Transactions of the ASME®

Transactions of the ASME, Journal of Fluids Engineering (ISSN 0098-2202) is published quarterly (Mar., June, Sept., Dec.) for $130.00 per year by The American Society of Mechanical Engineers, 345 East 47th Street, New York, NY 10017. Second class postage paid at New York, NY and additional mailing offices. POSTMASTER: Send address changes to Transactions of the ASME, Journal of Fluids Engineering, c/o THE AMERICAN SOCIETY OF MECHANICAL ENGINEERS, 22 Law Drive, Box 2300, Fairfield, NJ 07007-2300.
CHANGES OF ADDRESS must be received at Society headquarters seven weeks before they are to be effective. Please send old label and new address.
PRICES: To members, $40.00, annually; to nonmembers, $130.00. Add $24.00 for postage to countries outside the United States and Canada.
STATEMENT from By-Laws. The Society shall not be responsible for statements or opinions advanced in papers or . . . printed in its publications (B7.1, Par. 3).

INDEXED by Applied Mechanics Reviews and Engineering Information, Inc.
Canadian Goods & Services Tax Registration #126148048

Journal of Fluids Engineering

Published Quarterly by The American Society of Mechanical Engineers

VOLUME 116 • NUMBER 2 • JUNE 1994

(Contents continued on page 211)

(Contents continued)

Journal of Fluids Engineering

Technical Forum

Questions in Fluid Mechanics:

Mixed Mechanisms, Complex Shapes, and Transitional Regimes: Help Us Decipher the Devices of Organisms

by Steven Vogel[1]

Fluid mechanical phenomena provide both opportunities upon which organisms, through natural selection, have capitalized as well as constraints that selection, however intense, can't escape. We biologists who seek to identify these opportunities and constraints face what to an engineer must appear a queer situation. We see the solutions, and from them we try to infer the underlying problems.

Furthermore, by comparison with human technology, the solutions themselves commonly have a somewhat odd character. Nature has no antipathy toward analytically-awkward combinations of physical mechanisms and toward awkward regimes of flow. Problems of biological interest commonly combine viscous and inertial effects, vortices without true statistical turbulence, air-water interfaces, and non-steady flows—even where the fluids are decently Newtonian and the solids keep their shapes. Simplifying assumptions (beloved of both biologists and engineers) concomitant with simulations are especially hazardous at early stages of investigations, where just what matters is hard to guess. And the errors introduced by such assumptions are likely to have a peculiar bias when applied to any machine designed by natural selection. The latter is an optimization process operating in the context of a machine's normal operating conditions. Since simplifications represent deviations from normal conditions they'll usually not show the machine at its best. The most infamous example, of course, is the partly apocryphal demonstration that the bumblebee can't fly.

We've often found it most useful to use what one might call an "abstraction gradient," running from field data through measurements on organisms under controlled conditions to physical models and thence to computational and analytic modelling—again we reverse the normal design process of human technology. And we often use a tool of far greater analytic power for natural than for human technology. Where similar structural arrangements have evolved independently in several lineages ("convergence") we recognize these as strong evidence of some common functional imperative. For instance, we could make a very good guess about profiles appropriate for streamlined struts from a look at the legs of insects that cling to rocks in torrential streams and at the hammers of hammerhead sharks.

All of which is prefatory to a cry for help. Again and again I've felt the need for basic information on physical systems with which to compare our organisms or their bits and pieces. What's available too often applies to flow regimes too disparate from those with which I'm working to be confidently trusted as relevant. Readily available data and formulas for physical systems most often apply to Reynolds numbers higher or lower than those encountered by macroscopic biological systems—very roughly between one and a million. And they rarely take account of our world of mixed physical mechanisms. To give a few examples...

(1) Many sponges feed by pumping water into small peripheral holes, through a filter, and out a large apical hole; similarly some tropical termites ventilate their mounds by moving air in through peripheral porous regions and out apically. Both are arranged to make a primary ambient flow help out in generating their internal secondary flow, somewhat in the manner of an aspirator or carburetor. Many other cases of this use of winds and currents are known. Such secondary flows are easy to produce with devices for which the assumption of inviscid flow is adequate. But the organisms induce such flows in cases where viscous entrainment appears to be the main agency and with every mix of viscous and inertial effects in the velocity gradients near surfaces. Could we have something a little more powerful than small corrections for viscous entrainment at the static apertures of Pitot tubes?

(2) The pointed tips so common on the leaves of trees and shrubs appear to be (at least in part) devices to use the Coanda effect to help shed water. The scheme ought to matter most for leaves exposed to rain without simultaneous wind, helping them avoid bearing an unnecessary weight of water. Thus it's reasonable to find the greatest elaboration of what have been usually called "drip tips" convergently evolved on the understory leaves of rain-forest trees. The Coanda effect is commonly explained using Bernoulli's principle and inviscid flow. But it takes only a little experimentation on leaves to recognize the involvement of both surface tension and viscosity. How do these different physical mechanisms interact?

(3) Leaves, again. They're a little like flags—flexible objects

[1]Department of Zoology, Duke University, Durham, NC 27708-0325.

in flows—but flags suffer rather high drag relative to their areas. The drag of broad leaves is several times less than that of flags of the same area at the same speeds, and their shapes and flexibility appear to be specifically attuned to accomplishing the feat. In increasingly strong and turbulent winds (of speeds that might put a tree at hazard of toppling), many leaves reconfigure into increasingly tight cones or cylinders; these are quite stable and have far lower drag than leaves that have been prevented from reconfiguring. But leaves are multifunctional structures, and their forms reflect the combined demands of light interception, low-speed convective cooling, water shedding, and so forth—as well as drag minimization in storms. Leaf shape is certainly variable—but what options are open and attractive and what variations are maladaptive and inappropriate? We know too little about design versus performance of flexible surfaces with low drag.

(4) For that matter, relatively little information seems to be available on the design even of rigid, low-drag structures at low (but not creeping) Reynolds numbers. What are the possibilities open to the fuselage of a bird or insect, the body of a small, fast-swimming crustacean, and so on? And, once again, what rules apply when the physical conditions get a little more complicated? We know of least two cases, the lower bill of birds called "skimmers" and the hind legs of fishing bats, in which a structure penetrates the air-water interface and moves through the water at very high speeds. In both these latter, drag may be especially awkward because of the peculiar location of its line of action.

(5) And what about lift? We encounter lots of lift-producing devices at Reynolds numbers between about 100 and 100,000. Sometimes, as with most wings and with many fins and swimming legs, lift is highly desirable; sometimes, as with a flatfish or sand dollar on the bottom of a bay or a limpet or snail on a rock, lift is more hazardous to its purchase than is drag. Little data seem available for the design of lift-maximizing shapes in this range. Even less well-studied are the options for lift minimization for creatures that form protrusions from solid substrata.

(6) Unsteady flows are the inevitable products of valve-and-chamber pumps, of pulsating jets, of oscillating appendages, of predators that lunge, of prey that shrink swiftly, of suction-feeding fishes, of attached organisms subject to surging waves. We're beginning to take seriously the special character and consequences of these cases and of matters such as determination of the drag of a swimming creature by looking at how it decelerates when coasting. But what we have available are mainly tests designed to tell when it's safe to ignore unsteady flow and factors for the virtual mass of simple shapes in inviscid flows. Our shapes, though, aren't usually simple, and our flows are almost always viscous. For instance, I once encountered a significant added mass on flat plates moving nearly parallel to flow—on the extremely light-weight wings of a very small insect, where added mass seemed a simple proportion of boundary layer mass. Might someone take a careful look at virtual mass in oscillating, viscous flows?

Our world of concern may be a physically messy one, between the multiplicity of mechanisms and its location in the twilight zone between dependable order and describable chaos, but it's the world with which we're stuck. Professionals in fluid mechanics have been of great assistance to many of us in ways ranging from help with technology to extracting our feet from our mouths on conceptual matters. But gratitude for a history of help, although merited, isn't the present point. Rather I strongly urge upon fluid mechanists a more positive role—using biological situations to suggest where general phenomenological information might be useful to have, for biologists immediately and for engineers at least potentially. After all, technological imperatives have commonly provided impetus for basic work—why not the imperatives of biology as well? One's perspective on fluid mechanics can only be broadened in the process. I strongly urge, as well, a broad look at biology. For one thing, the world of organisms is exceedingly diverse, one not limited to humans or even vertebrates. For another, the successes of a few hundred million years of evolution can provide some assistance. Again, convergences upon specific designs are fingers pointing to salient physical devices, and they give better hints than those afforded by the empirical technology of one's human predecessors.

As introductions to the concerns of biologists (as well as references for all the cases mentioned), I suggest the two recent sources below.

References

Denny, M. W., 1993, *Air and Water: The Biology and Physics of Life's Media*, Princeton University Press, Princeton, NJ.

Vogel, S., 1994, *Life in Moving Fluids, 2nd Edition*, Princeton University Press, Princeton, NJ.

Comments on *Policy Statement on the Control of Numerical Accuracy*, Journal of Fluids Engineering, Vol. 115 (1993), pp. 339-340

by Wei Shyy[1] and Munir Sindir[2]

We read with interest an Editorial published in the September 1993 issue of the *Journal of Fluids Engineering* (Vol. 115, No. 3, pp. 339-340), authored by Dr. C. J. Freitas, regarding the revised *Policy Statement on the Control of Numerical Accuracy*. The statement has given explicit guidelines for the accuracy requirement and assessment of numerical computation for fluid flow problems to be published in JFE; it has also given preference to certain types of numerical methods, most notably those with at least second-order spatial accuracy. We feel that the goal of setting a standard to help control the quality of numerically oriented journal papers is definitely a very important one. We also appreciate the diligence of the Coordinating Group on Computational Fluid Dynamics (CGCFD), and particularly the efforts of Dr. Freitas. However, this *Policy* seems to be written in too restrictive a way, and will likely impose unnecessary constraints on JFE in the search for high-quality numerical work. We would like to convey some of our concerns about the above mentioned *Policy Statement*, hoping to promote further dialogue in the fluids engineering community.

The focus of the revised *Policy* seems mostly on the finite volume/difference/element methods. Besides these popular approaches, other methods have found successes in treating interesting and practically relevant problems. Some examples come to mind include stochastic methods, such as those based

[1]Department of Aerospace Engineering, Mechanics & Engineering Science, University of Florida, Gainesville, FL 32611-2031.

[2]Rocketdyne Division, Rockwell International Corporation, Canoga Park, CA.

in flows—but flags suffer rather high drag relative to their areas. The drag of broad leaves is several times less than that of flags of the same area at the same speeds, and their shapes and flexibility appear to be specifically attuned to accomplishing the feat. In increasingly strong and turbulent winds (of speeds that might put a tree at hazard of toppling), many leaves reconfigure into increasingly tight cones or cylinders; these are quite stable and have far lower drag than leaves that have been prevented from reconfiguring. But leaves are multifunctional structures, and their forms reflect the combined demands of light interception, low-speed convective cooling, water shedding, and so forth—as well as drag minimization in storms. Leaf shape is certainly variable—but what options are open and attractive and what variations are maladaptive and inappropriate? We know too little about design versus performance of flexible surfaces with low drag.

(4) For that matter, relatively little information seems to be available on the design even of rigid, low-drag structures at low (but not creeping) Reynolds numbers. What are the possibilities open to the fuselage of a bird or insect, the body of a small, fast-swimming crustacean, and so on? And, once again, what rules apply when the physical conditions get a little more complicated? We know of least two cases, the lower bill of birds called "skimmers" and the hind legs of fishing bats, in which a structure penetrates the air-water interface and moves through the water at very high speeds. In both these latter, drag may be especially awkward because of the peculiar location of its line of action.

(5) And what about lift? We encounter lots of lift-producing devices at Reynolds numbers between about 100 and 100,000. Sometimes, as with most wings and with many fins and swimming legs, lift is highly desirable; sometimes, as with a flatfish or sand dollar on the bottom of a bay or a limpet or snail on a rock, lift is more hazardous to its purchase than is drag. Little data seem available for the design of lift-maximizing shapes in this range. Even less well-studied are the options for lift minimization for creatures that form protrusions from solid substrata.

(6) Unsteady flows are the inevitable products of valve-and-chamber pumps, of pulsating jets, of oscillating appendages, of predators that lunge, of prey that shrink swiftly, of suction-feeding fishes, of attached organisms subject to surging waves. We're beginning to take seriously the special character and consequences of these cases and of matters such as determination of the drag of a swimming creature by looking at how it decelerates when coasting. But what we have available are mainly tests designed to tell when it's safe to ignore unsteady flow and factors for the virtual mass of simple shapes in inviscid flows. Our shapes, though, aren't usually simple, and our flows are almost always viscous. For instance, I once encountered a significant added mass on flat plates moving nearly parallel to flow—on the extremely light-weight wings of a very small insect, where added mass seemed a simple proportion of boundary layer mass. Might someone take a careful look at virtual mass in oscillating, viscous flows?

Our world of concern may be a physically messy one, between the multiplicity of mechanisms and its location in the twilight zone between dependable order and describable chaos, but it's the world with which we're stuck. Professionals in fluid mechanics have been of great assistance to many of us in ways ranging from help with technology to extracting our feet from our mouths on conceptual matters. But gratitude for a history of help, although merited, isn't the present point. Rather I strongly urge upon fluid mechanists a more positive role—using biological situations to suggest where general phenomenological information might be useful to have, for biologists immediately and for engineers at least potentially. After all, technological imperatives have commonly provided impetus for basic work—why not the imperatives of biology as well? One's perspective on fluid mechanics can only be broadened in the process. I strongly urge, as well, a broad look at biology. For one thing, the world of organisms is exceedingly diverse, one not limited to humans or even vertebrates. For another, the successes of a few hundred million years of evolution can provide some assistance. Again, convergences upon specific designs are fingers pointing to salient physical devices, and they give better hints than those afforded by the empirical technology of one's human predecessors.

As introductions to the concerns of biologists (as well as references for all the cases mentioned), I suggest the two recent sources below.

References

Denny, M. W., 1993, *Air and Water: The Biology and Physics of Life's Media*, Princeton University Press, Princeton, NJ.

Vogel, S., 1994, *Life in Moving Fluids, 2nd Edition*, Princeton University Press, Princeton, NJ.

Comments on *Policy Statement on the Control of Numerical Accuracy*, Journal of Fluids Engineering, Vol. 115 (1993), pp. 339-340

by Wei Shyy[1] and Munir Sindir[2]

We read with interest an Editorial published in the September 1993 issue of the *Journal of Fluids Engineering* (Vol. 115, No. 3, pp. 339-340), authored by Dr. C. J. Freitas, regarding the revised *Policy Statement on the Control of Numerical Accuracy*. The statement has given explicit guidelines for the accuracy requirement and assessment of numerical computation for fluid flow problems to be published in JFE; it has also given preference to certain types of numerical methods, most notably those with at least second-order spatial accuracy. We feel that the goal of setting a standard to help control the quality of numerically oriented journal papers is definitely a very important one. We also appreciate the diligence of the Coordinating Group on Computational Fluid Dynamics (CGCFD), and particularly the efforts of Dr. Freitas. However, this *Policy* seems to be written in too restrictive a way, and will likely impose unnecessary constraints on JFE in the search for high-quality numerical work. We would like to convey some of our concerns about the above mentioned *Policy Statement*, hoping to promote further dialogue in the fluids engineering community.

The focus of the revised *Policy* seems mostly on the finite volume/difference/element methods. Besides these popular approaches, other methods have found successes in treating interesting and practically relevant problems. Some examples come to mind include stochastic methods, such as those based

[1]Department of Aerospace Engineering, Mechanics & Engineering Science, University of Florida, Gainesville, FL 32611-2031.

[2]Rocketdyne Division, Rockwell International Corporation, Canoga Park, CA.

on the discrete vortex elements (Chorin, 1973), and Monte Carlo simulations for obtaining probability density functions (Pope, 1985), and spectral methods (Canuto et al., 1988). In general, spectral methods are of high formal order of spatial accuracy whereas, the particle methods improve the solution accuracy at slower rates as the number of particles/ensembles increase. Finite volume/difference/element methods, which have many different formulations with varying orders of accuracy, in time and in space, are often more effective for solving engineering problems involving complex physics *and* geometries. Evidences abound that the nominal order of accuracy of each of these above methods does not necessarily give adequate indications in terms of the relative merits among them. It appears clear that any official policy to be implemented by a journal should address the requirement regarding the control of *actual accuracy* of a reported solution rather than restricting the numerical schemes employed. This observation brings out our major concerns regarding the scope of the *Policy Statement*.

(i) It doesn't seem appropriate for this *Policy* to deal only with a restricted class of computational methods. Requirements such as "*Methods must be at least second order accurate in space*" shouldn't be applied as a universal criterion. Cost for obtaining accurate solutions is a more relevant measure which obviously is very hard to assess in a fair and objective way for many cases.

(ii) The order of accuracy requirement should not be applied to "space" only and further restricted to the "*nodes in the interior of the computational grid.*" Furthermore, in spatial coordinates, one needs to distinguish the treatments between convection, diffusion and source terms. For consistency one also has to maintain the true accuracy of the proposed schemes by accounting for the effects of zonal (for multi-zone or multi-block calculations) and physical *boundaries* in addition to the "*interior nodes.*" The collective order of accuracy of the schemes used to handle the various terms for entire fluid flow problems is more important. However, it is not easy at all to rigorously assess the true order of accuracy in a grid system utilizing non-uniform and curvilinear coordinates often needed for computing a practical flow problem. Adopting schemes which maintain high order of accuracy only on regular grids is not sufficient for complex flow computations.

(iii) The formal order of accuracy is useful mainly for solution with smooth profiles. Practical fluid flow problems frequently involve high gradients and discontinuities. For flows with such features, *formal order of accuracy* and *true accuracy* are not necessarily consistent. Furthermore, based on the same basic discrete operator, it is possible to devise different implementations which while possessing the same formal order of accuracy, produce solutions of very different *actual numerical accuracy* (Shyy, 1994).*

The basic issues in CFD should be accuracy, stability, and consistency. Furthermore, accuracy issues should include both numerical and physical model related considerations to provide a more meaningful assessment of the computations. Therefore, it seems more useful for JFE to implement a policy that stresses these basic requirements with appropriate quantification, and establishes a consistent, realistic and technically viable procedure. We believe the ASME CGCFD has laid out certain guidelines that could very well serve as a starting point for establishing this procedure. However, in finalizing this procedure we should, in our opinion, try to avoid vague statements such as "*assess and minimize*" and blanket rules such as "*Methods should be at least second order accurate in space.*" The current status of computational fluid dynamics is not easy to be regulated by some simple rules. Many sophisticated methods have been developed for solving difficult problems. On the other hand, many practical engineering problems are still heavily relying on methods classified as first order, and for good reasons. We should not decide *a priori* which methods to be preferred. Instead, we need to ensure that the solutions reported contain enough information to enable the readers to assess the confidence levels of such results. A practical goal of CFD is to produce solutions accurate enough, using the most *effective* methods, to gain new understanding and/or making new design. Personally, we do not promote first-order computational schemes, definitely appreciate the importance of searching for accurate methods, and have contributed to this topic. We are definitely not in favor of publishing work based on the computations on a single grid layout without a thorough investigation of the accuracy obtained, either. However, we recognize that the issues involved here are complicated in nature, and will take a concerted effort by our whole community to gradually clarify them. We do hope that JFE will adopt a policy which is fair, thoughtful and can be implemented by a larger segment of the CFD community while improving the standard of publishing the numerically oriented papers.

References

Canuto, C., Hussaini, M. Y., Quarteroni, A., and Zang, T. A., 1988, *Spectral Methods in Fluid Dynamics*, Springer-Verlag, New York.

Chorin, J. A., 1973, "Numerical Study of Slightly Viscous Flow," *Journal of Fluids Dynamics*, Vol. 57, pp. 785–796.

Pope, S. B., 1985, 'PDF Methods for Turbulent Reactive Flows," *Progress in Energy and Combustion Science*, Vol. 11, pp. 119–192.

Shyy, W., 1994, *Computational Modeling for Fluid Flow and Interfacial Transport*, Elsevier, Amsterdam, The Netherlands.

*This is true in practice for some cases even if one uses large number of grid points.

Response: To the Comments by Drs. W. Shyy and M. Sindir

by Pratap Vanka[1]

I have read with interest the recent note written by Dr. Shyy and Dr. Sindir. I believe that some of their statements are already stated in the new JFE Policy statement (Freitas, 1993). There is probably no doubt in anyone's mind that the papers published in a reputed journal such as the JFE should be scientifically accurate to the best of available technology. In experiments, the accuracy is dictated by available electronic and mechanical components. In numerical papers, the algorithm plays that part. Drs. Shyy and Sindir are correct in insisting that the order of the scheme is not the one which should be stressed. It is the accuracy. I agree. However, performing systematic grid-independent studies with first order schemes is very laborious because of the sluggish nature of error reduction. In the past (late seventies) several papers have appeared which have increased the number of grid nodes only by a small fraction in regions of steep gradients and have claimed grid-independent solutions using the hybrid scheme. These have promoted a sense of false security in subsequent papers and also in many current papers still being submitted to JFE. The second order accuracy in the interior is only a small requirement to now improve this trend. I do not think that papers with higher than second order accuracy will be

[1]Department of Mechanical and Industrial Engineering, University of Illinois at Urbana-Champaign, Urbana, IL 61801.

on the discrete vortex elements (Chorin, 1973), and Monte Carlo simulations for obtaining probability density functions (Pope, 1985), and spectral methods (Canuto et al., 1988). In general, spectral methods are of high formal order of spatial accuracy whereas, the particle methods improve the solution accuracy at slower rates as the number of particles/ensembles increase. Finite volume/difference/element methods, which have many different formulations with varying orders of accuracy, in time and in space, are often more effective for solving engineering problems involving complex physics *and* geometries. Evidences abound that the nominal order of accuracy of each of these above methods does not necessarily give adequate indications in terms of the relative merits among them. It appears clear that any official policy to be implemented by a journal should address the requirement regarding the control of *actual accuracy* of a reported solution rather than restricting the numerical schemes employed. This observation brings out our major concerns regarding the scope of the *Policy Statement*.

(i) It doesn't seem appropriate for this *Policy* to deal only with a restricted class of computational methods. Requirements such as "*Methods must be at least second order accurate in space*" shouldn't be applied as a universal criterion. Cost for obtaining accurate solutions is a more relevant measure which obviously is very hard to assess in a fair and objective way for many cases.

(ii) The order of accuracy requirement should not be applied to "space" only and further restricted to the "*nodes in the interior of the computational grid.*" Furthermore, in spatial coordinates, one needs to distinguish the treatments between convection, diffusion and source terms. For consistency one also has to maintain the true accuracy of the proposed schemes by accounting for the effects of zonal (for multi-zone or multi-block calculations) and physical *boundaries* in addition to the "*interior nodes.*" The collective order of accuracy of the schemes used to handle the various terms for entire fluid flow problems is more important. However, it is not easy at all to rigorously assess the true order of accuracy in a grid system utilizing non-uniform and curvilinear coordinates often needed for computing a practical flow problem. Adopting schemes which maintain high order of accuracy only on regular grids is not sufficient for complex flow computations.

(iii) The formal order of accuracy is useful mainly for solution with smooth profiles. Practical fluid flow problems frequently involve high gradients and discontinuities. For flows with such features, *formal order of accuracy* and *true accuracy* are not necessarily consistent. Furthermore, based on the same basic discrete operator, it is possible to devise different implementations which while possessing the same formal order of accuracy, produce solutions of very different *actual numerical accuracy* (Shyy, 1994).*

The basic issues in CFD should be accuracy, stability, and consistency. Furthermore, accuracy issues should include both numerical and physical model related considerations to provide a more meaningful assessment of the computations. Therefore, it seems more useful for JFE to implement a policy that stresses these basic requirements with appropriate quantification, and establishes a consistent, realistic and technically viable procedure. We believe the ASME CGCFD has laid out certain guidelines that could very well serve as a starting point for establishing this procedure. However, in finalizing this procedure we should, in our opinion, try to avoid vague statements such as "*assess and minimize*" and blanket rules such as "*Methods should be at least second order accurate in space.*" The current status of computational fluid dynamics is not easy to be regulated by some simple rules. Many sophisticated methods have been developed for solving difficult problems. On the other hand, many practical engineering problems are still heavily relying on methods classified as first order, and for good reasons. We should not decide *a priori* which methods to be preferred. Instead, we need to ensure that the solutions reported contain enough information to enable the readers to assess the confidence levels of such results. A practical goal of CFD is to produce solutions accurate enough, using the most *effective* methods, to gain new understanding and/or making new design. Personally, we do not promote first-order computational schemes, definitely appreciate the importance of searching for accurate methods, and have contributed to this topic. We are definitely not in favor of publishing work based on the computations on a single grid layout without a thorough investigation of the accuracy obtained, either. However, we recognize that the issues involved here are complicated in nature, and will take a concerted effort by our whole community to gradually clarify them. We do hope that JFE will adopt a policy which is fair, thoughtful and can be implemented by a larger segment of the CFD community while improving the standard of publishing the numerically oriented papers.

References

Canuto, C., Hussaini, M. Y., Quarteroni, A., and Zang, T. A., 1988, *Spectral Methods in Fluid Dynamics*, Springer-Verlag, New York.

Chorin, J. A., 1973, "Numerical Study of Slightly Viscous Flow," *Journal of Fluids Dynamics*, Vol. 57, pp. 785–796.

Pope, S. B., 1985, 'PDF Methods for Turbulent Reactive Flows," *Progress in Energy and Combustion Science*, Vol. 11, pp. 119–192.

Shyy, W., 1994, *Computational Modeling for Fluid Flow and Interfacial Transport*, Elsevier, Amsterdam, The Netherlands.

*This is true in practice for some cases even if one uses large number of grid points.

Response: To the Comments by Drs. W. Shyy and M. Sindir

by Pratap Vanka[1]

I have read with interest the recent note written by Dr. Shyy and Dr. Sindir. I believe that some of their statements are already stated in the new JFE Policy statement (Freitas, 1993). There is probably no doubt in anyone's mind that the papers published in a reputed journal such as the JFE should be scientifically accurate to the best of available technology. In experiments, the accuracy is dictated by available electronic and mechanical components. In numerical papers, the algorithm plays that part. Drs. Shyy and Sindir are correct in insisting that the order of the scheme is not the one which should be stressed. It is the accuracy. I agree. However, performing systematic grid-independent studies with first order schemes is very laborious because of the sluggish nature of error reduction. In the past (late seventies) several papers have appeared which have increased the number of grid nodes only by a small fraction in regions of steep gradients and have claimed grid-independent solutions using the hybrid scheme. These have promoted a sense of false security in subsequent papers and also in many current papers still being submitted to JFE. The second order accuracy in the interior is only a small requirement to now improve this trend. I do not think that papers with higher than second order accuracy will be

[1]Department of Mechanical and Industrial Engineering, University of Illinois at Urbana-Champaign, Urbana, IL 61801.

disqualified! I agree that when it comes to curvilinear grids and non-uniform grids, many methods can become first order. The new policy does not go that far in insisting that second-order accuracy needs to be demonstrated on arbitrary grids. However, if the grid is carefully chosen and the skewness minimized, second-order accuracy for convective/diffusive fluxes may be achievable. Drs. Shyy and Sindir correctly point out that the two schemes with the same order of formal accuracy can give different results on a given grid. I agree, but that is because of insufficient grid refinement with both schemes. Finally, results from both schemes must be coincident after sufficient grid refinement. I do not think that the journal will be merely satisfied with the use of a coarse grid with a second order accuracy scheme. Grid-independence must still have to be shown despite higher accuracy.

The goal of JFE should be to publish descriptions of fluid flow phenomena in engineering devices to the best scientific accuracy possible. I believe that it is not an unreasonable demand to insist accuracy checks on the numerical results. The insistence of at least second order accuracy only helps towards that goal, but if a first order scheme is used and sufficient number of tests are conducted to show grid-independence, I see no reason why such a paper will be rejected. Finally, I fail to see why cost of obtaining a solution should be an indicator of the accuracy of the flow fields, as we are talking about trusting the results rather than paying for them!

Response: To the Comments by Drs. W. Shyy and M. Sindir

by Christopher J. Freitas[1]

One of the covert objectives of the new Policy Statement on the Control of Numerical Accuracy was to incite an open discussion of the issue of numerical uncertainty. As chairman of the Coordinating Group on Computational Fluid Dynamics and as a past Associate Editor of the *Journal of Fluids Engineering*, I have seen too often the subject of numerical accuracy neglected or treated like an annoyance. I am glad to see that open discussion has broken out and is beginning to run rampant. I thank Drs. Shyy and Sindir for initiating this.

With regard to the comments of Drs. Shyy and Sindir, I do agree with them that the basic issues in CFD are those of accuracy, stability, and consistency. And that accuracy must address both numerical and modeling issues. However, I do not agree that the cost of a simulation is a relevant measure. Certainly, cost is important, but who cares what the cost is if the simulation is wrong or provides no realistic engineering or scientific insight to the problem? It has been my experience that clients do not care what the cost of a simulation is as long as it provides the information they need to design or enhance their process or equipment. The use of second-order spatial methods or their equivalent does not add a significant amount of overhead to the simulation, but does provide a significant improvement in accuracy. Drs. Shyy and Sindir confuse the issue of second-order spatial accuracy, by discussing the collective order of accuracy of the algorithm. If we were to require that the algorithm be second order, including the temporal accuracy and boundary condition implementation, then we would be overly restrictive. But, we intentionally specified that only the interior nodes be solved using second-order spatial methods, a reasonable first step toward a useful set of criteria for numerical accuracy.

We further agree with Drs. Shyy and Sindir that to formally determine the accuracy of methods for non-uniform and non-orthogonal grid systems is difficult. But then, that is why we are requiring a demonstration of accuracy through a grid refinement study. I don't believe that methods of the same formal accuracy will produce "very different" results at sufficient grid resolutions. If they do not give similar results at fine grid resolutions, then one or both are not satisfying consistency conditions. Certainly (and hopefully), a first-order spatial method using a sufficiently fine grid resolution will give the same results as a higher-order method at a coarser grid resolution. This, after all, is the fundamental premise of numerical methods, that as the grid resolution gets finer, it approaches the continuum solution, regardless of order of the method. It just may take a whole lot more nodes for a lower-order method than for a higher-order method. Certainly, in principal, a detailed grid convergence study may be performed for a first-order method, potentially demonstrating accuracy of results. However, to properly perform such a study would require excessive amounts of cpu time due to the slow rate of reduction in global error, and even then, numerical diffusion will still have a deleterious effect on the computed results even though it scales with grid spacing. Therefore, we have recommended to the Editor of this Journal to categorically eliminate first-order methods from papers published in it.

Finally, I agree with Drs. Shyy and Sindir that CFD is not easily regulated. Few complex methodologies are. However, CFD has advanced sufficiently and has taken a position equal to that of experimental methods in the solution of the problems of engineering and science. It is only fair and appropriate that we in the CFD community, require of ourselves equivalent standards for evaluation, like those that the experimental community has adopted for themselves. Again, we are not promoting methods or approaches, but are attempting to provide guidelines for the evaluation of scientific and engineering works. Certainly, first-order methods will be used to design and enhance engineered systems, and provide sufficiently accurate answers for this purpose. But, are these results then suitable for publication in an archival journal (to the level that these simulations are typically performed). In general, I believe the answer is no.

[1]Southwest Research Institute, San Antonio, TX 78284.

Response: To the Comments by Drs. W. Shyy and M. Sindir

by Patrick J. Roache[1]

The principal objection of the subject comment seems to be the categorical rejection of first-order accurate spatial differencing. To support this objection, the authors raise several points, none of which appear to this reader to support their position.

Contrary to the comment, the Policy does not "deal only with a restricted class of computational methods." It is true, as is well recognized by all, that the impetus for the Policy

[1]President, Ecodynamics Research Associates, Albuquerque, NM 87119.

disqualified! I agree that when it comes to curvilinear grids and non-uniform grids, many methods can become first order. The new policy does not go that far in insisting that second-order accuracy needs to be demonstrated on arbitrary grids. However, if the grid is carefully chosen and the skewness minimized, second-order accuracy for convective/diffusive fluxes may be achievable. Drs. Shyy and Sindir correctly point out that the two schemes with the same order of formal accuracy can give different results on a given grid. I agree, but that is because of insufficient grid refinement with both schemes. Finally, results from both schemes must be coincident after sufficient grid refinement. I do not think that the journal will be merely satisfied with the use of a coarse grid with a second order accuracy scheme. Grid-independence must still have to be shown despite higher accuracy.

The goal of JFE should be to publish descriptions of fluid flow phenomena in engineering devices to the best scientific accuracy possible. I believe that it is not an unreasonable demand to insist accuracy checks on the numerical results. The insistence of at least second order accuracy only helps towards that goal, but if a first order scheme is used and sufficient number of tests are conducted to show grid-independence, I see no reason why such a paper will be rejected. Finally, I fail to see why cost of obtaining a solution should be an indicator of the accuracy of the flow fields, as we are talking about trusting the results rather than paying for them!

Response: To the Comments by Drs. W. Shyy and M. Sindir

by Christopher J. Freitas[1]

One of the covert objectives of the new Policy Statement on the Control of Numerical Accuracy was to incite an open discussion of the issue of numerical uncertainty. As chairman of the Coordinating Group on Computational Fluid Dynamics and as a past Associate Editor of the *Journal of Fluids Engineering*, I have seen too often the subject of numerical accuracy neglected or treated like an annoyance. I am glad to see that open discussion has broken out and is beginning to run rampant. I thank Drs. Shyy and Sindir for initiating this.

With regard to the comments of Drs. Shyy and Sindir, I do agree with them that the basic issues in CFD are those of accuracy, stability, and consistency. And that accuracy must address both numerical and modeling issues. However, I do not agree that the cost of a simulation is a relevant measure. Certainly, cost is important, but who cares what the cost is if the simulation is wrong or provides no realistic engineering or scientific insight to the problem? It has been my experience that clients do not care what the cost of a simulation is as long as it provides the information they need to design or enhance their process or equipment. The use of second-order spatial methods or their equivalent does not add a significant amount of overhead to the simulation, but does provide a significant improvement in accuracy. Drs. Shyy and Sindir confuse the issue of second-order spatial accuracy, by discussing the collective order of accuracy of the algorithm. If we were to require that the algorithm be second order, including the temporal accuracy and boundary condition implementation, then we would be overly restrictive. But, we intentionally specified that only the interior nodes be solved using second-order spatial methods, a reasonable first step toward a useful set of criteria for numerical accuracy.

We further agree with Drs. Shyy and Sindir that to formally determine the accuracy of methods for non-uniform and non-orthogonal grid systems is difficult. But then, that is why we are requiring a demonstration of accuracy through a grid refinement study. I don't believe that methods of the same formal accuracy will produce "very different" results at sufficient grid resolutions. If they do not give similar results at fine grid resolutions, then one or both are not satisfying consistency conditions. Certainly (and hopefully), a first-order spatial method using a sufficiently fine grid resolution will give the same results as a higher-order method at a coarser grid resolution. This, after all, is the fundamental premise of numerical methods, that as the grid resolution gets finer, it approaches the continuum solution, regardless of order of the method. It just may take a whole lot more nodes for a lower-order method than for a higher-order method. Certainly, in principal, a detailed grid convergence study may be performed for a first-order method, potentially demonstrating accuracy of results. However, to properly perform such a study would require excessive amounts of cpu time due to the slow rate of reduction in global error, and even then, numerical diffusion will still have a deleterious effect on the computed results even though it scales with grid spacing. Therefore, we have recommended to the Editor of this Journal to categorically eliminate first-order methods from papers published in it.

Finally, I agree with Drs. Shyy and Sindir that CFD is not easily regulated. Few complex methodologies are. However, CFD has advanced sufficiently and has taken a position equal to that of experimental methods in the solution of the problems of engineering and science. It is only fair and appropriate that we in the CFD community, require of ourselves equivalent standards for evaluation, like those that the experimental community has adopted for themselves. Again, we are not promoting methods or approaches, but are attempting to provide guidelines for the evaluation of scientific and engineering works. Certainly, first-order methods will be used to design and enhance engineered systems, and provide sufficiently accurate answers for this purpose. But, are these results then suitable for publication in an archival journal (to the level that these simulations are typically performed). In general, I believe the answer is no.

[1] Southwest Research Institute, San Antonio, TX 78284.

Response: To the Comments by Drs. W. Shyy and M. Sindir

by Patrick J. Roache[1]

The principal objection of the subject comment seems to be the categorical rejection of first-order accurate spatial differencing. To support this objection, the authors raise several points, none of which appear to this reader to support their position.

Contrary to the comment, the Policy does not "deal only with a restricted class of computational methods." It is true, as is well recognized by all, that the impetus for the Policy

[1] President, Ecodynamics Research Associates, Albuquerque, NM 87119.

Review: Laminar-to-Turbulent Transition of Three-Dimensional Boundary Layers on Rotating Bodies

Ryoji Kobayashi
Department of Machine Intelligence and Systems Engineering, Faculty of Engineering, Tohoku University, Sendai, Japan

The laminar-turbulent transition of three-dimensional boundary layers is critically reviewed for some typical axisymmetric bodies rotating in still fluid or in axial flow. The flow structures of the transition regions are visualized. The transition phenomena are driven by the compound of the Tollmien-Schlichting instability, the crossflow instability, and the centrifugal instability. Experimental evidence is provided relating the critical and transition Reynolds numbers, defined in terms of the local velocity and the boundary layer momentum thickness, to the local rotational speed ratio, defined as the ratio of the circumferential speed to the free-stream velocity at the outer edge of the boundary layer, for the rotating disk, the rotating cone, the rotating sphere and other rotating axisymmetric bodies. It is shown that the cross-sectional structure of spiral vortices appearing in the transition regions and the flow pattern of the following secondary instability in the case of the crossflow instability are clearly different than those in the case of the centrifugal instability.

1 Introduction

Clarification of the transition process, and prediction of transition condition on axisymmetric rotating bodies, are significant not only in fundamental research interests in three-dimensional boundary layer transitions of rotating bodies, but also in technological developments concerned with internal flow in turbomachinery. Boundary layer flows over rotating bodies will be expected to show much more complicated structures in their transition region than those of two-dimensional, nonrotating bodies, since in the former case the external body forces, such as centrifugal force and Coriolis force, play an important role in the transition process.

In the present review, laminar-turbulent transition of the three-dimensional boundary layer, which develops over an arbitrary shaped axisymmetric body $R(x)$ as shown in Fig. 1, rotating with angular velocity ω in the uniform flow U_∞, is discussed. As has been established in the classical literature, the drag force of a slender ellipsoid increases as its rotating speed increases (Wieselsberger, 1927), and the critical Reynolds number of the rotating sphere where the drag force suddenly reduces, will decrease with increasing rotating speed (Luthander and Rydberg, 1935). These phenomena clearly indicate remarkable influences of the body rotation to boundary layer transition and separation. Recent rapid development in computer performance made it easier to calculate laminar boundary layers on rotating bodies numerically. Turbulence models contribute to calculations of turbulent boundary layers. In order to predict accurately a location of the laminar-turbulent transition on an arbitrary shaped body, it is essential to do systematic investigations on typical axisymmetric rotating bodies. In this paper, attention is, therefore, focused on considering non-dimensional parameters for prediction of transition regions on rotating bodies of rather simple profiles and also on comparing structures of the transition regions to each other.

For Couette flows, their instabilities and transitions between two coaxial rotating axisymmetric bodies, such as cylinders, disks, cones, and spheres, the reader is referred to Wimmer (1988).

2 Rotating Disk

Consider the laminar-to-turbulent transition problem for a three-dimensional boundary layer on a flat disk rotating with

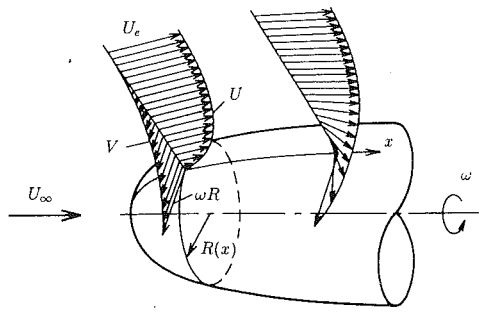

Fig. 1 Axisymmetric body rotating in axial flow

Contributed by the Fluids Engineering Division for publication in the JOURNAL OF FLUIDS ENGINEERING. Manuscript received by the Fluids Engineering Division October 16, 1992; revised manuscript received September 28, 1993. Associate Technical Editor: D. P. Telionis.

Table 1 Comparison of critical and transition Reynolds numbers measured

Investigators	Reynolds number: Critical $Re_{x,c}$	Reynolds number: Transition $Re_{x,t}$	Methods of measurement
Smith (1947)	2.32×10^5	—	Hot wire
Gregory et al. (1955)	1.90×10^5	2.84×10^5	China-clay, acoustical
Cobb-Saunders (1956)	2.0×10^5	2.4×10^5	Heat transfer
Gregory and Walker (1960)	1.35×10^5	2.75×10^5	Acoustical
Chin and Litt (1972)	1.7×10^5	3.50×10^5	Electrochemical
Fedrov et al. (1976)	4.5×10^4	2.65×10^5	Naphthalene
Clarkson et al. (1980)	3.3×10^5	3.9×10^5	Dye in water
Kobayashi et al. (1980)	8.8×10^4	3.2×10^5	Hot wire
Malik et al. (1981)	8.6×10^4	—	Hot wire

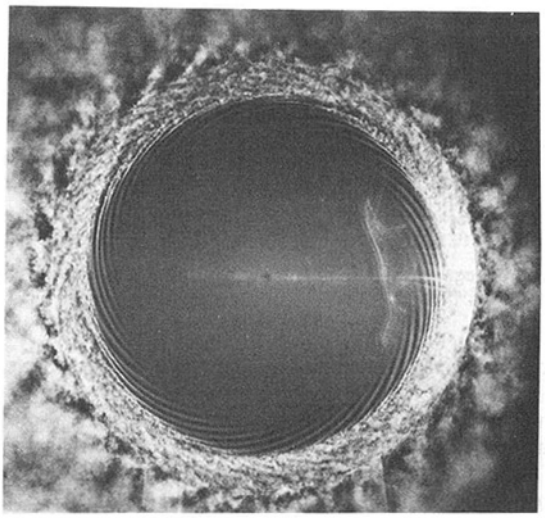

Fig. 2 Transition on rotating disk (anticlockwise rotation) (Kobayashi et al., 1980)

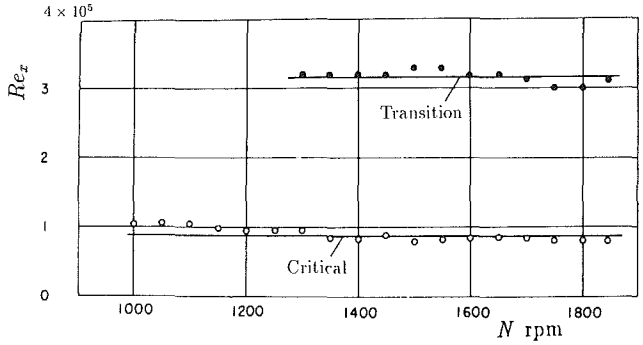

Fig. 3 Critical and transition Reynolds numbers in relation to rotating speed N (Kobayashi et al., 1980)

a uniform angular velocity ω in a fluid otherwise at rest. The laminar flow furnishes a simple, exact solution of the Navier-Stokes equations in the self-similar form. The flow moves axially toward the rotating disk, and the three-dimensional boundary layer builds up on the surface. The displacement thickness δ_1 and the momentum thickness δ_2 of the laminar boundary layer are $\delta_1 = 1.255\sqrt{\nu/\omega}$ and $\delta_2 = 0.657\sqrt{\nu/\omega}$, as calculated from the integrations of the circumferential component of the flow field $v(z)$ (Schlichting, 1979) and $v(z)^2$, respectively, where ν denotes the kinematic viscosity and z is a distance from the disk surface. The boundary layer thicknesses δ_1 and δ_2 remain constant in the radial direction, which allows simple applications of theory, experiment and computations. The rotating disk problem has been, therefore, considered often as a typical three-dimensional transition problem, which is related to three-dimensional boundary layers on swept wings. The transition is caused by the crossflow instability concerned with the radial velocity component $u(z)$.

Theodorsen and Regier (1944) measured a transition Reynolds number ($\omega R^2/\nu$) of 3.1×10^5 based on the disk radius, which was determined from the initial rise in disk moment coefficient. Using a hot wire probe, Smith (1947) observed sinusoidal waves propagating in a direction of approximately 14 deg with the outward radius vector, having a magnitude of 0.2 linear velocity of the disk at the same radius, and found first the local critical Reynolds number shown in Table 1. Gregory et al. (1955) indicated that the sinusoidal waves came from a structure of spiral vortices. They measured again the direction ϵ (about 14 deg) of the vortex axis with the circumferential direction and also the number n = about 30 of the vortices appearing on the rotating disk by means of a china-clay evaporation technique and a moving-coil microphone.

Figure 2 shows $TiCl_4$ smoke visualization picture on the rotating disk. Spiral smoke streaks, which represents the vortices coming from the crossflow instability, are visible in the transition region. Defining $Re_x = \omega r^2/\nu$, the critical local Reynolds number $Re_{x,c}$ as the onset of instability and the transition Reynolds number $Re_{x,t}$ as the end of transition measured by different investigators are listed in Table 1. The values for $Re_{x,c}$ and $Re_{x,t}$ remain unchanged when the rotating speed is varied, as shown in Fig. 3. Differences among the measured values in Table 1 might be caused by different measurement techniques or differences in the sensitivity of instruments used. The critical Reynolds number based on the momentum thickness δ_2, which

Nomenclature

N = rotational speed
Nu = Nusselt number
n = number of spiral vortices on circumference
Re = Reynolds number
R = local radius of body measured from axis of rotation
r = radial location
S = local rotational speed ratio ($\omega R/U_e$)
U_e = local flow velocity at edge of boundary layer
U_∞ = axial flow velocity
x = distance measured from leading edge
δ_1 = displacement thickness of boundary layer
δ_2 = momentum thickness of boundary layer
ϵ = angle of spiral vortex axis measured from circumferential direction
θ = half included angle of cone; central angle of sphere
ν = kinematic viscosity of fluid
ω = angular velocity of rotating body

Subscripts

c = critical condition
l = laminar state
s = separation
t = transition condition; turbulent state
x = based on x
2 = based on momentum thickness

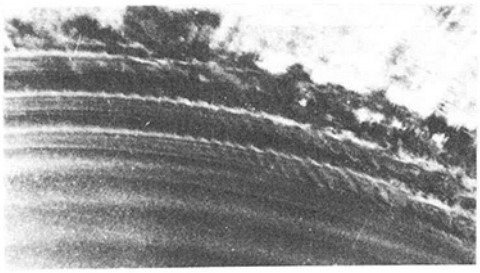

Fig. 4 Secondary instability of spiral vortices on rotating disk (Kobayashi et al., 1980)

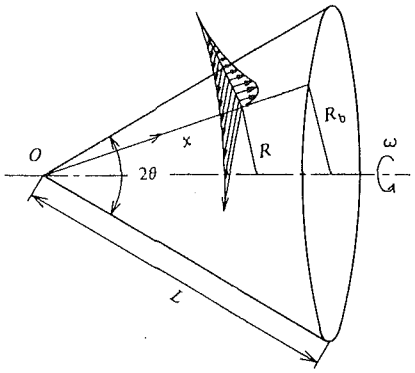

Fig. 5 Rotating cone in still fluid and notation

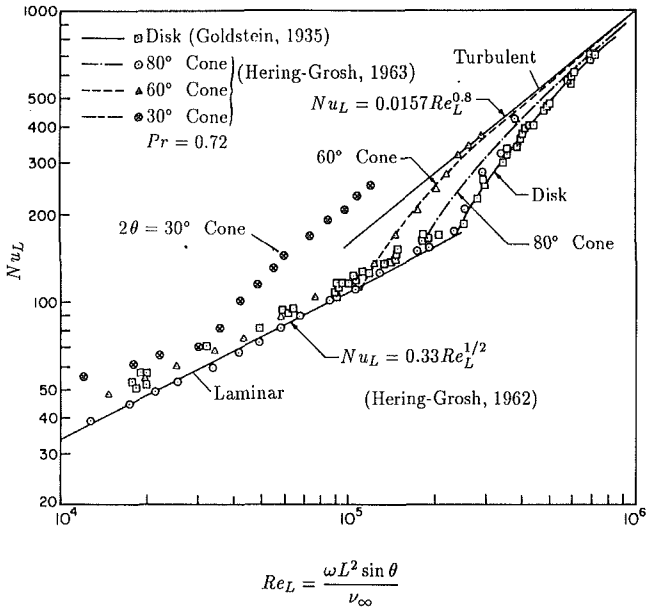

Fig. 6 Average Nusselt number for cones and disks rotating in still air (Kreith, 1966, 1968)

is calculated from the data $Re_{x,c} = 8.8 \times 10^4$ measured by Kobayashi et al. (1980), becomes $(\omega r \delta_2/\nu)_c = 195$.

The effects of a single, isolated roughness at a subcritical location on the transition was studied by Wilkinson and Malik (1985). Disturbances generated by the roughness evolve spatially as a wave packet. The wave packets spread rapidly around the disk, merge with each other, and eventually fill the entire circumference of the disk.

The theoretical investigation for instability of the boundary layer flow was carried out first by Stuart (see Gregory et al., 1955) by virtue of the Orr-Sommerfeld equation under inviscid condition. However, the neglect of viscosity resulted in the prediction of $n = 113$ to 140 vortices, which is about four times larger than the observed value (Gregory et al., 1955). Brown (1961) and Cebeci and Stewartson (1980), who solved the Orr-Sommerfeld equation for finite Reynolds number, obtained the critical Reynolds number $Re_{x,c}$ of 3.0×10^4 and 3.1×10^4, respectively. Kobayashi et al. (1980) and Malik et al. (1981) considered further the effects of Coriolis force and streamline curvature in their linear stability analyses and obtained $Re_{x,c} = 6.8 \times 10^4$ and 8.2×10^4, respectively. These theoretical predictions for stationary spiral vortices are very close to the measured values $(8.6 \sim 8.8) \times 10^4$ in Table 1. Subsequent theoretical predictions were made by Szeri and Giron (1984) with $Re_{x,c} = 8.0 \times 10^4$, by Malik (1986) with 8.1×10^4, by Itoh and Zhang (1987) with 7.9×10^4, and by Sahin (1988) with 8.1×10^4. The effects of nonlinearity on the growth of disturbances were considered by Itoh (1985), Hall (1986), and MacKerrell (1987). Recently, Balakumar and Malik (1990) examined theoretically the relative importance of the stationary and traveling disturbances and showed that the critical Reynolds number for the traveling disturbances is smaller than the one for the stationary spiral vortices, but the growth rate of the traveling disturbances is small.

The structure of the spiral vortices and their behavior were also studied in detail. Kohama (1984a) clarified the cross-sectional flow pattern of the spiral vortices, which were co-rotating, as predicted by Kobayashi et al. (1980), and confirmed that the spiral vortices are fixed relative to the rotating disk surface. Clarkson et al. (1980) also confirmed the fact using a flow visualization technique. The angle ϵ of the vortex axis with respect to the circumferential direction is about 14 deg at the beginning of the transition and decreases to about 7 deg as the vortices develops (Kobayashi et al., 1980). The number n of the vortices is 30 to 34, while Malik et al. (1981) measured 21 at the beginning ($Re_x = 8.4 \times 10^4$) and an increase to around 30 in the radial direction due to branching of individual vortices.

When the spiral vortices having the corotating structure are well developed, another organized fine structure wrapped around the spiral vortices appears as a secondary instability on each vortex, as shown in Fig. 4, which is followed by rapid transition to turbulence (Kobayashi et al., 1980; Kohama, 1984a, 1987). Further research is expected for a role of the secondary instability in the transition process to turbulence and for effects of surface roughness on the formation of the spiral vortices.

3 Rotating Cones in Still Fluid

Laminar flow field around a cone rotating in still fluid and its heat transfer characteristics can be obtained under boundary layer approximation directly from Kármán's differential equations for viscous flow on a rotating disk (Kármán, 1921) by a transformation, as pointed out by Wu (1959) and Tien (1960). The displacement thickness δ_1 and the momentum thickness δ_2, calculated from the circumferential velocity component in the boundary layer, are found to be $\delta_1 = 1.255\sqrt{\nu/(\omega \sin\theta)}$ and $\delta_2 = 0.657\sqrt{\nu/(\omega \sin\theta)}$, where 2θ is the included angle. The notation is given in Fig. 5.

The transition problem for the rotating cone in still fluid was studied first in terms of heat or mass transfer characteristics from the cone surface. Figure 6 shows experimental results of the average Nusselt number Nu_L over the slant length as a function of the cone Reynolds number Re_L. It can be said that the turbulent region on the cone surface becomes large with increasing cone Reynolds number for fixed cone angle, and that the transition starts at smaller Reynolds number as the cone angle is decreased.

Figure 7 shows the critical and transition Reynolds number (Re_c and Re_t). The Reynolds number is defined here as $Re = \omega R^2/\nu$, where $R = x \sin\theta$, and x is the distance measured from the apex of a cone along the surface to the critical and transition points. The values of Re_c and Re_t remain unchanged

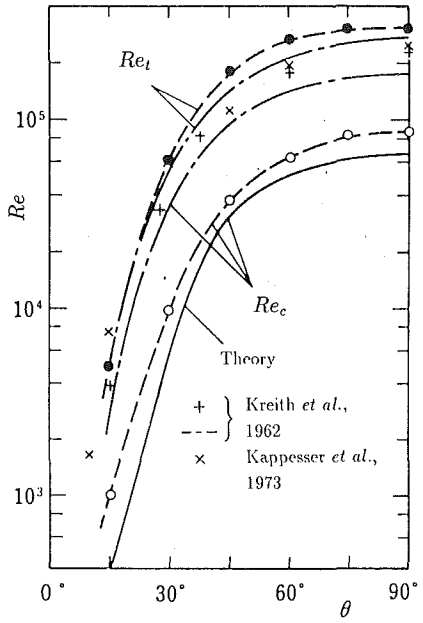

Fig. 7 Critical and transition Reynolds numbers in relation to half cone angle (Kobayashi and Izumi, 1983)

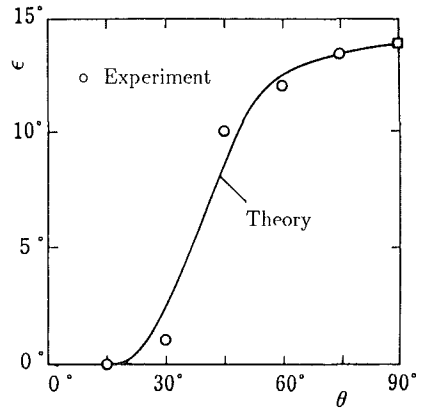

Fig. 8 Direction ϵ of spiral vortices (Kobayashi and Izumi, 1983)

as the rotational speed N of the cone is varied, which is similar to the case of a rotating disk (Kobayashi et al., 1980). Kreith et al. (1962) detected the transition region by using a small microphone and a hot-wire probe. Kappessor et al. (1973) determined the transition Reynolds number by measuring the mass transfer of oxygen to the rotating cone. Kobayashi and Izumi (1983) used a hot wire probe. Besides, Tien and Campbell (1963) gave $Re_c = (1.3 \sim 1.8) \times 10^5$ and $Re_t = (1.4 \sim 2.5) \times 10^5$ for $\theta = 45$ to 90 deg as well as $Re_t = 5 \times 10^4$ for $\theta = 30°$ using the mass transfer of naphthalene; these are not shown in Fig. 7.

It is clear that both the Reynolds numbers decrease rapidly when θ decreases below the value of 60 deg. This implies that the centrifugal instability plays a more important role in the transition than the crossflow instability. The theoretical value for Re_c, which was obtained from the linear stability theory, coincides fairly well with the measured value.

As seen in Fig. 8, the direction ϵ of the spiral vortices decreases from 14 deg ($\theta = 90$ deg, rotating disk) to 0 deg ($\theta \leq 15$ deg). The number n of the spiral vortices appearing on the cone also decreases with decreasing θ: $n = 31 \sim 32$ for $\theta = 90$ deg, $n = 30 \sim 31$ for $\theta = 75$ deg, $n = 26 \sim 27$ for $\theta = 60$ deg and $n = 22 \sim 23$ for $\theta = 45$ deg. The linear stability analysis, carried out by Kobayashi and Izumi (1983), gave the critical Reynolds number Re_c, the spiral-vortex axis ϵ and the number n of the

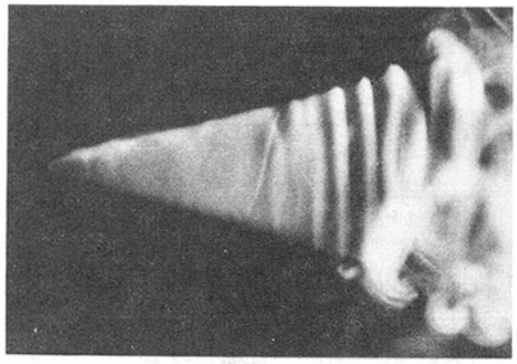

Fig. 9 Boundary layer transition on rotating cone in still fluid (Kobayashi and Izumi, 1983). $2\theta = 30$ deg.

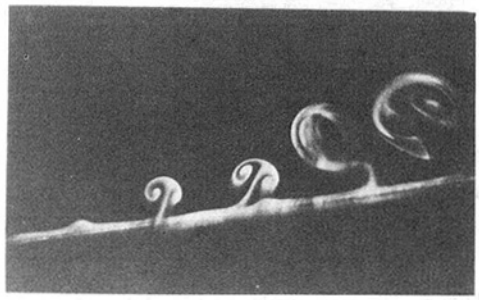

Fig. 10 Cross-sectional flow structure of spiral vortices (Kobayashi and Izumi, 1983). $2\theta = 30$ deg.

vortices as function of the cone angle θ, which were in agreement with the experimental findings.

Flow visualizations show that the flow pattern in the transition region in the case of $\theta > 30$ deg is similar to the one of the rotating disk, shown in Fig. 2, and cross-sectional flow of the spiral vortices is of the corotating type, which will be seen in Fig. 27, while another typical flow pattern appears in the case of $\theta < 30$ deg. Figure 9 shows the transition on a $\theta = 15$ deg cone where $\epsilon = 0$ deg. Cross-sectional flow structure in the vortices, shown in Fig. 10, indicates Taylor-vortex-like counter-rotating pairs of vortices, implying that the major instability which drives the transition is the centrifugal one. There exist both the co-rotating and counter-rotating vortices on a cone of $\theta = 30$ deg.

The critical Reynolds number Re_c for a rotating cylinder ($\theta = 0$ deg) is about 11, which was calculated by Walowit et al. (1964) using linear stability theory. Theodorsen and Regier (1944) obtained the transition Reynolds number $Re_t \approx 10$ by measuring the spinning moment of a cylinder. Chen and Christensen (1967), and Kirchner and Chen (1970) obtained the critical Reynolds number Re_c of about 30 via flow visualization. It is clear from Fig. 7 that the Reynolds number Re_c and Re_t are very small compared to those for the rotating cone, so that the boundary layer on the rotating cylinder is quite unstable.

4 Rotating Cone in Axial Flow

The laminar forced flow and heat transfer problem around a cone rotating in axial flow were studied by Koh and Price (1967) following contributions by Illingworth (1953) for a laminar compressible boundary layer over a slow rotating cone behind an attached shock wave and by Tien and Tsuji (1965) for the limiting cases of very slow and very fast rotating cones. The notation is shown in Fig. 11.

Figure 12 presents the transition region for a rotating cone ($2\theta = 30$ deg, clockwise spin) in uniform flow (Kobayashi et al., 1983). One can see regular spiral vortices in the transition region. The location of the transition region shifts in the di-

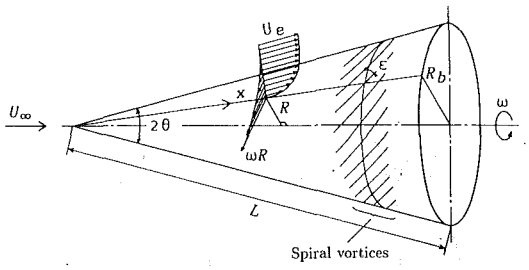

Fig. 11 Rotating cone in axial flow and notation

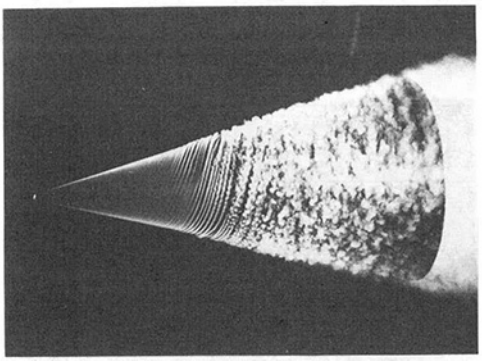

Fig. 12 Transition of boundary layer on rotating cone in axial flow (Kobayashi et al., 1983). Clockwise rotation, $2\theta = 30$ deg. $U_\infty = 1.7$ m/s, $N = 670$ rpm.

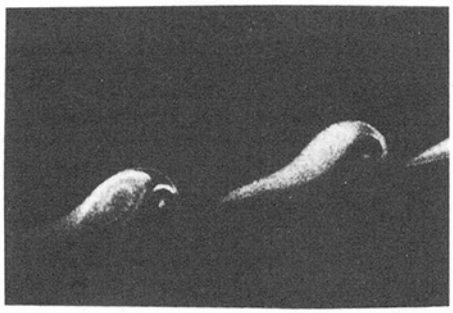

Fig. 13 Cross-sectional flow structure of spiral vortices (Kobayashi et al., 1983). $2\theta = 30$ deg.

rection of the cone apex as the rotating speed N of the cone is increased.

The structure of the spiral vortices is found to be in counter-rotating pairs as seen from a cross-sectional view shown in Fig. 13. Those spiral vortices are followed by the secondary instability as shown in Fig. 14, and soon after this stage, the entire flow field becomes fully turbulent. Appearance of this secondary instability observed on the rotating cone is obviously different from that of the rotating disk case shown in the Fig. 4. The difference in the appearance of the secondary instability comes from the difference of the cross-sectional flow pattern in the spiral vortices: co-rotating or counter-rotating. Kohama (1984b, 1985a) tried to explain the detailed process of the transition for the counter-rotating spiral vortices by using a schematic. It appears that a horseshoe pattern originates on the surface of the spiral vortices where a large velocity gradient with an inflection point created by the counter-rotation is expected. After the horseshoe pattern, breakdown to turbulence occurs rapidly.

Salzberg and Kezios (1965) first measured the transition point by experiment on local mass transfer from a $2\theta = 30$ deg naphthalene cone as shown in Fig. 15, and formulated it in the relation between the transition Reynolds number ($U_e x_t/\nu$) and the rotational parameter ($\omega R_b/U_\infty$) as followed:

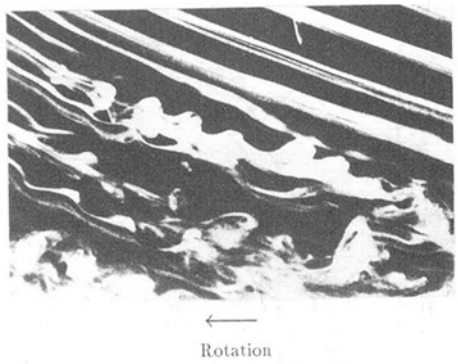

Fig. 14 Secondary instability of spiral vortices on rotating cone (Kobayashi et al., 1983). $2\theta = 30$ deg.

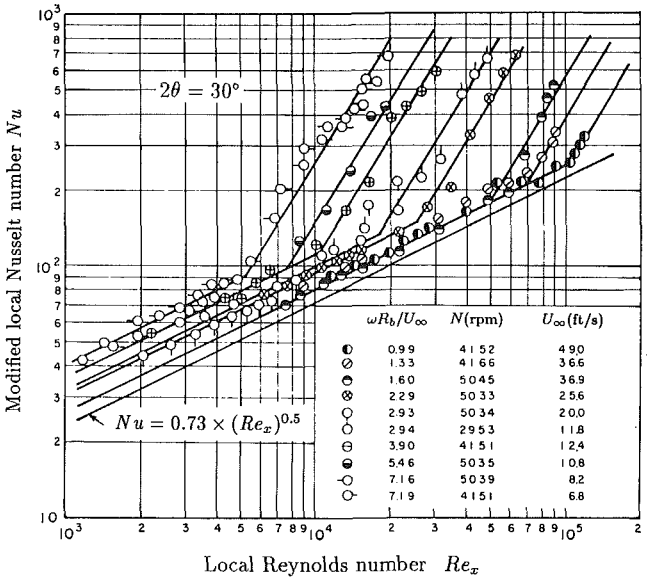

Fig. 15 Mass transfer from rotating cone in axial flow (Salzberg-Kezios, 1965)

$$\frac{U_e x_t}{\nu} = 110960\left\{0.73\left(\frac{\omega R_b}{U_\infty}\right)^{-2} + 0.08\left(\frac{\omega R_b}{U_\infty}\right)^{-1}\right\}^{6/7} \quad (1)$$

where R_b is the base radius of the cone, U_∞ is the axial flow velocity, U_e is the local flow speed at the edge of the boundary layer, and x_t is a distance measured from apex to the transition point. The transition point was determined from a deformation of the naphthalene surface due to mass transfer.

Kobayashi (1981) pointed out on the basis of his linear stability theory that the critical and transition points can be determined by using a relation between Re_x ($= xU_e/\nu$) and the local rotational speed ratio $S = \omega R/U_e$. Figure 16 shows the critical and transition Reynolds number on a $2\theta = 30$ deg cone with respect to the rotational speed ratio S (Kobayashi et al., 1983). Linear stability theory well predicts the tendency of the critical Reynolds number $\mathrm{Re}_{x,c}$ which decreases with increasing S, but there exists still a discrepancy quantitatively between the theoretical prediction and the experimental value of Fig. 16. From Fig. 16, $\mathrm{Re}_{x,c}$ and $\mathrm{Re}_{x,t}$ decrease rapidly with increasing S. This implies that the centrifugal instability becomes more dominant in the transition as S increases. Okamoto et al. (1976) measured the critical points for $2\theta = 15$ and 30 deg, and stated that the critical points can be given using a dimensionless parameter $(\omega R/U_\infty)_c$, which is independent from the rotational speed, for example, $(\omega R/U_\infty)_c = 1.45$ for $2\theta = 30$ deg. The value $(\omega R/U_\infty)_c = 1.45$ could be estimated to be $S_c = 1.4$

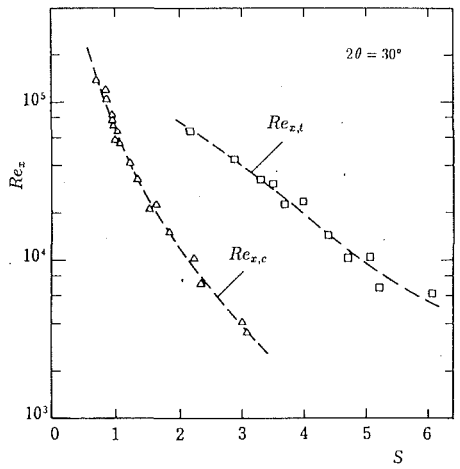

Fig. 16 Critical and transition Reynolds numbers ($Re_{x,c}$, $Re_{x,t}$) in relation to local rotational speed ratio $S = \omega R / U_e$ (Kobayashi and Izumi, 1983)

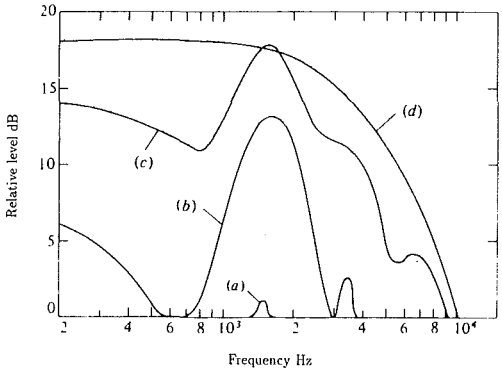

(a) $S = 2.01$, $Re_x = 2.18 \times 10^4$, (b) 2.41, 2.67×10^4
(c) 2.66, 2.92×10^4, (d) 3.50, 3.94×10^4

Fig. 17 Frequency spectra of velocity fluctuations in transition region (Kobayashi et al., 1983)

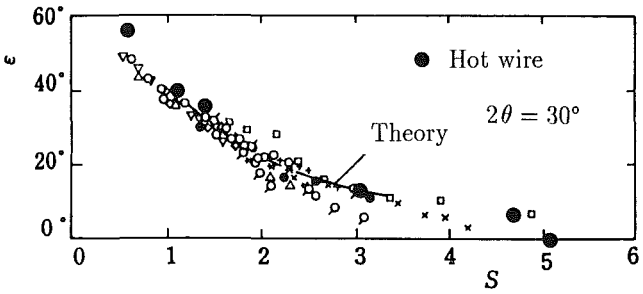

Fig. 18 Direction ϵ of spiral vortices (Kobayashi et al., 1983)

to 1.5 for any value of Re_x in Fig. 16. It should be further discussed what are reasonable dimensionless parameters in order to express the critical and transition locations for different values of the flow conditions, the cone size L and the cone angle θ.

Figure 17 shows frequency spectra of velocity fluctuations in the transition region. Curve (a) is the state just after the critical point and curve (d) at the transition point is the same as that for turbulent boundary layer. The clear peaks of curves (a) to (c) are owing to the appearance of the spiral vortices. The spiral vortices are relatively fixed to the rotating cone surface (Kobayashi and Kohama, 1984). Traveling disturbances are not yet found around the instability point of the laminar boundary layer.

Figure 18 shows the direction ϵ of the spiral vortices. Symbols except hot wire were measured by the flow visualization technique, in which the same symbols were plotted along the vortex axis in one photograph. The direction ϵ of the spiral vortices decreases as S increases, and drops to $\epsilon = 0$ deg when S exceeds the value of 5. Namely, the spiral vortices tend to become toroidal vortices. The number n of the spiral vortices also decreases with increasing S, as shown in Fig. 19, where the value of S is obtained near the critical point.

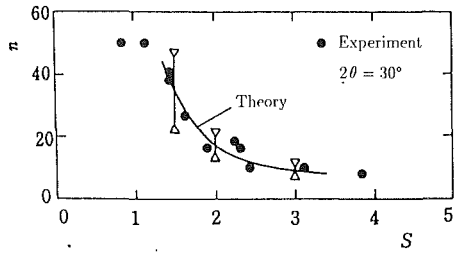

Fig. 19 Number n of spiral vortices (Kobayashi et al., 1983)

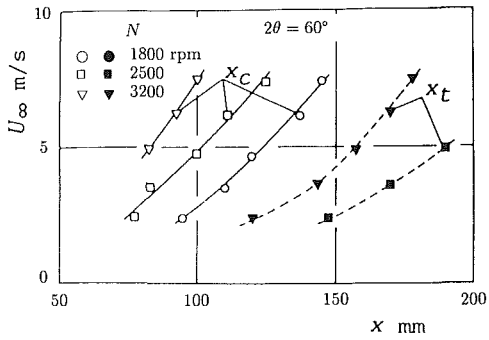

Fig. 20 Critical and transition points (x_c, x_t) of transition region (Kobayashi et al., 1987)

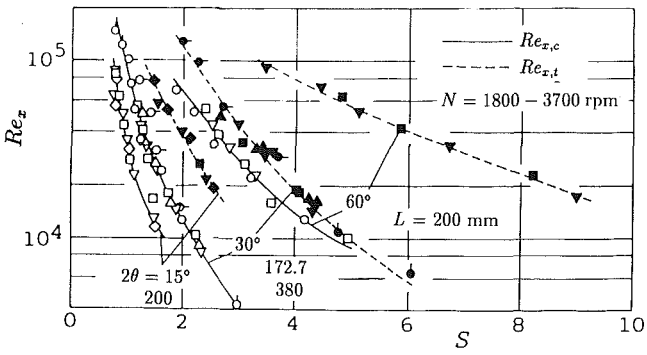

Fig. 21 Relation of critical Reynolds number $Re_{x,c}$ and transition Reynolds number $Re_{x,t}$ to rotational speed ratio S (Kobayashi et al., 1987)

For a cone angle of $2\theta = 60$ deg, Fig. 20 gives the critical and transition points (x_c, x_t). Both the points of the transition region move downstream as the external flow velocity U_∞ is increased, while they move upstream with increasing rotational speed N. Figure 21 expresses these results as the relation between the local Reynolds number ($Re_{x,c}$, $Re_{x,t}$) and the rotational speed ratio S for three cone angles of $2\theta = 15$, 30, and 60 deg. It is seen from Fig. 21 that the critical and transition points (x_c, x_t) can be expressed by using the relation of $Re_{x,c}$ and $Re_{x,t}$ to S for a fixed cone angle even if U_∞ and N are varied. The decrease of $Re_{x,c}$ and $Re_{x,t}$ with increasing S comes from the increase of the instability caused by the centrifugal force. While the cone angle increases from $2\theta = 15$ to 60 deg, $Re_{x,c}$ and $Re_{x,t}$ move to larger values of S. Figure 21 includes some experimental results for another large 30 deg cone of $L = 380$ mm. It shows that the relations of $Re_{x,c}$ and $Re_{x,t}$ to S are independent of L.

In Fig. 18, it should be noticed that the direction ϵ of the vortex axis appears to become zero at a finite value of S. For

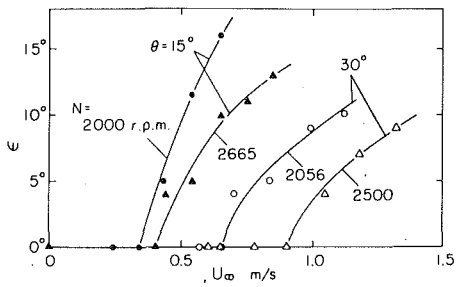

Fig. 22 Direction ϵ of spiral vortices against approaching flow velocity U_∞ (Kobayashi and Kohama, 1984)

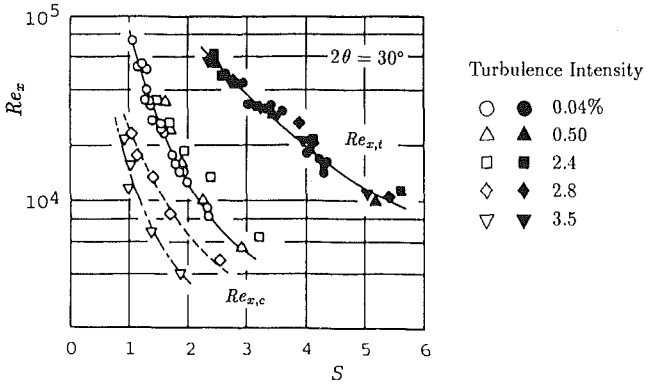

Fig. 23 Effect of free stream turbulence on $Re_{x,c}$ and $Re_{x,t}$ (Kobayashi et al., 1987)

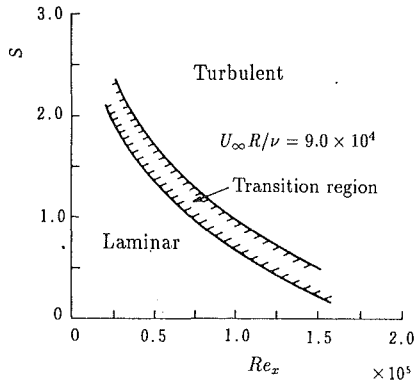

Fig. 24 Transition condition on circular cylinder rotating in axial flow (Yamato and Yamamoto, 1983)

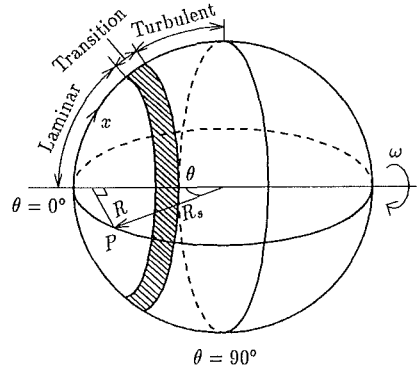

Fig. 25 Rotating sphere and notation

$S \to \infty$, which corresponds to the case of a rotating cone in still fluid, it was already clear that for a $2\theta = 30$ deg cone ϵ is equal to zero as shown in Fig. 8. We focus here attention to the condition of S, at which the spiral vortices change to the toroidal vortices. A similar phenomenon is known for viscous axial flow through an annulus having a rotating inner cylinder, where toroidal vortices transfer to spiral vortices at a definite value of axial Reynolds number (Snyder, 1965). Careful measurements were made by Kobayashi and Kohama (1984). As shown in Fig. 22, the direction ϵ remains zero until the flow velocity U_∞ reaches a definite value and then starts abruptly to increase with increasing U_∞. This definite value of U_∞ depends upon the cone angle θ and the rotational speed N. It corresponds to the local rotational speed ratio $S = 6$ to 8, which is independent of the cone angle θ and the rotational speed N. The scattering of the measured values results mainly due to fluctuations of the appearance of vortices.

The effect of free-stream turbulence was also studied by Kobayashi et al. (1987). Figure 23 shows the critical Reynolds number $Re_{x,c}$ and the transition Reynolds number $Re_{x,t}$ over a wide range of turbulence intensities from 0.04 to 3.5 percent. The experiment was carried out by using a low-turbulence wind tunnel at Tohoku University (Ito et al., 1980, 1985, 1992). It can be seen that there is no effect of turbulence intensity on the transition Reynolds number $Re_{x,t}$, while the critical Reynolds number $Re_{x,c}$ is found to vary in high levels of turbulence intensity. The spiral vortices appear uniformly over the circumference of the cone at the critical point x_c in the range of the lower turbulence intensity 0.04 to 2.4 percent, while at the higher turbulence intensity (2.8 and 3.5 percent) few spiral vortices initially appear on the circumference at the critical point x_c, but as the number of the vortices increases downstream, they finally appear uniformly over the circumference of the cone. Since the point x_c is located upstream compared with the case of the lower turbulence level, the corresponding critical Reynolds number $Re_{x,c}$ is smaller.

Transition region on a circular cylinder rotating in its axis in axial flow shifts upstream as the spin velocity is increased. Figure 24 shows the local Reynolds number Re_x with respect to the velocity ratio S (Yamato and Yamamoto, 1983). Here, $Re_x = xU_\infty/\nu$, $S = \omega R/U_\infty$, U_∞ is uniform flow velocity, R is a radius of the cylinder, and x is the distance measured from a leading edge to downstream.

5 Rotating Sphere in Still Fluid

When a sphere rotates in still fluid, a flow similar to that of the rotating disk is induced from the poles to the equator and radially released from the equator, namely, from $\theta = 0$ and 180 to 90 deg, as indicated in Fig. 25. The resulting stationary flow is three-dimensional. The induced flow is of fundamental interest in the fields of meteorology, astrophysics, fluid dynamics, and many others. Horwath (1951) first investigated this problem theoretically (limited to the case of laminar flow), introducing a boundary-layer approximation. Since then, many scientists (Nigam, 1954; Stewartson, 1958; Kobashi, 1957; Bowden and Lord, 1963; Kreith et al., 1963; Banks, 1965, 1976; Manohar, 1967; Singh, 1970; Sawatzki, 1970; Yamabe et al., 1982) have worked on this problem, both theoretically and experimentally, and the structure of the flow field in the case of a laminar boundary layer has been greatly clarified.

The actual flow field around a rotating sphere involves in general not only the laminar boundary layer, but also a transitional region and a turbulent boundary layer, because the flow condition near the equator is very unstable. It might be expected that the mechanism of the transition near the equator is mainly of the centrifugal instability, similar to the case of the rotating circular cylinder, while the one near the pole is of the cross-flow instability, similar to the case of the rotating disk. It should be, therefore, said that the present transition on the rotating sphere is caused by a combination of the centrifugal instability and the cross-flow instability.

Sawatzki (1970) first investigated this flow field experimentally using a hot-wire anemometer and a smoke method, and detected regularly spaced waves in the boundary layer transition region. He presumed the regular waves to be the same

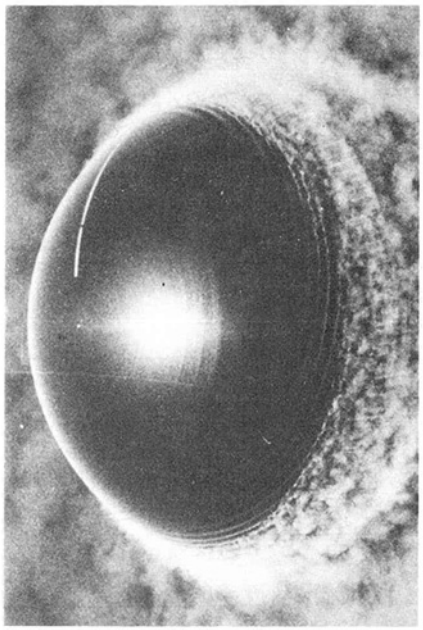

Fig. 26 Transition on sphere rotating in still fluid (Kohama and Kobayashi, 1983b). Clockwise rotation.

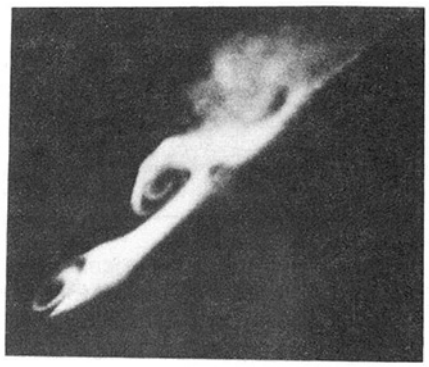

Fig. 27 Cross section of spiral vortices (Kohama and Kobayashi, 1983b). $D = 250$ mm; $N = 1500$ rpm.

kind of spiral vortices occurring on a rotating disk. The vortices were fixed relative to the surface of the rotating sphere. He also found that the transition region shifts toward the pole with rotating speed, and measured several properties of the vortices.

Later Kohama and Kobayashi (1983a) measured the transition process in detail. The transition region was visualized as shown in Fig. 26. One can see spiral streaks arranged regularly in the transition region. It was confirmed by further visualization of the cross-sectional flow pattern in those streaks, shown in Fig. 27, that they have the structure of vortices curling in the same direction. The secondary instability that follows develops into organized fine structure wrapping on the surface of the spiral vortices. The results were similar to those of the rotating disk case (Kobayashi et al., 1980). Transition to turbulence makes rapid progress soon after the appearance of the wrapping structure.

Figure 28 shows the location θ of the transition region versus the rotating speed N, which begins at the critical point θ_c and ends at the transition point θ_t, where θ is a central angle measured from the pole toward the equator, as shown in Fig. 25. It is clear from the figure that the transition region shifts from the equator ($\theta = 90$ deg) toward the pole ($\theta = 0$ deg) with increasing N, and also that the location of the transition region differs considerably among the diameters D of three spheres at the same rotating speed N.

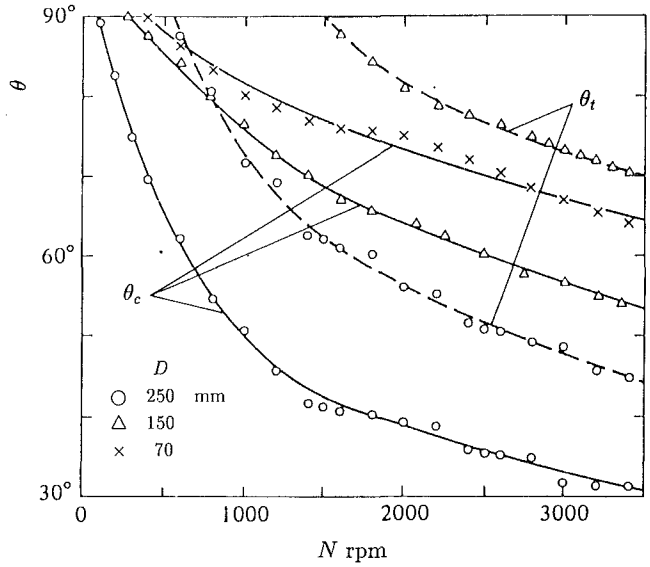

Fig. 28 Variation of critical point θ_c and transition point θ_t with rotation speed N (Kohama and Kobayashi, 1983a)

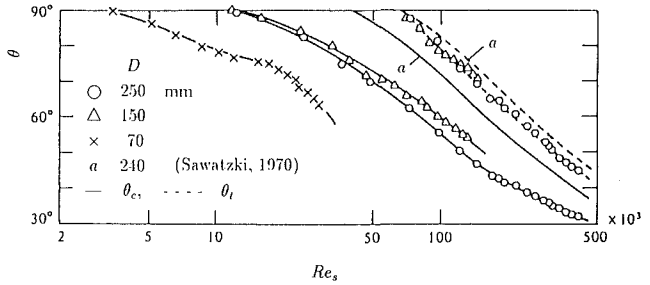

Fig. 29 Variation of critical point θ_c and the transition point θ_t with spin Reynolds number (Kohama and Kobayashi, 1983a)

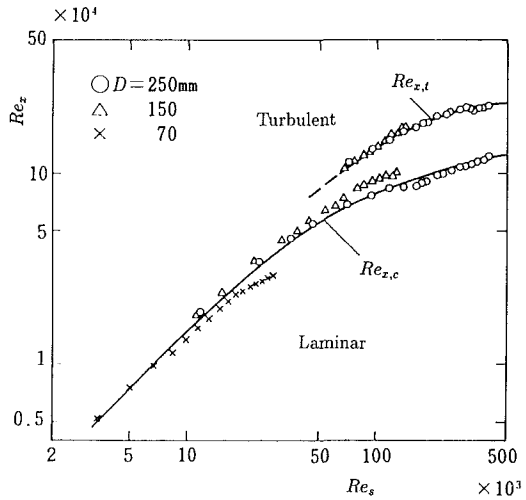

Fig. 30 Critical and transition Reynolds numbers ($Re_{x,c}$, $Re_{x,t}$) in relation to rotation Reynolds number Re_s (Kohama and Kobayashi, 1983a)

In Fig. 29, we plot the transition angles (θ_c, θ_t) in Fig. 28 versus the spin Reynolds number Re_s ($= \omega R_s^2/\nu$), based on the radius R_s of the sphere. The results of Sawatzki (1970) for $D = 240$ mm are also included. It can be said that the transition points are almost identical for different diameters in the expression of Fig. 29, while the critical points vary considerably. Kohama and Kobayashi (1983a) found finally that the nondimensional expression for the transition of the rotating sphere should depend upon the local Reynolds number Re_x ($= \omega\theta R_s^2 \sin\theta/\nu$) based on the distance θR_s measured along

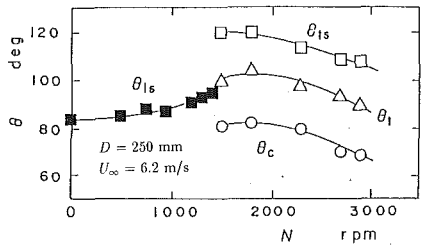

Fig. 31 Variations of laminar separation point (θ_{ls}), critical point (θ_c), transition point (θ_t), turbulent separation point (θ_{ts}) with rotational speed N of sphere (Kobayashi and Arai, 1990)

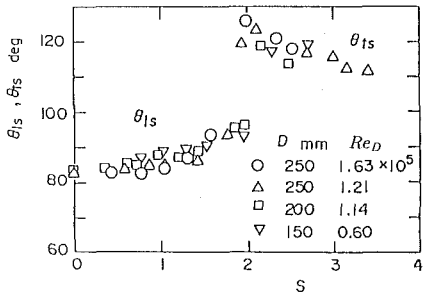

Fig. 32 Location of laminar separation (θ_{ls}) and turbulent separation (θ_{ts}) in relation to local rotational speed ratio S (Kobayashi and Arai, 1990)

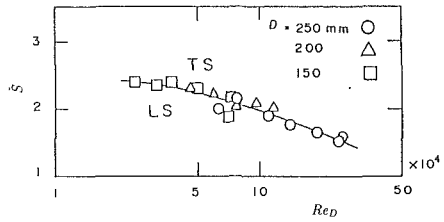

Fig. 33 Transfer condition $\tilde{S}$ of rotational speed ratio from laminar separation (LS) to turbulent separation (TS) in relation to free-stream Reynolds number Re_D (Kobayashi and Arai, 1990)

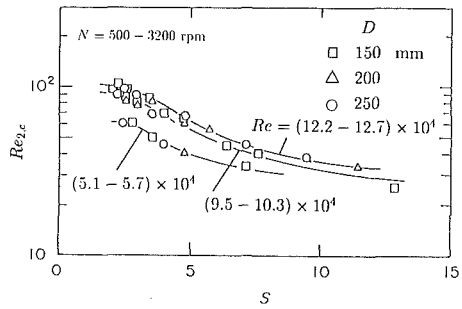

Fig. 34 Critical Reynolds number $Re_{2,c}$ in relation to $\tilde{S}$ (Kobayashi and Arai, 1990)

the sphere surface from the pole and the local peripheral velocity $\omega R_s \sin\theta$, as shown in Fig. 30, where the critical location $Re_{x,c}$ and the transition one $Re_{x,t}$ can be obtained from the two similar curves, independent of the size of the sphere diameter D and the rotating velocity ω.

The number n of the spiral vortices on the rotating sphere increases and tends to the value for the rotating disk ($n=30$) as the angular velocity is increased and the transition region shifts to the pole. The spiral angle varies from 14 deg at onset to 4 ~ 8 deg along the vortex axis in the transition region. This fact is almost independent of the rotating velocity.

6 Rotating Sphere in Axial Flow

The flow field for the steady laminar incompressible boundary layer on a sphere rotating in axial flow has been studied theoretically by Schlichting (1953), Hoskin (1955), Lee et al. (1978), Kumari and Nath (1982), and El-Shaarawi et al. (1985), and experimentally by Luthander and Rydberg (1935), and El-Shaarawi et al. (1987). Their results showed marked influence of rotation on laminar separation, drag, and the critical Reynolds number, for which the drag coefficient decreases abruptly. Axial flow with the uniform velocity U_∞ is directed from left to right along the axis of rotation in Fig. 25.

Kobayashi et al. (1988), and Kobayashi and Arai (1990) studied experimentally the effects of rotation on the transition and the separation of the three-dimensional boundary layer on the sphere rotating in axial flow. Figure 31 shows variations of the characteristic points measured at a fixed flow velocity for different values of the rotating speed N, where θ_{ls} denotes the location of laminar separation, θ_c is the critical point, θ_t is the transition point and θ_{ts} is the location of turbulent separation. At a definite value of N, the laminar boundary layer becomes unstable prior to laminar separation owing to cross-flow instability. This instability manifests itself as spiral vortices, similar to the cases of a circular disk and a sphere rotating in still fluid. The boundary layer then exhibits laminar-to-turbulent transition and turbulent separation.

Figure 32 shows a relation between the separation points (θ_{ls}, θ_{ts}) and the local rotational speed ratio $S(=\omega R/U_e=2\omega R_s/3U_\infty)$ for different values of D and the free-stream Reynolds number defined as $Re_D=DU_\infty/\nu$, where U_e denotes the local flow speed at the edge of the boundary layer. It is clear that the laminar separation point θ_{ls} increases from 83 deg for no rotation with increasing N, while the turbulent separation point θ_{ts} decreases as N is further increased. The transfer from laminar separation to turbulent separation occurs at a definite magnitude of the rotational speed ratio S, defined with $\tilde{S}$, which is given in Fig. 33. For a given Reynolds number, the flow pattern of the boundary layer on a rotating sphere would be of the laminar separation type if $S<\tilde{S}$, while it would be of the turbulent separation type if $S>\tilde{S}$. The relation of $\tilde{S}$ to Re_D is independent of the external flow velocity, the rotational speed and the sphere diameter.

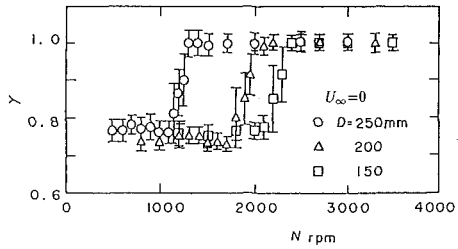

Fig. 35 Variations of relative angular speed (γ) of spiral vortices (Kobayashi and Arai, 1990)

Figure 34 shows the critical local Reynolds number $Re_{2,c}$ at the critical point θ_c (Fig. 31), which is based on the local meridional flow velocity at the outer edge of the boundary layer and the momentum thickness there. The rotational Reynolds number Re is defined as $Re=\omega R^2/\nu$. It is noticed that the relation between $Re_{2,c}$ and S depends somewhat upon the rotational Reynolds number Re.

For rotating disks (Kohama, 1984a) and rotating cones (Kobayashi et al., 1987; Kobayashi and Kohama, 1984), it was found that spiral vortices in their transition regions were fixed on the rotating solid surface. A relative angular speed $\gamma=\omega'/\omega$ of the spiral vortices for the rotating sphere in axial flow was measured as shown in Fig. 35, where ω' denotes angular speed of the spiral vortices. It is clear that the spiral vortices are fixed on the surface of the rotating sphere, i.e., $\gamma=1$, when the rotational speed N is large, while they move relatively on the sphere surface with the magnitude of $\gamma\doteq0.76$, when N is

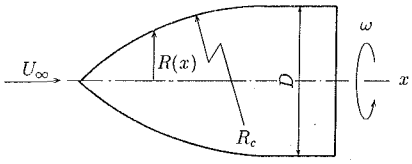

Fig. 36 Spinning ogival cylinder

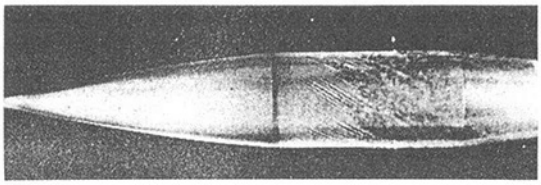

Fig. 37 Spin induced transition at zero angle of attack (Kegelman et al., 1983). $\omega D/2U_\infty = 0.658$, $Re_L = 0.928 \times 10^6$.

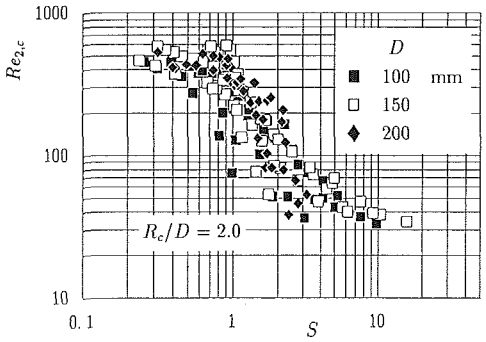

Fig. 38 Critical Reynolds number against rotating speed ratio for ogival cylinder (Kobayashi et al., 1991)

small. The rotational speed N at which γ increases from 0.76 to 1.0 varies with different values of the sphere diameter D and the external flow velocity U_∞. The mechanism of the change in the relative angular speed is not clarified.

7 Other Rotating Bodies

Besides basic rotating bodies, other more complex axisymmetric geometries have been experimentally studied. For a spinning ogival cylinder (Fig. 36), Mueller et al. (1981) and Kegelman et al. (1983) made a smoke visualization of the boundary layer transition as shown in Fig. 37 for $R_c/D = 18.6$. They observed a simultaneous appearance of Tollmien-Schlichting waves and spiral vortices in the transition region on the cylindrical part of the test model. The formation of spiral vortices is primarily dependent upon the rotational speed ratio S $(=\omega R/U_\infty)$ and relatively independent of Reynolds number based on the free-stream velocity. The spiral vortices were considered to come from the crossflow instability, though the cross-sectional flow pattern of the vortices was not visualized. Kohama (1985b) confirmed later for an ogival cylinder of $R_c/D = 8.1$ by means of flow visualization technique that the spiral vortices appearing on the rotating ogive nose cone are counter-rotating, a phenomenon similar to the one observed over a rotating cone in axial flow (Kobayashi et al., 1983).

Experiments by Kobayashi et al. (1991) found that the critical location of transition for the rotating ogival cylinder can be expressed, as shown in Fig. 38, primarily with a relation between the critical local Reynolds number $Re_{2,c}$ $(=U_e\delta_2/\nu)$ and the local rotational speed ratio S $(=\omega R/U_e)$ for different values of D, U_∞, and N, and that, for the rotating ellipsoids, the relation of $Re_{2,c}$ to S depends somewhat upon the slenderness a/b, as shown in Fig. 39.

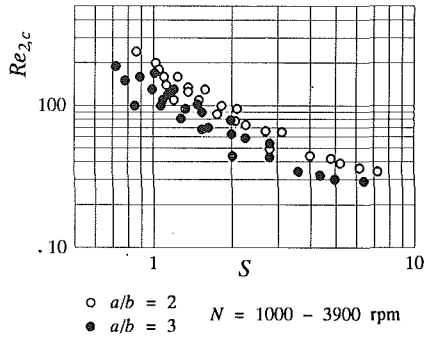

Fig. 39 Critical Reynolds number against rotational speed ratio for ellipsoid of slenderness 2 and 3 (Kobayashi et al., 1991)

8 Conclusions

The transition condition varies greatly depending on the body profile and the flow parameters, as shown in the present review. Of engineering interest should be to predict a location of boundary layer transition for an arbitrary body profile as shown in Fig. 1. The systematic investigations for typical profiles such as the rotating disk, the rotating cone, the rotating sphere and others provide useful data for the prediction. The data of the typical profiles are necessary to be expressed by using dominant dimensionless parameters. To find the dominant parameters becomes more complicated in case of more complex profile under more flow conditions, because the transition causes a combination of different magnitudes among the Tollmien-Schlichting instability, the centrifugal instability and the crossflow instability, as is seen in Fig. 21 for the rotating cone in axial flow. Another reason for the complexity comes from the fact that the instability occurs not only under a local condition at the critical point but also depending on a historical process from upstream to the critical point along a curved surface. What are dominant unified dimensionless parameters for predicting the transition location for arbitrary axisymmetrical body rotating in still fluid and in axial flow remains open for further discussion. Theoretical considerations for the present instability problem should be done in order to explain the experimental results systematically.

The transition process became clear for the three-dimensional boundary layers on the rotating typical axisymmetrical bodies. It was shown that spiral vortices appearing in the transition region have two kinds of structure; corotating when the cross-flow instability is dominant, and counter-rotating for the centrifugal instability dominant, and that fine organized structure appearing as the secondary instability is distinctly different between the corotating vortices and the counter-rotating vortices. The mechanism of the secondary instability and detailed transition process to turbulence should be discussed.

References

Balakumar, P., and Malik, M. R., 1990, "Traveling Disturbances in Rotating-Disk Flow," *Theoretical and Computational Fluid Dynamics*, Vol. 2, pp. 125–137.

Banks, W. H. H., 1965, "The Boundary Layer on a Rotating Sphere," *Quarterly Journal of Mechanics and Applied Mathematics*, Vol. 18, pp. 443–454.

Banks, W. H. H., 1976, "The Laminar Boundary Layer on a Rotating Sphere," *Acta Mechanica*, Vol. 24, pp. 273–287.

Bowden, F. P., and Lord, R. G., 1963, "The Aerodynamic Resistance to a Sphere Rotating at High Speed," *Proceedings of Royal Society of London*, Vol. A271, pp. 143–151.

Brown, W. B., 1961, "A Stability Criterion for Three-Dimensional Laminar Boundary Layers," *Boundary Layer and Flow Control*, G. V. Lachmann, ed., Pergamon, Vol. 2, pp. 913–923.

Cebeci, T., and Stewartson, K., 1980, "On Stability and Transition in Three-Dimensional Flows," *AIAA Journal*, Vol. 18, pp. 398–405.

Chen, C. F., and Christensen, D. K., 1967, "Stability of Flow Induced by an Impulsively Started Rotating Cylinder," *Physics of Fluids*, Vol. 10, pp. 1845–1846.

Chin, D.-T., and Litt, M., 1972, "An Electrochemical Study of Flow Instability on a Rotating Disk," *Journal of Fluid Mechanics*, Vol. 54, pp. 613–625.

Clarkson, M. H., Chin, S. C., and Shacter, P., 1980, "Visualization of Flow Instabilities on a Rotating Disk," *AIAA Journal*, Vol. 18, pp. 1541–1543.

Cobb, E. C., and Saunders, O. A., 1956, "Heat Transfer from a Rotating Disk," *Proceedings of the Royal Society of London*, Series A, Vol. 236, pp. 343–351.

El-Shaarawi, M. A. I., El-Refaie, M. F., and El-Bedeawi, S. A., 1985, "Numerical Solution of Laminar Boundary Layer Flow About a Rotating Sphere in an Axial Stream," ASME JOURNAL OF FLUIDS ENGINEERING, Vol. 107, pp. 97–104.

El-Shaarawi, M. A. I., Kemry, M. M., and El-Bedeawi, S. A., 1987, "Experiments on Laminar Flow About a Rotating Sphere in an Air Stream," *Proceedings of the Institution of Mechanical Engineers*, Vol. 201, pp. 427–438.

Fedrov, B. I., Plavnik, G. Z., Prokhorov, I. V., and Zhukhovitskii, L. G., 1976, "Transitional Flow Conditions on a Rotating Disk," *Journal of Engineering and Physics*, Vol. 31, pp. 1448–1453.

Goldstein, S., 1935, "On the Resistance to the Rotation of a Disc Immersed in a Fluid," *Proceedings of the Cambridge Philosophical Society*, Vol. 31, pp. 232–241.

Gregory, N., Stuart, J. T., and Walker, W. S., 1955, "On the Stability of Three-Dimensional Boundary Layers with Application to the Flow Due to a Rotating Disk," *Philosophical Transactions*, Vol. 248, pp. 155–199.

Gregory, N., and Walker, W. S., 1960, "Experiments on the Effect of Suction on the Flow Due to a Rotating Disk," *Journal of Fluid Mechanics*, Vol. 9, pp. 225–234.

Hall, P., 1986, "An Asymptotic Investigation of the Stationary Modes of Instability of the Boundary Layer on a Rotating Disc," *Proceedings of Royal Society of London*, Series A, Vol. 406, pp. 93–106.

Hering, R. G., and Grosh, R. J., 1962, "Laminar Free Convection from a Non-isothermal Cone," *International Journal of Heat and Mass Transfer*, Vol. 5, pp. 1059–1068.

Hering, R. G., and Grosh, R. J., 1963, "Laminar Combined Convection from a Rotating Cone," ASME *Journal of Heat Transfer*, Vol. 85, pp. 29–34.

Hoskin, N. E., 1955, "The Laminar Boundary Layer on a Rotating Sphere," *50 Jahre Grenzschichtforschung*, H. Görtler and W. Tollmien, eds., Friedr. Vieweg und Sohn, Braunschweig, pp. 127–131.

Howarth, L., 1951, "Note on the Boundary Layer on a Rotating Sphere," *Philosophical Magazine*, Vol. 2, pp. 1308–1315.

Illingworth, C. R., 1953, "The Laminar Boundary Layer of a Rotating Body of Revolution," *Philosophical Magazine*, Series 7, Vol. 44, pp. 389–403.

Ito, H., Kobayashi, R., Yuge, T., Honda, M., Hashimoto, H., Inooka, H., Masuda, H., Takayama, K., Nanbu, K., Imai, K., Sasaki, H., Higano, M., Kohama, Y., and Obinata, G., 1980, "The Design and the Performance of the Low-Turbulence Wind Tunnel, Tohoku University," *The Memoirs of the Institute of High Speed Mechanics*, Tohoku University, (in Japanese), Vol. 44, pp. 93–151.

Ito, H., Kobayashi, R., Oba, R., Tani, J., Masuda, H., Kohama, Y., and Imai, K., 1985, "The Velocity and Turbulence Distributions in Various Parts of the Low-Turbulence Wind Tunnel, Tohoku University," *The Memoirs of the Institute of High Speed Mechanics*, Tohoku University, (in Japanese), Vol. 85, pp. 67–104.

Ito, H., Kobayashi, R., and Kohama, Y., 1992, "The Low-Turbulence Wind Tunnel at Tohoku University," *The Aeronautical Journal of the Royal Aeronautical Society*, Vol. 96, pp. 141–151.

Itoh, N., 1985, "Stability Calculations of the Three-Dimensional Boundary-Layer Flow on a Rotating Disk," *Laminar-Turbulent Transition*, V. V. Kozlov, ed., pp. 463–470, New York, Springer-Verlag.

Itoh, M., and Zhang, Q., 1987, "Viscous Type Instability of the Boundary Layer on a Rotating Disk," *Transactions of the Japan Society of Mechanical Engineers* (in Japanese), Series B, Vol. 53, pp. 438–443.

Kappesser, R., Greif, R., and Cornet, I., 1973, "Mass Transfer to Rotating Cones," *Applied Scientific Research*, Vol. 28, pp. 442–452.

Von Kármán, Th., 1921, "Ueber Laminare und Turbulente Reibung," *Zeitschrift für Angewandte Mathematik und Mechanik*, Vol. 1, pp. 233–252; NACA TM 1092, 1946.

Kegelman, J. T., Nelson, R. C., and Mueller, T. J., 1983, "The Boundary Layer on an Axisymmetric Body With and Without Spin," *AIAA Journal*, Vol. 21, pp. 1485–1491.

Kirchner, R. P., and Chen, C. F., 1970, "Stability of Time-Dependent Rotational Couette Flow. Part 1. Experimental Investigation," *Journal of Fluid Mechanics*, Vol. 40, pp. 39–47.

Kobashi, Y., 1957, "Measurements of Boundary Layer of a Rotating Sphere," *Journal of Science of the Hiroshima University*, Series A, Vol. 20, pp. 149–157.

Kobayashi, R., Kohama, Y., and Takamadate, Ch., 1980, "Spiral Vortices in Boundary Layer Transition Regime on a Rotating Disk," *Acta Mechanica*, Vol. 35, pp. 71–82.

Kobayashi, R., 1981, "Linear Stability Theory of Boundary Layer Along a Cone Rotating in Axial Flow," *Bulletin of the Japan Society of Mechanical Engineers*, Vol. 24, pp. 934–940.

Kobayashi, R., Kohama, Y., and Kurosawa, M., 1983, "Boundary-Layer Transition on a Rotating Cone in Axial Flow," *Journal of Fluid Mechanics*, Vol. 127, pp. 341–352.

Kobayashi, R., and Izumi, H., 1983, "Boundary-Layer Transition on a Rotating Cone in Still Fluid," *Journal of Fluid Mechanics*, Vol. 127, pp. 353–364.

Kobayashi, R., and Kohama, Y., 1984, "Spiral Vortices in Boundary Layer Transition on a Rotating Cone," *Laminar-Turbulent Transition*, V. Kozlov, ed., IUTAM Symposium, Novosibirsk, Springer-Verlag, pp. 573–580.

Kobayashi, R., Kohama, Y., Arai, T., and Ukaku, M., 1987, "The Boundary-Layer Transition on Rotating Cones in Axial Flow with Free-Stream Turbulence," *JSME International Journal*, Vol. 30, pp. 423–429.

Kobayashi, R., Arai, T., and Nakajima, M., 1988, "Boundary-Layer Transition and Separation on a Sphere Rotating in Axial Flow," *Experimental Thermal and Fluid Science*, Vol. 1, pp. 99–104.

Kobayashi, R., and Arai, T., 1990, "Spiral Vortex Behavior in Transition Region and Separation of Three-Dimensional Boundary Layers on Spheres Rotating in Axial Flow," *Laminar-Turbulent Transition*, D. Arnal and R. Michel, eds., IUTAM Symposium Toulouse, France, Springer-Verlag Berlin Heidelberg, pp. 551–557.

Kobayashi, R., Fukunishi, Y., and Ohtani, F., 1991, "Prediction of Turbulent Transition of Boundary Layer on Rotating Axisymmetric Bodies," *Japan Society of Mechanical Engineers*, Tohoku Branch, Report No. 911-1, pp. 19–21.

Koh, J. C. Y., and Price, J. F., 1967, "Nonsimilar Boundary-Layer Heat Transfer of a Rotating Cone in Forced Flow," ASME *Journal of Heat Transfer*, Vol. 89, pp. 139–145.

Kohama, Y., and Kobayashi, R., 1983a, "Boundary-Layer Transition and the Behaviour of Spiral Vortices on Rotating Spheres," *Journal of Fluid Mechanics*, Vol. 137, pp. 153–164.

Kohama, Y., and Kobayashi, R., 1983b, "Behaviour of Spiral Vortices on Rotating Axisymmetric Bodies," *Reports of the Institute of High Speed Mechanics*, Tohuku University, Sendai, Japan, Vol. 47, pp. 27–38.

Kohama, Y., 1984a, "Study on Boundary Layer Transition of a Rotating Disk," *Acta Mechanica*, Vol. 50, pp. 193–199.

Kohama, Y., 1984b, "Behaviour of Spiral Vortices on a Rotating Cone in Axial Flow," *Acta Mechanica*, Vol. 51, pp. 105–117.

Kohama, Y., 1985a, "Turbulent Transition Process of the Spiral Vortices Appearing in the Laminar Boundary Layer of a Rotating Cone," *Physico-Chemical Hydrodynamics*, Vol. 6, pp. 659–669.

Kohama, Y., 1985b, "Flow Structure Formed by Axisymmetric Spinning Bodies," *AIAA Journal*, Vol. 23, pp. 1445–1447.

Kohama, Y., 1987, "Crossflow Instability in Rotating Disk Boundary Layer," *AIAA Paper*, No. 87-1340.

Kreith, F., Ellis, D., and Giesing, J., 1962, "An Experimental Investigation of the Flow Engendered by a Rotating Cone," *Applied Scientific Research*, Section A, Vol. 11, pp. 430–440.

Kreith, F., Roberts, L. G., Sullivan, J. A., and Sinha, S. N., 1963, "Convection Heat Transfer and Flow Phenomena on Rotating Spheres," *International Journal of Heat and Mass Transfer*, Vol. 6, pp. 881–895.

Kreith, F., 1966, "Friction Drag and Convective Heat Transfer of Rotating Cones in Mixed and Turbulent Flow," *Proceedings of the 1966 Heat Transfer and Fluid Mechanics Institute*, Stanford University Press, Stanford, Calif., pp. 29–43.

Kreith, F., 1968, "Convection Heat Transfer in Rotating System," *Advances in Heat Transfer*, Vol. 5, pp. 129–251.

Kumari, M., and Nath, G., 1982, "Nonsimilar Laminar Incompressible Boundary Layer Flow Over a Rotating Sphere," *Archiwum Mechaniki Stosowanej*, Warszawa, Vol. 34, pp. 147–164.

Lee, M. H., Jeng, D. R., and De Witt, K. T., 1978, "Laminar Boundary Layer Transfer Over Rotating Bodies in Forced Flow," ASME *Journal of Heat Transfer*, Vol. 100, pp. 496–502.

Luthander, S., and Rydberg, A., 1935, "Experimentelle Untersuchungen über den Luftwiderstand bei einer um eine mit der Windrichtung parallele Achse rotierenden Kugel," *Physikalische Zeitschrift*, Vol. 36, pp. 552–558.

MacKerrell, S., 1987, "A Nonlinear, Asymptotic Investigation of the Stationary Modes of Instability of the Three-Dimensional Boundary Layer on a Rotating Disk," *Proceedings of Royal Society of London*, Series A, Vol. 413, pp. 497–513.

Malik, M. R., Wilkinson, S. P., and Orszag, S. A., 1981, "Instability and Transition in Rotating Disk Flow," *AIAA Journal*, Vol. 19, pp. 1131–1138.

Malik, M. R., 1986, "The Neutral Curve for Stationary Disturbances in Rotating-Disk Flow," *Journal of Fluid Mechanics*, Vol. 164, pp. 275–287.

Manohar, R., 1967, "The Boundary Layer on a Rotating Sphere," *Zeitschrift für Angewandte Mathematik und Physik*, Vol. 18, pp. 320–330.

Mueller, T. J., Nelson, R. C., and Kegelman, J. T., 1981, "Smoke Visualization of Boundary-Layer Transition of a Spinning Axisymmetric Body," *AIAA Journal*, Vol. 19, pp. 1607–1608.

Nigam, S. D., 1954, "Note on the Boundary Layer on a Rotating Sphere," *Zeitschrift für Angewandte Mathematik und Physik*, Vol. 5, pp. 151–155.

Okamoto, T., Yagita, M., and Kamijima, Y., 1976, "Experimental Investigation on the Boundary-Layer Flow Over Rotating Cone-Cylinder Body in a Uniform Stream," *Bulletin of the Japan Society of Mechanical Engineers*, Vol. 19, pp. 930–937.

Sahin, I., 1988, "Application of Various Coordinate Transformations for Rotating Disk Flow Stability," *AIAA Journal*, Vol. 26, pp. 368–370.

Salzberg, F., and Kezios, S. P., 1965, "Mass Transfer From a Rotating Cone in Axisymmetric Flow," ASME *Journal of Heat Transfer*, Vol. 87, pp. 469–476.

Sawatzki, O., 1970, "Das Strömungsfeld um eine rotierende Kugel," *Acta Mechanica*, Vol. 9, pp. 159–214.

Schlichting, H., 1953, "Die laminare Strömung um einen axial angeströmten rotierenden Drehkörper," *Ingenieur-Archiv*, Vol. 21, pp. 227–244.

Schlichting, H., 1979, "Boundary Layer Theory," McGraw-Hill Book Co., p. 104.

Singh, S. N., 1970, "Laminar Boundary Layer on a Rotating Sphere," *Physics of Fluids*, Vol. 13, pp. 2452–2454.

Smith, N. H., 1947, "Exploratory Investigation of Laminar-Boundary-Layer Oscillations on a Rotating Disk," NACA Technical Note, No. 1127.

Snyder, H. A., 1965, "Experiments on the Stability of Two Types of Spiral Flow," *Annals of Physics*, Vol. 31, pp. 292–313.

Stewartson, K., 1958, "On Rotating Laminar Boundary Layers," *Grenzschichtforschung Symposium Freiburg*, Springer-Verlag Berlin, pp. 59–71.

Szeri, A. Z., and Giron, A., 1984, "Stability Flow Over a Rotating Disk," *International Journal for Numerical Methods in Fluids*, Vol. 4, pp. 989–996.

Theodorsen, Th., and Regier, A., 1944, "Experiments on Drag of Revolving Disks, Cylinders, and Streamline Rods at High Speed," NACA Report, No. 793, pp. 367–384.

Tien, C. L., 1960, "Heat Transfer by Laminar Flow from a Rotating Cone," ASME *Journal of Heat Transfer*, Vol. 82, pp. 252–253.

Tien, C. L., and Campbell, D. T., 1963, "Heat and Mass Transfer from Rotating Cones," *Journal of Fluid Mechanics*, Vol. 17, pp. 105–112.

Tien, C. L., and Tsuji, I. J., 1965, "A Theoretical Analysis of Laminar Forced Flow and Heat Transfer About a Rotating Cone," ASME *Journal of Heat Transfer*, Vol. 87, pp. 184–190.

Walowit, J., Tsao, S., and DiPrima, R. C., 1964, "Stability of Flow Between Arbitrarily Spaced Concentric Cylinder Surfaces Including the Effect of a Radial Temperature Gradient," ASME *Journal of Applied Mechanics*, Vol. 31, pp. 585–593.

Wieselsberger, C., 1927, "Ueber der Luftwiderstand bei gleichzeitiger Rotation des Versuchskörpers," *Physikalische Zeitschrift*, Vol. 28, pp. 84–88.

Wilkinson, S. P., and Malik, M. R., 1985, "Stability Experiments in the Flow over a Rotating Disk," *AIAA Journal*, Vol. 23, pp. 588–595.

Wimmer, M., 1988, "Viscous Flows and Instabilities Near Rotating Bodies," *Progress in Aerospace Sciences*, Vol. 25, pp. 43–103.

Wu, C. S., 1959, "The Three Dimensional Incompressible Laminar Boundary Layer on a Spinning Cone," *Applied Scientific Research*, Sect. A, Vol. 8, pp. 140–146.

Yamabe, H., Nishida, S., and Ito, J., 1982, "Laminar Boundary Layer on a Rotating Sphere," *Bulletin of the Japan Society of Mechanical Engineers* (in Japanese), Vol. 239, pp. 62–64.

Yamato, H., and Yamamoto, Y., 1983, "A Study on a Boundary Layer Around a Rotating Circular Cylinder in an Axial Uniform Flow," *Journal of the Society of Naval Architects of Japan*, No. 152, pp. 32–43.

R. W. Douglass

J. D. Ramshaw

Idaho National Engineering Laboratory,
EG&G Idaho, Inc.,
Idaho Falls, ID 83415-3808

Perspective: Future Research Directions in Computational Fluid Dynamics

The current state of computational fluid dynamics (CFD) has yet to reach its full promise as a general tool for engineering design and simulation. Research in the areas of code robustness, complex flows of real fluids, and numerical errors and resolution are proposed as directions aiming toward that goal. We illustrate some of the current CFD challenges using selected applications.

1 Introduction

Since the previous workshop on basic research needs in fluid dynamics (Jones et al., 1981), there have been dramatic advances in computing power and significant but less dramatic advances in numerical methodology. In view of these advances, it is remarkable how few changes there have been in our everyday use of computational fluid dynamics (CFD) to solve practical engineering problems. Computational fluid dynamics remains much more of an art than a science, and a rather fragmented and eclectic art at that. Here we wish to speculate on some of the further advances that will be required for computational fluid dynamics to evolve into a more mature, systematic, and user-friendly discipline.

At its inception, the field of numerical simulation envisioned for its maturity the ability to accurately model complicated phenomena, perhaps to the point of replacing expensive experiments. Certainly the hope was to be able at least to supply predictive information for experimental design and analysis. In the field of fluid dynamics, the vision is yet to be fully realized. There are many reasons why this is so, including limited computing resources, the inability to model complex phenomena involving turbulence, the challenge of multiple length and time scales within a single problem, and code reliability. In what follows, we identify three general areas in which we believe focused research can significantly advance computational fluid dynamics toward its mature vision. We take the view that future research directions should largely reflect current problems and known deficiences. Therefore our attempt is to identify some of the ways in which the current state of computational fluid dynamics is unsatisfactory, and their implications for future research.

2 Proposed Research Directions

In our judgment, the problems of code robustness, physical models for flows of real fluids in complicated domains, and numerical errors and resolution are the areas which are currently most challenging to computational fluid dynamics researchers and analysts. In the following subsections, we define more thoroughly our concerns and suggest areas where research might best be directed.

2.1 Robustness. In general, current computational fluid dynamics codes and methods lack robustness. They tend to be touchy and temperamental, and their successful use frequently requires an experienced staff who are intimately familiar with their vagaries. While this provides challenges for those involved in their development, it limits the degree to which the codes can be routinely used as "black boxes." This in turn limits their user base and prevents them from achieving their full potential for engineering analysis and applications.

In many situations, the lack of robustness can be traced to strong coupling, stiffness, and numerical instabilities. For example, in highly exothermic chemically reacting flows there is strong coupling between the chemistry and the fluid dynamics. Frequently the chemical time scales are much shorter than the fluid-dynamical ones, which gives rise to the additional problem of stiffness. Stiffness is dealt with by introducing implicitness into the numerical scheme. For example, Xu and Smooke (1993) used a fully implicit scheme for diffusion flame calculations. Usually this is done in a limited way, however, using, linearization and/or time-splitting approximations (such as the alternating direction implicit or ADI method) which are not always faithful to the physics. For example, the ADI method works best when the flame fronts align themselves with the designated mesh rows or columns (Kee et al., 1985, page 142), which is a rather severe restriction on the class of combustion problems solvable with the method. In practice, these approximations work better in some problems than others, which of course is the antithesis of robustness. When they break down, unphysical and/or marginally unstable solutions frequently result.

It has been known for some time that these problems are largely eliminated by the use of fully implicit (backward Euler) schemes in which all terms contributing to time derivatives are simultaneously evaluated at the new time level in their fully nonlinear forms. Such schemes require the solution of large sparse systems of nonlinear equations on each time step. Efficient and robust solution procedures for such systems have been elusive. Several investigators (Kee et al., 1985; Keyes, 1989; and Knoll and McHugh, 1992, for example) have made

Contributed by the Fluids Engineering Division for publication in the JOURNAL OF FLUIDS ENGINEERING. Manuscript received by the Fluids Engineering Division January 10, 1993; revised manuscript received June 29, 1993. Associate Technical Editor: O. C. Jones.

made significant recent advances in the area of fully implicit methods which appear particularly useful for stiff problems. These advances hold promise for fully implicit methods which are both robust and computationally efficient. This seems an exceptionally fruitful research area, in which further significant advances in the next few years are expected. One such area of research is applying domain decomposition and the associated distributed computing techniques to implicit schemes to more efficiently use local computing resources.

2.2 Complex Geometries and Complex Fluids. In spite of significant advances in finite element and finite difference methods on generalized meshes (particularly triangular and tetrahedral meshes), body-fitted coordinates, domain decomposition, and so on, capabilities to routinely perform practical three-dimensional simulations in complex geometries remain inadequate, especially for complex flows involving sharp interfaces, surface tension, compressibility, heat transfer, turbulence, multiple components and phases, chemical reactions, and radiation. In addition to the lack of robustness already discussed, existing codes for such problems tend to be based on simple and relatively inaccurate numerical schemes, rather than the more advanced schemes currently available. As an illustration, consider the SIMPLE (Patankar and Spalding, 1972) and SIMPLER (Patankar, 1980) algorithms which are in wide use today in many codes such as PHOENICS (a product of CHAM of North America). MacArthur and Patankar (1989) show that obtaining solutions becomes difficult for large Rayleigh numbers ($> 10^8$) when the SIMPLE and SIMPLER methods were applied to a natural convection model problem. Likewise, Xu and Smooke (1993) find similar difficulties with convergence of these methods which was attributed to their inability to handle large density variations in the reacting flow and the equation-by-equation iteration nature of the algorithms. Implicit Newton methods, which include all of the equations simultaneously in the iteration process, are shown to converge to smaller residual norms faster than the SIMPLER method (Xu and Smooke, 1993).

Reticence to adopt newer methods is due in part to the inherent time lag associated with code development, but it also reflects considerations of complexity and manageability. In most cases the advanced schemes are significantly more complicated than their predecessors, and the developers of large-scale codes must contend with so many complications of a physical nature that they frequently employ simple numerical schemes just to keep things manageable. Even so, such codes tend to be extremely complex; they typically contain thousands or tens of thousands of lines of FORTRAN, and require years or tens of person-years of development effort.

There is a clear need for a next generation of robust and economical computer codes, based on state-of-the-art numerical methods, for simulating three-dimensional flows of complex fluids in complex geometries. In order to meet this need, it will be necessary to develop and employ better methods for managing the complexity of code-development and debugging processes, which are currently far too time-consuming and error-prone. Such methods may possibly use symbolic manipulation to automatically generate discrete approximations, together with post-processors to automatically generate the corresponding source coding. This is tantamount to developing higher-level languages which bear the same relation to FORTRAN as FORTRAN does to machine language. The use of modular or object oriented coding languages (such as $C++$ or FORTRAN 90, for example) fill part of this need and will increasingly be used by code developers in the future.

Similarly, more systematic methods for debugging are also needed, including automated source-code consistency tests. Work is progressing in these areas and progress has been made, but it has not yet had a significant impact on the way most computational fluid dynamics codes are written. Further developments along these lines hold promise for completely revolutionizing future computational fluid dynamics code development, and we expect to see significant progress in this area in the next several years.

2.3 Resolution and Numerical Errors. Most computational fluid dynamics practitioners are more concerned with obtaining results than with either the order of accuracy of their numerical schemes or the need to refine the grid until converged grid-independent solutions are obtained. It is noteworthy that technical journals publishing numerical results are beginning to require a "systematic discussion of numerical errors" (ASME *Journal of Heat Transfer*, Information for Authors). However, these concepts are largely irrelevant to large-scale practical engineering applications of computational fluid dynamics, which typically involve such wide ranges of length and time scales that the use of cells and time steps small enough to fully resolve them is prohibitive. This situation requires new methodologies for estimating, bounding, and minimizing discretization errors in situations where one is forced to live with very coarse resolution. Sometimes errors in local flow variables are of less concern than errors in global parameters of primary interest (e.g., total drag). Local and global errors are not always simply related, so methods to separately quantify them would be desirable. Once the errors are quantified, adaptive strategies can be developed to minimize them subject to the constraints of the available resolution and computational resources. It may be possible to use current and future adaptive gridding methods for this purpose by replacing the error measures on which they are based.

3 Selected Computational Fluid Dynamics Applications

In this section, we discuss several specific computational fluid dynamics applications of current interest that illustrate the challenges described in Section 2. No attempt was made to thoroughly cover all significant areas of computational fluid dynamics application, nor to discuss each of the proposed research areas in depth. Notable omissions include high speed and hypersonic flows and the challenging field of thermal-fluid flows in materials processing. We have attempted, however, to select examples that accurately reflect the current-state-of-the-art in the areas discussed.

3.1 Tokamak Plasma Boundary Layer. The Tokamak is the mainline reactor concept for magnetic confinement fusion. The working fluid in the reactor is a plasma, a hot ionized gas, which comes in contact with portions of the reactor structure. When this happens, large heat and particle fluxes occur which cause thermal stresses. Since experiments are very costly, it becomes mandatory to model these flows so that the stresses can be determined. Such flows are modeled by solving a system of multidimensional multi-fluid, atomically reacting, magnetohydrodynamic equations coupled to equations for the transport of neutral species generated through plasma-wall interactions. Such a system can involve in excess of fifteen simultaneous, nonlinear equations on each computational cell. The modeling is further complicated by many time scales and a complex geometry. The resulting system is, not surprisingly, stiff and touchy to solve.

Knoll and McHugh (1992), Knoll et al. (1993), and others are working on a promising technique for solving these equations. They are investigating an advanced Newton method involving an efficient numerical evaluation of the Jacobian and multiple grids for generating good initial guesses on fine grids. Techniques for increasing the radius of convergence of the Newton method are also under investigation. Aspects of solving sparse matrix problems are a part of the ongoing research. These ideas have been successfully applied to Tokamak

edge plasma modeling with the desired results of solution speed-up and more numerically stable codes.

Since these difficulties are common to a wide variety of fluid dynamics problems, study of these ideas in other contexts holds promise for more robust algorithms for general computational fluid dynamics applications as well.

3.2 Internal Combustion Engines. The cover story in the May 1992 issue of *Mechanical Engineering* was "Computational Fluid Dynamics: CFD Comes To Engine Design." In an article in this issue, Leo O'Connor (1992) presented a survey of computational fluid dynamics tools used today by foreign and domestic automobile makers. When pointing to the future, the article suggests that although the art is fairly well developed, there is still room for research. In particular, the article suggests that two areas in need of work are solution adaptiveness and the physical models. In the author's words,

> "For example, in solution adaptiveness, some unstructured codes are advanced enough to generate the extra cells needed in simple simulations, But when it comes to the complex three-dimensional shapes associated with designing engines, the numerical models need further development. 'Modeling combustion in an engine is a complex problem because you have the movement of pistons to deal with as well as the combustion process itself,' said Michael Engelman, president of Fluid Dynamics International. '*In combustion, no one knows the right physical model to put in the code. You make all sorts of simplified assumptions because the process is so complex. There is still much physical modeling to be done no matter how advanced our numerical models are.*' (our italics)"

These comments, of course, are not limited to this application.

3.3 Dynamic Fluid Interfaces. Mixing of fluids has become an increasing topic of importance for real flow modeling (see Ottino, 1989 for an introduction). Of necessity, behavior of the mixing interface plays a key role in the evolution of the flow field through, for example, interfacial tension, chemical reaction, and energy and mass transport. The subject of multiphase flow relies heavily on interfacial dynamics. However, the state-of-the-art in modeling these kinds of problems is still evolving.

Consider the very recent work of Unverdi and Tryggvason (1992), which describes an up-to-date method of following interfaces via front-tracking. In this paper are striking examples of two- and three-dimensional flows of bubbles. As stated by the authors, the interfaces are sharp and the method appears to be robust and computationally efficient. Limitations are also identified which include resolution requirements, especially for three-dimensional flows, and the treatment of interacting interfaces. More specifically,

> "When the double interfaces are of dynamical significance, such as in the generation of froth when bubbles arrive at a free surface, or when a thin film between adjacent bubbles ruptures, either a subgrid model for the film behavior or a mechanism to decide on the rupture time and the subsequent changes in interface topology have to be added. The proper inclusion of rupture of thin films necessitates additional physical modeling."

3.4 Flow Past a Submarine. Challenges facing the computational fluid dynamics community include making realistic models for flows in complex geometries which are characterized by a wide range of the relevant parameters. A transient external flow over a maneuvering vehicle at large Reynolds number is one example (Swean et al., 1990). The important length scales range from the turbulent boundary layer at a Reynolds number of 10^7 at one extreme to the large scale vortices being shed at the other extreme. These length scales may span many orders of magnitude and the demands on the grid to effectively capture these scales within the available computer resources may be severe. In addition, flow structures such as moving shock waves may require the grid to adapt in time as well as space.

There are basically three ways of obtaining spatial resolution: refining the grid (h-refinement), increasing the order of the approximation (p-refinement), and grid clustering. These can all be done adaptively as the computations progress. The choice of type of interpolating polynomial used also requires consideration of accuracy versus simplicity. Simple (complete) polynomials have long been used, but the advantages of orthogonal polynomials are becoming noticed as in the spectral element codes.

Time scales, like spatial scales, may range over several orders of magnitude. In the present example, high-frequency oscillations caused by the propeller or time step restrictions due to fine grids in the turbulent boundary layer can cause the calculation to resolve temporal variations at an excessively fine level when only the low frequency vortex shedding from the vehicle body is desired.

4 Summary

We have discussed three areas which point to promising future research areas in fluid mechanics modeling. The issues of code robustness, complex flows of complex fluids, and resolution and numerical errors need to be addressed to advance the state-of-the-art. Specifically, we identify the need for efficient implicit methods, better physical models for reacting flows, ways of obtaining accurate solutions on coarse grids and for multiple length scale problems, and ways of estimating, bounding, and minimizing the discretization errors in situations where a coarse grid must be used. This list is clearly not exhaustive. Obvious omissions include further advances in vector, parallel and distributed computation, lattice-gas methods, graphics standardization, unstructed grids, free Lagrangian methods, and the vexing question of how to bring some semblance of order to the bewildering and rapidly proliferating variety of computational fluid dynamics codes and methods.

Acknowledgments

We are grateful to our colleagues in the Computational Fluid Dynamics Team at the INEL for their input. This contribution was supported by the U.S. Department of Energy DOE-Idaho Field Office, under DOE Contract DE-AC07-76ID01570 and by the INEL Long Term Research Initiative in Computational Mechanics.

References

Jones, O. C., Kreith, F., and White, F. M., 1981, "Basic Research Needs in Fluid Mechanics," ASME JOURNAL OF FLUIDS ENGINEERING, Vol. 103, No. 4, Dec., pp. 509–519.

Kee, R. J., Petzold, L. R., Smooke, M. D., and Grcar, J. F., 1985, "Implicit Methods in Combustion and Chemical Kinetics Modeling," *Multiple Time Scales*, J. H. Brackbill and B. I. Cohen, eds., Academic Press, New York, pp. 113–144.

Keyes, D. E., 1989, "Domain Decomposition Methods for the Parallel Computation of Reacting Flows," *Computer Physics Communications*, Vol. 53, pp. 181–200.

Knoll, D. A., and McHugh, P. R., 1992, "NEWEDGE: A 2-D Fully Implicit Edge Plasma Fluid Code for Advanced Physics and Complex Geometry," *Journal of Nuclear Materials*, Vol. 196–198, pp. 352–356.

Knoll, D. A., Prinja, A. K., and Campbell, R. B., 1993, "A Direct Newton Solver for the Two-Dimensional Tokamak Edge Plasma Fluid Equations," *Journal of Computational Physics*, Vol. 104, pp. 418–426.

MacArthur, J. W., and Patankar, S. V., 1989, "Robust Semidirect Finite Difference Methods for Solving the Navier-Stokes and Energy Equations," *International Journal of Numerical Methods in Fluids*, Vol. 9, pp. 325–340.

O'Connor, L., 1992, "Computational Fluid Dynamics: Giving a Boost to Engine Design," *Mechanical Engineering*, Vol. 114, No. 5, May, pp. 44–50.

Ottino, J. M., 1989, *The Kinematics of Mixing: Stretching, Chaos, and Trans-*

port, Cambridge Texts in Applied Mathematics, Cambridge University Press, New York.

Patankar, S. V., 1980, *Numerical Heat Transfer and Fluid Flow*, Hemisphere Publishing Co., New York.

Patankar, S. V., and Spalding, D. B., 1972, "A Calculation Procedure for Heat, Mass and Momentum Transfer in Three-Dimensional Parabolic Flows," *International Journal of Heat and Mass Transfer*, Vol. 15, p. 1787.

Swean, T., Sandberg, W., Löhner, R., Stewart, M., Ramamurti, R., Fung, T., Fyfe, D., and Patnaik, G., 1990, "Unsteady CFD Simulations of Submarine Flows," Final Report to the Naval Research Laboratory under ARPA Order No. 6604, Submarine Technology Program, DARPA, 1400 Wilson Blvd, Arlington, VA 2209–2308.

Unverdi, S., and Tryggvason, G., 1992, "A Front-Tracking Method for Viscous, Incompressible, Multi-fluid Flows," *Journal of Computational Physics*, Vol. 100, pp. 25–37.

Xu, Y., and Smooke, M. D., 1993, "Application of a Primitive Variable Newton's Method for the Calculation of an Axisymmetric Laminar Diffusion Flame," *Journal of Computational Physics*, Vol. 104, pp. 99–109.

Estimating Uncertainty in Computations of Two-Dimensional Separated Flows

Ayodeji O. Demuren
Mem. ASME.

Robert V. Wilson

Department of Mechanical Engineering,
Old Dominion University,
Norfolk, VA 23529

The present paper investigates sources of uncertainties in two-dimensional flow computations and presents methods for estimating them. A sample problem is used for illustration. The following categories are explored in detail: (i) Uncertainty due to truncation error in numerical schemes; (ii) Uncertainty due to discretization error; (iii) Uncertainty due to outflow boundary conditions; (iv) Uncertainty due to incomplete iterative convergence; (v) Uncertainty due to computational grid aspect ratio. The error estimates are based on requirements for internal consistencies in computed results. Therefore, they provide better judgement of the numerical solution integrity than comparisons to experimental data or "benchmark" solutions whose reliability may sometimes be questionable. Ideally, both approaches should be employed. A new method is presented for estimating the optimum grid-cell aspect ratio for computational accuracy and efficiency.

1 Introduction

The rapid development of computers over the past three decades has encouraged the development of computational fluid dynamics to such an extent that it has become a viable analytical tool in the solution or design process in several engineering and environmental applications. As investigated flow situations have become more complicated, the need for techniques for evaluating sources and magnitudes of uncertainties in computed results has grown.

Ferziger (1989) proposed some methods suitable for the estimation and reduction of numerical errors resulting from inadequate grid resolution or incomplete convergence of the iterative scheme. The former is based on the Richardson extrapolation method originally proposed by Richardson (1911) and Richardson and Gaunt (1927). This method has been used in a wide range of applications to improve numerical solutions or to estimate errors in numerical solutions. Churchill et al. (1981) and de Vahl Davis (1983) applied the method to estimate zero-grid-size solution in natural convection problems. Applications to aerodynamic flows are reported by Dang et al. (1989) and Zing (1991), among others. The common result is that the Richardson extrapolation method is reliable only when the numerical solutions on the different grids used in the procedure are smooth and display similar characteristics, which presupposes that the grids should be sufficiently fine to resolve all flow features.

In the present paper, we investigate a wider range of sources of uncertainty in numerical computations of separated flows. Possible errors resulting from each source are estimated and methods for eliminating or minimizing them are explored. The model problem is the steady, two-dimensional laminar flow over a backward facing step. The Reynolds number in the flow problem is at the high end of the laminar flow regime (equal to 400 based on the mean flow velocity and the channel height upstream of the step). The flow configuration and the boundary conditions are illustrated in Fig. 1. Present computed results are compared to a "benchmark solution" (BM) developed by Gartling (1990) based on second-order accurate fine grid computations, though more emphasis is placed on techniques for estimating errors in the absence of the other independent results.

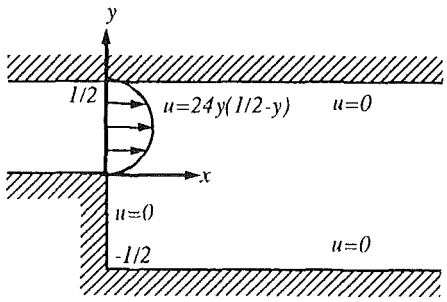

Fig. 1 Geometry for backward facing step

2 Numerical Method

The equations governing the steady, two-dimensional, incompressible flow can be written in dimensionless variables as:

$$\frac{\partial u}{\partial x}+\frac{\partial v}{\partial y}=0 \tag{1}$$

Contributed by the Fluids Engineering Division for publication in the JOURNAL OF FLUIDS ENGINEERING. Manuscript received by the Fluids Engineering Division December 3, 1992; revised manuscript received March 18, 1994. Associate Technical Editor: R. K. Agarwal.

Table 1 Grids used in uncertainty estimation

Grid	Section	Grid Size, $N_x \times N_y$	Domain Size, $L \times H$	ϵ_x, ϵ_y
1	3, 6	258×34	10×1	1, 1
2	3	130×18	10×1	1, 1
3	3	66×10	10×1	1, 1
4[a]	4, 5	480×41	30×1	1.01, 1.05
5	7	258×18	10×1	1, 1
6	7	258×66	10×1	1, 1
7	7	258×130	10×1	1, 1
8	7	258×258	10×1	1, 1

(a) For shorter domain lengths, the latter streamwise portion of this grid is truncated.

$$u\frac{\partial u}{\partial x}+v\frac{\partial u}{\partial y}=-\frac{\partial p}{\partial x}+\frac{1}{\mathrm{Re}}\left(\frac{\partial^2 u}{\partial x^2}+\frac{\partial^2 u}{\partial y^2}\right) \quad (2)$$

$$u\frac{\partial v}{\partial x}+v\frac{\partial v}{\partial y}=-\frac{\partial p}{\partial y}+\frac{1}{\mathrm{Re}}\left(\frac{\partial^2 v}{\partial x^2}+\frac{\partial^2 v}{\partial y^2}\right) \quad (3)$$

where Re is the Reynolds number. The equations are solved with modified versions of the popular TEACH computer code, which is based on the SIMPLE algorithm of Patankar and Spalding (1972). The grids and domain lengths used in various sections of the paper are presented in Table 1. Also given are the geometric grid expansion factors, with the grid spacing expanding by a constant factor, ϵ_x from the inflow to outflow plane, and by a factor, ϵ_y from the top and bottom walls towards the channel center-line.

3 Truncation Error in Numerical Schemes

Truncation error in a numerical scheme may result from errors in approximating the convection or diffusion terms, but in high Reynolds number flows convection usually dominates diffusion, except in the immediate proximity of a wall, so more attention needs to be placed on the former. Diffusion terms are simply approximated with central differences.

Four differencing schemes are applied to the two model problems. The differencing schemes are the hybrid, central, second-order upwind (2nd OU), and third-order upwind (3rd OU). On discretizing the governing Eqs. (1), (2), and (3) over a typical control volume, the four schemes lead to algebraic equations with the general form:

$$A_P\phi_P = A_E\phi_E + A_W\phi_W + A_N\phi_N + A_S\phi_S + A_{EE}\phi_{EE} + A_{WW}\phi_{WW} + A_{NN}\phi_{NN} + A_{SS}\phi_{SS} + S_u + B \quad (4)$$

where ϕ is any field property (velocity or temperature), S_u is the source term (pressure gradient or additional viscous terms), the A's are the convection/diffusion coefficients, and B is the fluid body force, where applicable. The subscripts stand for east, west, north, etc. Expressions for these coefficients for the various schemes can be found in the literature and are given in Demuren and Wilson (1992).

The four approximations of the convection terms outlined above are applied to the test problem over a streamwise computational domain length of 10. Computed locations of zero shear stress on the upper and lower walls are shown in Table 2. From the results, the hybrid scheme gives a large percentage difference compared to the "benchmark" result (20 percent for the top point and 17 percent for the bottom point). The artificial diffusion introduced by the first-order upwind (1st OU) part of the hybrid coefficients makes the effective Reynolds number lower and thus the eddy lengths are shorter, as would be the case in a flow with a somewhat lower Reynolds number. To obtain improved accuracy a higher-order method must be used. The central and third-order upwind schemes give percentage differences under 5 percent, and the second-order upwind scheme under 8 percent.

The order of the difference schemes can be estimated following generalizations of the Richardson extrapolation method.

Table 2 Points of zero shear stress

Difference Scheme	Top (% diff[a])	Bot. (% diff[a])
Hybrid	3.87 (20)	5.05 (17)
2nd OU	4.47 (7.8)	5.70 (6.6)
Central	4.64 (4.3)	5.88 (3.6)
3rd OU	4.61 (4.9)	5.84 (4.3)
BM	4.85	6.10

(a) Percent difference between value and benchmark solution.

Table 3 Estimated order of numerical schemes, @ Re = 100

Difference scheme	1st OU	Hybrid	2nd OU	Central	3rd OU
Order	0.8	1.9	2.0	2.0	2.2

Basically, the exact functional value can be approximated in terms of results on finite grids plus the leading term of the truncation error as:

$$\phi = \phi_h + h^n x_n + \ldots \quad (5)$$

$$\phi = \phi_{2h} + (2h)^n x_n + \ldots \quad (6)$$

$$\phi = \phi_{4h} + (4h)^n x_n + \ldots \quad (7)$$

where h is the grid spacing in the x-direction, n is the order of the scheme and x_n is a grid function, which is assumed to be equal for the h, $2h$, and $4h$ grids. The grid function contains spatial derivatives of ϕ with respect to x and y, which are also of order n. The statements above will be valid so long as h is sufficiently small for the leading term to be dominant. The order of the numerical scheme can then be estimated from:

$$n = \frac{\ln\left[\dfrac{(\phi_{2h}-\phi_{4h})}{(\phi_h-\phi_{2h})}\right]}{\ln(2)} \quad (8)$$

Computations were made on grids 1-3 at a Reynolds number of 100. The lower Reynolds number was chosen for economy because much finer grids are required for Eqs. (5)-(8) to be valid at the larger Reynolds number. Otherwise the leading term in the truncation series may not be dominant. Estimates of the order of the numerical scheme based on Eq. (8) are presented in Table 3. The results show that the 1st OU scheme is indeed first-order accurate, the 2nd OU and central schemes are second-order accurate, and the 3rd OU is only slightly better than the second-order accurate. The only possible surprise is that the hybrid scheme is almost second-order accurate. This is mainly due to the lower Reynolds number of the flow which enables the use of central differencing in major sections of the computational domain.

4 Discretization Error

The discretization error was investigated by employing a Richardson extrapolation method of analysis. The truncation of grid 4 to a domain length of 10 units was used as a base grid. This grid is defined as the $2h$ grid. A grid was generated with half the grid spacing in the x and y directions which is defined as the h grid, and one was generated with double the grid spacing, defined as the $4h$ grid. Central differencing was used for the convection terms of the governing equations. This scheme, described in the previous section, is second-order accurate. Following Ferziger (1989) (see also Demuren and Wilson (1992)), one can combine the solutions on the h and $2h$ grids to obtain a fourth-order accurate solution on the $2h$ grid:

$$\phi_{2h}|_{4\text{th}} = \frac{4}{3}\phi_h|_{2\text{nd}} - \frac{1}{3}\phi_{2h}|_{2\text{nd}} \quad (9)$$

Similarly, one can combine solutions on the $2h$ and $4h$ grids to yield a fourth-order accurate solution on the $4h$ grid:

Table 4 Points of zero shear stress

Grid	Top (% diff[a])	Bot. (% diff[a])
$h\|_{2nd}$[b]	4.72 (−2.6)	6.01 (−1.5)
$2h\|_{2nd}$	4.55 (−6.1)	5.79 (−5.1)
$4h\|_{2nd}$	3.61 (−25)	4.76 (−22)
$2h\|_{4th}$	4.78 (−1.4)	6.08 (−0.26)
$4h\|_{4th}$	4.87 (0.41)	6.13 (0.52)
$4h\|_{6th}$	4.77 (−1.6)	6.08 (−0.31)
BM	4.85	6.10

(*a*) Percent difference between value and benchmark solution.
(*b*) Results incompletely converged to $r_{max} = 1.5 \times 10^{-2}$ (maximum of u, v, and mass equation residual), all other results converged to $r_{max} = 2.0 \times 10^{-4}$.

$$\phi_{4h}|_{4th} = \frac{4}{3}\phi_{2h}|_{2nd} - \frac{1}{3}\phi_{2h}|_{2nd} \tag{10}$$

The fourth-order accurate solution can be combined to obtain a sixth-order accurate solution on the $4h$ grid:

$$\phi_{4h}|_{6th} = \frac{16}{15}\phi_{2h}|_{4th} - \frac{1}{15}\phi_{4h}|_{4th} \tag{11}$$

The procedure used to generate the more accurate results is equivalent to the extrapolation method used for estimating zero-grid-size results (see Churchill et al., 1981). The present results may also be interpreted as the $0h$ results for the second-order scheme.

As an example of the estimation of discretization error, the points of zero shear stress at the upper and lower walls are calculated. The results of these calculations as well as the extrapolated values using Eqs. (9)–(11) are displayed in Table 4, and compared to the "benchmark" solution.

The results using the Richardson extrapolation method show that combining the $2h|_{2nd}$ and $4h|_{2nd}$ results, yields an improved result. For the top wall point, the percentage difference improves from 6.1 percent ($2h$ grid) and 25 percent ($4h$ grid) to 0.41 percent ($4h$ grid, fourth-order accurate). For the bottom wall point, the percentage difference improves from 5.1 percent ($2h$ grid) and 22 percent ($4h$ grid) to 0.26 percent ($4h$ grid, fourth-order accurate). The initial results on the h grid are not converged to the same level as the $2h$ and $4h$ grid results. This may partly explain why the $2h|_{4th}$ results are not much better than the $4h|_{4th}$ results.

5 Outflow Boundary Conditions

Outflow boundary conditions pose a particular difficulty in elliptic problems. The usual practice is to locate the outflow plane far enough away from the region of interest which presumes a pre-knowledge of the solution. The question arises as to how far the outflow plane should be located in separated flows and what errors are introduced by too short a location. The effect of the location of the outflow boundary was investigated for the model problem by truncating the domain from 30, to 15, 10, and 7 units, respectively.

The outflow boundary conditions (OBC) consist of setting the first derivatives of u and v, in the direction normal to the outflow plane, to zero, while satisfying global conservation of mass at the outflow. Thus:

$$\Delta u = \int_{-0.5}^{0.5} (u_{2,j} - u_{n-1,j})\,dy \tag{12}$$

$$\frac{\partial u}{\partial x} \approx 0 \Rightarrow u_{n,j} = u_{n-1,j} + \Delta u \tag{13}$$

$$\frac{\partial v}{\partial x} = 0 \Rightarrow v_{n,j} = v_{n-1,j} \tag{14}$$

where the subscripts 2 and n denote the inflow and outflow locations, respectively, for the u variable. If global continuity is satisfied at the outflow $\Delta u = 0$ and $u_{n,j} = u_{n-1,j}$.

The points of zero wall shear stress are calculated and shown in Table 5, while the streamlines and pressure counters are shown in Figs. 2 and 3 for the various domain lengths. It is clear that with the outflow boundary conditions specified in Eqs. (12) to (14) the location of the outflow boundary has little effect on the computed solution. There was no difficulty in obtaining the correct results even though a recirculating eddy was dissected by this boundary for the domain length of 7.

Table 5 Points of zero wall shear stress

Domain length	30	15	10	7
1st Top	4.57	4.56	4.55	4.53
2nd Top	10.27	10.27	—	—
1st Bot.	5.80	5.80	5.78	5.76

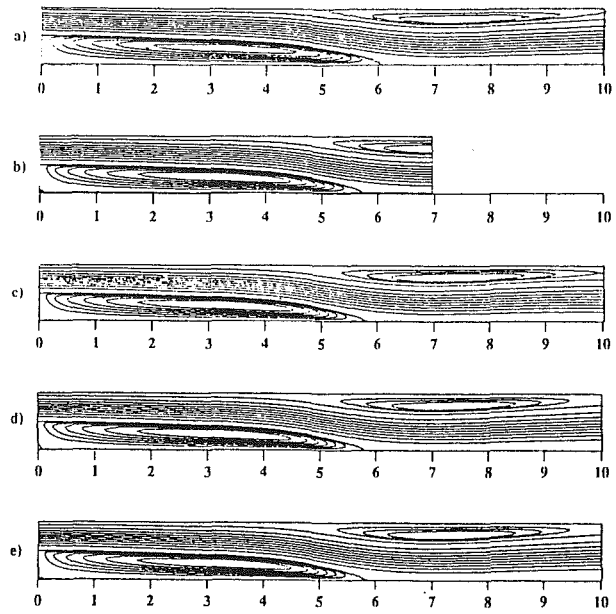

Fig. 2 Normalized streamlines. (*a*) "BM solution," (*b*) $L = 7$, (*c*) $L = 10$, (*d*) $L = 15$, (*e*) $L = 3$

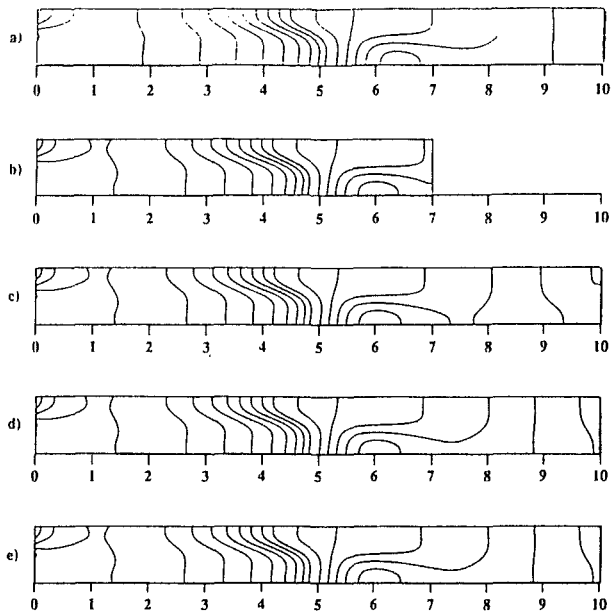

Fig. 3 Normalized pressure contours. (*a*) "BM solution," (*b*) $L = 7$, (*c*) $L = 10$, (*d*) $L = 15$, (*e*) $L = 30$

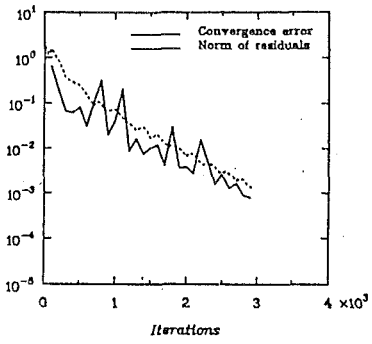

Fig. 4 Convergence error and L_2-norm of residuals of the u mom., v mom., and continuity equations

6 Incomplete Iterative Convergence

Uncertainty due to incomplete iterative convergence can be defined as the difference between the current and the exact solution of the discretized problem on the same grid. The discretized solution will never satisfy the continuous equations exactly. Therefore, there will be a point in the iterative process when further relaxation of the system of equations will not bring any additional improvement in the solution. Stopping criteria must be selected, and resulting errors from foregoing additional iterations, should be estimated. One stopping criterion, which is common in practice, is to terminate the iterative process when the difference in computed results, from one iteration to the next, falls below a pre-selected amount. Another stopping criterion is based on a measure of how well the discretized solution satisfies the discretized equations. This quantity is referred to as the residual of the discretized equation. In this method, when the residual falls below a preselected tolerance, the iterative process is terminated. However, it is not always obvious what the tolerance level should be.

Ferziger (1989) proposed to base the convergence criterion on the relative error which can be estimated as:

$$\epsilon^n \approx \frac{|\phi^{n+1}-\phi^n|_2}{\lambda_1 - 1} \tag{15}$$

λ_1 is the principal eigenvalue of the amplification matrix, which is presumed dominant and can be estimated as:

$$\lambda_1 \approx \frac{|\phi^{n+1}-\phi^n|_2}{|\phi^{n}-\phi^{n-1}|_2} \tag{16}$$

Thus the relative error depends on both the solution from iteration to iteration and the rate of convergence. If the convergence rate is slow λ_1 will be close to unity and the relative error could still be very large even with very small changes in the value of ϕ between iterates.

The convergence error was estimated for the model problem by using the u component of velocity for the general variable ϕ in Eqs. (15) and (16). The convergence error and the norm of the residuals of the u momentum, v momentum, and continuity equations are shown in Fig. 4. The latter was 2×10^{-3} when the former was about 1×10^{-3}. It appears that this is an appropriate stopping point, and both criteria appear to be equally applicable. The norm of the residuals and the convergence error have similar trends and values. This is not a surprising result, because, as pointed out by one of the reviewers, the norm of the residual can be shown analytically to be related to the convergence error. However, the main advantage of the latter is that it is computed in normalized form, whereas the normalization quantity for the residuals may not always be obvious.

7 Computational Grid Aspect Ratio

7.1 Choice of Grid-Cell Aspect Ratio. In most computational fluid flow problems, the choice of the grid-cell aspect ratio is not trivial. Convergence characteristics suggest that the aspect ratio should be of order unity, but the need to resolve boundary layers may dictate much higher aspect ratios. The natural way to carry out grid refinement is to halve the cell size in each direction, which automatically maintains the initial cell aspect ratio. What is the effect of this choice on the accuracy of computed results?

Assuming that the leading truncation error term is of second-order and that the grid spacing is sufficiently small, the functional value, ϕ, can be written as:

$$\phi = \phi_h + \frac{h_x^2}{2}\frac{\partial^2\phi}{\partial x^2} + \frac{h_y^2}{2}\frac{\partial^2\phi}{\partial y^2} + \ldots \tag{17}$$

where h_x and h_y are the grid spacing in the x and y directions, respectively.

Let the aspect ratio be defined as, $A_R = h_x/h_y$, also let $\beta = (\partial^2\phi/\partial y^2)/(\partial^2\phi/\partial x^2)$ then:

$$\phi = \phi_h + \frac{h_x^2}{2}\frac{\partial^2\phi}{\partial x^2}\left(1+\frac{\beta}{A_R^2}\right) + \ldots \tag{18}$$

The discretization error is then approximately:

$$\epsilon = \frac{h_x^2}{2}\frac{\partial^2\phi}{\partial x^2}\left(1+\frac{\beta}{A_R^2}\right) \tag{19}$$

For the same total number of grid points, refinement may be applied selectively in the x or y-direction. The choice would produce a change in the cell-aspect ratio. For example, if h_y is reduced by a factor m, with h_x $(=h)$ unchanged, A_R will be increased by the factor m. Then the discretization error would be approximately:

$$\epsilon_1 = \frac{h^2}{2}\frac{\partial^2\phi}{\partial x^2}\left(1+\frac{\beta}{m^2A_R^2}\right) \tag{20}$$

On the other hand, if h_y is unchanged while h_x is reduced by a factor m so that $h_x = h/m$ and A_R is also reduced by a factor m, the error is:

$$\epsilon_2 = \frac{h^2}{2}\frac{\partial^2\phi}{\partial x^2}\left(\frac{1}{m^2}+\frac{\beta}{A_R^2}\right) \tag{21}$$

The ratio of the errors is then:

$$\frac{\epsilon_1}{\epsilon_2} = \frac{1+\dfrac{\beta}{m^2A_R^2}}{\dfrac{1}{m^2}+\dfrac{\beta}{A_R^2}} = \frac{\dfrac{A_R^2}{\beta}+\dfrac{1}{m^2}}{\dfrac{A_R^2}{m^2\beta}+1} \tag{22}$$

The implication of this result is that:

$$\frac{\epsilon_1}{\epsilon_2} = 1, \text{ if } A_R^2 = \beta; \text{ and } \frac{\epsilon_1}{\epsilon_2} < 1, \text{ if } A_R^2 < \beta;$$

$$\text{and } \frac{\epsilon_1}{\epsilon_2} > 1, \text{ if } A_R^2 > \beta \tag{23}$$

Therefore the limiting cell aspect ratio for selective grid refinement is $\sqrt{\beta}$, or $\sqrt{(\partial^2\phi/\partial y^2)/(\partial^2\phi/\partial x^2)}$. So long as $A_R < \sqrt{\beta}$ grid refinement in the y-direction leads to more effective error reduction than in the x-direction. If $A_R > \sqrt{\beta}$ further grid refinement in the y-direction becomes less effective than that in the x-direction. In boundary-layer type flows $\beta \gg 1$, so the optimum value of $A_R > 1$. But in separated flows with no preferred direction $\beta \sim 1$ and the optimum A_R will also be about 1. Thus, the optimum value of A_R can be obtained simply from an estimate of β. This condition can be applied globally or locally.

7.2 Application to Model Problem. To test this hypothesis, computations of the model problem were made on several grids with cell aspect ratios in the range of 0.625 to 10.0. It

Table 6 Points of zero wall shear stress

Grid	Grid Size	Aspect ratio	1st Top (%[a])	1st Bot
5	258×18	0.625	—[b]	—[b]
1	258×34	1.25	4.64 (4.3)	5.88 (3.6)
6	258×66	2.5	4.80 (1.0)	6.05 (0.8)
7	258×130	5	4.84 (0.2)	6.08 (0.3)
8	258×258	10	4.84 (0.2)	6.09 (0.2)
BM	—	—	4.85	6.10

(*a*) Percent difference between value and benchmark solution.
(*b*) Solution not converged.

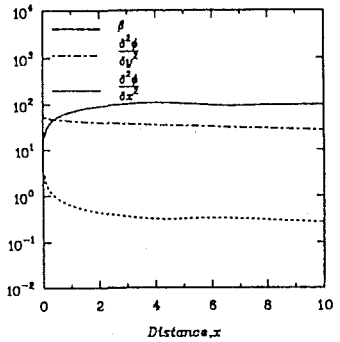

Fig. 5 Estimate of β based on L_2 norms of $\partial^2\phi/\partial x^2$ and $\partial^2\phi/\partial y^2$

was difficult to get converged solutions on coarser grids because of wiggles generated by the well-known "odd-even" decoupling problem. The results are presented in Table 6. The results show improved agreement with the benchmark solution with refinement in the y-direction corresponding to increased aspect ratio. This confirms the analysis for large β. The deviation from the benchmark was reduced each by a factor of 4, for grids 1 to 6 and 6 to 7, simply by halving the cell-size in the y-direction. For a second-order scheme, such a reduction would normally be expected from halving of the cell size in both directions. Clearly, the y-component of the truncation error is dominant and selective refinement in this direction is more cost effective than a global refinement. An estimate of the value of β based on the L_2 norm of results computed on grid 1 is shown in Fig. 5. The variation in x is based on the integration of the result from $x=0.05$. β is equal to 100, which implies that the optimum aspect ratio should be 10, in rough agreement with the present theory.

8 Concluding Remarks

Various sources of uncertainty in numerical computations of fluid flow have been examined. Specific estimates of numerical error magnitudes were computed with reference to a two-dimensional separated flow problem. Truncation error in numerical schemes can be estimated by comparing solutions from low and higher-order schemes. The effect of outflow boundary conditions can be estimated by varying systematically the location of the outflow boundary without changing the grid distribution or the numerical scheme. Discretization errors can be estimated by making computations on related grids with varying degrees of fineness and using Richardson extrapolation method. The solution can then be improved. The method can also be used to determine the global order of accuracy of a numerical method. The uncertainty in computed results due to incomplete convergence of the iterative scheme can be removed by computing an estimate of the convergence error and using this as a stopping criterion rather than the more widely used change in computed results between iterates. Grid aspect ratio effects on the solution are also important. Higher aspect ratios are more effective in generating accurate solutions in separated flows with elongated regions with boundary layer character. A method is presented for estimating the optimum cell aspect ratio for use in more general flow situations.

Acknowledgment

This research was supported by the National Aeronautics and Space Administration under NASA contract NAS1-18605 while the authors were in residence at ICASE, NASA Langley Research Center, Hampton, VA 23665. Computations were performed on Cray computers at the center.

References

Churchill, S. W., Chao, P., and Ozoe, H., 1981, "Extrapolation of Finite-Difference Calculations of Laminar Natural Convection in Enclosures to Zero Grid Size," *Numerical Heat Transfer*, Vol. 4, pp. 39–51.

Dang, A. L., Kehtarnavaz, H., and Coats, D. E., 1989, "The Use of Richardson Extrapolation in PNS Solutions of Rocket Nozzle Flow," AIAA Paper 89-2985.

de Vahl Davis, G., 1983, "Natural Convection of Air in a Square Cavity: A Bench Mark Numerical Solution," *International Journal for Numerical Methods in Fluids*, Vol. 3, pp. 249–264.

Demuren, A. O., and Wilson, R. V., 1992, "Estimating Uncertainty in Computations of Two-Dimensional Separated Flows," ICASE Report 92-69.

Ferziger, J. H., 1989, "Estimation and Reduction of Numerical Error, Forum on Methods of Estimating Uncertainty Limits in Fluid Flow Computations," ASME Winter Annual Meeting, San Francisco, CA.

Gartling, D. K., 1990, "A Test Problem for Outflow Boundary Conditions—Flow Over a Backward Facing Step," *International Journal for Numerical Methods in Fluids*, Vol. 11, pp. 953–967.

Richardson, L. F., 1911, "The Approximate Arithmetical Solution by Finite Differences of Physical Problems," *Philosophical Transactions of the Royal Society of London Serial A*, Vol. 210, pp. 307–357.

Richardson, L. F., and Gaunt, J. A., 1927, "The Deferred Approach to the Limit," *Philosophical Transactions of the Royal Society of London Serial A*, Vol. 226, pp. 299–361.

Patankar, S. V., and Spalding, D. B., 1972, "A Novel Finite Difference Formulation for Differential Expressions Involving both First and Second Derivatives," *International Journal for Numerical Methods in Fluids*, Vol. 4, pp. 551–559.

Zing, D. W., 1991, "Viscous Airfoil Computations Using Richardson Extrapolation," AIAA Paper 91-1559.

Optimum Suppression of Fluid Forces Acting on a Circular Cylinder

H. Sakamoto
Professor.
Department of Mechanical Engineering,
Kitami Institute of Technology,
Kitami, 090, Japan

H. Haniu
Associate Professor.
Department of Mechanical Engineering,
Kitami Institute of Technology,
Kitami, 090, Japan

The objective of this paper is to investigate the suppression of the fluid forces acting on a circular cylinder (hereafter called the main cylinder) by controlling the flow around it. Flow control was established by introducing a fine circular cylinder (hereafter called the control cylinder) near the main cylinder. Measurements were carried out with variation of the position of the control cylinder in the ranges of $G/d = 0.004 \sim 0.20$ (G is the gap between main cylinder and control cylinder, d is diameter of main cylinder) and $\alpha = 0 \sim 180$ deg (α is the angle along circumference from the front stagnation point of main cylinder) at a Reynolds number of 6.5×10^4. Subsequently, the steady and unsteady fluid forces, vortex shedding frequency and flow pattern were systematically examined. Furthermore, such matters as the mechanism of the flow control, the nature of the controlled wake, the relationship between the characteristics of the controlled fluid forces, and the behavior of the flow were discussed in detail on the basis of the obtained results regarding fluid forces, vortex shedding frequency and flow pattern.

1 Introduction

The study of the suppression of the fluid forces and vortex shedding over a circular cylinder has received much attention, since practical application is expected in various areas of engineering. Many methods have been developed to reduce the fluid forces and to suppress vortex shedding over a circular cylinder, and some of these have been successful (Zdravkovich, 1981). Recently, Strykowski and Sreenivasan (1990) reported that vortex shedding can be suppressed almost completely by simply inserting a small cylinder in the separated shear layer. The work of Strykowski and Sreenivasan was carried out in the range of Reynolds numbers less than $Re = 120$. The formation mechanism of vortices formed by the alternating rolling-up of separated shear layers is considered to be virtually the same for any bluff body and any Reynolds number. Therefore, it is assumed that the reduction of fluid forces by suppression of vortex shedding, as achieved by Strykowski and Sreenivasan, is quite possible over the circular cylinder even at large Reynolds numbers. Quite recently, Sakamoto et al. (1991) investigated the reduction of the time-averaged drag and the fluctuating lift and drag, acting on a square prism with the introduction of a small circular cylinder in a manner similar to that of Strykowski and Sreenivasan. They found that the maximum reduction of the time-averaged drag is 30 percent, and the maximum reduction in the fluctuating lift and drag are approximately 95 and 75 percent respectively. Thus, it is obvious that such methods are very effective to control the flow around a bluff body. However, the nature of the controlled flow, i.e., the structure of the wake, the behavior of the boundary layer and separated shear layer, and the stability of the controlled flow, is not yet fully clarified. Further work is required for a better understanding of this method.

The aim of the present work is to reduce the fluid forces acting on a circular cylinder at comparatively large Reynolds numbers with the introduction of the control cylinder near the main cylinder. The position of the control cylinder was changed systematically, and then the steady and unsteady fluid forces were examined in order to estimate the magnitude of the reduction of the forces and to identify the optimum position of the control cylinder. Furthermore, the mechanism of the flow control, the structure of the controlled wake, and the behavior of the controlled boundary layer and the separated shear layer were discussed in detail on the basis of the obtained vortex shedding pattern and visualized wake flow pattern. Subsequently, the applicability of the present method in reducing the fluid forces and suppressing the vortex shedding was evaluated.

2 Experimental Arrangement and Procedures

The experiments were carried out in a low speed, closed-circuit wind tunnel. The test section of the tunnel was rectangular, with a height of 0.6 m, a width of 0.4 m, and a length of 5.4 m. Two types of circular cylinders were used for the experiment: one cylinder with two load cell was used to measure the fluid forces, and the other cylinder was equipped with pressures tap of 0.8 mm diameter was used to measure the static pressure on the cylinder surface. Both cylinders had a

Contributed by the Fluids Engineering Division for publication in the JOURNAL OF FLUIDS ENGINEERING. Manuscript received by the Fluids Engineering Division September 22, 1993; revised manuscript received October 21, 1993. Associate Technical Editor: Ho, Chih-Ming.

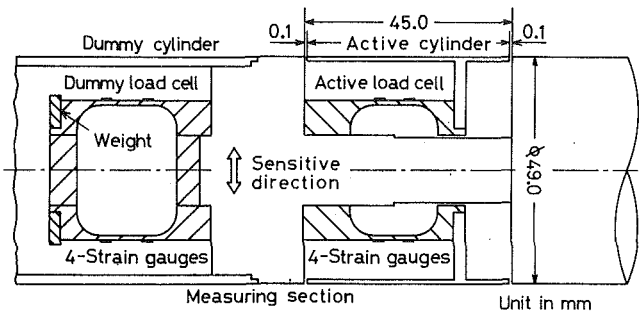

Fig. 1 Arrangement of load cell installed inside of the main cylinder

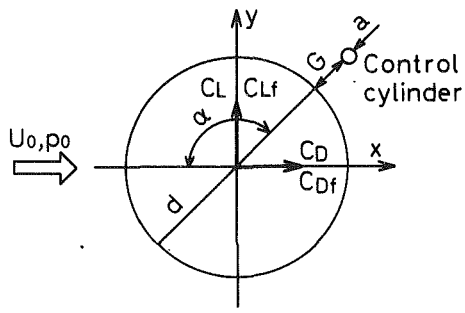

Fig. 2 Definition sketch and coordinate system

diameter of 49 mm and a length of 400 mm, in order to span the width of the test section. The circular cylinder used for the measurement of fluid forces, consisted of an active section and a dummy section as shown in Fig. 1. The load cells, on which four semiconductor strain gauges were attached were installed inside the main cylinder. The load cell installed inside the active section measured the combination of the fluid forces and other forces caused by the vibrations transmitted through the cylinder support. The load cell installed inside the dummy section measured only the forces caused by the vibrations transmitted through the cylinder support. Therefore, by subtracting the output of the load cell installed inside the dummy section from that of the load cell installed inside the active section, the fluid forces acting on the active cylinder only could be measured. The spanwise length of the active cylinder was 45 mm (0.92 of diameter of circular cylinder). This size was determined by taking into account the cross-correlation lengths of the fluctuating pressure in the spanwise direction of the cylinder surface, which were found to be (1.3 ~ 2.0)d (Surry, 1972), and (1.0 ~ 1.60)d (Batham, 1973). If the length of the active cylinder were to exceed these values. the load cell would not measure the correct fluctuating forces, because the fluctuating pressures are not always in phase at arbitrary distances in the spanwise direction. The natural frequency of the load cell was about 960 Hz. This value satisfied So and Savaker's criterion (So and Savakar, 1981), which requires the natural frequency of the load cell to be at least four times the frequency of the dominant force. The diameter of the control cylinder used in the present experiment was 3 mm. The control cylinder was set in tension at one side of the main cylinder as shown in Fig. 2. The vibrations of the control cylinder were not generated during measurements.

Experiments were carried out at a constant free-stream velocity $U_0 = 20$ m/s. The position of the control cylinder was varied in the range of $G = 0.2 \sim 10$ mm ($G/d = 0.004 \sim 0.20$) and $\alpha = 0 \sim 180$ deg. The corresponding Reynolds number, Re ($= U_0/d/\nu$), was 6.5×10^4. The turbulent intensity of the free-stream was below 0.2 percent. The flow in the axial plane through the mid-section of the cylinder was visualized by using smoke. Important symbols and the definition of the coordinate system used in the present study are shown in Fig. 2. The blockage effect of the test cylinder was 8.2 percent, and no corrections were made for it.

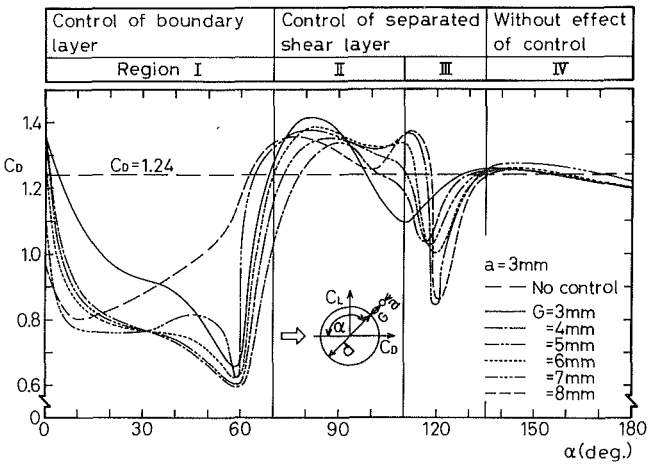

Fig. 3 Distribution of the time-averaged drag coefficient for different positions of the control cylinder. (Uncertainty in C_D: less than ±3 percent, in α: less than ±0.5 degree.)

3 Results and Discussions

3.1 Classification of Control Effects. Figure 3 shows the values of the time averaged drag coefficient C_D, which is defined by $C_D = D/(0.5\rho U_0^2 A)$, as a function of the position of the control cylinder. From these results, the distribution of the time-averaged drag coefficient due to the difference in the

Nomenclature

A = projected area of the active cylinder
C_D = time-averaged drag coefficient $= D/(0.5\rho U_0^2 A)$
C_{Df} = r.m.s.drag coefficient $= \sqrt{\overline{D_f^2}}/(0.5\rho U_0^2 A)$
C_L = time-averaged lift coefficient $= L/(0.5\rho U_0^2 A)$
C_{Lf} = r.m.s. lift coefficient $= \sqrt{\overline{L_f^2}}/(0.5\rho U_0^2 A)$
D = time-averaged drag acting on the active cylinder
D_f = fluctuating drag acting on the active cylinder
G = gap width between the main cylinder and the control cylinder
L = time-averaged lift acting on the active cylinder
L_f = fluctuating lift acting on the active cylinder
U_0 = free-stream velocity
a = diameter of the control cylinder
d = diameter of the main cylinder
p = time-averaged pressure acting on the surface of main cylinder
p_0 = static pressure of free-stream
x, y = Cartesian coordinate system (see Fig. 2)
α = position of the control cylinder measured along the circumference from front stagnation point of the main cylinder
θ = position of piezometric hole measured along the surface of the main cylinder
ρ = density of the fluid

setting angle α of the control cylinder is roughly classified into four regions, in accordance with the phenomenological mechanisms of the control. Region I is the range of 0 deg $< \alpha <$ 70 deg, in which the drag decreases, region II is the range of 70 deg $< \alpha <$ 110 deg, in which drag increases, region III is the range of 110 deg $< \alpha <$ 135 deg, in which the drag decreases, and region IV is the range of 135 deg $< \alpha <$ 180 deg, in which the drag is not varied. In region I, the effectiveness of the control cylinder is attributed to the control of the boundary layer on the main cylinder. In region II and III, the effectiveness of the control cylinder is attributed to the control of the free shear layer.

Figures 4(*a*) and (*b*) show the distributions of the surface pressure on the main cylinder. It can be seen in Fig. 4(*a*) that in region I the separation point is displaced downstream, from a position in front of the location $\theta = 90$ deg to a location a little downstream. This is due to the transition from laminar to turbulent flow along the surface of the main cylinder. Waka and Yoshino (1987) have investigated the flow around a circular cylinder with variation of the velocity and position of tangential blowing from a surface slot. Based on the measurements of the surface pressure distributions, they demonstrated that a large reduction in the time-averaged drag is due to the displacements of the separation points. Therefore, from the change of the surface pressure distributions in the region I as shown in Fig. 4(*a*), it can be concluded that the mechanism of the flow control by means of the present method is similar to that of tangential blowing from a surface slot. Furthermore, when the control cylinder is located at $\alpha = 63$ deg as shown in Fig. 4(*a*), the generation of the two flow patterns can be recognized from the existence of two different distributions of the surface pressure. The generation of the two flow patterns occurs in the vicinity of the boundary between regions I and II. These appear in the form of a bistable flow pattern, in which each pattern lasts a short period of time and in the form of an unstable flow pattern, in which each pattern appears alternately at very short intervals.

Next, in region II, the C_D increases considerably compared with that in the case without the control cylinder. This is due to the fact that the shear layer separated from the main cylinder is forced to bend by the control cylinder. The rolling-up of the shear layer is intensified, and the base pressure increases. In region III, as shown in Fig. 4(*b*), the shear layer which separates near $\theta = 90$ deg is forcibly reattached near $\theta = 130$ deg, and the reattached shear layer then adheres until near the rear stagnation point, so that the base pressure decreases. Also, as will be discussed later, when the control cylinder is located in the vicinity of the boundary between regions II and III, and region III and IV, two types of flow patterns are generated in the form of a bistable and an unstable flow pattern respectively. The C_D in region IV does not change because the control cylinder is located in the wake of the main cylinder.

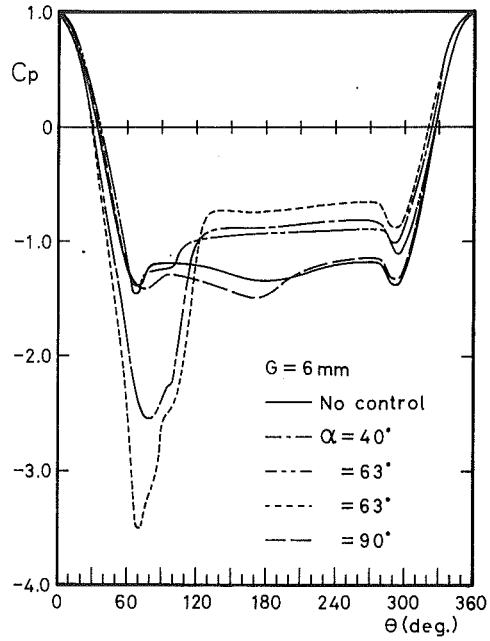

Fig. 4(*a*)

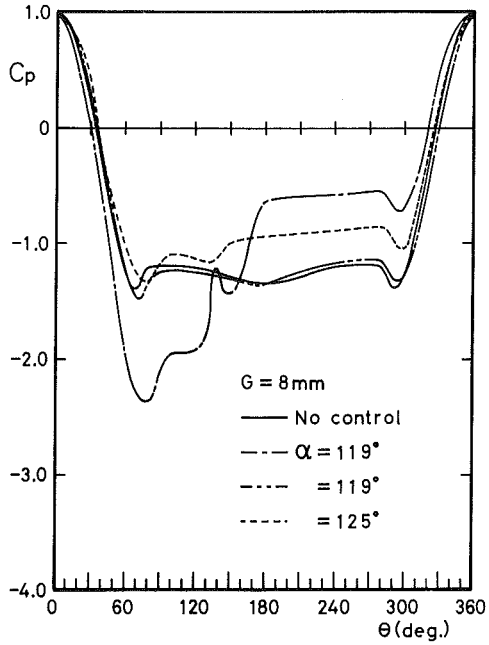

Fig. 4(*b*)

Fig. 4 Distribution of the time-averaged pressure coefficient for different positions of the control cylinder. (Uncertainty in C_p: less than ±2 percent, in θ: less than ±0.5 degree.)

3.2 Control of Time Averaged Drag and Lift. Figures 5 and 6 show the time-averaged drag coefficient C_D and lift coefficient C_L, when the gaps between the two cylinders G and the angle α vary in the ranges of $G = 0.2 \sim 10$ mm ($G/d = 0.004 \sim 0.02$) and $\alpha = 0 \sim 180$ deg. All results are presented in the form of contour diagrams which were obtained by interpolation between the measured values. The results of C_D are expressed as multiples of $C_D = 1.28$, which is the value of the main cylinder without the control cylinder, in order to quantify the effect of control.

First, C_D provides minimum values when the control cylinder is located near $\alpha = 60$ deg and near $\alpha = 120$ deg. In particular, the time-averaged drag is reduced to about 50 percent when the control cylinder is located near $\alpha = 60$ deg. In this case, the maximum reduction is caused by the displacement of the separation point due to the transition from a laminar to a turbulent boundary layer along the upper surface on the side where the control cylinder is set up. To reduce C_D by controlling the boundary layer of the cylinder surface, the tripping wire method, in which a small wire is attached to the cylinder's surface, has been available. The maximum reduction of C_D by the tripping wire method was about 30 percent (James and Troung, 1972) under the condition, at which the Reynolds number and the ratio of the main cylinder diameter to that of the control cylinder are the same as those of the present experiment. Next, when the control cylinder is located near $\alpha = 120$ deg, the time-averaged drag is reduced to about 30 percent as shown in Fig. 5. Igarashi and Tsutsui (1989) carried out detailed investigations on the control of the shear layer separated from a circular cylinder when the control cylinder was located near

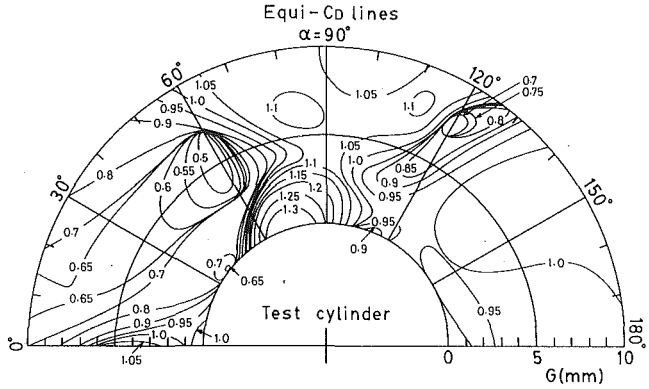

Fig. 5 Equi-line diagram of the time-averaged drag coefficient. (Uncertainty in C_D: less than ±3 percent, in G: less than ±0.05 mm, in α: less than ±0.5 degree.)

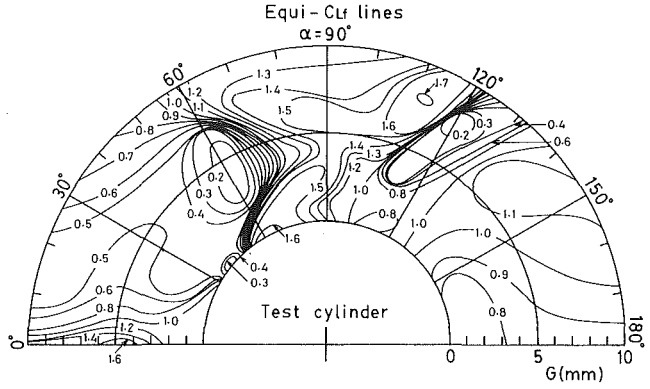

Fig. 7 Equi-line diagram of the fluctuating lift coefficient. (Uncertainty in C_{Lf}: less than ±3 percent, for further information, see the caption of Fig. 5.)

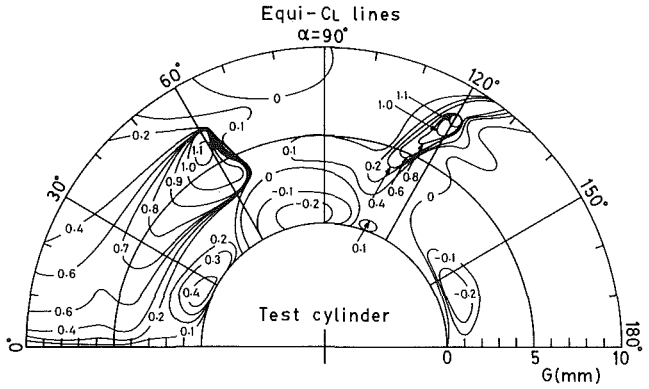

Fig. 6 Equi-line diagram of the time-averaged lift coefficient. (Uncertainty in C_L: less than ±3 percent, for further information, see the caption of Fig. 5.)

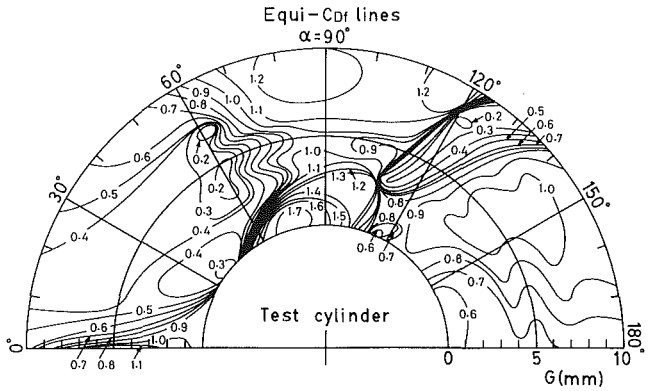

Fig. 8 Equi-line diagram of the fluctuating drag coefficient. (Uncertainty in C_{Df}: less than ±3 percent, for further information, see the caption of Fig. 5.)

$\alpha = 120$ deg. In their investigation, even if the diameter ratio of the cylinders is 0.05, which is smaller than the value 0.06 of the present experiment, an almost identical reduction of 30 percent was obtained. Similar measurements were carried out in the present experiment for a control cylinder of d = 1 mm diameter ratio: 0.02), and maximum reduction values of approximately 50 and 30 percent were obtained near $\alpha = 60$ and 120 deg, respectively.

We tried to estimate the total reduction rate of the drag, combining the drag of the control cylinder with the drag of the main cylinder since the control cylinder itself generates drag. To estimate the drag of the control cylinder, we adopted the actual velocity at the outer boundary of the separated shear layer as the velocity which approaches the control cylinder and 0.95 ($\mathrm{Re} = 5 \times 10^3$) as the drag coefficient. As a result, the drag of the control cylinder was estimated to be about 10 percent of that of the main cylinder. The total drag of two cylinders can be reduced by a maximum of 40 percent from the drag of an uncontrolled main cylinder when the control cylinder is located near $\alpha = 60$ deg and 20 percent near $\alpha = 120$ deg.

Next, the time-averaged lift coefficient C_L takes a maximum value when C_D becomes minimum near $\alpha = 60$ deg and near $\alpha = 120$ deg. These maximum values of C_L are caused by the following effects: near $\alpha = 60$ deg, the separation point of the boundary layer is greatly moved backward due to the accelerated gap flow between the cylinders, and near $\alpha = 120$ deg, the reattached shear layer on the main cylinder surface adheres until near the rear stagnation point. As a result, a large lift force of upward direction is generated, because the negative pressure on the upper-side surface is considerably larger than that of the lower-side surface.

3.3 Control of Fluctuating Fluid Forces and Vortex Shedding. Figures 7 and 8 show the r.m.s. values of the fluctuating lift coefficient C_{Lf} and the fluctuating drag coefficient C_{Df}, which are defined by the following equation: C_{Lf}, $C_{Df} = [\sqrt{\overline{L_f^2}}, \sqrt{\overline{D_f^2}}]/(0.5\rho U_0^2 A)$. All the results are reduced by the corresponding values of the undisturbed main cylinder, namely $C_{Lf} = 0.46$ and $C_{Df} = 0.12$. The fluctuating lift and drag are mostly suppressed when the control cylinder is located at the region of $G = 3 \sim 7$ mm, near $\alpha = 60$ deg and $G = 7 \sim 8$ mm, near $\alpha = 120$ deg, and then the maximum reductions of C_{Lf} and C_{Df} are approximately 85 percent. When the control cylinder is placed at these locations, it is possible to suppress the vortex shedding completely because the fluctuating lift and drag are virtually not generated.

Next, when the control cylinder is located in the region between $\alpha = 70$ deg and $\alpha = 110$ deg, the fluctuating fluid forces increase, and then the rate of increase in C_{Lf} and C_{Df} reaches values as high as 70 percent. As stated above, this is due to fact that the separated shear layer is forcibly bent by the control cylinder so that the rolling-up of the shear layer is intensified. When the control cylinder is located beyond $\alpha = 150$ deg, C_{Lf} and C_{Df} are considerably reduced. This suggests that the flow characteristics in the vortex formation region, where the alternate vortex shedding is created, namely the concentration of vorticity, the counterbalance of vorticity and inverse flow, change considerably due to the presence of the control cylinder.

Figure 9 shows the power spectrum of the fluctuating lift. When the control cylinder is located in the region near $\alpha = 60$ deg, where the fluctuating fluid forces are considerably reduced from the existence of a clear spectral peak as shown in Fig.

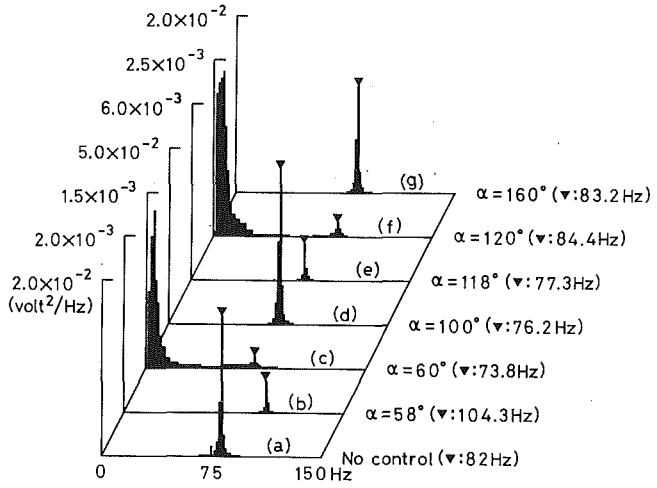

Fig. 9 Power spectrum of fluctuating lift

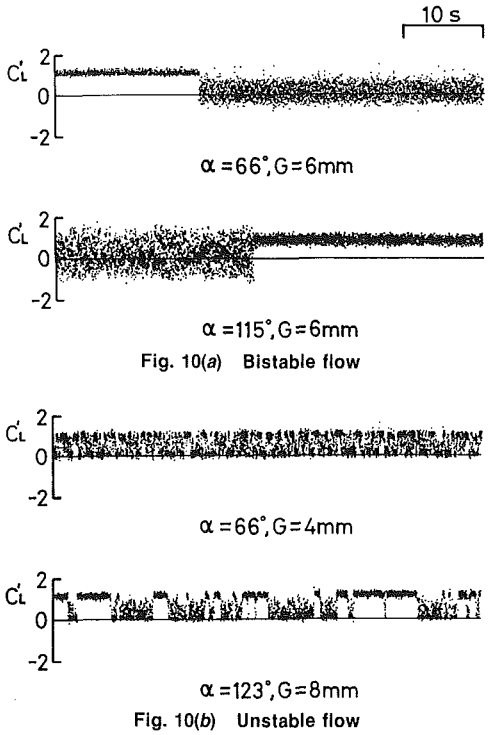

Fig. 10(*a*) Bistable flow

Fig. 10(*b*) Unstable flow

Fig. 10 Waveform of fluctuating lift for bistable and unstable flow

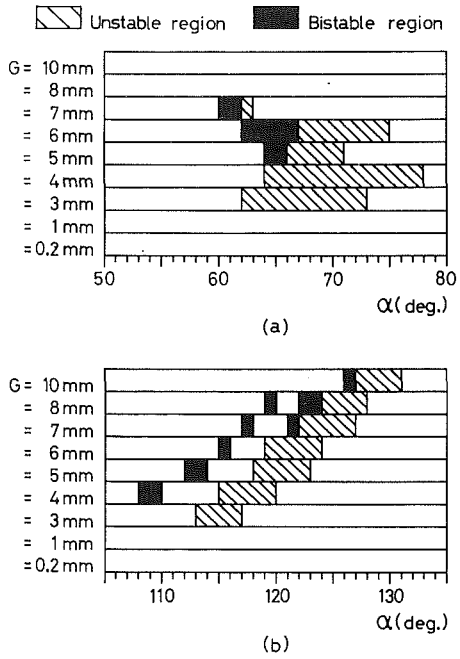

Fig. 11 Domain of bistable and unstable flow. For further information, see the caption of Fig. 5.

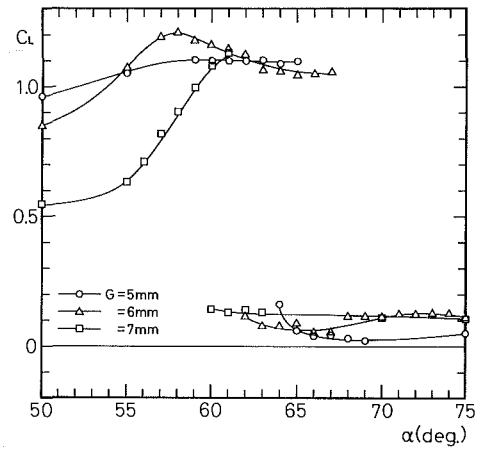

Fig. 12 Lift coefficient C_L when bistable flow occurs (near $\alpha = 60$ deg). For further information, see the caption of Fig. 6.

9(*b*), we can recognize that alternative vortex shedding has occurred. In this region, vortex shedding occurs with fairly high frequency. Thus, the wake fluctuation width is to be decreased substantially. Next, when the control cylinder is located at $\alpha = 60$ deg and $\alpha = 120$ deg, which provides the minimum fluctuating fluid forces, clear spectral peaks are almost absent as shown in Figs. 9(*c*) and (*f*). Thus, alternate vortex shedding is essentially suppressed. Finally, when the control cylinder is located within the wake of the main cylinder, a clear spectral peak is observed as shown in Fig. 9(*g*). However, the energy and frequency of the spectral peak are somewhat different from that without the control cylinder.

3.4 Generation of Bistable and Unstable Flow. As described in section 3.1, when the control cylinder is located near $\alpha = 60$ deg and near $\alpha = 120$ deg, two flow patterns develop in the form of bistable and unstable flow respectively. In this section, the relation between fluid forces and the flow patterns generated in these regions are clarified. Figures 10(*a*) and (*b*) show the waveforms of the fluctuating lift acting on the main cylinder when the control cylinder is located near $\alpha = 60$ deg and $\alpha = 120$ deg, respectively. It can be recognized that two kinds of the fluctuating lift are generated in the form of bistable flow, in which each waveform lasts for a length of time as shown in Fig. 10(*a*), and in the form of unstable flow, in which each waveform appears alternately at very short intervals as shown in Fig. 10(*b*), clearly indicating the generation of two flow patterns. The judgment of distinction between the bistable flow and unstable flow was based on the following guideline: if an identical flow pattern continued for more than 1000 cycles (one fluctuation by a pair of vortex shedding is defined as one cycle), it was designated as bistable flow, and if less than 1000 cycles, it was designated as unstable flow. Figures 11(*a*) and (*b*) show the positions of the control cylinder which corresponds to bistable and unstable flow. It is found that two flow patterns, forming bistable or unstable flow, correspond to the region of $G = 3$ mm to 7 mm when the control cylinder is located near $\alpha = 60$ deg, and in the region of $G = 3$ mm to 10 mm when the control cylinder is located near $\alpha = 120$

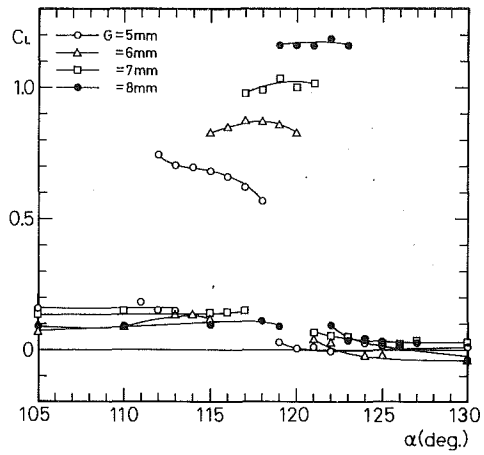

Fig. 13 Lift coefficient when bistable flow occurs (near $\alpha = 120$ deg). For further information, see the caption of Fig. 6.

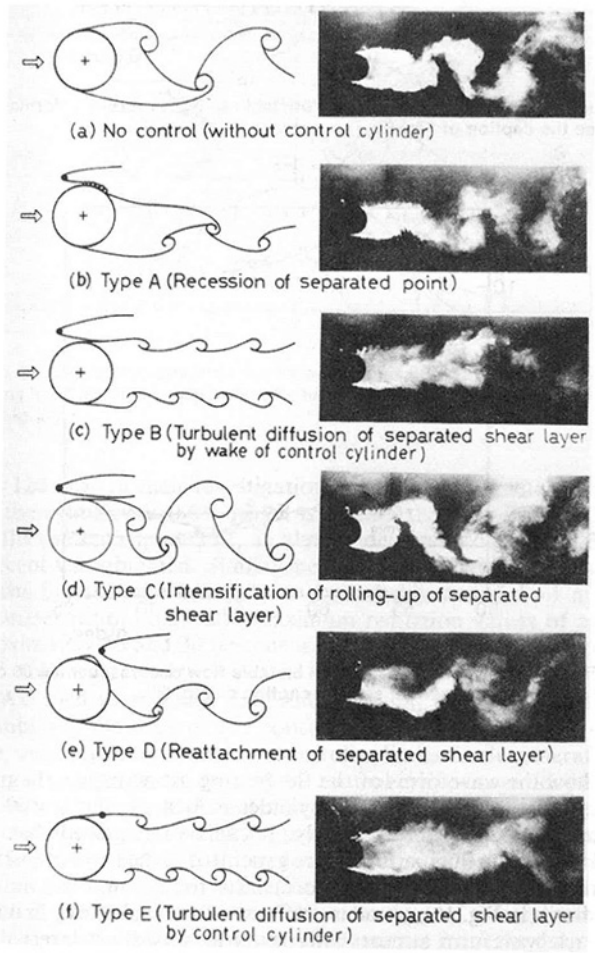

Fig. 14 Smoke patterns and schematic representation of wake flow for different positions of the control cylinder

deg. Accordingly, in these regions, two different values in the time-mean lift and drag, and the fluctuating lift and drag develop with the generation of two flow pattern.

Figures 12 and 13 show the time-averaged lift coefficient corresponding to the two flow patterns. Figure 14 also shows the observed smoke patterns and the configuration of the wake flow patterns. Here, the two values for only the bistable flow are presented, because the estimation of C_L is difficult for the unstable flow. First, when the control cylinder is located near $\alpha = 60$ deg, one of the two flow patterns is one in which the recession of the separated point of the boundary layer along the upper-side surface occurs as shown in Fig. 14 (*b*) (Type A). The pressure distribution on the upper and lower surfaces of the main cylinder is fairly asymmetrical, so that a large C_L develops. Also, minimum values develop for each C_D, C_{Lf}, and C_{Df} due to the suppression of the vortex shedding. The other pattern is one in which no interaction occurs between the upper and lower-side shear layer, due to the turbulent diffusion of the shear layer caused by the interference with the wake of the control cylinder as shown in Fig. 14(*c*) (Type B). In this case, the flow on the upper and lower-side is relatively symmetrical, so that the value of C_L is small, and C_D, C_{Lf}, and C_{Df} decrease substantially. As shown in Fig. 11(*b*), for example, these two patterns are generated in the form of the bistable flow at $\alpha = 52$ deg to 67 deg and in the form of the unstable flow at $\alpha = 67$ to 75 deg when the gap between two cylinders is 6 mm.

Next, when the control cylinder is located near $\alpha = 120$ deg, the bistable and unstable flow are generated in a form of the combination of two flow patterns among three flow patterns as shown in Figs. 14(*d*), (*e*) and (*f*). One of the flow patterns is one in which the separated shear layer is forced to bend by the control cylinder, so that its rolling-up is intensified as shown in Fig. 14(*d*) (Type C). In this case, the value of C_L is small, but the values of C_D, C_{Lf}, and C_{Df} increase as compared to those without the control cylinder. The next pattern is one in which the separated shear layer on the upper-side is forcibly reattached, so that the reattached shear layer adheres until near the rear stagnation point as shown in Fig. 14(*e*) (Type D). In this case, the value of C_L is large but those of C_D, C_{Lf}, and C_{Df} greatly decrease due to the suppression of the vortex shedding. In this last pattern no interraction occurs between the upper and lower-side shear layer because the growth and strength of the rolling-up of the shear layer on the upper-side is prevented by the control cylinder as shown in Fig. 14(*f*) (Type E). In this pattern, the vortex shedding is suppressed, and then C_D, C_{Lf} and C_{Df} are substantially reduced.

4 Conclusions

This objective of this paper was to investigate the suppression of the fluid forces acting on a circular cylinder by introducing a fine circular cylinder around the flow. The main results of the present study may be summarized as follows:

(1) The effect of the present method for suppressing the fluid forces is classified into two categories; one is due to the control of the boundary layer along the surface of the circular cylinder; the other is due to the control of the shear layer separated from its surface.

(2) The greatest reduction of the time-mean drag and the fluctuating lift and drag occurs when the control cylinder is located at two regions, i.e., $G = 3$ to 7 mm and near $\alpha = 60$ deg, and $G = 7$ to 8 mm and near $\alpha = 120$ deg. The maximum reduction of the time-averaged drag is 50 percent, and the maximum reduction in the fluctuating lift and drag is 85 percent, by using the control cylinder with a diameter of 3 mm, which is considerably smaller than the main cylinder with a diameter of 49 mm.

(3) The wake flow pattern due to the difference in position of the control cylinder is found to be classified roughly into five patterns. Furthermore, the relation between the behavior of the controlled wake flow and the characteristics of the controlled fluid forces is clarified.

(4) When the control cylinder is located near $\alpha = 60$ deg and $\alpha = 120$ deg, where the largest reduction of the time-mean drag and the fluctuating lift and drag occur, the two flow patterns are found to be generated with either the form of the bistable

flow, in which each flow pattern lasts a certain period of time, or the unstable flow, in which the duration of the existence of each flow pattern is very short.

Acknowledgment

The authors express their sincere thanks to Mr. Y. Obata of the Department of Mechanical Engineering, Kitami Institute of Technology, for his assistance in the construction of the experimental apparatus.

References

Batham, J. P., 1973, "Pressure Distributions on Circular Cylinders at Critical Reynolds Numbers," *Journal of Fluid Mechanics*, Vol. 57, Part 2, pp. 209–228.

James, D. F., and Troung, Q. S., 1972, "Wind Load on Circular with Spanwise Protrusion," Proc. ASCE, *Journal of Engineering Mechanics*, Vol. 98, No. EM6, pp. 1593–1589.

Igarashi, T., and Tsutsui, T., 1989, "Flow Control Around a Circular Cylinder by a New Method," *Transaction of JSME*, Vol. 55, No. 511, pp. 701–707.

Sakamoto, H., Tan, K., and Haniu, H., 1991, "An Optimum Suppression of Fluid Forces by Controlling a Shear Layer Separated from a Square Prism," Transaction of ASME, JOURNAL OF FLUIDS ENGINEERING, Vol. 113, No. 2, pp. 183–189.

So, R. M. C., and Savkar, S. D., 1981, "Buffeting Forces on Rigid Circular Cylinder in Cross Flows," *Journal of Fluid Mechanics*, Vol. 105, pp. 397–425.

Strykowski, P. J., and Sreenivasan, K. R., 1990, "On the Formation and Suppression of Vortex Shedding at Low Reynolds Numbers," *Journal of Fluid Mechanics*, Vol. 218, pp. 71–107.

Surry, D., 1972, "Some Effects of Intense Turbulence on the Aerodynamics of a Circular Cylinder at Subcritical Reynolds Number," *Journal of Fluid Mechanics*, Vol. 52, Part 3, pp. 481–563.

Waka, R., and Yoshino, F., 1987, "The Forced Reattachment of the Separated Shear Layer of a Circular Cylinder with Tangential Blowing," Transaction of JSME, Vol. 53, No. 490, pp. 1704–1710.

Zdravkovich, M. M., 1981, "Review and Classification of Various Aerodynamic and Hydrodynamic Means for Suppressing Vortex Shedding," *Journal of Wind Engineering and Industrial Aerodynamics*, Vol. 7, No. 2, pp. 145–189.

Chiang Shih
Department of Mechanical Engineering,
FAMU/FSU College of Engineering,
Florida A & M University and
Florida State University,
Tallahassee, FL 32316

Chih-Ming Ho
Mechanical, Aerospace and Nuclear
Engineering Department,
University of California, Los Angeles,
Los Angeles, CA 90024

Three-Dimensional Recirculation Flow in a Backward Facing Step

The flow field behind a small aspect ratio (channel width/step height = 3) backward-facing step is examined using laser Doppler anemometer. All three velocity components inside the separation region are surveyed in detail. The velocity profile just upstream of the step is laminar and two-dimensional. The velocity field reveals that the reattachment and the flow in the recirculation zone are highly three-dimensional due to the small aspect ratio.

1 Introduction

Flow fields associated with separation and reattachment have received significant attention because of their importance in many engineering applications. Examples include the flow behind flame holders in combustors, separated flow in diffusers, and separation bubbles on airfoils. Among these separation-reattachment configurations, the backward-facing step has been studied most extensively. A detailed review of the two-dimensional situations has been offered by Bradshaw and Wong (1972) and later by Eaton and Johnston (1981). The reattachment length, one of the important properties because it indicates the rate of mixing of the separated shear layer, has been found by Eaton and Johnston (1981) to be sensitive to many parameters, e.g., Reynolds number, background turbulence level, streamwise pressure gradient, etc. Near the reattachment region, the local turbulence intensity and Reynolds stresses reach their peak values, which can be attributed to the impingement of the unsteady shear layer onto the step's floor. The coherent structures in the shear layer were studied recently by Bhattacharjee et al. (1986) and Roos and Kegelman (1986). In a two-dimensional backward facing step with an aspect ratio of 16.24, the instantaneous velocity traces indicate that the coherent structures in the shear layer are correlated almost across the entire span (Bhattacharrjee et al., 1986).

Flow visualization by Cherdron et al. (1978) showed vortex pair structures behind a sudden expansion inside a symmetric duct. In a channel with a fully developed velocity profile before the step, Armaly et al. (1983) found multiple regions of separation downstream of the backward-facing step (aspect ratio = 18.1) on both the top and bottom sides of the channel walls. Their measurements showed that the appearance of a separation bubble on the wall opposite to the step destroyed the two-dimensionality of the flow, and wavy patterns of the spanwise separation-reattachment locations existed for both top and bottom separation bubbles. Their numerical results supported the existence of those additional separation regions. Several recent Navier-Stokes computational works (Kim and Monin, 1985 and Kaiktsis et al., 1991) also reported the appearance of a secondary separation bubble on the wall opposite to the step. This separation seems to be produced by the adverse pressure gradient imposed by the sudden expansion. Most of the existing research efforts have been focused on two-dimensional situations, though most of the realistic applications are practically dominated by three dimensional geometries. de Brederode and Bradshaw (1972) have systematically studied the side wall effects with top hat free stream velocity profile. They concluded that the three-dimensional features could be neglected if the aspect ratio of the step was larger than ten. They did observe, however, strong three-dimensional structures in their oil-film visualization for low aspect ratio cases.

In this work, we first establish the two-dimensionality of the flow before the step and then present the development of the three-dimensional features in the recirculation zone.

2 Experimental Apparatus

2.1 Water Channel. The present experiment was performed at the USC Fluid Mechanics Laboratory. A closed circuit water channel made of plexiglass was used in this investigation. The backward-facing step with a height of 19.05 mm is situated 50.8 mm downstream from the end of a two-dimensional 2.7:1 contraction. The aspect ratio (channel width/step height = W/H) is 3:1 with a channel width of 57.2 mm. The settling chamber before contraction is filled with foams and several fine mesh screens for turbulence reduction. Free stream turbulent intensity is found to be approximately 1 percent of the time-averaged velocity and this is also the limitation of the present LDA system. The whole assembly is positioned on a three-dimensional traversing mechanism. The x, y, and z coordinates are defined as the streamwise, the transverse and the spanwise directions, respectively.

2.2 Laser-Doppler Anemometer System. A single-component forward-scatter laser-Doppler anemometer (Dantec 55x modular optics system) was used for the velocity measurements and a Bragg-cell frequency shifter was employed to detect flow reversal. A counter-type processor (Dantec model no. 55L90a) translated the Doppler frequency information into velocity data which were then stored and analyzed on a PDP 11/23

Contributed by the Fluids Engineering Division for publication in the JOURNAL OF FLUIDS ENGINEERING. Manuscript received by the Fluids Engineering Division October 27, 1992; revised manuscript received March 2, 1993. Associate Technical Editor: D. M. Bushnell.

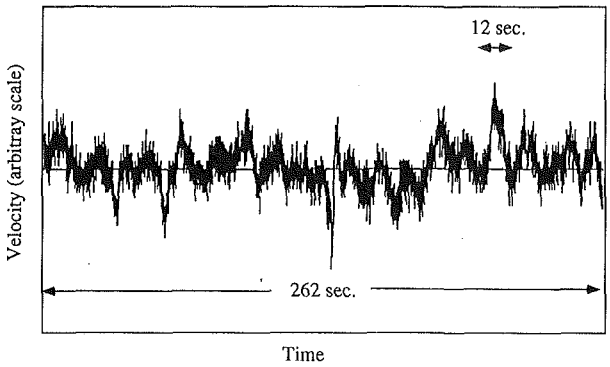

Fig. 1 Instantaneous velocity signal measured inside the separation region. The period of the most unstable shear layer instability waves is 0.5 second.

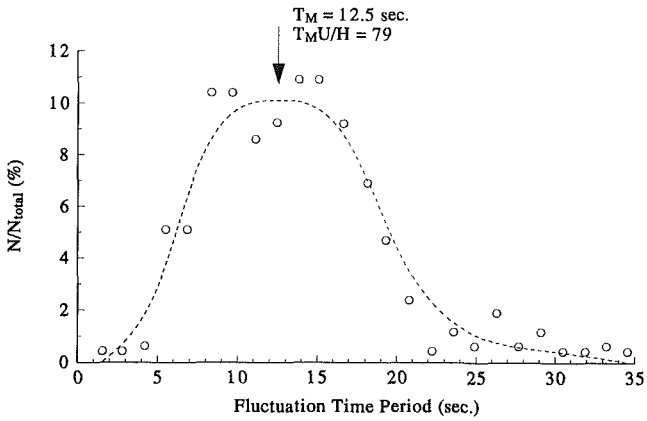

Fig. 2 Histogram of the fluctuation time period distribution inside the separation region

microcomputer. The probe volume of the present setup is approximately 0.08 mm in diameter and 0.68 mm in length along the optical axis. A 1-D residence-time weighting scheme is used to remove the LDA velocity bias. Streamwise and transverse velocity components were measured respectively by rotating the LDA optics 90 deg. The spanwise velocity was measured by turning the channel 90 deg about the streamwise axis. The Reynolds number, based on the step height and the free-stream velocity, was about 2300.

2.3 Experimental Uncertainties. The LDA system was calibrated using a rotating disk driven by a high-precision microstepping motor system. By using very long time average (more than 10 minutes) and 19,200 samples for each measurement, the estimated experimental uncertainties are 0.5 percent for the mean velocity and 1 percent for the turbulent intensity measurements. The relatively high value of the free-stream turbulence level is due to (1) the low contraction ratio of the channel, and (2) ineffectiveness of the screens, honeycombs and foams to reduce turbulence in this low velocity range. The spatial resolution of the traverse system is 0.5 mm in all three directions which is approximately 3 percent of the step height.

3 Experimental Results and Discussions

3.1 The Time Scales. Two time scales exist in this flow configuration. One is the instability frequency of the shear layer which can be determined by the free-stream velocity and the initial mixing layer thickness. In the present case, the initial instability period is 0.5 s. The other time scale is a low frequency fluctuation whose exact cause is not clear yet. This very low

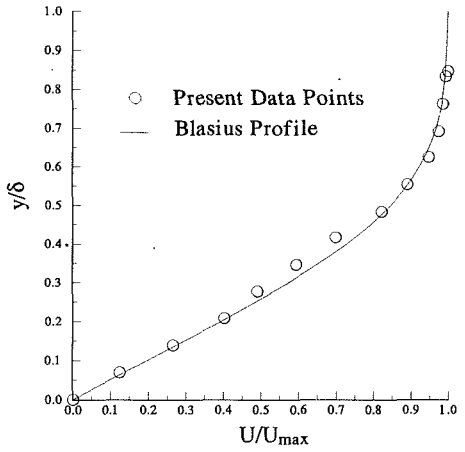

Fig. 3 Boundary layer velocity profile immediately upstream of the step

frequency fluctuation is detectable throughout the entire separation region but is clearest deep inside the recirculation zone where it receives minimum contamination from the shear layer fluctuating eddies which are at a much higher frequency range. Figure 1 shows a typical instantaneous velocity signal measured 10 mm downstream, $x/H = 0.53$, from the step and 6 mm above the step flow, $y/H = 0.31$. The low frequency fluctuations are represented by the quasi-periodic modulations which dominate the velocity trace. Superimposed on them are random turbulence and quasi-sinusoidal shear layer instability fluctuations. By examining a long record of the instantaneous velocity signals, a histogram of these low frequency fluctuation time period is presented in Fig. 2. Here N is the number of the fluctuations corresponding to time periods within a specific frequency window, and N_t is the total count of the number of fluctuations during the entire sample time. The estimated uncertainty in determining the fluctuation period is approximately 1 second. The total sample time for constructing this histogram is approximately half an hour, and N_t equals 140. A peak can be identified at $T_M \simeq 12.5$ s, which is about 25 times longer than the shear layer initial instability wave periods. A long tail extends toward the extremely low frequency end, suggesting the presence of even lower frequency motions. Limited studies (Eaton & Johnston, 1982; Cherry et al., 1984; and Kiya et al., 1985) suggest that a separation bubble shortening-lengthening process, i.e., the flapping of the separated shear layer at the separated region, could be responsible for this low frequency unsteadiness. If it is so, this long time scale should be scaled to the passage period of the vortices near the reattachment region. However, the T_M found is much longer than the reattaching shear layer passage period which is about 1 second. However, an interesting observation suggests a possible relation between this slow oscillation to the recirculation time scale of the entire bubble, which can be characterized by the turn-around time of the recirculation eddy of the step. From the velocity measurement, the estimated time scale in the recirculation bubble is about 6.5 s, which is approximately half of the long fluctuation period. However, more investigations will be needed in order to substantiate this observation. Due to the existence of this long time scale in the flow, the averaging times of the flow quantities are correspondingly increased such that statistical stability could be achieved. In the present experiment, the period with the maximum probability density, $T_M = 12.5$ s is used as the reference time scale and the flow properties are averaged at each measuring station for at least 48 periods of this long time scale, which corresponds to about 10 minutes.

3.2 The Two-Dimensionality Before the Step. The initial boundary layer profile just upstream of the step is shown in Fig. 3. It is fairly close to the Blasius laminar profile as rep-

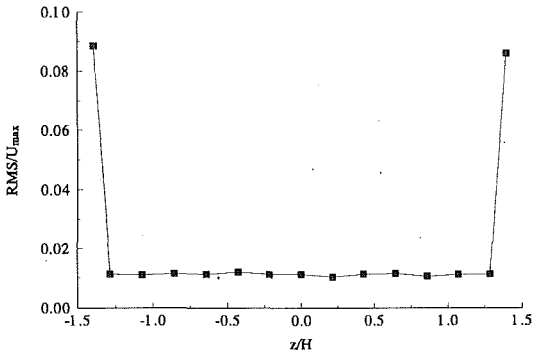

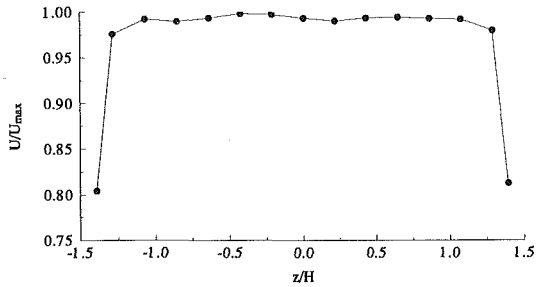

Fig. 4 Spanwise profiles of the free-stream velocity and turbulent intensity upstream of the step

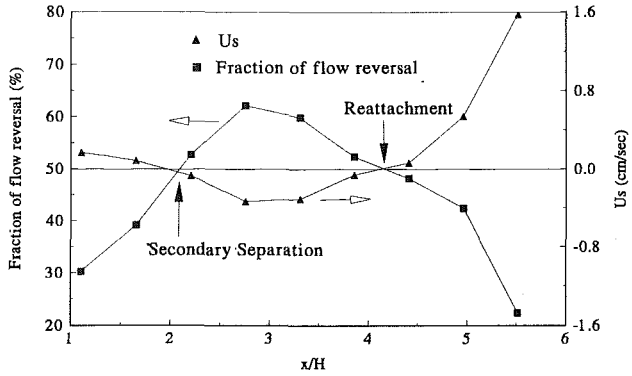

Fig. 5 Definitions of the shear layer reattachment location

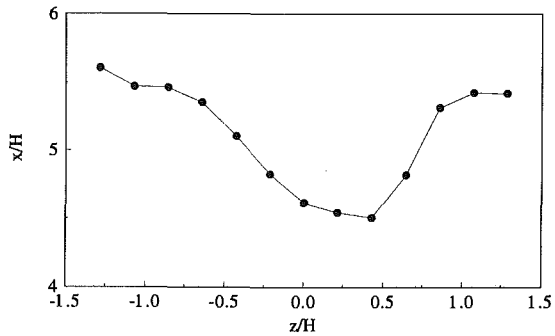

Fig. 6 Spanwise distribution of the shear layer reattachment locations

resented by the solid line. The slight deviation from the Blasius data could be due to the following two reasons: First, the relatively short developing distance between the contraction and the test section. Second, influences from the separated flow immediate downstream. The two-dimensionality of the inlet flow before the step was examined by measuring the spanwise distribution of the streamwise velocity components upstream of the step. As demonstrated by both the mean velocity and turbulence intensity profiles in Fig. 4, the incoming flow immediately before the step is indeed two-dimensional except very close to the side wall. The displacement thickness of the side wall boundary layer is of the same order of magnitude as that of the boundary layer before the step, which is about 1.7 mm, 3 percent of the channel width. Therefore, the three-dimensional distortion effect produced by the side wall boundary layer should be insignificant.

3.3 The Reattachment Length. The reattachment location is defined as the point where the separated shear layer reattaches to the surface. Two commonly accepted definitions (Kiya et al., 1982) are used to identify the time mean reattachment points; one method defines reattachment position as the point where the surface velocity, U_S, equals to zero. The surface velocity is defined as the time-averaged streamwise velocity component measured very close to the surface. In this experiment the measurements were taken at a distance of 2 mm above the bottom surface. The second method is to define the reattachment position at a point where the surface flow moves upstream 50 percent of the time. Alternatively, these two techniques can both be conceived as the determination of the position where the time mean separating streamline impinges onto the step's floor. both measurements were made in the present study and no appreciable difference (within 0.1 step height) could be found between the results. Figure 5 presents an example of these reattachment measurements which was taken along the centerline of the step. Two points simultaneously fulfill both criteria of the reattachment. Nevertheless, from a later shear layer profile measurement, the downstream point is identified as the correct one where the shear layer impinges onto the step floor as can also be shown in Fig. 7(*b*). The upstream point corresponds to the position where the reverse flow inside the recirculation zone separates again, forming a secondary eddy trapped near the step's corner.

The reattachment length is one of the most important parameters characterizing the global feature of a separated-reattached flow. For example, the reattachment length can be used as a measure of the level of the entrainment from the separated shear layer (Rothe and Johnston, 1979); the local maximum heat transfer rate is also found at the mean reattachment region. Therefore, information about the three-dimensional behaviors of the reattachment positions is critical in designing many engineering devices, e.g., a dump combustor. The spanwise distribution of the reattachment locations is given in Fig. 6. The reattachment points vary significantly across the span and their distribution is slightly asymmetrical. This asymmetry is found to be persistent throughout the entire experiment and is probably due to the non-uniformity of the facility upstream of the step. The reattachment point along the centerline is about 4.3 step heights which is considerably shorter than the typical two-dimensional cases in the same Reynolds number range, usually 6 to 9 step heights (Eaton and Johnston, 1981). The farthest reattached position occurs very close to one of the side walls and is at least 20 percent longer than those near the center. Armaly et al. (1983) reported a similar wavy distribution of the spanwise reattachment locations for a backstep flow with an initially parabolic velocity profile. In their measurement an additional separation bubble was found to exist at the wall opposite of the step, and was believed to be responsible for this wave like spanwise reattachment distribution. However, no such separation zone is detectable in the present study.

3.4 3-D Flow Pattern. Detailed velocity measurements are taken inside the recirculation region in order to understand this highly three-dimensional flow field. All three velocity components are measured by the LDA. Several cross-sectional measuring planes were chosen to display the inner structures

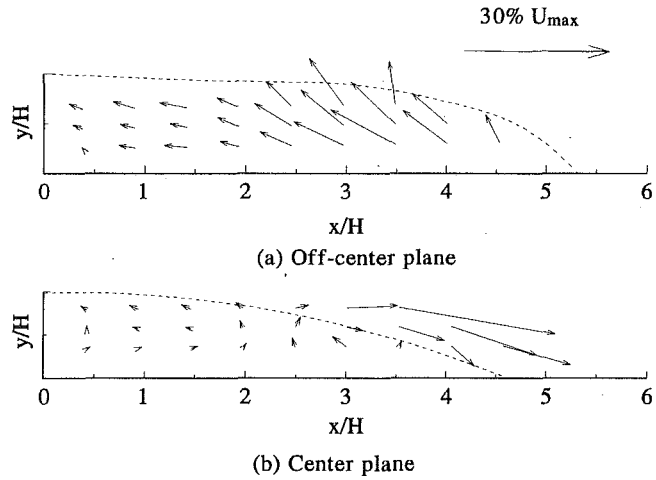

Fig. 7 Velocity vector plots measured at selective vertical planes

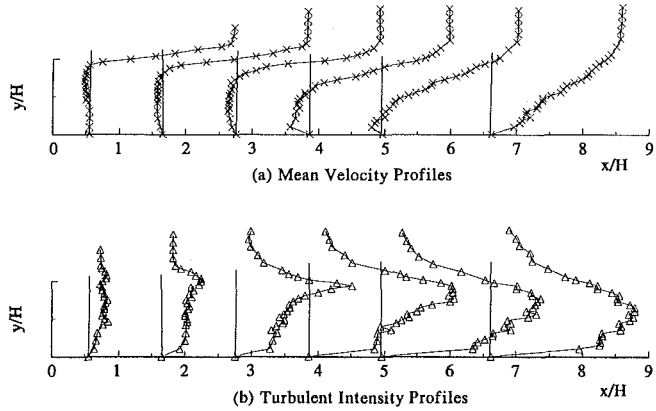

Fig. 8 Time-mean velocity and turbulent intensity profiles measured at the off-center plane

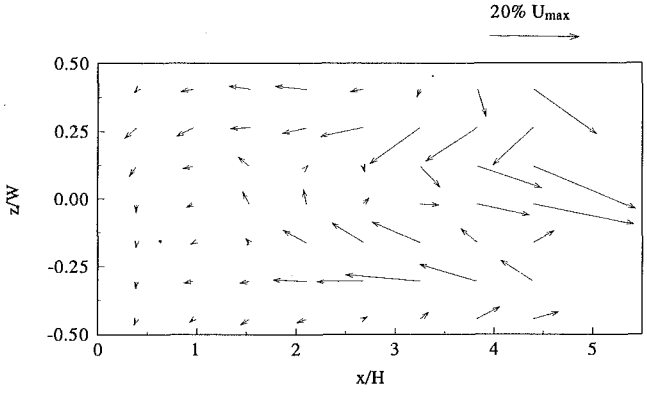

Fig. 9 Velocity vector plot measured at the horizontal plane, $z/H = 0.5$

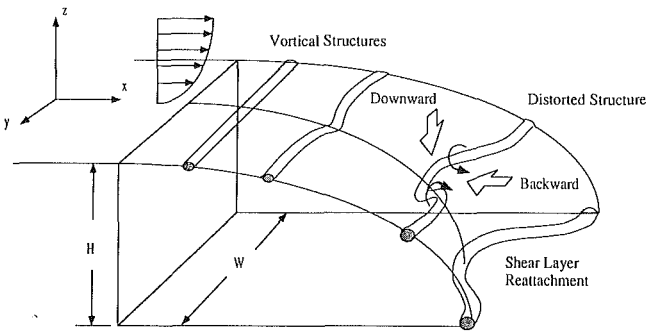

Fig. 10 Topological sketch of the three-dimensional separation region

of this complex flow field. Two vertical planes, one near the centerline and the other off the center, along with one horizontal cut at mid-height ($y/H = 0.5$) of the step are presented in Figs. 7 and 8. Figure 7(*a*) shows the vertical velocity field measured at a off-center plane located at $z/W = 0.25$. The vector-marks represent both the magnitudes and directions of the in-plane velocity components. The dashed line indicates the approximate location of the separating streamline as estimated based upon the time-averaged velocity profiles. At this section the flow field resembles the classical recirculation zone of a two-dimensional backward-facing step. Strong reversing flow, as high as 15 percent of the free-stream velocity, can be observed at specific locations inside the bubble.

The time-averaged velocity vectors plot taken at the center section [Fig. 7(*b*)], however, indicates a much more complicated flow structure. Near the corner of the step, there is a time-averaged counter-clockwise rotating eddy, which is the result of a secondary separation. This secondary recirculation region appears to be present only near the center region, see Fig. 7(*b*). The exact size of this region is about 2 steps downstream of the step, which can be identified from the surface velocity measurement, see Fig. 5. It can also be seen from Figs. 7 and 8 that the centerline region of the bubble is very quiet, in a time-averaged sense, as compared to the off-center regions. Based upon the instantaneous record, the centerline velocity is not as low as its time-averaged value would indicate, yet, it is still significantly lower than it off-center counterpart. This suggests that the three-dimensional separation bubble is virtually divided into two by a nearly motionless section along the centerline Time averaged velocity and turbulence intensity profiles of the off-center section, Fig. 8, are measured at several streamwise stations; these profiles resemble the two-dimensional cases.

Figure 9, the top plane view of the separation zone, measured at $y/H = 0.5$, reveals a very complex flow pattern; from which three distinct regions can be defined. First of all, one counter-rotating vortex pair can be recognized near the center. These two vortices are induced by the shear layer, which reattaches prematurely near the center and penetrates the horizontal measuring plane at these regions. Flow visualization is performed by injecting dye through holes located at the trailing edge of the step. Based upon the visualization, the vortical structures of the reattaching shear layer are observed to deform backward and downward first near the center plane, redirecting vorticity into the transverse (y) and streamwise (x) directions. The orientation of one of the distorted vortical structures in the reattaching shear layer is illustrated in Fig. 10. The vorticity redistribution spreads toward the wall and greatly increases the spanwise entrainment near the center of the step. Consequently, the separated shear layer reattaches earlier near the centerline as shown in Fig. 6. Strong spanwise movement is induced as fluid is entrained from the neighboring regions toward the center. The maximum spanwise velocity component is of the same order as the streamwise velocity component at that particular location, which is about 8 percent of the free stream velocity. Strong spanwise velocity also has been observed in a small aspect ratio rectangular sudden expansion by Hertzberg and Ho (1992). In that flow, the high level of spanwise flow obviates formation of a recirculation zone after the step and therefore has a zero reattachment length.

The off-center regions which are located almost symmetrically away from the centerline are responsible for recirculating most of the entrained fluid upstream inside the separation zone; this is consistent with the observations made from the vertical section velocity vector plot, Fig. 7(*a*). Most of the recirculating fluid moves backward and upward and was entrained again by the shear layer. A small portion of the fluid, however,

accumulates in the corner region near the centerline, forming the secondary flow region. This region is located closest to the step, see Fig. 8, which is also a comparatively quiet region compared to others. Typical time mean velocity is of the order of 3–7 millimeters per second, that is approximately 2.5–6 percent of the freestream velocity, within this quiet region.

4 Conclusions

A laser Doppler anemometer was used to measure the flow field behind a small aspect ratio backward-facing step; the incoming free stream-flow was two-dimensional. A time scale about 25 times longer than the period of the instability waves of the separating shear layer was detected throughout the entire separation region. Extensive measurements of the three velocity components indicate that the flow inside the separation region is highly three-dimensional: First of all, the mean reattachment line is highly distorted across the span with the shortest reattachment position locates along the centerline and is about 20 percent shorter. Secondly, strong spanwise movement that is of the same order of magnitude as compared to the local streamwise velocity component is induced inside the recirculation region.

Acknowledgment

This work was supported by a contract from the Air Force Office of Scientific Research.

References

Armaly, B. F., Durst, J., Pereira, J. C. F., and Schnung, B., 1983, "Experimental and Theoretical Investigation of Backward-Facing Step Flow," *Journal of Fluid Mechanics*, Vol. 127, pp. 473–496.

Bhattacharjee, S., Scheelke, B., and Troutt, T. R., 1986, "Modification of Vortex Interactions in a Reattaching Separated Flow;" *AIAA Journal*, Vol. 24, No. 4, pp. 623–629.

Bradshaw, P., and Wong, F. Y. F., 1972, "The Reattachment and Relaxation of a Turbulent Shear Layer," *Journal of Fluid Mechanics*, Vol. 52, Part 1, pp. 113–135.

Chardron, W., Durst, F., and Whitelaw, J. H., 1978, "Asymmetric Flows and Instabilities in Symmetric Ducts with Sudden Expansions," *Journal of Fluid Mechanics*, Vol. 84, pp. 13–31.

Cherry, N. J., Hillier, R., and Latour, M. E. M. P., 1984, "Unsteady Measurements in a Separated and Reattaching Flow," *Journal of Fluid Mechanics*, Vol. 114, pp. 13–46.

de Brederode, V., and Bradshaw, P., 1972, "Three-Dimensional Flow in Nominally Two-Dimensional Separation Bubbles I. Flow Behind a Rearward-Facing Step," I. C. Aero Report #72-19.

Eaton, J. K., and Johnston, J. P., 1981, "A Review of Research on Subsonic Turbulent Flow Reattachment," *AIAA Journal*, Vol. 19, No. 9, pp. 1093–1100.

Eaton, J. K., and Johnston, J. P., 1982, "Low Frequency Unsteadiness of a Reattaching Turbulent Shear Layer," *Turbulent Shear Flow III*, pp. 162–170.

Hertzberg, J., and Ho, C. M., 1992, "Vortex Dynamics in a Rectangular Sudden Expansion," *AIAA Journal*, Vol. 30, No. 10, pp. 2420–2425.

Kaiktsis, L., Karniadakis, G. E., and Orszag, S., 1991, "Onset of Three-Dimensionality, Equilibria, and Early Transition in Flow Over a Backward-Facing Step," *Journal of Fluid Mechanics*, Vol. 231, pp. 501–528.

Kim, J., and Moin, P., 1985, "Application of a Fractional-Step Method to Incompressible Navier-Stokes Equations," *Journal of Computational Physics*, Vol. 59, pp. 308–323.

Kiya, M., Sasaki, K., and Arie, M., 1982, "Discrete-Vortex Simulation of a Separation Bubble," *Journal of Fluid Mechanics*, Vol. 120, pp. 219–244.

Kiya, M., and Sasaki, K., 1985, "Structure of Large-Scale Vortices and Unsteady Reverse Flow in the Reattaching Zone of a Turbulent," *Journal of Fluid Mechanics*, Vol. 154, pp. 463–491.

Roos, F. W., and Kegelman, J. T., 1986, "Influence of Excitation on Coherent Structures in Reattaching Turbulent Shear Layers," AIAA paper No. 86-0112.

Rothe, P. H., and Johnston, J. P., 1979, "Free Shear Layer Behavior in Rotating Systems," ASME JOURNAL OF FLUIDS ENGINEERING, Vol. 120, pp. 219–244.

Flow in a Channel With Longitudinal Ribs

C. Y. Wang
Departments of Mathematics and Mechanical Engineering, Michigan State University, East Lansing, MI 48824
Mem. ASME

The laminar, viscous flow between parallel plates with evenly spaced longitudinal ribs is solved by an eigenfunction expansion and point-match method. The ribs on both plates may be symmetrically placed or staggered. For a given pressure gradient, the mean velocity is plotted as a function of the geometric parameters. We find the wetted perimeter and the friction factor—Reynolds number product are unsuitable parameters for the flow through ducts of complex geometry.

Introduction

The flow in ducts is a basic topic in fluid mechanics. Steady, parallel, laminar, fully developed, constant property flow has been solved for a variety of cross sections (Blevins, 1984; Shah and Bhatti, 1987). This paper studies the flow between parallel plates which have longitudinal ribs. Such ribs may serve as strengtheners or may be conduits or heating elements.

We shall use an eigenfunction expansion and point-match method. The earliest use of this method for parallel flow in a nonregular boundary was perhaps due to Sparrow and Loeffler (1959) although for certain geometries such a method may not be suitable (Sparrow, 1966). See Shah and London (1978) for a review.

On the other hand, complex regions may be decomposed into contiguous simpler sub-regions. The solutions to each sub-region can then be matched along their common boundary. The idea, in one dimension, is similar to using cubic splines to determine the shape of a constrained elastic rod. The earliest use of patching solutions of two dimensional regions seems to be due to Weil (1951) who studied the Stokes flow into a gap. Other applications include the works of Zarling (1976), Chen (1980), Trogdon and Joseph (1982). The matching processes used, however, were somewhat complicated.

The combination of using eigenfunction expansions for separate sub-regions and using simple point-match along the boundary is well suited for the present problem. As we shall see later, the algorithm is simple and highly efficient.

Formulation

Figure 1(a, b) shows the cross sections of channels with ribs on both plates. The ribs are evenly spaced either symmetrically or staggered. We normalize all lengths by the half period H. Due to symmetry only the L shaped regions in Fig. 1(c, d) need to be considered.

Let the velocity be normalized by H^2G/μ where G is the axial pressure gradient and μ is the viscosity. The governing equation for velocity w is the Poisson equation

$$\nabla^2 w = -1 \tag{1}$$

The L shaped regions are further sub-divided into two rectangular pieces I and II. For the symmetric case (Fig. 1(c)) the boundary conditions are

$$w_I\left(x, \frac{a}{2}\right) = 0, \quad \frac{\partial w_I}{\partial y}(x, 0) = 0, \quad \frac{\partial w_I}{\partial x}(0, y) = 0 \tag{2}$$

$$w_I(c, y) = 0, \quad \frac{a}{2} - b < y < \frac{a}{2} \tag{3}$$

$$w_{II}\left(x, \frac{a}{2} - b\right) = 0, \quad \frac{\partial \omega_{II}}{\partial y}(x, 0) = 0, \quad \frac{\partial w_{II}}{\partial x}(1, y) = 0 \tag{4}$$

Also both w_I and w_{II} and their derivatives match on their common boundary at $x = c$. For the staggered case (Fig. 1(d)) the boundary conditions are

$$w_I(x, a) = 0, \quad w_I(x, 0) = 0, \quad w_I(0, y) = w_I(0, a - y) \tag{5}$$

$$w_I\left(c - \frac{1}{2}, y\right) = 0, \quad a - b < y < a \tag{6}$$

$$w_{II}(x, a - b) = 0, \quad w_{II}(x, 0) = 0, \quad \frac{\partial w_{II}}{\partial x}\left(\frac{1}{2}, y\right) = 0 \tag{7}$$

In addition, velocities and its derivatives should match at $x = c - 1/2$.

Symmetric Case

We construct the following solutions which satisfy Eqs. (1), (2), (4)

$$w_I = \frac{1}{2}\left(\frac{a^2}{4} - y^2\right) + \sum_n A_n \cos(\alpha_n y)\left(e^{\alpha_n(x-c)} + e^{-\alpha_n(x+c)}\right) \tag{8}$$

$$w_{II} = \frac{1}{2}\left[\left(\frac{a}{2} - b\right)^2 - y^2\right] + \sum_m B_m \cos(\beta_m y)\left(e^{\beta_m(x-2+c)} + e^{-\beta_m(x-c)}\right) \tag{9}$$

Here A_n, B_m are constant coefficients and

$$\alpha_n \equiv (2n-1)\frac{\pi}{a}, \quad \beta_m \equiv \frac{(2m-1)\pi}{(a-2b)} \tag{10}$$

The other boundary conditions are Eq. (3) and

Contributed by the Fluids Engineering Division for publication in the JOURNAL OF FLUIDS ENGINEERING. Manuscript received by the Fluids Engineering Division October 5, 1992; revised manuscript received March 31, 1993. Associate Technical Editor: R. L. Panton.

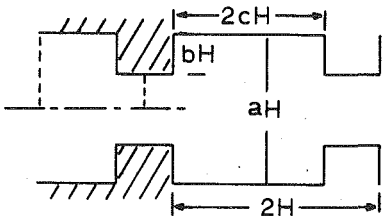

Fig. 1(*a*)

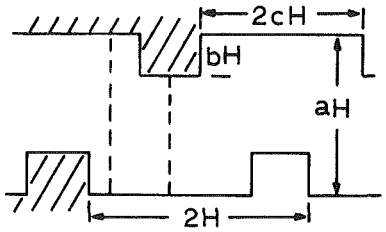

Fig. 1(*b*)

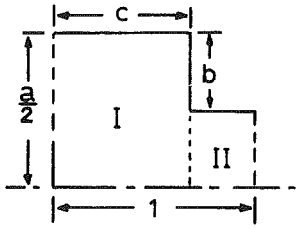

Fig. 1(*c*)

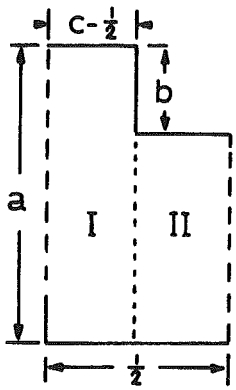

Fig. 1(*d*)

Fig. 1 (*a*, *b*) symmetric and staggered fins. (*c*, *d*) the corresponding computational regions.

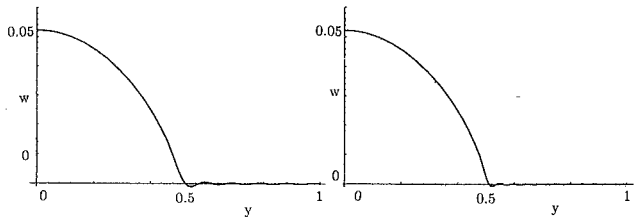

Fig. 2 Velocity along a mixed boundary (Fig. 3, at $x=0.5$). left: $N=20$, right: $N=40$.

$$w_I(c, y) = w_{II}(c, y), \quad 0<y<\frac{a}{2}-b \tag{11}$$

$$\frac{\partial w_I}{\partial x}(c, y) = \frac{\partial w_{II}}{\partial x}(c, y), \quad 0<y<\frac{a}{2}-b \tag{12}$$

We choose N points along the boundary at $x=c$

$$y_i = (i-1)a/(2N), \quad i=1, \ldots, N \tag{13}$$

and truncate A_n to N terms and B_m to M terms where

$$M = \text{Int}[N(1-2b/a)]+1 \tag{14}$$

Equations (3), (11), (12) become

$$\sum_1^N A_n \cos(\alpha_n y_i)(1+e^{-2\alpha_n c}) = \frac{1}{2}\left(y_i^2 - \frac{a^2}{4}\right), \quad i=M+1 \text{ to } N \tag{15}$$

$$\sum_1^N A_n \cos(\alpha_n y_i)(1+e^{-2\alpha_n c}) - \sum_1^M B_m \cos(\beta_m y_i) \times (1+e^{-2\beta_m(1-c)}) = \frac{1}{2}(b^2-ab) \quad i=1 \text{ to } M \tag{16}$$

$$\sum_1^N A_n \alpha_n \cos(\alpha_n y_i)(1-e^{-2\alpha_n c}) + \sum_1^M B_m \beta_m \cos(\beta_m y_i)(1-e^{-2\beta_m(1-c)}) = 0, \quad i=1 \text{ to } M \tag{17}$$

The linear system of $M+N$ equations and $M+N$ unknowns are solved for A_n and B_m. The accuracy of the solution depends on the number of points N. Figure 2 shows the velocity distribution along the boundary at $x=c$ ($a=1$, $b=0.25$, $c=0.5$). The error in w is less than 2 percent (as compared to the exact no-slip condition for $0.5<y<1$) for $N=20$ and decreases to 1 percent for $N=40$. Convergence is fairly fast. The corresponding constant velocity lines are shown in Fig. 3.

The mean velocity is integrated analytically:

Nomenclature

a = normalized distance between plates
A_n = constant coefficients
b = normalized height of ribs
B_m = constant coefficients
c = 1 − normalized width of ribs
C_n = constant coefficients
D_h = hydraulic diameter
$f\text{Re}$ = friction factor—Reynolds number product
G = axial pressure gradient
H = half period of ribs
i = integer index
m = integer index
M = integer
n = integer index
N = integer
u = normalized mean velocity
v = normalized mean velocity
v' = dimensional mean velocity
w = normalized velocity
x = Cartesian axis
y = Cartesian axis
z = $y - a/2$
α_n = eigenvalue Eq. (10)
β_m = eigenvalue Eq. (10) or Eq. (23)
γ_n = eigenvalue Eq. (23)
μ = viscosity

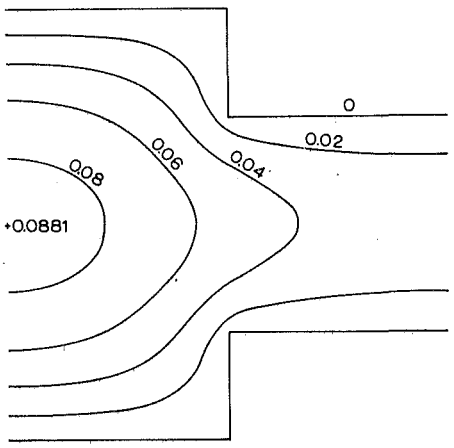

Fig. 3 Constant velocity lines for $a=1$, $b=0.25$, $c=0.5$

$$v=\frac{1}{\left[\frac{a}{2}-b(1-c)\right]}\left[\int_0^c\int_0^{a/2} w_I dydx+\int_c^1\int_0^{a/2-b} w_{II}dydx\right]$$

$$=\frac{1}{\left[\frac{a}{2}-b(1-c)\right]}\left\{\frac{1}{24}[ca^3+(1-c)(a-2b)^3]\right.$$
$$+\sum_1^N\frac{A_n}{(\alpha_n)^2}(-1)^{n+1}(1-e^{-2\alpha_n c})$$
$$\left.+\sum_1^M\frac{B_m}{(\beta_m)^2}(-1)^{m+1}[1-e^{-2\beta_m(1-c)}]\right\} \quad (18)$$

Staggered Case

The staggered case is slightly more complicated. We note that the solution to Region I, Fig. 1(*d*), has polar symmetry such that

$$w_I(x, z)=w_I(-x, -z) \quad (19)$$

where

$$z\equiv y-\frac{a}{2} \quad (20)$$

Guided by the boundary conditions, the following solutions are constructed

$$w_I=\frac{1}{2}\left(\frac{a^2}{4}-z^2\right)+\sum A_n\cos(\alpha_n z)[e^{\alpha_n(x-c+1/2)}+e^{-\alpha_n(x+c-1/2)}]$$
$$+\sum C_n\sin(\gamma_n z)[e^{\gamma_n(x-c+1/2)}-e^{-\gamma_n(x+c-1/2)}] \quad (21)$$

$$w_{II}=\frac{1}{2}y(a-b-y)$$
$$+\sum B_m\sin(\beta_m y)[e^{\beta_m(x+c-3/2)}+e^{-\beta_m(x-c+1/2)}] \quad (22)$$

Here A_n, C_n, B_m are to be determined and

$$\alpha_n=(2n-1)\frac{\pi}{a},\quad \gamma_n=2n\frac{\pi}{a},\quad \beta_m=\frac{m\pi}{a-b} \quad (23)$$

Similarly, $2N$ points are chosen along $x=c$

$$y_i=ia/(2N+1) \quad (24)$$

$$M=\text{Int}[2N(1-b/a)] \quad (25)$$

The algebraic equations to be solved are obtained from the conditions along the common boundary:

$$\sum_1^N A_n\cos\left[\alpha_n\left(y_i-\frac{a}{2}\right)\right][1+e^{-\alpha_n(2c-1)}]$$
$$+\sum_1^N C_n\sin\left[\gamma_n\left(y_i-\frac{a}{2}\right)\right][1-e^{-\gamma_n(2c-1)}]$$
$$=\frac{1}{2}y_i(y_i-a),\quad i=M+1\text{ to }2N \quad (26)$$

$$\sum_1^N A_n\cos\left[\alpha_n\left(y_i-\frac{a}{2}\right)\right][1+e^{-\alpha_n(2c-1)}]$$
$$+\sum_1^N C_n\sin\left[\gamma_n\left(y_i-\frac{a}{2}\right)\right][1-e^{-\gamma_n(2c-1)}]$$
$$-\sum_1^M B_m\sin(\beta_m y_i)(1+e^{-2\beta_m(1-c)})=\frac{-b}{2}y_i,\quad i=1\text{ to }M \quad (27)$$

$$\sum_1^N A_n\alpha_n\cos\left[\alpha_n\left(y_i-\frac{a}{2}\right)\right][1-e^{-\alpha_n(2c-1)}]$$
$$+\sum_1^N C_n\gamma_n\sin\left[\gamma_n\left(y_i-\frac{a}{2}\right)\right][1+e^{-\gamma_n(2c-1)}]$$
$$+\sum_1^M B_m\beta_m\sin(\beta_m y_i)(1-e^{-2\beta_m(1-c)})=0,\quad i=1\text{ to }M \quad (28)$$

There are $2N+M$ equations and $2N+M$ unknowns. The mean velocity is then

$$v=\frac{1}{\left[\frac{a}{2}-b(1-c)\right]}\left\{\frac{1}{12}\left[\left(c-\frac{1}{2}\right)a^3+(1-c)(a-b)^3\right]\right.$$
$$+\sum_1^N\frac{2(-1)^{n+1}A_n}{\alpha_n^2}[1-e^{-\alpha_n(2c-1)}]$$
$$\left.+\sum_1^M\frac{B_m[1-(-1)^m]}{\beta_m^2}[1-e^{-2\beta_m(1-c)}]\right\} \quad (29)$$

Results and Discussion

The conventional parameter to quantify flow rate is the friction factor—Reynolds number product

$$f\text{Re}=\frac{GD_h^2}{2\mu v'}=\frac{2[a-2b(1-c)]^2}{(1+b)^2v} \quad (30)$$

Here D_h is the hydraulic diameter equal to 4 (area)/(wetted perimeter). Since the presence of ribs greatly affects both flow rate and wetted perimeter, we find fRe, as defined, is an unsuitable parameter since the results would be unwieldy. This fact was also noted by Sparrow and Chukaev (1980) who used finite differences to solve the flow between a ribbed plate and a flat plate. In our results we shall quantify flow rate by the mean velocity normalized by the distance between the plates

$$u=\frac{v'}{(aH)^2G/\mu}=\frac{v}{a^2} \quad (31)$$

Figure 4 shows the mean velocity u for the symmetric case. When the ribs are absent ($b=0$), $u=0.08333$, from Eq. (30) $f\text{Re}=24$ for the flow between parallel flat plates. When $b/a=0.5$, opposite ribs touch and our results agree with published results of the flow through rectangular conduits. The mean velocity increases slightly when b is close to $0.5a$ is due to the elimination of the almost stagnant cross-sectional region between opposite ribs. The total flow still decreases with increased

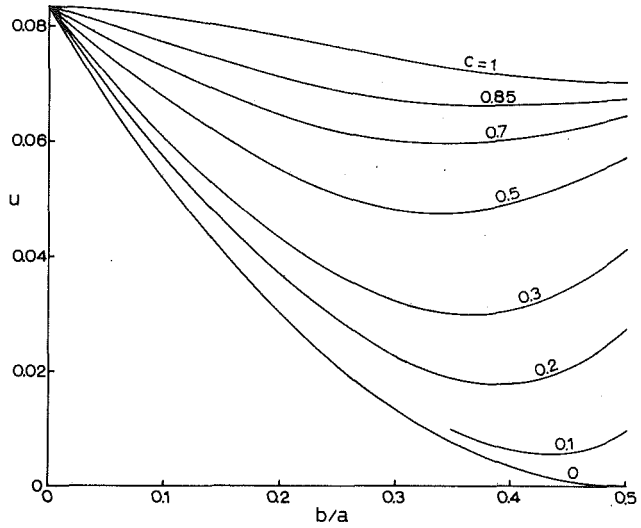

Fig. 4(*a*)

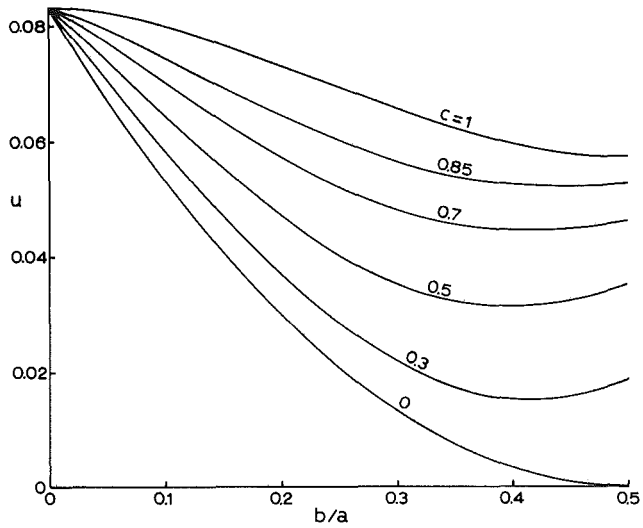

Fig. 4(*b*)

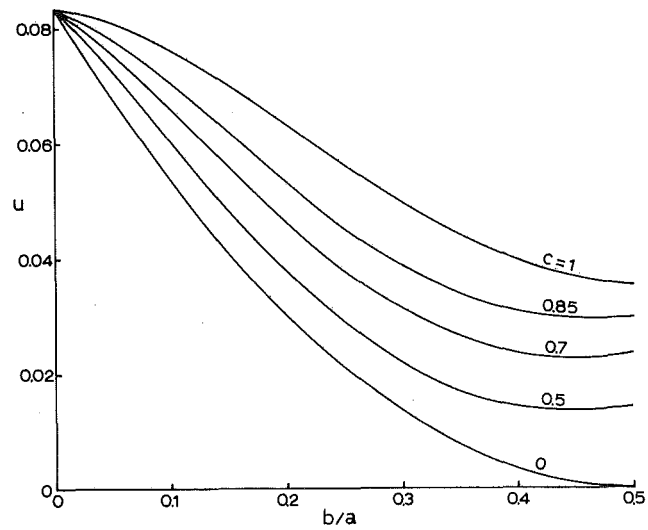

Fig. 4(*c*)

Fig. 4 Mean velocity for the symmetric case (*a*) $a=0.5$, (*b*) $a=1$, (*c*) $a=2$.

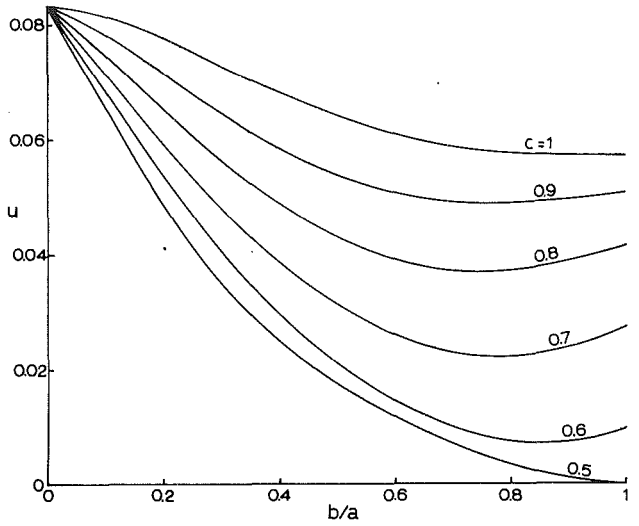

Fig. 5(*a*)

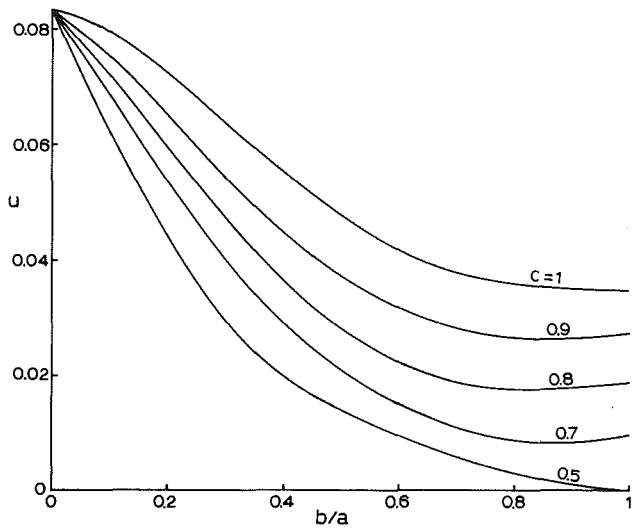

Fig. 5(*b*)

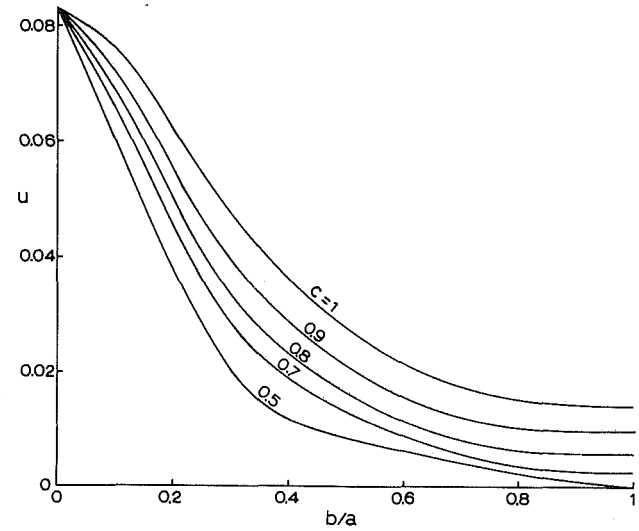

Fig. 5(*c*)

Fig. 5 Mean velocity for the staggered case (*a*) $a=0.5$, (*b*) $a=1$, (*c*) $a=2$.

b. Of interest is the $c=1$ case where the ribs become thin fins. The $c=0$ (all fin) case is equivalent to a narrower channel without fins.

Figure 5 shows the results for the staggered case where the ribs can reach the opposite plate ($b=a$) and thus c is limited to the range of 0.5 to 1. For the same values of a, b, c the staggered case yields lower flow than the symmetric case. The dependence of flow with phase shift (which changes neither cross sectional area nor wetted perimeter) was also noted by Wang (1976) for two plates with small wavy corrugations.

Conclusions

Our method used here is quite advantageous in comparison to direct numerical integration. The number of computations is less than the square root of that of finite differences. Also the double integral for flow can be evaluated analytically, eliminating another source of error. The method is simple enough such that other results, for values of the parameters not presented here, can be easily computed.

We find the cross-sectional area and the wetted perimeter alone could not have defined the flow rate. The use of $f\mathrm{Re}$ as the dependent variable is also unsuitable (compare Fig. 3.42 of Shah and Bhatti, 1987). We advocate using the normalized mean velocity to quantify the flow through a duct with complex geometry.

References

Blevins, R. D., 1984, *Applied Fluid Dynamics Handbook*, VanNostrand, New York.

Chen, Y. Z., 1980, "Solutions of Torsion Crack Problems of a Rectangular Bar by Harmonic Function Continuation Technique," *Engineering Fracture Mechanics*, Vol. 13, pp. 193–212.

Shah, R. K., and Bhatti, M. S., 1987, *Laminar Convective Heat Transfer in Ducts, in Handbook of Single-Phase Convective Heat Transfer*, S. Kakac, R. K. Shah, W. Aung, eds., Wiley, New York, Chapter 3.

Shah, R. K., and London, A. L., 1978, *Laminar Flow Forced Convection in Ducts. Advances in Heat Transfer*, Supplement 1, Academic, New York, Chapter 4.

Sparrow, E. M., 1966, Discussion to K. C. Cheng, "Analog Solution of Laminar Heat Transfer in Non Circular Ducts by Moiré and Point-Matching," ASME *Journal of Heat Transfer*, Vol. 88, p. 182.

Sparrow, E. M., and Chukaev, A., 1980, "Forced-Convection Heat Transfer in a Duct having Spanwise-Periodic Rectangular Protuberances," *Numerical Heat Transfer*, Vol. 3, pp. 149–167.

Sparrow, E. M., and Loeffler, A. L., 1959, "Longitudinal Laminar Flow Between Cylinders Arranged in Regular Array," *AIChE Journal*, Vol. 5, pp. 325–330.

Trogdon, S. A., and Joseph, D. D., 1982, "Matched Eigenfunction Expansions for Slow Flow Over a Slot," *Journal of NonNewtonian Fluid Mechanics*, Vol. 10, pp. 185–213.

Wang, C. Y., 1976, "Parallel Flow Between Corrugated Plates," *ASCE Journal of the Engineering Mechanics Division*, Vol. 102, pp. 1088–1090.

Weil, H., 1951, "On the Extrusion of a Very Viscous Liquid," ASME *Journal of Applied Mechanics*, Vol. 18, pp. 267–272.

Zarling, J. P., 1976, "An Analysis of Laminar Flow and Pressure Drop in Complex Shaped Ducts," ASME JOURNAL OF FLUIDS ENGINEERING, Vol. 98, pp. 702–706.

S. Acharya

S. Dutta

T. A. Myrum

R. S. Baker

Mechanical Engineering Department,
Louisiana State University,
Baton Rouge, LA 70803

Turbulent Flow Past a Surface-Mounted Two-Dimensional Rib

The ability of the nonlinear k–ϵ turbulence model to predict the flow in a separated duct flow past a wall-mounted, two-dimensional rib was assessed through comparisons with the standard k–ϵ model and experimental results. Improved predictions of the streamwise turbulence intensity and the mean streamwise velocities near the high-speed edge of the separated shear layer and in the flow downstream of reattachment were obtained with the nonlinear model. More realistic predictions of the production and dissipation of the turbulent kinetic energy near reattachment were also obtained. Otherwise, the performance of the two models was comparable, with both models performing quite well in the core flow regions and close to reattachment and both models performing poorly in the separated and shear-layer regions close to the rib.

Introduction

Ribs are frequently used to increase the heat transfer in turbulent duct flows by increasing the heat transfer area (fin effect) and by disturbing the laminar sublayer (roughness effect). The focus of the present investigation is on the roughness effect or, in particular, the flow behavior for a flow past a two-dimensional rib mounted on the bottom wall of a rectangular duct.

Numerous experimental studies have been conducted to understand the flow phenomena associated with flows past two-dimensional ribs. Castro (1979), Bergeles and Athanassiadis (1983), Antoniou and Bergeles (1988), Durst and Rastogi (1980), Tropea and Gackstatter (1985), Liou and Kao (1988) and Phataraphruk and Logan (1979) are representative of such studies.

A number of numerical studies have also been performed in order to predict the flow behavior in flows past two-dimensional ribs. Typical numerical studies with the linear k–ϵ model (Launder and Spalding, 1974) are: Durst and Rastogi (1980), Benodekar et al. (1985), Chung et al. (1987), Park and Chung (1989), Lee et al. (1988) and Leschziner and Rodi (1981).

The linear k–ϵ model is based on the Boussinesq approximation of the Reynolds stresses. The Boussinesq approximation does not account for the nonisotropic behavior of the turbulent stresses. Using flow past a backward-facing step as a test case, Thangam and Speziale (1991) found that inaccuracies in the Reynolds stresses, incurred by neglecting nonisotropic effects, play a strong role when trying to predict separated flow behavior. They also found that the nonlinear k–ϵ model, that includes higher order terms representing nonisotropic effects (Speziale, 1987), yields good predictions for backstep flows. Improved predictions of separated flows past backsteps using the nonlinear k–ϵ model have also been obtained by Speziale and Ngo (1988) and Thangam and Hur (1991).

As far as these authors know, no attempts have been made to apply the nonlinear k–ϵ model to flows past two-dimensional, surface-mounted ribs. Rather, as just pointed out, the application of the nonlinear model has been confined to relatively simple flow geometries, such as flows past backsteps, where only a single separation region exists. Flows past two-dimensional ribs possess two recirculation regions and, in this respect, are more complex than flows past backsteps.

The main objectives of the present investigation are to obtain detailed laser-Doppler measurements of the flow in the upstream and downstream recirculation regions of a separated duct flow past a wall-mounted, two-dimensional rib and to evaluate the ability of the nonlinear k–ϵ model to predict the flow behavior. The performance of the nonlinear model will be assessed through comparisons with the predictions of the standard k–ϵ model and with the results of the experiments of the present investigation and those of Antoniou and Bergeles (1988) and Castro (1979). Comparisons between the two models and the experimental data of this study will demonstrate the ability of the two models to predict the flow behavior in the upstream and downstream recirculation regions, while the comparisons involving the studies of Antoniou and Bergeles (1988) and Castro (1979) will demonstrate the ability of the two models to predict the flow behavior downstream of reattachment.

The Experimental Setup and Procedure

The test section is shown in Fig. 1. It was 101.6-cm long, 30-cm wide, and 6.1-cm high and was placed 40 hydraulic diameters downstream of the inlet. Air was drawn into the development duct through a 5.25-to-1 contraction section containing a honeycomb baffle and four screens. Laser-Doppler velocity measurements of the flow at the exit of the contraction section (i.e., the development duct inlet) confirmed a virtually uniform velocity profile. A 6.35-mm × 6.35-mm square steel rib was mounted on the lower wall, just downstream of the inlet to the test section, using double-sided tape.

Contributed by the Fluids Engineering Division for publication in the JOURNAL OF FLUIDS ENGINEERING. Manuscript received by the Fluids Engineering Division, January 2, 1993; revised manuscript received September 7, 1993. Associate Technical Editor: T. T. Huang.

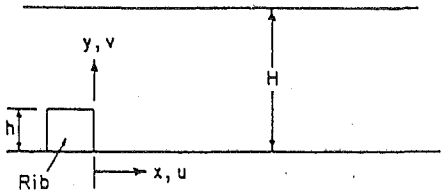

Fig. 1 Elevation view of test section

Table 1 Flow parameters and references for different case studies

Case	Reference	U_0 (m/s)	h (mm)	H (mm)	δ_u	Inlet/Outlet prescribed at
I	Antoniou and Bergeles (1988)	15	20	230	0.7h	−4.5h/+40h
II	Castro (1979)	3.1	25	647	5h	−34/+60h
III	Present study	3.6	6.35	61	3.3h	−15h/+30h

The flow measurements were performed using a conventional two-color DANTEC fiber-optic LDV system operating in the back-scatter mode. Each measurement consisted of 2000 samples at each location, recorded at sampling rate that varied from 25 samples/s in the near-wall recirculating region to 1500 samples/s at the outer edge of the shear layer. Measurements for samples sizes ranging from 2000 to 10,000 were performed at various locations with less than a one-percent difference in the mean and rms values. As recommended by Driver and Seegmiller (1982, 1985), the mean velocities and Reynolds stresses were obtained by ensemble averaging without bias correction. The uncertainties were calculated to a 95 percent confidence level (Kline and McClintock, 1953; Rood and Telionis, 1991) and were ±3.5 percent and ±3 percent for the mean $u-$ and v-velocities, ± 5 and ± 4.5 percent for the streamwise and cross-stream turbulence intensities, and ±8 percent for the turbulent shear stress.

The flow measurements of the present study were taken primarily at axial locations ranging from 1.4 rib heights upstream of the rib to 7.1 rib heights downstream of the rib; although limited measurements were also made between 7.1 to 13.4 rib heights downstream of the rib. These measurements, together with the corresponding model predictions of this study, will be referred to as Case III. Downstream of reattachment, the measurements reported by Antoniou and Bergeles (1988) and Castro (1979) were used in the comparisons with the model predictions of this study. The measurements of Antoniou and Bergeles (1988) and the associated model predictions will be referred to as Case I, while the measurements of Castro (1979) and the associated model predictions will be referred to as Case II. In both cases, a hot-wire anemometer was used, and the measurements were confined to the region downstream of reattachment. The experimental parameters for Cases I, II, and III are listed in Table 1.

The Standard k–ϵ Model. The standard k–ϵ model (Launder and Spalding, 1974) is based on the Boussinesq approximation:

$$\tau_{ij} = -\overline{\rho u_i' u_j'} = -\frac{2}{3}\rho k\delta_{ij} + \mu_t\left(\frac{\partial u_i}{\partial x_j}+\frac{\partial u_j}{\partial x_i}\right) \quad (1)$$

It involves solving the modeled k and ϵ equations along with the continuity and momentum equations. The equations expressing continuity and momentum are given by

$$\frac{\partial u_j}{\partial x_j}=0 \text{ and } \rho u_j\frac{\partial u_i}{\partial x_j} = -\frac{\partial p}{\partial x_i}+\mu\frac{\partial}{\partial x_j}\left(\frac{\partial u_i}{\partial x_j}+\frac{\partial u_j}{\partial x_i}\right)+\frac{\partial \tau_{ij}}{\partial x_j} \quad (2)$$

The modeled momentum equations for the standard k–ϵ model (Launder and Spalding, 1974), obtained by adopting the Boussinesq approximation are

$$\rho u_j\frac{\partial u_i}{\partial x_j} = -\frac{\partial p^*}{\partial x_i}+\frac{\partial}{\partial x_j}\left(\mu_{\text{eff}}\frac{\partial u_i}{\partial x_j}\right)+S_{u_i},$$

$$\text{where } S_{u_i}=\frac{\partial}{\partial x_j}\left(\mu_t\frac{\partial u_j}{\partial x_i}\right) \quad (3)$$

The modified pressure term p^* and the effective viscosity μ_{eff} are defined as

$$p^* = p+\frac{2}{3}\rho k,\ \mu_{\text{eff}}=\mu+\mu_t,\ \mu_t = C_\mu\rho\frac{k^2}{\epsilon} \quad (4)$$

The modeled transport equations for turbulent kinetic energy and dissipation (k and ϵ) are expressed as

$$\rho u_j\frac{\partial k}{\partial x_j}=\frac{\partial}{\partial x_j}\left(\frac{\mu}{\sigma_k}\frac{\partial k}{\partial x_j}\right)+\mu_t G-\rho\epsilon;\ \rho u_j\frac{\partial \epsilon}{\partial x_j}$$

$$=\frac{\partial}{\partial x_j}\left(\frac{\mu_t}{\sigma_\epsilon}\frac{\partial \epsilon}{\partial x_j}\right)+C_1\mu_t G\frac{\epsilon}{k}-C_2\rho\frac{\epsilon^2}{k} \quad (5)$$

In Eq. (5), the production of kinetic energy $P(=\mu_t G)$ is

$$\mu_t G=\tau_{ij}\left(\frac{\partial u_i}{\partial x_j}\right)=\mu_t\left[2\left(\left(\frac{\partial u}{\partial x}\right)^2+\left(\frac{\partial v}{\partial y}\right)^2\right)+\left(\frac{\partial u}{\partial y}+\frac{\partial v}{\partial x}\right)^2\right] \quad (6)$$

To account for the near-wall effects in the standard k–ϵ model, wall functions are used (Launder and Spalding, 1974). This requires the first interior grid point to be at a distance of $y^+ > 11.5$ from the wall and requires modifying the diffusion coefficient at the wall to satisfy the law-of-the-wall relationship. The near-wall dissipation value is prescribed from equilibrium as $\epsilon = C_\mu^{3/4}k^{3/2}/0.4y$, and the wall gradient of k is set to zero.

The Nonlinear k–ϵ Model. The nonlinear k–ϵ model of Speziale (1987) retains the tensorially invariant eddy viscosity of the standard k–ϵ model and adds the second-order derivatives of the streamwise and cross-stream velocities to the Boussinesq approximation to account for the nonisotropic behavior in the turbulent stresses. These extra second-order terms are incorporated as source terms in the momentum equations and in the k and ϵ transport equations.

For two-dimensional, separated flows, the individual com-

Nomenclature

C_1, C_2, C_μ = turbulence model constants; $C_1 = 1.44$, $C_2 = 1.92$, $C_\mu = 0.09$
C_D = nonlinear turbulence model constant, $C_D = 1.68$
D = hydraulic diameter, $D = 101.6$ mm
h, H = rib height, channel height
k = turbulent kinetic energy
P = production of kinetic energy, $\mu_t G$ (Eq. (7))
p = pressure
u, u' = mean and fluctuating streamwise velocities
U_0 = free-stream velocity
v, v' = mean and fluctuating cross-stream velocities
x_R = reattachment length
ϵ = dissipation of kinetic energy
μ, μ_t = viscosity, turbulent viscosity
ρ = density
σ_k, σ_ϵ = turbulence model constants, $\sigma_k = 1.0$, $\sigma_\epsilon = 1.3$
τ_{xx}, τ_{yy}, τ_{xy} = turbulent stresses

ponents of the stress terms in the nonlinear model (Speziale, 1987) can be written in Cartesian coordinates as

$$\tau_{xx} = -\frac{2}{3}\rho k + 2\rho\, C_\mu \frac{k^2}{\epsilon}\frac{\partial u}{\partial x} + 4C_D\rho C_\mu^2 \frac{k^3}{\epsilon^2}\left[-\frac{1}{3}\left(\frac{\partial u}{\partial x}\right)^2 - \frac{7}{12}\left(\frac{\partial u}{\partial y}\right)^2 - \frac{1}{6}\left(\frac{\partial u}{\partial y}\frac{\partial v}{\partial x}\right) + \frac{5}{12}\left(\frac{\partial v}{\partial x}\right)^2 + t_1\right] \quad (7)$$

$$\tau_{yy} = -\frac{2}{3}\rho k + 2\rho\, C_\mu \frac{k^2}{\epsilon}\frac{\partial v}{\partial y} + 4\, C_D\, \rho C_\mu^2 \frac{k^3}{\epsilon^2}\left[-\frac{1}{3}\left(\frac{\partial v}{\partial y}\right)^2 - \frac{7}{12}\left(\frac{\partial v}{\partial x}\right)^2 - \frac{1}{6}\left(\frac{\partial u}{\partial y}\frac{\partial v}{\partial x}\right) + \frac{5}{12}\left(\frac{\partial u}{\partial y}\right)^2 + t_2\right] \quad (8)$$

$$\tau_{xy} = \rho\, C_\mu \frac{k^2}{\epsilon}\left(\frac{\partial u}{\partial y} + \frac{\partial v}{\partial x}\right) + 4\, C_D\rho C_\mu^2 \frac{k^3}{\epsilon^2}\left[-\frac{\partial u}{\partial y}\frac{\partial v}{\partial y} - \left(\frac{\partial u}{\partial x}\frac{\partial v}{\partial x}\right) + t_3\right] \quad (9)$$

where

$$t_1 = \frac{\partial}{\partial x}\left(u\frac{\partial u}{\partial x}\right) + \frac{\partial}{\partial y}\left(v\frac{\partial u}{\partial x}\right);\ t_2 = \frac{\partial}{\partial x}\left(u\frac{\partial v}{\partial y}\right) + \frac{\partial}{\partial y}\left(v\frac{\partial v}{\partial y}\right);$$

$$t_3 = \frac{\partial}{\partial x}\left(u\frac{1}{2}\left(\frac{\partial u}{\partial y} + \frac{\partial v}{\partial x}\right)\right) + \frac{\partial}{\partial y}\left(v\frac{1}{2}\left(\frac{\partial u}{\partial y} + \frac{\partial v}{\partial x}\right)\right) \quad (10)$$

If the nonlinear approximations for the turbulent stresses are substituted into Eq. (2), the resulting equations will have the same form as in the standard k–ϵ model, but with more complicated expressions for the source terms in the x-momentum and y-momentum equations and for the turbulence production term. Near-wall effects are handled, as in the standard k–ϵ model, through the use of wall functions.

The inclusion of the terms t_1, t_2, and t_3 in Eqs. (7), (8), and (9) in the nonlinear model resulted in convergence difficulties. Speziale and Ngo (1988) observed that dropping these terms had "a relatively small effect on the turbulent stress intensity." In the present study, a 5.4-percent decrease was noted in the predicted recirculation length by neglecting these terms and no significant changes in the rms velocity fluctuations (less than 1 percent) were observed. Therefore, for the results presented in this paper, t_1, t_2, and t_3 are dropped from Eqs. (7), (8), and (9), respectively.

Boundary Conditions. Measured inlet boundary conditions were provided for all three cases. The inlet and outlet positions relative to the rib are given in Table 1. For Cases I and III, the measured inlet conditions fit the following profile:

$$\frac{u}{U_0} = \left(\frac{y}{\delta_u}\right)^{\frac{1}{5.6}} \text{ if } y/\delta_u < 1 \text{ and } y/\delta_u > \left(\frac{H}{\delta_u} - 1\right);$$

$$\frac{u}{U_0} = 1 \text{ if } 1 \le y/\delta_u \le \left(\frac{H}{\delta_u} - 1\right) \quad (11)$$

where the boundary layer thickness δ_u and the channel height H are given in Table 1 for the respective cases. The specified velocity profile fit the measured profiles to within 5 percent for Case III.

Of the three flows presented by Castro (1979), the flow characterized as F2L was selected because most of the data presented are for this case. The upstream profile is prescribed at 34 rib heights upstream of the rib from the data given for turbulent fully developed smooth duct flow.

The inlet ϵ profiles for the three cases were specified as $\epsilon = k^{1.5}/H$. For Cases II and III, the measured k profiles were used directly. However, for Case I, the measured fluctuations in u were available only at locations downstream of the rib, where the fluctuations were significantly higher than at the inlet. Therefore, the inlet value of k was prescribed as 10 percent of the measured u'^2 at 25 rib heights downstream of the rib, and ϵ was calculated from these values.

At the outlet, zero gradient flow conditions were specified for all quantities. No-slip conditions for the velocity and the wall conditions for the turbulence quantities were specified at all of the boundary surfaces, including the rib surfaces.

Computational Details

Numerical Scheme. The numerical solutions were obtained using the control-volume based formulation of Patankar (1980). In this procedure, the domain is discretized by a series of control volumes, with each control volume containing a grid point. The differential equation is expressed in an integral manner over the control volume, and profile approximations are made in each coordinate direction, leading to a system of algebraic equations that can be solved in an iterative manner. Pressure-velocity interlinkages are handled by the SIMPLER formulation (Patankar, 1980).

For a smooth approach to convergence, a box-filter (Clark et al., 1979) was necessary in computing the source terms for the nonlinear model. For a sufficiently fine mesh, as in this study, the box-filter does not affect the final converged results. The velocity field was filtered once before calculating the velocity gradients that appear in the source terms. The shear stress terms were filtered three times before using them in the source or generation terms.

More computer time was required for the nonlinear-model calculations than for the standard-model calculations because of the extra computations involved and because more iterations were required for convergence. For the same grid distribution, the nonlinear model required approximately three times the cpu time as the standard model.

Grid-Independence Studies. Grid-independence studies were performed for all three cases. For Case III, results for grid sizes of 75×28, 175×88, and 275×150 were obtained. In all cases, the grid points were nonuniformly distributed using a power-law expression such that the mesh in the x- and y-directions was packed toward the rib. The recirculation lengths predicted by the nonlinear model on the 175×88 and 275×150 meshes were within 9 percent of each other, while the corresponding deviation for the standard k–ϵ model was 6 percent. The standard k–ϵ model predictions for u/U_0 at two locations for the different grid sizes are shown in Fig. 2(*a*). Although the solutions on the 175×88 grid appear to be grid independent, all of the Case III solutions presented in this paper were obtained using the 275×150 grid.

For the Cases I and II the standard k–ϵ solutions were grid independent on grid sizes of 91×38 and 150×100, respectively (see Fig. 2(*b*) for Case II). The predicted reattachment lengths for the two grids were within 8.0 percent and 8.5 percent of each other for Cases I and II, respectively. The nonlinear model predictions were also found to be grid independent on a 150×100 grid. The results presented here for Cases I and II were obtained using the 150×100 grid.

Based on the foregoing studies, the results presented in this paper, for all three cases, are considered to be grid independent. The convergence criterion used requires that the residual of the mass conservation equation be less than 10^{-7} for all points in the flowfield, and that each variable, ϕ, satisfies the condition: $|\phi_{ij}^{n+1} - \phi_{ij}^{n}| \,/\, |\phi_{ij,\max}^{n}| \le 10^{-5}$.

Results and Discussion

Mean Velocities. Figure 3(*a*) compares the standard and

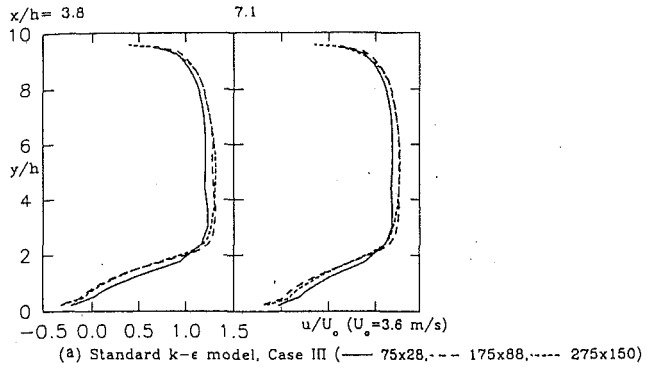

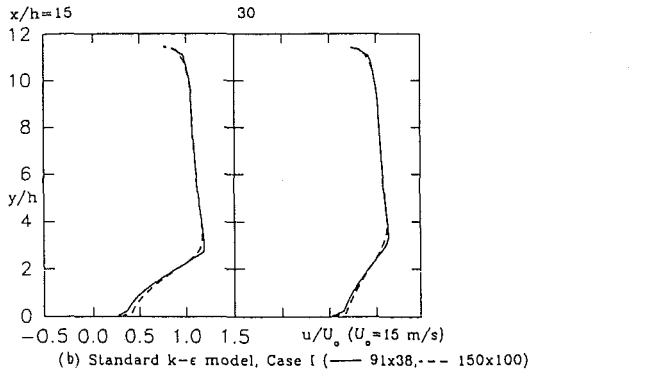

Fig. 2 u/U_0 **plots for different grid distributions**

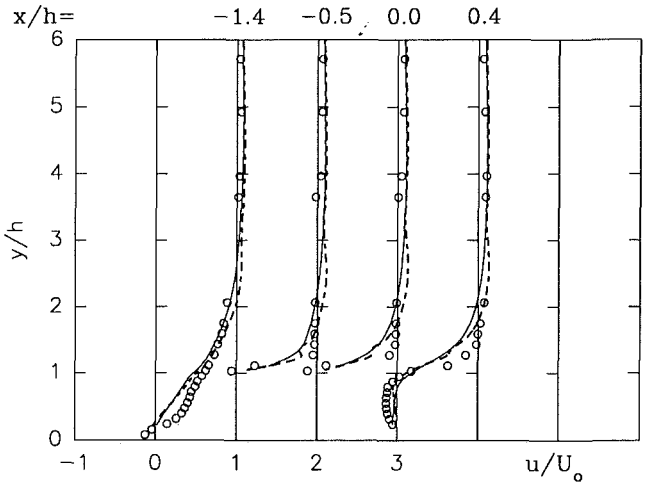

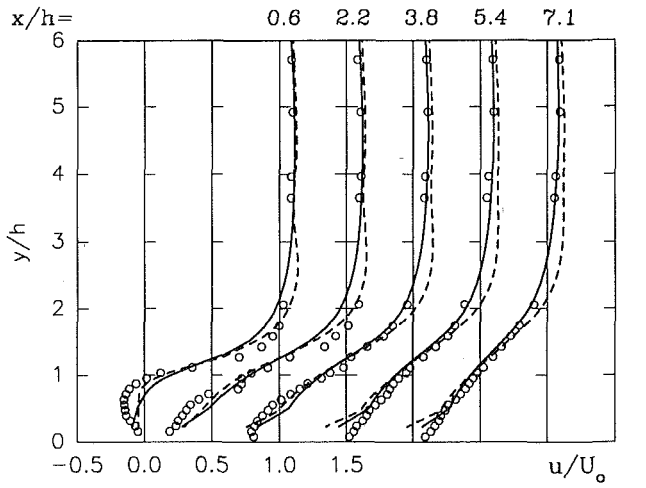

Fig. 3(*a*)

nonlinear k–ϵ model predictions of the mean streamwise velocities to the measured values. It is seen that the measurements at $x/h = -1.4$ indicate flow separation upstream of the rib. Directly above the rib, the measured velocity profiles at $x/h = -0.5$ and $x/h = 0.0$ indicate a small separation region blanketing the rib surface and a shear layer profile above it. Downstream of the rib, the profiles exhibit the expected trends of flow separation, shear layer growth, and reattachment (reattachment occurs at $x/h = 6.3 \pm 0.9$). In the recirculation region, u/U_0 reaches values up to 0.3. These observations are consistent with the backstep flow measurements of Chandrsuda and Bradshaw (1981).

Both models predict the mean streamwise velocities quite well, with the nonlinear model performing better directly above the rib and in the separated region ($x/h \leq 3.8$). Downstream of the flow separation, both models underpredict the magnitude of the velocity in the shear layer region, with the standard k–ϵ model exhibiting a larger degree of underprediction. In both the separated and shear layer regions, the measured velocity profiles recover more quickly than the predicted profiles between $x/h = 0.4$ and 3.8. Downstream of reattachment ($x/h \geq 5.4$), the predicted profiles appear to recover at the same rate as the measured values. Immediately above the rib ($x/h = -0.5, 0.0$), the predicted shear layer is thicker than measured shear layer. Moreover, the predictions do not show flow separation above the rib, but this is expected since the use of a high-Re turbulence model precludes the use of a fine mesh close to the wall ($y^+ < 11.5$). Therefore, the near-wall details ($y^+ < 11.5$) are not resolved.

The results for Case I are depicted in Fig. 3(*b*). Contrary to the experimental data, both models predict a velocity overshoot near the upper edge of the separated shear layer. However,

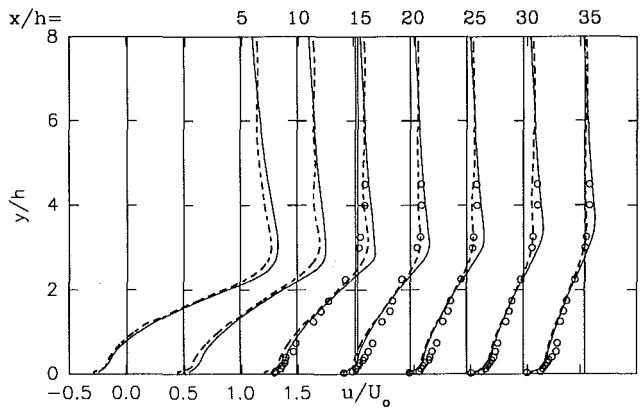

Fig. 3(*b*)

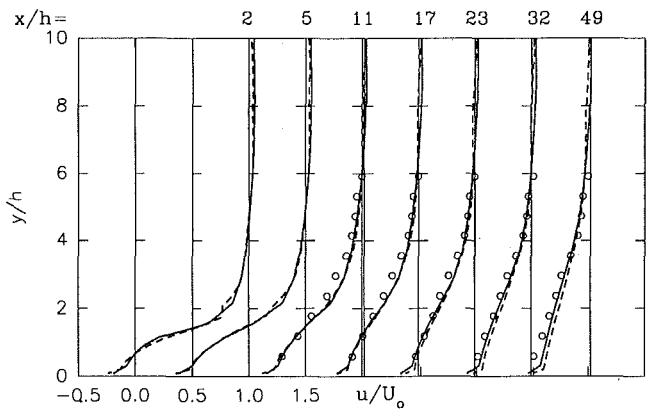

Fig. 3(*c*)

Fig. 3 u/U_0 **at different streamwise locations. (*a*) Case III, $U_0 = 3.6$ m/s; (*b*) Case I, $U_0 = 15$ m/s; (*c*) Case II, $U_0 = 3.1$ m/s. (○ experimental data, ——— standard k–ε model, · · · nonlinear model). (uncertainty in u/U_0 in Case III: ± 3.5 percent; Uncertainty in y/h and x/h = ±1.1 percent).**

the degree of overshoot is considerably less for the nonlinear model with the overshoot being virtually nonexistent at $x/h = 20$. At $x/h = 15$, the predictions and the measurements close to the wall ($y/h < 2$) are in good agreement, and the respective model predictions are identical. As x/h increases, the measured values for $y/h < 2$ appear to recover at a slightly faster rate than the model predictions.

An examination of the results for Case II (Fig. 3(*c*)) reveals no evidence of a velocity overshoot. This is because, compared to Case I, the mean velocity and the associated gradients are lower and the boundary layer is significantly larger than the rib height. The predictions of the respective models are virtually identical to one another and are in excellent agreement with the experimental data.

Castro (1979) (Case II) compared his measurements with those for a fully developed smooth duct flow and concluded that in the near-wall region, the velocity recovers to the undisturbed profile. However, the velocity defect on the high-velocity side of the shear layer persists beyond $x/h = 50$. The agreement between the present predictions and the measurements demonstrates that both models predict the velocity defect on the high-velocity side.

Cross-stream velocities were available for Case III only and are exhibited in Fig. 4. Upstream of the rib and above it the measurements reveal a strong positive v component and a curved flow deflected upward by the rib. Downstream of the rib, at $x/h = 0.4$ and 0.6, the positive velocities below $y/h = 1$ represent the separated eddy behind the rib, while the positive velocities above $y/h = 1$ represent the effect of the upward deflection of the flow by the rib. Although both numerical models underpredict the v velocity, they are generally in good qualitative agreement with the measurements. Note that the predictions of the respective models are fairly close to each other.

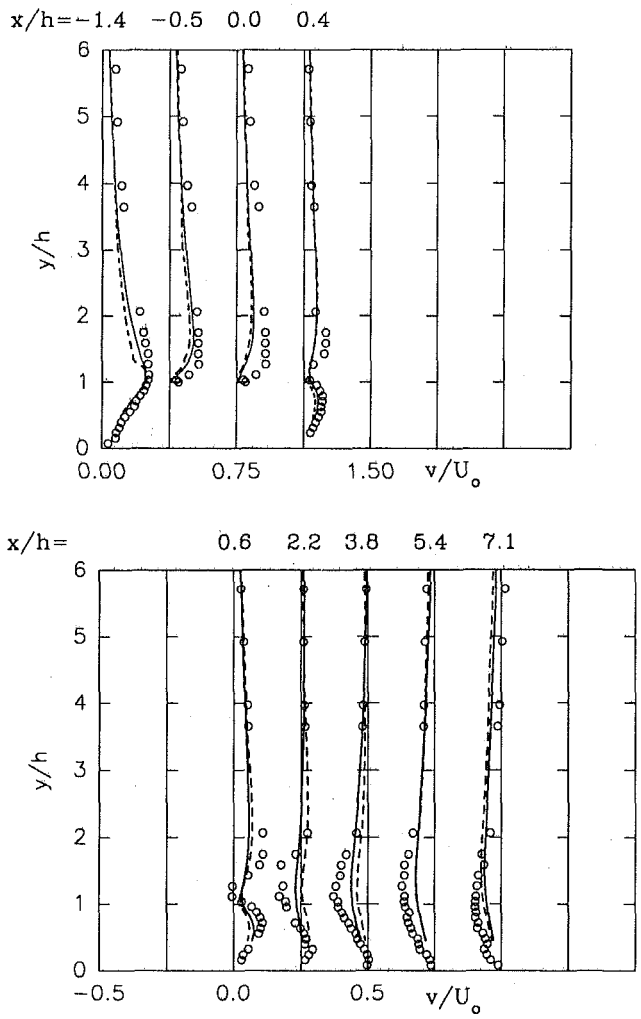

Fig. 4 v/U_0 **at different streamwise locations. Case III,** $U_0 = 3.6$ **m/s (○ experimental data, ——— standard** k–ϵ **model, · · · nonlinear model). (Uncertainty in** v/U_0**: ± 3 percent; uncertainty in** y/h **and** $x/h = \pm 1.1$ **percent).**

Reattachment Lengths. The mean reattachment lengths for the three cases are shown in Table 2. In the present experimental study, reattachment occurs at $x_R/h = 6.3 \pm 0.9$, while both Antoniou and Bergeles (1988) and Castro (1979) report x_R/h values of 10 but give no indication of the measurement uncertainty.

In order to rationalize the just reported reattachment lengths, it should be emphasized that in Cases II (Castro, 1979) and III the rib is fully immersed in the boundary layer ($\delta_u/h = 5$ for Case II and 3.3 for Case III) and the free stream streamwise turbulence intensity is low. The expansion ratio for Case II is, however, smaller than that for Case III and the Reynolds number based on either h or $2H$ is significantly higher for Case II ($\mathrm{Re}_{2H} = 25.2 \times 10^4$ for Case II and 2.8×10^4 for Case III). The Reynolds number effect appears to be important since x_R/h is greater for Case II. For Case I (Antoniou and Bergeles, 1988), the expansion ratio is nearly the same as that for Case III, but $\delta_u/\mathrm{h} = 0.7$, and the Reynolds number and the free stream turbulence intensities are significantly higher than for Cases I and II ($\mathrm{Re}_{2H} = 93 \times 10^4$, 0.4 percent freestream turbulence intensity). A higher Reynolds number implies larger x_R/h, but higher turbulence levels promote lateral turbulent transport and therefore reduce the reattachment length. The net effect appears to be that x_R/h for Case I is nearly the same as that for Case II.

The reattachment length predicted using the nonlinear model is larger than that predicted by the standard k–ϵ model. In view of the uncertainty associated with the experimental values, it is difficult to definitively assess whether the nonlinear model predictions of x_R/h are much better than the standard k–ϵ model values. For Case II, the nonlinear model predicts a reattachment length closer to the experimental value. However, for Case III, the standard-model prediction is within the experimental uncertainty, while the nonlinear prediction lies just outside the uncertainty band.

For flow past backsteps, it is generally agreed that the standard k–ϵ model underpredicts the reattachment length. The standard k–ϵ predictions of the present study are consistent with this observation. The nonlinear k–ϵ model predictions of Speziale and Ngo (1988), for flow past backsteps, gave reattachment lengths larger than the standard k–ϵ values, thus improving upon the predicted value of x_R/h.

Turbulent Stresses. The streamwise turbulence intensity results for Case III are shown in Fig. 5(*a*). Clearly, in the vicinity of the separation upstream of the rib, the measured turbulence levels are substantially higher than in the free stream, with the

Table 2 Measured and predicted reattachment lengths (x_R/h)

Case Study	Experiment (x_R/h)	Standard k–ϵ (x_R/h)	Nonlinear model (x_R/h)
I (Antoniou and Bergeles, 1988)	10	9.4	10.9
II (Castro, 1979)	10	7.8	9.0
III (Present work)	6.3 ± 0.9	5.9	7.5

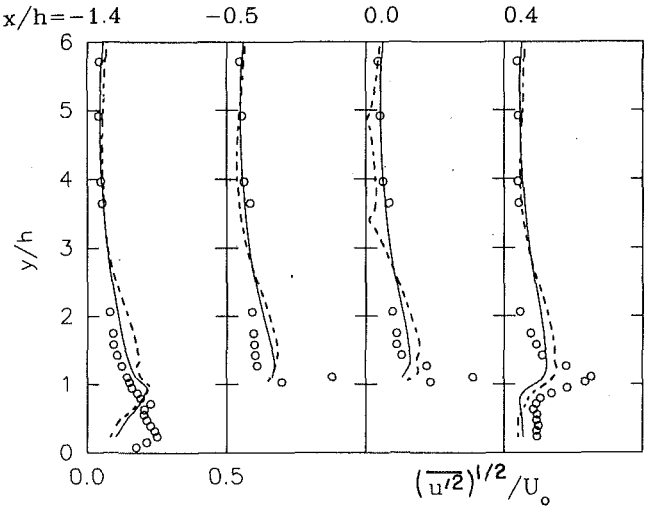

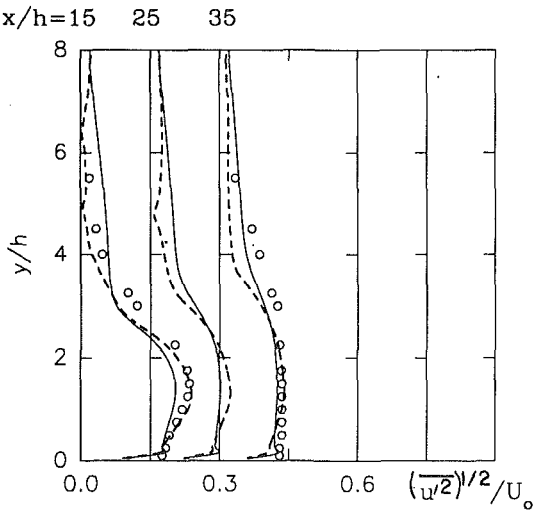

Fig. 5(*b*)

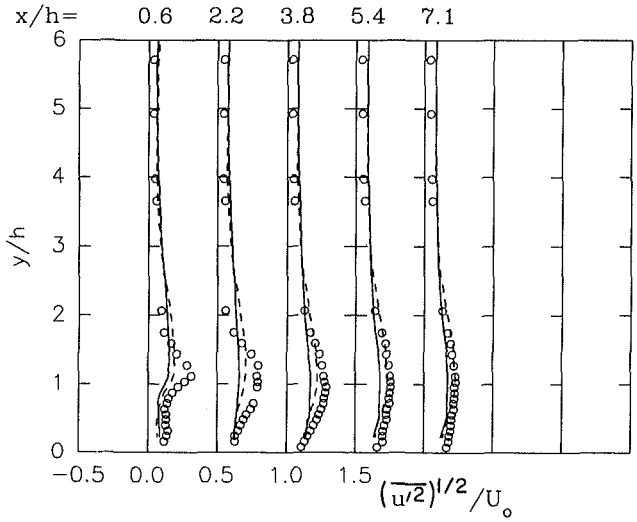

Fig. 5(*a*)

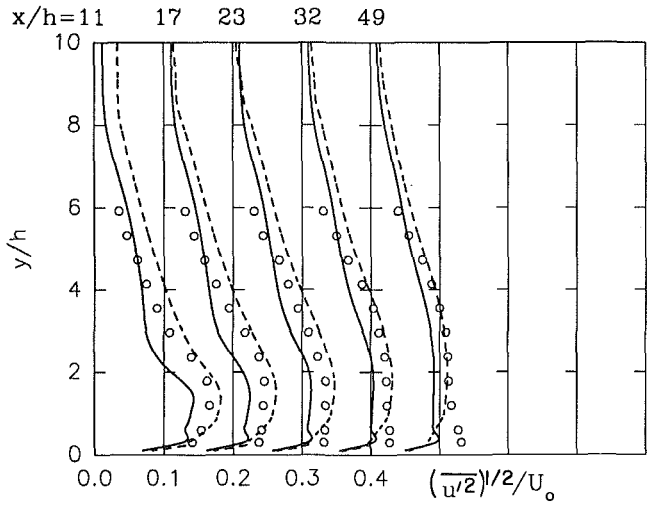

Fig. 5(*c*)

Fig. 5 $(\overline{u'^2})^{1/2}/U_0$ **at different streamwise locations. (*a*) Case III, $U_0 = 3.6$ m/s; (*b*) Case I, $U_0 = 15$ m/s; (*c*) Case II, $U_0 = 3.1$ m/s (○ experimental data, ——— standard k-ϵ model, · · · nonlinear model.) (Uncertainty in $(\overline{u'^2})^{1/2}/U_0$ in Case III: ± 5 percent, Uncertainty in y/h and $x/h = \pm 1.1$ percent).**

near-wall values reaching 0.25, about 2.5 times the free-stream values. The upward deflection of the flow by the rib leads to higher velocity gradients ($\partial u/\partial y$, $\partial v/\partial y$, and $\partial u/\partial x$) and thus to a higher production of turbulence.

Directly above the rib, the measured turbulence levels are further enhanced, with the streamwise intensity reaching a value of nearly four times the free-stream value. This increase in the peak intensity is significant and noteworthy. It can be explained by noting that along $y/h = 1$, as the flow approaches the rib, the no-slip constraint along the rib face leads to high values of $\partial u/\partial x$ and $\partial u/\partial y$. Since the two largest terms in the expression for the production of turbulence are proportional to $\partial u/\partial x$ and $\partial u/\partial y$, the turbulence levels are significantly enhanced in the region directly above the rib.

Downstream of the rib, as the flow separates, the peak values decay, and the locus of the peak droops downward with the shear layer toward reattachment. Just downstream of separation ($x/h \leq 0.6$), the profiles show a sharp peak in the shear layer and a flat profile in the recirculation region. With increasing x/h, the turbulence is diffused; the profiles become more uniform; and the peak turbulence level decays.

The general features of the aforedescribed observations are consistent with those for backstep flows (Chandrsuda and Bradshaw, 1981) and a flow through a pair of ribs (Liou and Kao, 1988). However, in these studies, the intensities increase in the initial part of the separated shear layer, but in the present measurements, the maximum streamwise turbulence intensity occurs directly above the rib.

Comparisons of the model predictions with the experiments show that the peak values are significantly underpredicted in the vicinity of the rib. However, further downstream of separation ($x/h \geq 3.8$), the predictions agree quite satisfactorily with the measured values. The nonlinear model predicts higher streamwise turbulence intensities than the standard k-ϵ model and, in general, shows better agreement with the measured data than the standard k-ϵ model. For $x/h \leq 0.0$, the nonlinear model displays a concavity in the intensity profile near $y/h \cong 3.5$. For a backstep flow, Thangam and Speziale (1991) observed similar behavior.

The streamwise turbulence intensities for Case I and II are shown in Figs. 5(*b*) and *c*, respectively. In both cases, the nonlinear-model predictions are generally in good agreement

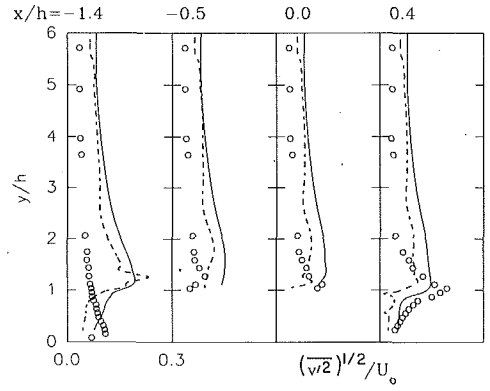

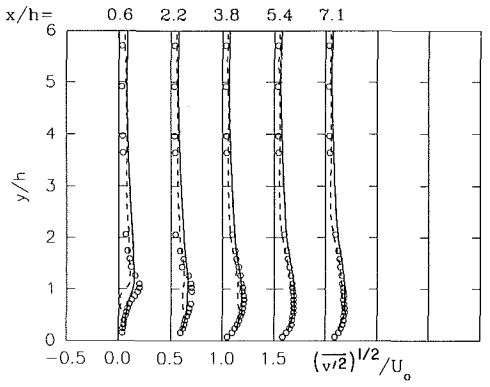

Fig. 6(*a*)

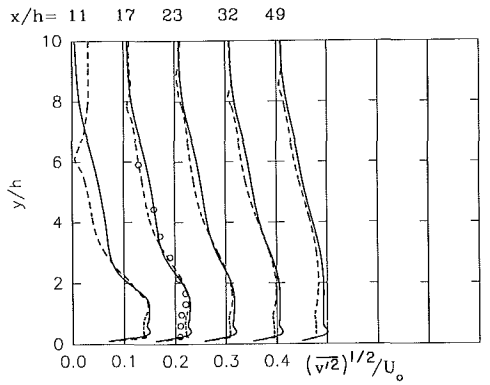

Fig. 6(*b*)

Fig. 6 $(\overline{v'^2})^{1/2}/U_0$ at different streamwise locations. (*a*) Case III, $U_0 = 3.6$ m/s; (*b*) Case II, $U_0 = 3.1$ m/s (○ experimental data, ——— standard k-ϵ model, --- nonlinear model). (Uncertainty in $(\overline{v'^2})^{1/2}/U_0$ in Case III: ± 4.5 percent; uncertainty in y/h and $x/h = \pm 1.1$ percent).

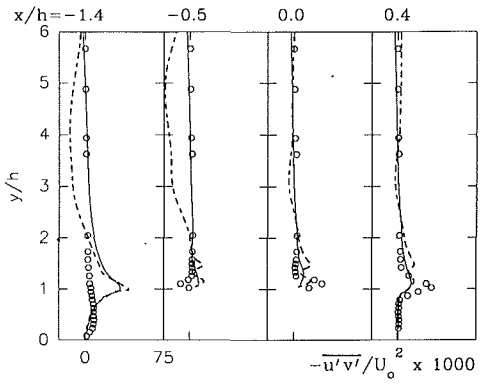

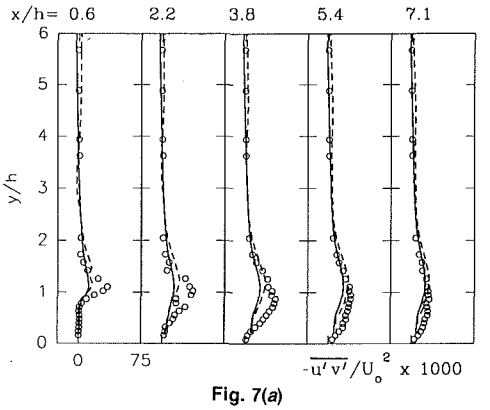

Fig. 7(*a*)

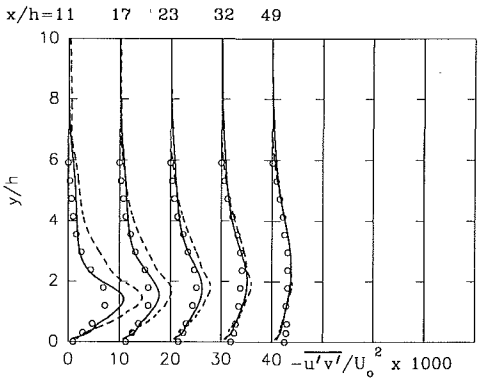

Fig. 7(*b*)

Fig. 7 $-\overline{u'v'}/U_0^2$ at different streamwise locations. (*a*) Case III, $U_0 = 3.6$ m/s; (*b*) Case II, $U_0 = 3.1$ m/s (○ experimental data, ——— standard k-ϵ model, ··· nonlinear model). (Uncertainty in $-\overline{u'v'}\,U_0^2$ in Case III: ± 8 percent; Uncertainty in y/h and x/h ± 1.1 percent).

with the data. They show distinct improvements compared to the standard k-ϵ model predictions in the recovery region. In examining Antoniou and Bergeles' (1988) data (Fig. 5(*b*)), it is seen that the standard k-ϵ model underpredicts the measured values in the inner boundary layer region and overpredicts the measured values in the outer-layer regions ($y/h > 4.5$). For Case II, the standard k-ϵ model underpredicts the measured values, particularly in the inner-layer region.

The cross-stream turbulence intensity ($(\overline{v'^2})^{1/2}/U_0$) profiles for Case III are shown in Fig. 6(*a*). First, it is observed that the measured cross-stream intensities are significantly smaller than the measured streamwise intensities, particularly in the near-rib region ($-1.4 < x/h < 2.2$), indicating the nonisotropic nature of the separated shear layer. Downstream of reattachment ($x/h > 5.4$), the cross-stream and streamwise intensities become more comparable, with the respective peaks at $x/h = 7.1$ being 0.18 and 0.23.

As for backstep flows, the maximum cross-stream intensity occurs downstream of the flow separation, not above the rib as observed in the measurements of the streamwise intensity. The explanation for this must invariably depend on the respective production terms for $\overline{u'^2}$ and $\overline{v'^2}$, that is $2[\overline{u'^2}\,\partial u/\partial x + \overline{u'v'}\partial u/\partial y]$ and $2[\overline{v'^2}\,\partial v/\partial y + \overline{u'v'}\partial v/\partial x]$, respectively. The former peaks above the rib, while the latter peaks downstream of it.

In the near-rib region ($-1.4 < x/h < 0.6$), the agreement between the predictions and measurements is less than satisfactory. However, directly above the rib, the nonlinear model predictions are in better qualitative agreement with the data. Immediately downstream of separation ($0.4 < x/h < 0.6$),

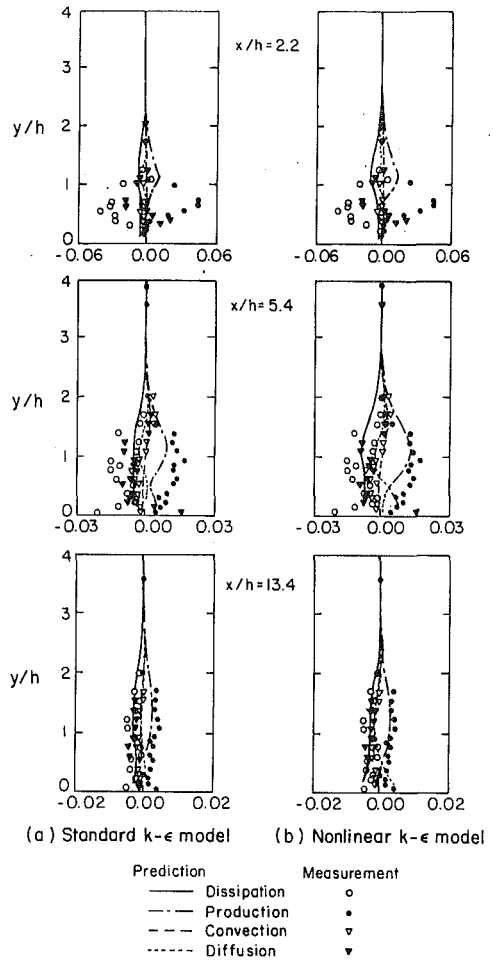

Fig. 8 Turbulent kinetic energy balances at different streamwise locations for Case III. (Uncertainty in balance terms ≅ ±12 percent).

the predicted turbulent intensities are smaller than the measured values.

Figure 6(*b*) shows cross-stream intensities for Case II. Cross-stream intensities have not been reported for Case I, and as seen in Fig. 6(*b*), only limited turbulent intensity data are available for Case II. The standard k–ϵ model predictions for $(\overline{v'^2})^{1/2}$ are close to $(\overline{u'^2})^{1/2}$, as expected, since the model reduces to $(\overline{u'^2})^{1/2} = (\overline{v'^2})^{1/2}$ for fully developed flows. The measured data and the nonlinear k–ϵ model predictions indicate that $(\overline{v'^2})^{1/2} < (\overline{u'^2})^{1/2}$, reflecting the nonisotropic nature of the flow and the nonlinear model. In general, the nonlinear-model predictions agree better with the experimental data shown in Fig. 6(*b*) than the standard-model predictions.

Turbulent shear stress results for Case III are presented in Fig. 7(*a*). The measured values of $\overline{u'v'}$ are consistent with the trends for $(\overline{v'^2})^{1/2}$, i.e., the shear stress peaks downstream of the separation, as observed for backstep flows. In the recirculation region, $x/h = 0.4$ and 0.6, the $\overline{u'v'}$ values are small, but with increasing x/h, both convection and diffusion lead to more uniform profiles.

For $x/h \leq 0$ and $y/h > 2$, the standard k–ϵ predictions are somewhat better than the nonlinear model predictions which show a concavity in the profile. Thangam and Speziale (1991) observed similar behavior in their nonlinear-model predictions of a flow past a backward facing step and argued that such behavior is consistent with experimental observations. However, the present experiments do not show a concavity in the $\overline{u'v'}$ profile. The peaks at locations downstream of the rib are underpredicted by both the models, with the nonlinear model performing slightly better.

No experimental data are available for Case I. However, comparisons between the predictions and measurements for Case II in Fig. 7(*b*) show that both models overpredict the measured values up to $x/h = 32$, beyond which the agreement is quite satisfactory.

Kinetic Energy Balances. The measured and predicted values of the various terms in the kinetic energy balance equation are shown in Fig. 8. The production of k can be calculated directly from the measured values of $\tau_{ij}\,\partial\overline{u}_i/\partial x_j$. Assuming $\overline{w'^2} = 1/2\,(\overline{u'^2} + \overline{v'^2})$, k can be approximated as $3/4\,(\overline{u'^2} + \overline{v'^2})$ and the turbulent diffusion $\overline{u'}\,1/2\,\overline{q^2}$ and $\overline{v'}\,1/2\,\overline{q^2}$ can be approximated as $3/4\,(\overline{u'^3} + \overline{u'v'^2})$ and $3/4\,(\overline{v'^3} + \overline{u'^2v'})$, respectively. The pressure diffusion is usually neglected. The dissipation, ϵ, is then the only unknown and is calculated from the balance equation.

In the separation region ($x/h = 2.2$), the production and dissipation terms are significant, but the turbulent diffusion term is also fairly large, with both positive and negative values. The convection, by comparison, is relatively small. Due to the significant contribution of the diffusion term, the turbulence in the separation region is not in equilibrium. In the vicinity of reattachment, the magnitude of the various terms decrease, but note that the turbulent diffusion is still quite significant. Downstream of the separated region, the turbulent diffusion terms decrease. However, even at $x/h = 13.4$, in the central part of the boundary layer ($0.5 < y/h < 1.5$), the diffusion terms are as large as the dissipation terms. Clearly, the assumption of turbulence equilibrium, even well downstream of reattachment, is questionable.

The predictions show that both the models underpredict the dissipation, the production, and the diffusion in the separated region. While there is a significant reduction in the measured quantities between $x/h = 2.2$ and $x/h = 5.4$, the predictions have a proportionately smaller reduction in the derived quantities. Far downstream of the rib ($x/h = 13.4$), the predictions and the measurements show a reduction in all the components of the turbulent kinetic energy balance. At this location ($x/h = 13.4$), the predictions agree quite well with the measured production of the turbulent kinetic energy, but the dissipation and diffusion are still underpredicted.

Conclusions

The ability of the nonlinear k–ϵ turbulence model to predict the duct flow past a wall-mounted, two-dimensional rib was assessed through comparisons with the standard k–ϵ turbulence model and the experimental flow results of this study (Case III) as well as the flow measurements of Antoniou and Bergeles (1988) (Case I) and Castro (1979) (Case II). The use of the nonlinear model resulted in improved predictions of the mean velocities near the upper edge of the shear layer of Case I. It also resulted in considerable improvements in the prediction of the streamwise turbulence intensity for all cases and gave improved predictions of the production and dissipation of the turbulent kinetic energy near reattachment. Otherwise, the performance of the two models was comparable, with both models performing quite well in the core flow region and close to reattachment, and both models performing poorly in the separated and shear-layer regions close to the rib. Both models grossly underpredicted the production, dissipation, and diffusion components in the recirculating region, but downstream of reattachment, they predicted the components of the turbulent kinetic energy reasonably well. The measurements demonstrated that the turbulence was far from equilibrium in the recirculation and shear layer regions, with nonequilibrium conditions persisting at least as far as 7 rib heights downstream of reattachment.

Acknowledgment

This work was supported by a grant from the National Science Foundation (CTS-8800736) and the Cornell Supercomputing Facility and under a contract with the Gas Research Institute (5090-260-1961). Their support is gratefully acknowledged.

References

Antoniou, J., and Bergeles, G., 1988, "Development of the Reattachment Flow Behind Surface-Mounted Two-Dimensional Prisms," ASME JOURNAL OF FLUIDS ENGINEERING, Vol. 110, pp. 127–133.

Benodekar, R. W., Goddard, A. J. H., Gosman, A. D., and Issa, R. I., 1985, "Numerical Prediction of Turbulent Flow Over Surface-Mounted Ribs," *AIAA Journal*, Vol. 23, No. 3, pp. 359–366.

Bergeles, G., and Athanassiadis, N., 1983, "The Flow Past a Surface-Mounted Obstacle," ASME JOURNAL OF FLUIDS ENGINEERING, Vol. 105, pp. 461–463.

Castro, I. P., 1979, "Relaxing Wakes Behind Surface-Mounted Obstacles in Rough Wall Boundary Layers," *Journal of Fluid Mechanics*, Vol. 93, pp. 631–659.

Chandrsuda, C., and Bradshaw, P., 1981, "Turbulence Structure of a Reattaching Mixing Layer," *Journal of Fluid Mechanics*, Vol. 110, pp. 171–194.

Chung, M. K., Park, S. W., and Kim, K. C., 1987, "Curvature Effect on Third-Order Velocity Correlations and Its Model Representation, *Physics of Fluids*, Vol. 30, No. 3, pp. 626–628.

Clark, R. A., Ferziger, J. H., and Reynolds, W. C., 1979, "Evaluation of Subgrid-Scale Models Using an Accurately Simulated Turbulent Flow," *Journal of Fluid Mechanics*, Vol. 91, Part 1, pp. 1–16.

Driver, D. M., and Seegmiller, H. L., 1985, "Features of a Reattaching Turbulent Shear Layer in Divergent Channel Flow," *AIAA Journal*, Vol. 23, No. 2, pp. 163–171.

Driver, D. M., and Seegmiller, H. L., 1982, "Features of a Reattching Turbulent Shear Layer Subject to an Adverse Pressure Gradient," AIAA/ASME 3rd Joint Thermophysics, Fluids, Plasma and Heat Transfer Conference, June 7–11, St. Louis, MO.

Durst, F., and Rastogi, A. K., 1980, "Turbulent Flow over Two-Dimensional Fences," *Turbulent Shear Flows 2*, Bradbury et al., eds., Berlin, Springer-Verlag, pp. 218–231.

Kline, S. J., and McClintock, F. A., 1953, "Describing Uncertainties in Single-Sample Experiments," *Mechanical Engineering*, Vol. 75, pp. 3–8.

Launder, B. E., and Spalding, D. B., 1974, "The Numerical Computation of Turbulent Flows," *Computer Methods in Applied Mechanics and Engineering*, Vol. 3, 1974, pp. 269–289.

Lee, B. K., Cho, N. H., and Choi, Y. D., 1988, "Analysis of Periodically Fully Developed Turbulent Flow and Heat Transfer by k–ϵ Equation Model in Artificially Roughened Annulus," *International Journal of Heat and Mass Transfer*, Vol. 31, No. 9, pp. 1797–1806.

Leschziner, M. A., and Rodi, W., 1981, "Calculation of Annular and Twin Parallel Jets Using Various Discretization Schemes and Turbulence Model Variations," ASME JOURNAL OF FLUIDS ENGINEERING, Vol. 103, pp. 352–360.

Liou, T. M., and Kao, C. F., 1988, "Symmetric and Asymmetric Turbulent Flows in a Rectangular Duct with a Pair of Ribs," ASME JOURNAL OF FLUIDS ENGINEERING, Vol. 110, pp. 373–379.

Park, S. W., and Chung, M. K., 1989, "Curvature-Dependent Two-Equation Model for Prediction of Turbulent Recirculating Flows," *AIAA Journal*, Vol. 27, pp. 340–344.

Patankar, S. V., 1980, *Numerical Heat Transfer and Fluid Flow*, Hemisphere Publishing Corporation, pg. 133.

Phataraphruk, P., and Logan, E., Jr., 1979, "Turbulent Pipe Flow Past a Rectangular Roughness Element," *Turbulent Boundary Layers*, Weber, H. E., ed., ASME.

Rood, E. P., and Telionis, D. P., 1991, "Journal of Fluids Engineering Policy on Reporting Uncertainties in Experimental Measurements and Results," ASME JOURNAL OF FLUIDS ENGINEERING, Vol. 113, pp. 313–314.

Speziale, C.G., 1987, "On Nonlinear *k-l* and *k-*ϵ Models of Turbulence," *Journal of Fluid Mechanics*, Vol. 178, pp. 459–475.

Speziale, C. G., and Ngo, T., 1988, "Numerical Solution of Turbulent Flow Past a Backward facing Step using a Nonlinear *k-*ϵ Model," *International Journal of Engineering Sciences*, Vol. 26,pp. 1099–1112.

Thangam, S., and Hur, N., 1991,"A Highly-Resolved Numerical Study of Turbulent Separated Flow Past a Backward-Facing Step," *International Journal of Engineering Services*, Vol. 29, pp. 607–615.

Thangam, S., and Speziale, C. G., 1991, "Turbulent Separated Flow Past a Backward-Facing Step: A Critical Evaluation of Two-Equation Turbulence Models," NASA Contractor Report, ICASE Report No. 91-23.

Tropea, C. D., and Gackstatter, R., 1985, "The Flow Over Two-Dimensional Surface-Mounted Obstacles at Low Reynolds Numbers," ASME JOURNAL OF FLUIDS ENGINEERING, Vol. 107, pp. 489–494.

Average Physical Parameters in an Air-Water Two-Phase Flow in a Small, Square-Sectioned Channel

J. K. Keska

R. D. Fernando

J. Keska Consultants,
P.O. Box 573,
Richland, WA 99352

This experimental study focuses on an adiabatic two-phase air-water flow generated in a small, horizontal, 6.35 mm square channel. Pressure and temperature were near standard conditions. Experimental data and correlations available in the literature, generally, do not consider the full range of concentration, small cross-sectional areas and direct physical parameters, such as concentration (void fraction) and/or phase velocities. Based on the direct measurement of in-situ spatial concentration (in a full range of concentrations, including gas and liquid phases only), and flow-pattern determination, the experimental data from the study are compared with data from the literature and with prediction by the generally accepted Lockhart-Martinelli's and Chen's models. Spatial concentration measurements were made with a computer-based system developed and built by the authors. Pressure drop over a length of the channel was also measured with pressure transducers. These measurements were made for a variety of flow conditions which encompassed bubble, slug, plug, and annular flow regimes. Flow patterns were established, and both mean and fluctuating components of the concentration measurements were used to objectively identify the flow patterns. These results, together with visual enhanced observation (stroboscope) supplemented with a high-speed CCD camera recording enhanced with dye injection, were used to obtain flow-pattern maps and compared with the literature. Spatial concentration is shown to be a key physical parameter in describing the state of the mixture in two-phase flow.

Introduction

Despite the numerous theoretical and experimental investigations on gas-liquid pipe flow, no reliable correlations between the frictional pressure gradient, spatial concentration, phase velocities, and flow pattern are available, mainly as result of the large number of variables involved and significant limitations and difficulties in measurement. Also, only a few studies have been concerned with small, horizontal, rectangular channels, which are of interest in heat exchanger design. Even fewer studies have reported in-situ measurements of spatial concentration and the velocities of the phases.

Current development of micromechanical devices, which includes micro-heat exchangers with rectangular or square channels that are easier to manufacture, are of interest in this study. Although numerous results exist in the engineering literature pertaining to two-phase flow in large-diameter channels, the size, geometry, and experimental approach (measurement techniques used and physical parameters) are significantly different in this investigation.

Therefore, any experimental results of two-phase flow in small channels, with precisely described experimental conditions and in-situ measured physical parameters (spatial concentration or phase velocities), are especially valuable. In a study of a two-phase gas-liquid mixture flow for the description of experimental conditions, the most important parameters are in-situ concentration (or its complement void fraction) and in-situ phase velocities. Measurement of either parameter allows the determination of the other and results in an umambiguous description of the experimental conditions. This requires the use of a concentration meter and/or a phase velocity meter.

Also in two-phase flows, it is necessary to be able to predict a priori the flow pattern that will be encountered for given flow conditions. Hence, much experimental and theoretical research has concentrated on this problem. Flow pattern, however, is a subjective parameter and thus various authors have defined flow patterns differently. In addition, the flow structure may be difficult to visualize because of the high velocity of a mixture and/or component flow and translucent liquid films. Also flow-pattern transitions may be influenced by a number of parameters such as channel geometry, orientation, flow parameters, and physical properties of the fluids. Various analytical, empirical and theoretical methods, which attempt to overcome the problems associated with flow-pattern prediction, have been proposed.

The aim of this study is to describe the flow of air-water in a square horizontal channel with the in-situ and physical pa-

Contributed by the Fluids Engineering Division for publication in the JOURNAL OF FLUIDS ENGINEERING. Manuscript received by the Fluids Engineering Division April 20, 1992; revised manuscript received September 8, 1993. Associate Technical Editor: T. T. Huang

rameters. Of the many parameters that could be considered in the study, the following were selected:

- the in-situ void fraction or spatial concentration that describes the state of the mixture
- in-situ phase and mixture velocities that are dynamic parameters associated with the flow
- pressure drop that is a measure of the transport energy consumption and that in turn is related to the dynamic and state parameters.

Furthermore, the flow pattern, which is an effect resulting from conditions described by these in-situ parameters, is considered. In the following, the authors have presented the data and results in terms of the commonly used parameters in the literature such as superficial velocities, quality, and Lockhart-Martinelli parameters. These are not considered as physical parameters within the realm of direct measurement and detection; they do, however, allow comparison with data published by others.

Flow-Pattern Characterization

From a survey of the literature related to flow-pattern definition and characterization, it is clear that visual flow-pattern definitions resulting in a flow-pattern map are ambiguous and vary from paper to paper (Barnea et al., 1980; Chen and Spedding, 1984; Lockhart and Martinelli, 1949; Mandhane et al., 1974; Richardson, 1958). Many different flow-map coordinates have been proposed with varying numbers of flow-pattern maps. Obviously, when flow-pattern definitions are used, they need to be described and defined in detail without ambiguity, with physical parameter definitions and standards, and be related to the experimental conditions in order for different researchers' results to be compared.

Many empirical, deterministic and statistical methods have been used in attempts to identify flow-pattern transitions. Almost all of the literature reports on studies of two-phase flow pattern are for channels with large diameters. Also, most of the results in literature include data on such superficial parameters as gas and liquid velocities or quality. Furthermore these superficial parameters are geometry- and system-related, and at least they are a function of spatial concentration, flow pattern, and in-situ phase velocities.

The work by Mandhane et al. (1974) identified six major flow patterns. Barnea et al. (1980) categorized five flow patterns with various sub-groups. They also propose an analytical model for flow-pattern prediction in horizontal two-phase flows. In another work, Barnea et al. (1983) produced flow-pattern maps based on the same categories for small diameter pipes. Mukherjee and Brill (1985) introduced a system of empirical equations for four flow patterns for inclined two-phase flow of kerosene and oil. Jepson (1989) attempted to model only the transition to slug flow using a physical model. Lin and Hanratty (1987) have studied pipe diameter effects on flow pattern in air-water horizontal flow employing various techniques in an attempt to identify the patterns and flow-pattern transitions accurately and less subjectively. More recently, Wambsganss et al. (1990 and 1991) examine flow in small horizontal rectangular channels.

Based on the authors' experience, visual identification of flow pattern in gas-water mixtures is very complicated. Attempts to identify them have been ambiguous, even when techniques such as using high speed CCD cameras with slow motion capabilities are used in parallel, thereby "freezing" the motions with a stroboscope and/or dye injection enhancement. To eliminate the subjectivity in flow-pattern identification, the authors used statistical methods in their study for the determination of the five commonly used flow patterns (Keska, 1991). These flow-pattern definitions follow those used by Richardson (1958).

Void Fraction (α)

The void fraction is essential in determining the state of a mixture flow. Its importance is highlighted by the number of correlations that exist in the literature from theoretical modelling, from phenomenological curve fitting, and from direct and indirect measurements. Mostly analytical and empirical models exist for void fraction prediction and mainly for well-defined flow patterns such as annular or bubbly flow.

Butterworth (1975) compares six models for void faction prediction proposed by others and comes to the conclusion that all are similar. However, he states that, if the flow pattern are taken into consideration when applying the models, the results may deviate from the predicted significantly. Chen (1986), taking the generalized form of the Butterworth equation, gives a simplified form for annular flow.

In some reported experimental results (Butterworth, 1975; Chen and Spedding, 1984, Wambsganss et al., 1990 and 1991), void fraction is calculated using parameters such as quality and fluid properties. One equation that is often used is the Butterworth (1975) form:

$$\alpha = \frac{1}{1 + K\left(\frac{1-x}{x}\right)^{p}\left(\frac{\rho_g}{\rho_L}\right)^{q}\left(\frac{\mu_l}{\mu_g}\right)^{r}} \tag{1}$$

where K, p, q, and r take on values suggested by their respective models, from which the above equation is formulated. It should

Nomenclature

A = cross-sectional area, m^2
c_v = in-situ volumetric spatial concentration, $c_v = \frac{V_w}{V_w + V_a}$
G = mass flux, kg/m^2s
k, n = constants
L = length, m
$\dot{M}$ = mass flow rate, kg/s
p = pressure, kPa
$\frac{\Delta p}{\Delta L}$ = pressure gradient kPa/m
$\dot{V}$ = flow rate, m^3/s
V = volume, m^3
v = velocity, m/s
S = slip ratio
x = mass quality
α = void fraction
ρ = density, kg/m3
μ = dynamic viscosity, kg/m s
ϕ, X = Lockhart-Martinelli parameters

Subscripts

g = gas
m = mixture
L = liquid
s = superficial
v = volumetric
w = water
I, II, III = first, second, third type
1, 2, . . . , i = 1st, 2nd, . . . , ith component or value

be noted that this equation does not take the flow regime into consideration.

The Lockhart and Martinelli ($L-M$) correlation is obtained by substituting $K = 0.28$, $p = 0.64$, $q = 0.36$, and $r = 0.07$. Hence,

$$\alpha = \frac{1}{1+0.28\left(\frac{1-x}{x}\right)^{0.64}\left(\frac{\rho_g}{\rho_L}\right)^{0.36}\left(\frac{\mu_L}{\mu_g}\right)^{0.07}} \tag{2}$$

or

$$\alpha = \frac{1}{1+X^{2/3}} \tag{3}$$

expressed in terms of the Lockhart-Martinelli parameter X. Chen and Spedding (1984) in their further examination of the void fraction correlations have incorporated an empirical parameter k to account for the deviation of the experimental data from the idealized annular flow model on which Eq. (3) is based. The modified equation is

$$\alpha = \frac{k}{k+X^{2/3}} \tag{4}$$

Slip Ratio

The in-situ slip ratio is important in determining the dynamic condition of a mixture flow because of the physical and independent character of the components. A single correlation by itself does not predict the slip ratio satisfactorily. The Butterworth form of the Lockhart-Martinelli (1949) correlation is

$$\frac{V_g}{V_L} = \left(\frac{1-x}{x}\right)\left(\frac{\rho_g}{\rho_L}\right)\left(\frac{\mu_L}{\mu_g}\right) \tag{5}$$

This has been shown to hold for most flow regimes by Spedding et al. (1986). Chen and Spedding (1984) have analyzed the general form of the Butterworth equation (empirical) and related it to the various flow patterns by substituting different values for the equation constants. The proposed correlations are presented in graphical form for horizontal air-water data in a 45.5 mm diameter pipe. They also claim that their correlations give good agreement with experimental data of others for pipes ranging from 25 mm to 52.5 mm diameters (5 sizes).

Pressure Drop

The main contributor to the pressure drop in adiabatic horizontal pipe flow is friction. This is the main assumption used in many of the commonly published analytical solutions. However, in two-phase flow, factors like the phase distribution, stratification, and degree of wetting also effect pressure drop. Lockhart and Martinelli (1949) were the first to suggest correlations for pressure drop in their 1949 paper. Subsequently, many authors have used these same correlations with modifications. The pressure drop in general is a function of a number of parameters including density, spatial concentration, temperature, phase velocities, channel dimensions and flow pattern. The Lockhart and Martinelli correlation introduces the parameters X and ϕ as a means of correlating the pressure drop data. These are related as follows:

$$\phi_L^2 = \frac{(\Delta P/\Delta L)_m}{(\Delta P/\Delta L)_L} \tag{6}$$

$$\phi_g^2 = \frac{(\Delta P/\Delta L)_m}{(\Delta P/\Delta L)_g} \tag{7}$$

$$X^2 = \frac{(\Delta P/\Delta L)_L}{(\Delta P/\Delta L)_g} = \left(\frac{\phi_g}{\phi_L}\right)^2 \tag{8}$$

Richardson (1958) in his thesis expresses the parameter X in terms of the quality and phase constituents thus:

$$X = \left(\frac{1-x}{x}\right)^{0.875}\left(\frac{\rho_g}{\rho_L}\right)^{0.5}\left(\frac{\mu_L}{\mu_g}\right)^{0.125} \tag{9}$$

Various researchers, such as Butterworth, Chen and Spedding, have adopted the L-M model and tested it against experimental data. While deviations exist, they have found that those deviations are acceptable. The limitations in the L-M correlations are due to neglecting the flow pattern and to the interaction and acceleration between the phases.

Experimental Apparatus

Experimental data was obtained by the authors for a two-phase flow of air-water mixture generated in a horizontal open loop flow test apparatus as shown on Fig. 1. The flow channel (12 in the figure) is square sectioned. The input parameters are measured at the entrance and the phases mixed in a chamber. The flow occurs through the channel where differential pressure is measured. The flow then passes through a capacitive sensor system and finally exits with phase separation.

The flow channel (12), shown in Fig. 1, is constructed from a square sectioned transparent acrylic tube and has internal dimensions of 6.35 mm. Two pressure taps are set 0.86 m apart on top of the channel. A mixing chamber (7) is fitted to the entrance end of the channel to intimately mix the air and water. The flow rates are controlled at a metering panel (2.5).

The capacitive sensor system (10) contains the capacitive sensors for the computer-based capacitive concentration meter. The body of the system is machined from a block of acrylic plastic. Two sensors (each consisting of 2 plates) are mounted in this channel flush with the walls, in non-intrusive contact with the mixture flow. In normal orientation, these sensors form type I and type III capacitors.

The instrumentation for the capacitive sensor system is based on capacitance meters (13) and consists of two separate systems. Each system consists of a primary electronic part connected to the sensor and secondary electronics (18) where the signal is conditioned and amplified to give an analog signal proportional to the capacitance of a sensor. The static and differential pressures between the two taps on the flow channel are measured using electrical pressure transducers (8 and 9), which provide an analog voltage signal proportional to pressure. All signals in the form of time traces are acquired and stored using a computer-based data acquisition system (DAS) (20).

Analog signals from the capacitive sensor system and pressure transducers are digitized using a 12 bit A/D converter installed in the IBM PC compatible system. The capacitance of a type I capacitive sensor bears a linear relationship with the volumetric spatial concentration (Keska, 1990). Thus calibration may easily be performed in-situ. The type III sensor bears a non-linear relationship with the film thickness, and this sensor must be calibrated separately. More details on capacitive sensors and their principles of operation are in many publications by Keska (1976, 1981, 1990, 1991). The flow pattern is observed visually with the help of a stroboscope (19) to "freeze" the motion. An air-driven dye injection system (17) is also used for flow-pattern observation enhancement in certain cases. A CCD camera system (15, 16) was used to record the flow pattern and the video record was analyzed in slow motion.

Results and Discussion

A large quantity of data was generated in this experimental

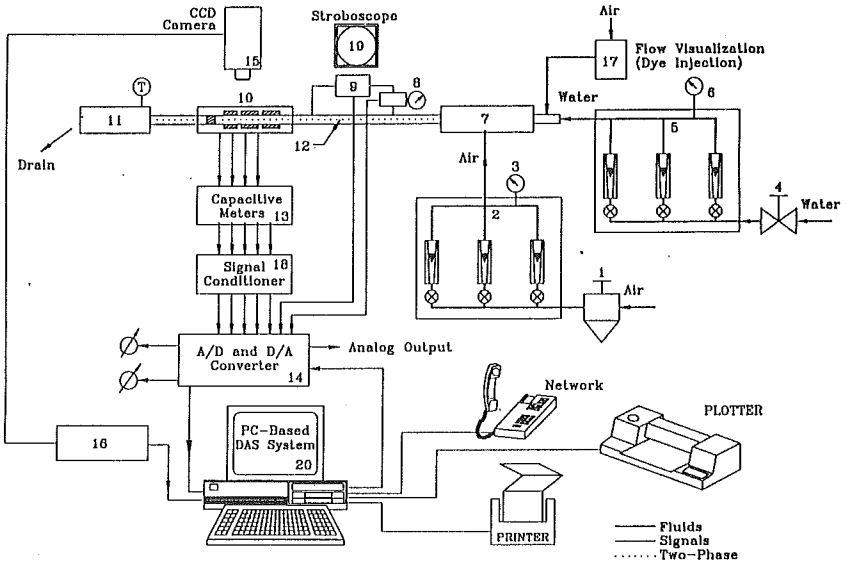

KEY					
1	reducer	10	capacitive sensor system	16	frame grabber
2,5	rotameters	11	separator	17	dye injection system
3,8	manometers	12	square channel	18	signal conditioner & interface
4	valve	13	capacitive meters	19	stroboscope
7	mixing chamber	14	A/D & DA converter	20	computer aided data acquisition system with peripherals
9	differential manometer	15	CCD camera		

Fig. 1 Experimental apparatus for two-phase flow used in experiments

study. Various flow conditions defined by the inlet air and water flow rates were set; then spatial concentration, pressure drop, static pressure near the sensor, and film thickness were measured and stored in the form of time traces by the data acquisition system. From this large pool of experimental data, 20 data sets, which represent most of the possible flow patterns, were chosen for detailed analysis and presentation.

Measured and calculated parameters for these data sets are shown in Table 1. The results are presented in the following with emphasis on the time averaged values of void fraction, slip ratio, pressure drop, flow pattern, and RMS values.

Flow Pattern

Figure 2 shows how the data obtained in this study compare to those in the literature. This figure shows the in-situ flow pattern of the measured data superimposed on the flow-pattern maps proposed by Wambsganss et al. (1990) and Mandhane et al. (1974) in the superficial velocity plane. Partial qualitative agreement is seen with results of Wambsganss while quantitative differences are observed with both. The large differences noticed with Mandhane may be caused by the effect of flow channel geometry on the flow pattern.

Void Fraction (α)

Many reported studies use the quality (x) as the only parameter which describes the state of the mixture. However, quality is a composition of the spatial concentration, phase velocities and densities. It is interesting at this point to examine the relationship between the concentration $c_v = (1-\alpha)$ and gas quality, x. From the definition for quality x, by substituting for M_g, M_L, V_g, and V_L we get the relation

$$x = \frac{\rho_g v_g (1 - c_v)}{\rho_g v_g (1 - c_v) + \rho_L v_L c_V} \tag{10}$$

Rearranging to express c_v in terms of x we get the following relation

$$c_v = \frac{\rho_g v_g (1 - x)}{\rho_g v_g (1 - x) + \rho_L v_L x} \tag{11}$$

These two equations show the interdependency of c_v and x, when the *in-situ* velocities and phase densities are known. It can be shown that the liquid (concentration) has little effect on the quality when the proportion of gas is relatively high, indicating that the flow may be treated as a single phase gas flow at high quality which is the case for annular flow. It is worthwhile to examine Eq. (11) for some special cases. If $\rho_g = \rho_L$, (equal phase densities) i.e., a homogeneous mixture, then

$$c_V = \frac{v_g (1 - x)}{v_g (1 - x) + v_L X} \tag{12}$$

which shows spatial concentration to be a function of the quality and *in-situ* velocities only. Further, if $v_g = v_L$ (equal phase velocities) i.e., a single phase flow, or a two phase flow assumed to behave as a single phase flow; then we have the trivial solution

$$c_v = (1 - x) \equiv (1 - \alpha) \tag{13}$$

where α is the void fraction. The implication of this equation is that the spatial concentration does not need to be determined if the two-phase flow is assumed to behave like a single-phase flow. The same dependency of x on c_v is seen when expressed in the Lockhart-Martinelli parameter X (Fig. 3) where the change in X is barely noticeable for high gas content mixture (90 percent of gas).

The void fraction data obtained experimentally is also presented in Fig. 4 along with the idealized annular flow model as described by Chen (1986) and data of Richardson (1958) and Wambsganss et al. (1990). To be able to represent the measured data in the form of the modified Eq. (4) by best fit criteria, a value of $k = 12$ was required; and a value of $k = 2.75$ was required for data of Wambsganss et al. (1990). Data of Richardson (1958) could not be well represented by a constant k value, however. The deviations from the model (Eq.

Table 1 Experimental data for an air-water two-phase flow in horizontal small channel. Flow pattern: A—annular, B—bubble, P—plug, S—slug, AS—annular/slug.

Rec. #	Flow pattern	Void fraction <α>	Spatial conc <cv> [-]	Superficial velocity Gas v_{sg} [m/s]	Superficial velocity Liquid v_{sl} [m/s]	*In situ* velocity v_g [m/s]	*In situ* velocity v_L [m/s]	Slip ratio v_g/v_L [-]	Mixture velocity v_{mix} [m/s]	Pressure drop Dp/DL Two ph [kPa/m]	Pressure drop Dp/DL Liquid [kPa/m]	Pressure drop Dp/DL Gas [kPa/m]	Mass flux G_{mix} [kg/m²s]	Quality x	Lockhart-Martinelli Parameters ϕ_L	Lockhart-Martinelli Parameters ϕ_g	Lockhart-Martinelli Parameters X (expt)	Lockhart-Martinelli Parameters X (Calc)	RMS values σ_{c_v}	RMS values σ_p
1	A	0.943	0.057	21.06	0.75	22.32	13.27	1.70	13.34	52.2	279.7	0.243	768	0.0315	5.40	5.35	0.99	1.13	0.013	4.933
2	A	0.906	0.094	14.30	1.10	15.77	11.70	1.35	11.77	52.3	224.6	0.142	1111	0.0150	3.85	12.56	3.26	2.21	0.030	7.410
3	B	0.675	0.325	0.43	0.19	0.64	0.59	1.13	0.57	0.5	1.1	0.025	184	0.0026	1.78	4.99	2.80	10.34	0.320	
4	B	0.526	0.474	0.85	0.65	1.61	1.37	1.17	1.38	4.1	5.3	0.052	656	0.0015	1.68	10.64	6.32	16.61	0.316	0.816
5	A	0.740	0.260	3.75	1.19	5.07	4.57	1.11	4.58	18.7	43.0	0.081	1193	0.0037	2.14	15.10	7.05	7.68	0.013	4.068
6	A	0.893	0.108	12.90	0.49	14.45	4.54	3.17	4.66	16.4	44.3	0.081	504	0.0298	4.37	8.86	2.03	1.19	0.046	2.818
7	A	0.963	0.037	24.70	0.21	25.64	5.68	4.68	6.11	19.6	71.2	0.073	229	0.1214	10.43	2.37	0.23	0.32	0.011	1.240
8	A	0.934	0.066	18.74	0.36	20.06	5.52	3.66	5.74	21.4	63.9	0.075	382	0.0565	6.51	4.38	0.67	0.66	0.023	1.769
9	P	0.456	0.544	1.03	1.36	2.26	2.50	0.90	2.51	10.5	15.1	0.074	1367	0.0009	1.42	15.80	11.11	26.80	0.254	0.408
10	A	0.880	0.120	10.51	0.28	11.94	2.34	5.21	2.37	5.7	13.6	0.072	287	0.0417	4.27	7.75	1.82	0.88	0.063	1.316
11	A	0.960	0.040	20.65	0.11	21.52	2.83	8.37	3.07	6.1	21.4	0.080	128	0.1736	10.37	1.91	0.18	0.22	0.016	0.667
12	B	0.311	0.689	0.50	1.36	1.60	1.97	0.81	1.99	8.7	9.9	0.066	1361	0.0004	1.30	19.60	15.12	50.59	0.083	0.063
13	S	0.745	0.255	3.86	1.27	5.18	4.97	1.04	5.00	23.8	50.1	0.079	1274	0.0035	2.28	17.00	7.46	7.92	0.180	5.077
14	A	0.949	0.051	22.15	0.33	23.35	6.51	3.62	6.83	24.5	86.7	0.068	354	0.0719	7.56	3.30	0.44	0.53	0.016	1.637
15	A	0.873	0.127	12.05	0.71	13.79	5.61	2.48	5.63	21.7	61.8	0.076	717	0.0193	3.65	11.78	3.23	1.76	0.050	4.367
16	A	0.948	0.052	21.37	0.69	22.54	13.20	1.69	13.61	54.5	289.4	0.265	717	0.0350	5.87	5.31	0.90	1.03	0.010	3.769
17	AS	0.834	0.166	7.96	0.78	9.54	4.66	2.09	4.61	17.9	43.5	0.081	768	0.0118	3.11	16.59	5.34	2.73	0.077	5.366
18	A	0.927	0.073	17.10	0.71	18.45	9.69	1.96	9.59	43.1	156.9	0.076	708	0.0273	5.25	7.61	1.45	1.29	0.020	4.285
19	AS	0.818	0.182	7.21	1.24	8.81	6.84	1.28	6.88	33.1	87.7	0.068	1254	0.0067	2.73	22.27	8.15	4.51	0.087	8.556
20	A	0.956	0.044	24.08	0.37	25.18	8.37	3.15	8.48	34.8	126.4	0.066	377	0.0711	8.54	3.32	0.39	0.53	0.010	1.434

(4)) for the bubble/plug regions for the measured data can be clearly seen. These are the regions where the liquid component plays a major part in determining the flow pattern and thus affects the relationship between void fraction and quality. The data obtained from Richardson seems to have a similar tendency; however, the values indicate differences that can be generated by different experimental conditions, void fraction determination, flow pattern, and other assumptions.

Slip Ratio

The slip ratio is defined as the ratio of the in-situ gas velocity to the in-situ liquid velocity. The relationship between in-situ water and air velocities with indications of the flow pattern for five discernable regions are shown graphically in Fig. 5. General transitions from bubble to annular flow follow the expected qualitative trends. Greater slip between the phases is more evident in the annular flow regime. Direct comparisons of correlations between slip ratio and void fraction with data in the literature are presented in Fig. 6 where for low void fraction the slip tends to one, indicating that the phases are moving with the same velocity in the cases of both Richardson (1958) and reported results.

The comparisons lead to the conclusion that, while there is qualitative agreement in the characteristics of slip ratio vs void fraction obtained by Richardson (1958), Wambsganss et al. (1990) and reported by the authors, the qualitative differences are demonstrated between Wambsganss et al. and our results. It is speculated that the poor agreement may be attributed to geometry and size effects; definition dependence of slip ratio, which for Wambsganss et al. (1991) is defined as the ratio of two superficial velocities; the lack of traceability of void fraction measurements and/or uncertainty estimations.

Pressure Drop

The obtained pressure drop data shown in Table 1 is presented in Fig. 7. Boundary curves for single-phase flows, i.e., with only water and only air flowing are displayed on the graph to show the relative positions of the two-phase data points. Data for these boundary curves were also obtained on the same experimental test rig.

The boundary curve for water is determined by employing a modified form of the Darcy-Weisbach and Blasius relations, and combining them to obtain

$$\left(\frac{\Delta P}{\Delta L}\right) = kv^n \tag{14}$$

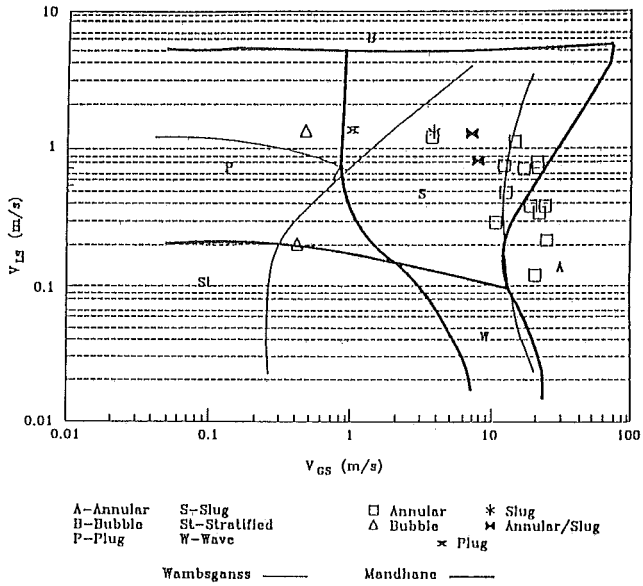

Fig. 2 Comparison of Mandhane et al. (1974) and Wambsganss et al. (1990) flow maps with experimental results. (Uncertainty in v_{LS} = ± 0.06 m/s and in v_{GS} = ± 0.01 m/s at 95 percent confidence level.)

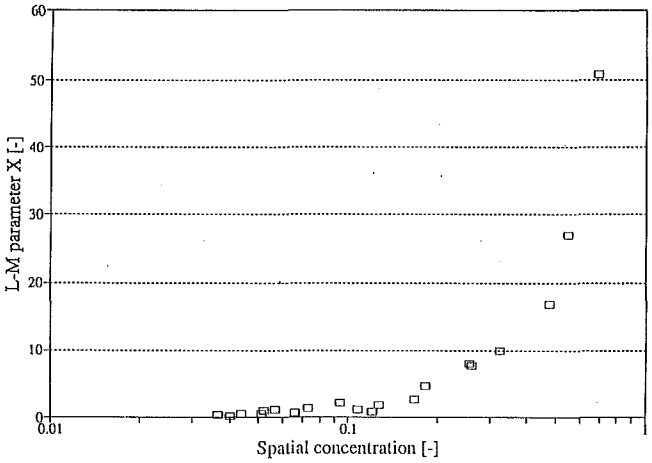

Fig. 3 Lockhart-Martinelli parameter versus measured spatial concentration. (Uncertainty in $X = \pm 0.05$ in spatial concentration $c_v = \pm 0.003$ at 95 percent confidence level)

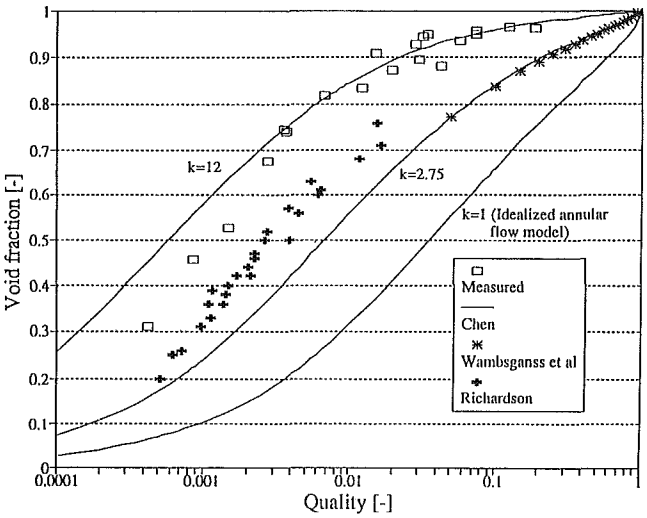

Fig. 4 Experimental data of void fraction versus quality for the measured data and that from literature with curves obtained with Chen's model (Uncertainty in $\alpha = \pm 0.003$ and in $x = \pm 0.06$ at 95 percent confidence level)

For water, to fit the measured data well, the exponent n was calculated in this equation and the constant $k = 3$ was required. Hence Eq. (14) may be written as

$$\left(\frac{\Delta P}{\Delta L}\right)_L = 3v_L^2 \tag{15}$$

The boundary curve for air is determined by fitting a cubic curve by the method of least squares to measured data with air flowing alone. The equation thus obtained is

$$\left(\frac{\Delta P}{\Delta L}\right)_g = (0.53v_g^3 - 9.5v_g^2 + 50v_g).10^{-3} \tag{16}$$

The measured data is compared with data from the literature (Richardson 1958; Wambsganss et al., 1990) in the form of the Lockhart-Martinelli parameters ϕ_L and X. The results compare fairly well as shown in Fig. 8.

Conclusion

In summary, from an investigation of the average in-situ components of spatial concentration, film thickness, pressure drop and phase component, and mixture velocities, experimental results were obtained using a specially constructed test loop with a specially developed and built computer-based concentration meter for an air-water mixture flow in a square horizontal channel. An analysis was performed on the data collected. Findings are as follows:

- Enhanced techniques used for flow-pattern recognition allowed comparison of the detected flow patterns with literature indicating only partial qualitative agreement.
- Mass quality (of the mixture) as a parameter shows a limitation in representing the concentration of that mixture component, especially when there is a high concentration of gas in the mixture. The in-situ measurement of spatial concentration has been shown to be a key factor in describing the state of the mixture in a two-phase flow. A general form of equation for void fraction in terms of mass quality found in the literature is shown to fit the measured data in the annular flow regions only as shown in Fig. 4.

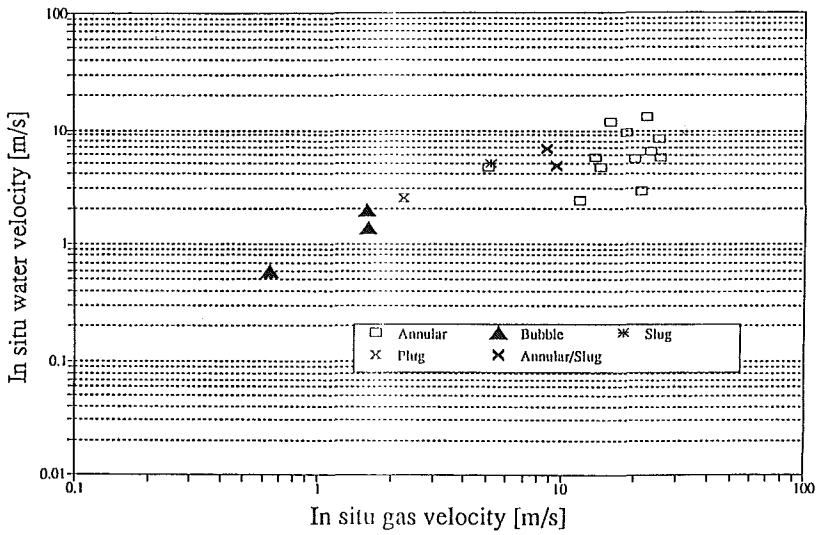

Fig. 5 Experimentally determined *in-situ* water velocity versus in-situ gas velocity with flow pattern indication (Uncertainty in $v_L = \pm 0.06$ m/s and in $v_g = \pm 0.01$ m/s at 95 percent confidence level)

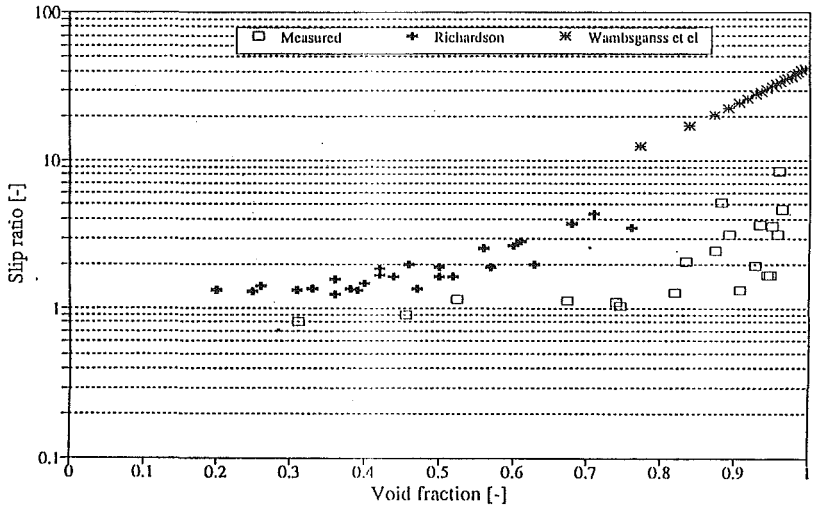

Fig. 6 Slip ratio versus void fraction measured in this experiment and that from the literature. (Uncertainty in slip ratio = ± 0.008 and in void fraction = ± 0.003 at 95 percent confidence level)

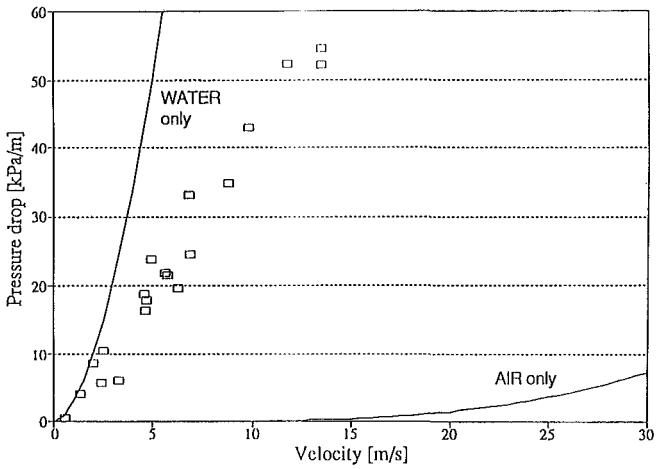

Fig. 7 Experimental data of pressure drop versus in-situ velocity. (Uncertainty in $\Delta P/\Delta L$ = ± 0.04 kPa/m and in v = ± 0.06 m/s at 95 percent confidence level)

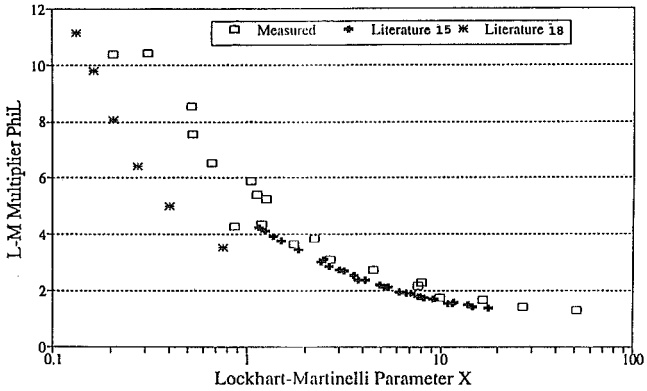

Fig. 8 Pressure drop data expressed in the Lockhart-Martinelli form for the experiment and literature. (Uncertainty for the measured data in both L-M parameters = ± 0.05 at 95 percent confidence level)

- Although qualitative agreement exists for slip velocities, the values obtained show differences with those from the literature at high void fractions, which indicates the need for futher investigations in this area.
- The assumptions in computing the in-situ mixture velocity are shown to have a great bearing on subsequent estimation of other parameters associated with two-phase flows.
- Analysis of the pressure drop indicates that the data expressed in the form of Lockhart-Martinelli parameters correlate well with those in the literature for conditions close to single-phase flow. However, a loss of sensitivity is seen when both phases influence the flow.

Acknowledgment

The research was funded by the Engineering Foundation, New York, and the University of Nebraska, and conducted during the time that the authors served at the University of Nebraska, Lincoln. The authors acknowledged J. W. Nageley's contribution in editing.

References

Barnea, D., Shoham, O., Taitel, Y., and Dukler, A. E., 1980, "Flow Pattern Transition for Gas-Liquid Flow in Horizontal and Inclined Pipes," *International Journal of Multiphase Flow*, Vol. 6, pp. 217–223.

Barnea, D., Luninski, Y., and Taitel, Y., 1983, "Flow Pattern in Horizontal and Vertical Two-Phases Flow in Small Diameter Pipes," *Canadian Journal of Chemical Engineering*, Vol. 61, pp. 617–620.

Butterworth, D., 1975, "A Comparison of Some Void-Fraction Relationships for Co-Current Gas-Liquid Flow," *International Journal of Multiphase Flow*, Vol. 1, p. 845.

Chen, J. J. J., 1986, "A Further Examination of Void Fraction In Annular Two-Phase Flow," *International Journal of Heat and Mass Transfer*, Vol. 29, No. 11, p. 1760.

Chen, J. J. J. and Spedding, P. L., 1984, "Holdup in Horizontal Gas-Liquid Flow," Multi-Phase Flow and Heat Transfer III, Part A—Fundamentals (1984), p. 333, *Process Technology Proceedings*, 1, Elsevier, Amsterdam.

Jepson, W. P., 1989, "Modelling the Transition to Slug Flow in Horizontal Conduit," *Canadian Journal of Chemical Engineering*, Vol. 67, pp. 731–740.

Keska, J. K., 1976, "Solids Concentration Measurement in Two-Phase Mixture," *3R-International*, Vol. 5, pp. 216–222.

Keska, J. K., 1981, "Two-Phase Mixture Flow. Theoretical and Experimental Aspects of Measurement, Mechanics and Methodics," *Scientific Bulletin of the University of Hannover*, Hannover, Vol. 53, pp. 246–449.

Keska, J. K., 1990, "Measurements of Two-Phase Flow Patterns and Void Fraction in a Small, Horizontal, Rectangular Channel," MCT Report, Argonne National Laboratory, p. 31.

Keska, J. K., 1991, "Void Fraction Fluctuation as an Indicator of Flow Patterns in Gas-Liquid Flow," *ASME-JSME Fluids Engineering Conference Proceedings*, FED-110, Portland, OR, pp. 89–95.

Lin, P. Y., and Hanratty, T. J., 1987, "Effect of Pipe Diameter on Flow Patterns for Air-Flow in Horizontal Pipes," *International Journal of Multiphase Flow*, Vol. 13, No. 4, pp. 549–563.

Lockhart, R. W., and Martinelli, R. C., 1949, "Proposed Correlation of Data For Isothermal Two-Phase, Two Component Flow in Pipes," *Chemical Engineering Progress*, Vol. 45, #1.

Mandhane, J. M., Gregory, G. A., and Aziz, K., 1974, "A Flow Pattern Map for Gas-Liquid Flow in Horizontal Pipes," *International Journal of Multiphase Flow*, Vol. 1, pp. 537–553.

Mukherjee, H., and Brill, J., 1985, "Empirical Equations to Predict Flow Patterns in Two-Phase Inclined Flow," *International Journal of Multiphase Flow*, Vol. 11, No. 3, pp. 299–313.

Richardson, B. L., 1958, "Some Problems in Horizontal Two-Phase Two-Component Flow," Ph.D. thesis, Purdue University, Argonne National Laboratory Report #ANL-5949.

Spedding, P. L., O'Hare, K. D., and Spence, D. R., 1986, "Prediction of Holdup In Two-Phase Flow," Paper direct from author, Queen's University of Belfast, Belfast N. Ireland.

Wambsganss, M. W., Jendrzejczyk, J. A., and France, D. M., 1991, "Two-Phase Flow Patterns and Transitions in a Small, Horizontal, Rectangular Channel," *International Journal of Multiphase Flow*, Vol. 17, No. 3, pp. 327–342.

Wambsganss, M. W., et al., 1990, "Two-Phase Flow Patterns and Frictional Pressure Gradients in a Small, Horizontal, Rectangular Channel," Report ANL-90/91, Argonne National Laboratory, Argonne, IL.

S. Abrahamson

S. Lonnes

Department of Aerospace Engineering
and Mechanics,
University of Minnesota,
Minneapolis, MN 55455

An Improved Model for Radial Injection Between Corotating Disks

Introduction

The flow field for this problem is illustrated in Fig. 1. The nature of the flow structure between corotating disks was investigated by Abrahamson et al. (1989, 1991). For the case of a solid (or nonventilated) hub, the flow between the disks contains three distinct annular regions. Most important to the current problem is the Inner region which extends from the hub (whose size is typically 1/3 to 1/2 of the disk radius) out to 3/4 of the disk radius. The Inner region is in solid body motion with the disks, and contains little or no mixing.

In an effort to eliminate the stagnant region adjacent to the hub, flow is introduced to the rotating cavity through a series of holes in the hub. The ventilation flow displaces the core flow radially, until all of the ventilation flow is entrained into the disk boundary layers and transported around the core flow. The radial extent of the core region affected by the ventilation flow is designated as the location where the radial velocity is zero. The flow in radii greater than this value is not addressed in this paper.

In a general paper on source-sink flows in rotating containers, Hide (1968) discussed the flow in a cylindrical, annular container. Hide used a linear analysis of the laminar Ekman layer flow to predict the extent of the radial penetration into the source layer. The model assumed a constant rotation rate in the source layer, (i.e., du_θ/dr = constant) and that the boundary layer entrainment did not depend on the radial velocity. Comparing to experimental measurements in an apparatus where S the ratio between the interdisk spacing t, and the hub radius r_h, was 1.8, the ratio between the source and sink radii was 1/4, and the Ekman number ($E = \nu/r_h^2\Omega$, where Ω is the disk rotation rate, and ν is the kinematic viscosity) was in the range from 1.4×10^{-7} to 3.4×10^{-8}, Hide showed fair agreement between his model and the measurements.

The problem of flow in a rotating cavity with a radial ventilation flow has been studied by several investigators with application to cooling of rotating disks in gas turbines. The review article of Owen (1988) gives a good overview of a large number of these studies. Of particular relevance is the experimental and analytical study of Owen and Pincombe (1980). Results were presented for two values of their ventilation flow coefficient C_w (352 and 643), with an aspect ratio of $S = 2.67$, and Rossby numbers in the range $5 < \epsilon < 30$. C_w is a dimensionless volumetric flow rate ($= Q/\nu r_h$), and $\epsilon = r_h^2 D\sqrt{E}/2$, where Q is the dimensional volumetric flow rate and D is the dimensionless flow coefficient used in the analysis below. The experimental measurements of the ventilation flow penetration were compared to Hide's (1968) model as well as their own which was based on the linear Ekman layer solution and Faller's (1963) model for the azimuthal velocity at moderate Rossby number. This model, coupled with the assumption that the boundary layer begins at $r = 0$ was used to develop an expression for the radial penetration of ventilation flow into the core region between two rotating disks by matching the source flow rate to the total boundary layer entrainment. This model predicts their data quite well, but contains no latitude for variation of the axial spacing of the disks. In other words, it does not account for the effects of radial velocity in the core. When the hub radius is a significant fraction of the disk radius the assumption that the boundary layer entrainment begins at $r = 0$ is no longer valid. The model can still be used by subtracting the entrainment from radii less than the hub radius.

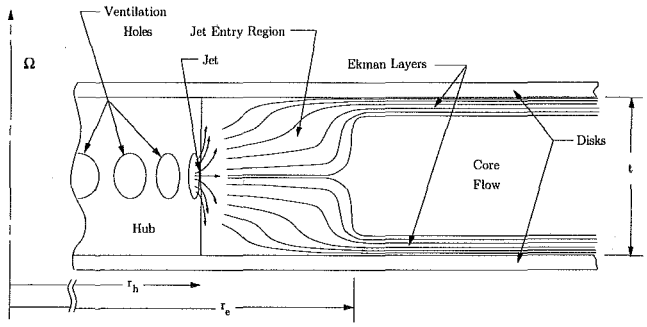

Fig. 1 Sketch of flow in the r-z plane

Chew et al. (1984) present an axisymmetric numerical calculation of the flow in the same rotating cavity as Owen and Pincombe (1980) with Re (based on cavity radius and tip speed) $= 2.5\times10^4$ and $79 < C_w < 605$.

Problem Formulation

The objective of the following analysis is to estimate the radial extent of the region affected by the injected fluid as a function of the dimensionless parameters E, D, and S. The problem is cast in a cylindrical coordinate system with the z

Contributed by the Fluids Engineering Division for publication in the JOURNAL OF FLUIDS ENGINEERING. Manuscript received by the Fluids Engineering Division April 28, 1992; revised manuscript received September 23, 1993. Associate Technical Editor: O. Baysal.

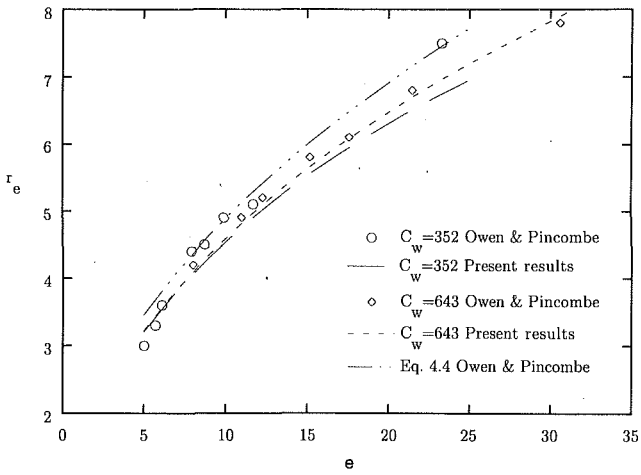

Fig. 2 Comparison to experimental data, $C_w = 352, 643$

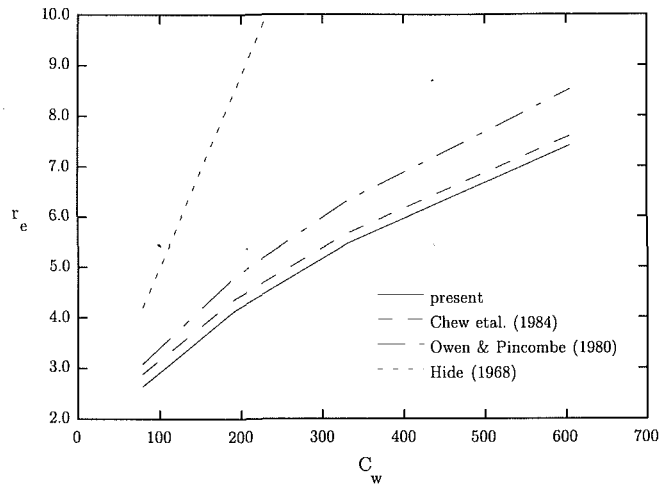

Fig. 3 Comparison to numerical results

axis coincident with the rotation axis of the disks. The r-z plane of the flowfield is sketched in Fig. 1, with streamlines indicated for the injected flow. It is assumed the entering fluid quickly mixes to provide a uniform radial flow, and at $r = r_h$ there is no tangential slip relative to the disks. The first assumption relies on the small Rossby number in the injection region so that Taylor-Proudman theorem ($\partial/\partial z \to 0$) applies, and that axial gradients continue to be small throughout the region of interest. The second assumption rests on the ability of the geometry to provide an inflow whose angular velocity is the same as the disks and hub, which in turn assures a small Rossby number. The inflow is assumed to be axisymmetric, and further, the boundary layers on the disks are assumed small relative to the axial separation between the disks. The flow is also assumed symmetric about the midplane between the disks.

The formulation of the problem for the jet entry region is governed by two conservation equations: continuity and angular momentum, with a model for the entrainment of fluid from the core between the disks into the disk boundary layers. These equations are derived for a cylindrical shell control volume of height t (which does not contain the disk boundary layers), radius r, and thickness dr.

Equations of Motion

The three relevant equations of motion are obtained from continuity, tangential momentum conservation, and model for boundary layer entrainment. The model used for the boundary layer entrainment is a composite of the entrainment from Greenspan (1968) and from a non-linear analysis of the boundary layer on a rotating disk with still fluid away from the disk, done by Cochran (1934). Before proceeding further, we cast the equations in dimensionless form by scaling the velocities by $r_h\Omega$, the hub tangential speed, and the lengths by the hub radius r_h. Continuity yields

$$\left\{\frac{du_r^*}{dr^*} + \frac{u_r^*}{r^*} + \frac{2u_z^*}{S}\right\} = 0 \tag{1}$$

where the $(\,)^*$ indicates a dimensionless variable. S is the aspect ratio $S = t/r_h$. Tangential momentum conservation yields

$$\frac{du_\theta^*}{dr^*} + \frac{u_\theta^*}{r^*} + 2 = 0 \tag{2}$$

Laminar boundary layer entrainment is modeled by

$$u_z^* = \pm 0.844\sqrt{E}\left(\frac{du_r^*}{dr^*} + \frac{du_\theta^*}{dr^*}\right) \tag{3}$$

For notational simplicity we omit the asterisks below.

Equations (1), (2), and (3) can be combined to form the simple differential equation,

$$\frac{du_r}{dr} + \frac{1}{1-C}\frac{u_r}{r} = -\frac{C}{1-C}\left(1 + r^{-2}\right) \tag{4}$$

where $C = 1.688\sqrt{E}/S$. Solving this equation and setting u_r equal to zero determines the end of the jet entry region. The resulting equation is,

$$\left[D + \frac{2S^2}{2S - 1.688\sqrt{E}}\right] r_e^{-1.688\sqrt{E}/(S-1.688\sqrt{E})} - \frac{1.688S\sqrt{E}}{2S - 1.688\sqrt{E}}\, r_e^2 - S = 0 \tag{5}$$

Results and Discussion

A comparison to the data of Owen and Pincombe (1980) is presented in Fig. 2, which is a plot of r_e as a function of the Rossby number at two ventilation flow rates, $C_w = 352$ and 643. Shown in the plot are the data points of Owen and Pincombe as well as their correlation, equation 4.4. For the lower ventilation rate, the figure shows that in terms of the number of data points on each curve, both the current calculation and their correlation perform equally well. When the ventilation flow coefficient is almost doubled, the current calculation gives better agreement with the data, probably because it accounts for the effects of radial velocity in the core.

The current calculation and the model of Owen and Pincombe (1980) are compared to the numerical calculations of Chew et al. (1984) in Fig. 3. The geometry is that of Owen and Pincombe and the Reynolds number (based on sink radius) is 2.5×10^4. In Fig. 3, the radial penetration is plotted as a function of the ventilation flow coefficient. Since the computations do not predict a zero radial velocity in the core, r_e is determined as the location where ru_r is 10 percent of its value at the source. Shown on the plot are the current results, the numerical predictions of Chew et al. (1984), equation 4.4 from Owen and Pincombe (1980) and Hide's (1968) solution. The models of Owen and Pincombe (1980) and Hide (1968) do not allow us to compute ru_r so their predictions are slightly biased away from the computations. From the figure it is clear that Eq. (5) closely agrees with the numerical predictions both in magnitude and slope.

The agreement between the calculations and the available data builds confidence in the validity of the calculations. Provided that the boundary layers are not a significant fraction of the disk separation, the results should apply. The von Kármán (1921) analysis provides a boundary layer scale of $\sqrt{\nu/\Omega}$ so the relative scale between the boundary layers and

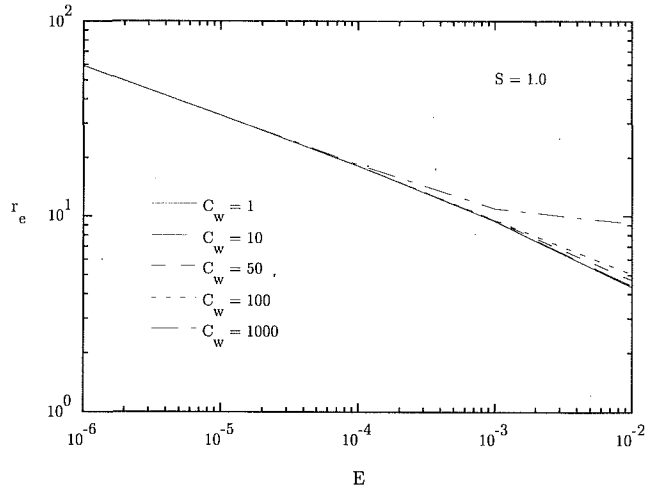

Fig. 4 Effect of rotation on penetration for fixed S and various C_w

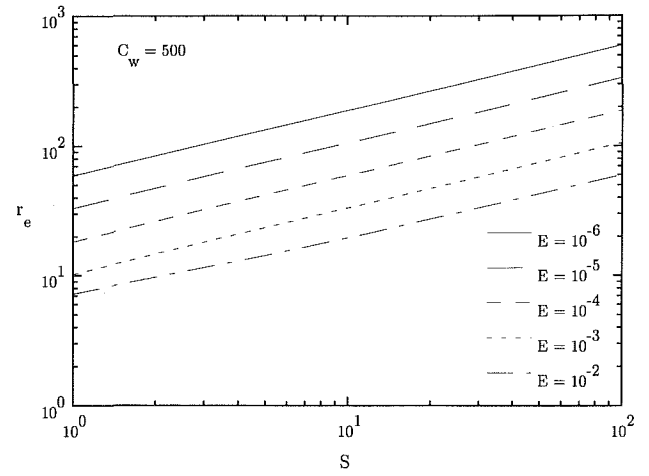

Fig. 5 Effect of axial separation for fixed C_w and various E

the disk separation is $\sqrt{E}/S$. If $\sqrt{E}/S << 1$ then the results of the calculations are applicable and we may explore the relationship between r_e, C_w, and E.

Figure 4 shows the relationship between the radial penetration and the rotation rate, at fixed $S = 1.0$ and parameterized by the ventilation flow coefficient C_w. In the figure, increases in the Ekman number correspond to decreases in the rotation rate. From the collapse of the curves at low Ekman number, it is apparent that the effect of C_w is minimal provided the rotation rate is fast enough. At low rotation rates the effect of increased ventilation flow is to increase the penetration distance, but this is only significant for extremely large C_w, and is probably due to the effects of the strong radial flow. Aside from these variations for large C_w, the figure shows r_e has a nearly exponential dependence on C_w.

Figure 5 shows the effect of S on r_e for various values of E at fixed C_w. The figure shows an exponential dependence of r_e on S which deviates slightly for the largest Ekman number at the smallest values of S. These values are in the range where $\sqrt{E}/S$ is around 0.1; the limit of the validity of the calculations.

Conclusions

In this paper relationships between the dimensionless radial penetration r_e of ventilation flow introduced at the hub, and the relevant parameters of the problem, E, S, and D (or C_w) for the case of laminar boundary layers on the disks were developed. A closed form expression was obtained, and the calculations were shown to agree well with experimental data. The radial penetration was shown to increase exponentially with increased S and decreased E (or increases in Ω or r_h) and for a fixed penetration, the ventilation flow rate C_w, increased with decreased E.

References

Abrahamson, S., Chiang, C., and Eaton, J., 1991, "Flow Structure in HDAs and implications for design," *ASME Advances in Information Storage Systems*, Vol. 1.

Abrahamson, S., Koga, D., and Eaton, J., 1989, "The Flow Between Shrouded Corotating Disks," *Physics of Fluids A*, Vol. 1, No. 2, pp. 241–251.

Chew, J., Owen, J., and Pincombe, J., 1984, "Numerical Predictions for Laminar Source-Sink Flow in a Rotating Cylindrical Cavity," *Journal of Fluid Mechanics*, Vol. 143, pp. 451–466.

Cochran, W., 1934, "The Flow Due to a Rotating Disc," *Proceedings of the Cambridge Philosophical Society*, Vol. 30, pp. 365–375.

Faller, A. J., 1963, "An Experimental Study of the Instability of the Laminar Ekman Boundary Layer," *Journal of Fluid Mechanics*, Vol. 15, pp. 560–576.

Girard, J., and Abrahamson, S., 1993, "On the Flow Structure Due to Corotating Disks with a Ventilated Hub," *Journal of Fluids Engineering*, Vol. 115, Sept.

Greenspan, H., 1968, *The Theory of Rotating Fluids*, Cambridge University Press, p. 46.

Hide, R., 1968, "On Source-Sink Flows in a Rotating Fluid," *Journal of Fluid Mechanics*, Vol. 32, No. 4, pp. 737–764.

Mochizuki, S., and Taneda, Y., 1979, "Unsteady Flow Phenomena in Multiple Disk Fans," ASME Paper No. 79-FE-10.

Mochizuki, S., and Yang, W., 1986, "Flow Friction on Corotating Parallel-Disk Assemblies with Forced Ventilation Flow," *Experiments in Fluids*, Vol. 4, pp. 56–60.

Owen, J. M., 1988, "Air-Cooled Gas-Turbine Discs: A Review of Recent Research," *International Journal of Heat and Fluid Flow*, Vol. 9, No. 4, pp. 354–365.

Owen, J. M., and Pincombe, J. R., 1980, "Velocity Measurements Inside a Rotating Cavity with a Radial Outflow of Fluid," *Journal of Fluid Mechanics*, Vol. 99, No. 1, pp. 111–127.

Owen, J. M., Pincombe, J. R., and Rogers, R. H., 1985, "Source-Sink Flow Inside a Rotating Cylindrical Cavity," *Journal of Fluid Mechanics*, Vol. 155, pp. 233–265.

Tsai, C.-J., Pui, D., and Liu, B., 1992, "Transport and Deposition of Wear Particles in Computer Disk Drives," *Particle and Particle System Characterization*, Vol. 9, No. 1, pp. 31–39.

von Kármán, T., 1921, "Über laminare und turbulente Reibung," *Zeitshcrift für Angwandte Mathematik und Mechanik*, Vol. 1, Aug. pp. 233–252.

R. N. Parthasarathy
Current Affiliation: Assistant Professor, School of Aerospace & Mechanical Engineering, The University of Oklahoma, 235 Felgar Hall, 865 Asp Avenue, Norman, OK 73019
Assoc. Mem. ASME

A. I. Sirviente
Graduate Research Assistant.
Mem. ASME

V. C. Patel
University of Iowa Foundation Distinguished Professor.
Fellow ASME.

Department of Mechanical Engineering and Iowa Institute of Hydraulic Research, The University of Iowa, Iowa City, IA 52242-1585

LDV Measurements in Separated Flow on an Elliptic Wing Mounted at an Angle of Attack on a Wall[1]

The flow around a half-ellipsoid with axes ratio 12:6:1 mounted on a plane wall at an angle of attack of 25° and at a Reynolds number of 47,000 (based on the maximum chord) was studied using a three-dimensional LDV system. In this paper the mean velocity distributions in a volume enclosing the separated region and the near wake are described. The flow is shown to be consistent with the findings of Johnson (1991) based on flow visualization and related topological analysis. The flow on most of the pressure side was attached and laminar, while that on the suction side and in the wake was separated and turbulent. The region of separation had mean negative streamwise velocities as large as 25 percent of the freestream velocity, and the reversed-flow region extended up to one chord length behind the body. The measurements clearly reveal the complex vortex structure that arises from the three-dimensional separation.

Introduction

Flow separation is an important phenomenon in fluid mechanics. Two-dimensional separation is straightforward and can be identified by the location where the surface shear stress vanishes. In three dimensions, however, separation points can become separation lines and the zero shear stress condition is no longer valid. Also, separation may occur by streamlines lifting off the surface to form a longitudinal vortex, or spiraling off the surface in the form of a tornado-like vortex.

Chapman and Yates (1991) classify three-dimensional flow-separation into primary separation, secondary separation, and compound separation, using concepts of topology. The topological approach is based on the fact that the surface shear-stress field comprises a continuous vector field. Within this shear stress field, a finite number of singular points, where the magnitude of shear stress is zero, may occur. The types of singular points occurring in the flow field and the connections between them constitute the topological structure of the flow. The above classification and studies of flow topology in three-dimensionally separated flows have been based primarily on flow visualization.

Detailed theoretical or numerical analysis and experimental measurements of three-dimensional flow separation are rare. As a first step toward understanding the structure of the flow associated with the frequently observed singularities of friction lines in separated flow over three-dimensional bodies, the flow around a half-ellipsoid mounted at an angle of attack on a horizontal wall was studied. This geometry has several advantages in addition to the simple mathematical representation of the shape and existence of exact solutions for potential flow. For example, both symmetric and asymmetric flows can be realized by a change of the angle of attack, generating a wide range of highly three-dimensional flows, with large-scale separations, and varied topology. The present investigation follows the comprehensive surface-flow visualization study of Johnson (1991) and Johnson and Patel (1993). This paper reports detailed three-dimensional laser-Doppler velocimeter (LDV) measurements of the mean-velocity field with the ellipsoid at an angle of attack of 25 deg, at which Johnson (1991) had found an array of singular points of the friction lines and attendant vortical structures. The measured velocity field is analyzed to illustrate the connection between the skin-friction topology on the surface, which is all that is usually observed in experiments, and the structure of the flow field, which is rarely measured in sufficient detail. Special emphasis is placed on the relationship between the flow topology and the phenomenon of three-dimensional flow separation.

Experimental Methods

One-half of an ellipsoid, of axes ratio 12:6:1, was mounted on a plane wall, as shown in Fig. 1. This semi-ellipsoid "wing" had a chord of 204 mm, a span of 204 mm, and was 34 mm thick at the root. The plane wall was a horizontal 12.5 mm thick plexiglass plate that spanned the width of the wind tunnel. The plate had a sharp leading edge to prevent flow separation and a 38 mm wide strip of sandpaper was glued on it at a distance of 155 mm from the leading edge to trip the boundary layer. LDV measurements close to the wall (without the ellipsoid) revealed that the plate boundary layer was turbulent with a momentum thickness Reynolds number, $R_\theta = 400$. The wind tunnel had a test section of 0.61 m × 0.61 m × 2.44 m long. Measurements in the freestream indicated that the flow

[1]A version of this paper was presented at the Symposium on Separated Flows, 1993 ASME Fluids Engineering Conference, Washington D.C., June 20–24, 1993.

Contributed by the Fluids Engineering Division for publication in the JOURNAL OF FLUIDS ENGINEERING. Manuscript received by the Fluids Engineering Division October 19, 1992; revised manuscript received September 7, 1993. Associate Technical Editor: T. T. Huang.

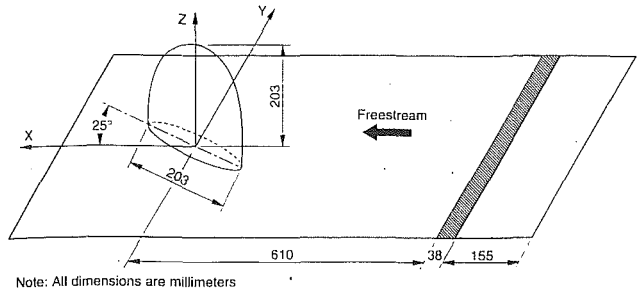

Fig. 1 Sketch of the ellipsoid on the wall

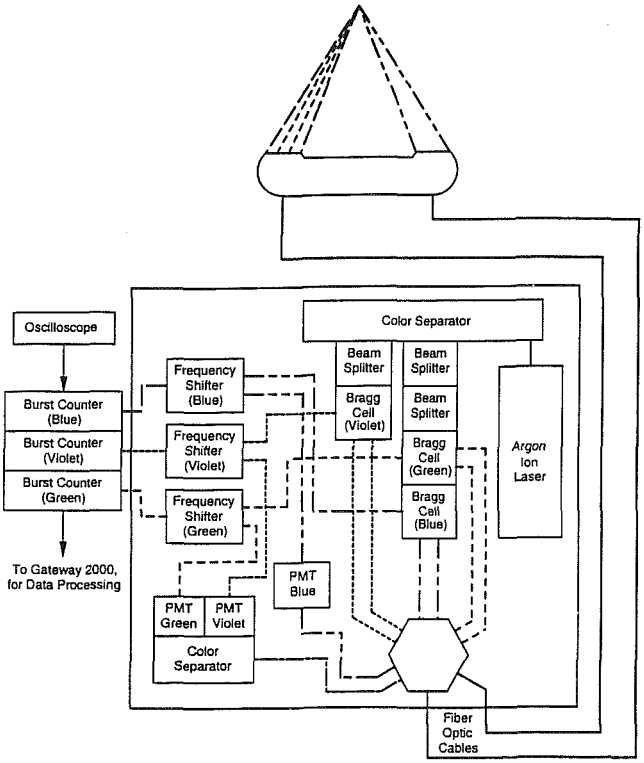

Fig. 2 Schematic of the LDV arrangement

was uniform within 2 percent in the central 0.3 m × 0.3 m section and the freestream turbulence intensity was 3 percent. This rather large value is due to the fact that the tunnel does not have extensive flow conditioning as it is often used to study problems of atmospheric icing. However, the glass walls of the tunnel test section make it ideal for use of LDV. For the present study, the ellipsoid was mounted at an angle of attack of 25 deg, and all measurements were taken at a freestream velocity, $U_0 = 3.5$ m/s, which resulted in a Reynolds number of 47,000 based on the maximum (wing-root) chord, $C = 204$ mm.

A three-dimensional LDV system with a fiber-optic probe was used to simultaneously measure the three velocity components. A schematic of the system is shown in Fig. 2. The LDV system was based on a 5-Watt argon-ion laser that was operated in the multiline mode. An external color separator was used to split the beam into the green (514.5 nm), blue (488 nm), and violet (476.5 nm) lines. Each of the green, blue, and violet lines was split into two beams, one of which was frequency shifted by passage through a Bragg cell. The six beams were transmitted to the probe through fiber-optic cables. The green and blue beams were in the horizontal plane and the violet in the vertical plane. The optical axes of the green and blue beams were at + 10.5 and − 10.5 deg, respectively, to the axis of the probe. Thus, the two orthogonal velocity components in the horizontal plane could be computed from the velocities measured in the blue and green systems, while the vertical velocities were measured directly by the violet system.

The fringe spacings were 5.35, 5.48, and 5.77 microns, respectively, on the green, blue, and violet systems. The fringe spacings and the angular transformations needed to resolve the two velocity components in the horizontal plane were verified by measuring the edge velocity of a plexiglass disc that was rotated at a known speed. The measurements using the LDV system were within 2 percent of the velocities computed using the disc rpm and the disc radius. The individual measuring volumes were $0.5 \times 0.5 \times 3$ mm. However, the actual measuring volume was smaller, since coincident measurements were made in the region crossed by all the three systems and since off-axis collection was used. The actual measuring volume was estimated to be $0.5 \times 0.5 \times 0.8$ mm. The scattered light from the crossing point was collected in backscatter by the same lens that focussed the beams. Since reversed flows needed to be measured, a frequency shift of 1 MHz was used on the green and blue systems, and 0.5 MHz was used on the violet system.

The signals were processed using a burst counter (TSI Model 1980). These were operated in the continuous mode and were digitally interfaced to a Gateway 2000 personal computer using TSI MI 990 interface and FIND software. Coincidence of signals from the three channels was ensured by verifying that the measurements from each system (green, blue or violet) occurred within 100 microseconds of each other. The measurements were number averaged (10,000 measurements in the separated region and 5000 measurements at other locations) and refined by eliminating all measurements that occurred outside ±3 standard deviations. Coincident data rates varied between 50 and 75 Hz in the separated region and were higher (150–250 Hz) in the freestream.

Water drops, generated by an ultrasonic humidifier, were used as the seeding particles. They were injected in the tunnel just downstream of the screens. A small amount of ethylene glycol added to the water prevented the water from evaporating and helped the drops to maintain their size. Measurements in the freestream indicated that the injecting device had negligible effect on the flow at the measurement location. Drop-size measurements using electron microscopy indicated a nominal diameter of 4 to 6 microns. Calculations showed that the terminal velocity of water drops of this size in air was 0.75 mm/s; since the flow displayed significant vertical velocities on the order of 0.1 to 0.3 m/s, the terminal velocity of the water drops did not add any significant error to the measured flow velocities. Frequency analysis of the governing equation of motion of the water drops illustrated that the drops could faithfully follow sinusoidal motions with frequencies up to 5 kHz; therefore, the drops were able to resolve most of the frequencies in the turbulent flow.

Experimental uncertainties in the velocity measurements were 4 percent for the streamwise component, 6 percent for the on-axis or transverse component when velocities were larger than 25 percent of the freestream velocity and 30 percent when the transverse velocities were smaller, and 5 percent for the vertical component. The uncertainties were large for the on-axis component when this velocity component was small since it was calculated by subtracting two large quantities. Increasing the angle between the optical axes of the green and blue systems would have helped to reduce this uncertainty. However, that would have resulted in an increase in the overall size of the probe and would have rendered its traverse unmanageable. It turns out that most of the interesting flow features were observed at locations with significant transverse velocities; therefore this did not pose a serious constraint.

The probe was mounted on a mechanical three-dimensional traverse that was capable of movement up to 200 mm in each direction. However, the region of interest was longer, partic-

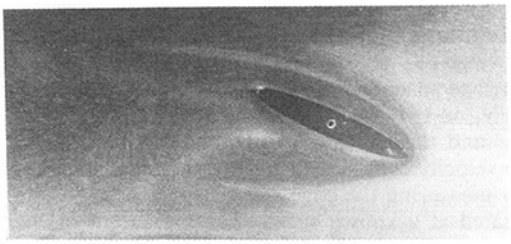

Fig. 3(*a*) Oil-flow photograph of the limiting streamlines at the wall

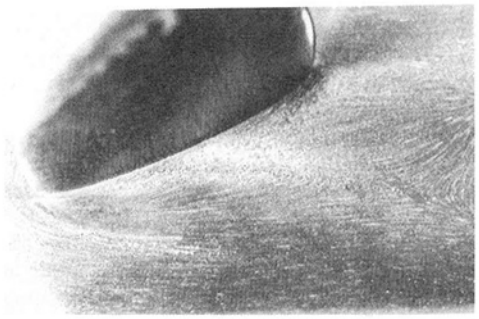

Fig. 3(*b*) Close-up of the flow on the wall on the suction side

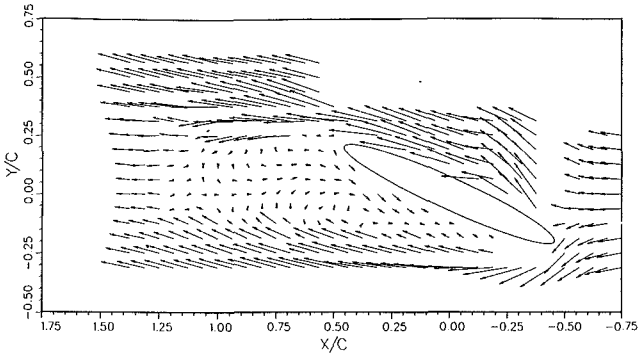

Fig. 4(*a*) Mean flow pattern at $Z/C = 0.02$

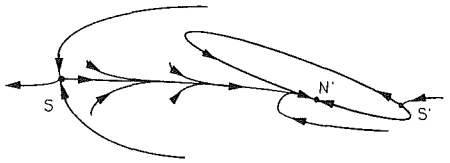

Fig. 4(*b*) Topological map of flow at $Z/C = 0.02$

ularly in the streamwise and vertical directions. To enable measurements in these regions, the wall on which the ellipsoid was mounted was supported by six legs whose heights could be varied. Also the wall could be moved as a whole in the streamwise direction in steps of 150 mm. Thus, measurements could be obtained from the wall till 25 mm beyond the tip of the ellipsoid in the vertical direction, and from 50 mm in front of the leading edge till 200 mm behind the trailing edge in the streamwise direction. Positioning accuracies were better than 2 mm. Velocity measurements were initially made on the suction side. The ellipsoid was then rotated and mounted at an angle of attack of -25 deg so that velocities on the pressure side could be measured. The velocities measured at the common locations (ahead of the leading edge and behind the trailing edge), after rotation of the ellipsoid, agreed with the measured velocities before rotation within the uncertainties stated above. Thus, it was possible to complete a comprehensive set of velocity measurements in a volume surrounding the ellipsoid.

Results

In the following discussion, Cartesian coordinates (X, Y, Z), with the origin at the centroid of the parent ellipsoid, X along the tunnel axis, Y parallel to the bottom plane, and Z measured from the plane toward the wing tip, are used. The corresponding mean-velocity components are denoted (U, V, W). The maximum wing chord C and the tunnel freestream velocity U_0 are used to normalize the lengths and velocities, respectively. To the extent possible, the observed topological features are described in terms of the 'pictorial dictionary' of flow features compiled by Perry and Steiner (1987).

From flow visualizations at the same Reynolds number, Johnson (1991) concluded that, at an angle of attack of 25 deg, the flow over the entire suction side was separated. The flow was highly three-dimensional and became turbulent on the suction side and in the wake. In an effort to understand the salient features of the flow, mean flow patterns in the constant Z planes (at different heights) and in the constant X planes (at different sections in the streamwise direction) are discussed sequentially. Presentation and discussion of the turbulence measurements is deferred to a later paper.

Mean Flow Patterns at Various Heights from the Wall (Z = Constant). Figure 3(*a*) shows an oil-flow photograph taken by Johnson (1991) of the limiting streamlines (friction lines) at the wall; a close-up view of the flow on the suction side is provided in Fig. 3(*b*). The present LDV measurements in a horizontal plane at a height of 3 mm ($Z = .02$) and their topological interpretation are shown in Fig. 4. This was the closest distance to the wall at which measurements could be obtained with reasonable signal-to-noise ratio. The vertical velocity could not be measured at this location, however, since one of the beams was blocked by the wall. It is clear that the LDV data confirm the observed surface-flow pattern. The flow around the leading edge could not be resolved by the LDV data partly due to inaccessibility of the pressure side to the laser beams in the present arrangement.

The measurements shown in Fig. 4 indicate no reverse flow on the pressure side. The separation (low friction and oil accumulation) line in the plane, wrapped around the body, which is seen in the photographs of Figs. 3(*a*) and 3(*b*), now appears as shear layers (regions of large velocity gradients) on the pressure and suction sides. These shear layers envelop a reversed flow region on the suction side. At the trailing edge, the flow from the pressure side is deflected toward the suction side, feeding the reversed flow region. From a preliminary look at the flow pattern in Fig. 4, it appears that there is a recirculating region in the suction side which would indicate the presence of a focus. However, careful examination of the velocity vectors and the flow visualization results (Figs. 3(*a*) and 3(*b*)) indicate only a line of flow convergence SN′ that lies roughly parallel to the freestream. A wall streamline or friction line into which friction lines converge from both sides is called a separation line. This designation is not appropriate, however, in the case of flow streamlines viewed in a plane. Following Perry and Steiner (1987), a flow line with these features is called a negative bifurcation line. The present measurements are consistent with the picture of Johnson (1991). A saddle point is observed at $X \approx 1.0$ and $Y \approx 0.0$. This coincides with the one seen in the surface streamlines in Fig. 3 and separates the flow proceeding downstream in the wake from the flow in the shear layer towards the body. In the wake, there is a region of relatively straight flow (with negligible transverse velocity) downstream of the saddle.

The topological map shown in Fig. 4(*b*) is based on the measured flow field and the flow visualization results, as well as consistency with the rules that govern the number of singular

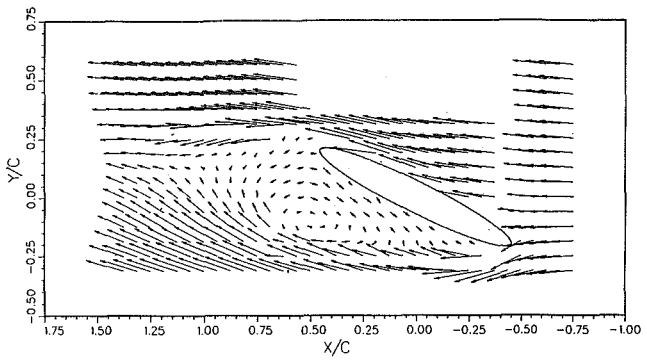

Fig. 5(*a*) Mean flow pattern at $Z/C = 0.13$

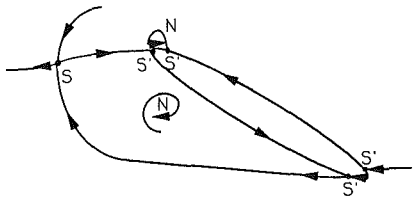

Fig. 5(*b*) Topological map of flow at $Z/C = 0.13$

points. Singular points which occur in isolation in the friction lines or in the flow lines viewed in a plane are termed nodes (N) and saddles (S), while those occurring on a body surface when cut by a plane are termed half-nodes (N') and half-saddles (S'). For friction lines and streamlines on a plane cutting a three-dimensional body, the rule states that (see, for example, Tobak and Peake, 1982)

$$(\Sigma N + 1/2\Sigma N') - (\Sigma S + 1/2\Sigma S') = -1 \qquad (1)$$

It is seen that Fig. 4(*b*) is consistent with this rule. In the absence of any discernible focus on the suction side, this represents the simplest topological map of the observed flow features. There is a half-saddle on the pressure side where the flow attaches to the body, a half-node on the suction side marking the end of the negative bifurcation line, and a saddle point in the wake. However, it should be noted that the LDV measurements around the leading and trailing edges were not detailed enough to capture all of the finer features which would imply additional singularities in the topological map. In this respect, the map shown here should be regarded as the simplest possible skeleton.

The flow pattern in a horizontal plane at a height of 26.5 mm ($Z = 0.13$) is shown in Fig. 5. The base of the ellipsoid is shown by a solid line and the local section is indicated by a broken line. Since the two sections are not greatly different at this height, the broken line is not seen in the figure. The entire flow on the suction side is separated and the extent of the reversed flow region can be seen in Fig. 5. At this height, there is no feeding of flow from the pressure side (as seen in Fig. 4) into the reversed flow region. Instead, reverse flow appears in a small region close to the trailing edge on the pressure side. This is in agreement with the findings of Johnson (1991), who located a short separation line on the pressure side to the trailing edge. The main saddle point on the suction side has moved forward and toward the pressure side at $X \approx 0.95$, $Y \approx 0.15$ and the region of reversed flow has mean velocities as high as 25 percent of the freestream velocity.

Figure 5(*b*) shows the topological map based on the measured velocity field. In comparison to the topology of Fig. 4(*b*), we see that several new singularities have appeared. Two foci (spiral nodes) centered in the separated regions on the suction and pressure sides and three more half-saddles can be identified. The number of singular points is consistent with Eq. (1). The prominent focus is associated with the negative bi-

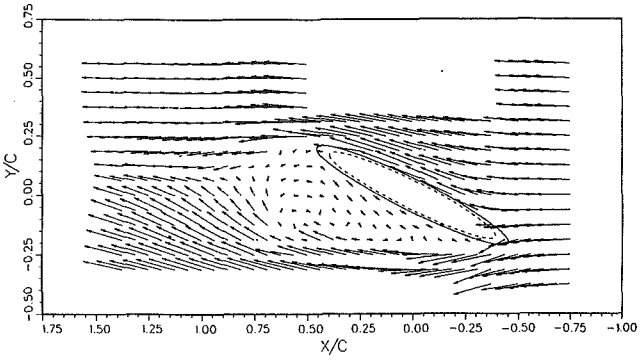

Fig. 6(*a*) Mean flow pattern at $Z/C = 0.50$

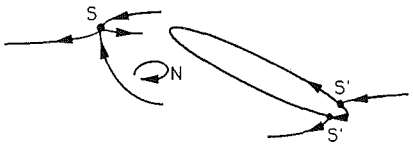

Fig. 6(*b*) Topological map of flow at $Z/C = 0.50$

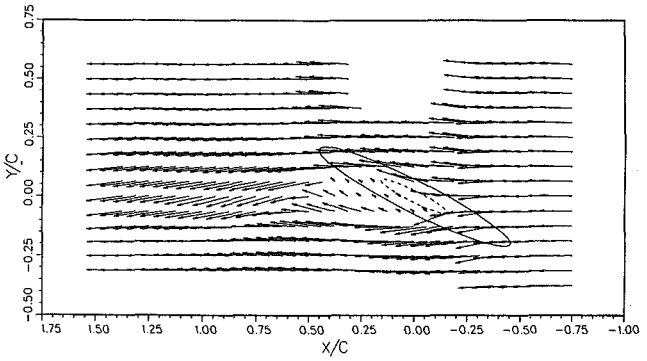

Fig. 7(*a*) Mean flow pattern at $Z/C = 0.94$

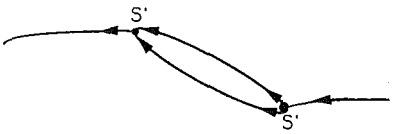

Fig. 7(*b*) Topological map of flow at $Z/C = 0.94$

furcation line SN' of Fig. 4(*b*), and begins to appear in the velocity vectors in horizontal planes around $Z = 0.06$ (height of 12 mm). Note that this focus was absent in the measurements close to the wall (Fig. 4). This is consistent with the surface flow visualizations of Johnson (1991), whose pictures showed that the separation line rolled up into a spiral node attached to the body close to the wall.

The flow pattern in the horizontal plane at increasing heights is topologically similar but the length of the reversed flow region becomes progressively smaller and the principal saddle point moves closer to the body. A qualitative change in the wake flow pattern is observed at $Z = 0.50$ (a height of 102 mm) as seen in Fig. 6. The topological features in Fig. 6(*b*) are essentially the same as those in Fig. 5(*b*), with the saddle point at $X \approx 0.65$, $Y \approx 0.1$, but there is much greater deflection of the wake flow from the pressure side towards the suction side. The flow from the suction side straightens itself in the wake (downstream of $X \approx 1.0$) while at sections $Z < 0.75$, the suction side flow in the wake has significant transverse velocities in the positive Y-direction.

The mean reversed flow region on the suction side vanishes at $Z = 0.88$. It should be emphasized that the flow is turbulent

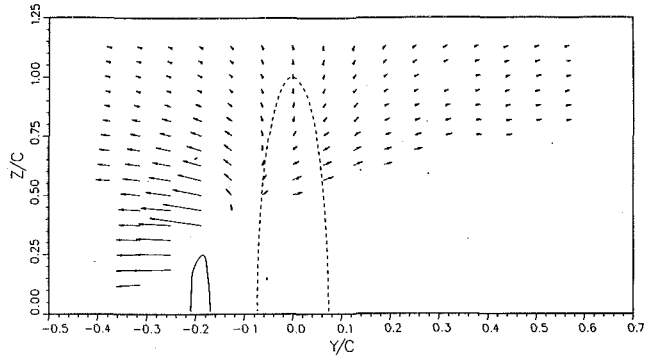

Fig. 8 Mean flow pattern at $X/C = -0.44$

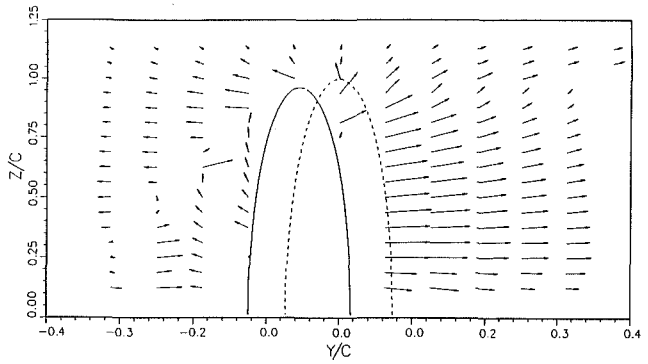

Fig. 9 Mean flow pattern at $X/C = -0.13$

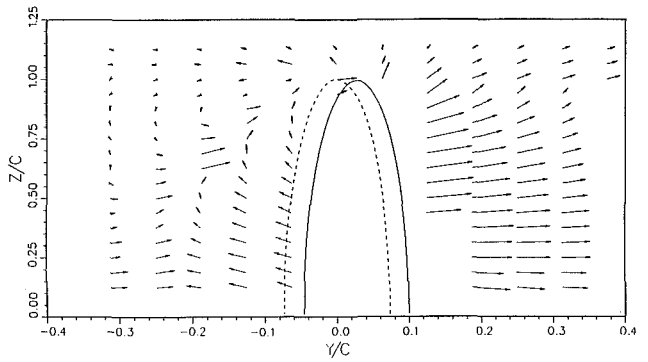

Fig. 10 Mean flow pattern at $X/C = 0.06$

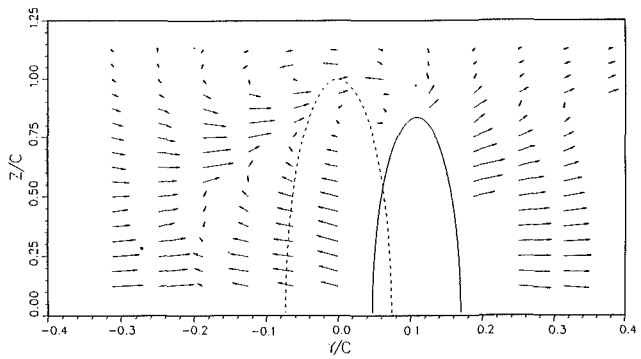

Fig. 11 Mean flow pattern at $X/C = 0.25$

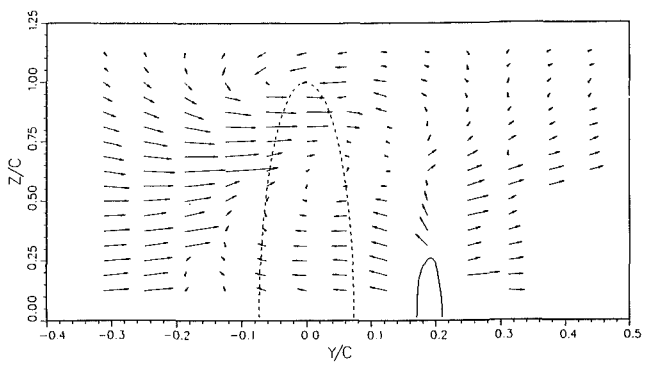

Fig. 12 Mean flow pattern at $X/C = 0.44$

and even though the mean velocity close to the body appears to be in the downstream direction (not separated), instantaneous negative values of streamwise velocity (reversed flow) occur. The flow at a height of $Z = 0.94$ is shown in Fig. 7 along with the topological map. There is no reversed mean flow. The flow attaches to the wing at a half-saddle at the leading edge and detaches at a half-saddle at the trailing edge. There is a region of small velocity and large deflection angles on the suction side, and the flow in the wake is deflected significantly towards the suction side. The wake appears to be sandwiched between straight flows with negligible transverse velocity.

The velocity vector plots presented and described above obviously give no information about the third, vertical component of velocity. However, it is important to keep in mind that the regions of reversed flow observed in each horizontal plane are no more than slices through a single, large, three-dimensional region of separated flow, a region that starts at the primary separation line on the wing along the locus of the half-saddles on the suction side. The locus of the clockwise (viewed from above) spiral nodes that appear in Figs. 5 and 6, in the vertical direction, may be thought of as the core of a vortex that emanates from the negative bifurcation line SN' in Fig. 4(*b*) and the corresponding line of separation on the plane. Since this vortex arises out of flow separation, the vortex is diffused and the velocities associated with it are necessarily small. Also, it should be emphasized that the features described above are based on the mean velocity measurements (averaged over long periods) and therefore may be smeared compared to the instantaneous flow structure. The velocities measured on the pressure side of the ellipsoid agreed well with the results of the potential-flow calculations, except very close to the ellipsoid and near the trailing edge. Also, the standard deviations of the velocities measured on the pressure side were comparable to freestream values, while those on the suction side and the near-wake were significantly larger than the freestream values. Therefore, it can be concluded that the flow on the pressure side was laminar.

Mean Flow Pattern in Constant X Planes. The vertical velocity components are visualized by examining the velocity vectors in planes normal to the freestream. Some typical results are presented below but, in the interest of brevity, only the most significant aspects of the mean flow are discussed. In particular, we no longer consider the many and varied topological features that are present when we look at the flow in vertical planes cutting through the body at various streamwise locations. As mentioned earlier, vertical velocities could not be measured close to the wall due to beam-blocking by the wall; the nearest location to the wall at which vertical velocities could be measured was $Z = 0.13$ (a height of 26.5 mm).

Figure 8 shows the flow in the vertical plane $X = -0.44$ which is close to the leading edge of the wing root. Both the local section (solid line) and the section through the center of the ellipsoid (broken line) are shown. Recall that positive Y is toward the pressure side. A line separating the flow going toward the pressure side from that going towards the suction side is seen around $Y = -0.1$. The flow is deflected outward on both sides, the large transverse velocities on the suction side at locations below $Z = 0.3$ being associated with the flow around the leading edge.

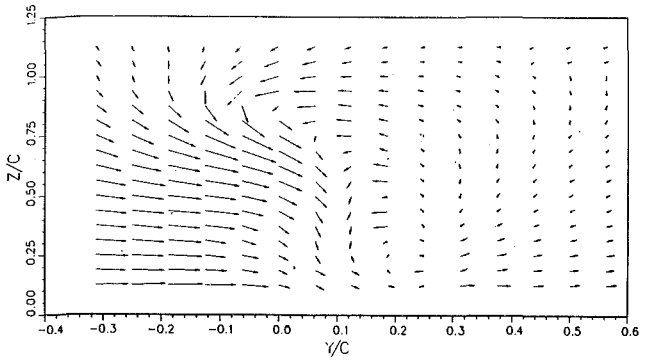

Fig. 13 Mean flow pattern at $X/C = 0.69$

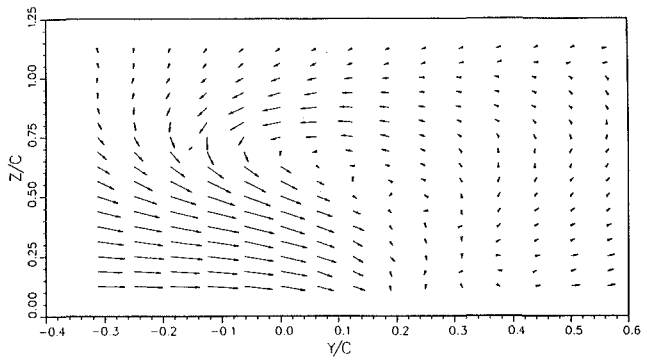

Fig. 14 Mean flow pattern at $X/C = 1.38$

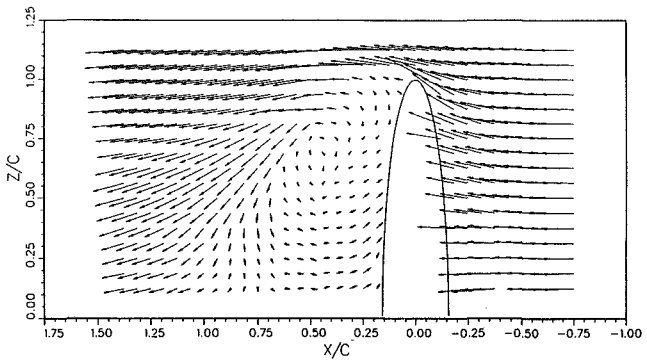

Fig. 15 Meanflow pattern at $Y/C = 0.0$

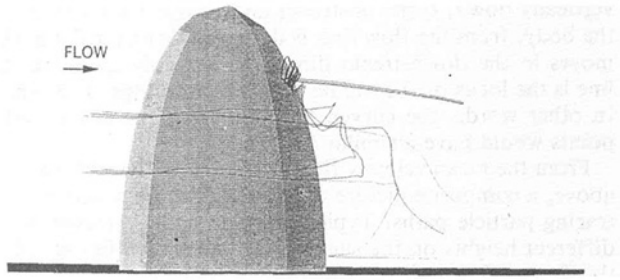

Fig. 16 Typical paths of particles released upstream of the body

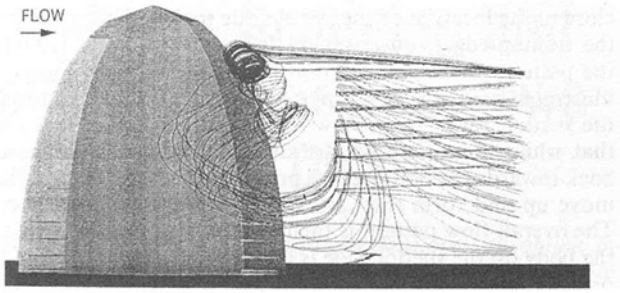

Fig. 17 Typical paths of particles released in the wake

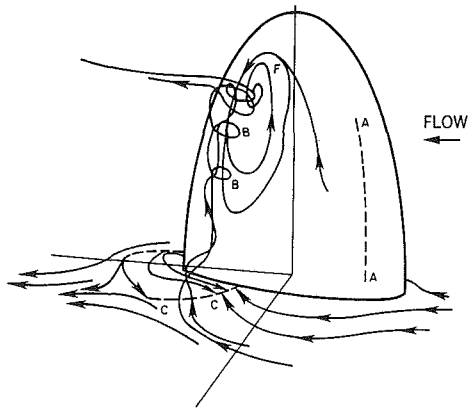

Fig. 18 Schematic of the flow pattern around the body

As we proceed downstream to $X = -0.13$ (Fig. 9), the transverse velocities on the pressure side become larger because the flow remains attached on that side. There is some evidence of a counterclockwise vortical structure near the tip centered around $Y \approx -0.05$, $Z \approx 1.0$ but the data density is not sufficient to resolve a vortex if one is indeed present. On the suction side, the velocity vectors near the wall reflect the presence of the separated flow.

At $X = 0.06$, which is just past mid-chord (Fig. 10) the data are qualitatively similar to those at the previous section and again there is no hint of a tip vortex. At $X = 0.25$ (Fig. 11), however, a new vortical structure, rotating in the clockwise sense and centered around $Y \approx 0.04$, $Z \approx 0.85$, is observed. In his flow visualizations, Johnson (1991) observed a prominent spiral node on the suction side on the body surface near the up and the trailing edge, and it was suggested that, in the neighborhood of the wing, the reversed flow rolled up into a vortex attached to the body at this node (much like a tornado). It is possible that the clockwise rotation observed in the velocity field is associated with that separation node. The lack of a well organized, tightly wound, tip vortex in the present case, in spite of the high incidence angle, is attributed to the massive separation on the suction side and the loss of lift associated with it.

At the next downstream station ($X = 0.44$, Fig. 12), which is just ahead of the trailing edge at the wing root, a large region of counterclockwise circulation is observed along with the clockwise circulation similar to that seen at the previous station. This new counterclockwise motion is presumably associated with the vortex arising from the primary separation on the wing, a vortex whose axis was identified with the spiral nodes in the velocity vectors in the horizontal planes.

Further downstream, at $X = 0.69$ (Fig. 13) and $X = 1.38$ (Fig. 14), the flow from the pressure side appears to interact with the two circulatory motions to produce one large vortical structure. The only difference between the flow in these two locations is that the vortical structure moves vertically down and towards the suction side as it proceeds downstream. When the flow is viewed in these sections, this vortical structure is the prominent feature of the body wake.

Flow Synthesis. The vortex resulting from the primary separation line on the wing can be seen in Fig. 15 which shows the flow pattern in the vertical plane $Y = 0.0$, parallel to the freestream, cutting through the center of the ellipsoid. The extent of the reversed flow region is readily seen in this figure. Also, there is a line that separates the flow that proceeds

vertically down, turns upstream and moves back towards to the body, from the flow that is deflected downward and then moves in the downstream direction. Roughly speaking, this line is the locus of the saddle points seen in Figs. 4, 5, and 6. In other words, the curved line that joins the actual saddle points would have a similar feature.

From the mean velocity field presented in the various views above, a composite picture of the flow can be constructed by tracing particle paths. Typical particle paths released at two different heights on the suction side are shown in Fig. 16. In this figure, flow is from left to right. Some of the particles are deflected vertically down and back to the suction side near the trailing edge while others are seen to swirl around, near the body, in a vortex-like flow. This region of swirling flow is close to the location of the spiral node (below the tip and near the trailing edge), observed by Johnson and Patel (1993) in the pattern of the skin-friction lines on the body. Figure 17 illustrates the paths of particles released in the wake toward the suction side. Again flow is from left to right. It is clear that while some particles are deflected vertically down and back towards the body before proceeding downstream, others move up and form the vortex-like region mentioned above. The overall flow pattern is then as shown in Fig. 18. Close to the body on the suction side is a vortex BB resulting from the primary separation line AA, the core of which is seen as the nodes in Figs. 5 and 6. This vortex is attached to the wall along the separation line CC (SN' in Fig. 4(*b*)) and fed by a part of the reversed flow in the separation region. This vortex interacts with another associated with a spiral node on the body and, as the flow proceeds downstream, interacts with the flow from the pressure side, producing one large diffused vortical structure in the wake.

Conclusions

The flow field around a half-ellipsoid mounted on a wall at an angle of attack of 25 deg at a Reynolds number of 47,000 measured using a three-dimensional LDV system was found to be consistent with the flow visualizations of Johnson (1991). The flow on the entire suction side was separated with a reversed-flow region extending to one-chord length behind the body and with mean reversed velocities as high as 25 percent of the freestream velocity. The primary separation line on the suction side of the body gave rise to a large vortex whose footprint was observed as a line of separation on the wall. Part of the reversed flow resulting from the primary separation moved towards the tip and interacted with another vortex attached to the suction side close to the trailing edge and below the tip in a spiral node of friction lines observed in the flow visualizations. The two vortices, together with the flow on the pressure side proceeded downstream forming one large vortical structure. This final vortex was found to be more diffused and less tightly wound than the tip vortex usually found in the wakes of lifting wings. A small separation zone close to the trailing edge was observed on the pressure side. The flow on the pressure side was laminar while the flow on the suction side and the near-wake was turbulent.

There are a number of other observations that can be made from this experiment. First of all, it is interesting to note that significant flow features can be identified even with the mean-velocity measurements although they may be smeared if the flow is unsteady. Further work is needed to quantify the unsteady features of the flow, which are undoubtedly present. Secondly, it is seen that an enormous amount of data is needed to fully visualize the flow structure that is associated with three-dimensional flow separation. In this regard, topological concepts applied to streamlines viewed in various planes cutting the flow domain are of somewhat limited help. In fact, they display a rich array of singular points and lines, and suggest a level of flow complexity that is far greater than reality. Construction and visualization of streamlines or particle paths in three-dimensional views using the measured flow field may turn out to be better vehicles for comprehending the true geometry of motion. Finally, it is suggested that the three-dimensional flow field around this simple geometry be used to develop and test advanced numerical methods for predicting such flows.

Acknowledgments

This research was sponsored by the Office of Naval Research, under grant N00014-91-J-1204, monitored by Dr. L. P. Purtell. The authors would like to acknowledge fruitful discussions with Mr. Timothy Johnson.

References

Chapman, G. T., and Yates, L. A., 1991, "Topology of Flow Separation on Three-Dimensional Bodies," *Applied Mechanics Reviews*, Vol. 44, No. 7, pp. 329–345.

Johnson, T. A., 1991, "Visualization of Topology of Separated Flow over a Semi-Elliptic Wing at Incidence Intersecting a Plane Wall," M.S. thesis, Mechanical Engineering, The University of Iowa, Iowa City, IA.

Johnson, T. A., and Patel, V. C., 1993, "Skin-Friction Topology Over a Surface Mounted Semi-Ellipsoidal Wing at Incidence," *AIAA Journal*, Vol. 31, pp. 1842–1849.

Perry, A. E., and Steiner, T. R., 1987, "Large-Scale Vortex Structures in Turbulent Wakes behind Bluff Bodies. Part 1. Vortex Formation Process," *Journal of Fluid Mechanics*, Vol. 174, pp. 233–270.

Tobak, M., and Peake, D. J., 1982, "Topology of Three-Dimensional Separated Flows," *Annual Reviews of Fluid Mechanics*, Vol. 14, pp. 61–85.

Particle Tracking Velocimetry Using Laser-Beam Scanning and Its Application to Transient Flows Driven by a Rotating Disk

S. Ushijima

N. Tanaka

Central Research Institute of Electric Power Industry (CRIEPI), 1646 Abiko, Abiko-shi, Chiba-ken, 270-11, Japan

A particle tracking velocimetry (PTV) system has been developed to obtain instantaneous two velocity components on several sections in three-dimensional space. The flow visualization is conducted by means of parallel laser-light sheets created by a scanning laser beam and the visualized particle images are taken by a high-speed video system synchronized with the scanning. In order to obtain higher accuracy in velocity measurements than usual PTV, some improvements are made on the analyzing procedures: the extraction of particle images, the determination of their center points, the derivation of velocity components and others. The present PTV was applied to the transient flows in a cylindrical tank with a rotating disk. As a result, two-dimensional transient flow patterns with large scale disturbances are continuously captured in three-dimensional space.

1 Introduction

Simultaneous velocity measurements over a certain area or in three-dimensional space are of great importance to understand nonuniform complicated flow patterns arising in experimental models. In order to perform such measurements, various digital image processing techniques have been extensively investigated as reviewed by Hesselink (1988). Among some principles to obtain velocity vectors from visualized images, particle image velocimetry (PIV) is one of the most effective techniques. PIV enables us to make accurate and high-quality measurements in a variety of laboratory-scale flows of gases and liquids over a wide range of velocity (Adrian, 1991). This paper deals with particle tracking velocimetry (PTV), classified as one of the PIV techniques, which utilizes relatively low-density particles scattered in a fluid so that the individual images can be identified. The velocity measurements based on PTV have been conducted by Imaichi and Ohmi (1983), Kobayashi et al. (1985), Chang et al. (1985), Agui and Jimenez (1987), Nishino et al. (1989) and many others up to the present.

While the area measured by PTV was usually a single two-dimensional plane visualized by slit light in the past, the area was expanded to three-dimensional space in recent years. Most of the PTV techniques applied to three-dimensional space (3D PTV) are based on stereoscopic visualization, which was first attempted by Chang and Tatterson (1983) and then improved by Racca and Dewey (1988), Nishino et al. (1989) and others. However, the identification of stereoscopically obtained particle images, as captured by multiple cameras, becomes difficult in such a flow as including many particles, which results in the dissatisfied spatial resolution. For instance, 3D PTV has a spatial resolution of at most 64 vectors in two-dimensional plane even if 512 ($=64^{3/2}$) vectors are obtained in three-dimensional space. The present PTV allows us to obtain instantaneously two components of velocity on several horizontal sections in three-dimensional space with the aid of a scanning laser beam. While the velocity component vertical to the visualized section is not measured, the spatial resolution, or the number of the available particles in a flow, is higher by nearly one order than that of 3D PTV in terms of the two-dimensional comparison.

The improvement of the accuracy of the derived velocity components is also mainly focused on in the present study. The first procedure of PTV is usually the binarization of particle images to determine their positions. Since the gray levels of the visualized many particles on a frame are generally different from one another, a single threshold which was often employed in previous works (e.g., Chang et al., 1985) is inappropriate to separate particle images from the background in good condition. Thus, in the present method, the binarization is carried out on 1,024 sub-regions consisting of 16×16 pixels using different threshold levels. Each threshold level is rationally determined on the basis of the discriminant and least squares threshold selection (Otsu, 1978). After taking logical product between the binarized and original images, particle images are finally extracted with having gray level distributions. The particle center position is calculated with sub-pixel accuracy from its second-order regression curvature fitted to its gray levels. The tracking method to specify the center points of an identical particle on multiple frames is conducted by setting a search region as done by Dracos and Malik (1992)

Contributed by the Fluids Engineering Division for publication in the JOURNAL OF FLUIDS ENGINEERING. Manuscript received by the Fluids Engineering Division January 12, 1993; revised manuscript received September 28, 1993. Associate Technical Editor: J. A. C. Humphrey.

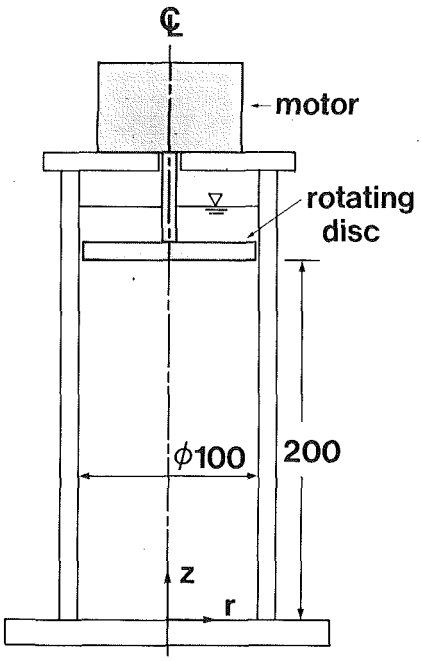

Fig. 1 Experimental tank

and Sata and Kasagi (1992), instead of the method utilizing particle trajectories (Kobayachi et al., 1985), which is not applicable when the velocity is relatively high and pathlines are intersecting each other. The identification of center points is conducted changing the number of the tracking frames so that the center points can suitably be detected in the visualized area where both high and low velocity regions coexist. The second-order polynomial approximation based on the method of least squares is applied to the specified center points of an identical particle and the direction of the velocity vector is determined from the derivative. In addition, the length of the velocity vector is calculated from the summation of the displacements of all center points. Thus the accuracy of the vector direction and length is improved compared with the previous method taking account of only initial and terminal positions as done by Imaichi and Ohmi (1982).

The present PTV was applied to the velocity measurement of the flow driven by a rotating disk in a cylindrical tank, where five horizontal sections were simultaneously visualized by parallel laser-light sheets generated from a scanning laser beam. Transient flow patterns were captured when the rotating direction of the disk was reversed after the steady state had been completed.

2 Experiments

2.1 Experimental Tank. Figure 1 shows the cylindrical tank used in the flow visualization experiments. A rotating disk driven by a motor is located in the upper region of the tank. The disk is made of acrylic plate and has a smooth surface which contacts with the confined fluid. The rotating direction and the angular frequency of the disk can be adjusted through a control unit. In the experiments, the steady-state condition was formed by rotating the disk in clockwise direction looking from above with an angular frequency of $(4/3)\pi$ radian per second for sufficiently long time. Then the rotating direction was instantaneously reversed at $t=0$ and the disk continued counter-clockwise rotation with the same angular frequency as that of the steady state. This procedure created the transient flow patterns lasting for a few minutes in the tank. The flow visualization was conducted both in the steady and transient conditions.

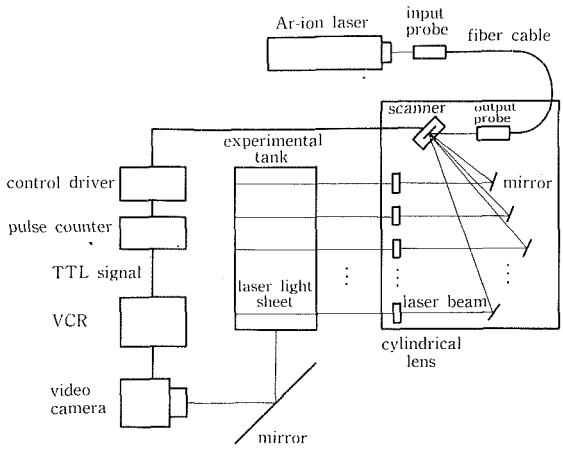

Fig. 2 Flow visualization system

Since the average fluid velocity in the steady state (U_0) measured by the PTV is 11.1 mm/s as described later, the Reynolds number may be derived as

$$\mathrm{Re}=\frac{U_0 D}{\nu}=1.1\times 10^3 \tag{1}$$

with the diameter of the tank (D) and the kinematic viscosity (ν). Accordingly the fluid in the tank is in turbulent condition. The representative time scale (T_0) defined in the following equation is calculated as 9.0 s.

$$T_0=\frac{D}{U_0} \tag{2}$$

2.2 Flow Visualization. The tracer particles scattered in the flow are made of high polymer (Eslen) with a specific gravity of 1.03. The shape of the particles is spherical and their average diameter is around 400 μm. They include fluorescent sodium which gives clear images in the presence of laser light. The working fluid in the tank is saline water with a suitable density so that the particles can take neutral buoyancy.

The tracer particles are visualized with parallel horizontal laser-light sheets generated by a scanning laser beam. The devices for the flow visualization are schematically shown in Fig. 2. The Ar-ion laser beam is transferred through a fiber cable and released from the output probe equipped with front lenses that can adjust the focus of the beam. The released laser beam is put on a small mirror of an optical scanner. The galvanometer scanner enables the mirror to take stepping movements at the frequency of 500 Hz. The laser beam, reflected by the scanner in different directions, is placed on the fixed mirrors in turn, which are arranged suitably on a mounting plate in order that the reflected laser beams should be parallel. Then the parallel laser beams are injected into cylindrical lenses, 3 mm in diameter, through which the beams turn into parallel laser-light sheets.

The visualized particles are recorded on video tapes with a high-speed video system consisting of a video camera and a video cassette recorder (VCR). This system is able to take 500 frames per second for 14 minutes. The VCR in the system sends TTL signals to the pulse counter. The pulse counter, in which the numbers of visualized sections and of the recording frames per section have been input beforehand, compares the TTL pulses with the input conditions and makes up analogue wave signals. The control driver, equipped with a servo amplifier which automatically selects PD/PID controls, operates the optic scanner according to the wave signals transferred from the pulse counter. Thus the stepping movements of the scanner are synchronized with the video-recording and the visualized sections are properly captured on the appointed frames.

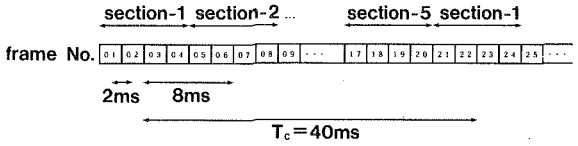

Fig. 3 Relationship between frames and recorded data

In the present case, five horizontal sections are visualized from $z=20$mm to 180mm with 40mm intervals, which are denoted by section-1 to section-5 from the lowest section. Four frames are taken per section and the relationship between the order of the frames and the recorded sections are shown in Fig. 3. The time interval between two adjacent sections is 8 ms and the scanning time period (T_C) corresponds to 40 ms. Since in a certain section the tracking frames, on which center points of an identical particle are found out, are selected every scanning cycle, their time interval (Δt_T) is same as T_C. The exposure time per frame is set at 200 μs with the aid of an electrical shutter.

The average particle distance (δ_i) on the ith frame may be estimated by

$$\delta_i = \left(\frac{S}{n_i}\right)^{1/2} \tag{3}$$

where S and n_i denote the visualized area ($2.5\times10^3\pi$ mm^2) and the number of the visualized particles on the ith frame, respectively. Since the the average particle distance in the steady state (δ_0) was 4.9 mm as described later, the particle spacing-displacement ratio (p) based on U_0 is evaluated as

$$p = \frac{\delta_0}{U_0\,\Delta t_T} = 11 \tag{4}$$

The spacing-displacement ratio based on the fluctuating velocity (Dracos and Malik, 1992) is expected larger than the value of Eq. (4). Thus the particle scattering is in suitable condition for their tracking.

3 Image Processing

3.1 Extraction of Particle Images. The visualized images recorded on video tapes are converted to digital data through an image processor controlled by a personal computer and stored on a magneto-optical disk with a capacity of 1 gigabytes. These procedures are performed in the devices shown in Fig. 4. The digitized data consist of 512×512 pixels with 256-gray-level resolution per a single pixel.

The procedure of the extraction of particle images is schematically shown in Fig. 5. Here the gray level distribution is expressed as one-dimensional, for convenience, though it is actually obtained on two-dimensional plane. First, smoothing filters and an image-enhancement filter based on digital Laplacian are applied to original images in order to delete noise patterns and to make clear the particle images (Rosenfeld and Kak, 1976). The binarization of the filtered images is conducted with the discriminant and least squares threshold selection (Otsu, 1978), which selects an optimum threshold level so that the summation of gray-level variances in two classes separated by the threshold should be minimum and that the variance between the two classes should be maximum on the basis of discriminant analysis. This binarization is applied to 1,024 subregions each consisting of 16×16 pixels, instead of a single threshold for a frame. Thus, as illustrated in Fig. 5(b), the different thresholds (T_m and T_n) may be selected for the particle images on a frame. The binarized particle images, shown in Fig. 5(c), have the area r_{pm} and r_{pn}, which may be slightly different according to the particles. The area of these images are then replaced by the average value r_p, 3×3 pixels in the present analysis, without changing the center points x_{cm} and

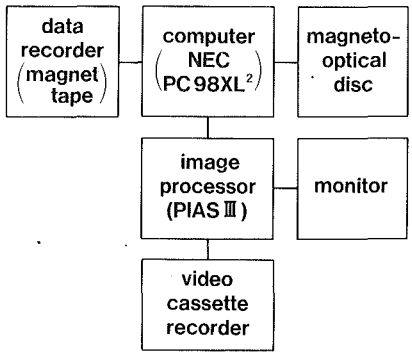

Fig. 4 Devices for digitization and pre-treatment

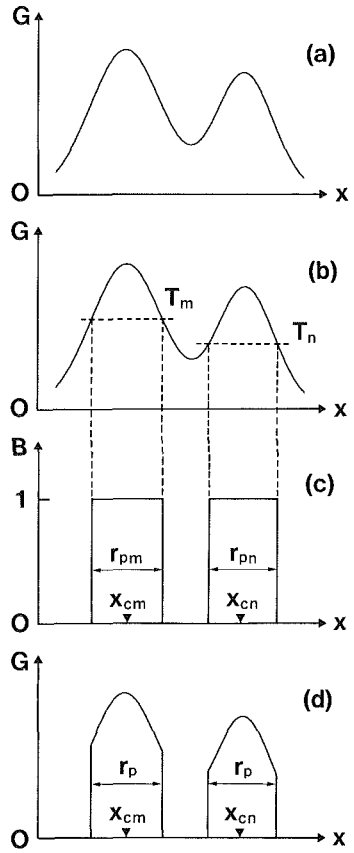

Fig. 5 Extraction of particle images

x_{cn}. Finally, the logical products are taken between the original images and the binarized images. As a result, the particle images having original gray-level distributions are separated from the background, as shown in Fig. 5(d). These image analyses are carried out on the devices shown in Fig. 4 and the final images are transferred to a high-speed computer (HITAC M680H).

3.2 Determination of Particle Center Points. The particle center points are determined using the extracted particle images sent to the high-speed computer. It is effective for their accurate positioning to make use of their gray-level distributions, rather than the binarized results. Since the error resulting from the incorrect positioning of the center points is a dominant factor for the total uncertainties of the derived velocity components (Ushijima, 1991), this procedure is improved to have sub-pixel accuracy in the present method.

Let $G(i, j)$ be the gray level at (i, j) on a particle image where i and j correspond to horizontal and vertical pixels

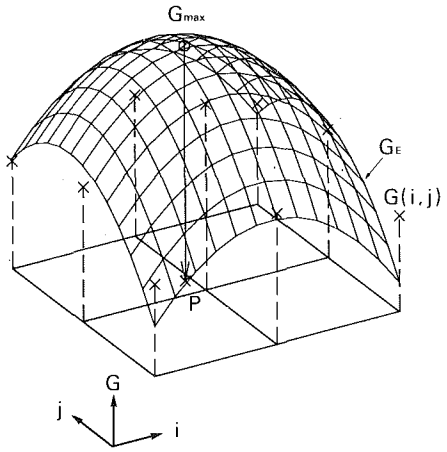

Fig. 6 Approximation of particle gray levels

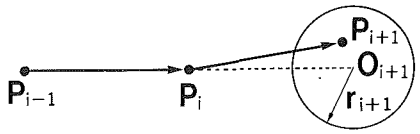

Fig. 7 Search region on $i+1$ frame

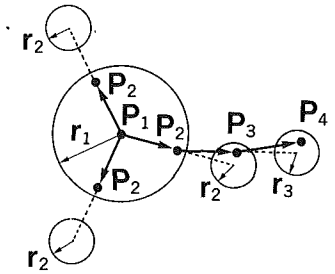

Fig. 8 Search region on the first frame

respectively. Here $1 \leqq i, j \leqq 3$, since a particle image has been extracted having its area of 3×3 pixels. The approximate gray level $G_E(i, j)$ is calculated from the second-order regression curvature derived with the method of least squares, as schematically shown in Fig. 6.

$$G_E(i,j) = a_0 + a_1 i + a_2 j + a_3 i^2 + a_4 j^2$$
$$\equiv a_0 + a_1 X_1(i,j) + a_2 X_2(i,j) + a_3 X_3(i,j) + a_4 X_4(i,j)$$
$$= a_0 + \sum_{m=1}^{4} a_m X_m(i,j) \quad (5)$$

While $G(i, j)$ and $X_m(i, j)$ are located at 9 points on two-dimensional image plane, these are converted to one-dimensional arrangements, for convenience:

$$G_1 = G(1,1),\ G_2 = G(1,2),\ \ldots,\ G_9 = G(3,3) \quad (6a)$$

$$X_{m1} = X_m(1,1),\ X_{m2} = X_m(1,2),\ \ldots,\ X_{m9} = X_m(3,3) \quad (6b)$$

Note that G_k and X_{mk} are defined at the same position. The four unknown constants (a_1, a_2, . . . , a_4) in Eq. (5) are determined by solving the following matrix equation:

$$\begin{bmatrix} c_{11} & c_{12} & c_{13} & c_{14} \\ c_{21} & c_{22} & c_{23} & c_{24} \\ c_{31} & c_{32} & c_{33} & c_{34} \\ c_{41} & c_{42} & c_{43} & c_{44} \end{bmatrix} \begin{bmatrix} a_1 \\ a_2 \\ a_3 \\ a_4 \end{bmatrix} = \begin{bmatrix} b_1 \\ b_2 \\ b_3 \\ b_4 \end{bmatrix} \quad (7)$$

with

$$c_{mn} = \sum_{k=1}^{9} (X_{mk} - \overline{X}_m)(X_{nk} - \overline{X}_n) \quad (8a)$$

and

$$b_m = \sum_{k=1}^{9} (X_{mk} - \overline{X}_m)(G_k - \overline{G}) \quad (8b)$$

Here the over-bar means taking average with respect to k. A remaining unknown constant a_0 is given by

$$a_0 = \overline{G} - \sum_{m=1}^{4} a_m \overline{X}_m \quad (9)$$

The particle center point P is determined where the approximate gray level G_E has a peak value $G_{\max}$, as indicated in Fig. 6.

The images recorded on video tapes are possibly distorted and their scales may slightly be different in accordance with the visualized sections. To correct the distortion and scales, nonlinear approximate functions, including third-order terms at the highest, are derived and the center points of particles on the image plane are transferred to those on the real plane. The unknown coefficients of the functions are determined with the method of least squares, as done in the derivation of the constants for the second-order regression curvature described above, utilizing the images of a calibration plate on which 21 standard points are regularly fixed.

3.3 Tracking of Center Points. The particle tracking procedure is conducted to specify the center points of an identical particle located on the multiple frames. In case that the particle spacing-displacement ratio, as defined by Eq. (4), is large enough, the tracking procedure becomes easier and the principle to utilize a search region is effective (Dracos and Malik, 1992). Figure 7 shows the search region on the $i+1$ frame, which is set up after the candidates of particle center points (P_1, P_2, . . . , P_i) have been specified. The center position of the circular search region is set at $2\mathbf{p}_i - \mathbf{p}_{i-1}$, where $\mathbf{p}_i$ is the position vector of P_i. The radius of the region may be determined by taking account of the average particle distances calculated by Eq. (3) and of the turbulence quantities as Lagrangian integral scales. In the present experiments where velocity measurements of transient flows are made, however, it is nearly impossible to estimate the exact turbulence quantities beforehand. Thus the radius of the search region r_{i+1} on the $i+1$ frame is calculated taking into account the particle distance on the $i+1$ frame alone as

$$r_{i+1} = \frac{1}{3}\,\delta_{i+1} \quad (10)$$

which is one of the criteria to determine the search region employed by Dracos and Malik (1992). When a single center point is located within the search region, this becomes a new candidate on the $i+1$ frame. In case that the multiple center points are included, the center point which gives the minimum variance of the local velocities calculated from P_{i-1}, P_i and P_{i+1} is selected. If there is no center point, all candidates (P_1, P_2, . . . , P_i) are discarded. This tracking procedure is repeated until the appointed final frame.

On the first frame of tracking, the circular search region is set up, having its center at P_1 and its radius r_1 equal to $(1/2)\delta_1$, as shown in Fig. 8. When multiple center points P_2 are included in the region, all of them are considered as valid and the tracking procedure described above continues to the following frames. While most of the misidentified center points are dropped in the process of the multiple trackings, a group of center points, which gives the minimum variance of local velocities derived from all center points, is selected if more than two groups are finally obtained. If there is no second

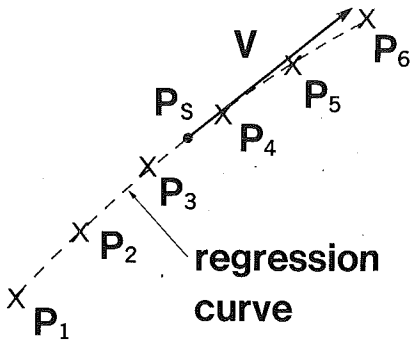

Fig. 9 Derivation of velocity vector

point P_2 in the search region, the corresponding first center point P_1 is discarded.

The particle tracking procedure for N_T frames, where N_T is referred to as tracking frame number, is carried out throughout all sampled frames, changing the first frame of tracking one by one, the number of total tracking procedures is given by $N_S - N_T + 1$, where N_S is the sampled frame number. In the present method, the lower and upper limitations (N_{T1} and N_{T2}, respectively) can be set for the tracking frame number in order to respond to high and low velocity regions coexisting in the visualized area. Thus the tracking procedure is conducted L_T times, which is given by

$$L_T = (N_S + 1)(N_{T2} - N_{T1} + 1) - \sum_{k=N_{T1}}^{N_{T2}} k \tag{11}$$

3.4 Derivation of Velocity Vectors. The velocity components were usually derived from the positions of the identified initial and terminal center points and their time interval in previous works (e.g., Imaichi and Ohmi, 1982; Kobayashi et al., 1985) after the particle tracking was completed. However, as indicated by Chen (1992), the shorter time interval makes the error associated with the positioning of center points relatively large, while the longer interval causes the loss of the information during it. To solve this problem, one may track the center points with sufficiently short time interval over several tracking frames and take into consideration all intermediate center points as well as the initial and terminal points to determine the velocity components.

The particle tracking over N_T tracking frames provides the same number of identified center points, where N_T is more than three in the present method. A quadratic function is approximated for these center points with the method of least squares and the direction of velocity vector is defined as its tangential direction. Figure 9 shows an example of the velocity vector determined from the regression curve in case of $N_T = 6$. When the regression curve is given by $y = f(x)$, the components of unit vector $\mathbf{n} = (n_1, n_2)$ at $P_S(x_S, f(x_S))$ is calculated by

$$n_1^2 = (1 + a^2)^{-1} \tag{12}$$

$$n_2^2 = a^2 (1 + a^2)^{-1} \tag{13}$$

where

$$a = \frac{df}{dx}\,[x = x_S] \tag{14}$$

The value of x_S is calculated as the average among x coordinates of N_T center points. The signs of the unit vector components and which coordinate should be selected as independent variable are determined from the spatial locations of the center points on the first and last frames. The length of the velocity vector V_{int} is calculated from the summation of all particle displacements as

$$V_{int} = \frac{1}{(N_T - 1)\Delta t_T} \sum_{k=1}^{N_T - 1} [(x_{k+1} - x_k)^2 + (y_{k+1} - y_k)^2]^{1/2} \tag{15}$$

Accordingly the velocity vector $\mathbf{V}$ is finally obtained as $V_{int} \cdot \mathbf{n}$.

3.5 Interpolation of Vectors on Boundary-Fitted Coordinates. The velocity vectors obtained by L_T times of tracking procedures are all superimposed and the average velocity vectors over the sampled frames are calculated at the appointed grid points. The grid points are generated using boundary-fitted coordinates (BFC) as proposed by Thompson (1977) in order to distribute the grid points as uniformly as possible in the circular visualized area.

The velocity components at the generated grids are obtained by interpolating the vectors randomly distributed in accordance with the particle positions. While various interpolation methods were employed in previous works, the weighted averaging based on the Gaussian window is utilized in the present interpolation, which was concluded advantageous by Agui and Jimenez (1987):

$$U_{mn} = \left(\sum_{k=1}^{n_v} w_k U_k\right) \Big/ \left(\sum_{k=1}^{n_v} w_k\right) \tag{16}$$

$$V_{mn} = \left(\sum_{k=1}^{n_v} w_k V_k\right) \Big/ \left(\sum_{k=1}^{n_v} w_k\right) \tag{17}$$

where (U_{mn}, V_{mn}) and (U_k, V_k) are velocity components interpolated at grid point P_{mn} (x_{mn}, y_{mn}) and those obtained by the particle tracking procedures at (x_k, y_k), whose total number is n_v, respectively. The weighting coefficient w_k is given by

$$w_k = \exp\left[-\frac{(x_k - x_{mn})^2 + (y_k - y_{mn})^2}{H_w^2}\right] \tag{18}$$

Here the window width H_w is $1.24\delta_v$ (Agui and Jimenez, 1987), where δ_v is the mean distance between velocity vectors given by

$$\delta_v = \left(\frac{S}{n_v}\right)^{1/2} \tag{19}$$

The average value of δ_v in the steady state is estimated as 2.6 mm, as described later. In terms of Nyquist sampling criterion, the resolution for the highest wave number is limited by $1/2\delta_v$ (Agui and Jimenez, 1987), which implies that meaningful grid intervals should be larger than $2\delta_v$. This condition is satisfied in the present case, since the average interval of the grids is about 7.4 mm, which is larger than $2\delta_v$.

The velocity components interpolated at the grid points are spatially smoothed within the error range which is given by bootstrap procedure (Efron, 1979; Diaconnis and Efron, 1983; Efron, 1983), as conducted by Agui and Jimenez (1987). The spatial smoothing is carried out by solving Laplace equations, $\nabla^2 U_{mn} = 0$ and $\nabla^2 V_{mn} = 0$. These Laplace equations are operated to the velocity components after they are converted to the transformed space with the relationships in BFC. In this procedure, the smoothed results must be within the error range estimated by the bootstrap method. The error range at each grid point is estimated from the frequency distribution created by the bootstrap procedure. This procedure is conducted by the following steps:

1) A set of synthetic samples S_k^1 $(k = 1, 2, \ldots, n_v)$ is created by selecting the original velocity components U_k $(k = 1, 2, \ldots, n_v)$ randomly. Since the number of samples is same as that of velocity components, some are possibly selected multiple times and others may not be chosen at all.

2) The n_S sets of synthetic samples are generated by repeating the same procedure n_S times. Thus the samples S_k^i $(k = 1, 2, \ldots, n_v;\ i = 1, 2, \ldots, n_S)$ are created.

3) One velocity component is obtained at every grid point by interpolating a set of synthetic samples S_k^i using Eq. (16). Since the number of sets is n_S, the n_S velocity components are obtained at every grid point by interpolating all sets of samples S_k^i one by one.

4) A frequency distribution can be drawn for the n_S velocity components at a grid point P_{mn}. From the frequency distribution, a mean value μ_{mn} and an error range σ_{mn} are finally determined for the velocity component U_{mn}.

5) The mean value and error range for V_{mn} are obtained in the same way.

Consequently, the smoothed result $U^{n+1}_{\text{ave},mn}$ at the $n+1$ step of the iteration is given by

$$U^{n+1}_{\text{ave},mn} = \max\{\mu_{mn} - \sigma_{mn}, \min(\mu_{mn} + \sigma_{mn}, U^{n}_{\text{ave},mn})\} \quad (20)$$

The error range σ_{mn} is determined on the basis of a confidence level of 68 percent which means 68 percent of the bootstrap samples are included in this range (Diaconnis and Efron, 1983). The similar procedure can be applied to another velocity component.

4 Application of PTV

4.1 Experimental Results. Two cases of analyses are performed for the obtained images; velocity vectors of the transient flow on section-1 at $z = 20$mm are continuously captured with short time intervals in Case A and the transition in three-dimensional space is evaluated on five horizontal sections in Case B. The sampling conditions and tracking frame numbers at each measurement are listed in Table 1.

Table 1 Sampling and tracking conditions

	Δt_T (ms)	N_S	N_{T1}	N_{T2}	L_T
Case A	40	5	3	5	6
Case B	40	10	3	6	26

The following statistical values are derived from the analyses of Case B for five horizontal sections in steady states.

1) number of particles per frame: $n_{p0} = 333$
2) particle distance calculated by Eq. (3) with n_{p0}: $\delta_0 = 4.9$ mm
3) number of total vectors per section: $n_{v0} = 4620$
4) average velocity: $U_0 = 11.1$ mm/s

Since the analyses of Case B was performed with four different tracking frame numbers, as presented in Table 1, the average number of velocity vectors obtained with a constant tracking frame number is $n_{v0}/4$ (= 1155). With this number, the mean distance of the vectors δ_v is estimated 2.6 mm from Eq. (19).

The numerical procedure for the image processing described in 3.2 to 3.5 is conducted with a FORTRAN code on HITAC 680H. The total CPU time to analyze one horizontal section in Case B where $N_S = 10$ and $L_T = 26$ as listed in Table 1, was about 40 minutes.

Figure 10 shows the transition of velocity vector distributions on section-1 obtained by the analyses of Case A, while the results shown in Figs. 10(*a*) and (*l*) are derived by Case B. The nondimensional time $t*$ is defined with the representative time T_0 given by Eq. (2). At $t* = 8.53$, the whole velocity decreases and eccentric flow pattern arises, as shown in Fig. 10(*b*), while the rotating direction is still same as that of the steady flow in Fig. 10(*a*). As the time proceeds, the shear stress in counter-clockwise direction transferred from the above fluid becomes gradually dominant against the remaining initial clockwise flow. As a result, the complicated transient flow patterns arise with large scale disturbance, which are continuously captured in a series of the results in Fig. 10. At $t* = 10.65$, as shown in Fig. 10(*k*), while the counter-clockwise flow has been dominant, the flow pattern is not yet fully stable and meandering flows

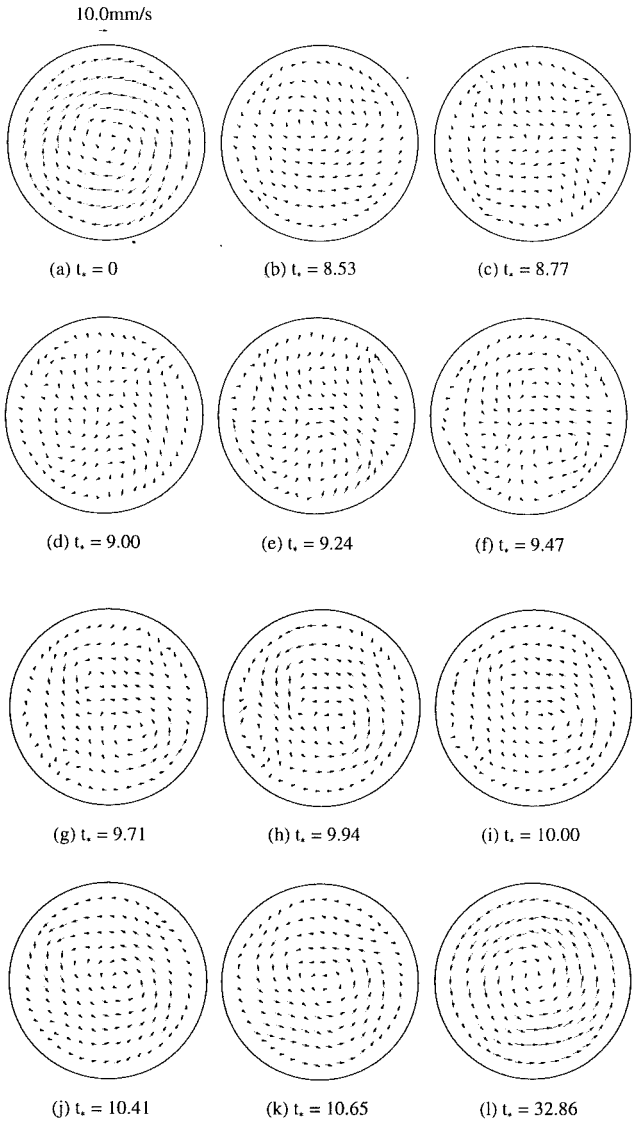

Fig. 10 Transition of flow patterns on section-1 (Case-A)

are observed. Finally, at $t* = 32.86$, flow pattern comes again to quasi-steady state as shown in Fig. 10(*l*).

Figure 11 shows the results of Case B. It is noted that section 1 and section 5 are the lowest and highest sections, respectively, and the vertical interval of two adjacent sections is 40 mm. In the steady states, as shown in Fig. 11(*a*), the instantaneous velocity on section-5, nearest to the rotating disk, is higher than those on the lower sections and slightly nonuniform owing to turbulence. The effect of the reversed rotating disk first appears on section-5. As shown in Fig. 11(*b*), the flow pattern on section-5 is completely disturbed at $t* = 1.67$ and slight affect extends to section-4 as well, yet the flows on the lower sections seem to be similar to those in the steady states. In the following results, as shown in Figs. 11(*c*) and (*d*), the transition of two-dimensional flow patterns is clearly captured in the three-dimensional space, in which the effect of the rotating disk proceeds toward lower sections. The counter-clockwise quasi-steady state is attained on all sections at $t* = 32.86$, as shown in Fig. 11(*e*).

4.2 Estimation of Uncertainty. Regarding the uncertainty involved in PTV techniques, several investigations have been made to specify the sources of errors and evaluate their quantities (e.g., Imaichi and Ohmi, 1983; Kobayashi et al., 1985; Chang et al., 1985; Agui and Jimenez, 1987; Nishino et

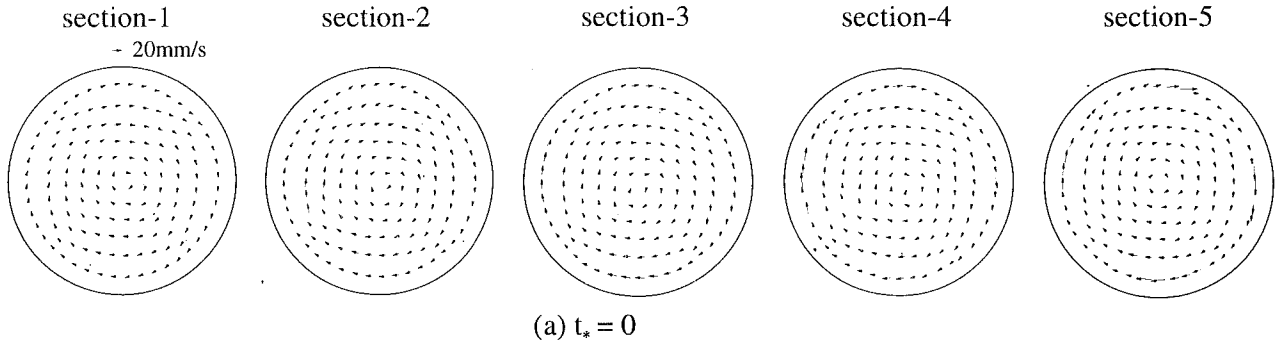

(a) $t_* = 0$

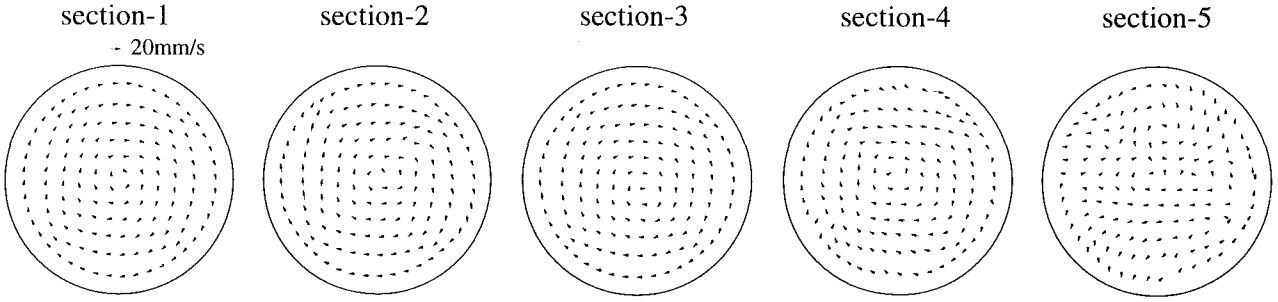

(b) $t_* = 1.67$

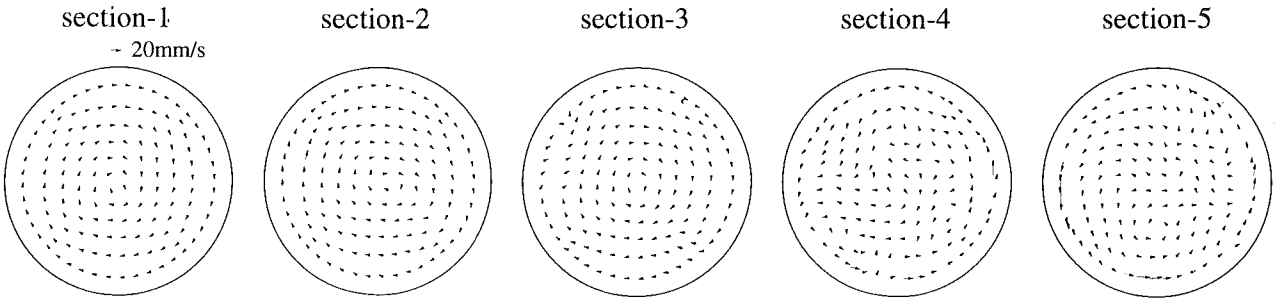

(c) $t_* = 3.33$

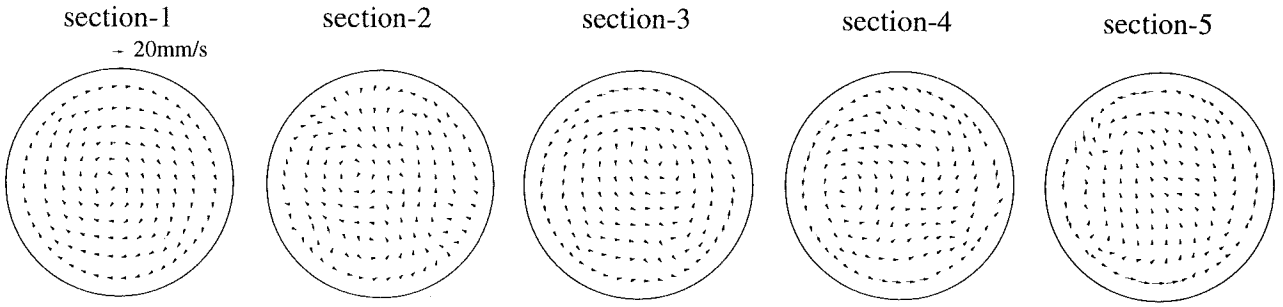

(d) $t_* = 6.66$

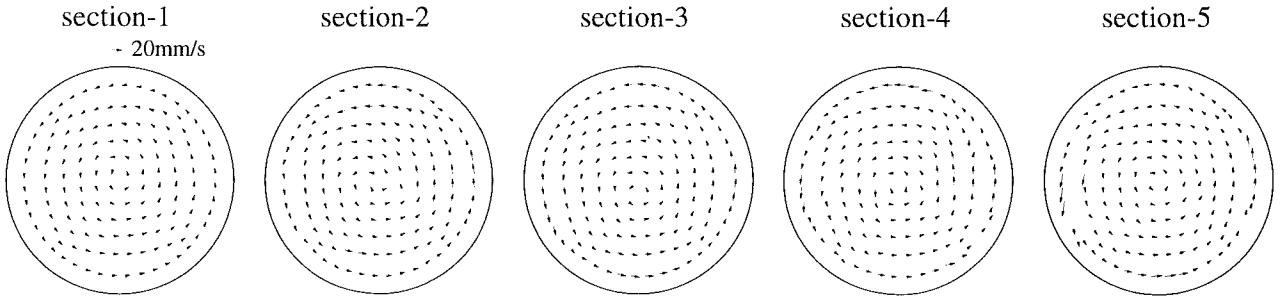

(e) $t_* = 32.86$

Fig. 11 Transition of 2D flow patterns in 3D space (Case-B)

al., 1989). As a result, it can be seen that a large amount of the uncertainties have been clarified up to the present.

According to Agui and Jimenez (1987), two different errors, visualization error ϵ_{vis} and sampling error ϵ_{sam}, need to be taken into account. The visualization error consists of the positioning error of the particle center points (ϵ_η) and the error associated with the traceability of particles to the fluid motion (ϵ_f). The positioning error is evaluated by

$$\epsilon_\eta = \frac{\eta}{\Delta} U_0 \tag{21}$$

with the precision for a particle position (η) and the average length of particle trajectories (Δ). Since the diameter of the visualized horizontal section is constructed by about 450 pixels on image plane, the scale of a pixel (Δ_p) corresponds to about 220 μm. The precision η is of the order Δ_p^2 owing to the present positioning with second-order accuracy. The average length of trajectories may be given by

$$\Delta = U_0 N_T \Delta t_T \tag{22}$$

Thus the length is estimated as 1.8 mm, assuming that the average tracking frame number is 4. Accordingly, the positioning error is given by

$$\epsilon_\eta = 2.7 \times 10^{-2} U_0 \tag{23}$$

The error ϵ_f is evaluated as

$$\epsilon_f^2 = 1.8 \times 10^{-2} \frac{\gamma_p}{S_0} U_0^2 \tag{24}$$

with $\gamma = (\rho_p - \rho_f)/\rho_f$, where ρ_p and ρ_f are the densities of particle and fluid respectively, and S_0 is the Stokes number given by $(\nu/\omega_0)^{1/2}/d$, where ω_0 and d are the angular frequency which may be calculated with D and U_0 and the particle diameter respectively. Although relative density γ is nearly zero, the following value is obtained for ϵ_f if assuming $\gamma = 0.03$:

$$\epsilon_f = 2.1 \times 10^{-4} U_0 \tag{25}$$

In addition, the sampling error is estimated as

$$\epsilon_{sam} = u' \left(\frac{3\eta U_0}{D u'} \right)^{(n-1)/(n+1)} = 2.5 \times 10^{-2} U_0 \tag{26}$$

where u' is the fluctuating velocity, assuming that $u'/U_0 = 0.1$ and $n = 5/3$. Consequently, the total error ϵ_T may be calculated from the summation of the squares, which yields

$$\epsilon_T = 3.7 \times 10^{-2} U_0 \tag{27}$$

5 Concluding Remarks

A PTV system has been developed to obtain instantaneous two velocity components on several sections in three-dimensional space. The flow visualization is conducted by means of parallel laser-light sheets created by a scanning laser beam and the particle images are taken by a high-speed video system synchronized with the scanning. This visualization method allows us to obtain higher spatial resolution than usual 3D PTV based on stereoscopical visualization, while the component vertical to the laser-light sheets are not derived. The unmeasured component will possibly be captured by adding another scanning system to visualize vertical planes or with the aid of some numerical procedures taking account of mass conservation.

The emphasis was also placed on the improvement of accuracy in the velocity measurements. The reformation of the procedures was conducted in the extraction of particle images, positioning of their center points, derivation of velocity components and others. Consequently, the accuracy is expected to be made higher than the usual velocity measurements by PTV. The present PTV was applied to the transient flows in a cylindrical tank with a rotating disk. As a result, two-dimensional transient flow patterns with large scale disturbances are continuously captured in three-dimensional space.

Acknowledgments

The authors are grateful to Mr. H. Karube for his contribution to the experiments.

References

Adrian, R. J., 1991, "Particle-Imaging Techniques for Experimental Fluid Mechanics," *Annual Review of Fluid Mechanics*, Vol. 23, pp. 261–304.

Agui, J., and Jimenez, J., 1987, "On the Performance of Particle Tracking," *Journal of Fluid Mechanics*, Vol. 185, pp. 447–468.

Chang, T. P., and Tatterson, G. B., 1983, "An Automated Analysis Method for Complex Three Dimensional Mean Flow Fields," *Proceedings 3rd International Symposium on Flow Visualization*, pp. 266–273.

Chang, T. P. K., Watson, A. T., and Tatterson, G. B., 1985, "Image Processing of Tracer Particle Motions as Applied to Mixing and Turbulent Flow—II. Results and Discussion," *Chemical Engineering Science*, Vol. 40, No. 2, pp. 277–285.

Chen, C. J., Chen, L. J., and Kim, Y. G., 1992, "Quantitative Flow Visualization of Three-Dimensional Flows," *Proceedings 6th International Symposium on Flow Visualization*, Springer-Verlag, pp. 3–11.

Diaconnis, P., and Efron, B., 1983, "Computer-Intensive Methods in Statistics," *Scientific American*, Vol. 248, No. 5, pp. 96–109.

Dracos, T., and Malik, N. A., 1992, "3D Particle Tracking Velocimetry—Its Possibilities and Limitations," *Proceedings 6th International Symposium on Flow Visualization*, Springer-Verlag, pp. 785–791.

Efron, B., 1979, "Computers and the Theory of Statistics: Thinking the Unthinkable," *SIAM Review*, Vol. 21, No. 4, pp. 460–480.

Efrok, B., 1983, "Estimating the Error Rate of a Prediction Rule: Improvement of Cross-Validation," *Journal of American Statistical Association*, Theory and Methods Section, Vol. 78, No. 382, pp. 316–331.

Hesselink, L., 1988, "Digital Image Processing in Flow Visualization," *Annual Review of Fluid Mechanics*, Vol. 20, pp. 421–485.

Imaichi, K., and Ohmi, K., 1983, "Numerical Processing of Flow-Visualization Pictures—Measurement of Two-Dimensional Vortex Flow," *Journal of Fluid Mechanics*, Vol. 129, pp. 283–311.

Kobayashi, T., Yoshitake, Y., Saga, T., and Segawa, S., 1985, "An Image Processing Technique for Determining Two-Dimensional Flow Fields with Reverse Flow," *Proceedings ASME Symposium on Physical and Numerical Flow Visualization*, pp. 39–46.

Nishino, K., Kasagi, N., and Hirata, M., 1989, "Three-Dimensional Particle Tracking Velocimetry Based on Automated Digital Image Processing," ASME JOURNAL OF FLUIDS ENGINEERING, Vol. 111, pp. 384–391.

Otsu, N., 1978, "Discriminant and Least Squares Threshold Selection," *Proceedings 4th International Joint Conference on Pattern Recognition*, pp. 592–596.

Racca, R. G., and Dewey, J. M., 1988, "A Method for Automatic Particle Tracking in a Three-Dimensional Flow Field," *Experimental Fluids*, Vol. 2, pp. 22.1.1–22.1.6.

Rosenfeld, A., and Kak, A. C., 1976, *Digital Picture Processing*, Academic Press, Inc.

Sata, Y., and Kasagi, N., 1992, "Improvement Toward High Measurement Resolution in Three-Dimensional Particle Tracking Velocimetry," *Proceedings 6th International Symposium on Flow Visualization*, Springer-Verlag.

Thompson, F., Thames, F. C., and Mastin, C. W., 1977, "Numerical Solution for Viscous and Potential Flow About Arbitrary Two-Dimensional Bodies Using Body-Fitted Coordinate System," *Journal of Computational Physics*, Vol. 24, pp. 245–273.

Ushijima, S., Takeda, H., and Tanaka, N., 1991, "Image Processing System for Velocity Measurements in Natural Convection Flows," *Nuclear Engineering and Design*, Vol. 132, pp. 265–276.

The Effect of Sensor Size on the Performance of Flush-Mounted Hot-Film Sensors

M. J. Moen

S. P. Schneider

School of Aeronautics and Astronautics,
Purdue University,
West Lafayette, IN

A parametric study was performed to determine the effect of sensor size on the performance of flush-mounted hot-film sensors, operated using constant-temperature anemometry. Three nickel sensors with surfaces of 12.5 × 125 microns, 25 × 250 microns, and 50 × 500 microns were deposited on glass flat-plate substrates. The frequency response and sensitivity of the sensors were measured using both electrical and flow testing. Electrical testing was performed using both sine and square waves. Flow testing was performed in a shock tube by subjecting the flush-mounted sensors to a shock-induced boundary layer. As the sensor size was decreased, frequency response increased and sensitivity decreased. These trends were observed for both electronic and flow testing conditions.

Introduction

Flush-mounted hot-film sensors are an established tool for the measurement of wall shear stress, yet the factors influencing their unsteady performance are not yet well understood (Hanratty and Campbell, 1983; Haritonidis, 1989; Diller and Telionis, 1989). It has been well accepted that the thermal properties of the substrate limit sensor operation (Alfredsson, et al., 1988; Reda, 1991). Computations have been performed assuming unsteady 2-D flow (Cole and Beck, 1988) and steady 3-D flow (Kalumuck, 1983), but no fully conjugated 3-D unsteady computations are known to us.

An experimental investigation was undertaken to aid in understanding the effect of sensor size on hot-film performance. Three nickel sensors with surfaces of 12.5 × 125 microns, 25 × 250 microns, and 50 × 500 microns (0.5 × 5 mil, 1 × 10 mil and 2 × 20 mil) were deposited on window-glass flat-plate substrates. The smaller of each sensor dimension is the length in the streamwise direction. All sensors had an aspect ratio of about 10 and were about 2800 angstroms thick, with resistances of about 4–5 ohms. The three sensors were thus identical except in size. Experiments using otherwise identical equipment should thus isolate the effect of sensor size.

Experimental Methods

For the electrical tests, a constant-temperature anemometer was connected to a function generator and the sensor. Convective currents over the sensor were minimized. An overheat was set; this was defined as the ratio between the operating resistance and the resistance at zero degrees Celsius. The anemometer was turned on and the steady-state voltage was monitored until the voltage level stabilized, in order to avoid transient heat transfer effects. Then, the square or sine wave test was initiated. A Gould DSO-400 8-bit oscilloscope was used to digitize a 500 point record at 500 kHz for each event. The record was analyzed on-screen or transferred to a computer. Two different constant-temperature anemometers were used (a custom-built anemometer called AC-2 and a TSI IFA-100). The figure captions include the anemometer used to obtain the data. The trends obtained with the two anemometers were in all cases the same, for all reasonable adjustments of the tuning capabilities, and for both electrical and flow tests.

Flow step tests were performed in a shock tube, using an experimental setup similar to that of Davies and Bernstein (1969). The sensor substrates were small flat plates with leading edges beveled at 30 degrees. All substrates were 51 mm (2 in.) long in the streamwise direction, 44.5 mm (1.75 in.) long in the spanwise direction and 3.18 mm (0.125 in.) thick. The sensor was located at mid-span 19.0 mm (0.75 in.) downstream of the leading edge. Each substrate was mounted on a 152 mm (6 in.) arm that extended upstream from the end of the shock-tube driven section. The beveled leading edges faced upstream toward the impinging shocks. As the normal shock passed over the plate, a shock-induced boundary layer developed. Since weak shocks were used, the flow behind the shock was in all cases subsonic. Because this unsteady flow was simple, well-characterized, and easy to set up, it was chosen as a basis for testing the sensor response.

The shock tube driver-section and driven-section pressures were recorded to determine the shock conditions. In addition, two high-speed pressure transducers on the driven section wall were used to measure the shock velocity. Using either the pressure-ratio data or the shock-speed data, the temperature and velocity of the flow behind the shock could be deduced. The two measurement methods gave consistent results to within one percent for nearly every run. The output voltage from the constant-temperature anemometer was again allowed to reach

Contributed by the Fluids Engineering Division for publication in the JOURNAL OF FLUIDS ENGINEERING. Manuscript received by the Fluids Engineering Division February 19, 1993; revised manuscript received August 17, 1993. Associate Technical Editor: W. S. Saric.

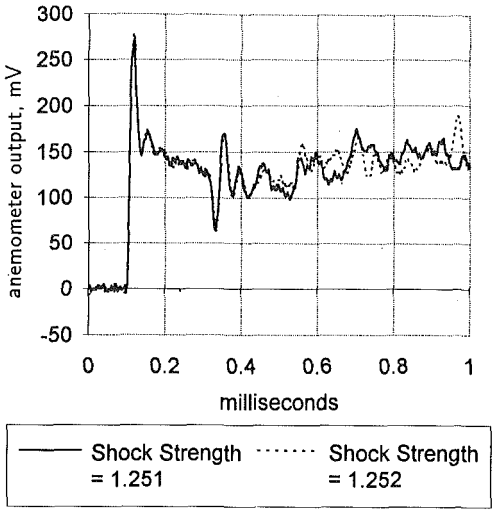

Fig. 1 Repeatability of anemometer response to shock passage, AC-2

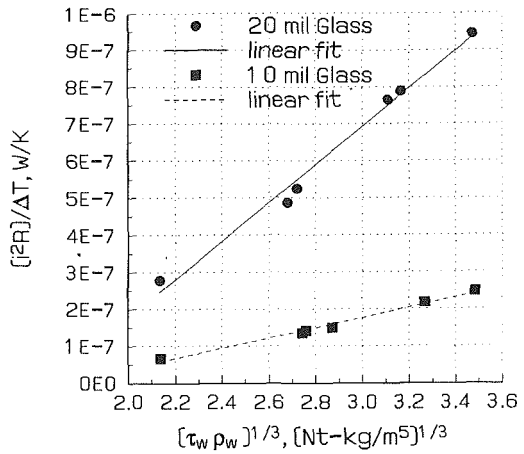

Fig. 2 Shear calibration, OHR = 1.4, IFA. Estimated accuracy for $i^2R/\Delta T$ is ±4 percent, for $(\tau_w \rho_w)^{1/3}$, ±4 percent

steady state before each run. The shock response was captured on the digital oscilloscope and transferred to a computer. Further details are reported in Moen and Schneider (1993). Uncertainty analyses were performed using the techniques described in Kline and McClintock (1953), and are reported in the text with the description of each figure. Trends were of primary interest; these trends were consistently observed in all the repeated and nearly-repeated trials.

Characterization of Test Flow

The repeatability of the anemometer shock-response was particularly important, since the shock strength was to be held constant for various runs during which the sensor model was varied. Figure 1 shows the results for two similar strength shocks. The response is nearly identical for the two shocks except after 0.4 ms, where the boundary layer is probably turbulent. At about 0.3 milliseconds, the signal fluctuates suddenly. This was due to a geometric step that existed in the juncture between the sensor plate and the mount, since data with an improved mount showed a reduced fluctuation. The fluctuation does not affect the results for the sensitivity or frequency response, which were obtained from the data for the first 0.2 ms after the shock arrival.

It was also desirable to compare our measurements to those of previous workers, to ensure the quality of the flow. Davies and Bernstein (1969) discuss the theoretical solution for the quasi-steady boundary layer behind a shock advancing into a stationary fluid, due to Mirels (1955). They show that this solution applies after the shock passage, for values of $x/(u_2 t) \geq 1$, where x is the distance from the leading edge of the plate, t is the time from the arrival of the shock at the leading edge, and u_2 is the velocity behind the shock. This is because all particles flowing in this region originate "on the plate," and have no knowledge of the plate leading edge. Conditions for the results presented here satisfy this criteria, since they were obtained using weak shocks or using only the small-time portion of the record. Mirels' theoretical expression for the laminar skin friction should therefore be applicable.

Hanratty and Campbell (1983) show that the output of a constant-temperature hot-film sensor operating in steady flow should correlate with the wall shear according to

$$\frac{i^2R}{\Delta T} = c_0(\rho_w \tau_w)^{1/3} + c_1, \tag{1}$$

where i is the sensor current, R is the sensor resistance, ΔT is the difference between the film and ambient temperatures, τ_w is the wall shear stress, ρ_w is the fluid density near the sensor, and c_0 and c_1 are proportionality constants determined experimentally. This relation is commonly used to calibrate flush-mount wall shear sensors, although the points are usually determined from steady-state values (Brown, 1967). Here, this relation was applied in a quasi-steady way, using Mirel's theory for the wall shear values. The calibration points were determined using the relatively flat area of the sensor response, approximately 0.1 milliseconds after the beginning of the response transient. Since the signal/noise ratio was limited, an 0.10 millisecond region containing 50 points was averaged to reduce the signal noise. The results are plotted in Fig. 2. The quality of the correlation suggests that the boundary layer is developing approximately in the manner described by Mirels' solution, and that the anemometer is responding normally. It remains to be determined whether this calibration is accurate

Nomenclature

A = anemometer response voltage
A_e = sensor area
AC-2 = data obtained using custom-built AC-2 anemometer
c_0, c_1, c_2 = empirical constants
i = sensor current
IFA = data obtained using TSI IFA anemometer
L = streamwise length of sensor
OHR = overheat ratio, R_{op}/R_{cold}
P = power dissipated in sensor by anemometer
P_{ref} = static power dissipation in stagnant air
P_s = total power dissipated in shock-response
P^* = non-dimensional unsteady portion of P_s, see Eq. (2)
R_{cold} = sensor resistance at zero degrees Celsius
R_{op} = sensor resistance at operating temperature
t = time from the arrival of the shock at the leading edge of the plate
T_{op} = sensor operating temperature
T_a = ambient temperature
T_2 = temperature of the air behind the shock
u_2 = velocity behind the shock
x = distance from the leading edge of the plate
ΔT = $T_{op} - T_a$
ρ_w = fluid density at the wall
τ_w = wall-shear stress

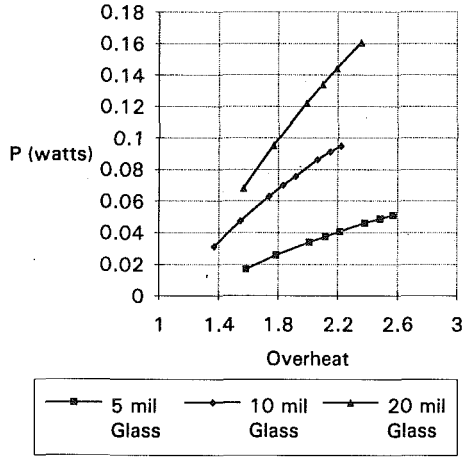

Fig. 3 Static power dissipation for various sensor sizes, AC-2. Estimated accuracy for P is ±4 percent, for overheat, ±2 percent.

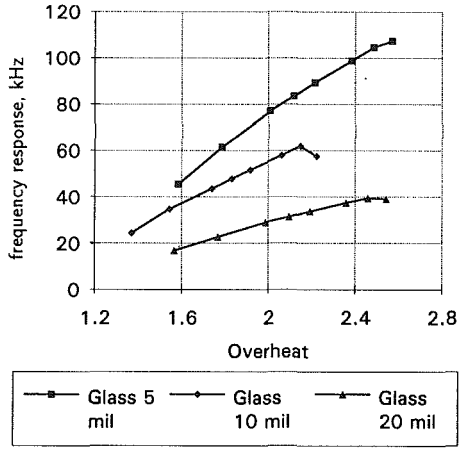

Fig. 5 Frequency response in square wave tests, AC-2. Estimated accuracy for frequency response is ±5 percent, for overheat, ±2 percent.

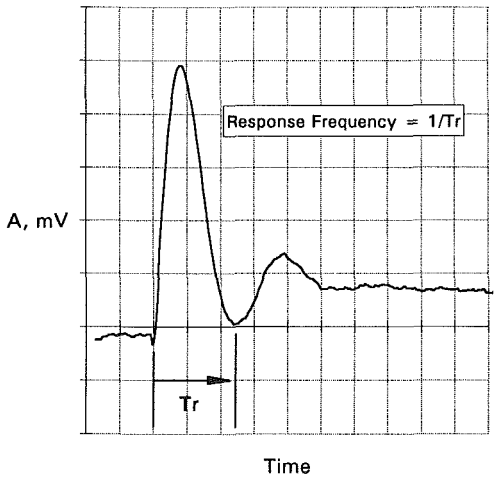

Fig. 4 Definition of frequency response used in square wave testing

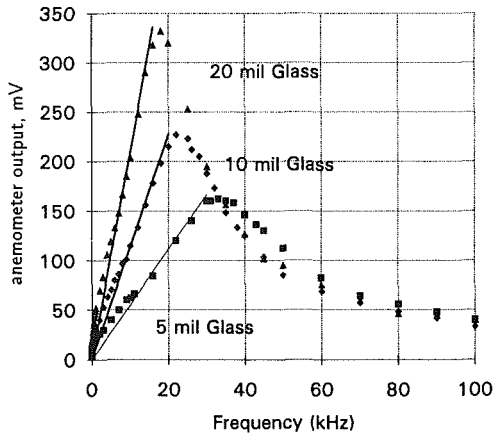

Fig. 6 Sine wave response against frequency, OHR = 1.4, AC-2. Estimated accuracy of anemometer output, ±3 percent, for frequency, ±1 percent.

in a time-resolved sense. The figure will be discussed further in connection with the other flow-testing results.

Results of Electrical Testing

Electrical testing was performed by perturbing the electronics with the sensor positioned in stagnant air.

Static Power Dissipation. Static power dissipation was determined using the sensor resistance and current. The sensor current is calculated using the output voltage and the sensor, cable, and bridge resistances. Figure 3 compares the static power dissipation for the 125, 250 and 500 micron glass-substrate sensors for a range of overheats. Dissipation increases with sensor size and overheat, as expected. Since only one pair of sensors was available, and only one of each pair was tested extensively, the effect of sensor variability is unknown. The three sensor sizes were varied by factors of 2 with the expectation that the variations among the sizes would be dominant. This was also the expectation of the sensor fabrication group at NASA Langley. These results also apply to the flow tests, since the pre-perturbation condition was the same.

Square Wave Tests. The square wave test is commonly used to determine frequency response, which can be defined in a number of ways. For example, Freymuth (1977) defines the frequency response using the point at which the output signal returns to 3 percent of the response maxima. For the present work, the response cut-off frequency was determined from the experimental curve as shown in Fig. 4. Here, A is the response voltage read from the anemometer. This definition was used consistently, and was chosen partly because it remained well-defined for both flow and electrical testing, and partly because it was insensitive to noise. The voltage at the end of the time pictured has not returned to the beginning level due to the higher-order behavior observed in the system. The voltage did return before the beginning of the next square wave, however.

The 125, 250, and 500 micron glass-substrate sensors were first tested for frequency response over a range of overheats. Figure 5 shows how the frequency response increases with increasing overheat for all three sensors. Frequency response increases with decreasing sensor size at all overheats. The curve slopes also increase with decreasing sensor size. For all three sensors, there appears to be a maximum obtainable frequency response. For the 125 and 500 micron sensor sizes, the curve levels out at an overheat of approximately 2.5. Film degradation is probably the cause of this limitation, for it was observed at this same overheat in earlier microscopic evaluations by Bartlett.

The same trends in frequency response were observed using both anemometers and for various adjustments of tuning parameters. In general, the frequency response was about 20 percent higher for any given overheat when using the IFA-100 rather than the AC-2. This may be attributed to the difference in bridge designs as well as the response tuning functions available on the IFA-100.

Sine Wave Tests. The sine wave test was administered to

Table 1 Sensor sizes compared to nominal time constants

Sensor dimension	Relative dimensions	Slope (from Fig. 6)	Slope ratio
12.5 × 125 microns	1	0.0056	1
25 × 250 microns	2	0.0114	2.04
50 × 500 microns	4	0.0210	3.77

the anemometer after it had been optimized using square wave testing. A constant amplitude sine wave was applied for various frequencies, for the 125, 250, and 500 micron glass-substrate sensors. Figure 6 shows the results. The figure shows that the response of the larger sensors rolls off at a lower frequency but with a larger peak amplitude. This suggests, in agreement with the other data, that the larger sensors have lower frequency response and higher sensitivity. However, the relation between the figure and any clear definition of frequency response or sensitivity remains unknown. The trends were independent of anemometer settings.

Freymuth (1977) defines a time constant that is linearly proportional to the slope of this amplitude-frequency curve at low frequencies. Although Freymuth's theory was developed for a hot wire this portion was applied to the hot film, by least-squares fitting the low-frequency data in Fig. 6 to determine the slope. The resulting slopes relate linearly to the dimension of the sensor as seen in Table 1. This suggests that the frequency response of such sensors is inversely proportional to their size, a result that was qualitatively confirmed in the shock-tube tests.

Results of Shock-Tube Testing

Experimental flow-step testing was also performed to compare the effects of sensor dimension for perturbations more nearly similar to those encountered in applications. The frequency response was again obtained by taking the inverse of the characteristic time, which was again defined as the time from when the anemometer first began to respond until the minimum point of the first signal overshoot.

The effect of sensor dimension in flow testing was identical to that observed during electrical testing. The consistency between the two very different tests was initially surprising. Figure 7 shows the frequency response of the 125, 250, and 500 micron glass-substrate sensors as they adjust to similar shock waves (flow steps) at different overheats. Again, the smaller sensors respond fastest, and their response curves also have higher slope. Even the numerical values are similar. Extrapolation suggests that fast frequency responses are possible for small sensors at high overheats.

To analyze the flow sensitivity, the 250 and 500 micron glass-substrate sensors were set at nearly identical overheats and a series of weak shock waves (flow steps) were passes over each sensor. The 125 micron sensor failed before flow-sensitivity data could be obtained. Two definitions of sensitivity are used to analyze the data. The first definition uses the peak of the overshoot amplitude, which was recorded for each flow step. This peak was converted into a nondimensional unsteady power dissipation defined as

$$P^* = \frac{P_s - P_{\text{ref}}}{P_{\text{ref}}}, \tag{2}$$

where P_{ref} is the static power dissipation, and P_s is the total power dissipation. The nondimensional unsteady power dissipation was then plotted against the freestream velocity behind the applied step, u_2, and fit with a power series curve. By representing this data as the differential power dissipation normalized to the reference power dissipation, a clear relationship can be drawn for the relative amount of power dissipated to the flow by each sensor in response to the step. The more power that is dissipated to the flow for a given flow step, the more sensitive a sensor is. This choice of a definition for sensitivity is simple, and relates the sensitivity directly to the

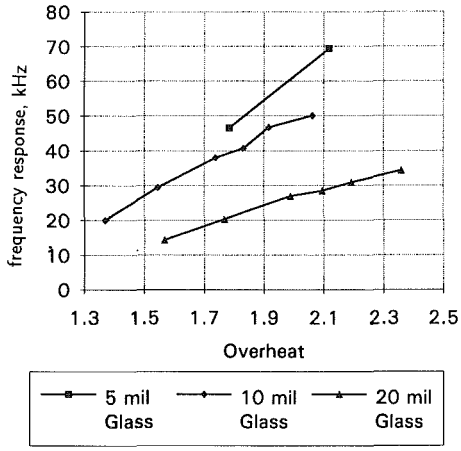

Fig. 7 Frequency response in flow tests, AC-2. Estimated accuracy for frequency response, ±5 percent, for overheat, ±2 percent.

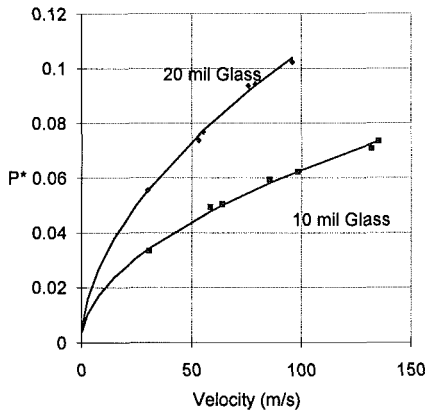

Fig. 8 Sensitivity in flow tests, OHR = 1.4, IFA. Estimated accuracy for P^* is ±2 percent, for velocity ±3 percent.

measureable quantity, the power fluctuations on the anemometer output. Figure 8 shows that the larger sensor has superior sensitivity. Again, not only are the values larger for the larger sensor, but the slopes are also larger. The inaccuracies in the velocity are principally due to boundary layer effects.

A second definition of flow sensitivity can be made using Eq. (1). Since a larger value of c_0 results in larger signals for a given wall-shear, the amplitude of c_0 can be called the sensitivity. Figure 2 shows the result of plotting the data in this form. Again, since the data for the larger sensor has a larger slope, the larger sensor is more sensitive. This results is in qualitative agreement with a theoretical expression given on page 588 of Hanratty and Campbell (1983),

$$c_0 = (c_2 A_e)/L^{1/3}, \tag{3}$$

where c_2 represents quantities not dependent on the sensor size, A_e is the surface area of the sensor, and L is the streamwise length of the sensor. Since the aspect ratio is the same for all sensors, the sensitivity should be directly proportional to $L^{5/3}$, or $A_e^{5/6}$. Thus, the theory given in Hanratty and Campbell (1983) appears to be in qualitative agreement with the results presented here.

The uncertainty in Fig. 2 must be given special attention. The values plotted on both axes are inferred indirectly from a combination of theory and measurement. Mirel's theory makes several assumptions whose accuracy is difficult to assess. We estimate, however, that the accuracy of $(\tau_w \rho_w)^{1/3}$ is of the order of a few percent. The computation of $I^2R/\Delta T$ is, however, more problematic. The principal difficulty is ΔT, which is normally the difference between the sensor temperature and the ambient

temperature. Here, the wall probably remains primarily at constant ambient temperature, T_a, during the short-duration run, but the temperature of the air behind the shock is higher, $T_2 > T_a$. Thus the wall and the air are not in equilibrium, as assumed in the derivation of equation 1, so the theoretical applicability of the calibration technique is limited. In fact, the curve given is obtained using $\Delta T = T_{op} - T_a$; if it is instead plotted using $\Delta T_2 = T_{op} - T_2$ the data show a pronounced nonlinearity. However, this ΔT_2 is highly uncertain, since it forms a small difference between two large and uncertain numbers, due in part to the limited accuracy of the experimental $R(T)$ data. The ΔT data plotted is probably accurate to within a few percent. No matter how the data was processed, the larger sensor clearly yielded a curve with a larger slope and higher values indicating that the larger sensor clearly had higher sensitivity.

Discussion of Results

The sensor-size effects observed are not surprising. A reduction in sensor size reduces the heated area of the plate, and thus the thermal capacity of the system. In the electrical tests, a fixed step in voltage corresponds to the injection of a fixed amount of heat, which can raise the temperature faster, due to the smaller thermal capacity. Since the smaller sensors are also able to respond faster to changes in the flow conditions, the thermal capacity must decrease faster than the surface area with reductions in size. This is not surprising, since the thermal capacity would be expected to scale with the cube of a typical sensor dimension. The reduction in flow-sensitivity with decreasing sensor size seems to be caused by the smaller area that is able to respond to perturbations in the flow, in agreement with existing theory (Hanratty and Campbell, 1983). A given change in the heat transfer rate between the surface and the fluid, measured in watts/m^2, causes a smaller change in the power draw from the anemometer, measured in watts. Sensors smaller than those used here should have even faster frequency response; fabrication of smaller sensors should be fairly straightforward, if the substrate surface is sufficiently smooth. It seems unlikely that the frequency response can increase indefinitely as the sensor size is reduced, but the practical limitations on the observed trends are as yet unknown.

The dynamic response of the hot-films involves responses to small-amplitude perturbations imposed on a steady mean condition; the qualities of the dynamic response may well depend on this pre-perturbation state. It is important to note that in all the measurements obtained here, the pre-perturbation condition involved stagnant fluid above the sensor; pre-perturbation heat transfer to the fluid was limited to free convection. The dependence of the results on this pre-perturbation condition remains to be determined. For example, the Reynolds number of the steady flow that exists prior to the perturbation is likely to affect the results in a significant manner. Studies of this effect are planned.

Conclusions

The performance of flush-mounted hot-film sensors has been studied by systematically varying sensor dimension. The experimental results for the three glass-substrate sensors show that frequency response increases with decreasing sensor size, while sensitivity decreases. Changes in sensor size thus involve a tradeoff between the sensitivity and frequency response, so that a high frequency-response sensor has poor sensitivity and vice versa. These results were consistent for both electronic and flow tests, the latter performed using the response to the shock-induced boundary layer set up on a small flat plate in a shock tube. The results suggest that it may be possible to obtain a useful system with high frequency-response using small sensors and low-noise electronics.

Acknowledgment

This work was supported in part by NASA Langley's Instrument Research Division under grant NAG-1-1201. The sensors were fabricated by Mr. J. Bartlett's group at NASA Langley, and technical support was lent by Mr. Michael Scott of the Instrument Research Division. Dr. Daniel Reda of NASA Ames provided helpful comments on an earlier version of the paper. The referees also provided helpful comments.

References

Alfredsson, P., Johansson, A., Haritonidis, J., and Eckelmann, H., 1988, "The Fluctuating Wall-Shear Stress and the Velocity Field in the Viscous Sublayer," *Physics of Fluids*, Vol. 31, pp. 1026–1033.

Brown, G. L., 1967, "Theory and Application of Heated Films for Skin Friction Measurement," *Proceedings of the 1967 Heat Transfer and Fluid Mechanics Institute*, Stanford Press, pp. 362–381.

Cole, K., and Beck, J., 1988, "Conjugated Heat Transfer from a Hot-Film Probe for Transient Airflow," ASME *Journal of Heat Transfer*, Vol. 110, pp. 290–296.

Davies, W., and Bernstein, L., 1969, "Heat Transfer and Transition to Turbulence in the Shock-Induced Boundary Layer on a Semi-Infinite Flat Plate," *Journal of Fluid Mechanics*, Vol. 36, pp. 87–113.

Diller, T., and Telionis, D., 1989, "Time-Resolved Heat Transfer and Skin Friction Measurements in Unsteady Flow," *Advances in Fluid Mechanics Measurements*, M. Gad-el-Hak, ed., Springer-Verlag, New York.

Freymuth, P., 1977, "Frequency Response and Electronic Testing for Constant-Temperature Hot-Wire Anemometers," *Journal of Physics E*, Vol. 10, pp. 705–709.

Hanratty, T., and Campbell, J., 1983, "Measurement of Wall Shear Stress," *Fluid Mechanics Measurements*, R. J. Goldstein, ed., Hemisphere Publishing, New York.

Haritonidis, J. H., 1989, "The Measurement of Wall Shear Stress," *Advances in Fluid Mechanics Measurements*, M. Gad-el-Hak, ed., Springer-Verlag, New York.

Kalumuck, K., 1983, "A Theory for the Performance of Hot-Film Shear Stress Probes, PhD thesis, M.I.T. Department of Aerospace Engineering.

Kline, S. J., and McClintock, F. A., 1953, "Describing Uncertainties in Single-Sample Experiments," *Mechanical Engineering*, Vol. 75, pp. 3–8.

Mirels, H., 1955, "Laminar Boundary Layer Behind Shock Advancing into Stationary Fluid," TN 3401, NACA.

Moen, M., and Schneider, S., 1993, "The Effect of Sensor Size and Substrate Properties on the Performance of Flush-Mounted Hot-Film Sensors," *Thermal Anemometry 1993, Proceedings of the Third ASME International Symposium on Thermal Anemometry*, American Society of Mechanical Engineers, FED Vol. 167, pp. 249–261.

Reda, D., 1991, "Rise-Time Response of Nickel-Foil-on-Kapton-Substrate, Hot-Film, Shear-Stress Sensors," AIAA Paper 91-0169, AIAA.

Michihisa Tsutahara
Professor.

Takeyoshi Kimura
Professor.

The Graduate School
of Science and Technology,
Kobe University,
Nada, Rokko, Kobe 657 Japan

Kideok Ro
Associate Professor,
National Fishers Junior College
of Tongyeong,
445 Inpyung-Dong, Chungmu,
Kyungnam 650-160 Republic of Korea

Ship's Propulsion Mechanism of Two-Stage "Weis-Fogh" Type

The dynamic properties of a ship's two-stage "Weis-Fogh" type propulsion mechanism are experimentally and numerically investigated. In order to study the effects of the interaction of the two wings, the wings are designed in a manner that enable them to move close to each other. The opening angle and the moving speed are the same for both wings. Two cases of the phase differences of the wings' motions are considered, the in-phase case and the out-of-phase case. The differences of the dynamic properties between the two wings are shown and the properties of this propulsion mechanism are discussed.

Introduction

The Weis-Fogh mechanism has been known as a novel and efficient mechanism of lift generation (Weis-Fogh, 1973 and Lighthill, 1973). This mechanism, which was first observed on the hovering flight of the Encarsia Formosa insect, indicates that when the insect's wings open, after touching their trailing edges, circulations are formed very quickly around each wing without shedding any vortices. Consequently, lift is generated very efficiently. The Weis-Fogh mechanism may be defined as the quick generating mechanism of circulations by the interaction of two wings, which results in effective lift generation. The Reynolds number for the insect's flight is around 30. However, this mechanism utilizes the inertia force, and thus it is more efficient for high Reynolds number flows. Efficiency is greater in the water than in the air.

Tsutahara and Kimura (1987) in a previous study, have proposed a ship's propulsion mechanism using the Weis-Fogh mechanism and have shown that this new propulsion equipment has a good potential for practical applications. In this paper, we propose an extension in which two units of the previously reported propulsion mechanism are mounted in a square channel and the dynamic properties are investigated by experiments and numerical analysis. The model of this propulsion mechanism is shown as in Fig. 1. The wings are set as shown in the figure, and the motion of each is as follows: A point p reciprocates in the channel along the dashed line. The wing with the trailing edge touching the side wall rotates (or opens up) to an angle α, the wing then translates keeping α constant, and then once the leading edge touches the other wall the wing rotates or closes.

It is obvious that the advantage of the two-stage type will be of importance in actual applications, and therefore, in this study, we will investigate the effects that will take place through the interaction of the two wings. In order to better understand the interaction between the wing, the distance between the two was decreased.

Furber and Ffowcs Williams (1979) reported that the properties of an axial pump were improved by making the clearance narrower between the rotor blades and the stator blades. The pump's improvement is due to the Weis-Fogh effect; this is based on the fact that sufficient circulations are formed when two blades pass each other. The qualitative analysis was based on the assumption that the circulation of each wing remains constant after their interaction. However, when two wings with opposite circulations interact, their circulations may be canceled and the magnitude of circulation about each wing may decrease.

Our results, especially our numerical analysis, indicate that it is doubtful that this type of the Weis-Fogh effect takes place. Therefore, it is recommended that the term, the Weis-Fogh mechanism, should indicate the mechanism of generating the circulations just when the wings start to move. In our case, that mechanism works when the wings are open with their trailing edges touching the side wall.

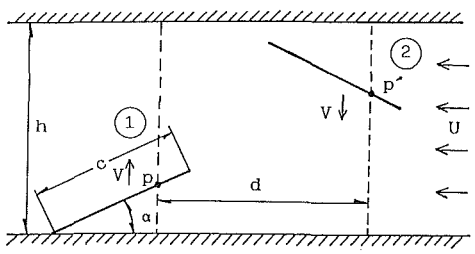

Fig. 1 Model of the propulsion mechanism

Contributed by the Fluids Engineering Division for publication in the JOURNAL OF FLUIDS ENGINEERING. Manuscript received by the Fluids Engineering Division January 3, 1989; revised manuscript received January 10, 1994. Associate Technical Editor: D. P. Telionis.

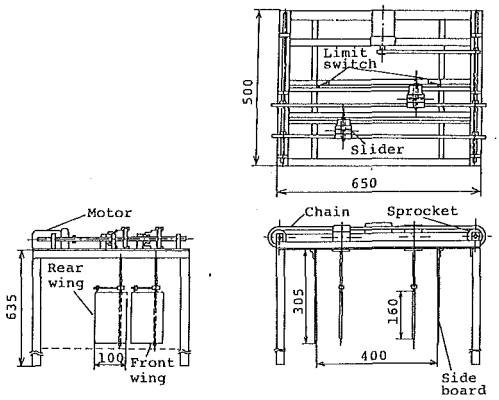

Fig. 2 Driving unit of the wings

Experimental Study

Apparatus and Method. A circulation tank is used in the experiments. A driving unit of the wings shown in Fig. 2 is mounted on the frame of the channel so that the wings can move in the flow. The sliders in the unit move reciprocally in the direction perpendicular to the flow by changing the direction of the current supplied to a DC motor. The movements of the two sliders are synchronized by a common rotating shaft. The phase difference between the motions of two wings can be chosen as the in-phase (or the phase difference 0 deg) and the out-of-phase (or the phase difference 180 deg). In the in-phase the two wings start to move from the same side of the channel and in the out-of phase they start to move from the opposite sides toward each other. The wings are pitched about their quarter-chord (Fig. 3).

In order to obtain some information on the flow field about the wings, the flow is visualized by the hydrogen bubble method. Hydrogen bubbles are continuously and also intermittently generated to obtain, respectively, the streamlines and timelines.

The balances are mounted on the rod, between the slider and the wing, to facilitate measurement of thrust and drag. The data are handled with a 16 bit personal computer (NEC 9801) through an AD converter. The definition of the thrust T and the drag D are given in Tsutahara and Kimura (1987), that is, the thrust is defined as the component of the force on the wing in the positive x-direction, and the drag as the y-component of the force in the direction opposite to the moving direction of the wing. This definition is the same as that in Tsutahara and Kimura (1987). The drag on the ship hull is not considered. The term "resistance" may be more suitable for the force referred to as "drag" here; but we shall once more use drag in this paper for the convenience of comparing the results with those in Tsutahara and Kimura (1987).

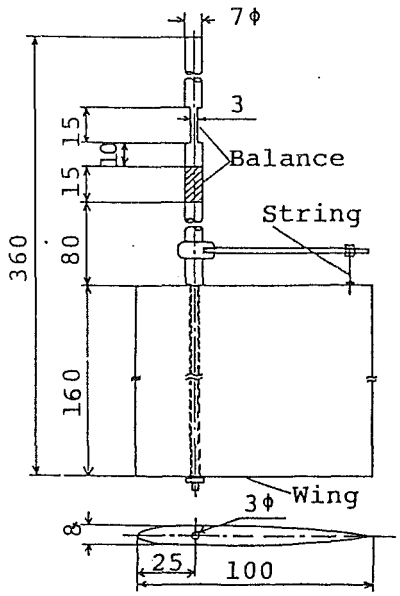

Fig. 3 Structure of the wing and balance

Two side boards 0.4 m apart from each other are equipped as in Tsutahara and Kimura (1987). The Weis-Fogh effect takes place between the wing and the wall or equivalently between the wing and its image with respect to the wall.

The conditions of the experiments are as follows. The distance d between the pitching axes of the two wings is taken to be 0.11 m. The opening angle is chosen every 5 deg, from 10 to 45 deg. The speed U of the water flow is varied from 0.16 to 0.31 m/s, and the speed V of the translation of the wings varies from 0.12 to 0.36 m/s.

Flow Patterns. We shall first present some examples of flow patterns obtained by the flow visualization, since it is helpful for understanding the whole flow.

Figure 4 shows the timelines and the streaklines when the wings are at standstill. The flow is quasi-steady and the separations occur at the leading edges of the wings. Figure 4 is shown for the sake of comparison with the results for moving wings, Figure 5 through 7, which are shown together with the numerical simulations, are described later in detail. In Figs. 5 to 7: $\alpha = 30$ deg, $V/U = 1$, $d = 1.15\ c$, and $h = 2.5\ c$.

Figure 5 shows the streaklines for the in-phase case obtained by the experimental and the numerical flow visualizations. The wings are translating in the direction of the arrows. There is no separation at the leading edges of the wings. This flow should be compared with that of the nonmoving wings shown

Nomenclature

p, p' = reference points
c = chord length of wing
h = width of channel
d = distance between two wings or points p and p'
T, D = thrust and drag
C_T, C_D = thrust coefficient and drag coefficient
$\overline{C_T}, \overline{C_D}$ = time averaged thrust coefficient and drag coefficient
ρ = density of water
S = area of wing
α = maximum opening angle
V = moving velocity of wing
U = flow velocity
η = propulsive efficiency
T_c = period of one cycle of wing motion
F = complex potential
κ_j = strengths of jth bound vortex in front wing
M = number of bound vortices
$\tilde{\kappa}_j$ = strengths of jth free vortex
N, N' = numbers of free vortices
z_j = position of jth vortex
ψ = stream function
Γ = circulation about wing
X, Y = forces
Δt = time increment for numerical calculation
Δr = distance between two bound vortices
M_p = moment about point p

Symbols

$'$ = values for rear wing
$-$ = complex conjugate
$\oint_B dz$ = integration along contour of wing surface

Subscripts

t = trailing edge
p = point p

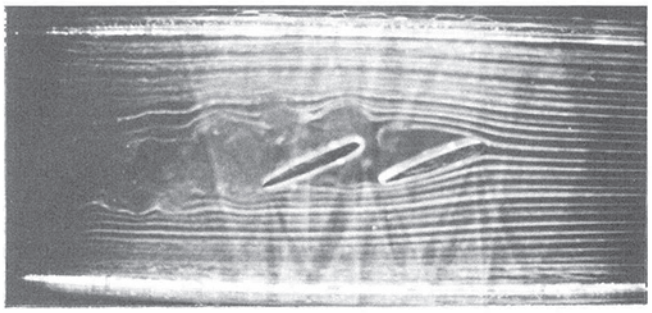

(a)

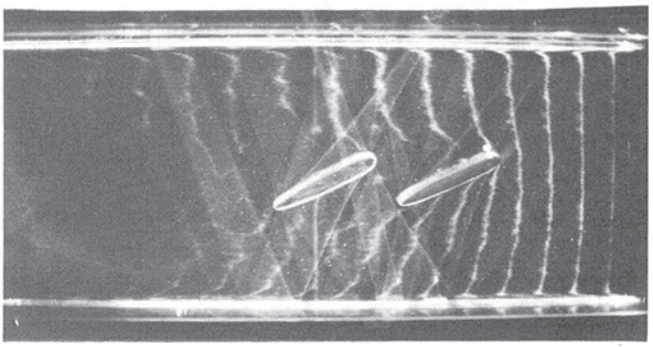

(b)

Fig. 4 Streamlines and timelines for stationary wings

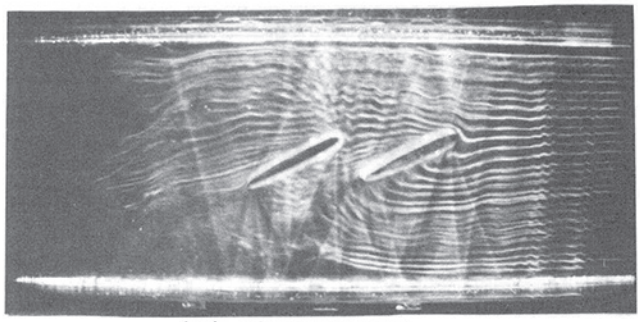

(a) Photograph

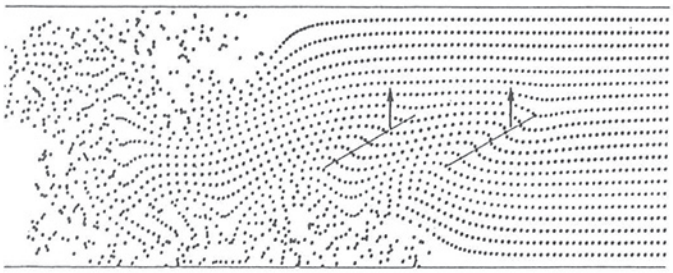

(b) Streak lines

Fig. 5 Streaklines for the in phase when the wings are translating

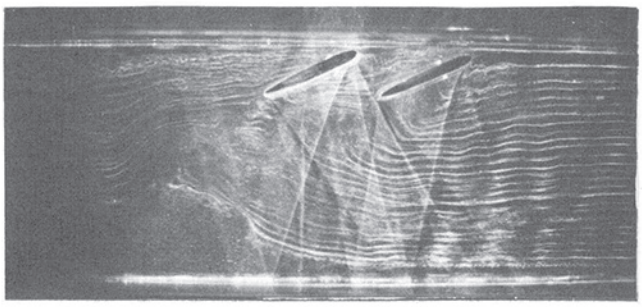

(a) Photograph

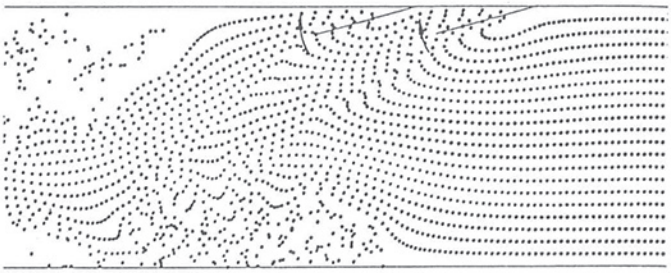

(b) Streak lines

Fig. 6 Streaklines for the in phase when the wings are closing

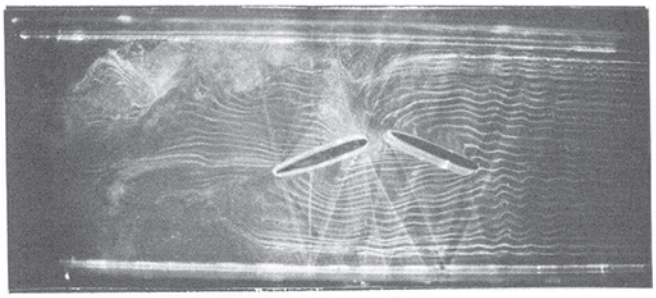

(a) Photograph

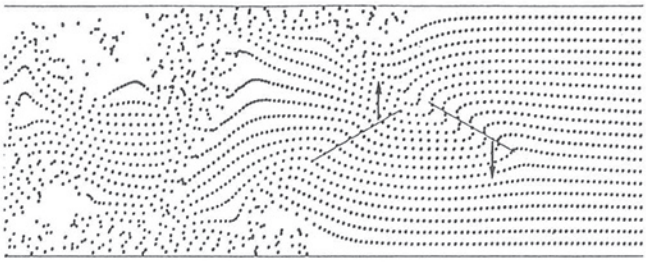

(b) Streak lines

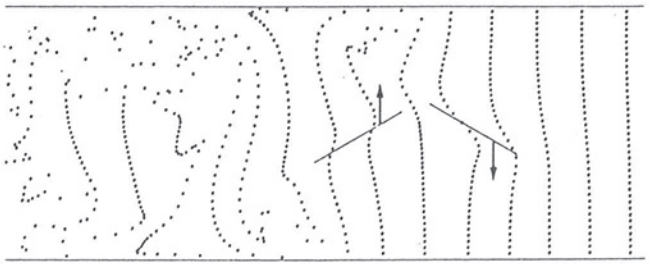

(c) Time lines

Fig. 7 Streaklines for the out of phase when the wings are translating

in Fig. 4. The streaklines when the wings are closing are presented in Fig. 6. Downstream of the wings, there are large clusters of vortices alternately near the upper wall and the lower wall, which are produced when the wings close and the flow is meandering between them. The wake from the each wing is also detectable.

For the out-of-phase case, Fig. 7 shows the streaklines when the wings pass each other. Figure 8 shows the streaklines and the timelines through the one stroke by the numerical simulation. In this case the meandering of the flow is not large, so the fluid is flowing near the center of the channel, and the clusters of vortices exist rather symmetrically with respect to the centerline.

Time Variation of the Thrust and the Drag. The thrust and the drag coefficients are defined, respectively, as

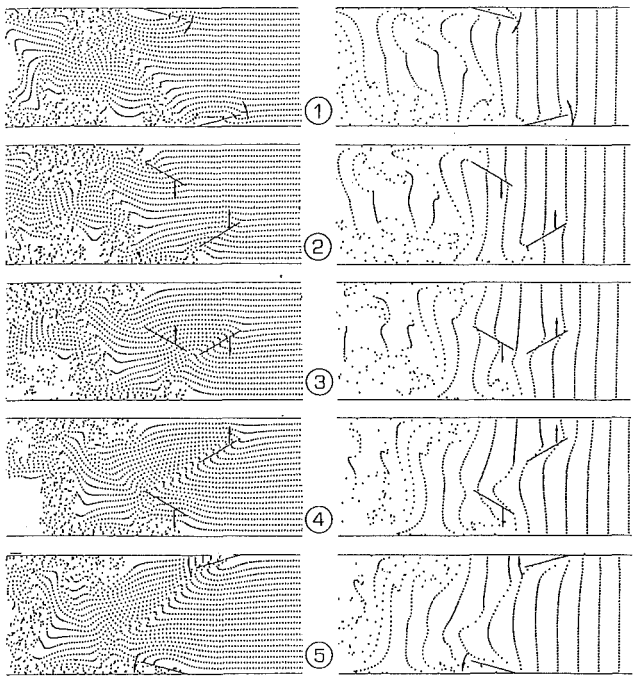

(a) Streak lines (b) Time lines

Fig. 8 Streaklines and timelines for the out of phase through one stroke

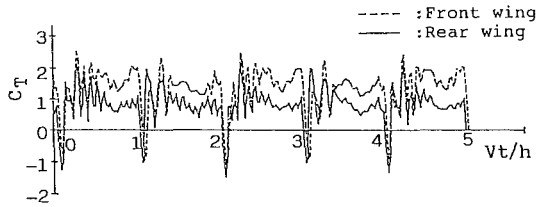

(a) Thrust coefficient

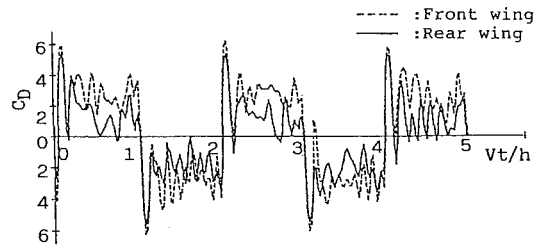

(b) Drag coefficient

Fig. 9 Thrust and drag coefficients for the in phase

$$C_T=\frac{T}{1/2\rho V^2 S},\quad C_D=\frac{D}{1/2\rho V^2 S}, \tag{1}$$

where ρ is the density of the water and S is the area of the wing. An example of the time variation of the thrust coefficient and the drag coefficient for the in-phase and the out-of-phase are shown in Fig. 9 and in Fig. 10, respectively. The opening angle α, and the ratio of the wing's moving velocity V to the flow velocity U, V/U, were given the values 30 deg and 1, respectively.

In Figs. 9 and 10, the dashed lines represent the values of the front wing and the solid lines represent those of the rear wing on the leeside. At the opening stage the thrust becomes negative. The same happens for the single stage type (Tsutahara and Kimura, 1987). This fact is also confirmed by the numerical analysis presented later.

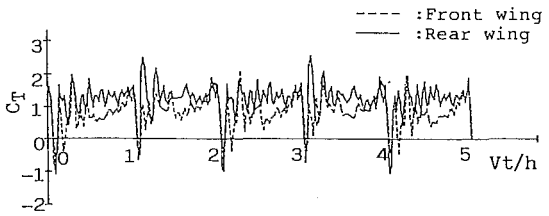

(a) Thrust coefficient

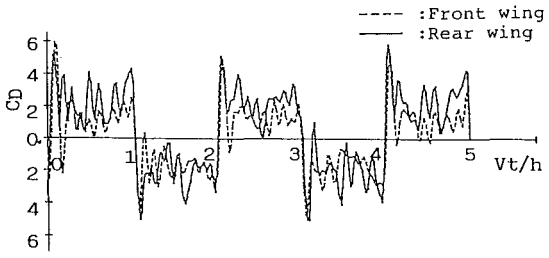

(b) Drag coefficient

Fig. 10 Thrust and drag coefficients for the out of phase

In the case of the mode of operation in-phase, the thrust and the drag on the front wing are larger than those of the rear wing for almost the entire duration. In the case of the out-of-phase mode, on the other hand, a striking phenomenon is observed. The thrust on the front wing decreases but increases on the rear wing when the two wings interact at the center of the channel. The same is true for the drag coefficient, although the difference between the characteristics of the two wings is not as clear as those of the thrust.

The measurement error was evaluated to be less than 25 percent, and the qualitative results, as described above, are true for all the trials.

Averaged Forces. The time average of the thrust and the drag coefficients over five cycles versus velocity ratio V/U are presented in Fig. 11 and Fig. 12 for the cases of in-phase mode and out-of-phase mode, respectively. In Fig. 11, both the thrust and the drag for the in-phase mode are larger on the front wing than on the rear, and the difference is clear. In Fig. 12, however, both are larger on the rear wing, although the difference is smaller. In both of these figures the opening angle of the wings is 15 deg and the trend is the same for other opening angles. These averaged forces have rather constant values versus V/U by nondimensionalizing them with the moving speed of the wing V. In the previous paper by Tsutahara and Kimura (1987), the definition of the thrust and the drag coefficients was incorrect since these quantities were not divided by V^2 and by U^2. The curves for those coefficients divided by U^2 versus V/U were similar to quadratic curves. So that, for the purpose of comparison in the thrust and the drag between the two wings, nondimensionalizing the V^2 will be more suitable.

Efficiency. The propulsive efficiency is defined as

$$\eta=\int_0^{T_c} C_T U\,dt \Big/ \int_0^{T_c} C_D V\,dt, \tag{2}$$

where T_c is the period of one cycle of the wing motion. In Figs. 13 and 14 the propulsive efficiency versus V/U for the three cases of the opening angles are shown. For the in-phase mode shown in Fig. 13, the front wing has a higher efficiency than the rear wing and the difference is as clear as in the thrust and the drag coefficients. However, for the out-of-phase mode (Fig. 14), the two wings have almost the same values. In all the cases, especially when the opening angle is small, the highest efficiency takes place when the ratio V/U less than unity, which

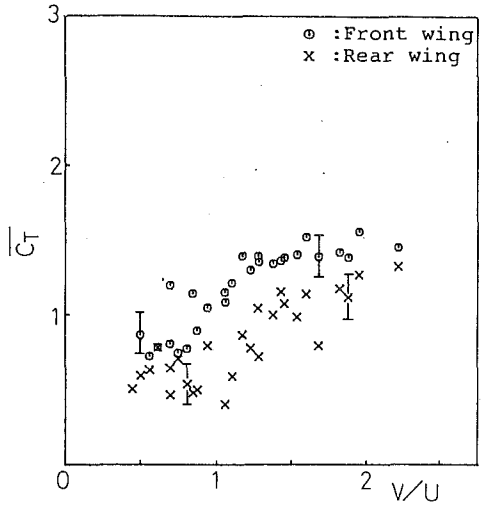

(a) Thrust coefficient

Fig. 11(*a*)

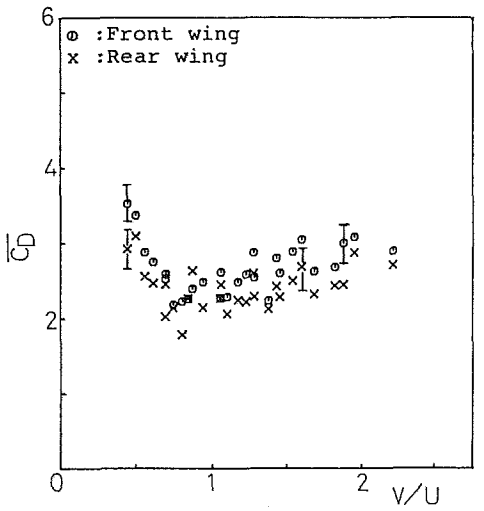

(b) Drag coefficient

Fig. 11(*b*)

Fig. 11 Average thrust and drag coefficients for the in phase

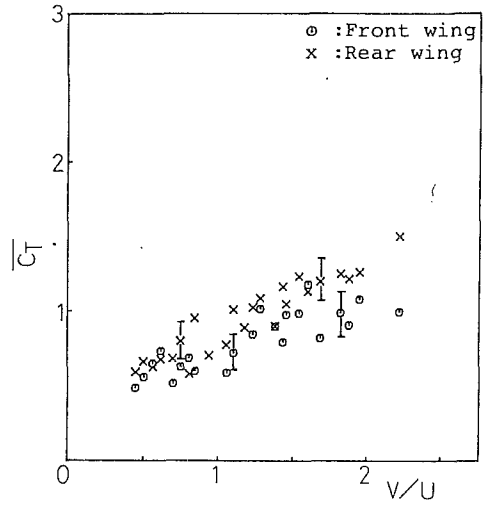

(a) Thrust coefficient

Fig. 12(*a*)

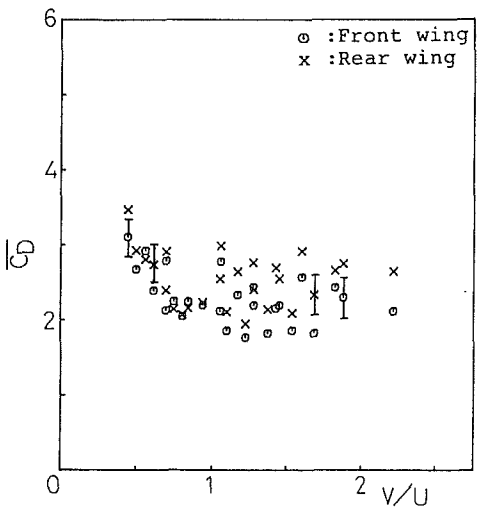

(b) Drag coefficient

Fig. 12(*b*)

Fig. 12 Average thrust and drag coefficients for the out of phase

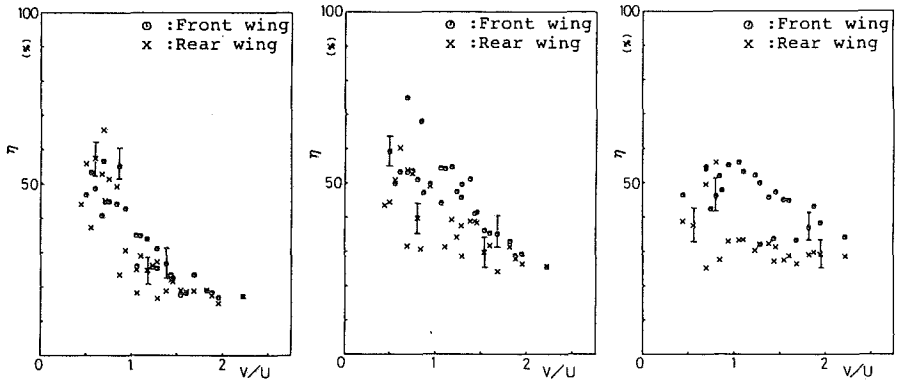

(a) α=15° (b) α=30° (c) α=40°

Fig. 13 Propulsive efficiencies for the in phase

is true for the single-stage type. It is also noted that as the opening angle becomes smaller the region of high efficiency becomes narrower, that is, the peak of the efficiency curve becomes sharp. This is again true for the single-stage type.

These facts may be explained by considering the velocity triangle often used in cascade theory (see, for example, Wislicenus, 1969). The incident angle is defined by U and V, and considering the opening angle which corresponds to the stagger

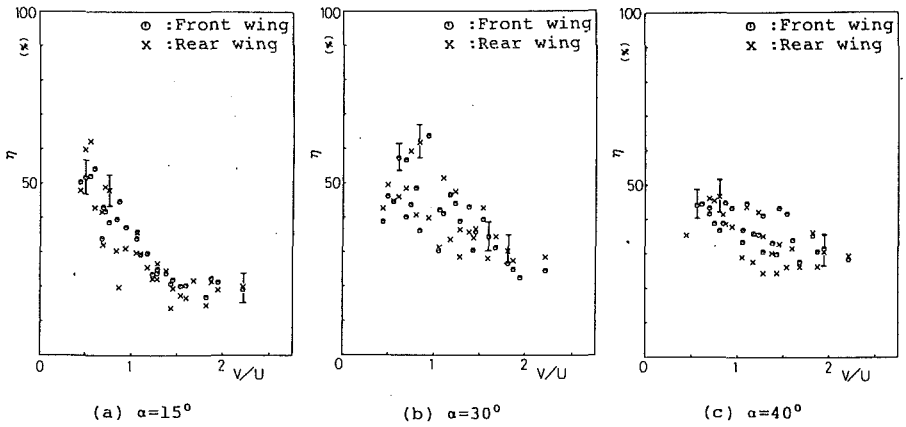

Fig. 14 Propulsive efficiencies for the out of phase

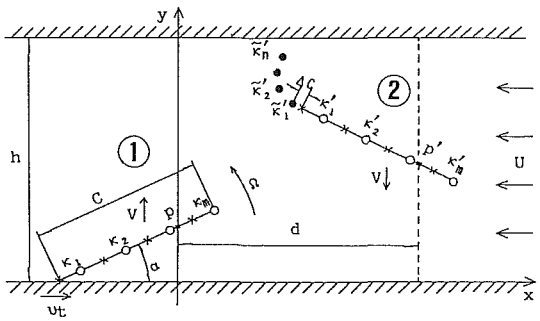

Fig. 15 Model of the numerical analysis

angle, the maximum efficiency is achieved when the attack angle is suitable for a given quasi-steady flow. However, the flow we are here dealing with is unsteady, and its configuration changes very quickly, so that the understanding of the mechanisms that affect the efficiency requires more detailed study.

It is noteworthy that with regards to efficiency, the qualitative difference between the two cases, the in-phase and the out-of-phase is clear. However, the average of the efficiencies of both wings, is almost the same for the two cases. This means that even for the case of the same phase the front wing increases its efficiency but the rear wing's decreases as compared to the single-stage type. Although the efficiencies for the single-stage type are not presented here, the values are closely identical to the above averaged values (in Tsutahara and Kimura, 1987, the efficiencies were higher because the model used in the previous experiment was larger and the loss due to the viscosity was less). This fact raises doubts on whether the Weis-Fogh effect takes place for this type of motion. This issue will be addressed further on.

Although the propulsive efficiency did not increase by designing this mechanism as a two-stage type, periodic accelerations on the ship hull induced by the periodic motion of the wing will be reduced by controlling the phases of the wings motions in the two-stage type. This fact is of importance in actual applications.

Numerical Analysis

Method of Numerical Analysis. The discrete vortex method (see Leonard, 1980; Sarpkaya, 1989) is used for calculating the flow field and the forces on the wing. The model of the analysis is shown in Fig. 15, in which the wings are considered to be flat plates and they are represented approximately by M bound point vortices for each wing. It is assumed that separation does not take place at the leading edges of the wings, so that the free point vortices representing the wake are introduced at a point Δc distant from the trailing edge of each wing.

We introduce the complex variable $z=x+iy$, where $i^2=-1$. The strengths and the positions of the bound vortices on the rear wing (marked 1) are expressed, respectively, by κ_j and z_j $(j=1, 2, \cdots, M)$, and those on the front wing (marked 2) are κ_j' and z_j' $(j=1, 2, \cdots, M)$. The strengths and the positions of the free vortices from the rear wing are, respectively, $\tilde{\kappa}_j$ and $\tilde{z}_j$ $(j=1, 2, \cdots, N)$, and those from the front wing are $\tilde{\kappa}_j'$ and $\tilde{z}_j'$ $(j=1, 2, \cdots, N')$, where N and N' have different values in general. The velocity v_t is the moving or sliding velocity in the x-direction of the trailing edge when the wing is at the opening stage. The other symbols are the same as those in Fig. 1.

Taking the infinite numbers of images with respect to the two solid walls, the complex potential can be expressed in a closed form as

$$F(z)=\sum_{j=1}^{M}\kappa_j\left\{\log\left[\sinh\frac{\pi(z-z_j)}{2h}\right]-\log\left[\sinh\frac{\pi(z-\bar{z}_j)}{2h}\right]\right\}+\sum_{j=1}^{M}\kappa_j'\left\{\log\left[\sinh\frac{\pi(z-z_j')}{2h}\right]-\log\left[\sinh\frac{\pi(z-\bar{z}_j')}{2h}\right]\right\}+\sum_{j=1}^{N}\tilde{\kappa}_j\left\{\log\left[\sinh\frac{\pi(z-\tilde{z}_j)}{2h}\right]-\log\left[\sinh\frac{\pi(z-\bar{\tilde{z}}_j)}{2h}\right]\right\}+\sum_{j=1}^{M}\tilde{\kappa}_j'\left\{\log\left[\sinh\frac{\pi(z-\tilde{z}_j')}{2h}\right]-\log\left[\sinh\frac{\pi(z-\bar{\tilde{z}}_j')}{2h}\right]\right\}+Uz. \quad (3)$$

where upper bars over the complex variables represent the complex conjugates.

The variables being determined at each time step are the $2M$ bound vortices and the newly introduced free vortex or vortices. The free vortices do not change their strengths once they are shed. One free vortex is introduced from each trailing edge at each time step since the separation is assumed to take place only from the trailing edges. When the trailing edges are on the wall, free vortices are not introduced.

The procedure for determining the variables is as follows (this is the same for the two wings, therefore only the conditions for one wing, i.e., the rear wing, will be presented): At the control points on the wing, located at the centers between adjacent bound vortices, the stream function ψ $(=\mathrm{Im}\{F(z)\})$ is represented by

$$\psi=\int_0^r v_n\,dr+\psi_t, \quad (4)$$

where Im refers to the imaginary part, v_n is the velocity component in the direction normal to the wing surface, and r is the distance along the wing surface from the trailing edge. The variable ψ_t represents the value of the stream function at the trailing edge, which is zero when the trailing edge is in contact with the lower wall and is $-Uh$ when it is in contact with the upper wall, otherwise ψ_t must be determined at each time step. When the trailing edge is in contact with the walls the value of ψ_t is satisfied automatically by Eq. (3). Therefore, in this case, the following condition should be used:

$$\mathrm{Re}\left(\frac{dF}{dz}\right)_{z=z_t} = v_t, \tag{5}$$

where Re refers to the real part, and the moving velocity v_t of the trailing edge at z_t can be evaluated by $v_t = V\tan\alpha$.

When the wing is translating in the flow conditions (4) are imposed at the control points, and at the trailing edge the Kutta's condition

$$-\mathrm{Im}\left(\frac{dF}{dz}\right)_{z=z_t} e^{i\alpha} = V\cos\alpha, \tag{6}$$

is satisfied instead of Eq. (5). One more condition is necessary for determining the value of the stream function at the trailing edge ψ_t. This is Kelvin's circulation theorem

$$\sum_{j=1}^{M}\kappa_j + \sum_{l=1}^{N}\tilde{\kappa}_1 = \frac{\Gamma_0}{2\pi}, \tag{7}$$

where Γ_0 is the circulation around the wing just before the wing detaches from the wall.

When the wing is closing, with the leading edge in contact with the wall, the discussion is the same as that when it is opening with slight changes in the definition of Eqs. (4) and (5). In this case, ψ_t in Eq. (4) should be the stream function at the leading edge, and r is taken as a distance from the leading edge. Therefore v_t in Eq. (5) is also the sliding velocity of the leading edge.

The conditions presented above are for one wing only. Similar conditions for the other wing must also be satisfied. These conditions for the two wings are implemented at each time step. The free vortices move with the local velocity of the flow.

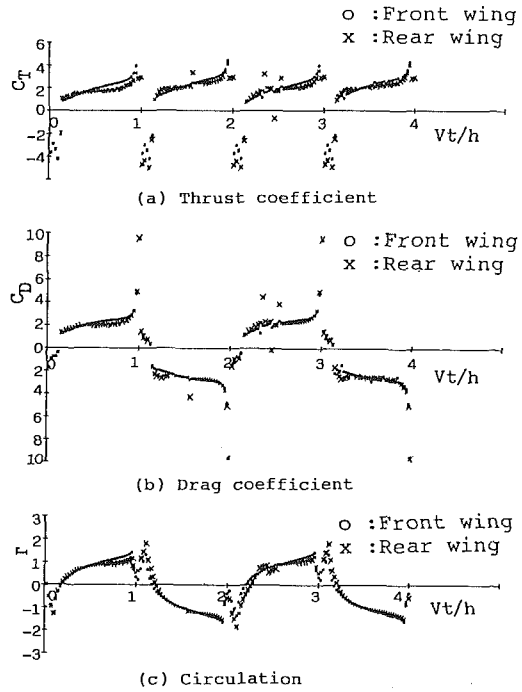

Fig. 16 Thrust and drag coefficients and circulations. Motions of the wings are in the in phase and the distance $d = 2c$.

Forces and Moment on the Wing. Let X and Y be the components of the force on the wing in the x-direction and the y-direction, respectively, which are expressed, by integrating the pressure around the wing surface, as

$$X - iY = \frac{i\rho}{2}\oint_B \left(\frac{dF}{dz}\right)^2 dz + i\rho\oint_B \frac{\partial F}{\partial t}\overline{dz}, \tag{8}$$

where B represents the contour of integration along the wing surface and $\overline{dz}$ is the complex conjugate of dz. The first term on the right-hand side in Eq. (8) can be evaluated easily by the theorem of residue and the second term is calculated by a technique in which the wing is considered to be cuts of the logarithmic functions and the arguments of these functions are estimated at the cut surface. The result for the rear wing is written in the form

$$\begin{aligned} X - iY = &-\pi\rho\left[\frac{\pi}{h}\sum_{j=1}^{M}\kappa_j^2\cosh\frac{\pi(z_j-\overline{z_j})}{2h} - \frac{\pi}{2h}\sum_{j=1}^{M}\kappa_j\right. \\ &\times\left\{\sum_{\substack{j=1\\k\neq j}}^{M}\kappa_k\left[\cosh\frac{\pi(z_j-z_k)}{2h} - \cosh\frac{\pi(z_j-\overline{z_k})}{2h}\right]\right\} \\ &-\sum_{j=1}^{M}\kappa_j\left\{\sum_{k=1}^{M}\kappa_k'\left[\cosh\frac{\pi(z_j-z_k')}{2h} - \cosh\frac{\pi(z_j-\overline{z_k'})}{2h}\right]\right\} \\ &-\sum_{j=1}^{M}\kappa_j\left\{\sum_{l=1}^{N}\tilde{\kappa}_1\left[\cosh\frac{\pi(z_j-\tilde{z}_1)}{2h} - \cosh\frac{\pi(z_j-\overline{\tilde{z}_1})}{2h}\right]\right\} \\ &-\sum_{j=1}^{M}\kappa_j\left\{\sum_{l=1}^{N'}\tilde{\kappa}_1'\left[\cosh\frac{\pi(z_j-\tilde{z}_1')}{2h} - \cosh\frac{\pi(z_j-\overline{\tilde{z}_1'})}{2h}\right]\right\} \\ &-2Ui\sum_{j=1}^{M}\kappa_j - 2i\sum_{j=1}^{M}\kappa_j\dot{\overline{z}}_j - 2ie^{-i\alpha}\left\{\sum_{j=1}^{M}\left[\sum_{q=1}^{M}\dot{\kappa}_q\Delta r_j\right]\right. \\ &\left.\left.+\frac{\tilde{\kappa}^{\mathrm{new}}}{\Delta t}\cdot c\right\}\right], \end{aligned} \tag{9}$$

where Δr_j is the distance between κ_j and κ_{j-1}, and $\tilde{\kappa}^{\mathrm{new}}$ represents the newly introduced free vortex. The expression for the front wing is similar to the above equation.

The moment about the point p or p' in Fig. 15 can be obtained in a similar manner to that of the forces, and we shall omit here the detailed expression.

The forces obtained by Eq. (9) are strictly due to the pressure of the fluid, so that when the wing is in contact with the wall at the leading edge or at the trailing edge, the reaction from the wall must be added to the forces. If we assume that there is no friction between the wing edge and the wall, only the drag must be modified. In this case, the reaction or the side force from the wall is the component in the y-direction, that is, the direction perpendicular to the flow only. If we let M_p be the moment about the point p, the reaction Y_w will be expressed by

$$Y_w = M_p\cos\alpha/r_p, \tag{10}$$

where r_p represents the distance between the point p and the edge touching the wall. When the sign of the moment changes and the wing does not act the force on the wall Y_w should be zero. We should note here that in Eq. (10) we neglect the mass of the wing but the virtual mass of the fluid is of course considered, and Eq. (10) will be reasonable because the latter is much larger than the former.

The definitions of the thrust and drag coefficients are, respectively, $C_T = X/\{(1/2)\rho V^2 c\}$ and $C_D = (Y + Y_w)/\{(1/2)\rho V^2 c\}$. The average thrust and the drag coefficients are defined as those averaged over four cycles and the propulsive

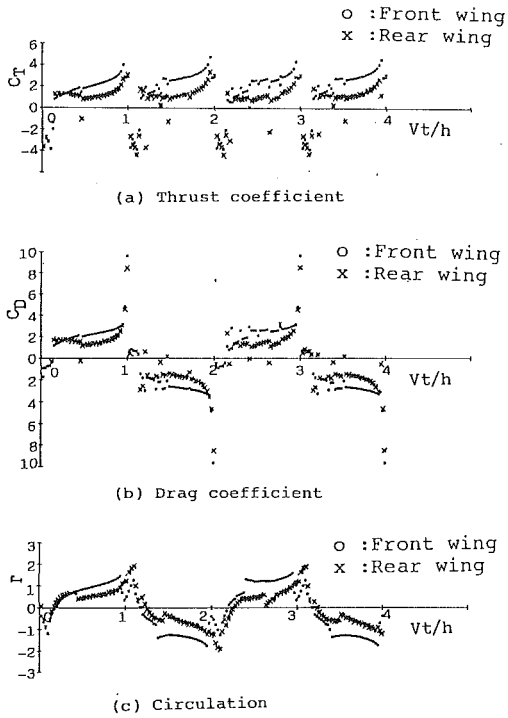

Fig. 17 Thrust and drag coefficients and circulations for the in phase. ($d = 1.1c$)

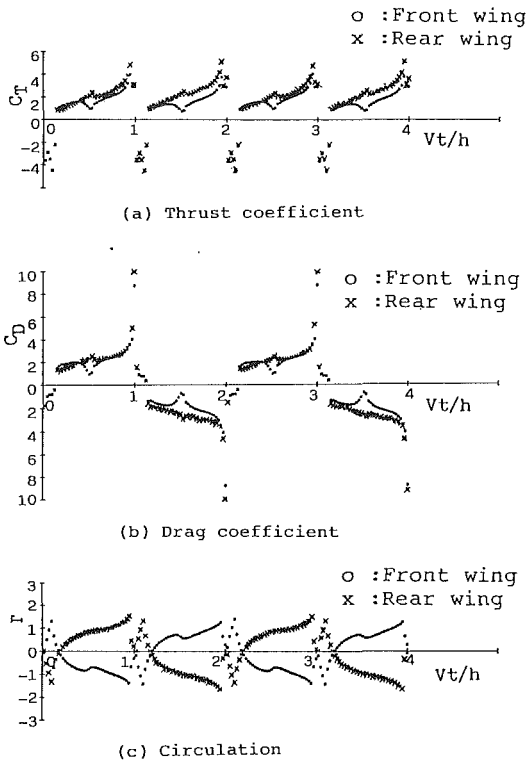

Fig. 18 Thrust and drag coefficients and circulations for the out of phase. ($d = 1.1c$)

efficiency is given in Eq. (2). The circulation about the wing is

$$\Gamma = 2\pi \sum_{j=1}^{M} \kappa_j. \tag{11}$$

Numerical Results and the Forces. The conditions of the numerical calculations are matched with the experiments. The time histories of the thrust and the drag coefficient and the circulations about the wings, in the case of the two wings at a distance $d = 2c$ moving in the in-phase, are shown in Fig. 16.

The error of the numerical simulation is hard to evaluate for the discrete vortex method. It strongly depends on the value of the time increment and on the point where the free vortices are introduced. A reliable method to obtain the optimum parameters has not established so far. Therefore, we chose the values of these parameters by several trials, and the error was evaluated less than 30 percent by comparing with the experimental data.

The differences between the forces on the two wings are almost indistinct; therefore the two wings do not affect each other even in such a short distance and the forces are almost identical to those in the single-stage type. The thrusts become negative when the wings open and become large positive when the wings close, and the same is true for all cases. These facts are detected in experiments, and more clearly in the single stage type reported in Tsutahara and Kimura (1987). It should be noted that the rear wing does not even get affected by the wake of the front wing. The same is also true for the out-of-phase case.

The same coefficients and the circulations in the case of the wings close to each other are shown in Fig. 17. Both the thrust and the drag of the front wing are much larger than those of the rear wing. This may be due to the fact that the circulation of the front wing is larger than that of the rear wing.

For the out-of-phase case, Fig. 18 shows that when the two wings meet at the center of the channel the thrust on the front wing decreases and that on the rear wing increases; and the average thrust on the rear wing is slightly larger than the front.

Table 1 Averaged thrust, drag coefficients and propulsive efficiencies by numerical calculation

ΔT	Wing	$\overline{C_T}$	$\overline{C_D}$	$\overline{\eta}$ (%)
0°	②	1.6(1.3)	2.6(2.4)	62(54)
	①	0.9(0.7)	2.1(1.8)	43(39)
180°	②	1.2(0.8)	2.3(1.8)	52(44)
	①	1.6(1.1)	2.7(2.0)	59(55)

These calculation results agree well qualitatively with the experimental data.

When the wings meet at the center of the channel the circulation of the front wing decreases, on the other hand, that of the rear wing is not affected. This can be explained as follows. The essential factor determining the circulation about the wing is the flow in the vicinity of its trailing edge, because the vorticity on the surface of the wing is shed there. Therefore the front wing is strongly affected when the two wings pass each other, but the rear is not.

The above fact implies that when two wings approach each other from the opposite direction and separate, the circulations about the wings are not necessarily strengthened but in general weakened because the directions of these circulations are opposite. This idea contradicts the hypothesis by Furber and Ffowcs Williams (1979) and this will be considered again in discussion.

In Table 1, the averaged thrust and drag coefficients and the propulsive efficiency for $\alpha = 30$ deg, $V/U = 1$, and $d = 1.1c$ are presented with the experimental values for comparison. All the values of the numerical calculations are somewhat larger than those of the experiments. The differences may be explained as follows: The wings are assumed to be flat plates in the numerical analysis and when the wings are closing, the

forces will have large values, because the pressure of the fluid between the wing and the side wall becomes very high; whereas in the experiments the wings are streamlined and some clearance exists between the wings and the walls even when the wings close. Another reason may be that in the experiments there is the free surface in the water tank, so that the two-dimensionality is not strictly preserved at this stage. For efficiency in the calculation the separations occur only at the trailing edges and the loss is estimated to be lower than that in the experiments.

Discussion

Forces. We shall consider here the difference between the forces of the two wings qualitatively by examining the circulations about the two wings. When the wings are moving in-phase, the direction of the circulations are the same (Fig. 17), so that the flow velocity in the area between the two wings will become lower and the static pressure will become higher; then the two wings receive a repulsive force as shown in Fig. 9. This is the reason why the thrust and the drag on the front wing are larger.

For the out-of-phase case, the circulations have opposite directions (Fig. 18), so that a suction force exerted on the two wings in a similar manner (Fig. 10). In the former case, the wings always interact, but in the latter case they interact only when they pass each other. Therefore, the difference between the forces of the two wings is clearer for the in-phase case.

In the above discussion, we only considered the force due to the velocity, that is, the first term in Eq. (8). The term representing the unsteadiness, or the virtual mass, is not considered. Nevertheless, the above qualitative discussion roughly explains the different characteristics of the two wings.

The Weis-Fogh Effect Between the Two Wings. When two wings separate, circulations of opposite directions about the wings are produced immediately without any vortices shed, but not violating the Kelvin's circulation theorem. This is called the Weis-Fogh effect. When two wings originally at rest start to move and separate, this mechanism always works. But when the two wings which have already enough circulations come across, this mechanism does not always work, because if the circulations are determined by Kutta's condition when the wings pass then the circulation are not always strengthened and could even be weakened by canceling. In a realistic estimation, even if the circulations are strengthened, the thrusts on the two wings will not increase at the same time, as argued earlier in terms of the pressure change in the area between the two wings.

Conclusions

The dynamic properties of a two-stage type propulsion system using the Weis-Fogh mechanism have been studied experimentally and numerically. The following results have been obtained:

(1) The interaction between the two wings takes place when the wings are close to each other, but when the two separate, no effect of the wake of the front wing on the rear wing is detected.

(2) When the phases of the two wings' motions are in phase, the thrust, the drag, and the propulsive efficiency of the front wing are higher than those of the rear wing.

(3) When the phases are apart by 180 deg, the result is the reverse of the in phase and the differences between the characteristics of the two wings are slight.

(4) For both cases of phase differences, the propulsive efficiencies of the two wings do not increase at the same time, that is, one gains and the other looses, and the averaged value of the efficiencies of the two is almost the same as that of the single-stage type.

Acknowledgments

The authors thank Professor T. Kida of the University of Osaka Prefecture for his valuable comments, and they also thank Dr. K. Takahashi and Messrs. M. Ohashi and Y. Omori for their assistance in carrying out the experiments.

References

Furber, S. B., and Flowcs Williams, J. E., 1979, "Is the Weis-Fogh Principle Exploitable in Turbomachinery?" *Journal Fluid Mechanics*, Vol. 94, pp. 519–541.

Leonard, A., "Vortex Method for Flow Simulation, 1980," *Journal of Computational Physics*, Vol. 37, pp. 289–335.

Lighthill, M. J., 1973, "On the Weis-Fogh Mechanism of Lift Generation," *Journal of Fluid Mechanics*, Vol. 60, pp. 1–17.

Sarpkaya, T., 1989, "Computational Methods with Vortices," ASME JOURNAL OF FLUIDS ENGINEERING, Vol. 111, March, pp. 5–52.

Tsutahara, M., and Kimura, T., 1987, "An Application of the Weis-Fogh Mechanism to Ship Propulsion," ASME JOURNAL OF FLUIDS ENGINEERING, Vol. 109, pp. 107–113.

Weis-Fogh, T., 1973, "Quick Estimates of Flight Fitness in Hovering Animals, Including Novel Mechanism for Lift Production," *Journal of Experimental Biology*, Vol. 59, pp. 169–231.

Wislicenus, G. F., 1969, *Fluid Mechanics of Turbomachinery*, Vol. 1, Dover Publications, New York, pp. 226–259 and pp. 398–407.

Yukimaru Shimizu
Professor,
Department of Mechanical Engineering,
Mie University,
Kamihama-cho, Tsu-shi,
Mie-ken, 514 Japan

Takaya Yoshikawa
Engineer,
Nippon Spark Plug Co., LTD

Shinji Matsumura
Engineer,
Mitsubishi Motors Co., LTD,
Shiga Factory

Power Augmentation Effects of a Horizontal Axis Wind Turbine With a Tip Vane—Part 1: Turbine Performance and Tip Vane Configuration

This paper describes the experimental results of output power augmentation of a horizontal axis wind turbine with a tip vane. In order to find the relationship between the performance of the turbine and the configuration of the tip vane, various types and sizes were used. It was found that V-type and S-type tip vanes can improve turbine performance. Also, the dimensions of V- and S-type tip vanes were investigated. The maximum improvement achieved was a 25 percent increase in power in an existing wind turbine without a tip vane.

1 Introduction

The idea of augmenting the power output of a horizontal axis wind turbine by installing a tip vane on the blade tip was proposed by Van Bussel (1986) and Von Holten (1976) ten years ago. Although it has been proven theoretically that output power can be increased through the use of tip vanes, the idea is difficult to implement in wind turbines. Following an extensive review of the literatures our experimental work has led to an increase of 20 to 25 percent in power over the power obtained without a tip vane. In a nutshell, we deduced that

(1) To decrease induced drag, the induced vortex on blade tip must be kept as small as possible.

(2) tip vane increases the flow rate across the rotor surface.

Although these ideas differ from those proposed by Von Holten, their implementation leads to an increase in power.

2 Experimental Equipment and Method

Figure 1 illustrates the open jet wind tunnel used in the experiment. Over the whole outlet surface the maximum deviation is 2.5 percent from average velocity. This nonuniformity is due to turbulence. The relative nonuniform deviation is divided by the tip-speed ratio, leaving an operational turbulence of approximately 0.5 percent (at a tip-speed ratio of $\phi = 6$) over the whole outlet. The horizontal axis wind turbine with a rotor diameter 1.160 m is placed 1.2 m from the tunnel outlet.

To prevent downstream effects, we provided a distance of 4.6 m behind the wind turbine. Figure 2 shows the interior of nacelle in detail. It consists of a double-geared drive; the gear ratio is 2:1. The main shaft goes through the drive. At the end of the shaft, a slip ring is installed to measure the force on the blade. A torque meter is used. The braking load is provided by an electromagnetic brake. Figure 3 shows an example of

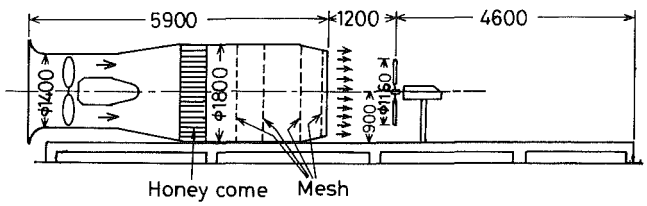

Fig. 1 Schematic diagram of open jet wind tunnel and test wind turbine

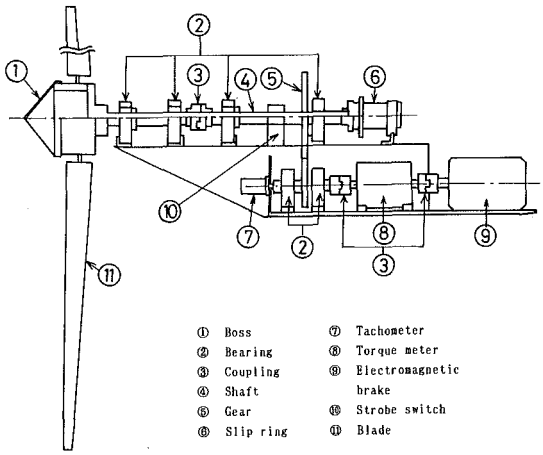

Fig. 2 The interior of nacelle in detail

Contributed by the Fluids Engineering Division for publication in the JOURNAL OF FLUIDS ENGINEERING. Manuscript received by the Fluids Engineering Division December 5, 1990; revised manuscript received November 18, 1993. Associate Technical Editor: W. Tabakoff.

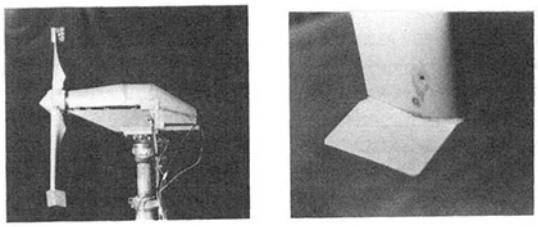

Fig. 3 Wind turbine with tip vanes and a tip vane on the blade tip

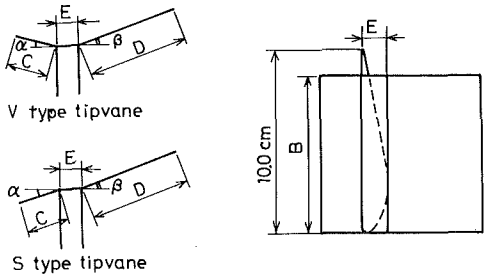

Fig. 4 Definitions of V and S type tip vanes, camber angles of leading edge α and trailing edge β and the fitting state on the blade tip

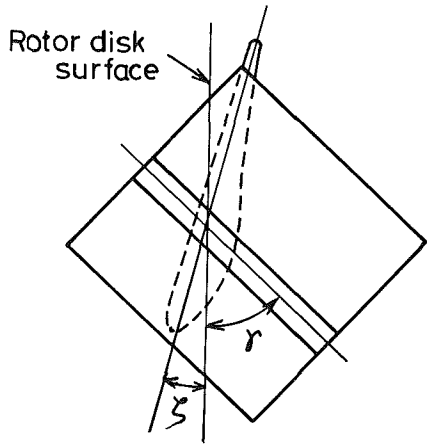

Fig. 5 Definitions of pitch angle of the blade ζ to the rotor disk surface and fitting angle of tip vane γ on the blade tip

the wind turbine and tip vane. Table 1 lists the configuration of the wind turbine blade used in the experiment.

In order to check the effects of a tip vane on the performance of the wind turbine, we constructed various types of tip vanes for our experiment. Table 2 shows the dimensions of tip vane used in the experiment. These tip vanes were constructed systematically, based on the many configurations of tip vanes that have been reported earlier. Through trial and error, we found that V-type and S-type tip vanes were the most effective in increasing power output. Figure 4 is a definition graph, where α is the camber angle of leading edge, and β is the camber angle of trailing edge. With the V-type tip vane, both α and β, the leading edge and the trailing edge open to outside ($\alpha \geqq 0$ deg, $\beta \geqq 0$ deg). With the S-type tip vane, α, the leading edge opens to inside, and β, the trailing edge opens to outside.

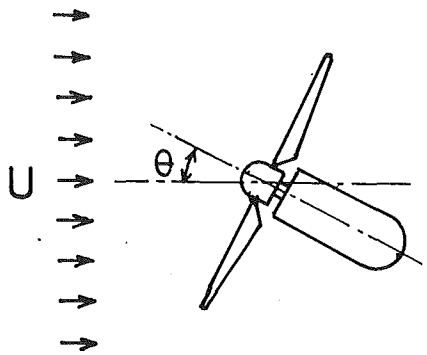

Fig. 6 Definition of inclination angle of rotor disk surface θ to wind direction

Table 1 Dimensions of test blade

Plane form of blade	Equi-chord length Twisted blade
Material	Wood
Weight (kg)	0.350
Length of blade (m)	0.500
Tip chord length (m)	0.100
Aspect ratio	5.000
Taper ratio	0
Airfoil section	FX74C16140

Torsion angle of blade $\delta = \tan^{-1}(300/573 \times 2\pi \times r_x)$ rad where r_x (m) is the length from blade root

Table 2 Dimensions of test tip vane

	$V(A*B)$	$S(A*B)$
$A(=C+D+E)$	6 ~ 10 cm	8 ~ 14 cm
B	6 ~ 12 cm	8 ~ 10 cm
α	0 ~ 90 deg	−30 ~ 0 deg
β	0 ~ 90 deg	〃
D/C	0.56 ~ 3.67	〃
γ	0 ~ 90 deg	0 deg

The relationship between the performance of the wind turbine and the configuration of the tip vane will be described in the following order.

(1) The effect on performance of the longitudinal and transverse dimensions (B, $C + D + E$) (refer to Fig. 4).

(2) The effect on performance of the camber angles α and β (refer to Fig. 4).

(3) The effect on performance of the ratio of the leading edge length C to the trailing edge length D (refer to Fig. 4).

(4) The effect on performance of the fitting angle γ of the tip vane on the blade tip (refer to Fig. 5).

(5) The effect on performance of the inclination angle θ of the rotary surface of the blade to the wind flow (refer to Fig. 6).

Table 2 lists the dimensions of tip vanes used in the experiment. The experimental results are detailed in the next section.

Tip speed ratio (ratio of peripheral speed) is defined as

$$\Phi = R\Omega/U$$

Power coefficient is defined as

$$Cp = T\Omega/0.5\ \rho U^3 \pi R^2 \quad (1)$$

Nomenclature

U = inlet wind speed
R = radius of rotor
T = resultant torque
Ω = angular velocity
ρ = air density
Φ = ratio of peripheral speed (tip speed ratio)
γ = angle of tip vane
θ = angle between main flow and rotary axis
Cp = power coefficient
Cp' = ratio of power coefficient
Cp'' = ratio of power coefficient

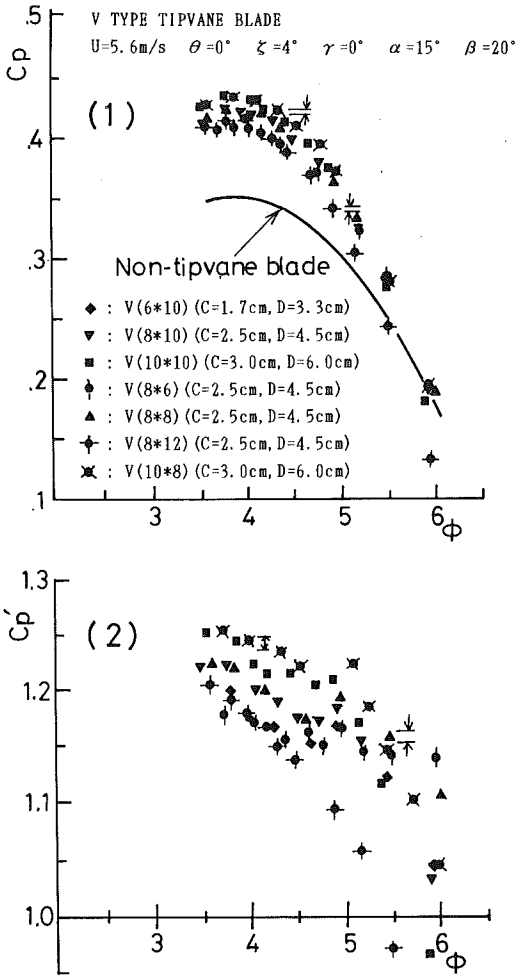

Fig. 7 Relationships between performance and aspect ratio of V type tip vanes on the wind turbine with V type tip vanes. (1) Relationship between power coefficient Cp and tip-speed ratio ϕ. (2) Relationship between power coefficient ratio Cp' and tip-speed ratio ϕ. (Uncertainty in $Cp = 0.4 \pm 0.002$, $Cp' = 1.2 \pm 0.006$ and $\phi = 4 \pm 0.02$.)

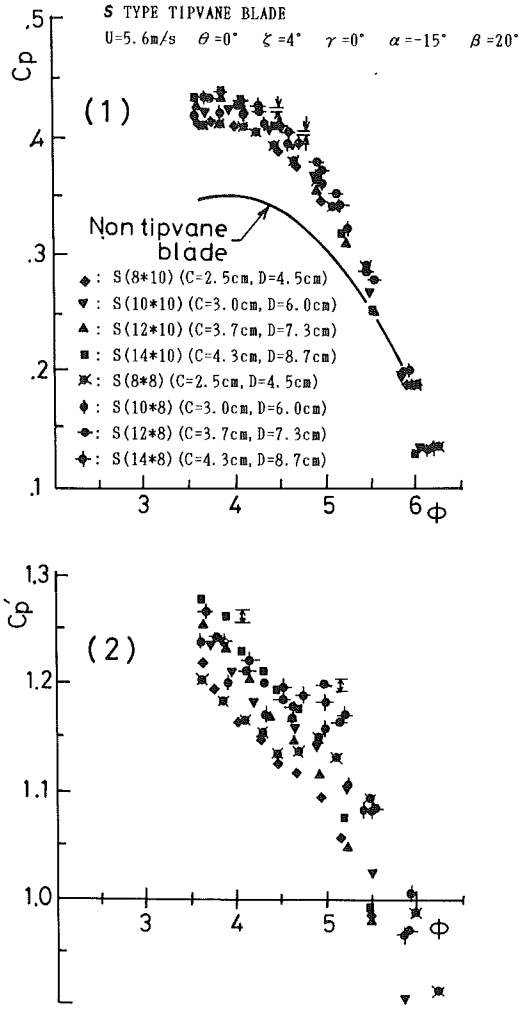

Fig. 8 Relationships between performance and aspect ratio of S type tip vanes on the wind turbine with S type tip vanes. (1) Relationship between power coefficient Cp and tip-speed ratio ϕ. (2) Relationship between power coefficient ratio Cp' and tip-speed ratio ϕ. (Uncertainty in $Cp = 0.4 \pm 0.002$, $Cp' = 1.2 \pm 0.006$ and $\phi = 4 \pm 0.02$.)

3 Experimental Results and Discussion

Figure 7 shows the relationship between the aspect ratio and performance. In Fig. 7-1, typical results of the V-type tip vane are shown, with the dimensions used as parameters. The maximum power coefficient obtained is 0.43 with the V(10*10)- and V(10*8)-type tip vanes. For the V(8*8)- and V(8*10)-type tip vanes, the power coefficient is slightly smaller than the maximum. The power coefficient of the others is again smaller in the order of V(8*6), V(8*12). Figure 7-2 shows the relationship between the ratio of the output coefficient Cp' and the tip speed ratio, where Cp' is defined as the ratio of the power coefficient with a tip vane to that without a tip vane with the same tip speed ratio (see Eq. (1)). This figure indicates that the maximum value is 1.25 for the V(10*10)- and V(10*8)-type tip vanes. This means that we can achieve 25 percent augmentation of the power coefficient by using one of these tip vanes. For the V(8*8)- and V(8*10)-type tip vanes, the Cp' value is 1.23.

Figure 8 shows the power coefficient Cp (Fig. 8-1) and the ratio of the power coefficient Cp' (Fig. 8-2) for the S-type tip vane. In Fig. 8-1, the maximum value is approximately 0.43 to 0.44, nearly the same as that for the V-type tip vane. The tip vanes with large Cp values are S(14*10) and S(14*8), followed by S(12*8) and S(12*10). We concluded that the power coefficient is larger when the tip vane length D is longer.

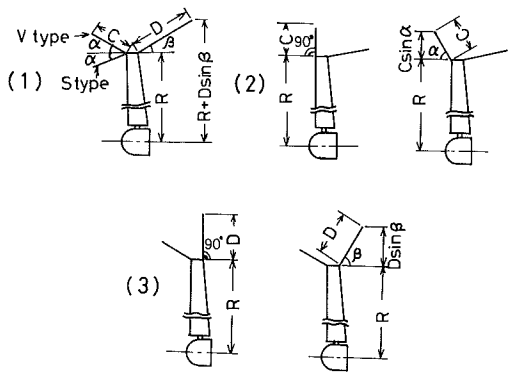

Fig. 9 Relationships between outer diameter $R + D \sin\beta$ or $R + C \sin\alpha$ of rotor with tip vanes and configurations of various tip vanes, camber angles of leading edge and trailing edge α and β are changed

However, if D is too long, the tip vane will bend by centrifugal force. Furthermore, vibration intensity will be intensed. The maximum Cp value in Fig. 8-2 is 1.27, indicating that the power coefficient is 27 percent larger than that without a tip vane. This value is slightly larger than that achieved with the V-type tip vane.

In Figs. 7 and 8, the experimental results with optimal performance are shown. In next figure, we discuss the effect on

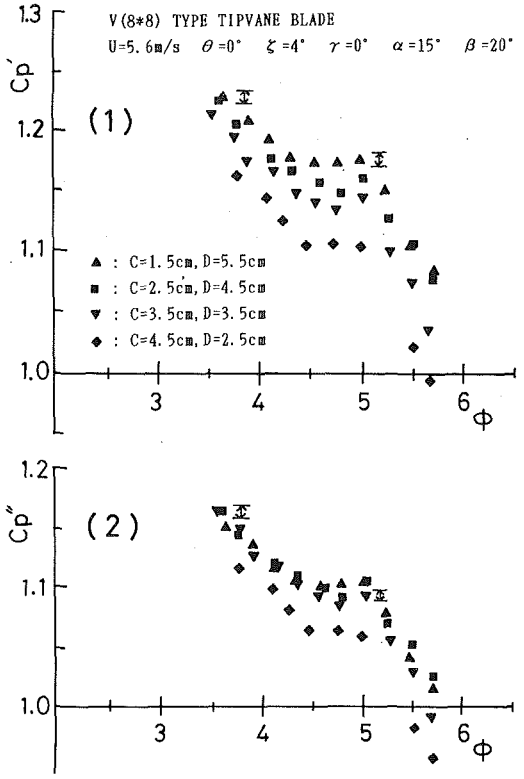

Fig. 10 In case of V type tip vane. Relationships between leading and trailing edge lengths C and D and (1) the ratio of power coefficient Cp', and (2) the ratio of power coefficient Cp''. (Uncertainty in Cp' = 1.2 ± 0.006, Cp'' = 1.1 ± 0.0055 and ϕ = 4 ± 0.02.)

performance of the ratio of the leading edge length C and the trailing edge length D (where $C + D$ = constant). As shown in Fig. 9, with the tip vane length $C + D$ remaining constant, the outside diameter is altered by the change in the ratio of C to D. The change in performance due to C and D will be presented, using parameters Cp' and Cp'', which are defined as follows:

$$Cp' = \frac{\text{power coefficient with a tip vane [where input area is } \pi R^2]}{\text{power coefficient without a tip vane}} \quad (2)$$

$$Cp'' = \frac{\text{power coefficient with a tip vane [where the input area is } \pi (R+dR)^2]}{\text{power coefficient without a tip vane}} \quad (3)$$

where dR expresses the increase of the outside diameter of the tip vane. Therefore, as shown in Fig. 9-2, $dR = C \sin \alpha$ when $C \sin \alpha > D \sin \beta$, and as shown in Fig. 9-3, $dR = D \sin \beta$ when $D \sin \beta > C \sin \alpha$.

As a typical example, Fig. 10-1 shows the ratio of the power coefficient Cp' for a V(8 * 8)-type tip vane, when $C + D$ = 7 cm. The lengths of C and D vary: (C, D) = (1.5 cm, 5.5 cm), (2.5 cm, 4.5 cm), (3.5 cm, 3.5 cm), (4.5 cm, 2.5 cm), where α = 15 deg and β = 20 deg. Figure 10-1 shows that the Cp' value reaches its maximum at C = 1.5 cm, and D = 5.5 cm. The next highest Cp' value is at C = 2.5 cm, and D = 4.5 cm. When the leading edge is longer than the trailing edge, for instance at C = 4.5 cm, and D = 2.5 cm, the Cp' value becomes small.

Considering the outside diameter of wind turbine with tip vane as $R + dR$, we get ratio of power coefficient Cp''. The results are shown in Fig. 10-2. The difference between the various symbols becomes considerably small. Based on these results, we have chosen the V(8 * 8)-type tip vane as the standard tip vane.

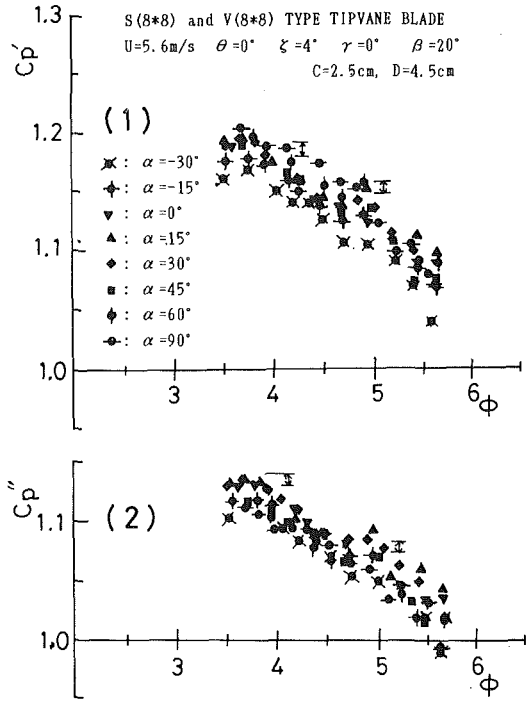

Fig. 11 In case of S type tip vane. Relationships between the camber angle of leading edge α, and (1) the ratio of power coefficient Cp' and (2) the ratio of power coefficient Cp''. (Uncertainty in Cp' = 1.2 ± 0.006, Cp'' = 1.1 ± 0.0055 and ϕ = 4 ± 0.02.)

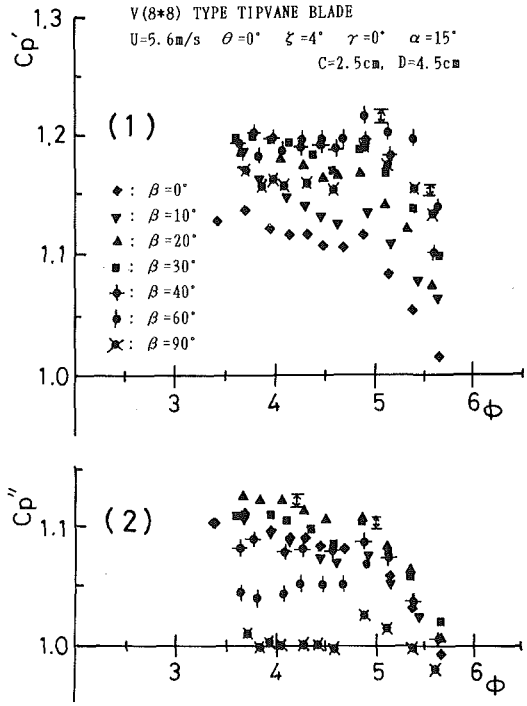

Fig. 12 In case of V type tip vane. Relationships between the camber angle of trailing edge β, and (1) the ratio of power coefficient Cp', and (2) the ratio of power coefficient Cp''. (Uncertainty in Cp' = 1.2 ± 0.006, Cp'' = 1.1 ± 0.0055 and ϕ = 4 ± 0.02.)

As shown in Fig. 9-1, if $\alpha \geqq 0$, the tip vane is a V-type, otherwise, it is an S-type. Performance varies with α and β. Even if the lengths of C and D are kept constant, the outside diameter of the wind turbine depends on α and β.

Figure 11-1 shows the ratio of the power coefficient where β = 20 deg and α varying between − 30 and 90 deg. The largest

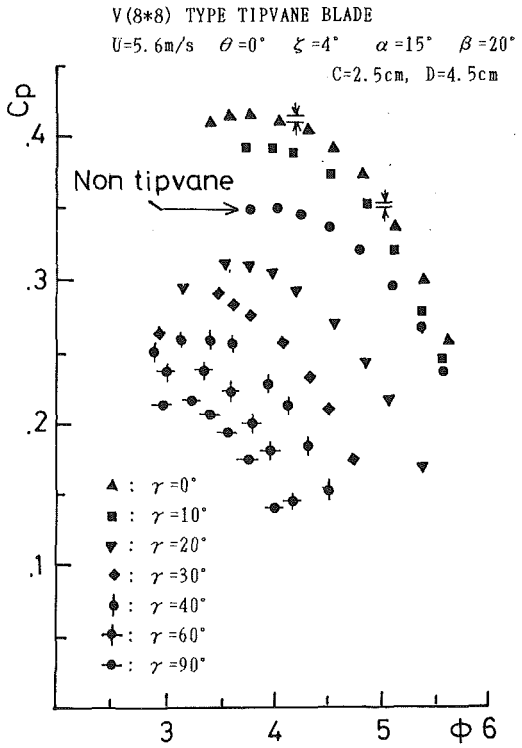

Fig. 13 In case of V type tip vane. Relationships between the fitting angle of tip vane γ on the blade tip and power coefficient *Cp*. (Uncertainty in $Cp = 0.4 \pm 0.002$.)

Cp' value is when $\alpha = 90$ deg, whereas the smallest value is when $\alpha = -30$ deg. When $\alpha = 90$ deg, the outside diameter is $R + C$, as shown in Fig. 9-2. By taking the practical outside diameter as $R + dR$, we get Cp'' ratio of the power coefficient, where, $dR = C \sin \alpha$ or $dR = D \sin \beta$ (see Fig. 9). These results shown in Fig. 11-2 are very different from those shown in Fig. 11-1. The largest Cp'' value is when $\alpha = 15$ or $\alpha = 30$ deg, but the Cp'' value when $\alpha = 90$ deg is much smaller.

Next, the relationship between the camber angle of trailing edge β and performance is discussed. In Fig. 12-1, keeping $\alpha = 15$ deg, β between 0 and 90 deg. The largest Cp' value was achieved when $\beta = 40$ or $\beta \fallingdotseq 60$ deg., and the smallest Cp' value when $\beta = 0$ deg. Figure 12-2 shows the ratio of power coefficient Cp'', when the outside diameter is $R + dR$. Since $Cp'' \fallingdotseq 1$ when $\beta = 90$ deg, and $Cp'' \fallingdotseq 1.05$ when $\beta = 60$ deg, there is little improvement in performance. Referring to Fig. 9-3, the practical length of blade is larger by D, when $\beta = 90$ deg and the length is larger by $D \sin 60$ deg, when $\beta = 60$ deg than the corresponding quantities without a tip vane.

We can then conclude from Figs. 11 and 12 that; (1) The effects of augmenting output are very reasonable when $\alpha = 15$ to 30 deg and $\beta = 10$ to 30 deg, with $\alpha = 15$ deg and $\beta = 20$ deg being particularly effective; and (2) when β is large, i.e., between 60 and 90 deg, it becomes ineffective in augmenting the output power. Likewise, the augmentation effects are very small when $\alpha = 90$ deg.

As shown in Fig. 5, the fitting angle γ can be changed. Figure 13 shows the power coefficient *Cp* for different γ values. *Cp* is largest when $\gamma = 0$ deg. Figure 13 shows that as γ increases, *Cp* becomes smaller. This observation suggests that the tip vane has a braking effect by changing the fitting angle γ. Therefore, in response to wind speed, we can control the tip vane in order to keep the rotary speed of the turbine constant, similarly to controlling the pitch angle of the blade.

We will now discuss performance when the rotary surface of the blade is inclined to the wind direction. Figure 14 shows the relationship between the power coefficient and the tip speed ratio of the wind turbine with a V-type tip vane; Figure 15 shows the same with an S-type tip vane. Furthermore, the ratio of the power coefficient Cp' is shown for four characteristic values of θ.

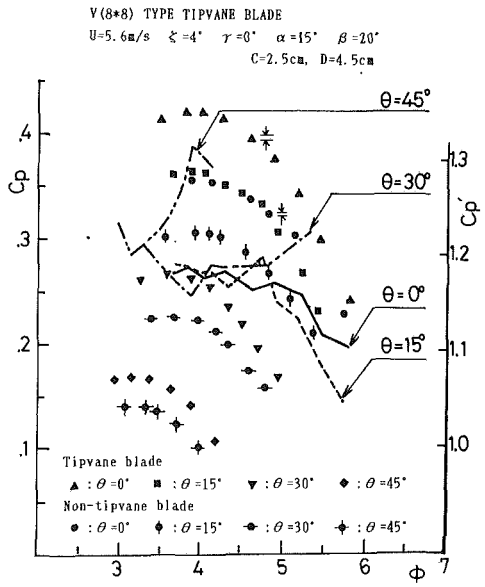

Fig. 14 In case of V type tip vane. Relationships between the inclination angle of rotor surface θ and power coefficient *Cp*. (Uncertainty in $Cp = 0.4 \pm 0.002$ and $Cp' = 1.1 \pm 0.0055$.)

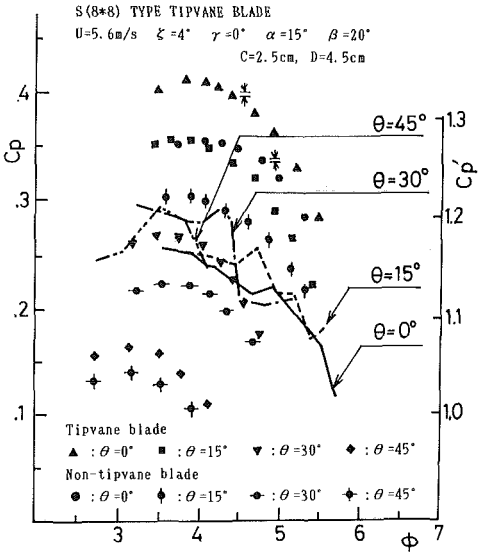

Fig. 15 In case of S type tip vane. Relationships between the inclination angle of rotor surface θ and power coefficient *Cp*. (Uncertainty in $Cp = 0.4 \pm 0.002$ and $Cp' = 1.1 \pm 0.0055$.)

For both the V-type and the S-type, the power coefficient *Cp* is reduced when θ is large. But, regardless of the value of θ, Cp' is greater than 1 for both types. This indicates that even when the rotary surface of the blade is inclined to the wind direction, the effect of the tip vane can be achieved, although the percentages of augmentation will differ. For the V-type shown in Fig. 14, the percentage is largest when $\theta = 45$ deg, whereas it has almost the same value when $\theta \fallingdotseq 0$ to 30 deg. For the S-type, the percentage is largest when $\theta = 30$ to 40 deg, and it becomes smaller when $\theta = 0$ to 15 deg.

4 Conclusions

(1) Although there are many types of tip vanes, the V-type and the S-type plate tip vanes that we have been proposed are

most effective in augmenting power output. By using the optimum configurations, we achieved 20 to 25 percent increase in power output than would be possible with a wind turbine without a tip vane.

(2) For V-type and S-type tip vanes, the aspect ratio to the chord length of the blade tip is an important parameter.

(3) The camber angles α and β of the tip vane are important factors. The optimum camber angle values are $\alpha = 15$ deg and $\beta = 20$ deg.

(4) Output power is affected by the fitting angle γ of the tip vane. Therefore, by varying the fitting angle we can control power output or maintain a constant rotation speed.

(5) Even when the angle between the rotary surface of the blade and the wind flow is changed, the blade with a tip vane yields higher performance than that without a tip vane.

References

Shimizu, Y., Yoshikawa, T., and Matsumura, S., 1990, "Power Augmentation Effects of Horizontal Axis Wind Turbine by Tip Vane—2nd Report," *Trans. of JSME*, Vol. 56-522B, pp. 502-507.

Van Bussel, G. J. W., 1986, "Status Rep. Tipvane Res," EWEA Conference, Rome, pp. 691-695.

Von Holten, Th., 1976, "Windmills with Diffuser Effect Induced by Small Tip Vanes," *Proceedings Ins. Symposium Wind Energy Syst.*, Cambridge, U.K.

Von Holten, Th., 1978, "Tipvane Research at T. U. Delft," *Proceedings 2nd Int. Symp. Wind Energy*, Paper F-2, Amsterdam.

Yukimaru Shimizu
Professor,
Department of Mechanical Engineering,
Mie University,
Kamihama-cho, Tsu-shi, Mie-ken, 514
Japan

Takaya Yoshikawa
Engineer,
Nippon Spark Plug Co., Ltd.

Shinji Matsumura
Engineer,
Mitsubishi Motors Co., Ltd.,
Shiga-Factory

Power Augmentation Effects of a Horizontal Axis Wind Turbine With a Tip Vane— Part 2: Flow Visualization

This paper presents a discussion of the physics of the flow discussed in our first report (Shimizu, Y. et al., 1990). By visualizing the flow around the tip vane, the following results were drawn: 1) The strength of the tip vortex, the induced drag and turbulence on the blade tip can be diminished with a tip vane. 2) The inflow rate to the rotary surface of wind turbine can be increased with the tip vane.

1 Introduction

In the accompanying first part of this paper (Shimizu et al., 1990), we reported on the experimental results of augmenting the output power of a horizontal axis wind turbine by using a tip vane. In this paper, we provide flow visualization results to explain the physical aspects of the modifications with the addition of tip vanes. As described in our first report, following goals were set:

(1) Decreasing the induced drag;

(2) Increasing the inflow rate across the rotary surface. Here, we will discuss whether our goal was realized using the flow visualization method around the wind turbine.

2 Experimental Equipment and Method

In this experiment, we used the same wind tunnel that was described in our first report (Shimizu et al., 1990). Figure 1 shows the equipment employed in the wind tunnel in order to visualize the flow.

The surface tuft method and the smoke method were employed for flow visualization. For the surface tuft method, cotton embroidery thread was used. The tuft is unraveled to adjust its length. For the smoke method, we constructed a high-performance smoke generator especially for our purposes.

Figure 2 shows the configuration of the smoke generator. First, compressed air is generated from a compressor ①. Then, air air tank ② is attached. A valve ③ adjusts the air volume sent to the nozzle. The area enclosed by a dashed box in Fig. 2 is the heart of the smoke generator. Copper pipe ⑥ is filled with liquid paraffin. Part of the pipe has heat-resistant putty glued to it and a 600 W nichrome wire wound around it. It is here that the liquid paraffin is heated and vaporized.

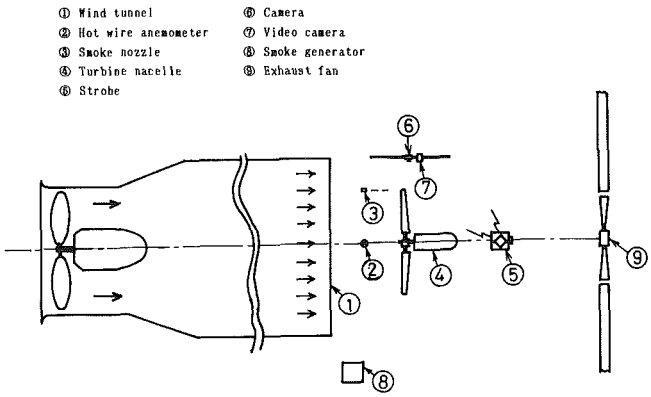

Fig. 1 Schematic diagram of experimental equipment of flow visualization in wind tunnel

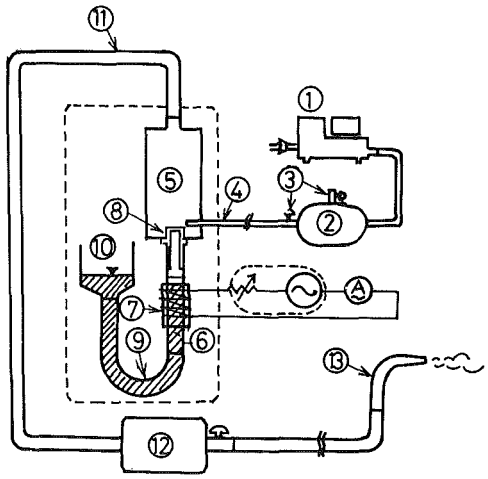

Fig. 2 Details of smoke generator equipment

Contributed by the Fluids Engineering Division for publication in the JOURNAL OF FLUIDS ENGINEERING. Manuscript received by the Fluids Engineering Division December 5, 1990; revised manuscript received November 18, 1993. Associate Technical Editor: W. Tabakoff.

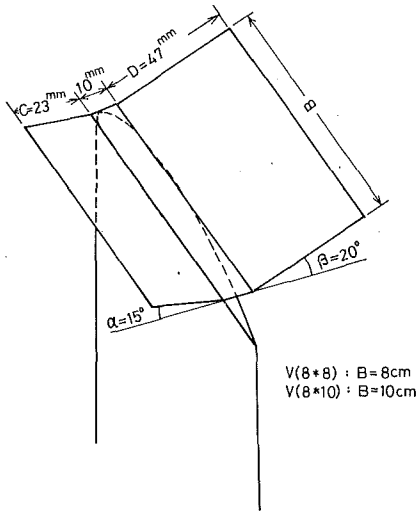

Fig. 3 Shape and dimension of V type tip vane used in the experiment

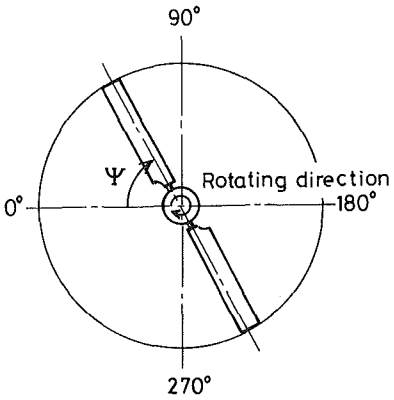

Fig. 4 Definition of azimuth angle Ψ

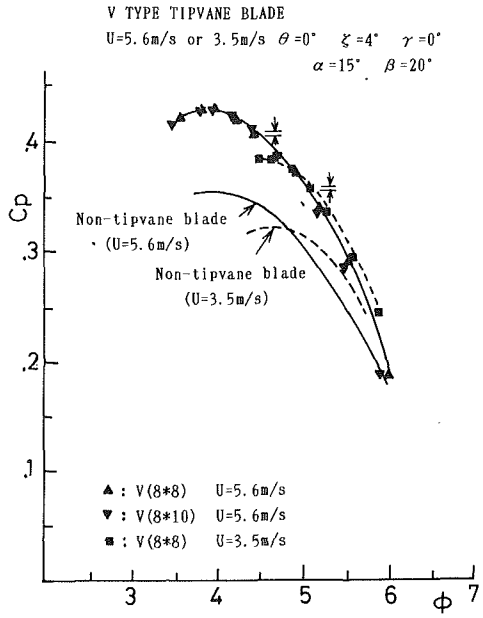

Fig. 5 Effects of Reynolds number to power coefficients *Cp* (Uncertainty in $Cp = 0.4 \pm 0.002$ and $\phi = 4 \pm 0.02$)

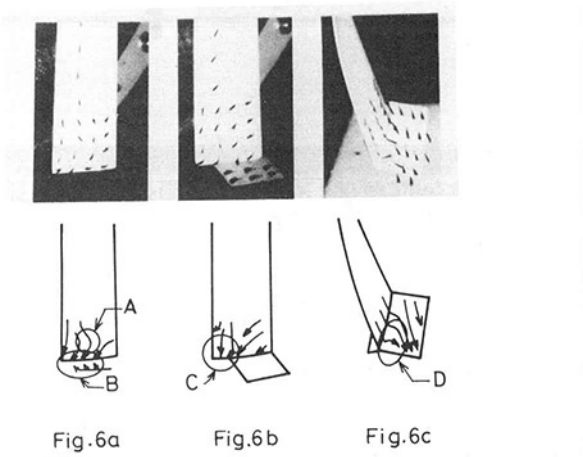

Fig. 6 (*a*) Tuft picture around blade tip without tip vane; (*b*) tuft picture around blade tip with V(8 × 8) tip vane; (*c*) tuft picture around blade tip with V(8 × 10) tip vane

The smoke from the vaporized liquid paraffin is directed to the nozzle ⑧ where it mixes with the compressed air from another nozzle ④. In order to provide a constant smoke density, it is necessary to maintain a constant height of the liquid surface. A tank with large free surface is connected to the copper pipe by a coupling pipe. The smoke generated in this way is sent to the smoke tank ⑫ through a heat-resistant hose ⑪ (silicon based). The smoke tank is required to prevent the vaporized paraffin from returning to a liquid state, which would block the hose. Finally, that smoke is sent through the nozzle ⑬.

Figure 3 shows the shape and dimensions of V-type tip vane used in our experiment. By using this tip vane, the highest power coefficient can be obtained (refer to our first report, Shimizu et al., 1990). The same result can be obtained with the S-type tip vane. The reason for this is the same as with the V-type tip vane.

Figure 4 shows the definition of the azimuth angle Ψ (which is defined as the angle as viewed from upstream of the rotary surface). The pictures taken by the smoke method were obtained with a wind speed of 3.5 m/s, at a rotation speed of approximately 270 rpm, which is the most efficient point. A V(8 * 8)-type tip vane was used and the nozzle was set at an azimuth angle of $\Psi = 0$ deg. The horizontal axis wind turbine has two blades. Each blade is named A or B.

3 Experimental Results and Considerations

3.1 The Effect of Wind Speed for the Performance of Wind Turbine. Here we will discuss the relationship between wind speed and the performance of the wind turbine with the V(8 * 8) – and V(8 * 10)-type tip vanes, which demonstrated high performance in the experiment described in our first report. Until now, the wind speed in our experiment was 5.6

Nomenclature

U = inlet wind speed
R = radius of rotor
T = resultant torque
Ω = angular velocity
ρ = air density
Φ = ratio of peripheral speed (tip speed ratio)
γ = angle of tip vane
θ = angle between main flow and rotary axis
Cp = power coefficient

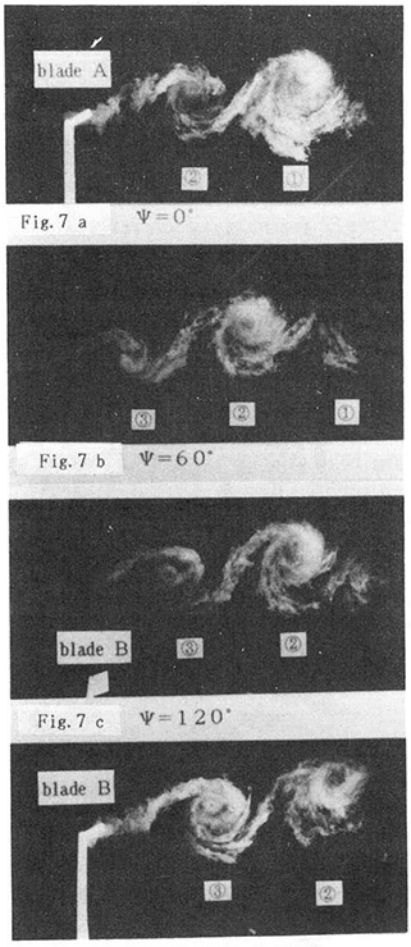

Fig. 7 With V(8∗8) tip vane. Relationships between tip vortex and azimuth angle Ψ. Flow visualization by smoke line method.

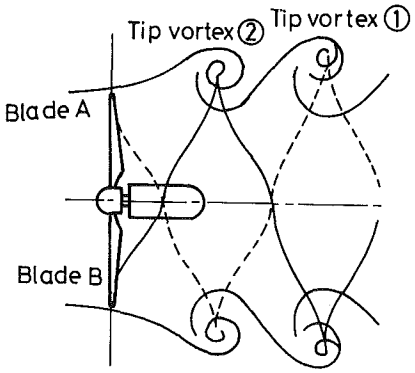

Fig. 8 Smoke line model of tip vortices behind rotor

m/s. Reynolds number for blade tip on the maximum power coefficients are about 1.5×10^5. However, for the smoke visualization method, this speed would cause the smoke to diffuse. The present experiment was performed with a wind speed of 3.5 m/s. Reynolds number is about 1.05×10^5. Figure 5 shows the relationships between *Cp* (power coefficient) and Φ (tip speed ratio) for different wind speed. Though some differences for *Cp* are seen the results of this visualization experiment are similar to those for speeds over 5 m/s.

3.2 Flow Visualization on the Blade Surface. We visualized the flow on the blade surface using the surface tuft method as shown in Fig. 6. In this figure, the upper row of

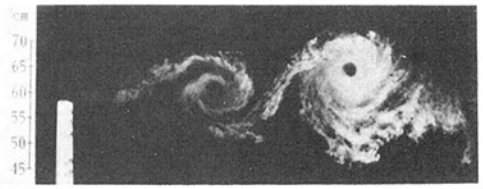

Fig. 9(*a*) Picture of tip vortex. Without tip vane on the blade tip. By smoke line method.

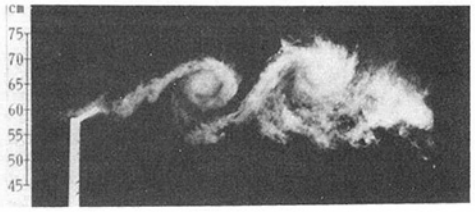

Fig. 9(*b*) Picture of tip vortex. With V(8 × 8) type tip vane on the blade tip. By smoke line method.

frames presents tuft photographs and the lower a model of the streamlines.

Figure 6a shows the flow on the blade surface of a plain tip at the point of maximum efficiency. The flow on the blade surface takes the same shape as the blade tip in the picture. Furthermore, it turns toward the leading edge at point A. Near the blade tip at point B, the tufts flap violently. The tip vortices are exhibiting random-motion behavior. This is difficult to understand from the picture

The V(8∗8)-type tip vane showed the highest performance in our experiment. Compared to the previous case in Fig. 6(*a*), Fig. 6(*b*) shows that the air flows along the chord at the blade tip. Furthermore, it no longer exhibits random-motion behavior, so that high performance can be obtained.

With a V(8∗10)-type tip vane (Fig. 5), it is clear that this type of tip vane yields nearly the same performance as the V(8∗8)-type tip vane. In Fig. 6(*c*), a little separation area can be seen from the motion of tufts at the corner of blade tip (D area in Fig. 6(*c*)), in which tuft directions become random, but not enough to diminish the output.

3.3 Smoke Visualization of the Flow Around the Blade Tip and the Tip Vortex

3.3.1 The Behavior of the Tip Vortex. The previous section presented flow visualizations of the flow on the blade surface using the surface tuft-method. Here, we provide pictures of the flow behind the rotary surface and analyze them in detail. First, in order to present a model of wind flow, we analyzed the relationship between the azimuth angle Ψ and the tip vortex.

Figure 7(*a*) is a picture at an azimuth angle of Ψ = 0 deg. The tip vortex near the blade will be referred to as vortex ①. Tip vortex ② is generated by blade B, and tip vortex ① is generated by blade A in the previous rotation. Figure 7(*b*) is taken at an azimuth angle of Ψ = 60 deg. From this picture, it can be seen that a new vortex ③ is generated just between vortex ② and the rotary surface. This tip vortex ③ is generated by blade A. Figure 7(*c*) shows that with an azimuth angle of Ψ = 120 deg, tip vortex ③ and tip vortex ② grow larger than before.

Although Fig. 7(*d*) seems similar to Fig. 7(*a*), the tip vortex has been changing. In Fig. 7(*a*), tip vortex ① is generated by blade A and tip vortex ② is generated by blade B. In Figs. 7(*b*) and 7(*c*), tip vortex ③ is generated by blade A.

In Fig. 7(*d*), another new tip vortex is generated by blade B. Figure 8 shows a model combining the previous pictures,

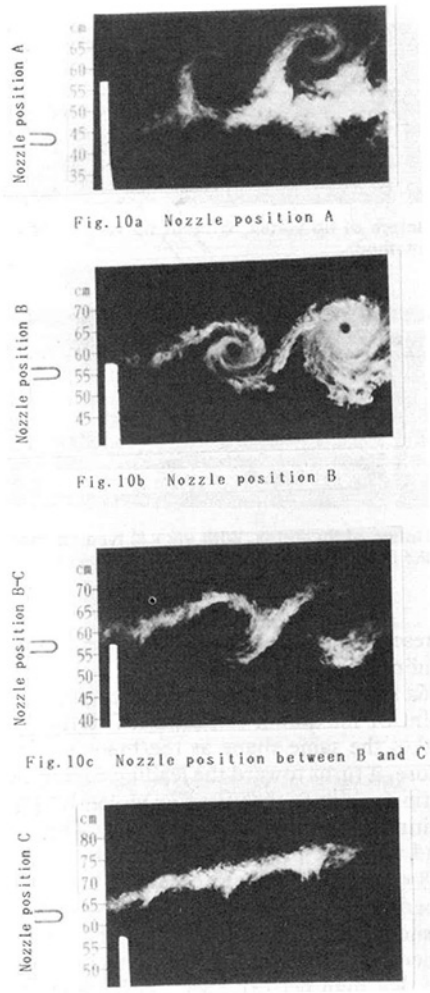

Fig. 10 Without tip vane. Flow visualization around blade tip by smoke line method

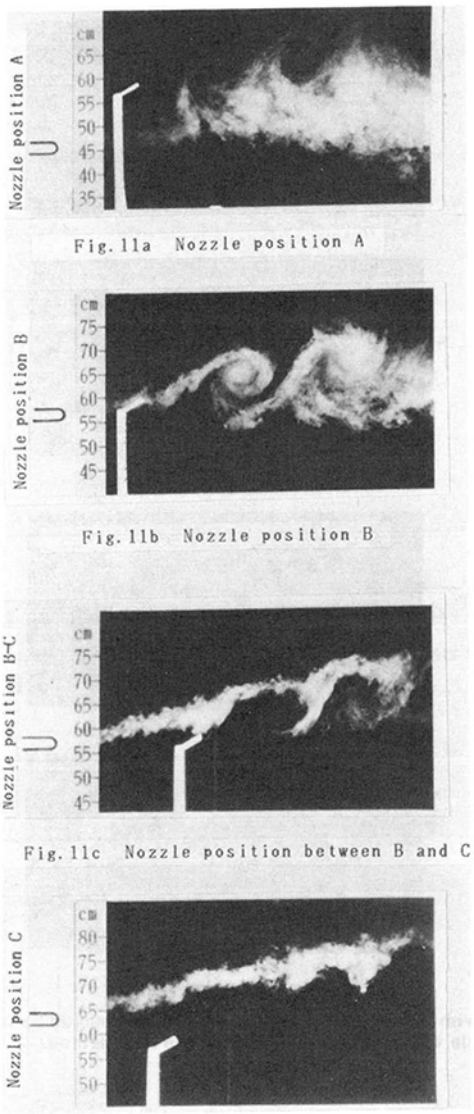

Fig. 11 With tip vane. Flow visualization around blade tip by smoke line method

i.e., a cross section of the spiral of vortices emanating from the blade tips.

3.3.2 Comparison of the Blades With and Without Tip Vane. We compared the flow of a blade with a tip vane and without a tip vane, taking into account the mechanism of the tip vortex generation described in the previous section. The pictures in Fig. 9 were taken at a wind speed of 3.5 m/s, an azimuth angle of $\Psi = 0$ deg, and a rotation speed near the most efficient point (270 rpm).

(*a*) Fig. 9(*a*) shows the induced vortex generated at the blade tip without a tip vane. In this picture, a strong vortex with clear core, like the eye of a typhoon or hurricane, is apparent. When a V(8 * 8)-type tip vane was used (Fig. 9(*b*), the generation of a tip vortex is restrained. No strong tip vortex like that in Fig. 9(*a*) can be found. This means that the tip vane can restrain the generation of a vortex at the blade tip.

(*b*) From Fig. 9, we examined the position of the vortex core generated by the blade tip. Compared with the blade without a tip vane, the vortex core with the V(8 * 8)-type tip vane is spread 4 cm to outside. From this picture, we understand that by using a tip vane, not only can the tip vortex be restrained, but the downstream flow can be spread successfully as well.

(*c*) Fig. 10 (without a tip vane) and Fig. 11 (with a tip vane) were shown to investigate the difference of the tip or trailing vortices. As shown in Fig. 12, the position of the smoke nozzle

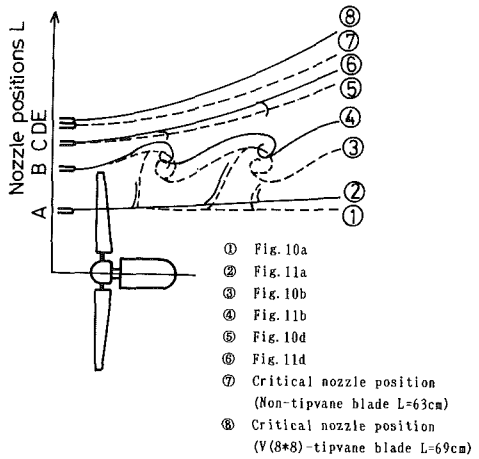

Fig. 12 The model of smoke lines around turbine rotor

is displaced in the radial direction upstream of the rotary surface. The solid line shows the position of the stream line when a tip vane is used, and the dashed line shows the position when no tip vane is used. By checking the relationship between the position of the smoke nozzle and how the induced vortices are generated, the extent of flow drawn to the rotary surface can be ascertained. Furthermore, by moving the nozzle further outside, we determined the position at which no effect of the tip vortex would appear. This position is 63 cm from the rotary center without a tip vane and 69 cm from the rotary center with a tip vane. This means that, when a tip vane is not used, the tip vortex can be found within 63 cm; beyond this the flow line bends only slightly. When a V(8 * 8)-type tip vane is used, though the generation of a tip vortex is restrained, the critical point of the tip vortex effect is expanded to 69 cm. This result shows that the flow expands radially by 6 cm when tip vane is used.

It is deduced from the above results and the velocity distributions around blade tip with and without tip vane, measured by authors [see references, Shimizu, Y., et al. 4 (1993)], that more air enters into the rotary surface when tip vane is set. The reference paper [Shimizu, Y., et al., 4 (1993)] shows the improved and increased axial velocity distributions near blade tip with tip vane, comparing the result without a tip vane.

4 Conclusions

We investigated the effect of tip vane through the flow visualization method and drew the following conclusions:

(1) The generation of the tip vortex is restrained. Flow turbulence near the blade tip and induced drag are reduced.

(2) The flow downstream of the wind turbine is spread successfully, by tip vanes.

(3) More air is drawn into the rotary surface.

(4) In order to achieve the above effects efficiently, a suitably shaped tip vane is required.

References

Shimizu, Y., Yoshikawa, T., and Matsumura, S., 1990, "Power Augmentation Effects of Horizontal Axis Wind Turbine by Tip Vane-2nd Report," *Trans. of JSME*, Vol. 56-522B, pp. 502-507.

Shimizu, Y., Imamura, H., Matsumura, S., Maeda, T., and Van Bussel, G. J. W., 1993, "Power Augmentation of Horizontal Axis Wind Turbine by Mie (Tip) Vane: Velocity Distribution around Tip of HAWT Blade With and Without Mie (Tip) Vane," SED-Vol. 14, *Wind Energy*, ASME 1993, pp. 143-148.

Van Bussel, G. J. W., 1986, "Status Rep. Tipvane Res," EWEA Conference, Rome, pp. 691-695.

Von Holten, Th., 1976, "Windmills with Diffuser Effect Induced by Small Tip Vanes," *Proceedings Ins. Symp. Wind Energy Syst.*, Cambridge, U.K.

Von Holten, Th., 1978, "Tipvane Research at T.U. Delft," Proceedings 2nd International Symp. Wind Energy, Paper F-2, Amsterdam.

ERRATA

T. S. Lu, "Steady Laminar Fluid Flow Through Variable Constrictions in Vascular Tube," *Journal of Fluids Engineering*, Vol. 116, March 1994, p. 66.

In the above paper the Associate Technical Editor was O. Baysal. The editor was incorrectly identified in the journal.

N. Ma
Department of Mechanical and Industrial Engineering, University of Illinois, Urbana, IL 61801

T. J. Moon
Mechanical Engineering Department, University of Texas, Austin, TX 78712-1063

J. S. Walker
Department of Mechanical and Industrial Engineering, University of Illinois, Urbana, IL 61801

Electromagnetic Pump With Thin Metal Walls

This paper treats a liquid-metal flow in a rectangular duct with a strong, uniform, transverse magnetic field and with thin metal walls, except for two finite-length, perfectly conducting electrodes in the side walls, which are parallel to the magnetic field. There are large velocities inside the boundary layers adjacent to the thin metal side walls, but not inside the layers adjacent to the electrodes. Upstream and downstream of the electrodes, a significant fraction of the total flow leaves and enters the side-wall boundary layers, respectively. For the particular duct treated here, the fully developed side layers, which carry 38.8 percent of the total flow, are realized at a distance of three characteristic lengths from the ends of the electrodes.

Introduction

A liquid metal can be pumped by the electromagnetic (EM) body force due to the interaction of an electric current between a pair of electrodes and a magnetic field produced by an external magnet. The pump treated here has a rectangular cross section, a uniform magnetic field applied perpendicular to the top and bottom walls, and a pair of perfectly conducting electrodes with an externally applied voltage difference in the side walls. A longitudinal and two cross sections are shown in Fig. 1. The characteristic length L is half the distance between the side walls, $2a$ is the dimensionless distance between the top and bottom, $2b$ is the dimensionless length of each electrode, and t is the thickness of all walls except the electrodes. The electrical conductivities of the liquid metal, non-electrode metal walls and electrodes are σ, σ_w, and ∞. The externally applied magnetic field is $B\hat{\mathbf{y}}$, where B is the magnetic flux density, while $\hat{\mathbf{x}}$, $\hat{\mathbf{y}}$, and $\hat{\mathbf{z}}$ are the Cartesian unit vectors. The dimensionless electric potential function ϕ has the constant values $\pm\phi_o$ for the electrodes at $z = \pm 1$.

We assume that the magnetic Reynolds number $R_m = \mu_p \sigma UL$ is sufficiently small that we can neglect the magnetic field produced by the electric currents in the liquid metal and duct walls. Here μ_p is the magnetic permeability of the liquid metal, and the characteristic velocity U is the average of the x component of the velocity. We assume that the Hartmann number $M = BL(\sigma/\mu)^{1/2}$ is large so that viscous effects are confined to Hartmann layers with $O(M^{-1})$ dimensionless thickness adjacent to the top and bottom, and to side layers with $O(M^{-1/2})$ dimensionless thickness adjacent to the side walls (Roberts, 1967). Here μ is the viscosity of the liquid metal. We also assume that the interaction parameter $N = \sigma B^2 L/\rho U$ is sufficiently large that inertial effects can be neglected everywhere, where ρ is the density of the liquid metal. Since the side layers adjacent to the thin metal side walls involve large, $O(M^{1/2})$ values of the dimensionless axial velocity u, the last assumption requires that $N \gg M^{3/2}$ (Walker et al., 1971).

Treatments of pumps with electrically insulating nonelectrode walls ($\sigma_w = 0$) are included in several textbooks (Shercliff, 1962). With $R_m \ll 1$, $M \gg 1$ and insulating walls, $u = 1$ everywhere, except in the viscous boundary layers which play no

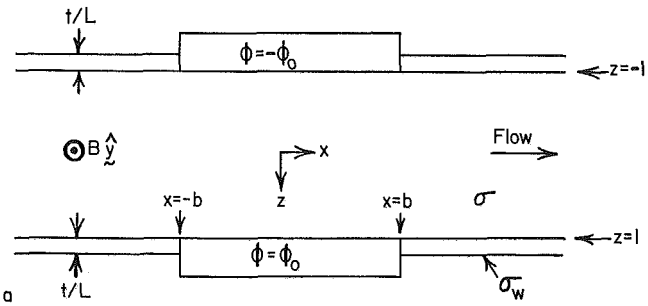

Fig. 1(*a*)

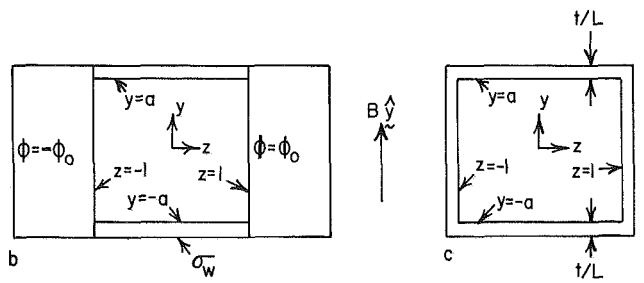

Fig. 1(*b*)

Fig. 1 Sections of an electromagnetic pump showing dimensionless coordinates and distances. (*a*) Longitudinal section perpendicular to the magnetic field, (*b*) cross section for $|x| < b$, (*c*) cross section for $|x| > b$.

Contributed by the Fluids Engineering Division for publication in the JOURNAL OF FLUIDS ENGINEERING. Manuscript received by the Fluids Engineering Division December 15, 1992; revised manuscript received October 27, 1993. Associate Technical Editor: R. L. Panton.

significant role in the problem. For this slug flow, ϕ is independent of y and is governed by Laplace's equation in x and z, with the prescribed values at the electrodes and with $\partial\phi/\partial z = 1$ at $z = \pm 1$ for $|x| > b$. In many uses of EM pumps, such as feed pumps for liquid sodium in fast breeder reactors, electronically insulating ceramic materials are not compatible with hot liquid metals, and duct walls must be metal. Since the pressure drop for a rectangular duct is proportional to the wall conductance ratio $c = \sigma_w t/\sigma L$, the design objective is to minimize c by minimizing t. With liquid sodium and stainless steel walls, strength limitations generally keep values of c at roughly 0.1 for typical pumps. With thin metal walls, the flow is not slug flow, a significant fraction of the total flow is carried by $O(M^{1/2})$ values of u inside the side layers for $|x| > b$, flow leaves and enters these layers upstream and downstream of the electrodes, respectively, and flow is redistributed in the y direction inside the side layers. Therefore the flows in EM pumps with insulating and thin-metal walls are quite different.

In the inviscid core region, the dimensionless EM body force, $\mathbf{j} \times \hat{\mathbf{y}}$, exactly balances the pressure gradient, ∇p, where $\mathbf{j}$ is the dimensionless electric current density. All or part of the electric current entering or leaving each thin metal wall at $z = \pm 1$ flows in the y direction inside the side wall, and this requires a voltage difference between $y = 0$ and $y = \pm a$. Since voltage is continuous at the liquid-solid interfaces, the y-variations of ϕ inside the side layers drive currents in the y direction and thus locally reduce the value of j_z from its core value. The corresponding reduction in the side-layer EM body force from its core value leaves part of the pressure gradient unbalanced, so that the side-layer flow accelerates until $u = O(M^{1/2})$ and viscous forces restore the force balance. For fully developed flow with $c = 0.1$ and $a = 2$, 38.8 percent of the total flow is carried by the high-velocity side layers, so that $u = 0.612$ in the inviscid core (Walker, 1981). Since ϕ is constant throughout each electrode, there are no significant y-variations of ϕ and no $O(M^{1/2})$ values of u inside the side layers adjacent to the electrodes, and the average value of u in the core for $|x| < b$ is 1. Downstream of the electrodes, 38.8 percent of the total flow enters the side layers from the core. The flow entering a side layer has a uniform distribution in y, while the fully developed side layer has a parabolic flow distribution from zero at $y = \pm a$ to a maximum at $y = 0$. Therefore there is a redistribution of the flow in the y direction inside the high-velocity side layers adjacent to the thin metal side walls for $|x| > b$.

There have been many analytical, numerical and experimental studies of liquid-metal flows in EM pumps with insulating walls or thin metal walls. For the three-dimensional flows in pumps with thin metal walls, the numerical solution of the full Navier-Stokes and electromagnetic equations becomes progressively more challenging as the magnetic field strength is increased and the thickness of each boundary layer decreases. Some researchers have ignored variations along magnetic field lines and have developed numerical solutions of the full equations for the resultant two-dimensional problems for strong magnetic fields (Winowich and Hughes, 1983). In this paper we present a numerical solution for the three-dimensional flow with a magnetic field which is sufficiently strong that inertial effects are negligible. Our approach complements the numerical solution of the full Navier-Stokes equations: for moderate magnetic-field strengths, inertial effects are important, our approach is invalid, and the solution of the full equations is both necessary and practical because boundary-layer thicknesses are modest; for strong magnetic fields, the solution of the full equations becomes extremely difficult, but our approach is then valid.

While many future applications with superconducting magnets and low-density liquid metals will have very large interaction parameters, most EM pump experiments to date have involved relatively weak magnetic fields and often high-density mercury. Alexion and Keeton (1985) present experimental measurements of pressure in an EM pump with thin metal walls and large values of the interaction parameter. Their pressure variations agree well with out results, but quantitative comparisons are not possible because their magnetic-field strength decreases to zero near the end of the electrodes while we assume a uniform magnetic field everywhere.

Analysis

For $R_m \ll 1$, $M \gg 1$, and $N \gg M^{3/2}$, the dimensionless equations governing the core variables are

$$\nabla p = \mathbf{j} \times \hat{\mathbf{y}}, \quad \mathbf{j} = -\nabla\phi + \mathbf{v} \times \hat{\mathbf{y}}, \quad \nabla \cdot \mathbf{v} = \nabla \cdot \mathbf{j} = 0, \quad (1a\text{–}d)$$

where $\mathbf{v} = u\hat{\mathbf{x}} + v\hat{\mathbf{y}} + w\hat{\mathbf{z}}$ is the velocity normalized by U, while p, $\mathbf{j}$, and ϕ are normalized by σUB^2L, σUB and UBL, respectively. Equation (1a) is the momentum equation without the inertial and viscous terms, (1b) is Ohm's law, Eq. (1c) is the continuity equation and Eq. (1d) is the conservation of charge equation. The flow is symmetric about the $y = 0$ and $z = 0$ planes, and, without inertial effects, it is also symmetric about the $x = 0$ plane. Therefore we need only treat the flow for $0 \le x < \infty$, $0 \le y \le a$, and $0 \le z \le 1$, with appropriate symmetry conditions at the $x = 0$, $y = 0$ and $z = 0$ planes.

For thin walls $t \ll L$. Neglecting $O(t^2/L^2)$ terms, the electric potential of the top wall at $y = a$ for $x \ge 0$, ϕ_t, is independent of y, and the electric potential of the thin metal side wall at $z = 1$ for $x > b$, ϕ_s, is independent of z (Shercliff, 1956). The tangential components of the dimensionless electric current density in the top and thin metal side are

$$j_{xt} = -\frac{\sigma_w}{\sigma}\frac{\partial\phi_t}{\partial x}, \quad j_{zt} = -\frac{\sigma_w}{\sigma}\frac{\partial\phi_t}{\partial z}, \quad (2a,b)$$

$$j_{xs} = -\frac{\sigma_w}{\sigma}\frac{\partial\phi_s}{\partial x}, \quad j_{ys} = -\frac{\sigma_w}{\sigma}\frac{\partial\phi_s}{\partial y}. \quad (2c,d)$$

With an electrical insulator at the outside surface of each thin metal wall, integration of Eq. (1d) through the top or side yields boundary conditions on the ϕ and $\mathbf{j}$ in the liquid metal (Walker, 1981),

$$\phi = \phi_t(x,z), \quad j_y = -c\left(\frac{\partial^2\phi_t}{\partial x^2} + \frac{\partial^2\phi_t}{\partial z^2}\right), \text{ at } y = a, \quad (3a,b)$$

$$\phi = \phi_s(x,y), \quad j_z = -c\left(\frac{\partial^2\phi_s}{\partial x^2} + \frac{\partial^2\phi_s}{\partial y^2}\right), \text{ at } z = 1, \text{ for } x > b. \quad (3c,d)$$

While we neglect $O(t^2/L^2)$ terms in order to derive the conditions (3b,d), we keep $c = \sigma_w t/\sigma L$ as an O(1), specifiable parameter (Moon and Walker, 1990).

The Hartmann layer at $y = a$ satisfies the no-slip conditions at the top and matches any core values of u and w. The jumps in v, j_y and ϕ across the Hartmann layer are $O(M^{-1})$, $O(M^{-1})$, and $O(M^{-2})$, respectively (Walker et al., 1971), so that the core variables must satisfy the conditions (3a,b) and

$$v = 0 \text{ at } y = a, \quad (4)$$

neglecting $O(M^{-1})$ terms. The solution of the core Eqs. (1) which satisfies the conditions (3a,b, 4) and the symmetry conditions that $j_y = v = 0$, at $y = 0$, is

$$p = p_c(x,z), \quad \phi = \phi_t(x,z), \quad j_x = \frac{\partial p}{\partial z}, \quad j_y = 0, \quad j_z = -\frac{\partial p}{\partial x}, \quad (5a\text{–}e)$$

$$u = \frac{\partial\phi}{\partial z} - \frac{\partial p}{\partial x}, \quad v = 0, \quad w = -\frac{\partial\phi}{\partial x} - \frac{\partial p}{\partial z} \quad (5f\text{–}h)$$

where p_c and ϕ_t are governed by

$$\frac{\partial^2 p_c}{\partial x^2} + \frac{\partial^2 p_c}{\partial z^2} = 0, \quad \frac{\partial^2\phi_t}{\partial x^2} + \frac{\partial^2\phi_t}{\partial z^2} = 0, \quad (6a,b)$$

for $0 \le x < \infty$ and $0 \le z \le 1$. The symmetry conditions are

$$p_c=0, \quad \frac{\partial \phi_t}{\partial x}=0, \text{ at } x=0, \quad \frac{\partial p_c}{\partial z}=0, \quad \phi_t=0, \text{ at } z=0. \tag{7a-d}$$

The boundary conditions on p_c and ϕ_t at $z=1$ are different for $x<b$ and $x>b$.

For $0\le x\le b$, there are no $O(M^{1/2})$ velocities inside the side layer and the jumps in ϕ and w across the side layer are $O(M^{-1/2})$ (Walker et al., 1971). Therefore the boundary conditions are

$$\phi_t=\phi_o, \quad \frac{\partial p_c}{\partial z}=0, \text{ at } z=1, \text{ for } 0\le x\le b, \tag{8}$$

neglecting $O(M^{-1/2})$ terms. The separation of variables solutions for the boundary value problems (6-8) are

$$\phi_t=\phi_o z+\sum_{n=1}^{\infty} A_n \frac{\cosh(n\pi x)}{\cosh(n\pi b)} \sin(n\pi z), \tag{9a}$$

$$p_c=(\phi_o-1)x+\sum_{n=1}^{\infty} B_n \frac{\sinh(n\pi x)}{\cosh(n\pi b)} \cos(n\pi z), \tag{9b}$$

for $0\le x\le b$. The constants $[\cosh(n\pi b)]^{-1}$ are included in each term in order to avoid exponentially large terms in the matching at $x=b$ which determines the coefficients A_n and B_n.

For $x>b$, the jump in j_z across the side layer is $O(M^{-1/2})$ (Moon and Walker, 1990), so that the condition (3*d*) becomes an equation governing ϕ_s,

$$\frac{\partial^2 \phi_s}{\partial x^2}+\frac{\partial^2 \phi_s}{\partial y^2}=\frac{1}{c}\frac{\partial p_c}{\partial x}(x,1), \tag{10}$$

for $b<x<\infty$ and $0\le y\le a$. The symmetry condition is

$$\frac{\partial \phi_s}{\partial y}=0, \text{ at } y=0. \tag{11}$$

As long as there is no electrical insulator between the top and side walls at the corner, the values of ϕ here must be the same, and the electric current into the corner from the side (2*d*) must equal the current into the top from the corner (2*b*), so that

$$\phi_t(x,1)=\phi_s(x,a), \quad \frac{\partial \phi_t}{\partial z}(x,1)=-\frac{\partial \phi_s}{\partial y}(x,a). \tag{12a,b}$$

The details of the high-velocity side layer for $x>b$ can be ignored if we guarantee conservation of mass for the entire flow (Moon and Walker, 1990). In the side layer, u_{SL}, ϕ_{SL} and j_{zSL} are $O(M^{1/2})$, O(1) and O(1), respectively, so that the z component of Ohm's law (1*b*) gives $u_{SL}=\partial\phi_{SL}/\partial\zeta$, where $\zeta=M^{1/2}(z-1)$ is the stretched coordinate. The fraction of the total flow carried by the side layers at any $x=$ constant cross section is

$$Q_{SL}=\frac{1}{a}\int_0^a\int_{-\infty}^0 u_{SL}\,d\zeta dy=\frac{1}{a}\int_0^a \phi_s(x,y)dy-\phi_t(x,1). \tag{13}$$

The fraction of the total flow carried by the core is given by the integral of the solution (5*f*),

$$Q_c=\frac{1}{a}\int_0^a\int_0^1 u\,dz dy=\phi_t(x,1)-\int_0^1 \frac{\partial p_c}{\partial x}(x,z)dz. \tag{14}$$

Since the mass flux deficiency in the Hartmann layers is $O(M^{-1})$,

$$Q_{SL}+Q_c=\frac{1}{a}\int_0^a \phi_s(x,y)dy-\int_0^1 \frac{\partial p_c}{\partial x}(x,z)dz=1, \tag{15}$$

for $x>b$. The condition (15) is a solubility condition which guarantees the existence of a side-layer solution with (1) $\phi_{SL}=\phi_s$ at $\zeta=0$, (2) $\phi_{SL}\to\phi_t(x,1)$, as $\zeta\to-\infty$, and (3) a volumetric flow rate whose sum with the core flow rate gives a value which is independent of x.

The solution for $x>b$ is given by the superposition of fully developed flow in a rectangular duct with thin metal walls (Walker, 1981) and a three-dimensional disturbance which decays exponentially as $x\to\infty$. The separation of variables solutions for Eqs. (6), (10) and the symmetry conditions (7*c*,*d*, 11) are presented by Moon et al. (1992),

$$p_c=P_o-\frac{cK}{a}(x-b)+\sum_{n=1}^{\infty} D_n \cos(\lambda_n z)\exp[-\lambda_n(x-b)], \tag{16a}$$

$$\phi_t=Kz+\sum_{n=1}^{\infty} C_n \sin(\lambda_n z)\exp[-\lambda_n(x-b)], \tag{16b}$$

$$\phi_s=K\left[1+\frac{1}{2a}(a^2-y^2)\right]+\sum_{n=1}^{\infty}\left[E_n\cos(\lambda_n y)-\frac{D_n}{\lambda_n c}\cos(\lambda_n)\right]\times\exp[-\lambda_n(x-b)], \tag{16c}$$

where

$$K=\left(1+\frac{a}{3}+\frac{c}{a}\right)^{-1}.$$

The volumetric flow condition (15) and the continuity of potential condition (12*a*) give expressions for D_n and C_n in terms of E_n,

$$D_n=\frac{E_n c\sin(\lambda_n a)}{a[\cos(\lambda_n)-\lambda_n c\sin(\lambda_n)]}, \tag{17a}$$

$$C_n=\frac{1}{\sin(\lambda_n)}\left[E_n\cos(\lambda_n a)-\frac{D_n}{\lambda_n c}\cos(\lambda_n)\right]. \tag{17b}$$

We introduce the solutions (16, 17) into the electric current continuity condition (12*b*) to obtain a characteristic equation for the eigenvalues λ_n

$$a\lambda_n\cos[\lambda_n(a+1)][\lambda_n c\sin(\lambda_n)-\cos(\lambda_n)]+\sin(a\lambda_n)\cos^2(\lambda_n)=0. \tag{18}$$

There are an infinite number of discrete, real, positive values of λ_n which satisfy Eq. (18). We use the first 50 eigenvalues and the corresponding expressions (17) for D_n and C_n in the series solutions (16) truncated at $n=50$ (Moon et al., 1992).

We truncate the upstream series solutions (9) at $n=24$, and we match the solutions at $x=b$ with the method of weighted residuals in order to determine the coefficients, A_n, B_n, E_n, and P_o. At $x=b$, ϕ_t, p_c and their axial derivatives are continuous, while $\phi_s(b^+,y)=\phi_o$. The weighted residual is

$$\begin{aligned} R=\int_0^1 \{ & w_v[\phi_t(b^-,z)-\phi_t(b^+,z)]^2 \\ & + w_v w_p[p_c(b^-,z)-p_c(b^+,z)]^2 \\ & + \left[\frac{\partial \phi_t}{\partial x}(b^-,z)-\frac{\partial \phi_t}{\partial x}(b^+,z)\right]^2 \\ & + w_p\left[\frac{\partial p_c}{\partial x}(b^-,z)-\frac{\partial p_c}{\partial x}(b^+,z)\right]^2\Big\}dz \\ & + w_v\int_0^a [\phi_s(b^+,y)-\phi_o]^2 dy, \end{aligned} \tag{19}$$

where values at $x=b^-$ and at $x=b^+$ are evaluated from the solutions (9) and the solutions (16), respectively. Values are weighted with the factor w_v relative to their axial derivatives, and p is weighted with the factor w_p relative to ϕ. The series expansions for the axial derivatives involve factors of λ_n or $n\pi$, and these factors are large for the last terms in each series. Without w_v, the method of weighted residuals produces an excellent match of the axial derivatives, but a very poor match of the values. The magnitudes of ϕ and p may be quite different, so w_p is needed to insure that equally good matches are achieved. As the values of w_v and w_p are changed, certain

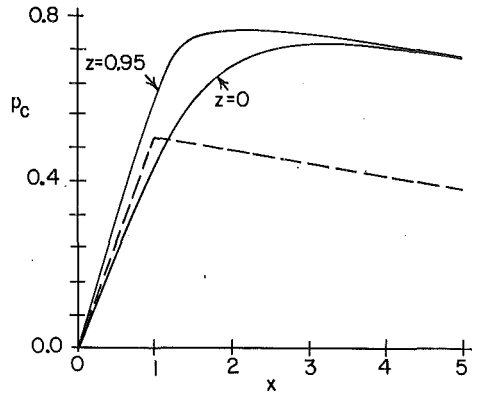

Fig. 2 The pressure p_c at $z=0$ and $z=0.95$. The dashed line is p_c for two different locally fully developed flows.

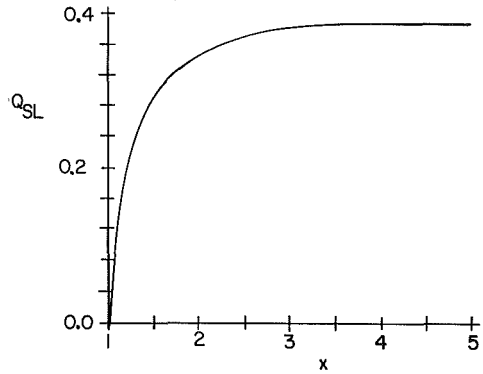

Fig. 3 Fraction of the total flow carried by the side layers at each cross section

matches improve at the cost of other matches, and the values are adjusted by trial and error until all matches involve a comparably small error.

The residual is minimized for this set of coefficients with the equations

$$\frac{\partial R}{\partial P_o}=0; \quad \frac{\partial R}{\partial A_n}=\frac{\partial R}{\partial B_n}=0, \text{ for } n=1 \text{ to } 24;$$

$$\frac{\partial R}{\partial E_n}=0, \text{ for } n=1 \text{ to } 50.$$

This minimization gives 99 simultaneous, linear, algebraic equations for the 99 unknown coefficients P_o, A_n, B_n, and E_n. Once the values of the coefficients are determined by Gauss elimination, the solutions (9, 16) give p_c, ϕ_f and ϕ_s, while the expression (5, 13) give the core variables and the flow rate in the side layer for $x>b$.

Results

We present some typical results for the case with $a=2$, $b=1$, $c=0.1$ and $\phi_o=1.5$. For this case, excellent matching at $x=b$ is achieved with $w_v=2$ and $w_p=0.5$. The pressure p_c at $z=0$ and $z=0.95$ is presented in Fig. 2. The dashed line represents p_c for locally fully developed flow, namely $p_c=(\phi_o-1)x$, for $x<b$, and $p_c=(\phi_o-1)b-(cK/a)(x-b)$, for $x>b$. For the locally fully developed flow, the electric current between the electrodes is artificially confined to the axial region $|x|<b$. In reality, this current fringes into the regions $|x|>b$, so that more current flows between the electrodes for a given value of ϕ_o, which produces a larger pressure rise than that for locally fully developed flow. Since more current flows between the electrodes, the actual magnitude of j_z at $z=1$ for $0\le x\le b$ is larger than that for locally fully developed flow and the pressure gradient is larger, as illustrated by p_c at $z=0.95$ for $x<1$ in Fig. 2. However, at $x=b$, the electrode ends, and j_z at $z=1$ abruptly changes signs, so that the pressure gradient becomes negative. At $z=0$, the current between the electrodes is spread over a large axial distance, so that the magnitude of j_z is everywhere less than that for locally fully developed flow with $j_z=-(\phi_o-1)$. Therefore the pressure gradient at $z=0$ is less than that for locally fully developed flow, but the pressure continues to rise until $x=3$. The difference between p_c at $z=1$ and $z=0$ is equal to the total axial current for $0\le z\le 1$, due to fringing. This axial current reaches a maximum at $x=b$.

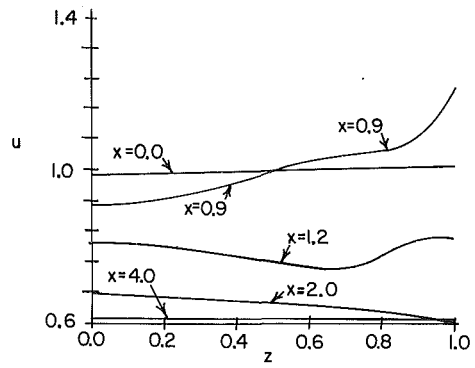

Fig. 4 Core velocity y at various cross sections

The fraction of the total flow carried by the side layers, $Q_c(x)$, is presented in Fig. 3. As x increases from $b=1$, Q_c increases quickly from 0 and has essentially reached the fully developed value of 0.388 by $x=4$. The axial core velocity u at various cross sections is presented in Fig. 4. For $x<b$, there is no flow inside the side layers, so that the average value of u is 1 at every cross section. However, as x increases from 0, the flow begins to migrate toward the sides, so that $u=1.2$ and 0.9 at $z=1$ and $z=0$, respectively, at $x=0.9$. As x increases from b, flow enters the side layer, and the average value of u decreases. The values of u decreases throughout the core, but the decrease is initially largest near $z=1$ as the local flow enters the side layer. The fully developed value of 0.612 is realized by $x=4$.

Conclusion

In an electromagnetic pump with a strong, uniform, transverse magnetic field and with electrically insulating walls (except for the electrodes), $u=1$ and $w=0$ throughout the core, and we need only solve a two-dimensional potential problem. However, with thin metal walls, the flow is a complex three-dimensional one. There are no high-velocity layers adjacent to the electrodes, so that the average value of u is 1 here, but the flow begins to concentrate near the sides as it approaches the ends of the electrodes. Beyond the ends of the electrodes, part of the flow enters the high-velocity side layers at $z=\pm 1$ and is vertically redistributed toward the $y=0$ plane inside these layers. For the present duct with $a=2$ and $c=0.1$, the side layers eventually carry 38.8 percent of the total flow, so that u decreases to 0.612. The flow essentially reaches fully developed flow after three characteristic lengths beyond the ends of the electrodes.

Acknowledgments

This research was supported by the National Science Foundation under grants CTS 91-20448 and DDM 92-58413, by the Bureau of the Engineering Research at The University of Texas at Austin, and by the Fusion Power Program at Argonne National Laboratory.

References

Alexion, C. C., and Keeton, A. R., 1985, "Experiments on a Large Thin-Wall Duct," *Single- and Multi-Phase Flows in an Electromagnetic Field*, H. Branover, P. S. Lykoudis and M. Mond, eds., American Institute of Aeronautics and Astronautics, New York, pp. 516–532.

Moon, T. J., Hua, T. Q., Walker, J. S., and Picologlou, B. F., 1992, "Liquid Metal Flow in a Simple Manifold with a Strong Transverse Magnetic Field," *Applied Scientific Research*, Vol. 49, pp. 49–65.

Moon, T. J., and Walker, J. S., 1990, "Liquid Metal Flow Through a Sharp Elbow in the Plane of a Strong Magnetic Field," *Journal of Fluid Mechanics*, Vol. 213, pp. 397–418.

Roberts, P. H., 1967, *An Introduction to Magnetohydrodynamics*, American Elsevier, New York.

Shercliff, J. A., 1956, "The Flow of Conducting Fluids in Circular Pipes under Transverse Magnetic Fields," *Journal of Fluid Mechanics*, Vol. 1, pp. 644–666.

Shercliff, J. A., 1962, *Theory of Electromagnetic Flow Measurement*, Cambridge University Press, Cambridge.

Walker, J. S., 1981, "Magnetohydrodynamic Flows in Rectangular Ducts with Thin Conducting Walls. Part 1. Constant Area and Variable Area Ducts with Strong Uniform Magnetic Fields," *Journal of Mécanique*, Vol. 20, pp. 79–112.

Walker, J. S., Ludford, G. S. S., and Hunt, J. C. R., 1971, "Three-Dimensional MHD Duct Flows with Strong Transverse Magnetic Fields. Part 2. Variable Area Rectangular Ducts with Conducting Sides," *Journal of Fluid Mechanics*, Vol. 46, pp. 657–684.

Winowich, N. S., and Hughes, W. F., 1983, "A Finite Element Analysis of Two-Dimensional MHD Flow," *Liquid Metal Flows and Magnetohydrodynamics*, H. Branover, P. S. Lykoudis and A. Yakhot, eds., American Institute of Aeronautics and Astronautics, New York, pp. 313–322.

C. H. Liu
Research Student.
Present Address: Chung Shan Institute of Science and Technology, Lung-Tan, Taiwan

C. Vafidis
Research Fellow.
Present Address: Centro Ricerche Fiat, Orbasano, Torino, Italy

J. H. Whitelaw
Professor.

Department of Mechanical Engineering, Imperial College of Science, Technology and Medicine, Exhibition Road, London SW7 2BX, U.K.

Flow Characteristics of a Centrifugal Pump

Measurements of velocity have been obtained in a centrifugal pump in terms of angle-resolved values in the impeller passages, the volute, the inlet and exit ducts and are presented in absolute and relative frames. The pump comprised a radial flow impeller with four backswept blades and a single volute, and the working liquid had the same refractive index as the transparent casing to facilitate the use of a laser-Doppler velocimeter. The flows in the impeller passages were found to depart from the curvature of the blade surfaces at off-design conditions with separation from the suction surface and from the shroud. Secondary flows from the suction to pressure surfaces were dominated by the influences of the relative motion between the shroud and impeller surfaces and the tip leakage. Geometric differences of 0.5 mm and one degree in spacing of the four blades caused differences in passage velocity of up to 6 percent of the impeller tip velocity close to the design flowrate and up to 16 percent at the lowest discharge. The flowrate from each impeller passage varied with volute circumferential position by up to 25 percent at an off-design flowrate. Poor matching of the impeller and volute at off-design conditions caused swirl and separation in the inlet and exit pipes.

Introduction

There have been many investigations of velocity characteristics of pump flows including those of Hamkins and Flack (1987), Sideris and van dem Braembussche (1987), and Flack Hamkins and Brady et al. (1987), and they have been paralleled by measurements in compressors Eckhardt (1976), Adler and Levy (1979), and Kjork and Lofdahl (1989). In general, however, the measurements have been limited so that little has been revealed of the flow within blade passages. A summary of some of the findings has been provided by Liu (1992) who also gives further details of the present work.

Here we are concerned with the inlet, blade passages and volute of a centrifugal pump which was modified to allow optical access and, thereby, measurements by laser-Doppler velocimetry. In particular, the inlet and exit ducts, casing and volute of the present pump were manufactured from acrylic with the same refractive index as the working fluid to allow detailed velocity measurements for a range of conditions extending from the design condition to near shutdown.

The following section describes the flow configuration, the instrumentation, and possible sources of measurement uncertainty. The results are presented and discussed in the third section with separate consideration given to the inlet and exit flows, the absolute and relative flows in the impeller passages and the flow in the volute passage. The report ends with a summary of the more important conclusions.

Contributed by the Fluids Engineering Division for publication in the Journal of Fluids Engineering. Manuscript received by the Fluids Engineering Division October 17, 1992; revised manuscript received October 6, 1993. Associate Technical Editor: L. Nelik.

Flow Configuration and Instrumentation

The experimental arrangement comprised the pump, the circuit for the temperature-controlled liquid, the laser velocimeter and the encoder which identified the shaft angle and rotating speed of the impeller. The centrifugal pump (Price model SC100-150) was driven by an electric motor running at 2910 rpm and circulated liquid from and to a 70 litre tank through 36 and 28.5 mm inlet and exit pipes, respectively. The flow was regulated by a valve downstream of the exit pipe and measured by a sharp edge orifice meter, calibrated to an accuracy of better than 3 percent. The impeller of Fig. 1 had four backswept blades of 2.5 mm thickness with the blade height tapered from 11.2 mm at an inner radius of 21 mm to 6.2 mm at the outer radius of the impeller of 62.7 mm. The clearance between the impeller tip and shroud was adjusted to 0.5 mm, smaller than the manufacturer's nominal value. The curve of the impeller blade was a logarithmic spiral with an entrance angle of the flow of around 30 degrees and an exit angle of 58 degrees which was near-constant between radii of 40 and 62.7 mm.

The original cast stainless steel casing of the pump was replaced by a cast acrylic component of rectangular external shape and internal dimensions identical to those of the metal components. This was achieved by moulding a core of the metal casing in silicon rubber, creating a casting of plaster of Paris, moulding a core of low melting-point alloy (MCP 70) and a second casting, this time of acrylic. The final cast was machined to provide flat external surfaces and polished on its internal and external surfaces. The finished acrylic casing was annealed at 82°C for 35 hours with slow heating and cooling. The final internal dimensions were measured and found to be within 0.5 mm of those of the original casing and volute.

However, the head of the pump was found to be around 17 percent higher with the perspex casing due probably to the smaller impeller tip clearance and the machined and polished inner surfaces.

The working fluid was a mixture of 31.8 percent by volume of 1, 2, 3, 4-tetrahydronapthalene (tetraline) and oil of turpentine with density and kinematic viscosity of 0.893 kg/m^3 and 1.74×10^{-6} m^2/s, respectively, at 25°C. The Reynolds number based on the impeller diameter of 125.4 mm and tip velocity of 19.1 m/s was 1.38×10^6. The mixture was maintained at a temperature of 25 ± 0.2°C by a temperature controller (Eurotherm, type 818), with a heater and cooler installed within the storage tank and a platinum resistance sensor near the pump outlet to maintain a refractive index of 1.49, identical to that of the cast acrylic. The design point of the pump was determined based on the criteria of equal angular momentum of the flow at the impeller discharge and at the throat of the volute see Karassik et al. (1976). For the present speed of 2910 Rpm, the design flowrate was 2.72×10^{-3} m^3/s (Q_n), equivalent to a flow coefficient, F, of 0.058, and the experimental conditions comprised a range of flowrates between 93 and 15 percent of the design value, see Table 1.

The laser-Doppler velocimeter was similar to that used in the investigation of Liu et al. (1990) and comprised a one-watt region argon-ion laser (514.5 nm wavelength) and a transmitting optics based on diffraction grating to provide beam splitting and frequency shifts up to 13 MHz. The collection optical system comprised a lens of 200 mm focal length, a 100 μm diameter pinhole and a photomultiplier (EMI model 9817B). The combination of the transmitting and receiving optics and a near 90 deg scattering angle led to a measurement volume of 52 and 200 μm in diameter and length, respectively. The optical components were secured to an optical bench which was translated in three orthogonal directions with accuracy of location better than 0.1 mm in each direction. The Doppler signal, based on natural contaminants in the liquid, was processed by a frequency counter (TSI model 1990c) and interfaced to a microcomputer (IBM PC-AT), together with the pulse train from the optical shaft encoder with its resolution of 0.25 degrees. The digital information was collected in sequences of up to 1.4×10^6 velocity values and used subsequently to provide angle-resolved velocity traces of up to 2300 rotation cycles or ensemble averaged values based on angular windows of one degree. The ensemble averaged velocity statistics in each angular window were calculated from sample sizes between 1000 and 4000 velocity values depending on the magnitude of the rms of the fluctuations.

The possible sources of uncertainty associated with the measurements of velocity were considered in detail by Liu and by Liu et al., and include aspects of the optical arrangements, the signal and data-processing systems and the particles which represent the flow. The velocity fluctuations occurred at moderate frequency so that the particles were able to follow the flow so that no inaccuracy should be attributed to this source. Similarly, the signal processing system is unlikely to have given rise to important uncertainties except where the software logic tended to restrict the number of measurements per unit time; operation over a time sufficient to realize the number of velocity values indicated in the previous paragraph limited the magnitude of the resulting uncertainty. Nevertheless, statistical effects, together with velocity-gradient broadening due to the finite dimensions of the measuring volume were responsible for maximum uncertainties in the ensemble-averaged mean and rms velocities of 2 and 5 percent of the local values respectively with smaller values away from surfaces. The use of refractive index matching reduced position errors to less than 0.2 mm.

Results and Discussion

The coordinate systems of Fig. 1 were chosen to facilitate presentation of the flows in different regions of the pump: the inlet and exit flows are described by the Cartesian coordinates, x-y-z, with the origins shown in the figure; the absolute flows in the impeller and the volute are described by the cylindrical coordinates, r-θ-z, in the volute, with an additional set of cylindrical coordinates for the relative flow in the impeller. The measurement stations of the flows in the impeller and volute are identified by the circumferential angle Ψ measured counter-clockwise from the cutwater. The impeller shaft angle ϕ was measured counter-clockwise with the zero on each revolution identified by a marker pulse from the shaft encoder, which was purposely aligned with the plane of $\Psi=330$ deg and with one of the impeller blade tips. The relative angular coordinate Ω on the impeller was measured from suction (SS) to pressure surface (PS) with its origin at the center of the blade thickness. The velocity values are normalized by the impeller

Nomenclature

C_n = relative cross-stream mean velocity
C_s = relative streamwise mean velocity
D_e = exit pipe diameter (= 28.5 mm)
D_i = inlet pipe diameter (= 36 mm)
H = head
n = number of blade
N = impeller rotation speed (= 2910 rpm)
Q = flowrate
Qn = design flowrate
r = radius
R = radius of inlet pipe, $Di/2$
Re = Reynolds number ($=UD/\nu$)
R_t = impeller outer diameter (= 62.7 mm)
t = impeller blade thickness (= 2.5 mm)
U, V, W = absolute mean velocities
u', v', w' = absolute rms of velocity fluctuations
U_e = bulk mean velocity in the exit pipe
U_i = bulk mean velocity in the inlet pipe
V_R = theoretical radial velocity at R_t, $\left(S=\dfrac{Q}{\left(2pR_t-n\dfrac{t}{\cos\beta}\right)(Z_t+\delta)}\right)$
$\hat{v}$ = area averaged radial velocity, $\left(=\dfrac{1}{A}\int_A V\,dA\right)$
W_R = theoretical absolute tangential velocity at R_t, ($=W_t-V_R\tan\beta$)
W_t = impeller peripheral velocity at R_t (= 19.1 m/s)
$\tilde{w}$ = mass averaged tangential velocity, $\left(=\dfrac{\int_A V\,W\,da}{\int_a V\,da}\right)$
Z_t = impeller blade height at R_t (= 6.2 mm)
β = blade angle (= 58 deg for $r \geq 40$ mm)
δ = blade tip clearance ($\approx$ 0.5 mm)
Φ = flow coefficient $\left(=\dfrac{Q}{2p\,R_t\,Z_t\,W_t}\right)$
ϕ = impeller shaft angle
ν = kinematic viscosity of the liquid ($=1.74\times10^{-6}$ m^2/s)
ρ = density of the liquid (= 0.893 kg/m^3)
ω = impeller angular velocity
Ω = relative angular coordinate on the impeller
Ψ = volute circumferential angle

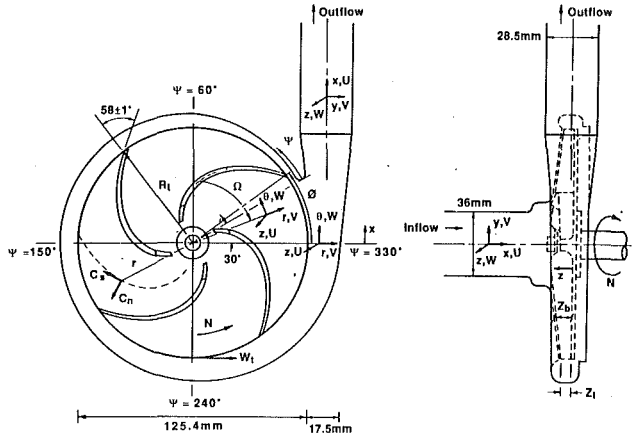

Fig. 1 Dimensions of the centrifugal pump and coordinate systems

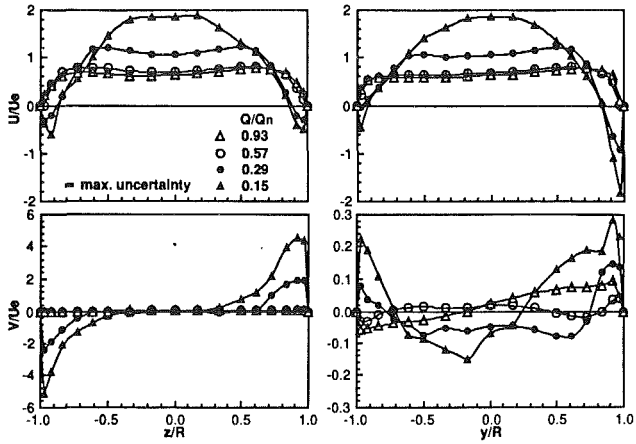

Fig. 2 Radial profiles of x-component (U/U_e) and y-component (V/U_e) of mean velocity in the inlet pipe

Table 1 Experimental conditions

Flow conditions	I	II	II	IV
$Q(m^3/s)$	2.52×10^{-3}	1.57×10^{-3}	8×10^{-4}	4×10^{-4}
Q/Q_n	0.93	0.57	0.29	0.15
F	0.054	0.034	0.017	0.0086
G	0.446	0.512	0.554	0.568
Inlet pipe				
U_i(m/s)	2.47	1.54	0.79	0.39
Re_i	54500	34000	17300	8670
Exit pipe				
U_e(m/s)	3.94	2.46	1.25	0.63
Re_e	69000	43000	22000	11000
Impeller passages				
V_R/W_t	0.056	0.035	0.018	0.009
W_R/W_t	0.9	0.94	0.97	0.98

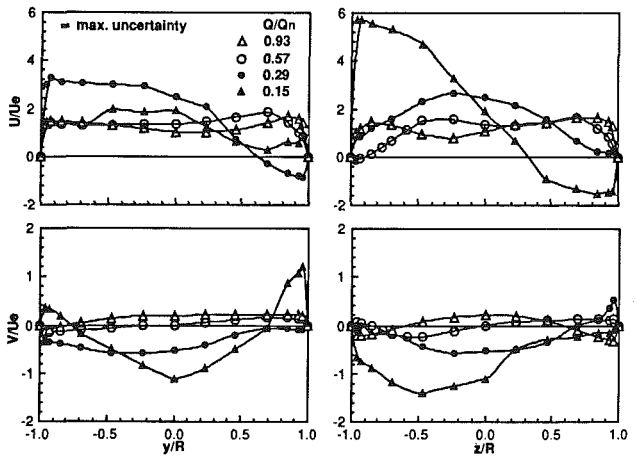

Fig. 3 Radial profiles of x-component (U/U_e) and y-component (V/U_e) of mean velocity at the axial station x/D_e of 1.8 in the exit pipe

tip velocity ($W_t = 19.1$ m/s), except in the inlet and exit pipes where the bulk mean velocity in the exit pipe (U_e) is used, Table 1.

Inlet and Exit Pipes. The velocities in the inlet and exit pipes were found to be insensitive to the circumferential orientation of the impeller, and the values reported in this subsection are ensemble-averaged over 360 degrees. The profiles of axial mean velocity in the inlet pipe 25 mm upstream of the impeller hub and on two orthogonal planes, Fig. 2, confirm symmetry in the z-direction and asymmetry in the y-direction and this was reflected by the asymmetric pressure distribution in the volute. The boundary layer thickened with evident regions of flow reversal and swirl near the pipe wall and larger normalised cross-stream velocities at $0.29Q_n$ and $0.15Q_n$, in contrast to the more uniform flow at $0.93Q_n$ and $0.57Q_n$. Integration of the radial profiles of the axial component resulted in mass flowrates within 1 and 4 percent of the values measured by the flow meter for $0.93Q_n$ and $0.57Q_n$, respectively, and with poorer agreement at lower flowrates due to increased asymmetry and flow separation. Typical rms values of the velocity in the inlet pipe were around 8, 11, 20, and 43 percent of the local bulk-mean velocities, U_i, for the four decreasing flowrates.

The distributions of axial mean velocity in the diverging section of the exit pipe of Fig. 3 show qualitative axial symmetry with a minimum in the central region at the flowrate of $0.93Q_n$. A region of streamwise flow separation occurred close to the wall ($z/R = -1$) at $0.57Q_n$ and changed position and increased at lower flowrates. The region of separated flow occupied up to 5, 20 and 35 percent of the pipe diameter with negative velocity values up to $-0.15U_e$, $-0.88U_e$ and $-1.49U_e$ for $0.57Q_n$, $0.29Q_n$ and $0.15Q_n$, respectively. The streamwise flow separation at lower flowrates was accompanied by increased cross-stream velocities and caused the location of the separated flow to vary in the downstream straight pipe. The poor match of impeller discharge flow and volute geometry in the upstream passage at off-design flowrates was responsible for the separation in the exit pipe. The exit flow was fully turbulent with typical values of the rms of velocity fluctuations of $0.17U_e$, $0.2U_e$, $0.65U_e$ and U_e for the four decreasing flowrates, and corresponding to around 4 percent of the impeller tip velocity.

Impeller Passages. The discharge flow of the impeller is characterized in Figs. 4 and 5 by the circumferential profiles of the three components of mean velocity at the middle of passage width, with Fig. 5 highlighting the effects of flowrate. Figure 4 shows that the blade-to-blade variations and the passage-to-passage velocity differences increased with decrease of flowrate, with the maximum differences between passages occurring close to the blade surfaces. Inspection of the impeller geometry showed maximum differences of 0.5 mm in passage width and up to one degree in circumferential spacing of the blades. The maximum differences in the radial and tangential velocities between passages were, in terms of the tangential velocity of the tip, $0.025W_t$ and $0.06W_t$, respectively, at $0.93Q_n$, and increased to $0.03W_t$ and $0.16W_t$ at $0.15Q_n$. The blade-to-blade variations in the W, V, and U velocity components are up to $0.16W_t$, $0.14W_t$, and $0.09W_t$, respectively, at $0.93Q_n$ and increased to $0.25W_t$, $0.32W_t$ and $0.12W_t$ at $0.15Q_n$.

Figure 5 considers one impeller passage, as in the remainder of the paper, and shows uniform tangential and axial components of velocity, except close to the surfaces of the blades,

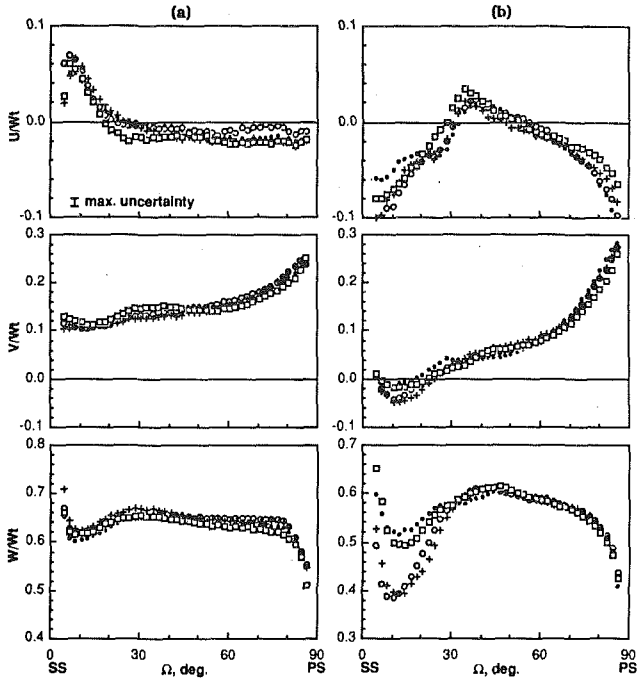

Fig. 4 Blade-to-blade distributions of angle-resolved axial (U/W_t), radial (V/W_t) and tangential (W/W_t) components of mean velocity on the mid-plane of the impeller passage at discharge, $z/Z_t = 0.5$ and $r/R_t = 1$, measured at $\Psi = 330$ degrees of the flowrates at (*a*)$0.93Q_n$ and (*b*) $0.29Q_n$. Symbols for each of the four impeller passages.

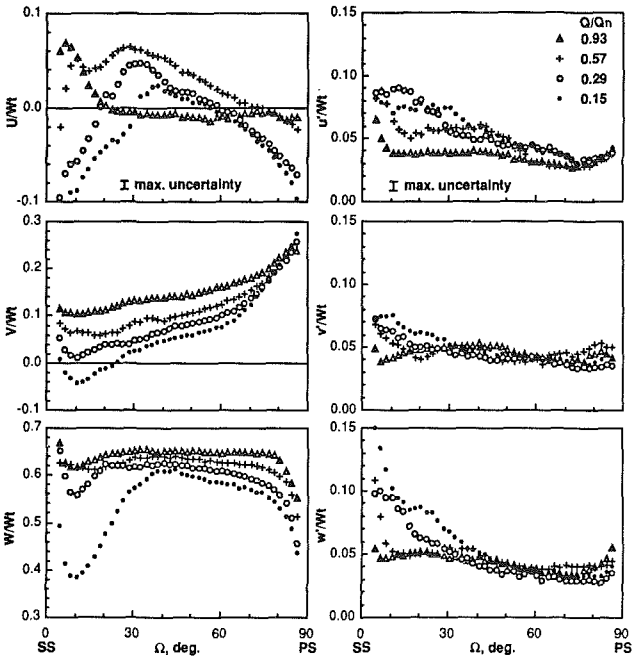

Fig. 5 Blade-to-blade distributions of angle-resolved axial (U/W_t), radial (V/W_t) and tangential (W/W_t) components of mean and rms velocities at the discharge, $r/R_t = 1$ and $z/Z_t = 0.5$, measured at $\Psi = 330$ deg

with the radial component increasing from suction to pressure surfaces at the flowrate of $0.93Q_n$. With these absolute velocities, the tangential component is much larger than the other two and the normalized value is unity at the blade surfaces, i.e., $\Omega = 2$ and 88 deg. The radial and tangential components decreased with flowrate and the axial component formed vortices close to the surfaces of the blades. The gradient of the radial velocity between blade surfaces increased with decreasing flowrate, leading to radial flow reversal near the suction surface at $0.15Q_n$. The rms of velocity fluctuations, ensembled in one degree intervals, were near-uniform and near-isotropic at high flowrates, and decrease in flowrate caused the increase of rms values and the blade-to-blade variations, with peak values close to the suction surface and in the wake region, as in the rotating diffuser of Iversen et al. (1960), the centrifugal pump of Flack et al. and the centrifugal fan of Kjork and Lofdhl. It is clear that these complexities and blade-to-blade variations of velocity, limit the value of investigations by methods which do not resolve in terms of angle and that ensemble-averages over 360 degrees can lead to over- or under-estimation of the local velocity by more than 100 percent, as reported by Liu et al.

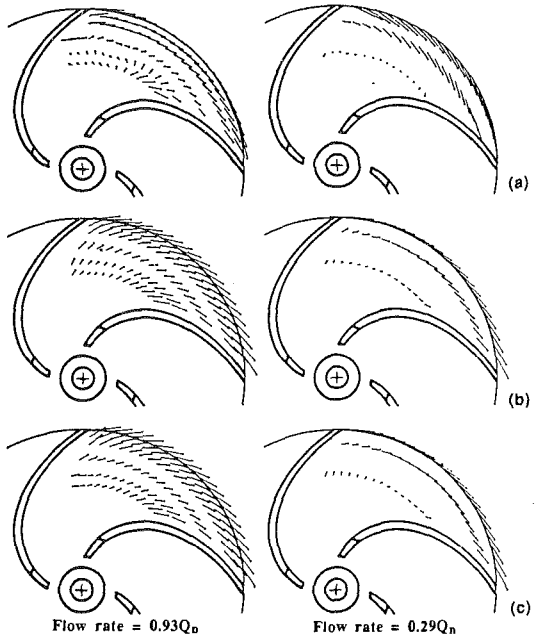

Fig. 6 Mean velocity vectors of the relative flow in an impeller passage at the flowrates of $0.93Q_n$, and $0.29Q_n$, measured at $\Psi = 330$ deg. Radial locations $r/R_t = 0.65$, 0.71, 0.81, 0.9, 0.95 and 1. (*a*) Plane 1 mm from the shroud; (*b*) Mid-plane of the blade height; (*c*) Plane 1 mm from the hub.

A clear picture of the impeller flow is given by Fig. 6 in terms of vectors of mean values of the angle-resolved relative velocities at $0.93Q_n$ and $0.29Q_n$, measured at six radial and three axial locations on the plane of $Y = 330$. The relative flow on the mid-plane of the passage follows the curvature of the blade at $0.93Q_n$ with departure from blade curvature at inner radii close to the hub and a less regular flow close to the shroud. A reduction of flowrate ($0.29Q_n$) decreased the velocity vectors and increased the flow angle, and the flow tended to decelerate towards the suction side of the passage and to accelerate towards the pressure side. The flow angles of Fig. 7(*a*) indicate the extent to which the flow was guided by the curvature of the blades at $0.93Q_n$ and shows values smaller than the blade angle of 58 at inner radii and larger than the blade angle at discharge with the flow close to the blade angle near the pressure surface. The flow angles at discharge, Fig. 7(*b*), decreased almost linearly from suction to pressure surfaces and increased monotonically with decreasing flowrate, leading to values larger than 90 deg at $0.15Q_n$ where the radial flow was reversed.

The tendency for the velocity vectors to change direction and to form vortices at small radii and close to the shroud is also evident from Fig. 6. The inward velocity vectors close to the shroud, common for an unshrouded impeller design due to the radial pressure gradient and the relative motion of the shroud and impeller, increased in magnitude and angle as the flowrate was decreased leading to radial flow reversal at radii

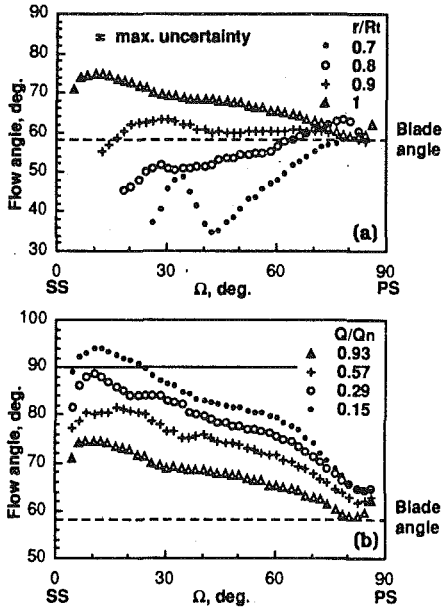

Fig. 7 Blade-to-blade distributions of mean flow angle, on the mid-plane of the impeller passage, $z/Z_t = 0.5$. (*a*) Variation with radius at the flowrate of $0.93Q_n$.

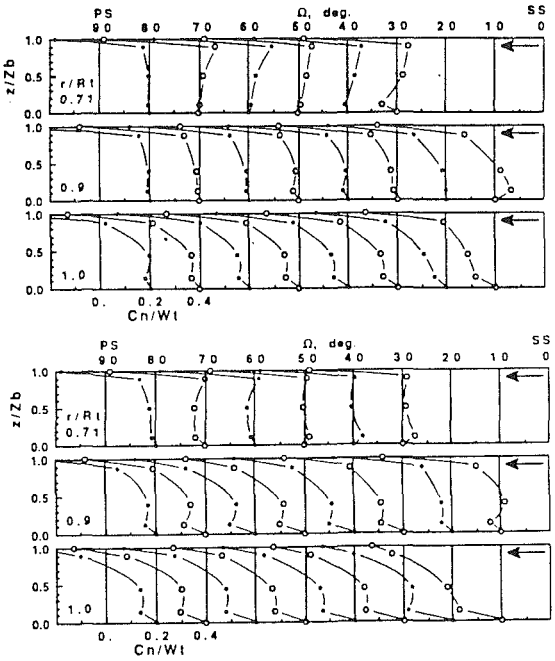

Fig. 8 Angle-resolved cross-stream mean velocity (C_n/W_t) in the impeller passage measured at $\Psi = 330$ deg with the radial planes of r/R_t of 0.71, 0.9 and 1 and the flowrates of (*a*) $0.93Q_n$ and (*b*) $0.29Q_n$.

up to $0.71R_t$ at the smallest flowrate. The velocity vectors at $r/R_t = 0.71$ had a tendency to diminish on the pressure side of the passage at the lower flowrate, in contrast to the larger vectors on the suction side of the passage. The potential flow in the impeller passages can be represented by superposition of a through-flow and a relative eddy caused by the irrotational nature of the flow. The relative eddy causes departure of streamlines from blade curvature, so that the flow angles were larger than the blade angle at discharge and the impeller head output was less than the theoretical value. The existence of the relative eddy is evidenced by the vectors at small radii and lower flowrate; it rotates in a clockwise direction and moves towards the suction surface due to the backswept geometry of the blades, enhancing the radial flow on the pressure side at discharge. Similar trends exist at the higher flowrate, but the vortex was less obvious due to the stronger through-flow.

The tendency for the impeller flow to follow the curvature of the blade surface was examined in terms of streamwise and cross-stream components of velocity by resolving the mean values of the radial and tangential components. The streamwise component (not shown) increased uniformly with radius with smaller variations between hub and shroud and across the passage than the radial component, and this result suggests that the secondary flow was responsible for the non-uniform distributions in radial component. The cross-stream component, C_n, of Fig. 8 had positive and negative values at $r/R_t = 0.71$ and only negative values at discharge and increased from hub to shroud and from pressure to suction surfaces due mainly to the relative motion of the impeller and shroud surfaces. The secondary flow at $r/R_t = 0.9$ and 1 increased with decrease in flowrate, but less so at $r/R_t = 0.71$, and the changes of sign suggest the formation of vortices due to pressure gradients and leakage flow.

Effect of Volute on the Relative Flow in the Impeller. The asymmetric shape of the volute generated circumferential pressure distributions which depended on the operating condition, and off-design operation resulted in larger pressure variations which, in turn, affected the flow in the impeller and pump performance, as expected from previous investigations including those of Bowerman and Acosta (1957), Iversen et al. and Sideris and van den Braembussche. The measurements on the

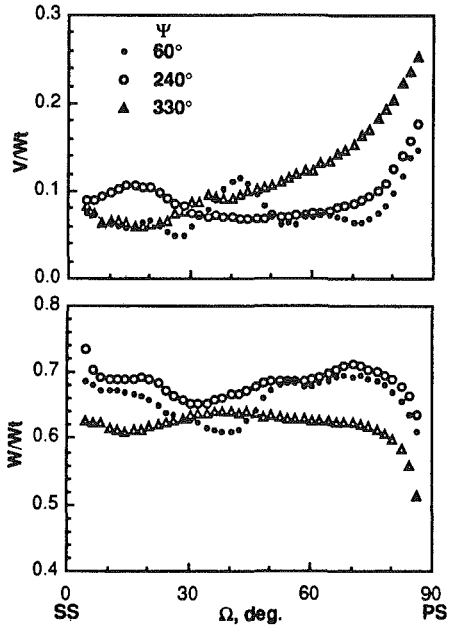

Fig. 9 Blade-to-blade distributions of angle-resolved radial (V/W_t) and tangential (W/W_t) components of mean velocity on the mid-plane of the impeller passage at discharge, $z/Z_t = 0.5$ and $r/R_t = 1$, at the flow rate of $0.57Q_n$.

planes of $\psi = 60$, 240, and 330 deg confirm the influence of the volute, with the velocity vectors and flow angles smaller at 60 and 240° deg.

A sample of the results for the flowrate of $0.57Q_n$ Fig. 9, shows smaller radial and larger tangential velocities at discharge for $\Psi = 60$ and 240 deg. The radial velocity profiles, averaged over 360 degrees, resulted in values of $0.08W_t$, $0.092W_t$, and $0.116W_t$ for $\Psi = 60$, 240, and 330 deg respectively. Area averages of the radial velocity profiles obtained on three axial planes, $z/Z_t = 0.15$, 0.5, 0.92, over the peripheral area of the passage at discharge resulted in lower values of $0.044W_t$, $0.053W_t$, and $0.059W_t$ due to velocity gradients from hub to shroud. These results confirmed variations of passage flowrates with circumferential angles of the volute, and those

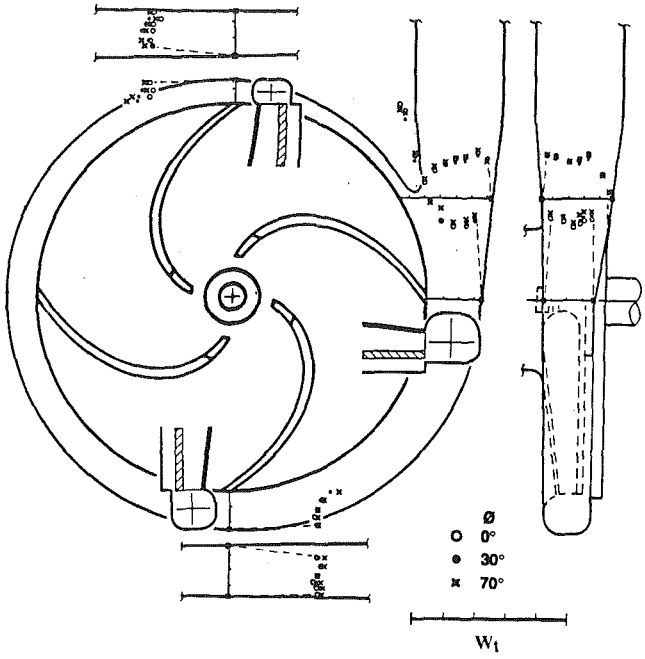

Fig. 10 Angle-resolved tangential component of mean velocity (W/W_t) in the volute passage at the flowrate of $0.57Q_n$

at $\Psi = 60$ and 240 are 25 and 10 percent, respectively, lower than that at $\Psi = 330$ deg.

Volute Passage. Figure 10 shows that the streamwise velocity in the volute had a tendency to decelerate along the passage and varied with impeller shaft angle at the flowrate of $0.57Q_n$. The radial profiles were characterized by velocity maxima at the impeller discharge with near-uniform distributions close to the volute wall, and the variations with shaft angle decreased with radius. The deceleration along the volute was due to the geometry and operating conditions so that the static pressure increased in circumferential direction at flowrates below the design point. The profile close to the cutwater, $x/D_e = 1.15$, has a sharp gradient towards the cutwater where local values of the rms of velocity fluctuations were up to $0.94W_t$, suggesting the effects of interaction between the cutwater and the impeller. The deceleration on the back surface of the wall ($z = -1$, Fig. 1) was caused by the geometry of the outlet ducts and was related to the flow separation in the downstream region of Fig. 3. Further examination of the flow suggested that the stagnation point on the cutwater occurred on the outer surface of the lip at $0.57Q_n$ and moved toward the inner surface at higher flowrates; the decreases of flowrate resulted in general decrease in streamwise velocity and increased variation with shaft angle due to less uniform discharge flow of the impeller which caused the cross-stream vortices in the volute.

The variations of velocity with impeller rotation decreased in the outlet towards the values of the 360-degree averages of Fig. 3. Measurements at two exit diameters downstream of the cutwater confirmed that the variations of mean velocity with impeller rotation were around 4 percent of the impeller tip velocity at the design flowrate and decreased to around 1 percent at lower flowrates.

Slip Factors. The angle-resolved radial and tangential velocities quantified the transfer of angular momentum to the flow and slip effect. The normalized angular momentum of the flow (M) and slip factor (S) were defined by Hamkins and Flack as;

$$M = \frac{r\tilde{w}}{R_t^2\omega} \quad \text{and} \tag{1}$$

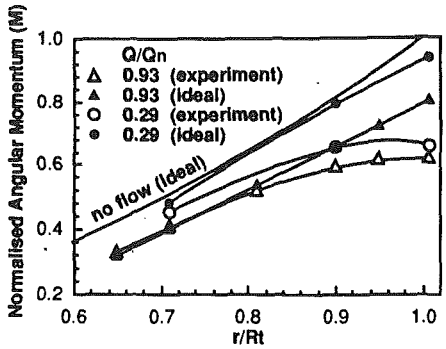

Fig. 11 Radial distributions of angular momentum (open symbols: experiment; block symbols: theoretical value)

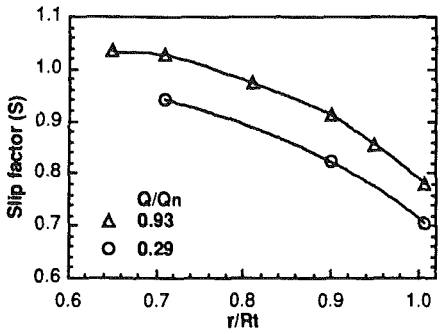

Fig. 12 Radial distributions of slip factor

$$S = \frac{\tilde{w}}{rw - \hat{v}\tan\beta} \tag{2}$$

and they were calculated from the area- and mass-averaged velocity values by integration of the angle-resolved values at each radial station.

Figure 11 shows that the angular momentum of the flow increased with radius to maxima of 0.62 and 0.66 at the discharge of $0.93Q_n$ and $0.29Q_n$, respectively. The ideal value of angular momentum based on the area-averages of measured radial velocity was obtained by dividing Eq. (1) by Eq. (2), and suggests that the flow loses momentum along the radius with larger loss for the lower flowrate, due partly to the slip effect and partly to friction. The slip factor, quantified in Fig. 12, has a trend opposite to that of angular momentum, and is larger than unity at small radii, supporting the effect of a relative eddy and in contrast to that reported by Hamkins and Flack. The slip factors at the impeller discharge increased with flowrate to around 0.71 at $0.29Q_n$ and 0.78 at $0.93Q_n$, and these values may be compared with the theoretical values of Busemann's and Stodola's, that is 0.69 and 0.58, respectively. The slip factors calculated by the velocities measured at $\Psi = 60$, 240 and 330 deg and $0.57Q_n$ (not shown) were within 6 percent in spite of variations in passage flowrate of up to 25 percent.

Concluding Remarks

Velocity characteristics of the turbulent flow in a centrifugal pump have been determined experimentally for operating conditions close to the design point to near shutdown. A transparent casing, with refractive index identical to that of the working liquid, allowed detailed measurements in the inlet and exit ducts, a large part of the inter-blade region and the volute by laser-Doppler velocimetry. The more important findings of the experiment are summarised in the following paragraphs.

1. The impeller flow departed from the curvature of the

surfaces of the blade at off-design conditions with increased blade-to-blade variations of relative velocity, in contrast to a generally well-guided flow close to the design flowrate. Decrease of flowrate from the design point caused deceleration of radial flow on the shroud surface and on the suction surface of the blades and increase of secondary flows and vorticity in the passages. The radial velocity reversed close to the suction surface at flowrates below 30 percent of the design point and close to the shroud surface at all flowrates. The velocity measurements confirmed the influence of the relative eddy by higher values on the suction surface and near-stagnation flow close to the pressure surface at small radii and lower flowrates. However, the geometry of the passage enhanced the influence of the relative motion between the shroud and impeller surfaces and the viscous effects, which, together with the leakage through the tip clearance, caused the secondary flow to be mainly from suction to pressure surface with vortices close to blade surfaces at smaller radii.

2. The unsteady effects of the impeller discharge were caused by turbulence, by variations in blade-passage geometry and by the position of the impeller relative to the volute. The measurements confirmed differences of the angle-resolved velocities between the four impeller passages, which increased with decrease of flowrate to 2.5 and 6 percent of the impeller tip velocity for the radial and tangential components, respectively, close to the design flowrate and to 3 and 16 percent at the flowrate close to shut-down. They were related to the differences of up to 0.5 mm in blade dimensions and up to one degree in blade circumferential spacing. Variations of relative flow in the passages with the circumferential angle of the volute were identified and reached 25 percent of the discharge, at 57 percent of the design flowrate.

3. The velocities in the volute passage decreased in the circumferential direction at off-design flowrates for which the volute was over-sized.

4. The angular momentum of the impeller flow increased with radius to a maximum at discharge close to the design flowrate with increasing departures of the angular momentum from the ideal value at smaller flowrates. The slip factor was larger than unity inside the impeller, decreased with radius and increased monotonically with flowrate at impeller discharge. Its value of 0.78 at 93 percent of the design flowrate was around 15 and 25 percent larger than the theoretical values of Busemann and Stodola respectively.

Acknowledgment

The authors benefited from discussions with Drs. H. McDonald and D.G.N. Tse of Scientific Research Associates Inc., U.S.A. Thanks are also due to Mr. P. Stanley for his contribution to the manufacture of the acrylic model, and to Mr. J. Laker for his construction of electronic components of the instrumentation.

References

Adler, D., and Levy, Y., 1979, "A Laser-Dopper Investigation of the Flow Inside a Backswept, Closed, Centrifugal Impeller," *Journal of Mechanical Engineering Science*, IMechE, Vol. 21, No. 1, p. 1.

Bowerman, R. D., and Acosta, A. J., 1957, "Effect of the Volute on the Performance of a Centrifugal-Pump Impeller. *Trans. ASME*, Vol. 79, p. 1057.

Eckhardt, D., 1976, "Detailed Flow Investigations within a High-Speed Centrifugal Compressor Impeller," ASME JOURNAL OF FLUIDS ENGINEERING, Vol. 98, p. 390.

Flack, R. D., Hamkins, C. P., and Brady, D. R., 1987, "Laser Velocimeter Turbulence Measurements in Shrouded and Unshrouded Radial Flow Pump Impellers." *International Journal of Heat and Fluid Flow*, Vol. 8, No. 1, p. 16.

Hamkins, C. P., and Flack, R. D., 1987, Laser Velocimeter Measurements in Shrouded and Unshrouded Radial Flow Pump Impeller," ASME *Journal of Turbomachinery*, Vol. 109, p. 70.

Iversen, H. W., Rolling, R. E., and Carlson, J. J., 1960, "Volute Pressure Distribution, Radial Force on the Impeller, and Volute Mixing Losses of a Radial Flow Centrifugal Pump," ASME *Journal of Engineering for Power*, Vol. 82, p. 136.

Karassik, I. J., Krutzsch, W. C., Fraser, W. H., and Messina, J. P., eds. 1976, *Pump Handbook*, McGraw-Hill, New York.

Kjork, A., and Lofdahl, L., 1989, "Hot-Wire Measurements Inside a Centrifugal Fan Impeller, ASME JOURNAL OF FLUIDS ENGINEERING, Vol. 111, p. 363.

Liu, C. H., 1992, "Applications of Laser-and Phase-Doppler Velocimetry," Ph.D. thesis, University of London.

Liu, C. H., Nouri, J. M., Vafidis, C., and Whitelaw, J. H., 1990, "Experimental Study of the Flow in a Centrifugal Pump," *Proc. 5th International Symposium on Appl. of Laser Techniques to Fluid Mechanics*, Lisbon, Portugal, 9–12 July, 1990.

Moore, J., 1973, "A Wake and An Eddy in A Rotating, Radial-Flow Passage, Part 1: Experimental Observations," ASME *Journal of Engineering for Power*, Vol. 95, p. 205.

Sideris, Th. M., and Van den Braembussche, R. A., 1987, "Influence of a Circumferential Exit Pressure Distortion on the Flow in an Impeller and Diffuser," ASME *Journal of Turbomachinery*, Vol. 109, p. 48.

Preliminary Design of Centrifugal Impellers Using Optimization Techniques

Sarim AL-Zubaidy
Associate Professor,
Department of Mechanical Engineering,
UAE University,
United Arab Emirates
Mem. ASME

The paper proposes a design method which may be used to evaluate the detailed geometry of an impeller (handling compressible and perfect fluid) from a prescribed mean streamline velocity distribution. The analysis makes use of numerical optimization, firstly in the step by step channel geometry calculation, and secondly in controlling the manner in which the relative velocity components are permitted to vary along the mean streamline for the condition of minimum entropy generation along the flow path. The components distribution of the relative velocity were not allowed to take arbitrary values, the variation of the radial, axial and tangential components was governed in such a way that the prescribed diffusion schedule is satisfied at every calculation point. The general configuration of the example design shows it to be well proportional and should not be difficult to manufacture.

Introduction

In order to meet the growing need for fuel efficient, reliable, and low cost small gas turbine engines for a variety of applications, there has been a flurry of interest in recent years to improve the design and performance of centrifugal compressors. This is because the centrifugal compressor is claimed to be cheaper to manufacture and inherently capable of producing higher stage pressure ratio than its axial counterpart. However, the design of a centrifugal compressor stage for improved or high efficiency is by no means simple. The number of variables involved in the design process may be divided into three main categories as follows:

1 Geometrical parameters
2 Operating conditions
3 Performance parameters.

The above division of variables is a convenient way to formulate the design problem. For example, one may investigate the effect of geometrical parameters on performance while the operating conditions would be constraints. Alternatively, the geometry may be kept constant and the effect of changing the operating conditions may be investigated.

For a specified set of operating conditions, it is necessary to optimize geometry to achieve best performance. However, it must be noted that optimum solution will be found only within the design given set of constants. Much progress has been made in employing various optimization techniques for problem solving in a number of engineering aspects e.g., Vanderplats (1976) and Biggs (1972) and many numerical optimization algorithms are now in existence. The author has developed a direct computer aided design procedure which uses an optimization algorithm reported in Biggs (1974) and the Optima manual (1976) to obtain the impeller detailed geometry for a prescribed total velocity diffusion.

Contributed by the Fluids Engineering Division for publication in the JOURNAL OF FLUIDS ENGINEERING. Manuscript received by the Fluids Engineering Division October 1, 1992; revised manuscript received June 10, 1993. Associate Technical Editor: L. Nelik.

The overall procedure consists of two main stages: stage 1 deals with the choice of the impeller principal dimensions, and stage 2 determines the hub, shroud and blade profile for the prescribed diffusion rate along the mean streamline.

Preliminary Design

The preliminary design study is usually carried out to examine a number of candidate impellers with different inlet and outlet geometry that will satisfy the given design requirements usually specified by the total-to-total pressure ratio and mass flow rate. In some cases rotational speed is also specified. Other constraints on the design might be given such as maximum permissible Mach number at the inducer tip, hub tip diameter, impeller matching requirements etc.

The energy, continuity, and Newton's second law may be combined and solved at the impeller inlet and exit, assuming the flow to be one-dimensional, steady and the working fluid to be a perfect gas to give expressions that relates geometrical, flow variables, and performance parameters. These could be then used to investigate the effects of the basic design variables on the principal geometric parameters. Details may be found in Jawad (1987). A computer program has been written in FORTRAN to solve the governing equations, some of the results are discussed briefly in the following:

Figure 1 shows the variation of the dimensionless mass flow parameter and the inducer tip blade angle β_e, with the inducer tip to the impeller tip diameter ratio and a variable outlet flow angle (for $P_{02}/P_{01} = 6{:}1$ and $m = 1$ kg/s). The curves shown are also plotted for the condition of zero pre-whirl at the impeller inlet and the following assumed (constant) values:

dimensionless speed parameter	$= d_2N/\sqrt{C_pT_{01}}$	$= 0.3193$
slip factor	$= \phi_s$	$= 0.82$
hub inlet diameter	$= d_{h1}$	$= 27$ mm

The variation of the dimensionless mass flow parameter has

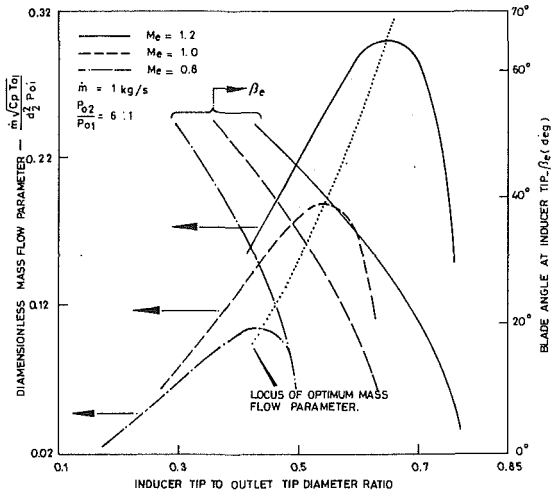

Fig. 1 An impeller design chart

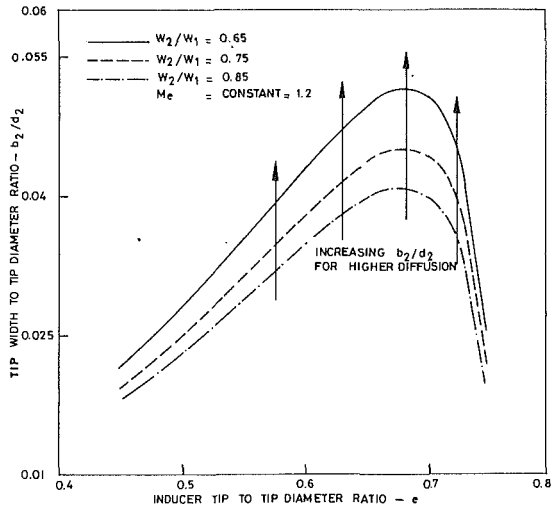

Fig. 2 Effect of inducer tip to impeller tip diameter ratio on tip width to tip diameter ratio for various diffusion ratios

been plotted for three values of the inducer tip Mach number ranging from $M_e = 0.8 - 1.2$. It can be seen that there is a unique optimum value of mass flow parameter for every value of the tip Mach number. The locus of the optimum points is highlighted by a dotted line. Also shown in the figure is the variation of the inducer tip blade angle for the same specified range of the inducer tip Mach number.

Figure 2 shows the variation of the impeller tip width to the impeller tip diameter against the inducer to tip diameter ratio. The figure was obtained for a single value of the inducer tip Mach number ($M_e = 1.2$) and varying overall relative velocity diffusion ($W_2/W_1 = 0.65$–0.85) for the same previously mentioned conditions. It is also noteworthy that the position of the maximum value of the blade tip to tip diameter ratio occurs at a unique value of the inducer to tip diameter ratio. The preliminary design stage mentioned above will allow to establish the practical region of variation of principal dimensions. The next stage, is to optimize these parameters within the imposed design limits.

The principal dimensions optimization program used, is based on the assumption that the flow inside the impeller is controlled by the maximum achievable diffusion which for a given geometry defines the separation point location. Downstream of this point the flow splits into a jet and wake. It is further assumed that the jet flow has a constant Mach number in the flow direction and the only losses are due to friction along the passage walls. The wake static pressure is fixed by a tangential equilibrium between jet and wake taking into account centrifugal and coriolis forces. This non-uniformity of relative velocity at the exit will give rise to mixing losses at diffuser entrance. Clearance losses were assumed to increase linearly with relative clearance. The calculation procedure allowed the impeller efficiency to be closely related to the impeller geometry (which permitted the complete mapping of the range specified in the previous stage, Figs. 1 and 2). Table 1 gives the optimum values of an example design.

Nomenclature

b = width (m)
C = absolute velocity (m/s)
C_d = dissipation coefficient
C_n = blade loading coefficient
C_p = specific heat at constant pressure (kJ/kgK)
d = diameter (m)
e = inducer tip to tip diameter ratio
$F(\bar{X})$ = objective function
f = function of. . .
g = basic design constraints, acceleration due to gravity (m/s^2)
H = stagnation enthalpy (kJ)
i_r, i_z, i_θ = unit vectors in the radial, axial and tangential directions
K = numerical constant
M = Mach number
m = length of the projection of mean streamline in the r-z plane (m)
m = mass flow rate (kg/s)
N = impeller rotational speed (rev/s)
n_b = number of blades
P = pressure (N/m^2), penalty function (Eq. (15))
q = index
r = radius (m)
S = entropy per unit mass (kJ/Kkg)
s = distance along flow path (m)
T = temperature (K)
t = time (s)
U = blade speed (m/s)
W = relative velocity (m/s)
$\bar{X}$ = independent design variables (X_1, X_2, X_3. . .)
Z = distance along axis of rotation (m)
α = angle between tangent to streamline and axis of rotation (deg). All angles are defined from tangential direction.
β = relative flow angle (deg)
δ = boundary layer thickness (m)
η = efficiency
θ = relative angular coordinate (rad)
ρ = fluid density (kg/m^3)
μ = fluid viscosity (kg/ms)
φ_s = slip factor
ω = angular speed of rotation (rad/s)

Subscripts

0 = stagnation conditions
1 = impeller inlet
2 = impeller exit
abs = absolute
c = curvature
e = inducer tip condition
h = hub
$i, i+1, \ldots$ = index
m = meridional
n = index
q = index
r = radial direction
rel = relative
rms = root mean square value
s = shroud
t = total
z = axial direction
θ = tangential direction
$\bar{}$ = vector, matrix elements

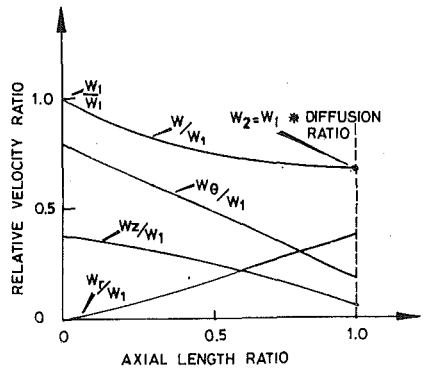

Fig. 3 Prescribed velocity distribution and components

The Design Theory

The choice of a suitable flow path for a centrifugal impeller is almost prerequisite for completely defining the entire passage geometry. The boundary values of the relative velocity components are known from the inlet and outlet velocity vector diagrams (analysis carried out assuming zero prewhirl) which resulted from the previous preliminary design stage. For a specified value of the impeller length along its axis of rotation a desirable total relative velocity schedule is prescribed. The choice is mainly based on achieving acceptable uniform rate of diffusion. Figure 3 shows the example design with the prescribed velocity ratio distribution along the impeller axial length ratio. The components distribution of the total relative velocity schedule between inlet and outlet can be initially independently assigned. However, the following simple relation must be satisfied at any points along the flow path:

$$\overline{W} = W_z\bar{i}_r + W_r\bar{i}_r + W_\theta\bar{i}_\theta \tag{1}$$

The equations of motion relative to the rotating impeller in which axial symmetry is assumed and neglecting blade body forces in r, θ, and z directions could be written as:

$$\frac{d}{dt}(W_r) - (W_\theta + \omega r)^2/r = -(1/\rho)(\partial P/\partial r) \tag{2.1}$$

$$\frac{1}{r}\frac{d}{dt}(rW_\theta + \omega r^2) = -(1/\rho r)(\partial P/\partial\theta) \tag{2.2}$$

$$\frac{d}{dt}(W_z) = -(1/\rho)(\partial P/\partial Z) \tag{2.3}$$

where d/dt refers to the total or substantial derivative.

The equation of motion normal to the mean streamline in the radial-axial plane for the condition of zero pressure gradient could be written as:

$$d^2r/dZ^2 = (1 + (dr/dZ)^2)^{1.5}/r \cos\alpha((\omega r/W_m) - \cot\beta)^2 \tag{3.1}$$

Equation (3.1) could be solved as a nonlinear, ordinary second-order differential equation if the meridional velocity as a function of the impeller axial length is known and if it is assumed that the flow angle is equal to the blade angle along the flow path for the known end conditions. The fluid density was calculated using the following relation:

$$\rho_{i+1} = \left[\frac{(T_{i+1})_{\text{abs}}}{(T_{oi})_{\text{abs}}}\right]^{1/\gamma-1}(\rho_{oi})_{\text{abs}} - \left[\left(\frac{(T_{i+1})_{\text{abs}}}{(T_{oi})_{\text{abs}}}\right)\left(\frac{(T_{oi})_{\text{abs}}}{(T_{oi}+1)_{\text{rel}}}\right)\right]^{1/\gamma-1} * \left[\frac{(\Delta P_o)_{\text{rel}}}{R(T_{oi})_{\text{abs}}}\right] * \left[\frac{(T_{oi})_{\text{abs}}}{(T_{oi}+1)_{\text{rel}}}\right] \tag{3.2}$$

The relative pressure drop in the above expression was estimated in accordance with the following:

Table 1 Optimized dimensions

Tip width to tip diameter ratio	b_2/d_2	0.0399
Inducer to tip diameter ratio	d_{e1}/d_2	0.58
Inducer tip angle	B_e	38
Hub to tip diameter ratio	d_{h1}/d_2	0.16
Number of blades	n_b	16

$$(\Delta P_o)_{\text{rel}} = f(\Delta S) \tag{3.3}$$

Equation (2.2) can also be simplified and solved for the blade loading parameter distribution ($\partial P/\partial\theta \approx \Delta P/\Delta\theta = f(Z)$) since all parameters in Eq. (2.2) can now quite easily be determined. From the mathematical point of view, the original partial differential equation has been reduced to an ordinary differential equation solvable in a step by step manner along the flow path.

The theoretical pressure rise along the flow direction can in general be written as:

$$dP = \frac{\partial P}{\partial r}dr + \frac{\partial P}{\partial Z}dZ + \frac{\partial P}{\partial\theta}d\theta \approx \frac{\partial P}{\partial r}dr + \frac{\partial P}{\partial Z}dZ + \frac{\Delta P}{\Delta\theta}d\theta \tag{4}$$

by substituting from Eqs. (2.1), (2.2), and (2.3) in (4) the differential pressure rise can be calculated at each step.

It should be mentioned that there are two relatively simple methods for estimating the variation of relative velocity components along the hub and shroud streamlines. The first is by consideration of the fact that zero circulation should exist within the fluid up the streamline along the shroud or back wall and back down the mean streamline. Alternatively, it can be assumed that the meridional curvature along the shroud effectively increases the maximum suction surface velocity gradient (Rodgers, 1978). Therefore, any alteration of the velocity component along the mean streamline will cause a corresponding change to the calculated values of the relative velocity along the hub and shroud streamlines. The radius distribution along the hub and shroud surfaces can now be calculated using the equation of continuity of flow in the meridional plane together with the assumed variation of the radial-axial velocity component perpendicular to the mean streamline in the radial-axial plane following Rodgers (1978).

As was mentioned above, the pressure calculated using Eq. (4) neglects all irreversibility which take place along the passage length. It may be said that the creation of entropy by irreversible effects will always reduce the efficiency of the machine. The loss in efficiency for an adiabatic compressor can be directly related to the entropy change via:

$$\eta = \frac{(\Delta H - T_2\Delta S)}{\Delta H} \tag{5}$$

To account for the drop in the ideal pressure, a mean streamline efficiency estimator approach is adopted. The value of entropy increase at any step is calculated by integrating the model described by Traupel (1977) (assuming the flow to be compressible, adiabatic with constant stagnation temperature and a Prandtl number approaching unity), which was rewritten in terms of a selected group of design variables to give the following relation:

$$dS = C_d\left[\frac{W_\theta}{\sin\beta}\right]^3\left[\frac{\left(\tan\alpha(r_s - r_h) + \frac{\pi}{2n_b}(r_s + r_h)\sin\alpha\right)}{W_rT_{01}\left(\pi(r_s^2 - r_h^2)\left(1 - \left(\frac{W^2 - U^2}{2C_pT_{01}}\right)\right)\right)}\right]dm \tag{6}$$

It should be mentioned here that subsequent detailed geometry calculation (leading to the optimized design) seems to be rather insensitive to moderate variation of the dissipation coefficient.

In addition, the blockage factor due to boundary layer was also calculated. The model used was that of Pampreen (1981),

the model assumes that the spanwise distribution of the blockage factor is constant.

Optimization Procedure

In the present context, the optimization term is limited to those situations where the measure of achievement can be quantified and can be calculated and alternative courses of action can be represented by assigning different values to a set of parameters $X_1, X_2, X_3, \ldots, X_n$. The design objective function is designated by $F(\overline{X})$, where $\overline{X}$ denotes the vector with elements $X_1, X_2, X_3, \ldots, X_n$.

In most practical optimization problems, the parameters are not allowed to take entirely arbitrary values. Some limitations are usually imposed as simple or complicated relationships connecting these parameters may exist. These are denoted by two sets of parameters:

$$\begin{aligned} g_i(\overline{X}) &= 0 \qquad i = 1, 2, 3, \ldots, q \\ g_{i+1}(\overline{X}) &\geq 0 \qquad i = q+1, q+2, q+3, \ldots, n \end{aligned} \tag{7}$$

The objective function in the present paper was selected to be:

$$F(\overline{X}) = \sum_{\text{inlet}}^{\text{outlet}} dS \tag{8}$$

Six independent design variables have been selected that describe the basic geometry of the blades and the manner in which the relative velocity components along the major axis may vary. The chosen independent design variables are given by:

$$(\overline{X}) = \begin{Bmatrix} X_1 \\ X_2 \\ X_3 \\ X_4 \\ X_5 \\ X_6 \end{Bmatrix} = \begin{Bmatrix} r_{\text{rms}} \\ r_c \\ \alpha \\ \beta \\ W_\theta \\ Wr \end{Bmatrix} \tag{9}$$

The constraints imposed could be basically divided into:

1 Equality constraints which are mainly the various relations between the various variables (dependent and independent).

2 Inequality constraints which are mainly positivity constraints to ensure manufacturability, positive values of velocities, lengths etc. In addition, an approximate empirical formula to delay flow separation is used (given by the following relation):

$$\frac{dP}{dS} \leq \frac{K\mu((W_r^2 + W_\theta^2 + W_z^2)^{0.5})}{\delta^2} \tag{10}$$

It should be mentioned here that nearly all optimization routines require the partial derivatives of F and $g(\overline{X})$ with respect to all elements X_i of $\overline{X}$. In many instances obtaining analytical differentiation is not possible and therefore an approximate derivative has to be obtained by a method using finite differences. In the present work, a subroutine for calculating the partial derivatives has been used to aid the solution.

The algorithm used in this paper is a subroutine in the Optima suite for Recursive Quadratic Programming (OPRQP) and is suitable to solve constrained nonlinear programming problems. It is run under the assumption that the selected objective function and constraints are continuously differentiable. It is also necessary that the objective function be computable at points which do not satisfy the constraints. The method is iterative and its description is beyond the intended scope of this paper (Biggs, 1974 and Optima Manual, 1976). It is sufficient to say for the purpose at hand that in addition to a solution, the algorithm estimates every constraint and records the number of times a derivative calculation subroutine has been called. This is a conventional way of measuring the efficiency of an optimization algorithm.

During numerous runs of the above mentioned optimization algorithm and on examining the many solutions, it was noticed that on rare occasions one or more constraints have not been obtained within the desired tolerance, while the remaining constraints and the free gradient are small. It is then advisable to rescale the constraints to give the difficult ones greater weight in the penalty function. Multiplying them by a factor of ten is usually sufficient.

Design Results

By examining the development of the optimization solution it was noticed that the greatest improvement were achieved in the first three iterations. At the end of the third iteration, a suitable impeller geometry was nearly found.

The progress of some selected design variables during the optimization process is shown in Figs. 4 to 7. Figure 4 shows the initial assumed distribution of the radial component ratio of the relative velocity along the nondimensional meridional distance. This distribution experienced the greatest range of variations during the optimization process compared with the other relative velocity components. The solution progress at iteration number 0, 1, 2 and 9 is shown. It can be seen that the optimum distribution of the relative velocity (iteration #9) accelerates relatively slowly at the beginning then starts to accelerate rapidly, while near the exit, the acceleration is achieved in a gradual manner to the design exit velocity. Figure 5 shows the blade angle distribution at iteration number 1, 2, and 9. It is interesting to note that the final form of the blade angle distribution (calculated at iteration #9) does agree very well with the blade distribution that achieved good results reported in the comprehensive findings of Ingham (1973) for a similar class of total-to-total pressure ratio and mass flow rate. In addition, optimum distribution does seem to be in line with the pressure balanced blade design reported in the study of Balje (1970).

Figure 6 shows the distribution of the blockage factor for three blade distributions shown in the previous figure. Pampreen's (1981) method has been used for calculating the blade blockage factor. From this figure, it can be seen that the blade distribution calculated at iteration #9 (optimum for the specified constraints) should produce minimum overall calculated blockage along the shroud streamline.

Equation (7) was evaluated for each interval along the mean streamline. Figure 7 shows the blade loading coefficient distribution along the nondimensional meridional distance. The loading coefficient is defined in a similar manner to Morris and Kenny (1971) as:

$$C_n = (P_{\text{pressure}} = P_{\text{suction}})/\rho W^2 \tag{11}$$

The figure shows the initial (iteration #0), (#1) and the final (optimized, #9) distribution of the blade loading coefficient. Here, it must be said that as a rule of thumb, the design of impeller suggests that the value of the blade loading coefficient should not exceed 0.7 (Morris and Kenny, 1971). However, in all shown cases this value has been exceeded. It can be seen that the optimized distribution reaches the critical value well after the first half of the flow path, while the initial and first iteration solutions reach the critical value before and at the half way points, respectively. This suggest that the flow separation point was successfully delayed in the optimized design, where Schuster (1980) has pointed out that this critical value of the coefficient is usually reached near the point of separation. It can also be observed that the maximum value of the blade coefficient in the optimized design is considerably less than the initial value.

To verify the configuration of the example design, a quasi-three-dimensional flow analysis proposed by Katsanis (1964) and (1965) was performed and Fig. 8 show the results of the flow analysis. It can be seen that the velocity distribution is

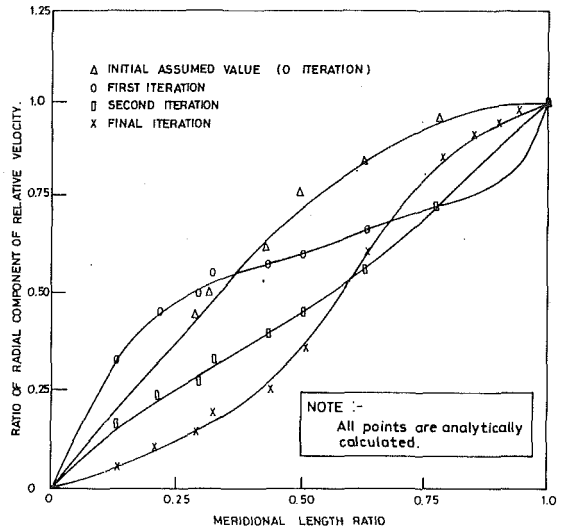

Fig. 4 Variation of the radial velocity component along the meridional length

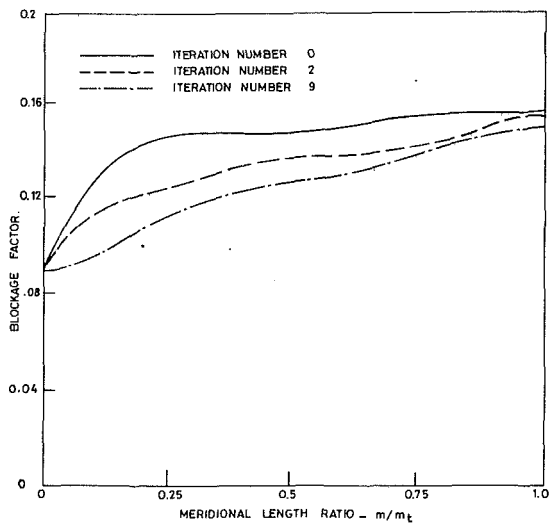

Fig. 6 Blockage factor distribution calculated at iterations number 0, 2, and 9

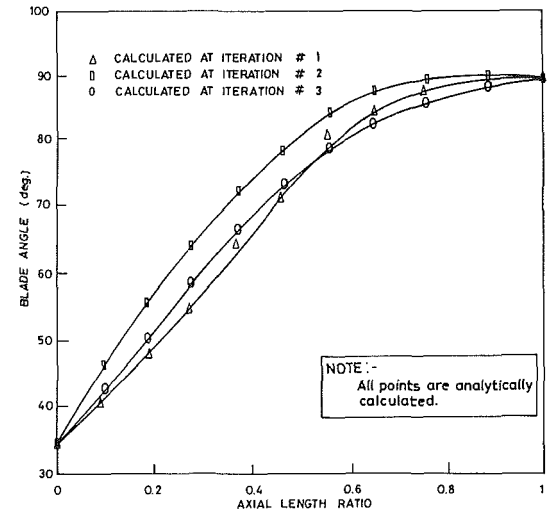

Fig. 5 Blade angle distribution along mean streamline

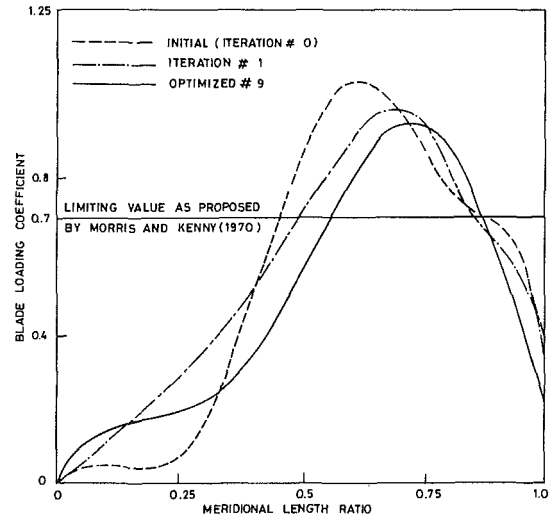

Fig. 7 Distribution of the blade loading coefficient along length ratio

quite smooth and free from sharp increases or decreases. Closer examination reveals that the diffusion was mainly achieved in the axial portion of the passage and it is kept minimum at the turning point from axial to radial. The general shape of the pressure ratio variation along the meridional coordinate experienced similar trend to pressure schedules of existing successful designs that are known to have good performances.

Concluding Remarks

The paper describes a preliminary direct design method for centrifugal compressor impellers based on a prescribed rate of deceleration. The method employs optimization techniques for obtaining the detailed geometry of the example radial impeller. The proposed method does allow the designer to observe and assess the effect of the various distributions of the relative velocity components (very rapidly) on the overall blade shape such as the degree of blade wrapping, the front view of the impeller, the radial-axial profile of the impeller and the space rate of turning of the three basic flow lines (hub, mean and shroud). The method can also provide a quantitative idea of the magnitude and the detailed distribution of the blade loading for each individual design. The described method has been used to design an example impeller. Its geometric proportions

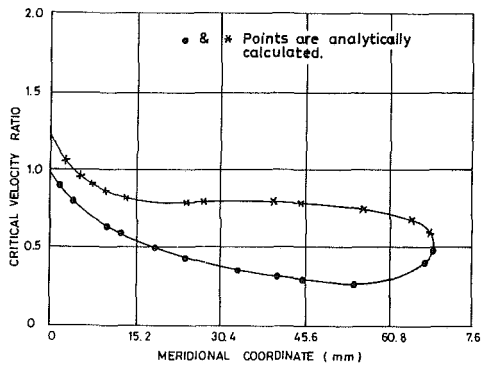

Fig. 8 Velocity ratio versus meridional coordinate

appear to be in line with existing impellers (designed using indirect approach) that are known to have good performance.

Finally, it must be emphasized that the main aim of this investigation was to develop the use of numerical optimization techniques to impeller design based on a prescribed mean stream velocity distribution, hence the available loss models were used.

However, more refined models may quite easily be substituted in the overall procedure.

References

Balje, O. E., 1970, "Loss and Flow Path Studies on Centrifugal Compressors—Part II," ASME *Journal of Engineering for Power*, pp. 287–299.

Biggs, M. G., 1974, "Constrained Mininisation Using Recursive Quadratic Programming: Some Alternative Sub-Problem Formulation," Report No. T. R. 51, Numerical Optimization Center (N.O.C.), Hatfield Polytechnic Inst., England.

Biggs, M. G., 1972, "Constrained Minimization Using Recursive Equality Quadratic Programming," *Numerical Methods for Nonlinear Optimization*, F. A. Lootsma, ed., Academic Press.

Ingham, D. R., 1973, "An Investigation Into the Effect of an Inducer Design on the Performance of Centrifugal Compressor Impeller," Ph.D. thesis, the Hatfield Polytechnic Inst., England.

Jawad, S. N., 1987, A Direct Design Method for High Pressure Ratio Centrifugal Compressor Impeller," SAE paper No. 871390.

Katsanis, T., 1965, "Use of Arbitrary Quasi-Orthogonals for Calculating Flow Distribution on a Blade-to-Blade Surface in a Turbomachine," NASA TN D-2809.

Katsanis, T., 1964, "Use of Arbitrary Quasi-Orthogonals for Calculating Flow Distribution on in the Meridional Plane of a Turbomachine," NASA TN D-2546.

Morris, R. E., and Kenny, D. P., 1971, "High Pressure Ratio Centrifugal Compressors for Small Gas Turbine Engines," ASME *Advanced Centrifugal Compressors*.

Optima Manual, 1976, "Routines for Optimization Problems," Numerical Optimization Center (N.O.C.), the Hatfield Polytechnic Inst., Hatfield, England.

Pampreen, R. C., 1981, "A Blockage Model for Centrifugal Compressor Impellers," ASME *Journal of Engineering for Power*, Vol. 94, No. 1, pp. 43–59.

Rodgers, C., 1978, "A Diffusion Factor Correlation for Centrifugal Impeller Stalling," ASME *Journal of Engineering for Power*, Vol. 100, pp. 592–603.

Schuster, P., and Schmidt-Eisenlohr, U., 1980, "Flow Field Analysis of Radial and Backswept Centrifugal Compressor Impellers. Part 2: Comparison of Potential Flow Calculations and Measurements," ASME Gas Turbine Conference book: *Prediction of Centrifugal Pumps and Compressors*, pp. 87–95.

Traupel, W., 1977, *Thermische Turbomachinen*, Vol. 1, 3rd edition, Springer-Verlag, Berlin.

Vanderplats, G. N., 1976, "The Computer for Design Optimization," *Computing and Applied Mechanics AMD*, ASME, Vol. 18, pp. 25–48.

Two-Phase Velocity Distributions and Overall Performance of a Centrifugal Slurry Pump

T. Cader
Graduate Student.

O. Masbernat

M. C. Roco[1]
Professor.

Department of Mechanical Engineering,
University of Kentucky,
Lexington, KY 40506

Back-scattering LDV has been used to investigate particulate two-phase flow in a centrifugal slurry pump. The measurements reported here have been made with a dilute suspension of 0.8 mm glass beads at the impeller-casing flow interface. This interface is of practical importance because the corresponding velocity and concentration results can be used to determine the pump head and flowrate. The present study evaluates the connection between the liquid and solids velocity distribution measured around the impeller and the pump performance determined from measurements at the pump inlet and outlet. The analysis of the velocity triangles for both phases shows the effect of the pump flowrate and inlet recirculation on the pump head at the impeller outlet, as well as the effect of particle slip on pump energy efficiency. A separate group of characteristic curves is proposed to represent the periodical fluctuations of the pump flowrate, head, and loss of efficiency due to particle slip, as a function of the impeller position.

Introduction

In order to evaluate the characteristic curves of a centrifugal pump, it is necessary to have a better understanding of the connection between the velocity distribution within the pump and the parameters measured at the pump extremities. The cylindrical surface separating the impeller outlet and casing inlet has been used as a representative area for this purpose in previous modeling and design studies (for instance see Karassik et al., 1976). In this paper, experimental results on velocity distributions for liquid and solids are presented as a function of the impeller position, and the solids influence on the pump head and efficiency is discussed. Previous experimental studies on the solids effect have been reported using pressure, flowrate and concentration measurements at the pump extremities (Wiedenroth (1970), Vocadlo et al. (1974), Walker and Goulas (1984), Roco et al. (1986), and Sellgren and Vappling (1986)). Velocity measurements for single fluids have shown a nonuniform jet-wake flow pattern at the impeller outlet, for shrouded and unshrouded impellers, in casings of different shapes, for liquids (see for instance Hamkins and Flack, 1987; Paone et al., 1989) and gases (see for instance Eckardt, 1975). Similar experimental results on solids and solids slip velocity distributions have not been found in previous publications, and are object of this paper. The pump head for the two-phase mixture at the impeller outlet is evaluated only from the velocity distributions assuming inertial forces as dominant in the pump channels and no prerotation at the pump inlet. The reduction of energy efficiency by particle slip assumes the interface between the impeller and casing flow as a representative domain for particle slip velocities and concentration. The corresponding approximation is satisfactory for showing the qualitative effects of solids and of velocity distributions. This is the first evaluation of efficiency reduction by solids made by starting from the two-phase flow microstructure.

A schematic of the centrifugal pump tested in laboratory is shown in Fig. 1 (after Roco et al., 1993). The pump is of radial type, and has a casing concentric to impeller. Its dimensionless specific speed calculated as $NQ^{0.5}/(gH)^{0.75}$ is 0.46. The impeller of diameter $D_{2i}=280$ mm is shrouded, with plane shrouds and three blades of simple curvature. The width of each shroud is 25 mm, and the blade width is 35 mm. The inlet clearance between the front impeller shroud and casing is about 5 mm. The pump has an inlet diameter of $D_1=100$ mm, and a discharge diameter of $D_2=76.2$ mm. The blades have an inlet angle of 26 degrees and an outlet angle of 23 degrees. The casing flow cross-section is rectangular, with Δr_{max} ($=60$ mm at window W2, and 32.6 mm at windows W3 to W8) and $B_c=100$ mm, as shown in Fig. 1(*c*). The power is transmitted to the pump from a 15 kW motor with variable speed between $N=0$ and 2000 rpm. The experiments presented here were run at $N=1000$ rpm. The nominal flow rate is $Q_n=63.6$ m^3/h and the corresponding pump head is $H_n=9.7$ m. The pump theoretical head at Q_n is 16.7 m. At $Q_n/2$, the effective and theoretical heads are 10.97 m and 17.93 m, respectively. The pump Reynolds number based upon the linear velocity of the impeller outlet surface ($U_{2i}=\pi D_{2i}N/60=14.67$ m/s) and the impeller diameter is $4\cdot10^6$. The pump is mounted in a closed circuit, with a feeder and a separation system for solids. The water temperature was maintained at 20 ± 0.5°C.

[1]Presently, National Science Foundation, Engineering Directorate, Room 525, 4201 Wilson Blvd., Arlington, VA 22230.

Contributed by the Fluids Engineering Division and presented at the Fluids Engineering Division Summer Meeting, Second Pumping Machinery Symposium, Washington, D.C., June 1993 of the AMERICAN SOCIETY OF MECHANICAL ENGINEERS. Manuscript received by the Fluids Engineering Division March 6, 1993; revised manuscript received August 27, 1993. Associate Technical Editor: J. A. C. Humphrey.

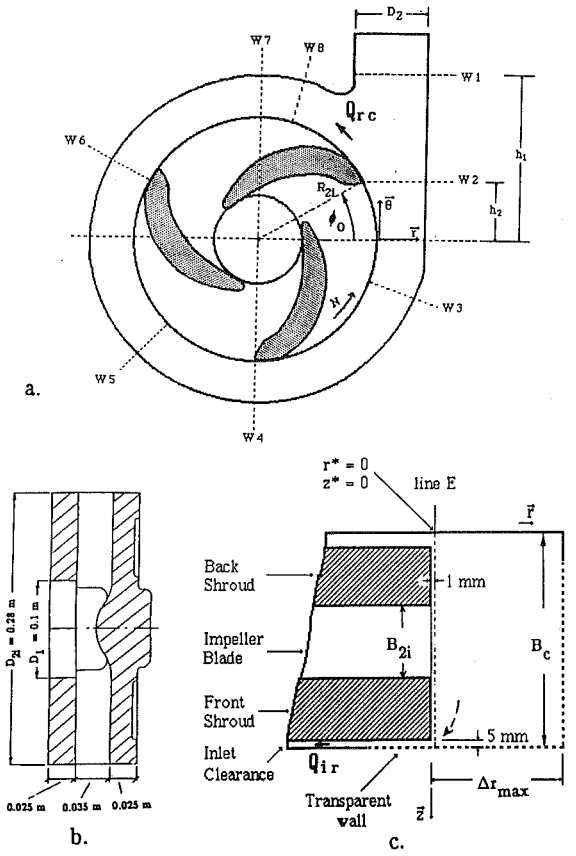

Fig. 1 The pump model: (*a*) casing axial cross-section, (*b*) casing radial section, (*c*) impeller radial section

The θ-axis is tangential to the impeller circumference, the r-axis is in the impeller radial direction, and the z-axis is directed from the impeller back shroud to the front shroud (Fig. 1(*c*)). The axial coordinate was normalized by the axial width of the casing ($z^* = z/B_c$) and the radial coordinate by the radial gap ($r^* = \Delta r/\Delta r_{max}$), respectively. The dimensionless impeller angle ϕ_0^* is measured counter-clockwise from window W2, and is normalized by the blade-to-blade interval $\Delta\phi_b = 360$ degrees/Z (number of blades) = 120 degrees:

$$\phi_0^* = (\phi - \phi_0)/\Delta\phi_b. \quad (1)$$

The angle $\phi_0 = 23.7$ degrees corresponds to the location of window W2, as shown in Fig. 1(*a*).The normalized impeller angle is denoted simply by ϕ^* if the impeller angle (encoder position) is measured with reference to the casing location of a current window. The dimensionless angle in casing, θ^*, has the same origin as ϕ:

$$\theta^* = (\theta - \phi_0)/360 \text{ degrees}. \quad (2)$$

By considering the origin at window W2, the access windows have the following normalized angles:

Window #	2	8	7	6	5	4	3	2
θ^* (-)	0	0.12	0.19	0.36	0.56	0.69	0.88	1

The particles in suspension are 0.8 mm glass beads ($S_s = 2.48$, $v_\infty = 0.082$ m/s, $\mathrm{Re}_\infty = 65$) and have a quasi-uniform size distribution. The results presented here are for a dilute suspension, 0.16 percent solids by volume, where the particle interactions are negligible.

The liquid (in the presence of solids) and solid velocities were measured using a discrimination method based on the laser-Doppler signal amplitude (Cader et al., 1992). All three particle slip velocity components were obtained in a dilute water-glass beads mixture flow. The laser beams have access through eight transparent windows mounted flush into the casing wall. In order to obtain a better signal-to-noise ratio and to increase wear resistance, optical grade quartz with optimum light transmittance to the green and blue laser beams was chosen instead of plexiglass. In order to increase the amount of light back-scattered from the particles, the surfaces of the 0.8 mm glass beads were made opaque by increasing their roughness using a mill with finer sand particles.

General Flow Pattern and Particle Slip Velocity

Several qualitative aspects of the flow pattern have been identified in the previous experimental study (Roco et al., 1993):

(*a*) Large-scale periodical, two-phase flow structures develop in the entire casing, and are dominated by stationary waves. The stationary waves have two prominent maxima at the casing tongue and in the "bottle-neck" sector (at windows W8 and W3 in Fig. 1(*a*), respectively). They are determined by a combined effect of the impeller blade motion, impeller-casing flow interaction, and secondary currents in pump. Between windows W8 and W4 counterclockwise, there is a sector in casing where the flow is accelerated, and velocity fluctuations are relatively smaller;

(*b*) The particles generally lead the fluid in the radial direction and lag in the circumferential direction;

Nomenclature

A_{2i} = impeller outlet cross-sectional area, $\pi D_{2i} B_{2i}$
B_{2i} = blade width at the impeller outlet
D_{2i} = impeller outlet diameter
H = pump head
N = pump rotational speed
r, θ (degrees), z = coordinates
Q, Q_n = flow rate, and its nominal value
Q_{rc} = casing recirculation flowrate past the cut-water (Fig. 1(*a*))
Q_{ir} = inlet clearance recirculation flow (Fig. 1(*c*))
Re_∞ = particle Reynolds number calculated with the terminal settling velocity v_∞
u = velocity normalized with U_{2i} at a given ϕ_0
u_{sL} = slip velocity at a given ϕ_0 ($= u_s - u_L$)
U = average of u over the blade-to-blade interval
U_{sL} = average of u_{sL} over the blade-to-blade interval
U_{2i} = peripheral impeller tip speed
v_∞ = terminal settling velocity at $\alpha_s = 0$
S_s, S_m = specific density of solids and mixture, respectively
Z = number of blades on impeller
α_s = volumetric solids concentration
δA = uncertainty of A
Δr_{max} = maximum radial gap (Fig. 1(*c*))
$\Delta\phi$, $\Delta\phi_b$ = angular interval, and the blade-to-blade angular interval, respectively
$\Delta\eta_{slip}$ = loss of efficiency due to particle slip
ϕ_0, ϕ = impeller angle measured from window

(*c*) The measured circumferential velocity distribution at the impeller-casing flow interface, averaged over the blade width (B_{2i}) and pump circumference ($\theta^* = 0$–1) correlates well with the head obtained from the pressure measurements over the pump inlet and outlet. The velocity averages over the casing width (B_c) underestimate the pump head. All averages reported in the following sections have been performed over the blade width. By integrating the corresponding radial velocity distributions over B_{2i}, one obtains the sum of the discharge flowrate (Q) and of the inlet recirculation flowrate (Q_{ir} in Fig. 1(*c*)).

(*d*) The periodical and turbulent velocity fluctuations have a complexity which is not fully reflected in the present flow simulations. This paper presents only the periodical velocity fluctuations and their averages which are relevant to the overall pump performance.

Particle slip velocities cause a change in the mixture velocity triangle and a supplementary energy loss because of the work performed by the drag forces. Slip velocity at a point is a function of the blade position relative to that measurement location in casing. From the general analysis of the blade-to-blade velocity data, three ϕ^* intervals have been identified:

— $\phi^* = 0$ to 0.5, the wake interval after the displacement of a blade. This interval is generally marked by larger velocity gradients for liquid velocity components and maxima of their standard deviations. The liquid radial velocity tends to increase, and the circumferential velocity to decrease. The velocity standard deviation increases after the blade displacement at $\phi^* = 0$ to 0.3, which suggests an increase of the turbulence intensity for the same interval. The radial and circumferential particle slip velocities are larger immediately after $\phi^* = 0$, and then decrease;

— $\phi^* = 0.5$ to 0.82, the interval before the arrival of the leading face of the next blade. In this interval the liquid velocity and its standard deviation have a continuous decrease. This interval corresponds to the boundary layer formed on the pressure face of the blade. The particle slip decreases to a minimum at both Q_n and $Q_n/2$, while the absolute circumferential slip reaches a minimum in this interval only at $Q_n/2$;

— $\phi^* = 0.82$ to 1, corresponding to the displacement of the cylindrical surface of the blade trailing edge past the measuring point.

Periodic Characteristic Curves

Usually, the pump performance at flanges (Φ_p, Ψ_p η) or at the impeller outlet (Φ_b, Ψ_b η) is given in average over all impeller rotations for the duration of the acquisition, i.e. averaged over the impeller angle (ϕ_0^*). For instance:

$$\Phi_b = \int_0^1 \Phi_b'(\phi_0^*) \cdot d\phi_0^* \tag{3}$$

The periodical variation of the pump head, flowrate and efficiency loss caused by particle slip, can be determined by using the measured velocity distributions as a function of the impeller angular position. The pump dimensionless coefficients may be plotted versus ϕ_0^*: $\Phi_b'(\phi_0^*) = Q_b(\phi_0^*)/(U_{2i}A_{2i})$, $\Psi_b'(\phi_0^*) = gH_b(\phi_0^*)/U_{2i}^2$, and $\Delta\eta_{slip}'(\phi_0^*)$. This group of characteristic curves, identified in the present study, is important when the pump vibrations and the pressure fluctuations in an hydraulic system as a whole are relevant. The periodical fluctuations of the pump head and flowrate during the impeller rotation can induce pump vibrations, which may be amplified if the pump-pipe system attains its resonance frequency. By volume-time averaging the velocities to get the pump flowrate coefficient, and mass-time averaging the velocities to get the pump head coefficient at the impeller outlet, at a given impeller angle, and neglecting the fluid prerotation at the impeller inlet, one obtains for a liquid-solid particle mixture

$$\Phi_b' = (1-\alpha_s) < u_{L,r} >_{b,\mathrm{av}} + \alpha_s < u_{s,r} >_{b,\mathrm{av}} \tag{4}$$

$$= < u_{L,r} >_{b,\mathrm{av}} + \alpha_s < u_{sL,r} >_{b,\mathrm{av}} = \Phi_{Lb}' + \Delta\Phi_{sb}'$$

$$\Psi_b' = [(1-\alpha_s) < u_{L,\theta} >_{b,\mathrm{av}} + \alpha_s S_s < u_{s,\theta} >_{b,\mathrm{av}}]/S_m \tag{5}$$

$$= [< u_{L,\theta} >_{b,\mathrm{av}} + \alpha_s (S_s < u_{s,\theta} >_{b,\mathrm{av}} - < u_{L,\theta} >_{b,\mathrm{av}})]/S_m$$

$$= \Psi_{Lb}' + \Delta\Psi_{sb}'$$

The velocities in Eqs. (4) and (5) are normalized by the peripheral impeller tip speed, U_{2i}, and averaged over the blade width (B_{2i}) and over all windows around the casing

$$< u >_{b,\mathrm{av}} = \frac{1}{2\pi B_{2i}} \int_{B_{2i}} dz \int_{2\pi} u \cdot d\theta \tag{6a}$$

The particle slip velocity in the i direction is

$$u_{sL,i} = u_{s,i} - u_{L,i} = u_{sL,i}^* \cdot v_\infty / U_{2i} \quad (i = r, \theta) \tag{6b}$$

The liquid and solids slip velocities from the right-hand side of Eqs. (4) and (5) were determined from the LDV measurements. Only the velocities averaged over B_{2i} are used in these equations. However, the velocity distributions as a function of z have strong, typical nonuniformities, as previously presented (Cader et al., 1992; Roco et al., 1993). Figure 2 illustrates the periodical blade-to-blade change of water velocity and particle slip velocity in the radial direction at window W6 as a function of the impeller angle ϕ^* relative to that window. The velocity changes with ϕ^* at this window are representative for

Nomenclature (cont.)

W2, and from a current window, respectively

Φ = pump flange-to-flange flowrate coefficient

Ψ_b = pump head coefficient at the impeller outlet, averaged over B_{2i}

Ψ_p = pump flange-to-flange head coefficient

η = hydraulic pump efficiency ($g\rho QH$/shaft power)

ν = kinematic viscosity

θ = angular position in casing

Subscripts

av = averaged around the impeller (over $\theta = 0$ to 360 degrees)

b = blade, averaged over B_{2i}

i = impeller; or $i = r, \theta$

ir = inlet circulation

L, s, m = liquid, solids and mixture, respectively

p = pump, flange-to-flange

r, θ, z = radial, circumferential and axial direction, respectively

rc = recirculation in casing past the cutwater

$< >_b$ = average over B_{2i} ($z^* = 0.35$ to 0.7)

$< >_c$ = average over B_c ($z^* = 0$ to 1)

$2i$ = at the impeller outlet

Superscripts

r^*, θ^*, z^* = normalized coordinates

u_{sL}^* = dimensionless u_{sL} at a given ϕ_0 ($= u_{sL} \cdot U_{2i}/v_\infty$)

U_{sL}^* = dimensionless U_{sL} ($= U_{sL} \cdot U_{2i}/v_\infty$)

ϕ_0^*, ϕ^* = normalized ϕ_0 and ϕ by $\Delta\phi_b$, respectively

$\Phi', \Psi', \Delta\eta_{slip}'$ = define Φ, Ψ, $\Delta\eta_{slip}$ at a given angle ϕ_0

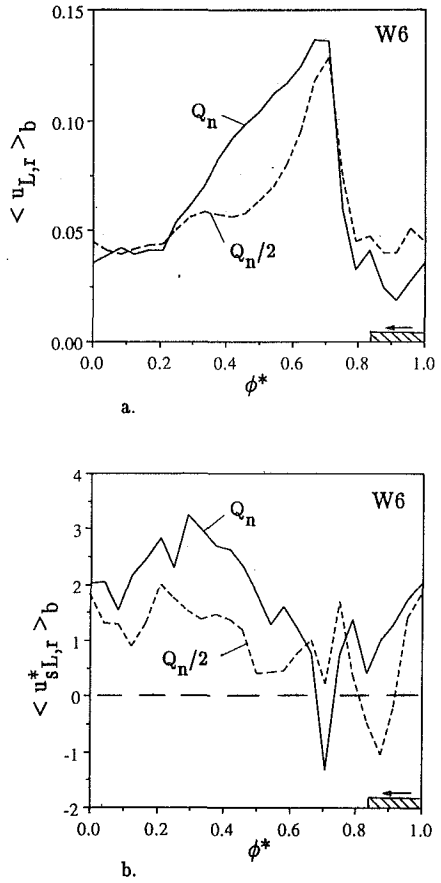

Fig. 2 Periodical fluctuations of radial velocities at window W6: (*a*) $<u_{L,r}>_b$ at Q_n and $Q_n/2$; (*b*) $<u^*_{sL,r}>_b$ at Q_n and $Q_n/2$ (uncertainties: $\delta\phi^* = 0.001$; $\delta < u_{L,r} >_b = 0.03$; $\delta < u^*_{sL,r} >_b = 0.04$)

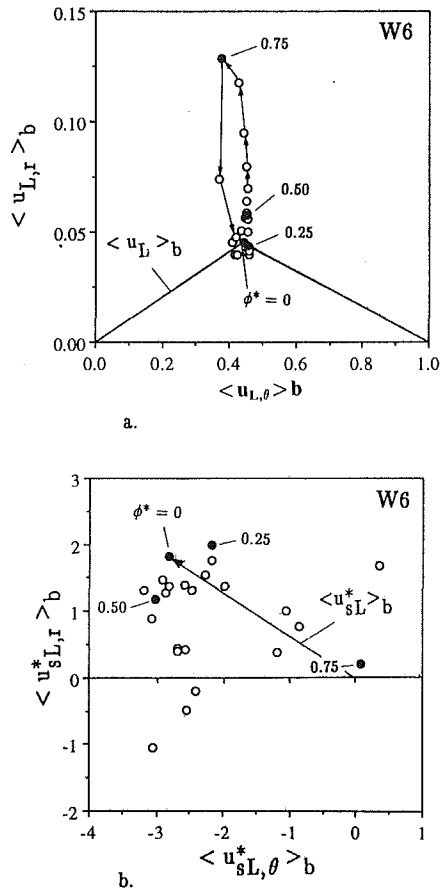

Fig. 3 Effect of ϕ^* on the velocity vectors at window W6: (*a*) water velocity triangles at $Q_n/2$; (*b*) particle slip velocity vector at $Q_n/2$; each circular dot is for a value ϕ^*, for instance 0, 0.25, 0.50, and 0.75 (uncertainties: $\delta < u_{L,i} >_b = 0.03$; $\delta < u^*_{sL,i} >_b = 0.04$; $i = r,\theta$)

the whole pump (Roco et al., 1993). The water radial velocities increase after the displacement of a blade, reaching a maximum at about $\phi^* = 0.7$, for both Q_n and $Q_n/2$. The particle slip velocity is larger in the wake interval ($\phi^* = 0$–0.5). In average over ϕ^*, the radial slip velocity is about 80 percent larger at Q_n than at $Q_n/2$.

The water velocity triangle and corresponding particle slip vector are functions of the location in casing. The effect of the impeller angular position (ϕ^*) on the water velocity triangle and particle slip vector is illustrated in Fig. 3 for window W6, at $Q_n/2$, by representing the vector extremities at intervals of $\Delta\phi^* = 0.05$. The dimensionless slip velocities $u^*_{sL,i}$ ($i = r$ or θ) are normalized by the particle settling velocity v_∞. The periodical water and particle slip velocity fluctuations, starting from $\phi^* = 0$ to 0.25, 0.5, 0.75, and again to 0, have a characteristic pattern. It is noticeable in Fig. 3(*a*) that the radial velocity increases more than three times when ϕ^* changes from 0 (when a blade's suction side passes by window W6) to 0.75 (before the arrival of the next blade at window W6). The increase is more than five times at Q_n, and the domain covered in the $<u_\theta>_b$ direction is also larger (Roco et al., 1993). The modulus of the particle slip velocity is larger in the wake interval ($\phi^* = 0$–0.5) as compared to $\phi^* = 0.75$ (Fig. 3(*b*)).

By averaging the fluid and particle slip velocity vectors given in Fig. 3 over the blade-to-blade interval ($\phi^* = 0$ to 1), one obtains a pair of mean vectors corresponding to window W6 (Fig. 4). Figures 4 (*a* and *b*), show the mean water and particle slip velocity vectors at all windows around the casing (from window W2 to W8) at $Q_n/2$. The circumferential water velocity is slightly larger at W3 and W4 and smaller at W6, W7, and W8, as compared to the average for all windows. The mean radial velocity is about zero at window W8, and maximum at windows W6 and W7 (Fig. 4(*a*)). In average over the casing circumference, the particle slip velocity vectors have negative circumferential components and positive radial components at $Q_n/2$ (Fig. 4(*b*)). Both the norms and angular positions of the slip velocity vectors at $Q_n/2$ are more dispersed as compared to Q_n. The circumferential components vary between $< U^*_{sL,\theta} >_b \approx -7$ at window W8 and ≈ 2 at window W3. If at Q_n the maximum angle between the slip velocity vectors is 75 degrees, at $Q_n/2$ the corresponding angle between the particle slip velocity vectors at W8 and W3 is larger than 90 degrees. The radial and circumferential velocities averaged over ϕ^* have a nonuniform distribution around the casing circumference (see Fig. 4 (*c* to *e*)). A progressive increase of the liquid circumferential velocity is observed between window W7 (after the casing tongue) and window W3 (before the discharge pipe). The liquid radial velocity has a peak at window W6–W7, and another at window W2. The absolute value of the radial particle slip velocity reaches its maximum at window W3, and the corresponding circumferential component at window W8, at the tongue (Fig. 4 (*d* and *f*)). While the radial liquid velocity $< U_{L,r} >_b$ is larger at Q_n as compared to $Q_n/2$ (Fig. 4(*c*)), the corresponding circumferential component is larger at $Q_n/2$ because of the recirculation flowrate past the cutwater Q_{rc} (Fig. 4(*e*)). This is true also at window W2 near the casing outlet, from where the flowrate splits into Q and Q_{rc}. The recirculation Q_{rc} develops similar to a vortex flow around the impeller, and is relatively large, particularly at off-duty flowrates, as in any pump with concentric impeller and casing.

The effect of solids on the characteristic curves can be determined from the second term of Φ'_b and Ψ'_b in Eqs. (4) and (5). The results are plotted in Figs. 5 and 6. The flowrate and

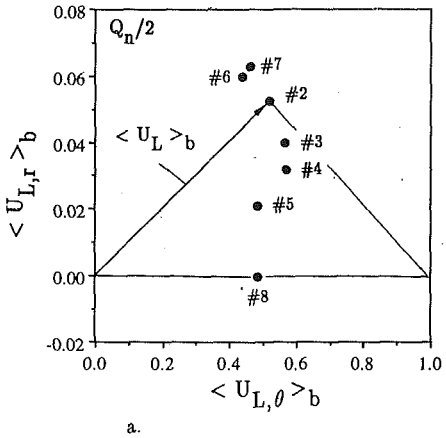

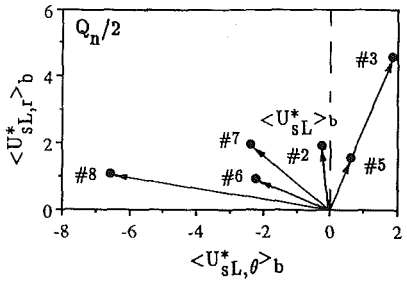

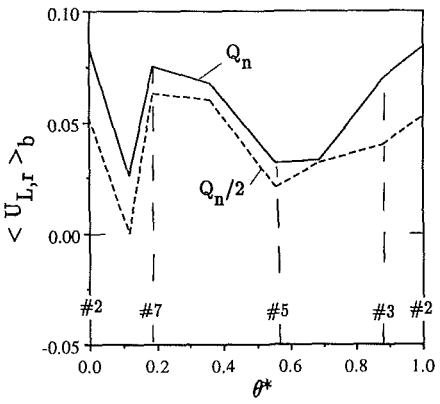

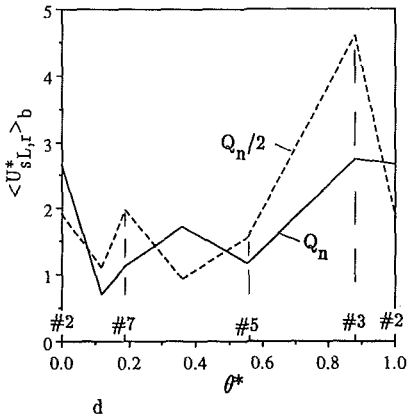

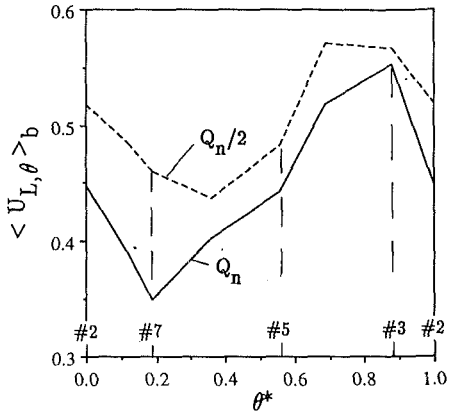

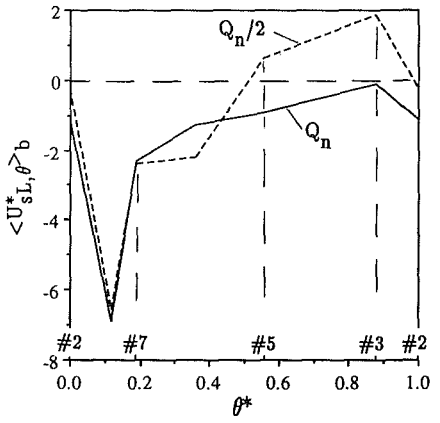

Fig. 4 Variation of the liquid velocity triangle and slip velocity vector, averaged over B_{2l}, at windows W2 to W8, at $Q_n/2$: (*a*) water velocity triangle; (*b*) particle slip velocity vector *c*, *d*, *e*, *f*. $< U_{L,r} >_b$, $< U^*_{sL,r} >_b$, $< U_{L,\theta} >_b$, and $< U^*_{sL,\theta} >_b$. at $Q_n/2$ *versus* Q_n.(uncertainties: $\delta < U_{L,i} >_b = 0.03$; $\delta < U^*_{sL,i} > = 0.04$; $i = r,\theta$; and $\delta\theta^* = 0.001$)

pump head have periodical fluctuations because of the finite number of blades. The standard deviation of the liquid flow coefficient $\Phi'_{Lb}(\phi^*_0)$ is almost the same at $Q_n/2$ and Q_n (40 to 45 percent), while the standard deviation of liquid head coefficient $\Psi'_{Lb}(\phi^*_0)$ is smaller at $Q_n/2$ (4 percent) than at Q_n (7 percent). The largest variations of Φ'_{Lb} and Ψ'_{Lb} occur at $\phi^*_0 = 0.7$–0.85, which corresponds to the arrival of the leading face of a blade at window W2. The standard deviation of $\Phi'_{sb}(\phi^*_0)$ and $\Psi'_{sb}(\phi^*_0)$ are between 45 percent and 71 percent. The most significant variations of ϕ'_{sb} and Ψ'_{sb} are in the wake interval ($\phi^*_0 = 0$–0.5) of a blade passing by window W2. Overall, the standard deviation of the total head coefficient Ψ'_b (Eq. (5)) derived from the velocity distributions is about 10 percent at Q_n, and about 5 percent at $Q_n/2$. The periodical velocity fluctuations at each window are an order of magnitude larger, but most velocity fluctuations cancel each other by averaging around the casing.

The work required to overcome the solid-liquid drag forces results in a reduction of the pump energy efficiency, $\Delta\eta_{slip}$. The corresponding energy dissipation due to particle slip was evaluated assuming that the impeller-casing flow interface is a representative area in the pump. This implies that the average particle slip velocity and concentration at that interface are assumed equal to the corresponding averages in the whole pump. This approximation is adopted in order to make a first evaluation of the effect of solids and of the impeller blade position. The energy dissipated per unit volume of fluid at the impeller outlet is obtained by multiplying the number of par-

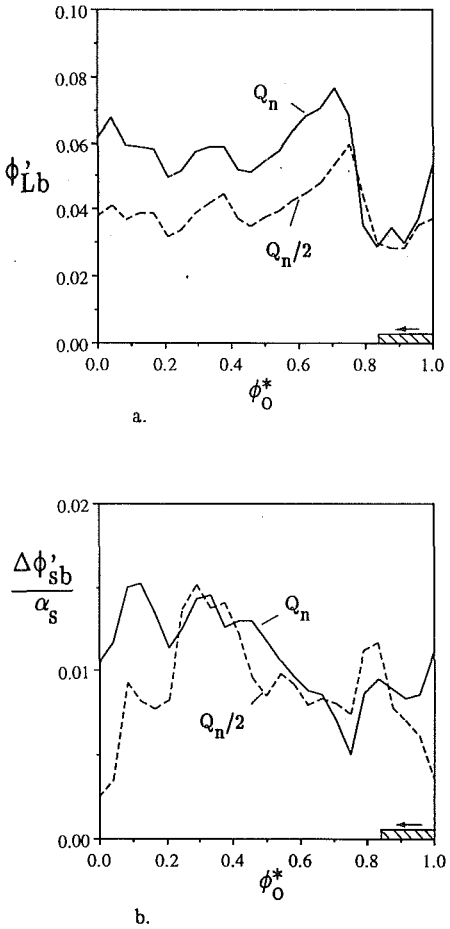

Fig. 5 Effect of ϕ_0^* on the flowrate coefficient at the impeller outlet (averaged over all circumferential windows): (*a*) for water, Φ'_{Lb}, (*b*) for solids, Φ'_{sb} (uncertainties: $\delta\Phi'_{Lb} = 0.03$; $\delta\Phi'_{sb} = 0.04$; $\delta\Phi^* = 0.001$)

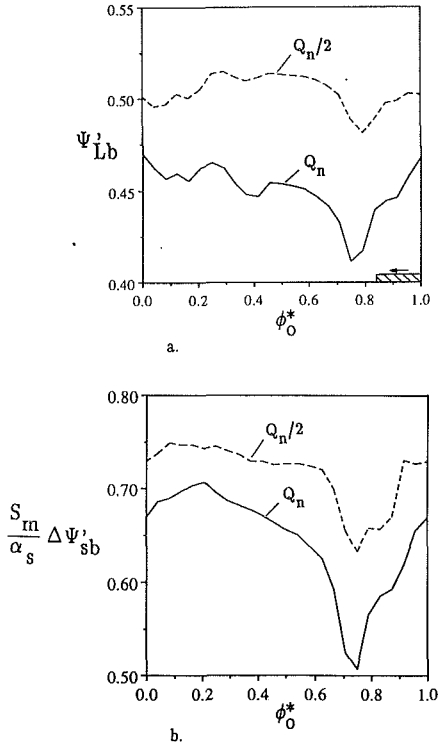

Fig. 6 Effect of ϕ_0^* on the head coefficient at the impeller outlet (averaged over all circumferential windows): (*a*) for water, ψ'_{Lb}, (*b*) for solids, ψ'_{sb} (uncertainties: $\delta\Psi'_{Lb} = 0.03$; $\delta\Psi'_{sb} = 0.04$; $\delta\phi^* = 0.001$)

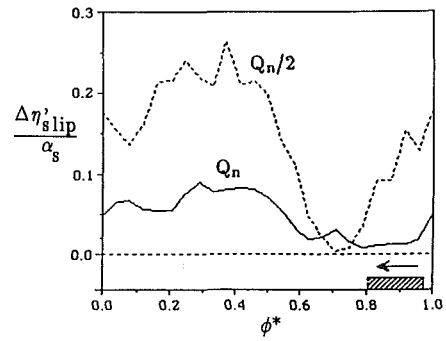

Fig. 7 Effect of ϕ_0^* on loss of energy efficiency by particle slip in the pump, $\Delta\eta'_{slip}/\alpha_s$ (uncertainty 0.06)

ticles per unit volume of mixture ($6\alpha_s/(\pi d_s^3)$) with the modulus of the drag force and the measured slip velocity. The drag force is estimated by assuming a drag coefficient equal to 0.44, corresponding to developed turbulent flow around the particle. The result is multiplied by the volume of mixture in the pump, and normalized by the total hydraulic power of the pump (ρgQH). For dilute slurries with negligible particle interactions, $\Delta\eta'_{slip}$ is proportional to solids concentration. The ratio $\Delta\eta'_{slip}/\alpha_s$ averaged over the casing circumference, is represented as a function of the blade-to-blade angular position ϕ^* in Fig. 7. The energy dissipation is larger in the blade wake (interval $\phi^* = 0$–0.5) especially at $Q_n/2$, and decreases before the arrival of the next blade (interval $\phi^* = 0.5$ to 0.82) where energy dissipation is about the same at both flowrates.

The periodicity due to the finite number of blades has a significant effect on the local velocity distribution. In the present experiments, the blade-to-blade velocity fluctuations are of the same order of magnitude as the mean velocity. However, due to averaging around the casing, the fluctuations of the pump dimensionless coefficients ϕ'_b and Ψ'_b are about 40 and 10 percent of the mean, respectively. If the impeller has a smaller number of blades, it is estimated that the periodical fluctuations of the characteristic curves would increase.

Head-Flowrate Performance Curve

The dimensionless pump flow rate and head coefficients given in (4) and (5) are now averaged over ϕ_0^*. By denoting $\Phi_b = Q_b/(U_{2i}A_{2i})$ and $\Psi_b = gH_b/U_{2i}^2$, one has:

$$\Phi_b = \int_0^1 \Phi'_b \, d\phi_0^* = (1-\alpha_s) < U_{L,r} >_{b,\mathrm{av}} + \alpha_s < U_{s,r} >_{b,\mathrm{av}}$$
$$= < U_{L,r} >_{b,\mathrm{av}} + \alpha_s < U_{sL,r} >_{b,\mathrm{av}} \tag{7}$$

$$\Psi_b = \int_0^1 \Psi'_b \, d\phi_0^*$$
$$= [(1-\alpha_s) < U_{L,\theta} >_{b,\mathrm{av}} + \alpha_s S_s < U_{s,\theta} >_{b,\mathrm{av}}]/S_m$$
$$= [< U_{L,\theta} >_{b,\mathrm{av}} + \alpha_s (S_s < U_{s,\theta} >_{b,\mathrm{av}} - < U_{L,\theta} >_{b,\mathrm{av}}]/S_m \tag{8}$$

where

$$U_{sL,i} = U_{s,i} - U_{L,i} = U^*_{sL,i} \cdot v_\infty / U_{2i} \quad (i = r,\theta) \tag{9}$$

and α_s is solids concentration by volume, S_s is the solids specific density, $< U_{L,i} >_{b,\mathrm{av}}$ $(i = r,\theta)$ are the Eulerian averages for the liquid velocity components in the presence of solids, and $< U^*_{sL,i} >_{b,\mathrm{av}}$ $(i = r,\theta)$ are the Eulerian averages for the particle slip velocity components normalized by v_∞.

By introducing the circumferential averages of the LDV measured velocities plotted in Fig. 4 (*c*-*f*) into Eqs. (7) and

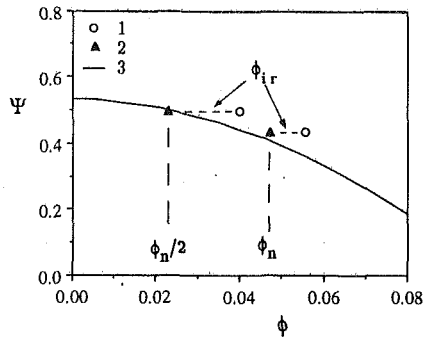

Fig. 8 Head versus flowrate coefficient averaged over the impeller rotation: 1. Φ_b and Ψ_b from LDV measurements over B_{2i}; 2. Φ_p from magnetic flowmeter, and Ψ_b; 3. flange-to-flange Φ_p and Ψ_p coefficients (uncertainties: $\delta\Phi$ and $\delta\Psi \leq 0.03$)

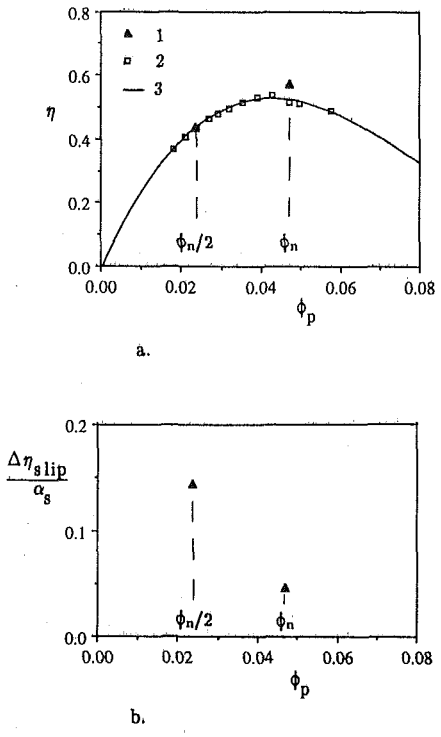

Fig. 9 Energy efficiency loss due to particle slip: (*a*) $\eta(\Phi_p)$; (*b*) $\Delta\eta_{slip}/\alpha_s(\Phi_p)$; 1. calculated with Φ_b and Ψ_b from LDV measurements over B_{2i}; 2. calculated with the flange-to-flange Φ_p and Ψ_p coefficients; 3. best fit curve of 2 (uncertainties: $\delta\eta \leq 0.03$; $\delta\Delta\eta_{slip}/\alpha_s = 0.06$; $\delta\Phi_p = 0.03$)

(8), one obtains two points (Φ_b, Ψ_b) corresponding to Q_n and $Q_n/2$. The points are marked by circles in Fig. 8. Since the velocity distribution was measured between the impeller shrouds, the resulted flowrate is the sum of the discharge flowrate (Q) and inlet recirculation flowrate (Q_{ir}). The solid triangles in Fig. 8 correspond to the head determined from the LDV velocity measurements, Ψ_b, and the discharge flowrate Q measured with a magnetic flowmeter mounted on the discharge pipe, Φ_p. The points marked by circles and triangles are compared to the $\Psi_p(\Phi_p)$ curve, which was obtained by using the flange-to-flange manometer pressure measurement (for Ψ_p) and the magnetic flowmeter (for Φ_p). It is obvious that the differences in flowrate between the points marked by circles and triangles are due to the inlet recirculation (dimensionless coefficient Φ_{ir}). This recirculation is larger at $Q_n/2$ ($Q_{ir} = 33.2$ m^3/h) as compared to Q_n ($Q_{ir} = 18.8$ m^3/h). By considering the average of the velocities over the impeller blade width (B_{2i}) to determine the head coefficient, the agreement with Ψ_p obtained from pressure measurements is within 5 percent. The difference between Ψ_b and Ψ_p includes the headlosses in the pump casing. If the averages had been taken over the entire casing width (B_c) the pump head coefficient predicted from the velocity distribution would have been lower because the mean circumferential velocity over B_c is lower than over B_{2i}.

Previous experimental results (including Sellgren and Vappling, 1986; Walker and Goulas, 1984; Roco et al., 1986), were based only on the pressure, flowrate and concentration measurements at the pump inlet and outlet. The present analysis shows the origin of the characteristic curve $\Psi_p(\Phi_p)$, and how the internal two-phase flow structure dictates its shape.

Efficiency Loss by Particle Slip

The pump efficiency curve $\eta(\Phi_p)$ obtained from the measured parameters on the pump is represented by a solid line (3) in Fig. 9(*a*). This is the best fit curve for η calculated with Ψ_p from pressure measurements, Φ_p from the magnetic flowmeter, and power measured at the pump shaft. The solid triangles (1) correspond to η calculated with Ψ_b results from the LDV velocity measurements (see Eq. (8) and Fig. 8), while Φ_p and power are measured in the same way.

The energy dissipation caused by particle slip for a full impeller rotation is obtained by integrating the results presented in Fig. 7 over ϕ^*. The dissipation is about three times larger at $Q_n/2$ than at Q_n. The averages over the blade-to-blade interval are: $\Delta\eta_{slip}/\alpha_s = 0.047$ for Q_n, and 0.144 for $Q_n/2$ (see Fig. 9(*b*)).

Experimental Uncertainty

The complexity of the measurements gives rise to numerous sources of uncertainty, from which only the most important are considered here. These sources are related to the LDV device (optical system and signal processors), and the statistical error involved in the choice of sample size. The Doppler frequency processors have an uncertainty of 1 percent for an individual measurement. The optical components of the LDV (TSI) also have an uncertainty of 1 percent. These optical components and the quality of the surfaces of the windows inserted into the pump casing affect the positioning of the probe volume in the pump. Several single-phase measurements at different locations were repeated, giving rise to differences of less than 1 percent between measurements at the same location. By setting the confidence level for an Eulerian average at 95 percent, the sampling uncertainty varies between 0.1 and 1 percent as a function of the local variance of the velocity histograms. The radial velocity component, measured at the impeller outlet, has a ratio of the standard deviation to mean of about 1. The same ratio for the circumferential component is about 0.1. The uncertainty of velocity fluctuation of an individual measurement was found to be 1 percent of the mean velocity (same as Hamkins and Flack, 1987). The uncertainty of the $r-\theta$ cross-correlation of the velocity fluctuations was found to be 2 percent of the square of the mean velocity.

Conclusions

The velocity distributions at the interface between the impeller and casing flow can be used to evaluate the pump head-flowrate characteristic curve at the impeller outlet. The relevant averaging surface for velocities is at the impeller outlet over the blade width (B_{2i}), and not over the casing width (B_c) as one may be intuitively inclined to choose.

The periodical fluctuations of the pump flowrate and head as a function of the impeller angle may cause pump vibrations, which could be amplified if the pump-pipe system is in resonance. It is proposed that $\Phi_b'(\phi_0^*)$, $\Psi_b'(\phi_0^*)$, and $\Delta\eta_{slip}'(\phi_0^*)$ be considered as a supplementary set of "periodic characteristic curves." Similar curves may be defined for the corresponding

flange-to-flange characteristics. The flowrate and head fluctuations at the pump discharge are about ten times smaller than those of the velocity fluctuations at the impeller-casing interface because of the averaging effect around the casing.

The main features of the liquid velocity distributions at Q_n and $Q_n/2$ are similar, with smaller periodical fluctuations and with larger inlet clearance recirculation at $Q_n/2$ (see Figs. 5, 6, and 8).

Besides the scientific relevance, the performed velocity measurements in a slurry pump model may be of interest in design and operation: for modifying the empirical formula of the impeller-casing slip factor, understanding the effect of the pump construction and particle size on the characteristic curves, defining areas with larger fluctuating and particle slip velocities in wear analysis, or calibrating computer codes.

Acknowledgments

This study was partially supported by Dresser Pump and NSF.

References

Cader, T., Masbernat, O., and Roco, M. C., 1992, "LDV Measurements in a Centrifugal Slurry Pump: Water and Dilute Slurry Flow," ASME JOURNAL OF FLUIDS ENGINEERING, Vol. 114, No. 4, pp. 606–615.

Eckardt, D., 1975, "Instantaneous Measurements in the Jet-Wake Discharge Flow of a Centrifugal Compressor Impeller," ASME *Journal of Engineering for Power*, July, pp. 337–346.

Hamkins, C. P., and Flack, R. D., 1987, "Laser Velocimeter Measurements in Shrouded and Unshrouded Radial Flow Pump Impellers," ASME *Journal of Turbomachinery*, Vol. 109, pp. 70–76.

Karassik, I. J., Krutzsch, W. C., Fraser, W. H., and Massina, J. P., 1976, *Pump Handbook*, McGraw-Hill, New York.

Paone, N., Riethmuller, M. L., and V. den Braembussche, R. A., 1989, "Experimental Investigation of the Vaneless Diffuser of a Centrifugal Pump by Particle Image Displacement Velocimetry," *Experiments in Fluids*, Vol. 7, pp. 371–378.

Roco, M. C., Cader, T., and Masbernat, O., 1993, "Periodic Liquid-Solid Flow Microstructure in a Centrifugal Pump," *Particulate Two-Phase Flow*, Chapter 13, Butterworth-Heinemann, Boston, pp. 391–493.

Roco, M. C., Marsh, M., Addie, G. R., and Maffet, J. R., 1986, "Dredge Pump Performance Prediction," *Journal of Pipelines*, Vol. 5, pp. 171–190.

Sellgren, A., and Vappling, L., 1986, "Effects of Highly Concentrated Slurries on the Performance of Centrifugal Pumps," *International Symposium on Liquid-Solid Flows*, M. C. Roco and W. Wiedenroth, eds., ASME, FED-38, New York, pp. 143–148.

Vocadlo, J. J., Koo, J. K., and Prang, A. J., 1974, "Performance of Centrifugal Pumps in Slurry Service," *Proc. Hydrotransport 3 Conf.*, BHRA, Cranfield, UK, Paper J2, pp. 17–32.

Walker, C. I., and Goulas, A., 1984, "Performance Characteristics of Centrifugal Pumps When Handling non-Newtonian Homogeneous Slurries," *Proceedings of the Institute of Mechanical Engineers*, Series 198 A, pp. 41–49.

Wiedenroth, W., 1970, "The Influence of Sand and Gravel on the Characteristics of Centrifugal Pumps, and Some Aspects of Wear in Hydrotransport," *Proc. Hydrotransport 1 Conf.*, BHRA, Cranfield, UK, Paper E1, pp. 1–28.

Hydrodynamic Design Considerations for Hydroacoustic Facilities: Part I—Flow Quality

J. M. Wetzel

R. E. A. Arndt

St. Anthony Falls Hydraulic Laboratory,
University of Minnesota,
Minneapolis, MN 55414-2196

Design studies are described for two recently completed large scale hydroacoustic test facilities (one of which is the world's largest). These recirculating water tunnels have a different configuration than conventional tunnels, and special hydrodynamic design studies were required to evaluate and optimize the performance of some critical components. This paper considers the flow quality in the test section as influenced by the design of the contraction and the turbulence management system. Numerical modeling and experimental work were used to arrive at an acceptable nonsymmetrical nozzle design. Studies were also made of a turbulence management system using honeycombs rather than screens as typically used. Although design goals for turbulence levels were met, this study indicated that additional research in the area of turbulence management is necessary before there is a complete understanding of the overall process of turbulence attenuation.

I Introduction

There has been a resurgence of interest in the development of flow facilities for laboratory research and testing. Although water tunnels have been used successfully in the past for cavitation research, their use in the field of hydroacoustics has been limited. This is primarily associated with the fact that the older water tunnels were not designed for that purpose. However, some modifications have been made to reduce the noise levels and thereby increase their utility.

Recently, specific efforts have been directed toward the design and construction of "quiet" water tunnels. These efforts have resulted in some new facilities now in operation, e.g., the Large Cavitation Channel (LCC) for the U.S. Navy, and the Hydrodynamics and Cavitation Channel (HYKAT) for the Hamburg Ship Model Basin (HSVA) in Hamburg, Germany. These facilities utilized a number of design features that deviated from conventional water tunnel design practice. For example, it was necessary to design a nonsymmetrical nozzle that could produce a uniformity of flow in the test section that was equal to or better than what could be achieved with a conventional nozzle. Special attention was also given to the development of a turbulence management system that would reduce test section turbulence levels to about 0.1 percent without introducing significant amounts of self-generated noise.

Anticipated design problems were evaluated by both numerical and physical modeling. The physical model for the LCC included the contraction, test section, and diffuser at a scale ratio of 1 to 10. The HYKAT model included the portion of the flow circuit from the vaned elbow preceding the settling chamber to the pump intake, thereby including three of the four elbows in the loop; the scale ratio for this model was 1 to 5. Both models used air as the test fluid. Further details are presented by Wetzel et al. (1983), Arndt et al. (1984), Song et al. (1987, 1988), Wetzel and Arndt (1990, 1991). Some results for these two models and comparison with the numerical models are discussed in the following sections. In this paper only the contraction and the turbulence management system are considered. Studies of the rest of the flow circuit are described in a companion paper (Wetzel and Arndt, 1993).

II. General Considerations

A. Specifications. Typical performance specifications for state-of-the-art facilities are:

1. Test section velocity uniformity within 1 percent of mean value of the longitudinal velocity excluding the boundary layer.
2. A turbulence level of 0.1 percent or lower
3. Model test configurations top mounted or sting mounted for propellers
4. Velocity regulation ($\pm 1/2$ percent of full scale)
5. Test section pressure 3.4 KPa to 414 KPa, 0.03 to 4.0 bar
6. Water quality (particle size < 5 microns)
7. Extremely low noise levels in the test section

B. Configuration. In order to meet these specifications, consideration must first be given to the general overall configuration. To satisfy the requirements for a top-mounted test body such as a ship hull, it is convenient to have the entire top of the upper leg of the tunnel flat. In this manner it is possible to enter the test section without a major draining of the tunnel circuit. The use of a flat top also removes the static head which exists for a symmetrical contraction. Thus, lower cavitation numbers can be obtained in the test section; this is particularly important for the lower velocities.

The two configurations studied by the authors are shown in

Contributed by the Fluids Engineering Division for publication in the JOURNAL OF FLUIDS ENGINEERING. Manuscript received by the Fluids Engineering Division January 11, 1993; revised manuscript received September 24, 1993. Associate Technical Editor T. T. Huang.

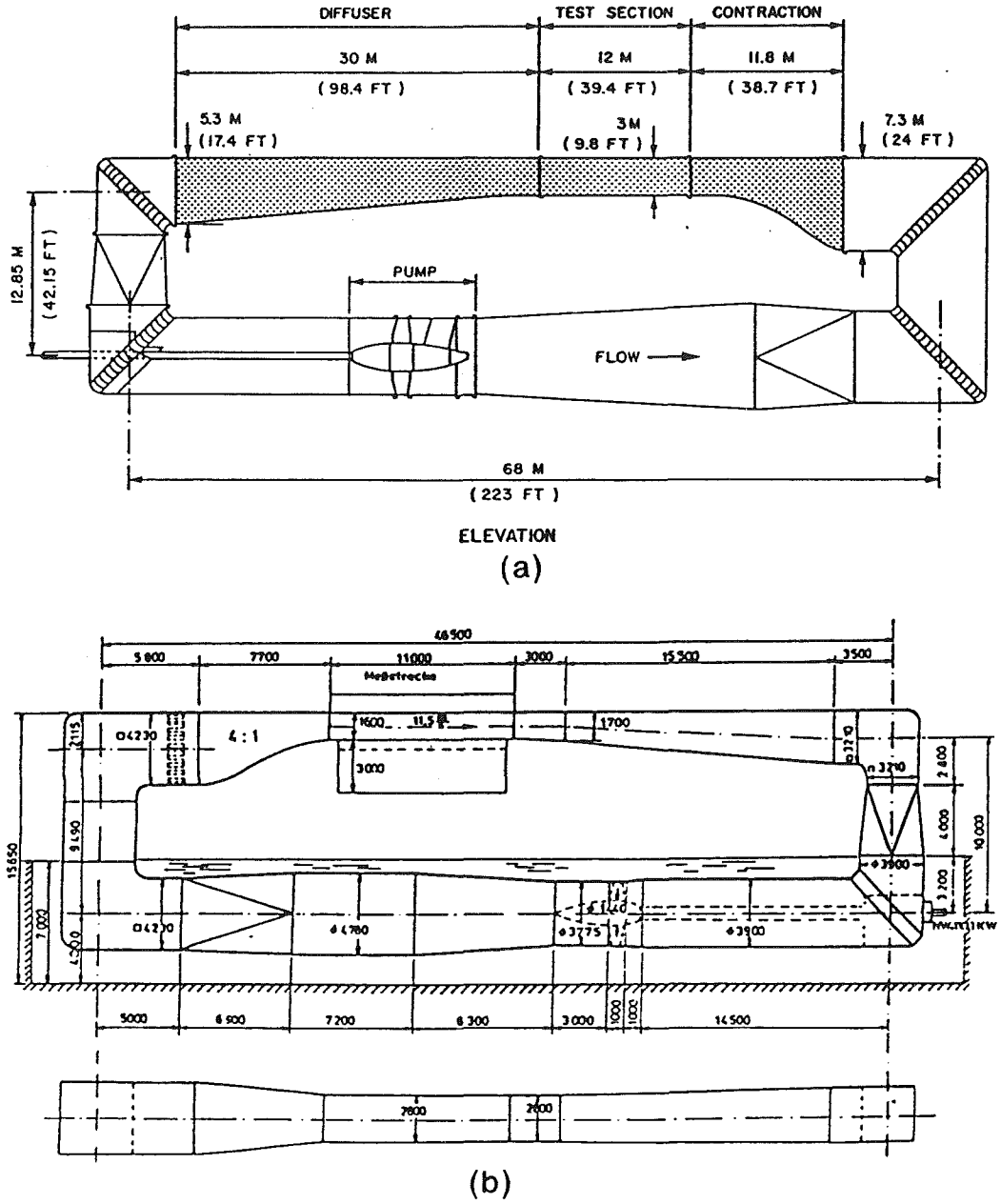

Fig. 1 Configurations of new cavitation facilities. (*a*) LCC (*b*) HYKAT

Fig. 1. (The shaded region in Fig. 1a indicates the components physically modeled for the LCC.) Although they are similar in appearance, there are some differences as indicated in Table 1.

Tests on existing water tunnels have indicated that the pump is the most significant noise source in the flow circuit. Therefore pump cavitation is an important consideration (see Wetzel and Arndt, 1993). The location of the pump in the lower leg

Nomenclature

c = nozzle contraction ratio
C_p = pressure coefficient $= (P - P_0)/(1/2)\rho U^2$
f = frequency
M = honeycomb cell size
P = pressure
P_0 = reference pressure
Re = Reynolds number
St = Stratford number
u = fluctuating velocity
u_1, u_2, u_3 = components of fluctuating velocity
U = mean stream velocity
x = streamwise direction
x_i = position of inflection point
y = vertical direction
η = turbulence reduction factor
μ = dynamic viscosity or non-isotropy factor
ν = kinematic viscosity, or nonisotropy factor
ρ = fluid density

Subscripts

e = exit
i = inflection point (see test)
I = inlet
l = local
P = plenum
T = test section

Table 1 Comparisons of LCC and HYKAT

	LCC	HYKAT
Test section LWH, m	12×3×3	11×2.8×1.6
Test section velocity, m/s	15	11.5
Contraction ratio	6	4
Main diffuser area ratio	3.12	2.3
Second elbow	Round	Square

of the flow circuit is also of importance. In conventional designs the pump is usually installed immediately downstream of the second elbow. (The elbows are numbered starting with number one following the main diffuser in the upper leg.) Such an installation provides the maximum length possible for the flow to stabilize before entering the main contraction in the upper leg. However, the inflow velocity distribution at this location may not be symmetrical; thereby increasing the likelihood of pump cavitation and unsteady flow. A compromise is therefore made to locate the pump at some distance from the second elbow to improve the inflow velocity characteristics. This is a compromise since this configuration requires the pump drive shaft to be lengthened, which may require an additional support bearing. For a given overall length of the water tunnel, the diffuser following the pump is reduced in length, resulting in an increase of the included angle of the diffuser for a given area ratio. This decreases the pressure recovery from the pump outflow so that these features must be considered in the tradeoff analysis.

The configuration of the test section, i.e., cross-section shape, size, and length, is determined by the particular type of testing and test bodies for which the facility is to be used. Current trends are for either a rectangular or square cross-section of considerable length. The cross-sectional area is determined from an analysis of the blockage corrections required for given test bodies. For a closed test section of constant cross sectional area, a longitudinal pressure gradient exists due to the development of the wall boundary layers. Compensation for boundary layer growth can be made by diverging the walls in the direction of flow, or if corner fillets are employed, the fillet size can be diminished in the flow direction. In either case, the solution is valid only for a given flow velocity, and therefore is not commonly employed.

The quality of the flow in the test section is directly related to the contraction design, which involves consideration of contraction ratio, shape, and length. As mentioned above, other considerations dictate the design of a nonsymmetrical contraction.

To achieve the desired turbulence level, attention must also be directed towards the turbulence control system (honeycomb and/or screens) upstream of the contraction. A considerable amount of literature on turbulence management is available that can be utilized, for example, Loehrke and Nagib (1976), Ramjee and Hussian (1976), Tan-Atichat and Nagib (1982), and Lumley and McMahon (1967).

In the above considerations, it must be stressed that a state-of-the-art facility design requires careful evaluation of many individual components, and the iteraction between these components to an extent that has probably not been previously considered.

In the past most designs were developed from experience, physical model tests, and to a limited extent, theoretical computations based on potential flow theory. The latter was used particularly for design of axisymmetric contractions and turning vanes in cascade. Fortunately, sufficient progress has now been made in numerical modeling so that computations can be made for 3-D flow in contractions, including effects of non-uniform inlet velocity profiles. These computational procedures have been verified by experimental measurements and are now a valuable tool in the design of hydrodynamic test facilities.

III Contraction Design

Several parameters are of importance in the determination of a nozzle design which includes contraction ratio, length, and shape. The contraction ratio essentially sets the physical dimensions of many other parts of the flow circuit. Large contraction ratios permit the use of large cross-section conduits in other parts of the circuit and thus reduce headloss. In general, the larger contraction ratios tend to contribute to better flow uniformity and lower turbulence levels in the test section. However, compromises must be made in the interest of economy. Wind tunnels are usually provided with relatively large contraction ratios; greater than 10 is quite common (Morel, 1977; Pope, 1966; Pankhurst and Holder, 1952). In the design of large water tunnels, lower ratios are employed due in part to the physical structure required to hold the large volume of water involved.

The length of the contraction should be as short as possible to reduce the boundary layer development, and yet prevent boundary layer separation due to adverse pressure gradients. Short length is also desirable for economic considerations, but may not be compatible with other flow requirements. Length and shape of the contraction are closely related parameters. Here reference to shape is more directed towards the boundary shape rather than the cross-sectional shape.

Numerical modeling techniques based on the inviscid Euler equations based on the inviscid Euler equations have been applied to the analysis of three-dimensional non-symmetrical contractions and have included the influence of non-uniform entrance velocity distributions on contraction performance. These techniques have been discussed by Song and Yuan (1988) and have been experimentally verified (Wetzel et al., 1986). Contractions with ratios of 4 and 6 were of particular interest for the HYKAT and LCC. The tops of these contractions were flat, with curvature confined to the sidewalls and bottoms. For the larger contraction ratio, the cross section was square (LCC), whereas for the smaller ratio, the cross section changed from square to rectangular at the test section (HYKAT).

Several boundary shapes were selected for detailed study. The first nozzle shape has been suggested by Wille (1963) and is given by

$$\frac{y}{y_0} = 2\left(\frac{x}{L}\right)^3 - \left(\frac{x}{L}\right)^6 \tag{1}$$

with the origin at the nozzle exit. L is the nozzle length and y_0 is the maximum ordinate at the nozzle entrance ($x = L$). The point of inflection is located at $x_1 = x/L = 0.737$. (x is measured upstream in Eqs. (1) and (2).)

During development of the LCC, a physical model was constructed and evaluated using this contour and a contraction ratio of six. Measurements were made of boundary pressures and the exit velocity profiles. Although the exit velocity profiles were essentially uniform, the pressure distribution near the inlet indicated a possibility of boundary layer separation due to the adverse pressure gradient. Consequently, several other contraction shapes were investigated using the numerical model. The overall length and contraction ratio were not changed.

The boundary curves selected for this purpose were defined by fifth-order polynomials, i.e.,

$$\frac{y}{y_0} = A\left(\frac{x}{L}\right)^3 + B\left(\frac{x}{L}\right)^4 + C\left(\frac{x}{L}\right)^5 \tag{2}$$

where $A = 10\ x_i(4x_i - 3)/D$, $B = -2A + 5$, $C = A - 4$, and $D = 10x_i^2 - 12x_i + 3$, where x_i is the position of the inflection point.

The family of fifth order polynomials given by Eq. (2) as a function of x_i was selected to improve the boundary layer separation characteristics. As the flow enters the contraction, the wall pressure rises and then decreases as the flow is accelerated. The magnitude and spatial rate of change of the

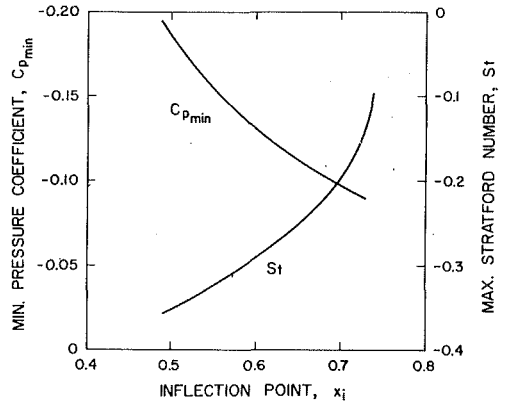

Fig. 2 Effect of inflection point location on Cp_{min} and separation parameter for contours given by Eq. (2) (LCC)

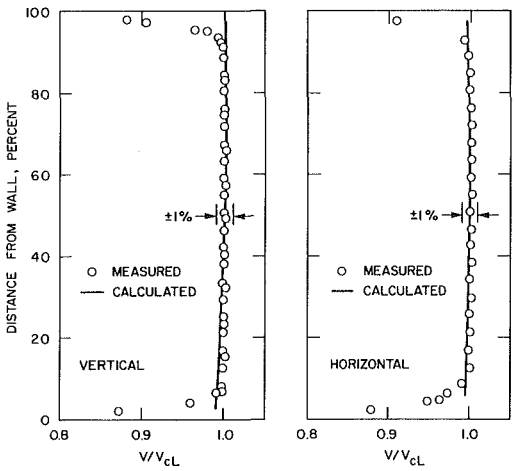

Fig. 3 Comparison of measured and calculated mean test section velocity distributions, $x_i = 0.5L$ (LCC)

pressure, if excessive, can lead to boundary layer separation. Near the exit of the contraction, an overshoot of velocity occurs, resulting in a further decrease in boundary pressure before rising to the test section pressure. This pressure minimum can lead to local cavitation if sufficiently low. The magnitude of the pressure coefficients can be changed by varying the location of the inflection point, x_i. It can be shown that with $x_i = 0.5$, the second derivative of Eq. (2) is zero at $x/L = 1$. For any other x_i, this condition is not satisfied.

According to Stratford (1959), the turbulent boundary layer separates at the point where

$$C_p\left(x\frac{dCp}{dx}\right)^{1/2} = 0.35(10^{-6}\,\mathrm{Re})^{1/10} \qquad (3)$$

where $d^2p/dx^2 \geq 0$ and $Cp \leq 4/7$.

In the above equation, Cp is the pressure coefficient and $\mathrm{Re} = Ux/\nu$. To test the likelihood of boundary layer separation, the Stratford number was computed along the centerline and corner line of the bottom surface.

$$\mathrm{St} = Cp(xdCp/dx)^{1/2} - 0.35(10^{-6}\mathrm{Re})^{1/10} \qquad (4)$$

Thus, the boundary layer will separate if $\mathrm{St} \geq 0$ with no separation predicted for $\mathrm{St} < 0$.

The minimum pressure coefficient occurring near the exit of the contraction has been determined for various x_i using test section wall and dynamic pressures as reference values. Equation (4) has also been calculated near the entrance to the contraction with entrance wall and dynamic pressures used for reference and at typical full-scale Reynolds numbers. The results of these computations for the LCC are shown in Fig. 2. As the inflection point is moved closer to the entrance, the pressure coefficient becomes less negative, which is desirable for cavitation resistance. However, the tendency for boundary layer separation increases as ST also becomes less negative. Thus, for a contraction of given length and area ratio, a compromise must be made as to the location of the inflection point.

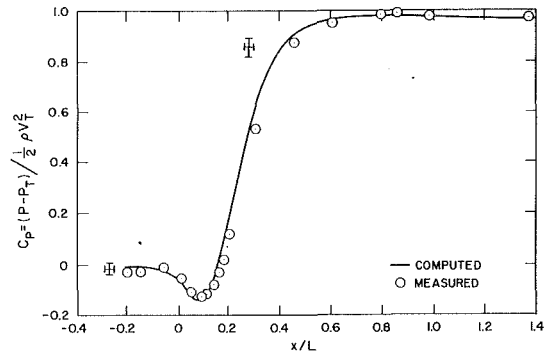

Fig. 4 Comparison of measured and computed contraction wall pressures. Bottom centerline, $x_i = 0.5L$ (LCC). Error band shown with bracketed lines.

The experimental data for the velocity distribution along the horizontal and vertical centerlines at mid-distance in the LCC test section are plotted in Fig. 3. The velocity profiles are quite flat outside the boundary layer regions, and the experimental data agree well with the computations of the math model. The variations are within the ±1 percent required by the specifications.

The wall pressures along the bottom centerline are shown in Fig. 4 with the pressure coefficient referenced to test section pressure and velocity. Good agreement between the measured and calculated pressures was obtained. No evidence of any boundary layer separation was noted. However, the pressure minimum near the contraction exit was of concern. As the numerical model was sufficiently accurate in the prediction of boundary pressures, it was used to determine the performance of the final contraction shape. It can be noted in Fig. 2 that St approaches zero quite rapidly as x_i increases. For example, St is approximately doubled if x_i/L is reduced to 0.7 from 0.737 with only a slight change in the minimum Cp. Near the exit region of the contraction, calculations of St for various x_i indicated a nearly constant value of about -0.6, which is sufficiently negative to indicate that separation would not be expected. Therefore, the governing factor at the exit is the magnitude of the minimum pressure coefficient and the impact on cavitation inception.

Additional studies were made during the development of the HYKAT. A parametric study has been made to evaluate the performance of three-dimensionsal contractions using the numerical model. The contraction ratio was fixed at four with an inlet section 4.23 m square and two slightly different contraction lengths were used. Of particular interest was the minimum pressure coefficient occurring near the downstream end of the contraction. Results of these computations are listed in Table 2 for the inflection point located 0.6 times the contraction length from the exit. The influence of upstream velocity nonuniformity was also examined by using a linear profile with the velocity at the bottom 20 percent greater than the mean velocity.

The velocities, u_{max} and u_{min}, are the maximum and minimum velocities, wherever they occur across the section, and $\bar{u}$ is the mean velocity at the section. The pressure coefficient is referenced to test section pressures and velocities.

Runs 1 and 2 show the effect of changing the exit section from rectangular to square and keeping the inlet section square. This changed the minimum C_p by about 7 percent. Results for

Table 2

Run no.	Contraction length, m	Test section, m	Inflow $u_{max}-\bar{u}/\bar{u}$, percent	Outflow $u_{max}-\bar{u}/\bar{u}$, percent	Outflow $\bar{u}-u_{min}/\bar{u}$, percent	Min Cp.
1	7.7	2.8×1.6	0	0.69	0.27	−0.113
2	7.7	2.12×2.12	0	0.94	0.62	−0.121
3	7.7	2.8×1.6	0	1.1	0.58	−0.038
4	8.7	2.8×1.6	0	0.91	0.50	−0.022
5	8.7	2.8×1.6	20	2.37	1.30	−0.032
6	8.7	2.8×1.6	0	0.29	0.30	−0.085
7	8.7	2.8×1.6	20	1.72	1.47	−0.089

a symmetrical contraction of two different lengths are listed as Runs 3 and 4. Here the magnitude of C_p has been reduced from the value of the non-symmetrical configuration of Run 1 and also the increased length has resulted in further reduction of C_p. Computations for the symmetrical contraction with a non-uniform inflow velocity distribution are summarized in Run 5. A small change is noted in C_p, but a larger change is noted in the outflow velocity distribution as evidenced by comparison of Runs 4 and 5.

Data for the longer non-symmetrical contraction with a uniform and non-uniform inlet velocity distribution are listed in Runs 6 and 7. Only a slight change in C_p is observed, again with a larger change in the outlet velocity distribution. The minimum pressure coefficient occurs in the bottom corner. The calculated cavitation number for an extreme case, assuming vapor pressure at the top of the test section is about 0.25. This is considerably in excess of the magnitude of the pressure coefficient, and therefore cavitation should not occur at that location.

Other alternatives were examined to evaluate cavitation, velocity uniformity, and boundary layer separation. These were a nonsymmetrical design with a flat top, an intermediate design with 1/3 of the contraction from the top and 2/3 from the bottom, and a symmetrical design with equal contraction from the top and the bottom. In terms of velocity uniformity and boundary layer characteristics, all were about equally good. However, it is normally desired to have cavitation occurring in the test section before any other locations in the tunnel. In the case of HYKAT, it was found that with a flat top surface, cavitation initiates at the test section for any velocity, whereas for the other two cases, cavitation will start first at the contraction entrance if the velocity is below about 5 and 7 m/s, respectively. On this basis, non-symmetrical sections with a flat top have been found to be acceptable.

VI Turbulence Management

Low turbulence levels in the test section are very desirable for modern water tunnels. The high turbulence levels in ordinary water tunnels make it difficult to interpret and apply to design the results of research on a variety of topics ranging from cavitation to boundary layer control. While considerable information on turbulence management exists for wind tunnels, information on water tunnels is sparse. In addition, the use of screens, the most commonly used device for turbulence control in wind tunnels, is not possible in water tunnels because of their tendency to "sing" in water flow. The literature contains information on retrofitted turbulence management systems. In these cases the incoming turbulence was a measured quantity. In the design of a new tunnel, the incoming turbulence is an unknown and can only be estimated. It is therefore desirable to carry out physical modelling of the turbulence management system since the experience with designing low turbulence water tunnels is very limited. Fortunately, there is sufficient information available in the literature to make a first cut at design which can then be "fine tuned" with physical model studies. The approach has been to use the theory of Lumley and McMahon (1967) and Batchelor (1960). Application of this theory was experimentally verified by Robbins (1978) during the retrofit of the turbulence management system in the Garfield Thomas Water Tunnel at the Pennsylvania State University.

The turbulence intensity in the test section is due primarily to three factors: 1) the scale and magnitude of the turbulence entering the management system, 2) the attenuation of turbulence by the honeycomb and the generation of new, finer scale turbulence leaving the honeycomb, 3) the decay of turbulence in the stilling basin and the contraction. Lumley (1964) has developed a procedure for determining the attenuation of incoming turbulence by a honeycomb. This is summarized in Lumley and McMahon. Primarily three factors are important: 1) the ratio of intergral scale of the incoming turbulence to the honeycomb cell size, 2) the length to diameter ratio of the honeycomb cells, and 3) the Reynolds number based on cell size. Lumley and McMahon suggest that the attenuated incoming turbulence and the self-generated turbulence can be added linearly. They propose this on the basis that the scales of the residual incoming turbulence and the self-generated turbulence are so different that little interaction occurs. For a distance, x_P downstream of a honeycomb, the turbulence intensity in the plenum is given by

$$\left[\frac{\overline{u^2}}{\overline{U^2}}\right]_P = \eta\left[\frac{\overline{u^2}}{\overline{U^2}}\right]_I + \frac{0.0072}{x_P/M} \tag{5}$$

where M is the mesh size of the honeycomb. The turbulence level in the test section is a result of viscous dissipation and the effects of the contraction on the turbulence in the plenum. Unfortunately, theory and data are only available for symmetrical nozzles of circular cross section. If the nozzle is idealized as conical, the equivalent straight section is 1/3 the total length. To this must be added the length of the stilling basin. Thus, the viscous decay is given by

$$\frac{(\overline{u^2})_T}{(\overline{u^2})_P} = \frac{2_P}{x_T} \tag{6}$$

where x_T is the length of the stilling basin plus the equivalent length of nozzle. The effect of the contraction was derived by Batchelor (1960) as

$$\left(\frac{\overline{u^2}}{\overline{U^2}}\right)_T = \frac{\mu+2\nu}{3c^2}\left(\frac{\overline{u^2}}{\overline{U^2}}\right)_P \tag{7}$$

where c is the contraction ratio of the nozzle, μ and ν are factors due to the nonisotropy of the turbulence, which are a function of the contraction ratio:

$$\mu \cong \frac{3}{4}c^{-2}(\log 4c^3 - 1) \tag{8}$$

$$\nu \cong \frac{3}{4}c \tag{9}$$

Batchelor provides a plot of μ and ν as a function of contraction ratio for convenience. The attenuation factors in Eqs. (6) and (7) must be multiplied together to obtain the turbulence level in the test section.

The design procedure would appear to be relatively straight-

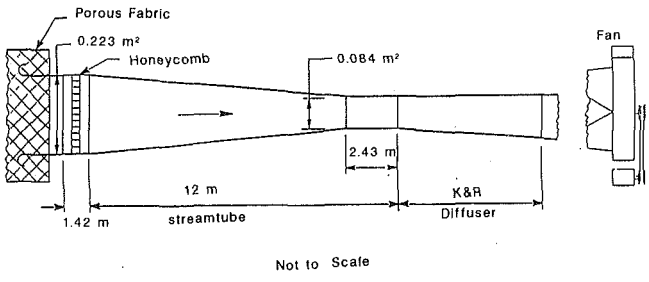

Fig. 5 Schematic of streamline model

forward. Given the scale, and amplitude of the incoming turbulence, η can be determined on the basis of the selected honeycomb characteristics. Equation (5) is used to determine the plenum turbulence level and Eqs. (6) and (7) are used to determine the final test section turbulence intensity. Unfortunately, there is little evidence to support the use of this procedure in the design of the LCC or the HYKAT since the problem is complicated by the use of tandem honeycombs and the fact that the nozzles are non-symmetrical and noncircular in cross section. It was therefore deemed prudent to experimentally verify the design procedure. During the design of the LCC, a rather unique experimental program was carried out which allowed the evaluation of full-scale honeycomb to minimize scale effects. Only a representative stream tube could be investigated in the laboratory. The stream tube has the same contraction ratio and the same contraction length as the prototype nozzle. The experimental apparatus is shown schematically in Figure 5. A representative section of full-scale honeycomb contained more than 800 cells. Thus, the stream tube model was deemed to be a reasonable simulation of the effects of contraction on the turbulence. A grid of quarter round bars were placed horizontally just downstream of the bellmouth inlet, oriented so that the rounded ends simulated the leading and trailing edges of a system of turning vanes. Turbulence was measured using hot-wire anemometry at twenty-one stations along the stream tube. Representative data obtained with two different honeycombs are shown in Figs. 6 and 7. The attenuation of plenum turbulence for a contraction ratio of 6 is expected to be from Eq. (7):

$$\frac{\left(\overline{\frac{u^2}{U^2}}\right)_T}{\left(\overline{\frac{u^2}{U^2}}\right)_P} = 0.0835 \tag{10}$$

which must be multiplied by the viscous decay factor. For the experimental setup this is estimated to be

$$\frac{(\overline{u^2})_T}{(\overline{u^2})_P} = 0.2 \tag{11}$$

Thus, the overall attenuation is found to be

Nozzle Attenuation factor

$$= \frac{\left(\sqrt{\overline{u^2}}/U\right)_T}{\left(\sqrt{\overline{u^2}}/U\right)_P} = \sqrt{0.0835 \times 0.2} = 0.129 \tag{12}$$

Neglecting the influence of the contraction on the structure of the turbulence and neglecting viscous dissipation, the nozzle attenuation factor would be simply $1/c = 0.167$. The data in Fig. 6 indicate this factor to be 0.13 for $M = 5.08$ cm in agreement with calculations. On the other hand, the data for the 2.54 cm grid (Fig. 7) indicate that the finer mesh honeycomb is more effective in attenuating upstream turbulence (as expected), but the resulting turbulence is less effectively attenuated in the nozzle. However, care must be given to the interpretation of these results. Only the axial component of turbulence was measured. The turbulence must be isotropic at the inlet and outlet of the contraction for the ratios of $\sqrt{\overline{u_1^2}}/U$ and $\sqrt{\overline{u^2}}/U$ to be comparable since

$$\overline{u^2} \equiv (\overline{u_1^2} + \overline{u_2^2} + \overline{u_3^2}) \tag{13}$$

More detailed analysis due to Arndt et al. (1983) indicate that there is a more complete return to isotropy for the finer scale turbulence downstream of the 2.54 cm honeycomb and the ratio of turbulence intensity between the test section and plenum are more closely representative of the ratio of *total* turbulence intensity. This study only provided guidance but unfortunately was not directly applicable to the design of the LCC since a tandem honeycomb design was selected.

Further experimental studies were made during the design of HYKAT. A tandem honeycomb design is also used. After considerable analysis, the upstream honeycomb was selected

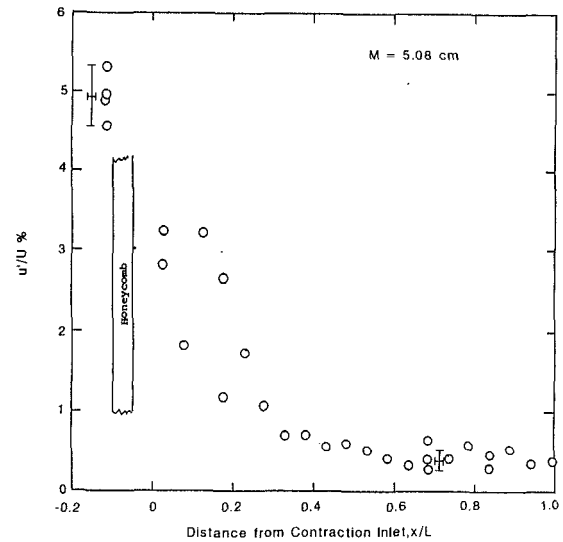

Fig. 6 Variation of u_i/U based on local velocity along axis of streamtube, $M = 5.08$ cm. Error band shown with bracketed lines.

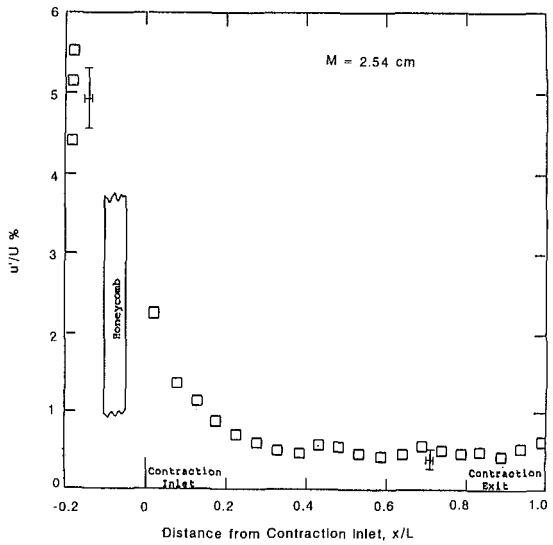

Fig. 7 Variation of u_i/U based on local velocity along axis of streamtube, $M = 2.54$ cm

Table 3 Comparison between measured and calculated turbulence levels in the 1:5 HYKAT model

Location	Turbulence level Measured	Calculated
Upstream of both honeycombs	0.130	—
Downstream of first honeycomb	0.090	0.041
Downstream of second honeycomb	0.060	0.023
Test section	0.0015	0.0029

to have a cell diameter of 2 cm and a length of 40 cm. The second honeycomb positioned 40 cm downstream has a length of 20 cm and a cell diameter of 1 cm. Studies were made in a 1:5 air model of most of the HYKAT circuit (described earlier). Verification of the HYKAT design is not possible in the model because of the mismatch in Reynolds nubmber, the difficulty in obtaining scaled-down honeycombs, and the fact that the entire flow circuit was not modeled. Therefore, it was decided to verify the *design procedure* instead. Two sections of honeycomb, properly spaced and having a length to cell diameter ratio of 24 was used in the model. Turbulence was simulated upstream of Elbow No. 4 by placing a coarse grid in the entrance section of the model. Turbulence levels were measured upstream of the first honeycomb, between the honeycomb, downstream of the second honeycomb, and at the entrance of the test section. These data were used to verify predictions of η, and self-generated turbulence for both honeycombs (Eq. (5)) and to determine the viscous dissipation and modification of the turbulence converted through the contraction (Eqs. (6) and (7)). The measured results and the design equations are compared in Table 3. The measured overall attenuation appears to be very good, i.e., 13 percent at the inlet to the turbulence management system results in only 0.15 percent in the test section compared to a predicted value of 0.29 percent in the test section. Again caution should be exercised since the theoretical comparisons are based on the turbulence returning to isotropy at each station, whereas in actuality different degrees of anisotropy probably exist at each measurement point in the model. Inspection of the data in Table 3 indicate that the honeycomb is less effective than predicted, but the contraction is more effective than expected leading to an overall performance of the turbulence management system that is suspiciously good. the results for the nozzle are especially in contradiction with the LCC tests. This is not entirely unexpected since the HYKAT nozzle departs markedly from the assumption of uniform contraction inherent in the LCC stream tube model. Unfortunately, full-scale verification of the turbulence management design has not been carried out in either the LCC or the HYKAT to date (January, 1993).

The important message to be obtained from this discussion is that our understanding of the details of turbulence management are incomplete. Time and budgetary constraints often force the design program to depend on limited one-dimensional turbulence data, when a more extensive program of turbulence research is necessary before the design procedure can be improved.

IV Conclusions

An extensive review of the literature and design experience with two very large hydroacoustic design facilities indicate the following:

1. An inviscid Euler model is an effective computational tool for contraction design. This technique is superior to potential flow analysis because flow distortion at the nozzle inlet can be simulated. Design studies to date indicate that nonsymmetrical nozzles with contraction ratios as low as four can be developed that have good flow properties.

2. Existing theory can be used for preliminary design of turbulence management systems. More research is necessary before test section turbulence levels can be predicted with accuracy. It is highly recommended that physical modeling of water tunnels include extensive measurements of all three components of turbulence at select positions in the water tunnel circuit.

Acknowledgment

This paper is based on extensive studies of the LCC and HYKAT over an extended period. This work could not have been accomplished without extensive collaboration with our colleagues at SAFHL including Professor C. C. S. Song and his students, Dr. John Killen, Mr. David Bintz and many others. We were fortunate to have the opportunity to collaborate with acoustic designers at Bolt Beranek and Newman, Inc. and Atlantic Applied Research Corporation. Mr. Paul Brott of DMJM (Daniel, Mann, Johnson & Mendenhall) and Mr. Richard Richter of SSV&K (Seeley Stevenson Value and Knecht), successfully blended our efforts with other subcontractors in acoustics, structural design, instrument design etc. during the LCC program. Dr. Ernst Weitendorf and his colleagues at the Hamburg Ship Model Basin provided us with a unique opportunity to introduce new and high-risk computational methods into the HYKAT program. Their confidence in our abilities is sincerely appreciated. R. E. A. Arndt acknowledges the support of the Office of Naval Research under Contract No. N000014-91-J-1239 in the preparation of this paper.

References

Arndt, R. E. A., Bintz, D., and Morel, T., 1983, Studies of the Turbulence Management System, Final report on Phase A-2, Task A-1, Naval Facilities Engineering Command, Contract N62477-82-C-0259, Aug.

Arndt, R. E. A., Song, C. C. S., Silberman, E., Killen, J. M., Wetzel, J. M., and Yuan, M., 1984, "Extended Phase A-2, Large Cavitation Channel," St. Anthony Falls Hydraulic Laboratory, University of Minnesota, Project Report 230, Aug.

Batchelor, G. K., 1960, *The Theory of Homogeneous Turbulence*, The University Press, Cambridge, England.

Loehrke, R. I., and Nagib, H. M., 1976, "Control of Free-Stream Turbulence by Means of Honeycombs: A Balance Between Suppression and Generation," ASME JOURNAL OF FLUIDS ENGINEERING, Vol. 98, No. 38, pp. 342–355.

Lumley, J. L., 1964, "Passage of a Turbulent Stream Through Honeycomb of Large Length-to-Diameter Ratio," ASME *Journal of Basic Engineering*, Vol. 86, pp. 218–220.

Lumley, J. L., and McMahon, J. R., 1967, "Reducing Water Tunnel Turbulence by Means of a Honeycomb," ASME *Journal of Basic Engineering*, Vol. 89, Dec., pp. 764–770.

Morel, T., 1977, "Design of Two-Dimensional Wind Tunnel Contractions," ASME JOURNAL OF FLUIDS ENGINEERING, June, pp. 371–378.

Pankhurst, R. C., and Holder, D. W., 1952, *Wind-Tunnel Technique*, Sir Isaac Pitman and Sons, Ltd.

Pope, Alan, and Harper, John J., 1966, *Low Speed Wind Tunnel Testing*, John Wiley & Sons, Inc., NY.

Ramjee, V., and Hussian, A. K. M. F., 1976, "Influence of the Axisymmetric Contraction Ratio on Free-Stream Turbulence," ASME JOURNAL OF FLUIDS ENGINEERING, Vol. 98, Sept., pp. 506–515.

Robbins, Basil, 1978, "Water Tunnel Turbulence Measurements behind a Honeycomb," *Journal of Hydronautics*, Vol. 12, No. 3, July, pp. 122–128.

Song, C. C. S., Wetzel, J. M., Yuan, M., Arndt, R. E. A., and Killen, J. M., 1987, "Hydrodynamics Analysis of the HYKAT," St. Anthony Falls Hydraulic Laboratory, University of Minnesota, Project Report No. 261, June.

Song, Charles C. S. and Yuan, Mingshun, 1988, "A Weakly Compressible Flow Model and Rapid Convergence Methods," ASME JOURNAL OF FLUIDS ENGINEERING, Vol. 110, pp. 441–445.

Song, C. C. S., Wetzel, J. M., Killen, J. M., and Arndt, R. E. A., 1988, "Physical and Mathematical Modeling of the HYKAT," St. Anthony Falls Hydraulic Laboratory, University of Minnesota, Project Report No. 282, Dec.

Stratford, B. S., 1959, "The Prediction of Separation of the Turbulent Boundary," *Journal of Fluids Mechanics*, Vol. 5, Pt 1.

Tan-atichat, J., Nagib, H. M., and Loehrke, R. I., 1982. "Interaction of Free Stream Turbulence with Screens and Grids: A Balance Between Turbulence Scales," *Journal of Fluid Mechanics*, Vol. 114, pp. 501–528.

Wetzel, J. M., Bintz, D., Arndt, R. E. A., Morel, T., Song, C. C. S., Gavali,

S., and Killen, J. M., 1983, Phase A-2, Large Cavitation Channel, St. Anthony Falls Hydraulic Laboratory, University of Minnesota, Project Report No. 229, Aug.

Wetzel, J. M., Song, C. C. S., and Arndt, R. E. A., 1986, "Hydrodynamics Design of a Large Cavitation Channel," *Proceedings, Advancement in Aerodynamics, Fluids Mechanics, and Hydroacoustics*, ASCE, Minneapolis, MN, p. 26–34.

Wetzel, J. M., and Arndt, R. E. A., 1991, "Hydrodynamic Design Considerations for Hydroacoustic Facilities," *Proceedings ASME Symp on Hydroacoustic Facilities*, Instrumentation and Experimental Techniques, Atlanta, GA, Dec.

Wetzel, J. M., and Arndt, R. E. A., 1993, "Hydrodynamic Design Considerations for Hydroacoustic Facilities: II. Pump Design Factors," ASME JOURNAL OF FLUIDS ENGINEERING, published in this issue pp.

Wille, R., 1963, Beiträge zur Phänomenologie der Freistrablen," *Zeitshrift für Fluawissen-schaften*, Band 11, pp. 222–233.

Hydrodynamic Design Considerations for Hydroacoustic Facilities: Part II—Pump Design Factors

J. M. Wetzel

R. E. A. Arndt

St. Anthony Falls Hydraulic Laboratory,
University of Minnesota,
Minneapolis, MN 55414-2196

The St. Anthony Falls Hydraulic Laboratory has been involved in the hydrodynamic design of large cavitation facilities, which require a high performance axial flow pump that is cavitation free to meet stringent design conditions. As cavitation has been shown to be the largest noise source in an otherwise well designed facility, it must be eliminated for the design range of flow conditions. To reduce the possibility of blade cavitation it is desirable to have a near uniform, or at least, a near symmetrical approach velocity distribution at the pump inlet. The design of flow facilities to achieve such an inflow was the subject of extensive investigations. These investigations consisted of both numerical and physical modeling of critical components in the test loop. The influence of these components, which included the contraction, diffuser, and turning vanes was carefully documented. The combination of the two modeling techniques will be demonstrated as an effective design tool for a high performance, hydrodynamic test facility.

1 Introduction

There has been an increasing interest in the development of high-speed flow facilities for research and testing. These facilities have been previously used primarily for cavitation research but are now being designed so that hydroacoustic research also can be conducted. The requirements for a quiet, recirculating flow facility place severe design restrictions on various components in the flow circuit. A slight amount of cavitation that may have been acceptable in earlier designs is no longer tolerable. It has been determined from noise measurements in many different water tunnels that cavitation of the main drive pump is the major source of noise. Therefore, the design of the pump becomes a critical item and requires special attention. The criteria for cavitation performance and noise are generally less stringent for most commercial pump applications than required for the flow facilities considered here. Thus, special consideration must be given to the inflow velocity distribution to the pump and attempt to make it as symmetrical as possible.

Wetzel and Arndt (1993) discuss in detail the overall design requirements for hydroacoustic facilities. In that paper, consideration was given to the design of the contraction, test section, and the turbulence management system with examples drawn from two major design programs: the U.S. Navy's Large Cavitation Channel (LCC) and the German Hydrodynamic and Cavitation Tunnel (HYKAT). This paper addresses the design of the remaining critical components such as the diffuser and turning vanes and their impact on pump inflow and pump head requirements. The overall design program included both physical and numerical modeling of selected critical components in the flow loop including the diffuser. The two modeling techniques were complementary in that one guided the other during the optimization of the flow elements. To the authors' knowledge, this is the first time that a numerical model based on a cell averaged eddy simulation approach (Song and Yuan, 1990) was used interactively with an experimental program to optimize the design including improving the pump inflow. The physical model for the LCC included the contraction, test section, and diffuser at a scale ratio of 1 to 10. The HYKAT model included the portion of the flow circuit from the vaned elbow preceding the settling chamber to the pump intake, thereby including three of the four elbows in the loop; the scale ratio for this model was 1 to 5. For further reference, a sketch of the HYKAT model is given in Fig. 1. Additional details are presented in Arndt et al. (1984), Arndt and Weitendorf (1990), Song et al. (1988), Weitendorf et al. (1987), and Wetzel and Arndt (1990, 1991, 1993).

II General Considerations

The focus of this paper is on the requirement for extremely low noise levels in the test section. Cavitation-free pump operation requires a well designed pump impeller operating in a distortion-free inflow and sufficient net positive suction head (NPSH) at the pump impeller.

The location of the pump in the lower leg of the flow circuit

Contributed by the Fluids Engineering Division for publication in the JOURNAL OF FLUIDS ENGINEERING. Manuscript received by the Fluids Engineering Division January 11, 1993; revised manuscript received September 24, 1993. Associate Technical Editor: T. T. Huang.

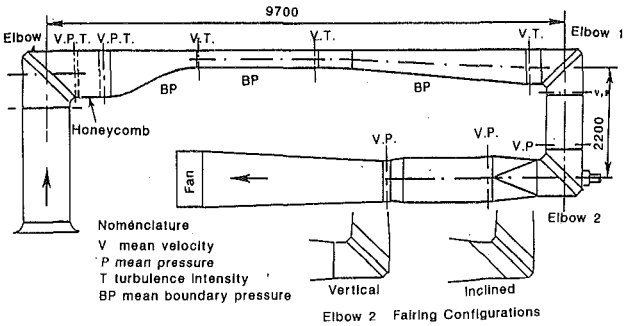

Fig. 1 Sketch of 1 to 5 physical model

is also of importance. In conventional designs the pump is usually installed immediately downstream of the second elbow. (The elbows are numbered starting with number one following the main diffuser in the upper leg.) Such an installation provides the maximum length possible for the flow to stabilize before entering the main contraction in the upper leg. However, the inflow velocity distribution at this location may not be symmetrical; thereby increasing the likelihood of pump cavitation and unsteady flow. A compromise is therefore made to locate the pump at some distance from the second elbow to improve the inflow velocity characteristics. However, the pump drive shaft must be lengthened and may require an additional support bearing. For a given overall length of the water tunnel, the diffuser following the pump is reduced in length, resulting in an increase of the included angle of the diffuser for a given area ratio. Since this decreases the pressure recovery from the pump outflow, these features must be considered in the trade-off analysis.

The high-speed flow from the test section must be reduced in velocity before it enters the pump. The main diffuser is used for this purpose, and it must be carefully designed to avoid flow separation and instabilities. The flow quality at the exit of the diffuser has a direct impact on the design of the vaned elbows with regard to vane strength, cavitation susceptibility, and turning action. If the test section is noncircular in cross-section, a shape transition must occur somewhere before the pump. It is generally most desirable to accomplish the shape transition in a separate component, rather than include it in a component designed for other purposes as well.

Decisions must also be made regarding the shape of the vaned elbows, i.e., circular or noncircular, vane profile, angle of inclination, and spacing based on an analysis for cavitation, turning capability, headloss, and structural integrity. Both steady and unsteady loads are of concern. Trailing edge vibration should be eliminated by proper design to prevent "singing" and consequent noise generation.

Extensive numerical modeling has been carried out for vaned elbows, including effects of the walls and non-uniform inlet velocity profiles. Recent developments in numerical modeling allowed for direct numerical simulation of the diffuser flow as well. These computational procedures have been verified by experimental measurements and are now a valuable tool in the design of hydrodynamic test facilities. Specific examples are given in the following sections.

III Component Design

A. Main Diffuser. The component that has the most influence on velocity distributions throughout the tunnel circuit is the main diffuser, which is also responsible for a major portion of the headloss in the circuit, typically 25 to 50 percent. Thus, the diffuser has an impact on both the head requirement of the pump and its subsequent cavitation performance.

A two-dimensional numerical model for turbulent flows was developed to analyze the performance of diffusers (Yuan et al., 1991; He and Song, 1991; Song et al., 1991; He et al., 1991). The flow in a diffuser is affected by a number of factors including: (1) inflow velocity distribution, (2) Reynolds number, (3) exit pressure distribution, (4) lateral diffusion, (5) inflow turbulence level, etc. The effect of inflow turbulence level on diffuser performance was not analyzed. The lateral diffusion affects the diffuser performance because it reduces the mean velocity over a cross section and increases the adverse pressure gradient. In the model, the effect of reduced mean velocity is partially accounted for by comparing the results based on normalized values. The effect of increased adverse pressure gradient is ignored. Of the first three factors listed above, the effect of inflow velocity distribution has been found to be most important.

Because the diffuser flow is so sensitive to the variation in the inflow velocity profile, model calibration was most effectively done by adjusting the inflow velocity distribution. A very minor adjustment in the inflow velocity distribution was needed to make the calculated exit velocity profile match the values measured in the physical model.

The experimental results that were used for comparison with the numerical model were obtained for diffusers with a horizontal top and the bottom sloped at an angle of 5.4 degrees. These measurements consisted of mean boundary pressures and velocity profiles. It is expected that turbulence levels may be quite high at the exit of a diffuser, and therefore may have a strong influence on the performance and stability of the turning vanes in the elbow attached to the diffuser exit. To arrive at an estimate of these turbulence levels, measurements were made on the non-symmetric diffuser to be used in the LCC. This diffuser was square in section with an area ratio of 3.2. Similar measurements were not made during the HY-KAT program since the general trends were expected to be the same.

Turbulent velocity components were measured with eight TSI, Inc. Model 1240, x-wire probes. A 16-channel constant temperature anemometer designed and fabricated in-house was connected to the probes. Anemometer output voltages were sampled by an Analogic A-D converter with simultaneous sample and hold input amplifiers. Sampling rates of 2000 and 500 samples per second were used. The digital samples were stored and subsequently processed by a PDP 11/34 computer.

Turbulence intensities of axial and vertical velocity com-

Nomenclature

C_p = pressure coefficient = $(P-P_0)/1/2\rho U^2$
f = frequency
H = diffuser height
P = pressure
P_0 = reference pressure
Q_{top} = discharge, top half of cross section
Q_{btm} = discharge, bottom half of cross section
R = radius
Re = Reynolds number
u = fluctuating velocity
u_1, u_2, u_3 = components of fluctuating velocity
U = mean stream velocity
x = streamwise direction
y = vertical direction
θ = angle-diffuser vane, circumferential
ν = kinematic viscosity
ρ = fluid density

Subscripts

B = bottom wall
e = exit
i = inlet
l = local
T = top wall, also test section

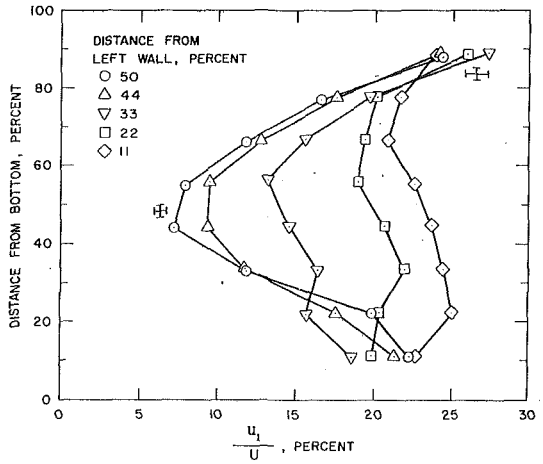

Fig. 2 Turbulence intensity of axial velocity component diffuser exit. Error band shown with bracketed lines.

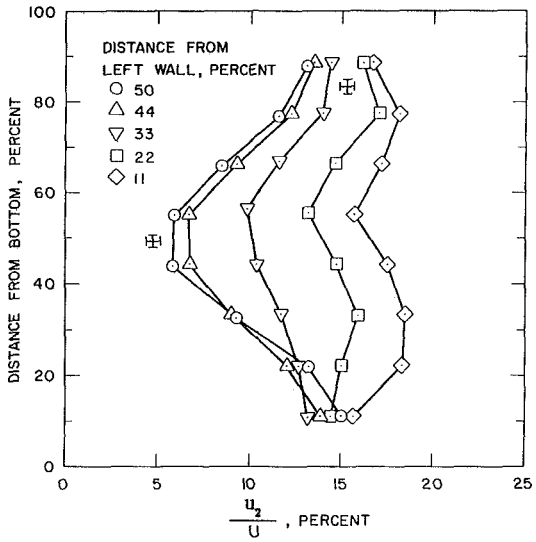

Fig. 3 Turbulence intensity of vertical velocity component diffuser exit. Error band shown with bracketed lines.

ponents, u_1, u_2, are shown in Figs. 2 and 3 for five vertical stations. Each of the RMS values of the unsteady components have been normalized with the local mean axial velocity. The lowest intensity occurs near the diffuser centerline, and the intensity increases as the walls are approached. The u_1 component is considerably greater than the u_2 components, with values up to about 25 percent being measured near the wall.

The arctangent of the vertical velocity component is representative of the angle of attack sensed by the first set of turning vanes. The angle of attack at the vertical centerline is about 4 degrees near the middle of the diffuser exit. The angles increase near both the top and bottom walls, reaching a value of about 10 degrees near the top and 9 degrees near the bottom.

These angles are quite large, and are to be considered very conservative. The instantaneous angles of attack and the resulting changes in the lift on a turning vane are considerably less due to the effects of unsteadiness. A more complete analysis is given by Greeley et al. (1984) and Norman et al. (1985).

The mean velocity profiles and the changes in angles of attack are important in the design of cavitation-free turning vanes in the elbow. Although there is a pressure rise along the diffuser axis, the centerline velocity is about 1.6 times the average velocity. Vane profiles must be selected that have a negative pressure peak of low magnitude to avoid the occurrence of local cavitation. The analysis of the turning vanes is discussed in the next section.

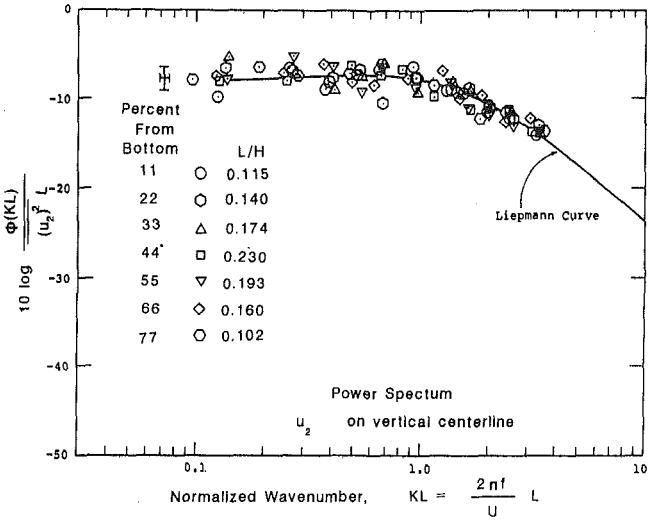

Fig. 4 Normalized power spectrum for vertical velocity component along vertical centerline of diffuser. Error band shown with bracketed lines.

The data samples for the u_2 component were transformed into a power spectrum by applying fast Fourier transform (FTT) program to the sample data. It was found that a Liepmann spectrum (Amiet, 1970) would fit the low frequency very well is properly shifted. The shift necessary to match the Liepmann spectrum with the estimated spectrum gave a value for a time scale at each probe location. The time scale was converted to a length scale by using the local measured mean velocity U_l. This estimated length scale was combined with the measured mean square average vertical component to give a dimensionless ordinate $\phi(KL)/\overline{u_2^2}L$ and abscissa $2\pi fL/U_l = KL$ as shown in Fig. 4. The length scale, L, varied from about 0.12 m at the centerline to about 0.06 m at the walls. In terms of the diffuser exit height, these values correspond to L/H of about 0.25 to 0.1. The ratio of the length scale to the semi-chord length of the turning vanes is an important parameter in the unsteady analysis referred to above. For the LCC vanes, this ratio varied from about 2 at the centerline to about 1 near the wall.

B. Vaned Elbows. The turning vanes in the elbow at the exit of the main diffuser are the most critical of the four elbows. They are exposed to the highest velocity and the lowest pressure. As previously shown, the velocity distribution is far from uniform across the cascade, and turbulence levels are high at the diffuser exit. Criteria used in selection of turning vanes include flow turning ability, resistance to cavitation and separation, flow induced vibration, headloss, and structural strength.

Initial attempts to select a suitable profile were based on the NACA four-digit airfoil series, as some experimental data were available for some particular shapes in a finite cascade (Silberman, 1949, 1953). These experiments also indicated that a ratio of the vane spacing to chord length of about 0.5 resulted in low headloss in the elbow. The desired section should have a small, negative pressure peak near the leading edge, and be relatively insensitive to angle of attack changes. The vane profiles selected were first evaluated using potential flow calculations for an infinite cascade in a uniform flow. The best candidates were further evaluated numerically in a two-dimensional finite cascade including the top and bottom walls of the elbow (Song et al., 1986).

The vane profile selected from the 4-digits series for a 87.5 degree turn for the first elbow in the LCC had a parabolic mean line with maximum camber of 19 percent located 30

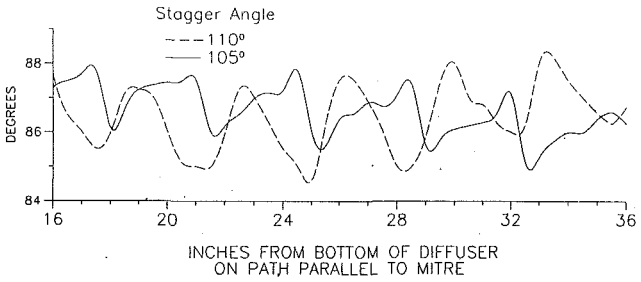

Fig. 5 Measured turning angles for the 19-315 vane in LCC 87-5 degree elbow

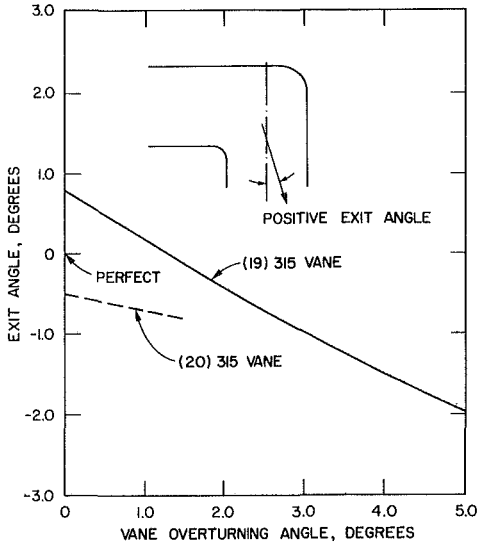

Fig. 6 Calculated flow exit angle

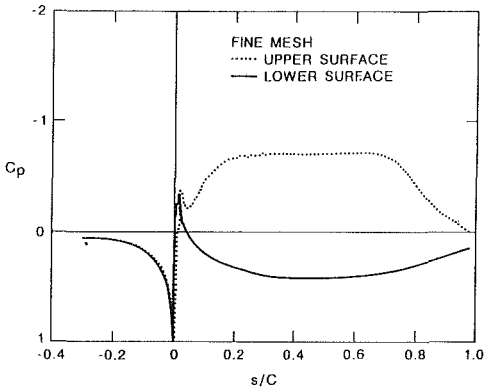

Fig. 7 Computed pressure distribution on recommended circular arc vane

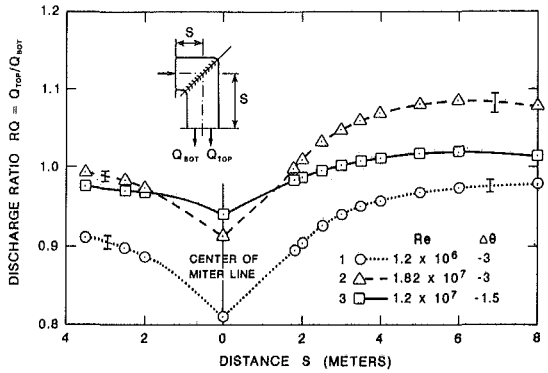

Fig. 8 Computed variation of discharge ratio with vane angle. Error band shown with bracketed lines. Symbols are computed points.

percent from the leading edge and a maximum thickness of 15 percent. All percentages are referenced to the chord length. They were installed with the chord line of each vane making an angle of 105 degrees with the cascade axis and spaced at 0.5 chord lengths from meanline to meanline along the cascade axis. Some experimental measurements were made with this configuration in a wind tunnel simulation of the LCC to establish the turning action (Cary, 1985). Results are shown in Fig. 5. The average turning angle is close to the desired angle, with a slight underturning action. The turning action has also been calculated for several angles referenced to the design angle, as shown in Fig. 6 for the LCC. These calculations indicate that the vanes should be set at about an additional degree to achieve the desired turning angle.

In contrast to the LCC, the turning vanes in the HYKAT consisted of circular arcs of different radii for the pressure and suction surfaces, thereby providing a chordwise variation in vane thickness. In this case, experimental measurements were made of the turning performance of the vanes for various stagger angles. The calculated pressure distribution on the upper and lower surface of a circular arc vane with a 14 percent thickness ratio is shown in Fig. 7. The pressure coefficient, C_p, is referenced to the average pressure and velocity at the elbow entrance. Computations of the cavitation number at the axial centerline of the diffuser exit for maximum flow conditions resulted in a value of 1.8 at the minimum test section cavitation number of 0.12. If the magnitude of the negative pressure coefficient is less than this value, cavitation should not occur. Considerable margin against cavitation can be noted.

Measurements of the velocity profiles at the diffuser exit of the HYKAT generally showed that the velocity distribution was skewed with higher velocities near the inner wall than the outer wall of the tunnel circuit. This asymmetric velocity distribution is expressed as a discharge ratio, $RQ = Q_{top}/Q_{btm}$ where Q_{top} and Q_{btm} is the discharge through the top and bottom half of a cross section, respectively. Thus, the discharge ratio RQ was less than one. As it was desired to have a near symmetrical profile at the pump intake, attempts were made to modify the velocity distribution by changing the angle of the vanes from their design position. This possibility was evaluated numerically with a hypothetical elbow and a long, straight channel as shown in Fig. 8. The first computations were made using model results for the inlet velocity profile to the elbow with RQ of about 0.91. The angle of the turning vanes was decreased by 3 degrees from their design value, as indicated by the circular symbols and $\Delta\theta = -3$. It can be seen that far downstream of the miter line that RQ has increased and is slightly less than one. At higher Reynolds numbers, typical for the full scale water tunnel, the velocity profile at the entrance to the elbow was anticipated to be more symmetrical. To confirm this, computations of the exit velocity profile has been made for the HYKAT diffuser at model and full-scale Reynolds number using the numerical model. The vertical centerline profiles are shown in Fig. 9 and the increased symmetry at higher Reynolds number is apparent. Using the results in Fig. 9 for guidance, computations were made with the inlet RQ of about one and again with the vane angles set 3 degrees less than the design angle. These results are also plotted in Fig. 8. For this case, the 3 degree underturning overadjusted the flow downstream. Therefore it can be seen that the turning vanes can be used to modify the velocity profiles, but should be done with care. As a reasonable design target for the HYKAT, a Reynolds number of about 65 percent of the design maximum was used to select a vane setting. After several trials, it was found that the best condition was obtained by setting the vanes for 1.5 degree underturning as shown in Fig. 8.

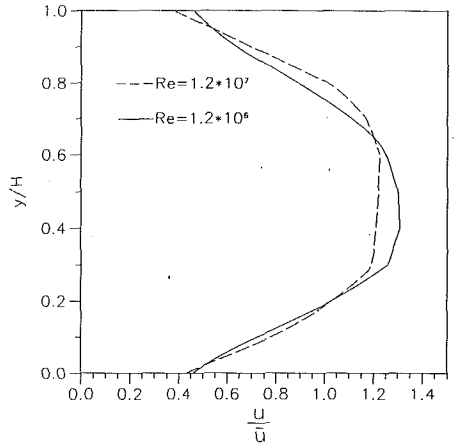

Fig. 9 Computed HYKAT diffuser exit velocity profiles at model and full-scale Reynolds number

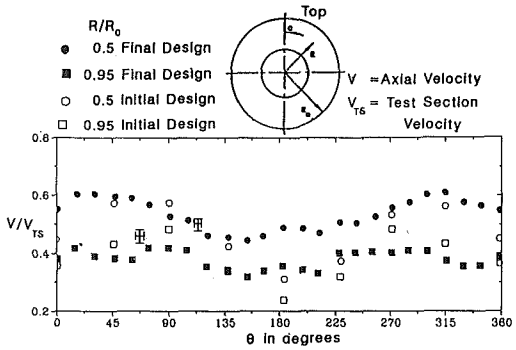

Fig. 10 Measured pump intake axial velocity distribution comparison between initial and final designs, HYKAT. Error band shown with bracketed lines.

C. Pump Inflow Velocity Distribution. The temporal mean inflow velocity distribution to the pump is of particular interest to the pump designer in order to provide a cavitation-free pump. During the design of HYKAT, velocities were measured along radial lines from the pump shaft to the outer housing of the pump impeller. A number of radial lines were selected for these measurements, and the circumferential position of the lines has been referenced to top center.

Extensive measurements were made in the 1 to 5 scale HYKAT model (Fig. 1). All velocity measurements were made using a TSI hot wire anemometer Model 1050 and Model 1240-T1.5 hot wire probes. A LeCroy analog to digital converter Model 8210 was used in conjunction with an AT&T 3B2 computer. The A/D converter sampling rate was 10,000 Hertz and the anemometer filter's cut-off frequency was set at 5000 Hertz. A linearizing program was used to convert the signal to velocity data which were then averaged over the sample. Velocity readings were referenced to the measured mean velocity in the test section with the same probe, if possible (Song et al., 1988).

The first measurements indicated considerable variation of the velocity in the circumferential direction with a deficiency of velocity at the bottom which was deemed unacceptable. This resulted in an extensive search for the source of the non-symmetry. Experimental results showed that the non-symmetry originated at the exit of the main diffuser, and was transmitted essentially unchanged through the two vaned elbows. Therefore, attempts were made to alter the velocity profile by reducing the turning action of the vanes, and thus directing more flow to the outside of the tunnel. The numerical model was used to guide the direction of the physical model tests as described previously in III.B.

As the vanes in the first elbow are most critical for cavitation susceptibility, it was decided that the adjustment of vane angle should be made at the second elbow where lower velocity and higher pressures are present. A comparison of the final and initial designs is shown in Fig. 10. These data were obtained in the HYKAT model. The improved uniformity of the final design justifies the interactive experimental-computational design procedure used here.

As an added benefit, the final design model test data were extrapolated to full-scale Reynolds number using the calculated differences in the diffuser exit profile shown in Fig. 9 (Wetzel and Arndt, 1990).

D. Component Headloss. The pump designer also needs the head requirement for the pump, as determined from the headlosses in the system. A summary of the component headlosses for the HYKAT at the design test section velocity of 11.5 m/s without a test body is given in Table 1. About 70 percent of the total loss occurs in the upper leg.

Table 1 Summary of measured headlosses

Component	H_l (m)
Test section	0.310
Main diffuser	0.727
1st elbow	0.178
Downcomer diffuser	0.019
2nd elbow	0.132
Pump diffuser	0.065
3rd and 4th elbow	0.118
Turbulent management	0.549
Contraction	0.008
Acoustic grids (optional)	0.381
Misc. piping	0.053
$\Sigma =$	2.54 m

IV Conclusions

Extensive design experience with two very large hydroacoustic design facilities indicate the following:

1. Typical designs include a diffuser in the upper leg. The diffuser is responsible for approximately 25 to 50 percent of the total headloss in the tunnel circuit. Nonsymmetrical diffusers have skewed velocity profiles at the exit which are a primary cause of flow distortion at the pump inlet. Satisfactory nonsymmetrical diffusers can be designed but deviations from conventional design must be approached with caution. Diffuser performance is very sensitive to the inflow velocity profile and Reynolds number. Work to date indicates that a numerical model of the diffuser flow coupled with physical model studies can be a very effective design tool.
2. Turning vanes set at the proper angle will turn the flow without velocity distortion. Moderate changes in the exit velocity profile can be made by adjustment of the vane angle. Predictions of the turning angle can be made with a numerical model.
3. The velocity distribution of the pump intake can be improved by adjustment of the turning vanes in the elbows preceding the pump. Improvements in pump inflow can result in the design of cavitation-free pumps that are essential in hydroacoustic test facilities.
4. The calibrated numerical models of the main diffuser and guide vanes were used to extrapolate the pump inlet profile measured in the physical model to the prototype condition. This provides the pump designer with the best possible input data for achieving a cavitation-free pump design.

Acknowledgment

This paper is based on extensive studies of the LCC and HYKAT over an extended period. This work could not have been accomplished without extensive collaboration with our

colleagues at SAFHL including Professor C.C.S. Song and his students, Dr. John Killen, Mr. David Bintz and many others. We were fortunate to have the opportunity to collaborate with acoustic designers at Bolt Beranek and Newman, Inc. and Atlantic Applied Research Corporation. Mr. Paul Brott of DMJM (Daniel, Mann, Johnson & Mendenhall) and Mr. Richard Richter of SSV&K (Seeley, Stevenson, Value & Knecht) successfully blended our efforts with other subcontractors in acoustics, structural design, instrument design etc. during the LCC program. Dr. Ernst Weitendorf and his colleagues at the Hamburg Ship Model Basin provided us with a unique opportunity to introduce new and high-risk computational methods into the HYKAT program. Their confidence in our abilities is sincerely appreciated. Roger E. A. Arndt acknowledges the support of the Office of Naval Research in the preparation of this paper.

References

Arndt, R. E. A., Song, C. S. S., Silberman, E., Killen, J. M., Wetzel, J. M., and Yuan, M., 1984, "Extended Phase A-2, Large Cavitation Channel, David Taylor Naval Ship Research and Development Center," St. Anthony Falls Hydraulic Laboratory, University of Minnesota, Project Report No. 230.

Arndt, R. E. A., and Weitendorf, E. A., 1990, "Hydromechanical Considerations in the Design of the New Cavitation Research Facility at the Hamburg Ship Model Basin," *Schiffstechnik Bd. 37*, Aug.

Amiet, R. K., 1970, "Acoustic Radiation from an Airfoil in a Turbulent Stream," *Journal of Sound and Vibration*, Vol. 41, No. 4, pp. 407–420.

Cary, C. M., 1985, "BBN Phase A-2 (Extended) Experiments in Support of LCC Turning Vane Design," Bolt Beranek and Newman, Inc., Tech. Memorandum No. 854.

Greeley, D. S., Abbot, P. A., and Cary, C. M., 1984, "Contributions to the Design of Turning Vanes for the Large Cavitation Channel (LCC)," Bolt Beranek and Newman, Inc., Memorandum No. 822.

He, J., Song, C. C. S., Yuan, M., and Wang, Q., 1991, "A Quasi-Three-Dimensional Method for Predicting the Effects of Parallel Walls and Lateral Diffusion on a Diffuser Flow," University of Minnesota Supercomputer Institute Research Report UMSI, 91/282.

He, J., and Song, C. C. S., 1991, "Numerical Simulation and Visualization of 2-D Diffuser Flow," University of Minnesota Supercomputer Institute Research Report UMSI 91/77.

Norman, T., and Johnson, W., 1985, "Estimating Unsteady Aerodynamic Forces on Cascade in a Three-Dimensional Turbulence Field," NASA TM-86701.

Silberman, E., 1949, "Fluid Flow Diversion by Guide Vanes in Miter Bonds," St. Anthony Falls Hydraulic Laboratory, University of Minnesota, Project Report No. 8.

Silberman, E., 1953, "Importance of Secondary Flow in Guide Vane Bends," *Proceedings*, Third Midwestern Conference on Fluid Mechanics, University of Minnesota.

Song, C. C. S., Wetzel, J. M., Yuan, M., and Arndt, R. E. A., 1986, "Mathematical Modeling for a Vaned Miter Elbow," *Proceedings, Advancement in Aerodynamics, Fluids Mechanics, and Hydroacoustics*, ASCE, Minneapolis, MN, pp. 26–34.

Song, C. C. S., Wetzel, J. M., Killen, J. M., and Arndt, R. E. A., 1988, "Physical and Mathematical Modeling of the HYKAT," St. Anthony Falls Hydraulic Laboratory, University of Minnesota, Project Report No. 282.

Song, C. C. S., and Yuan, M., 1990, "Simulation of Vortex-Shedding Flow About a Cylinder at High Reynolds Numbers," ASME JOURNAL OF FLUIDS ENGINEERING, Vol. 112, pp. 155–161.

Song, C. C. S., He, J., and Larson, E., 1991, "Numerical Simulation of Flow Regimes in Two-Dimensional Diffusers," University of Minnesota Supercomputer Institute Research Report UMSI 91/78.

Weitendorf, E. A., Friesch, J., and Song, C. S. S., 1987, "Considerations for the New Hydrodynamics and Cavitation Tunnel (HYKAT) of the Hamburg Ship Model Basin (HSVA)," Int'l. Symposium on Cavitation Research Facilities and Techniques, ASME, New York, NY.

Wetzel, J. M., and Arndt, R. E. A., 1990, "Cavitation Free Pumps for Very Large Hydroacoustic Test Facilities," *Proceedings, IAHR Symposium Model Tech. in Hyd. Energy Prod.*, Belgrade, Yugoslavia.

Wetzel, J. M., and Arndt, R. E. A., 1991, "Hydrodynamic Design Considerations for Hydroacoustic Facilities," ASME Winter Annual Meeting, Atlanta, GA.

Wetzel, J. M., and Arndt, R. E. A., 1993, "Hydrodynamic Design Considerations for Hydroacoustic Facilities. Part I—Flow Quality," ASME JOURNAL OF FLUIDS ENGINEERING, published in this issue, pp. 324–331.

Yuan, M., Song, C. C. S., and He, J., 1991, "Numerical Analysis of Turbulent Flow in a Two-Dimensional Nonsymmetric Plane-Wall Diffuser," ASME JOURNAL OF FLUIDS ENGINEERING, Vol. 113, June, pp. 210–215.

Splattering During Turbulent Liquid Jet Impingement on Solid Targets

Sourav K. Bhunia

John H. Lienhard V

W. M. Rohsenow Heat and Mass Transfer Laboratory, Department of Mechanical Engineering, Massachusetts Institute of Technology, Cambridge, MA 02139

In turbulent liquid jet impingement, a spray of droplets often breaks off of the liquid layer formed on the target. This splattering of liquid alters the efficiencies of jet impingement heat transfer processes and chemical containment safety devices, and leads to problems of aerosol formation in jet impingement cleaning processes. In this paper, we present a more complete study of splattering and improved correlations that extend and supersede our previous reports on this topic. We report experimental results on the amount of splattering for jets of water, isopropanol-water solutions, and soap-water mixtures. Jets were produced by straight tube nozzles of diameter 0.8 – 5.8 mm, with fully developed turbulent pipe-flow upstream of the nozzle exit. These experiments cover Weber numbers between 130-31,000, Reynolds numbers between 2700-98,000, and nozzle-to-target separations of $0.2 \leq l/d \leq 125$. Splattering of up to 75 percent of the incoming jet liquid is observed. The results show that only the Weber number and l/d affect the fraction of jet liquid splattered. The presence of surfactants does not alter the splattering. A new correlation for the onset condition for splattering is given. In addition, we establish the range of applicability of the model of Lienhard et al. (1992) and we provide a more accurate set of coefficients for their correlation.

1 Introduction

Liquid jets which impinge on solid surfaces often splatter violently, expelling a shower of droplets from the liquid film formed on the target. These airborne droplets are indicative of lowered cooling efficiency, lessened cleaning ability, or reduced coating efficiency, depending on the specific application of the impinging jet. In cleanroom situations, where impinging jets are used for post-etching debris removal, splattered liquid can produce airborne contaminants. In metal-jet forming operations, splattering is a primary cause of reduced yield. In situations involving toxic chemicals, the splattered droplets create a hazardous aerosol whose containment may necessitate significant air filtration costs.

Previous studies of splattering have demonstrated that it is driven by the disturbances on the surface of the impinging jet (Errico, 1986; Lienhard et al., 1992). Thus, undisturbed laminar jets do not splatter, unless they are long enough to have developed significant disturbances from capillary instability. Turbulent jets, on the other hand, develop surface roughness as a result of liquid-side pressure fluctuations driven by the turbulence, and they are highly susceptible to splattering.

Errico (1986) induced splattering of laminar jets by creating surface disturbances with a fluctuating electric field. His results showed that splattering commenced at progressively lower jet velocities when the amplitude of disturbance was increased. He also showed that splattering appeared on the liquid film on the target as the disturbances from the jet spread radially. When a turbulent jet strikes a target, similar travelling waves originate near the impingement point and travel outward on the liquid film (see Fig. 1). When the jet disturbances are sufficiently large, these waves sharpen and break into droplets (Fig. 2). All observations indicate that the amplitude of these disturbances on the jet govern splattering. They further indicate that splattering is a non-linear instability phenomenon, since the liquid film is clearly stable to small disturbances but unstable to large ones (Varela and Lienhard, 1991).

Lienhard et al. (1992; called LLG hereinafter) reported measurements of the splattered liquid flow rate for turbulent

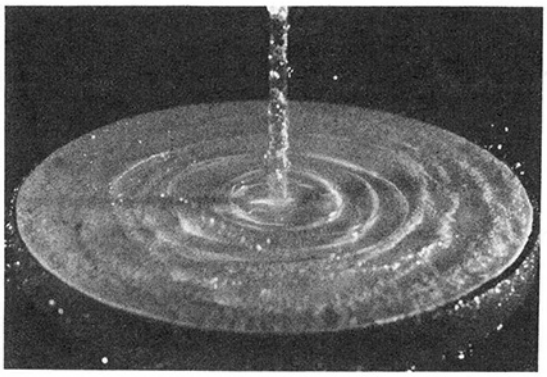

Fig. 1 Waves on the liquid layer and splattering. Water jet with $We_d = 2475$, $l/d = 31$, and $\xi = 0.108$ (Courtesy: X. Liu)

Contributed by the Fluids Engineering Division for publication in the JOURNAL OF FLUIDS ENGINEERING. Manuscript received by the Fluids Engineering Division October 27, 1992; revised manuscript received June 15, 1993. Associate Technical Editor: M. W. Reeks.

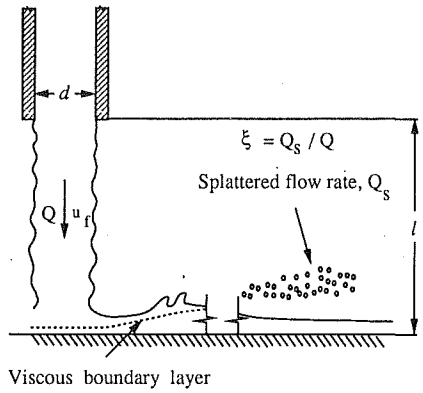

Fig. 2 Turbulent jet impingement and splattering: instantaneous liquid surface

jets in the form of the ratio of splattered flow rate, Q_s, to the incoming flow rate, Q:

$$\xi = \frac{Q_s}{Q} \tag{1}$$

LLG also proposed a model for splattering that related the rms amplitude of jet surface disturbances to the rate of splattering. In this model, turbulent pressure fluctuations in the jet formed an initial surface disturbance on the jet, which was then assumed to evolve by Rayleigh's capillary instability (Drazin and Reid, 1981) as the jet travelled to the target. The model produced a scaling parameter, ω, that characterized the rms amplitude of disturbances reaching the target:

$$\omega = \mathrm{We}_d \exp\left(\frac{.971}{\sqrt{\mathrm{We}_d}}\frac{l}{d}\right) \tag{2}$$

Here,

$$\mathrm{We}_d = \rho u_f^2 d/\sigma \tag{3}$$

is the jet Weber number based on the average jet-velocity at the nozzle exit, u_f, the nozzle diameter[1], d, and the liquid surface tension, σ. The nozzle-to-target separation is l. LLG obtained good correlation between ξ and ω, leading to the result:

$$\xi = -0.0935 + 3.41\times10^{-5}\omega + 2.25\times10^{-9}\omega^2 \tag{4}$$

for $2120 \le \omega \le 8000$, with no splattering for $\omega < 2120$. LLG also noted that splattering occurred within a few diameters of the point of impact and that viscosity (in the form of a jet Reynolds number) appeared to have no role in the splattering process, presumably owing to the thinness of the wall boundary layer in the stagnation region.

In spite of the LLG model's apparent success, several ambiguities accompany it. The model is based on data covering $1.2 \le l/d \le 28.7$ and $1000 \le \mathrm{We}_d \le 5000$, and its validity outside that range is unestablished. The onset point for splattering shows significant scatter as a function of ω and is not in complete agreement with all observations by other investigators. Furthermore, the model is predicated on exponential growth of capillary disturbances at the rate corresponding to Rayleigh analysis' most unstable wavelength ($\lambda = 4.51d$). That assumption is obviously flawed, since the turbulent pressure fluctuations driving instability cover a broad range of much shorter wavelengths ($\lambda < d$), the most energetic of which should be stable according to Rayleigh's results.

The present paper examines splattering over a much broader range of Weber number and nozzle-to-target separations ($130 < \mathrm{We}_d < 31{,}000$; $0.2 < l/d < 125$). Surface tension is independently varied. In contrast to LLG, we treat We_d and l/d as independent parameters. Our objectives are to establish the range of applicability of the LLG model and to obtain a more generally applicable criterion for the onset of splattering beneath a turbulent impinging liquid jet. In addition, we attempt further explanation of the overall phenomenon of splattering in terms of the available data on the evolution of surface-disturbances on turbulent jets.

2 Experiments

A schematic diagram of the measurement system is given in Fig. 3. All the measurements were made with water jets issuing into still air. Tube nozzles having diameters between 0.8-5.8 mm were used to produce the jets. The tubes were made 70-100 diameters long so as to ensure fully developed turbulent flow at the tube outlet. The outlets were carefully deburred to prevent the introduction of mechanical surface disturbances. The tube nozzles received water from a pressurized plenum with disturbances dampers and honeycomb flow straighteners at its upstream inlet.

Nozzle-target separation was varied from 2 to 300 mm. This corresponds to nondimensional nozzle-target separations, l/d, between 0.2 and 125 for all the nozzles other than the 0.84 mm diameter nozzle, for which l/d reached 500.

Splattering takes place over a limited range of radial positions upstream of the hydraulic jump, typically within a few diameters of the point of impact. The target radius was between 2 and 50 cm, and always slightly larger than the radial location of the hydraulic jump. The amount of liquid that remained in the liquid sheet on the target after splattering was measured by collecting it in a container beneath the target. The splattered liquid, on the other hand, remained airborne and fell well beyond the rim of the container. Flow rates of the jet and of

[1]The contraction coefficient for turbulent jets leaving pipe nozzles is nearly unity. Throughout this study, we treat nozzle diameter and jet diameter interchangeably.

Nomenclature

d = nozzle diameter (m)
f = Darcy friction factor
l = nozzle-to-target separation (m)
l_b = jet breakup length (m)
l_c = length of the jet at which splattering reaches its asymptotic limit (m)
l_o = length of the jet corresponding to onset of splattering (5 percent threshold) (m)
Q = jet flow rate (m^3/s)
Q_s = flow rate of splattered liquid (m^3/s)
u_f = average jet velocity at the nozzle exit (m/s)
u' = rms fluctuating component of velocity (m/s)
u_* = friction velocity based on wall shear stress, $u_f\sqrt{f/8}$ (m/s)
x = distance along the jet axis from the nozzle exit (m)
δ = rms height of the jet surface disturbances (m)
λ = jet surface disturbance wavelength (m)
μ = liquid dynamic viscosity (kg/m·s)
ξ = splattered fraction of incoming jet's liquid, Q_s/Q
ρ = liquid density (kg/m^3)
σ = surface tension between liquid and the surrounding gas (N/m)
ω = splattering parameter defined by Eq. (2)
Re_d = jet Reynolds number, $\rho u_f d/\mu$
We_d = jet Weber number, $\rho u_f^2 d/\sigma$

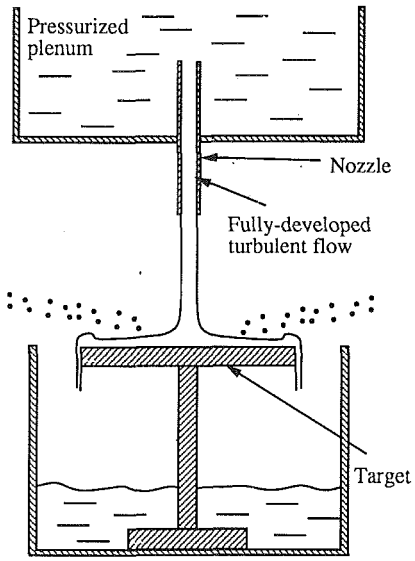

Fig. 3 Measurement of the fraction of jet liquid splattered

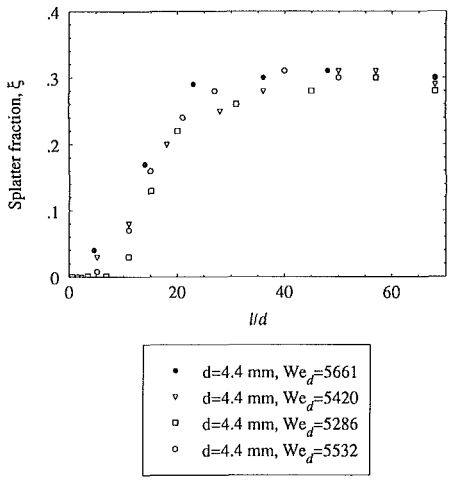

Fig. 4 Scatter in the measurements of splatter fraction for water jets of nearly the same Weber numbers

the unsplattered liquid were both obtained by measuring the time required to collect a known volume of liquid. From this, the amount of splattering was calculated.

The liquids used in these experiments were water, an isopropanol-water solution, and water containing a surfactant detergent. The liquid temperature was between 21 and 27°C. Surface tension was measured several times during the experiments using a platinum-ring surface tension meter. Tube diameters were measured and checked for roundness, and these measured values of diameter were used in an all subsequent calculations.

This technique facilitated quite precise measurements of the amount of splattering. Typically the uncertainty in ξ (at 95 percent confidence) was below ± 5 percent for $\xi > 10$ percent and below ± 25 percent for $\xi < 4$ percent. Uncertainties in the Reynolds numbers and the Weber numbers were below ± 2 and ± 3 percent, respectively. These low uncertainties may be credited to the direct measurement of liquid flow rate. Uncertainties in l/d and ω were below ± 2 and ± 3 percent, respectively. Some of the measurements were repeated using two different pumps to verify the reproducibility of the data and their independence from upstream pressure fluctuations. Figure 4 shows the typical scatter in the measurements of splatter fraction for several different runs at nearly the same jet Weber

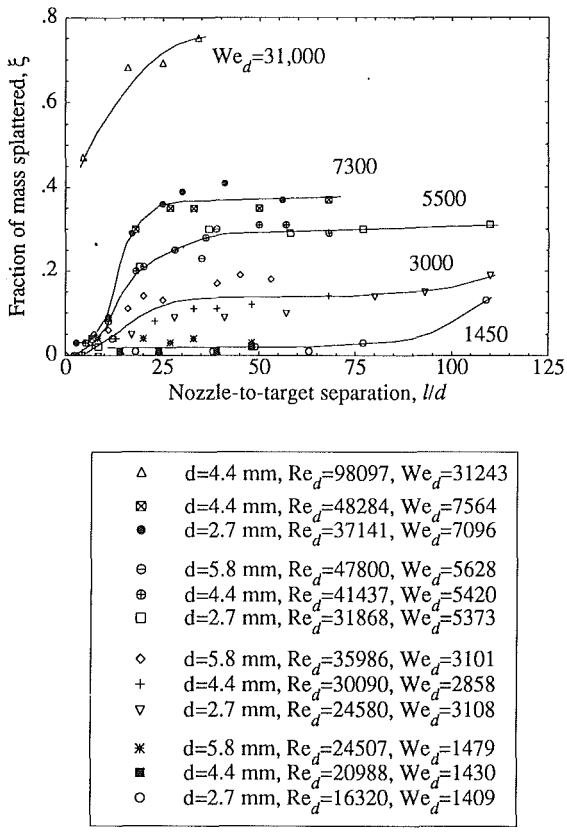

Fig. 5 Splattering as a function of nozzle-target separation and jet Weber number. Solid lines are fitted curves for Weber number constant to within ± 3 percent (which is the uncertainty of the experimental We_d): $We_d = 1450$ (1409, 1430, 1479); 3000 (3108, 2858, 3101); 5500 (5373, 5420, 5628); 7300 (7096, 7564); 31000 (31243).

numbers. (The values are all within the ± 3 percent uncertainty limits of We_d.) The rms scatter in ξ from run to run is ± 4 percent of the maximum value of ξ of about 0.3.

The independent physical parameters involved in this problem are l, d, ρ, u_f, σ, and μ. Dimensional analysis based on these parameters shows that the fraction of liquid splattered, ξ can depend only on three dimensionless groups, namely l/d, Re_d, and We_d. Independent variation of these three groups was accomplished by independent variation of d, l, σ, and u_f.

3 Splattering and Its Relation to Jet Disturbances

Figure 5 shows the amount of splattering at different nozzle-target separations for several nozzle diameters and Reynolds numbers. Each solid line represents data for a narrow range of Weber numbers, varying by less than ± 3 percent around the stated mean value, a range equal to the experimental uncertainty of We_d. Splattering of as much as 75 percent of the incoming fluid is observed at a Weber number of 31,000 and a Reynolds number of 98,000 for a nozzle-target separation of $l/d = 34$.

At any given Weber number and nozzle-target separation, the splatter fraction, ξ, depends extremely weakly on the Reynolds number, if at all. For example, in the data set for $We_d = 5500$, the Reynolds number increases by a factor of 1.5 without any discernible change in the splatter fraction, ξ. In contrast, a factor of 1.3 increase in the Weber number (from 5500 to 7300) produces a significant increase in the splatter fraction (roughly +25 percent).

An influence of Reynolds number would be expected to arise primarily from viscous effects near solid boundaries, either in setting the pipe turbulence intensity or as an influence of the viscous boundary layer along the target. Past work (e.g., Lien-

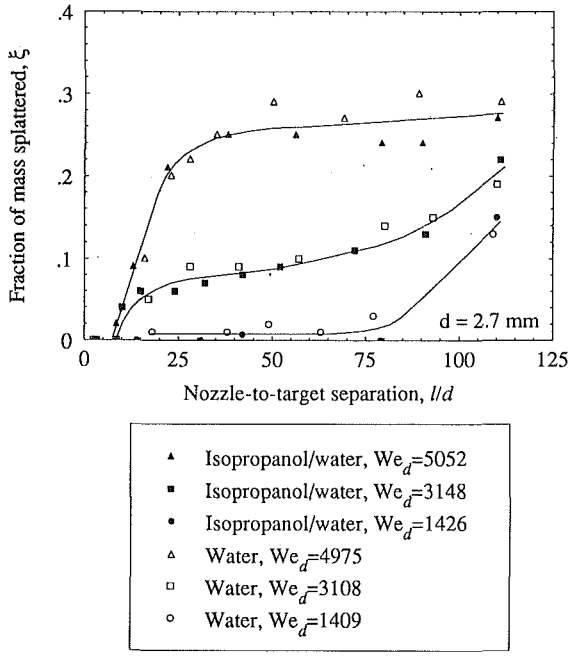

Fig. 6 (*a*) The Weber number correlates the splatter fraction, ξ, as the surface tension of the jet liquid is varied (0.072 N/m for water and 0.042 N/m for isopropanol/water solution): *d* = 2.7 mm

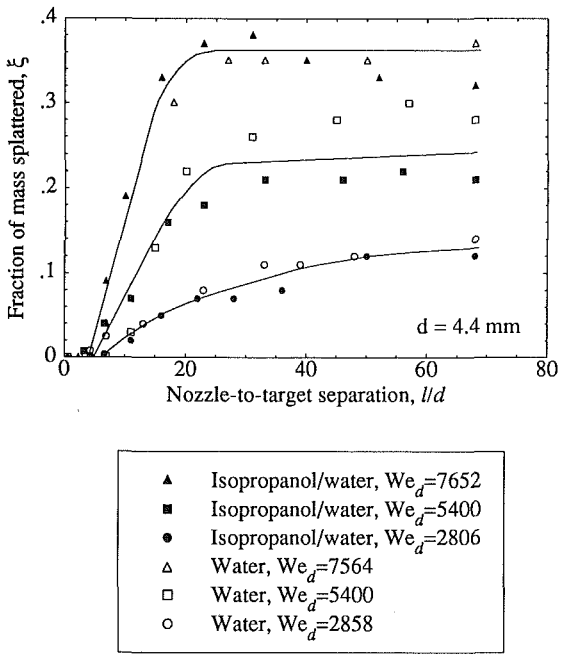

Fig. 6 (*b*) The Weber number correlates the splatter fraction, ξ as the surface tension of the jet liquid is varied (0.072 N/m for water and 0.042 N/m for isopropanol/water solution): *d* = 4.4 mm

hard et al., 1992) has established that the stagnation-point boundary layer is extremely thin relative to the liquid layer, and it thus may have little effect on the surface waves near the stagnation-point. To examine the effect of Reynolds number on turbulence intensity we refer to Laufer (1954). His measurements show the ratio of rms turbulent speed to friction velocity, u'/u_*, to be nearly independent of Reynolds number in fully-developed turbulent pipe-flows. Therefore

$$\frac{u'}{u_f} \propto \frac{u_*}{u_f} \propto \sqrt{f} \propto \mathrm{Re}_d^{-1/8}$$

where we have used the definition of $u_*(=u_f\sqrt{f/8})$ and the

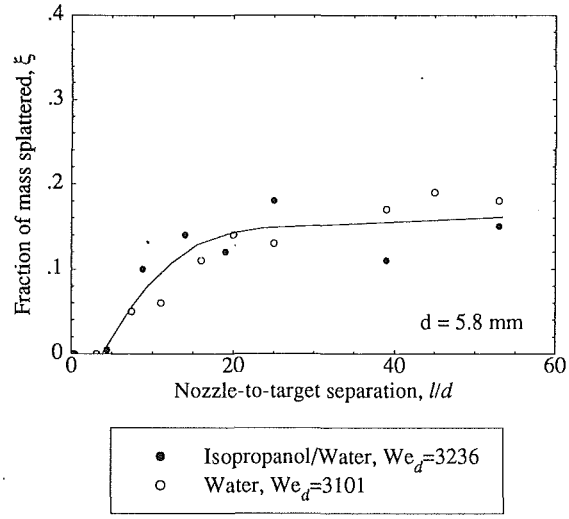

Fig. 6 (*c*) The Weber number correlates the splatter fraction, ξ, as the surface tension of the jet liquid is varied (0.072 N/m for water and 0.042 N/m for isopropanol/water solution): *d* = 5.8 mm

Blasius friction factor equation ($f = .316\mathrm{Re}_d^{-1/4}$ for $4000 < \mathrm{Re}_d < 10^5$). This weak dependence of the turbulence intensity on the Reynolds number may be the reason that we observe no significant dependence of splattering on the jet Reynolds numbers over the present range of Re_d.

To study the effect of surface tension variation on splattering, a solution of approximately 10 percent by volume of isopropanol in water was used. The surface tension of the solution was measured before each run of the experiment; it was thus maintained at 0.042 N/m within ± 5 percent accuracy (versus 0.072 N/m for pure water). Density was also measured. The data show (Figs. 6 *a*, *b*, *c*) that the splatter fraction, ξ, still scales with Weber number, We_d, as observed before for the water jets. The splatter fraction data for water and for an isopropanol-water solution, at a given jet Weber number, agree to within the experimental uncertainty in all but one case (Fig. 6*b*, $\mathrm{We}_d = 5368$).

Referring to Figs. 5 and 6, we see that very little splattering occurs close to the jet exit (small l/d), typically less than 5 percent. Beyond this region, the amount of splattering at first increases with distance, l/d. Farther downstream, it reaches a plateau. To explain these observations we refer to some recent measurements of the amplitude of turbulent liquid jet surface disturbances (Bhunia and Lienhard, 1993). The rms amplitude of jet surface disturbances at different axial locations of the jet, were obtained from the measurements of the instantaneous disturbance amplitude, using a non-intrusive optical instrument. Starting from nearly zero near the nozzle exit, the rms amplitude of jet surface disturbances initially grows rapidly as the jet moves downstream; farther downstream the growth rate diminishes and the rms disturbance tends to an asymptotic limit. Earlier Chen and Davis (1964) attempted to measure the amplitude of surface disturbances on turbulent liquid jets by an electric conductivity probe. Although that method is less accurate owing to the interference of the probe with the flow, those measurements are qualitatively consistent with the optical data. This growth of disturbances is the probable cause of the increase in the splatter fraction as the jet moves downstream. The steadily decreasing rate of amplitude growth results in a plateau of the disturbance amplitude which corresponds to that in the splatter fraction data.

For very long, low Weber number jets the plateau of splattering ends and ξ again increases with l/d (Fig. 6*a*). This may reflect the appearance of ordinary capillary instability on these jets. Specifically, when the Weber is low, the asymptotic turbulence-generated surface roughness is small compared to the

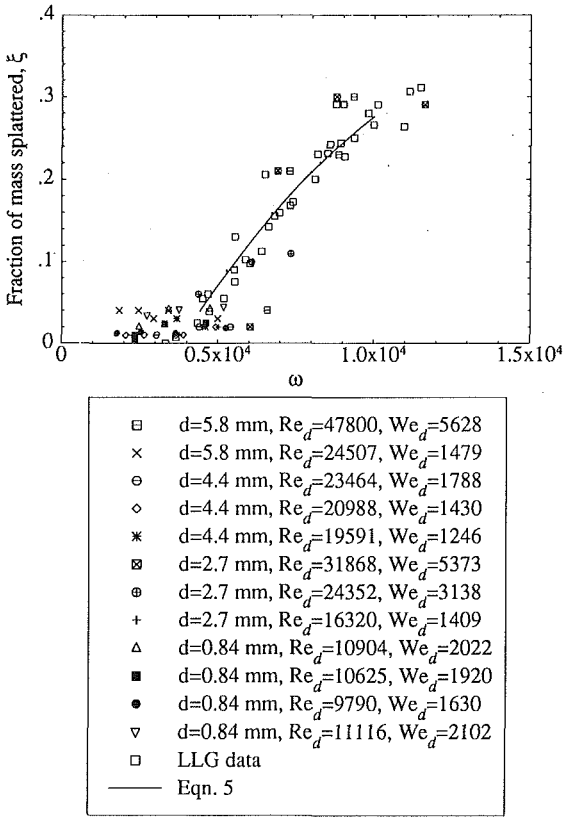

Fig. 7 Comparison of the LLG model's scaling with the present data for $l/d < 50$

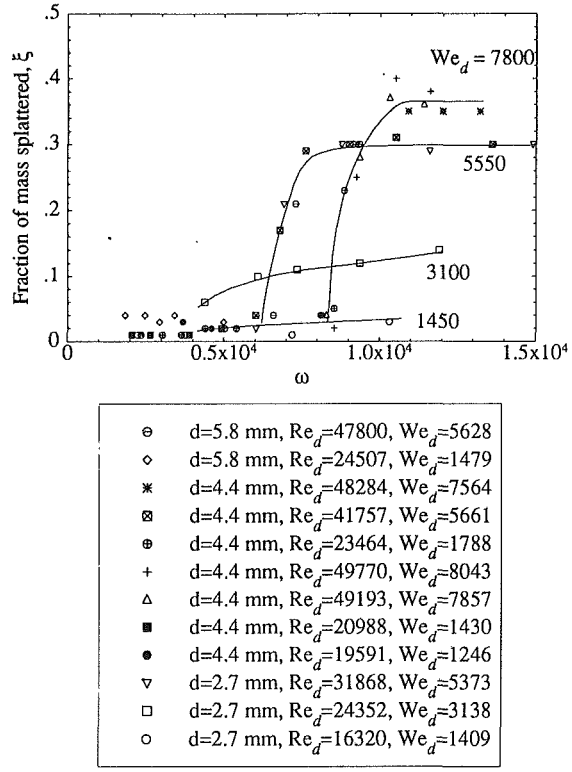

Fig. 8 Breakdown of the LLG model for $l/d > 50$ or $We_d > 5000$

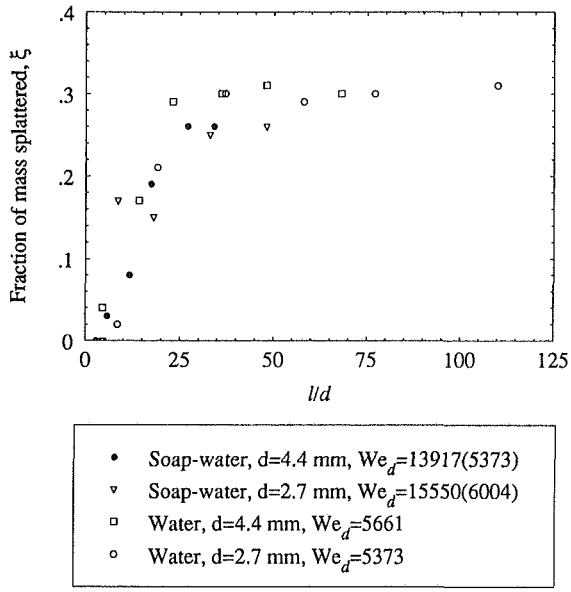

Fig. 9 Effect of surfactants on splattering. The Weber number in parentheses is based on the surface tension of pure water.

jet radius. Thus, the still nearly-cylindrical jet can give up surface energy by the usual Rayleigh-type instability. In contrast, at higher Weber number the turbulent disturbances grow to be as large as the jet radius, effectively breaking up the jet. In the low Weber number case, the splattering plateau ends when capillary instability further raises the jet roughness. In the high Weber number case, the plateau is reached when the jet is essentially broken up into drops.

Once the jet is broken up, the splattering is effectively due to the impact of individual droplets. For a given Weber number, the size and velocity of those droplets remain nearly constant with increasing l/d (excluding the effect of air drag); thus the amount of splatter reaches an asymptotic value. Presumably, this asymptote depends on droplet Weber number (which is roughly equal to jet Weber number).

On the basis of the present experiments, we find that the range of applicability of the LLG model is $10^3 < We_d < 5 \times 10^3$, $l/d < 50$ and $4400 < \omega < 10{,}000$. Figure 7 shows both the present data and the LLG data in $\xi - \omega$ coordinates. The scaling with ω correlates the data reasonably well in this range. While LLG used nominal tube diameter in their data reductions, all data in Fig. 7 are scaled with measured diameter. On this basis, we offer the following improved correlation for $\xi(\omega)$ in the range $4400 < \omega < 10{,}000$:

$$\xi = -0.258 + 7.85 \times 10^{-5}\omega - 2.51 \times 10^{-9}\omega^2 \qquad (5)$$

The lower limit in terms of ω is chosen to ensure that the predicted ξ is at least 4 percent. Below this level there is considerable scatter and high uncertainty in the measurements.

For larger l/d or We_d, the ω model fails (Fig. 8), but a different pattern emerges. For We_d = constant, ω becomes a function of l/d only and we see curves similar to the ones in Fig. 5.

3.1 The Influence of Surfactants. Surfactants lower liquid surface tension by forming a surface-absorbed monolayer at the liquid surface. When a new liquid surface is formed, some time is required for surfactant molecules to diffuse to the surface in sufficient concentration to alter the surface tension. To study the role of surfactants in splattering, a mixture of approximately 0.2 percent detergent in water was used. This reduced the surface tension of the static solution (liquid surface at rest) to 0.027 N/m and corresponded to a saturated concentration of surfactant. Figure 9 shows that the presence of the surfactant does not alter the amount of splattering. The splatter friction for the surfactant-laden jet is identical to that for a pure water jet of the same velocity, diameter and length; in fact, if the surfactant-jet Weber number is calculated on

the basis of pure-water surface tension, the curves for the surfactant-jets are identical to those of the pure jets. From the standpoint of splattering, the surface tension of the surfactant-jet is effectively the surface tension of the pure liquid.

Possible reasons for this behavior are as follow. Inside the nozzle, the surfactant is in the bulk of the liquid. When the liquid exits the nozzle, a new free surface is formed which is not initially saturated with surfactant. Because a finite time is required for the surfactant to diffuse from the bulk to the free surface, the surface remains unsaturated over some initial length of the jet. In this initial region, the surface tension remains near that of pure water.

The time required for the surface concentration of surfactant to reach saturation was estimated for turbulent diffusion from the bulk to the free surface under the assumption that all surfactant reaching the surface is captured by and remains on the surface. Using Köhler's (1993) correlation for interphase mass transfer across free surface, this model yields an unsaturated length of only 3 to 4 diameters for the two cases in Fig. 9. However, the model is unreasonable in that it neglects any turbulent reentrainment of surfactant from the surface, to the bulk, an effect that is probably quite large. Thus it seems likely that the time required to achieve saturation is significantly longer, if saturation is reached at all. In consequence, only the surface tension of the bulk liquid appears to play a role in splattering, at least for the lengths of the jets in this study. The data show clearly that the presence of a surfactant does not alter the splattering characteristics.

To help resolve this issue, measurements of the jet surface-roughness evolution with surfactants could be compared to those without surfactant. The present data and the belief that the splattering is driven by surface disturbances together imply that a surfactant has no impact on roughness evolution. These measurements will be the subject of future work.

3.2 The Onset of Splattering. Some problems arise in defining the onset point of splattering. Since the process of splattering involves turbulent flow, sporadic splattering of droplets occurs at much lower jet velocities than those that would cause any significant amount of sustained splattering (other parameters remaining the same). Consequently, the onset point is more accurately definable in terms of a non-zero level of splattering. Owing to the finite accuracy of measurement systems, this threshold should not be so low as to have substantial uncertainty. We chose to define the onset of splattering as the point where 5 percent of the incoming fluid is splattered. In view of our earlier observation that, for a given l/d, the amount of splattering depends strongly on the jet Weber number and not on the Reynolds number, we expect the onset point to be uniquely identifiable by its l/d and We_d. In other words, for a jet of a given Weber number, the onset point is reached at a certain l/d.

Figure 10 shows the data for onset points. A correlation for the onset point data is

$$\frac{l_o}{d}=\frac{130}{1+5\times10^{-7}\mathrm{We}_d^2} \tag{6}$$

For low Weber numbers, where surface tension dominates, comparison to the capillary breakup length is appropriate. When aerodynamic forces are negligible, the capillary breakup length of a uniform-velocity jet is given by (Weber, 1931)

$$\frac{l_b}{d}=12\sqrt{\mathrm{We}_d}\left(1+\frac{3\sqrt{\mathrm{We}_d}}{\mathrm{Re}_d}\right) \tag{7}$$

For the turbulent jets in this study, produced by fully-developed turbulent pipe-flows, Re_d exceeds 2000. In such jets, when $\mathrm{We}_d \sim 100$ we find $l_b/d \sim 120$. Thus, the observed onset point at low Weber numbers is close to the capillary breakup point. In this range, splattering is essentially of drop impingement type. Apparently, turbulent disturbances are strongly damped

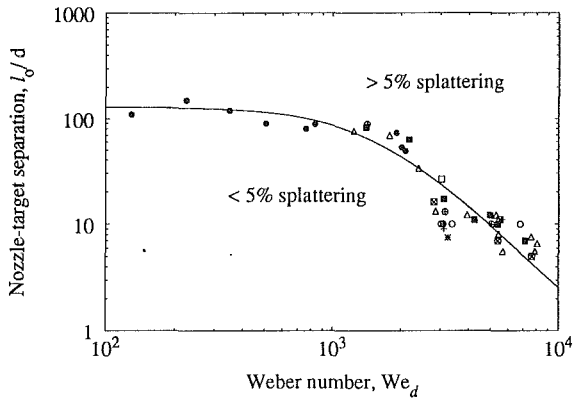

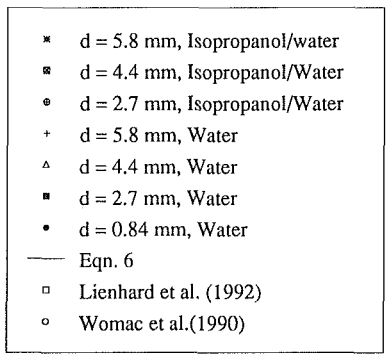

Fig. 10 Onset of splattering

Table 1 Comparison of observed upper-limit lengths to predicted capillary/aerodynamic breakup lengths of Miesse (1955)

We_d	Re_d	l_c/d	l_b/d	l_b/l_c
5373	31868	25	61	2.44
5661	41757	24	53	2.2
7564	48284	20	56	2.8
8043	49770	18	56	3.1

by surface tension in these low Weber number jets, and capillary instability is dominant.

The relative importance of turbulence and surface tension is characterized by a balance of the rms turbulent dynamic pressure and the capillary pressure. Thus, the appropriate Weber number for characterizing the splattering mechanism is based on the rms fluctuating component of the velocity, u', and the rms height of the surface disturbances, δ:

$$\mathrm{We}'=\frac{\text{turbulent dynamic pressure}}{\text{capillary pressure}}=\frac{\rho u'^2}{\sigma/\delta}=\frac{\rho u'^2\delta}{\sigma} \tag{8}$$

We' should be $\mathcal{O}(1)$ or greater when turbulence drives splattering. However, u' and δ are not easily available, while u_f and d are, so we have used

$$\mathrm{We}_d=\frac{\rho u_f^2 d}{\sigma}=\mathrm{We}'/\left[\frac{\delta}{d}\left(\frac{u'}{u_f}\right)^2\right]>>1 \tag{9}$$

which is 100-1000 times larger than the Weber number, We', that actually characterizes physical processes involved here (since u'/u_f is a few percent in magnitude and $\delta/d<0.5$).

The only other quantitative data on onset in literature – LLG and Womac et al. (1990)—compare very well with the present study. Some data in the text and in an accompanying figure in the paper by Womac et al. were combined to obtain the onset points for their study. Apparently, they indentified the onset points by visual observations. This is likely to provide slightly different l_o/d than by our method. Also, the visual determination of onset point depends on the size of the splattered droplets and their optical properties, which in turn in-

troduce additional uncertainties. These factors may account for the slight discrepancies between their results and ours.

Stevens and Webb (1989) did not observe any splattering for their turbulent jets (Webb, 1991). The most likely reason for this is that, in their study, l/d was almost always smaller than l_o/d. Only two of their reported data points lie within our splattering region (specifically, $\mathrm{Re}_d = 5 \times 10^4$, $d = 5.8$ mm, $l/d = 12.8$, $\mathrm{We}_d \simeq 6.2 \times 10^3$ and $\mathrm{Re}_d = 4 \times 10^4$, $d = 4.1$ mm, $l/d = 18.5$, $\mathrm{We}_d \simeq 5.6 \times 10^3$).

LLG reported an onset criterion of $\omega \geq 2120$ for the appearance of *any* splattering. In contrast, the present data show onset of any splattering over a range of values of ω, $2000 < \omega < 8000$. Within the range of applicability of the LLG model that was mentioned above, the onset of 5 percent splattering occurred for ω between 4100 and 5100.

3.3 The Upper Limit of Splattering for High Weber Number Jets. As previously explained, the upper limit of splattering for high Weber number jets should be reached near the breakup length of the jet. The breakup length of turbulent jets is known to depend on Reynolds and Weber numbers (Lienhard and Day, 1970). Miesse (1955) reported correlations for breakup lengths, l_b, of turbulent liquid jets subject to strong aerodynamic forces. From the data on jets from industrially-used converging-orifice type nozzles in a Reynolds number range similar to ours, he reported

$$\frac{l_b}{d} = 540 \sqrt{\mathrm{We}_d}\, \mathrm{Re}_d^{-5/8} \tag{10}$$

The jets in the present study were produced by tube nozzles with fully developed turbulent flow, so their breakup lengths can be predicted only in order of magnitude by this correlation. Table 1 compares the breakup lengths predicted by this correlation to the nozzle-target separations, l_c, at which the asymptotic upper limit of splattering is reached.

The predicted breakup lengths l_b are larger than the upper limit lengths l_c roughly by a factor of 2.6. This may be because this correlation overestimates the breakup lengths for the different nozzle geometry involved here. Alternatively, it may be that the splattering mechanism changes from jet impingement splattering to drop impingement splattering somewhat before the jet breakup location. In either case, the comparison shows a consistent relation between the jet breakup length and the upper-limit length of splattering.

4 Conclusions

Splattering has been measured for turbulent liquid jets impacting solid targets. Data span the range $0.2 \leq l/d \leq 125$, $2700 \leq \mathrm{Re}_d \leq 98{,}000$ and $130 \leq \mathrm{We}_d \leq 31{,}000$. The present results have been compared to the previous studies and improved correlations have been developed.

- For a turbulent jet, the amount of splattering is governed by the level of surface disturbances present on the surface of jet. This observation is similar to those for laminar jets with externally-imposed disturbances.
- The amount of splattering at a given nozzle-target separation depends principally on the jet Weber number.
- The presence of surfactants in the jet does not alter the amount of splattering. Only the surface tension of the bulk fluid plays a role in splattering.
- The model proposed by Lienhard et al. (1992) is applicable for $1000 < \mathrm{We}_d < 5000$ and $l/d < 50$. An improved version of their correlation is $\xi = -0.258 + 7.85 \times 10^{-5} \omega - 2.51 \times 10^{-9} \omega^2$, for $4400 < \omega < 10{,}000$. Outside this range, We_d and l/d should be treated as independent parameters.
- The onset point of splattering for a 5 percent threshold is given by the correlation $l_o/d = 130/(1 + 5 \times 10^{-7} \mathrm{We}_d^2)$.
- The upper-limit length of splattering, beyond which ξ is constant, appears to be related to the jet breakup length.
- Over the range of Reynolds numbers in this work, no significant effect of jet Reynolds number is identifiable. However, a very weak dependence on Reynolds number is likely to be present in all of the conclusions and the correlations presented in this study. Extrapolation above $\mathrm{Re}_d = 100{,}000$ should be done skeptically.

Acknowledgments

We gratefully acknowledge the support of the National Science Foundation under grant number CBT 8858288.

References

Bhunia, S. K., and Lienhard V, J. H., 1993, "Surface Disturbance Evolution and the Splattering of Turbulent Liquid Jets," *Heat Transfer—Atlanta, 1993*, AIChE Symposium Series, Vol. 89, No. 295, pp. 1–8.

Chen, T.-F., and Davis, J. R., 1964, "Disintegration of a Turbulent Water Jet," *Journal of Hydraulics Division, Proceedings of ASCE*, HY 1, Jan. pp. 175–206.

Drazin, P. G., and Reid, W. H., 1981, *Hydrodynamic Stability*, Cambridge University Press.

Errico, M., 1986, "A Study of the Interaction of Liquid Jets with Solid Surfaces," Ph.D. thesis, University of California, San Diego.

Köhler, J., 1993, "Heat and Mass Transfer in a Two-Phase Flow of a Binary Mixture," Heat Transfer Lab Internal Report, Department of Mechanical Engineering, MIT, Cambridge, MA.

Laufer, J., 1954, "The Structures of Turbulence in Fully Developed Pipe Flow," NACA Technical Report No. 1174.

Lienhard, J. H., and Day, J. B., 1970, "The Breakup of Superheated Liquid Jets," ASME *Journal of Basic Engineering*, pp. 515–522.

Lienhard V, J. H., Liu, X., and Gabour, L. A., 1992, "Splattering and Heat Transfer During Impingement of a Turbulent Liquid Jet," ASME *Journal of Heat Transfer*, Vol. 114, May, pp. 362–372.

Miesse, C. C., 1955, "Correlation of Experimental Data on the Disintegration of Liquid Jets," *Industrial and Engineering Chemistry*, Vol. 47, Sept., pp. 1690–1701.

Stevens, J., and Webb, B. W., 1989, "Local Heat Transfer Coefficients Under an Axisymmetric, Single-Phase Liquid Jet," *Heat Transfer in Electronics*-1989, ASME HTD, Vol. 111, pp. 113–119 (National Heat Transfer Conference, Philadelphia, PA).

Varela, D. A., and Lienhard V, J. H., 1991, "Development of Non-Linear Waves on a Non-uniform Axisymmetric Film," *Bulletin of American Physical Society*, A18, Vol. 36, No. 10; 44th Annual Meeting of Division on Fluid Dynamics, Scottsdale, AZ.

Weber, C. 1931, "Zum Zerfall eines Flüssigkeitsstrahles," *Zeitschrift für angewandte Matematik und Mechanik*, Vol. 2, pp. 136–154.

Webb, B. W., 1991, personal communication, July.

Womac, D. J., Aharoni, G., Ramadhyani, S., and Incropera, F. P., 1990, "Single Phase Liquid Jet Impingment Cooling of Small Heat Sources," *Proceedings 9th International Heat Transfer Conference*, Jerusalem, Israel, Vol. 4, pp. 149–154.

High Speed Liquid Impact Onto Wetted Solid Surfaces

H. H. Shi[1]

J. E. Field

C. S. J. Pickles

Physics and Chemistry of Solids,
Cavendish Laboratory,
Departement of Physics,
Madingley Road, Cambridge, CB3 0HE,
United Kingdom

The mechanics of impact by a high-speed liquid jet onto a solid surface covered by a liquid layer is described. After the liquid jet contacts the liquid layer, a shock wave is generated, which moves toward the solid surface. The shock wave is followed by the liquid jet penetrating through the layer. The influence of the liquid layer on the side jetting and stress waves is studied. Damage sites on soda-lime glass, PMMA (polymethylmethacrylate) and aluminium show the role of shear failure and cracking and provide evidence for analyzing the impact pressure on the wetted solids and the spatial pressure distribution. The liquid layer reduces the high edge impact pressures, which occur on dry targets. On wetted targets, the pressure is distributed more uniformly. Despite the cushioning effect of liquid layers, in some cases, a liquid can enhance material damage during impact due to penetration and stressing of surface cracks.

1 Introduction

It is well known that a thin liquid layer has a cushioning effect on the friction stresses between two sliding or impacting surfaces (see, for example, Bowden and Tabor 1954, 1964; Clark and Burmeister, 1992).This cushioning effect also appears during liquid impact on solids. A technique of forming a thin water layer on rotor blade surfaces has been successfully applied in the low pressure region of large steam turbines to minimize blade erosion (Troyanovski, 1973). Pioneering work on high speed liquid jet impact onto wetted solids was done by Brunton (1967). He found that the depth of deformation for impacts on aluminium plates was decreased with increasing liquid layer thickness; and that on wetted PMMA plates, the shear damage caused by side jetting was greatly reduced.

On a dry surface (rigid target), the impact pressure at the centre of contact is ρCV (Bowden and Field, 1964), while at the contact edge, pressures as high as $3\rho CV$ can develop due to the shock wave detachment geometry (Brunton and Rochester, 1979; Heymann, 1969; Lesser, 1981; Lesser and Field, 1983; Field et al., 1985), where ρ and C are the liquid density and shock wave velocity, and V is the impact velocity. When a liquid layer is present, the propagation of the shock wave through the layer and its reflection at the solid boundary become important. Brunton (1967) showed that as the liquid layer increases in thickness the contact pressure reduces from ρCV (rigid target) to $0.5\rho CV$ (water impact onto deep water). However, the problem of high speed liquid impact onto wetted solids has yet to be understood thoroughly, because of the transient nature of the phenomenon and the difficulties in designing a well-controlled experiment.

2 Experimental Method

The method for producing liquid jets was the one first devised by Bowden and Brunton (1961) and subsequently placed on a sound quantitative basis by Field and co-workers (Field et al., 1979; Hand et al., 1989). The gas gun for producing the liquid jet and the high speed photography system are shown schematically in Fig. 1. A lead slug accelerated by high pressure nitrogen gas was fired into a water-filled stainless steel nozzle forcing the water to flow through a small orifice. Special care was taken to produce a convex water meniscus at the nozzle exit in order to produce a jet with a curved front. Both 0.8 mm and 1.7 mm nozzles were used. Such jets simulate 4 mm and 10 mm diameter drops respectively (Field et al, 1979; Hand et al., 1991). Both a gel layer and a water film were used to cover the solids. The gel layer was prepared by dissolving 12 percent by weight of gelatin in water at 330 K and then pouring the mixture into a mold. Each of the mold faces had been lightly greased and covered with a thin plastic film. After slow cooling, the mold was dissassembled and the gel sheets placed horizontally on the target. By changing the distance of the mold gap, gel layers with different thicknesses were obtained. It has been shown that the flow properties of such a gel are not significantly different from those of pure water once the impact velocities exceed a few meters per second (see, for example, Field et al., 1989).

The gas gun was mounted vertically to allow the liquid jets to be fired at horizontal specimens covered by layers of chosen thickness. To produce thin water films, PTFE was sprayed onto the specimen to which a 10 mm × 10 mm paper label had already been applied. After drying, a 70 μm thick PTFE coating was formed. The label was removed and water was spread on the specimen. By removing water gradually with a syringe, the remaining water automatically moved into the uncoated area. The thickness of water was the same as the coating to within ± 10 μm.

The impact sequences were recorded with a Hadland Imacon 792 high speed camera operating at a framing rate of one

[1]Present address: Shock Wave Research Center, Tohoku University, Sendai, 980 Japan.

Contributed by the Fluids Engineering Division for publication in the JOURNAL OF FLUIDS ENGINEERING. Manuscript received by the Fluids Engineering Division October 16, 1992; revised manuscript received August 15, 1993. Associate Technical Editor: A. Prosperetti.

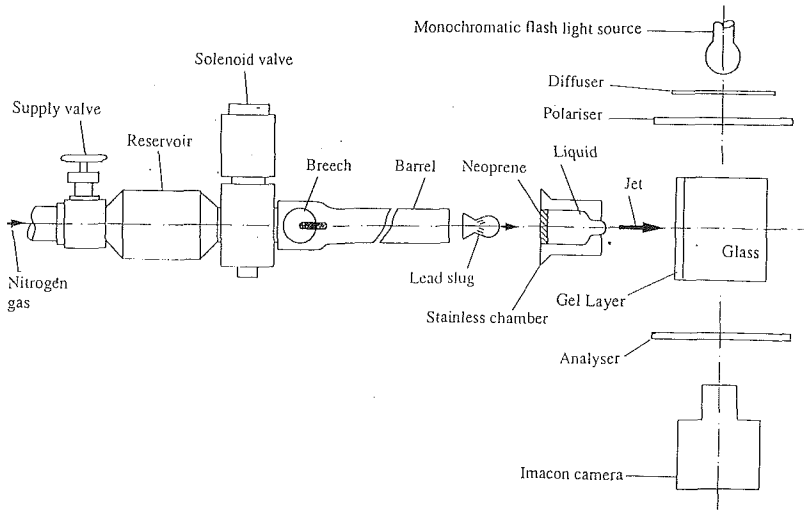

Fig. 1 Schematic diagram of the gas gun system and the experimental arrangement to observe the stress waves

million frames per second. Polarized back-lighting was used to visualize the stress waves in the solids. The measurement errors in the side jetting velocity and the wave velocities were less than ±5 percent. During high speed photography, the stand-off distance between the nozzle exit and the liquid layer was 15 mm and for the damage studies the distance was kept to 10 mm. The impact velocity of thc liquid jet versus firing pressure was calibrated using both optical fibre guided light beams with photodiodes and separately high speed photography.

3 Results

Figure 2 shows a 450 m/s water jet impact from a 0.8 mm nozzle onto a dry soda-lime glass block. The jet impact direction is indicated by one arrow in frame 2. The impact generates a compressive stress wave C and a shear stress wave S in the solid. When the compressive wave expands laterally along the free surface, it causes a head wave labeled, h, in frame 4. The measured velocities of C and S were 5700 m/s and 3000 m/s, respectively. The lateral side jetting labeled, J, appears in frame 3. Its velocity reaches 1600 m/s, i.e., about 3.5 times the impact velocity. Figure 3 shows a 450 m/s water jet impact from a 0.8 mm nozzle impact on to a wetted soda-lime glass block covered by a 3 mm-thick gel layer. In this case, the stress waves intensities are reduced, especially the head wave. The velocity of the side jetting (J, in frame 2) which is directed along the free gel surface is only ~100 m/s. Note that the impacting jet has contacted the gel surface in frame 1 but the side jetting does not appear until frame 2. This delay is similar to the process observed for impacts on compliant surfaces (Field et al., 1989).

Figure 4 shows damage marks on four 10 mm thick soda-lime glass plates caused by impacts with 680 m/s water jets from a 1.7 mm nozzle. Figure 4(a) is for a dry surface and Figs. 4(b), (c) and (d) for glass covered by different types of layer. It is interesting to note that the damage patterns on the dry and wetted surfaces are essentially similar: a central area surrounded by short circumferential cracks (Bowden and Field, 1964). However, the crack density is reduced as the thickness of the layer increases. The diameter of the main ring crack in Fig. 4(a) is 3.5 mm compared to 5.2 mm in Fig. 4(d). The increase of ring crack diameter with layer thickness can be explained by considering the broadened loading area when the shock wave propagates through the layer.

The cracks caused by liquid impact on brittle materials are due to the interaction between the Rayleigh surface wave and pre-existing defects; the crack density depends on the Rayleigh

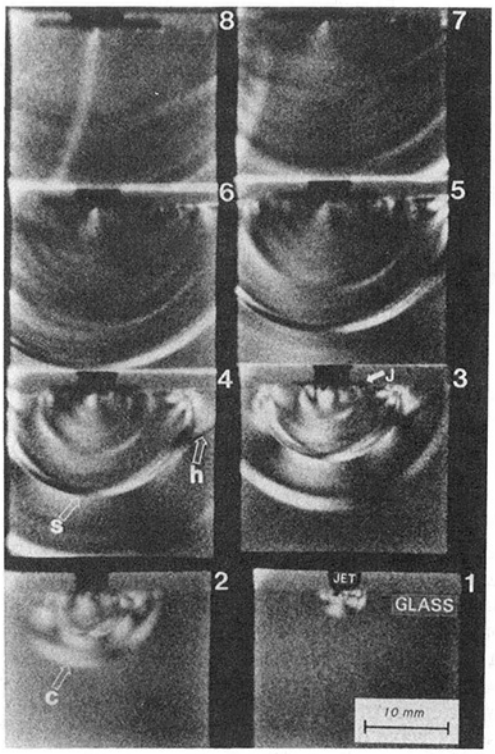

Fig. 2 Imacon sequence of the impact of a 450 ms^{-1} water jet from 0.8 mm nozzle onto a dry soda-lime glass block. C, compressive stress wave; S, shear stress wave; h head wave; J, outward side jetting. 1 μs per frame.

pulse duration and peak intensity (Bowden and Field, 1964; van der Zwaag and Field, 1983). Since the Rayleigh pulse peak intensity is proportional to the impact pressure, Fig. 4 suggests that when the liquid jet impacts a solid surface covered by a liquid layer a lower amplitude pressure pulse reaches the solid surface. See also the conclusions section.

Figure 5 compares the damage on dry and wetted (70 μ thick water film) PMMA plates caused by the impact of a 850 m/s water jet from a 0.8 mm nozzle. On the dry PMMA plate, an annular depression is formed at the position of the main ring crack (Bowden and Brunton, 1961). The annular depression for this range of impact velocities is due to the way the polymer recovers after loading. The material at the centre can withstand higher pressures during loading because the flow

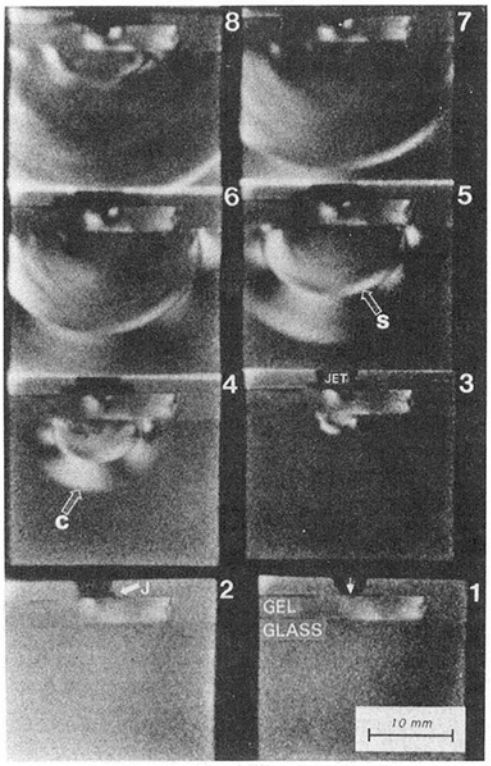

Fig. 3 Imacon sequence of the impact of a 450 ms^{-1} water jet from 0.8 nozzle onto a wetted soda-lime glass block, covered by 3 mm gel layer. *C*, compressive stress wave; *S*, shear stress wave; *J*, outward side jetting. 1 μs per frame.

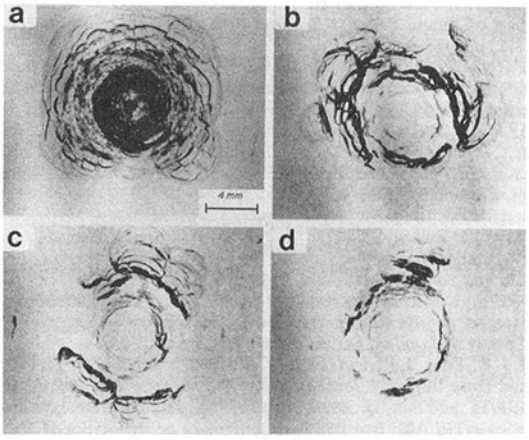

Fig. 4 The liquid impact damage on a 35 mm × 35 mm × 10 mm soda-lime glass plate. 680 ms^{-1} water jet from 1.7 mm nozzle. (*a*) dry surface; (*b*) 0.5 mm gel layer on the surface; (*c*) 0.7 mm gel layer on the surface; (*d*) 1.5 mm gel layer on the surface.

stress of the polymer is increased by the hydrostatic pressure there. However, around the periphery of the contact there is no hydrostatic pressure and the material in the annulus flows plastically and remains deformed. The annulus is not due primarily to the high "edge" pressures since their duration is very short. For a fuller discussion of liquid impact damage on polymers, see Gorham et al. (1979).

The removal of material in the form of chips is due to the side jetting. It has been shown that the circumferential cracks form steps on the surface of a few hundred nanometers which act as sites for erosion (Field, 1967). On the wetted PMMA plate, both the annular depression and chipping are greatly reduced. The reasons for these effects are the lower velocity of the side jetting; the fact that the side jetting flows along the water film, not the solid surface (see Fig. 3); and a lower

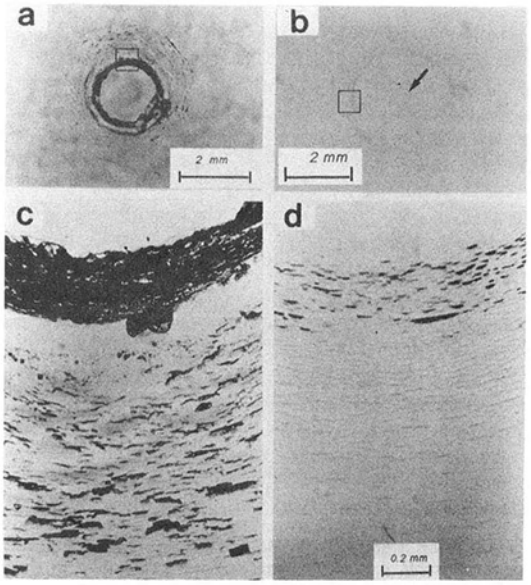

Fig. 5 The liquid impact damage on a 6 mm thick PMMA plate. 850 m/s water jet from 0.8 mm nozzle. (*a*) dry surface; (*b*) wetted surface covered by a 70 μm thick water film; (*c*) and (*d*) are the enlargements marked in (*a*) and (*b*) respectively. The subsurface shear failure regions marked with black arrows can be seen in both cases.

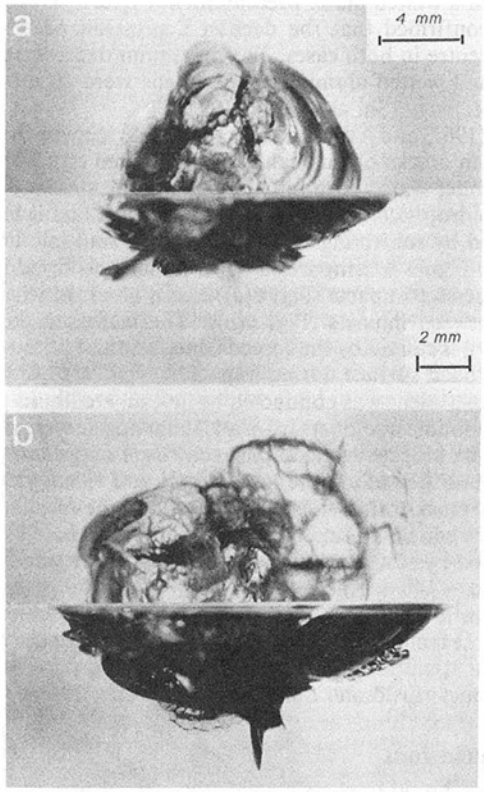

Fig. 6 The accelerated damage of PMMA block due to liquid adhering to the eroded surface after 5 impacts of 680 ms^{-1} water jet from 1.7 mm nozzle. Top view (upper part) and side view (below part). (*a*) specimen was dried between successive shots; (*b*) specimen was not dried during the impact sequence.

impact pressure at the position of the main ring crack. The subsurface shear failures marked with black arrows appear beneath the surfaces at the impact centres in both cases. This form of sub-surface failure in PMMA was described by Bowden and Brunton (1961).

On a dry aluminium plate, the shear force induced by the side jetting causes wave-like ripples in the outer annular region

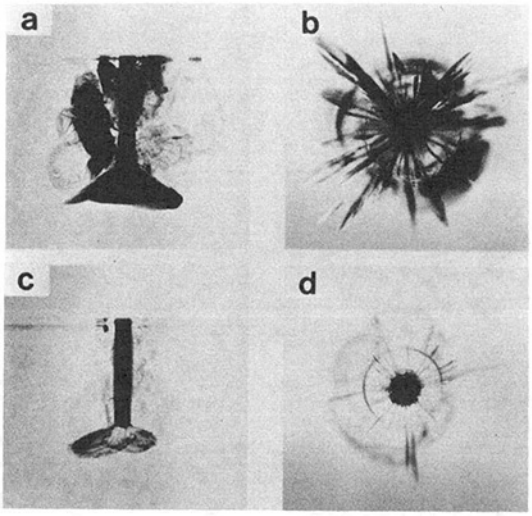

Fig. 7 Liquid penetration in PMMA blocks and the formation of the Hertzian cone crack. A 1 mm diameter hole was drilled in the blocks and was filled with red ink before the impact. (*a*) 575 m/s water jet from 1.7 mm nozzle; (*c*) 345 m/s water jet from 1.7 mm nozzle. (*b*) and (*d*) are the top views of (*a*) and (*c*) respectively.

(Wilson and Brunton, 1970). This wavy structure is not observed on a wetted plate. Measurement of surface profiles on metals confirmed that the deepest depression occurs at the impact centre in both cases. The maximum depression depths of dry and wetted aluminium specimens were 40 μm and 35 μm respectively (Shi and Field, 1992).

Field (1967) and Adler and Hooker (1978) showed that liquid trapped in cracks or pits can cause enhanced damage of materials under water drop impact if the crack sizes are smaller than the drop size. This destructive role of a liquid layer was examined by subjecting PMMA blocks to multiple liquid jet impacts. Figure 6 compares a block which was dried between five successive impacts (Fig. 6(*a*)) and a block which was not dried between impacts (Fig. 6(*b*)). The increased erosion in (Fig. 6(*b*)) is caused by the forced penetration of liquid trapped in the eroded surface during impact.

An experiment was conducted to investigate liquid penetration into solids: liquid jets from a 1.7 mm nozzle were impacted on PMMA blocks; at the impact centre a 1 mm diameter hole had been drilled along the impact axis and filled with ink to trace the crack trajectories. Figure 7 shows the results. A Hertzian type cone crack appears at the end of the hole. The cone angles were ~110 deg at the 575 m/s impact velocity (Fig. 7(*a*)) and ~140 deg at 345 m/s (Fig. 7(*c*)). The precise value can be influenced by the end geometry of the hole, but in general the cone angle is smaller the higher the impact velocity. A similar trend has also been found for solid particle impact on ceramics (Field and Sun, 1989; Akimune, 1990).

4 Conclusions

When a liquid impacts a solid, the central pressure is given by

$$P=\frac{\rho_1 C_1 \rho_2 C_2 V}{\rho_1 C_1+\rho_2 C_2} \tag{1}$$

where the subscripts 1 and 2 are for the liquid and solid, respectively. For a rigid solid, this reduces to $P=\rho_1 C_1 V$ and for the impact of water onto a thick water layer $P=0.5\rho_1 C_1 V$. For layers of intermediate thickness, repeated reflections from the liquid/solid and liquid surfaces increase the pressures to values between these extremes. This is essentially the result discussed by Brunton (1967). The reduced stress level means that with brittle solids the crack density and depth of cracking are both reduced, while with metals the depth of the plastic crater is reduced.

The lateral side jetting flows along the liquid layer free surface rather than on the solid surface when a liquid layer is present and the reduced compliance reduces the side jetting velocity. As a result the shear damage on materials is greatly reduced.

For repeated impacts, particularly onto partly damaged surfaces, liquid trapped in cracks or pits can be forced to penetrate and cause increased damage.

Acknowledgments

H. H. Shi thanks Xi'an Jiaotang University of China for a Tang Zhao-Qian Scholarship and the Cavendish Laboratory, Cambridge for support. The research was supported from grants from the UK, DRA, and SERC.

References

Adler, W. F., and Hooker, S. V., 1978, "Rain Erosion Behaviour of PMMA," *Journal of Materials Science*, Vol. 13, pp. 1013–1025.

Akimune, Y., 1990, "Hertzian Cone Crack in SiC Caused by Spherical Particle Impact," *Journal of Materials Science Letter*, Vol. 9, pp. 659–662.

Bowden, F. P., and Brunton, J. H., 1961, "The Deformation of Solids by Liquid Impact at Supersonic Speeds," *Proceedings of the Royal Society of London*, Series A, Vol. 263, pp. 433–450.

Bowden, F. P., and Tabor, D., 1954, 1964, *The Friction and Lubrication of Solids, Parts I and II*, Clarendon Press, Oxford.

Bowden, F. P., and Field, J. E., 1964, "The Brittle Fracture Solids by Liquid Impact, by Solid Impact and by Shock," *Proceedings of the Royal Society of London*, Series A, Vol. 282, pp. 331–352.

Brunton, J. H., 1967, "Erosion by Liquid Shock," *Proceedings of the Second International Conference on Rain Erosion and Associated Phenomena*, Fyall, A. A., and King, R. B., eds., RAE, Farnborough, England, pp. 535–560.

Brunton, J. H., and Rochester, M. C., 1979, "Erosion of Solid Surfaces by the Impact of Liquid Drops," *Erosion*, Preece, C. M., ed., Academic Press, New York, pp. 185–248.

Clark, H. McI., and Burmeister, L. C., 1992, "The Influence of the Squeeze Film on Particle Impact Velocities in Erosion," *International Journal of Impact Engineering*, Vol. 12, pp. 415–426.

Field, J. E., 1967, "The Importance of Surface Topography on Erosion Damage," *Proceedings of the Second International Conference on Rain Erosion and Associated Phenomena*, Fyall, A. A., and King, R. B., eds., RAE, Farnborough, England, pp. 593–603.

Field, J. E., Gorham, D. A., Hagan, J. T., Matthewson, M. J., Swain, M. V., and van der Zwagg, S., 1979, "Liquid Jet Impact and Damage Assessment for Brittle Solids," *Proceedings of the Fifth International Conference on Erosion by Liquid and Solid Impact*, Field, J. E., Paper 13.

Field, J. E., Lesser, M. B., and Dear, J. P., 1985, "Two-Dimensional Liquid Wedge Impact and Its Relevance to Liquid Drop Impact," *Proceedings of the Royal Society of London*, Series A, Vol. 401, pp. 225–249.

Field, J. E., Dear, J. P., and Ogren, J. E., 1989, "Effect of Target Compliance on Liquid Drop Impact," *Journal of Applied Physics*, Vol. 65, pp. 533–540.

Field, J. E., and Sun, Q., 1989, "Ballistic Impact on Ceramics," Institute of Physics Series No. 102, International Conference on Properties of Materials at Hight Rate of Strain, Oxford, pp. 387–394.

Gorham, D. A., Matthewson, M. J., and Field, J. E., 1979, "Damage Mechanics in Polymers and Composite Under High-Velocity Liquid Impact," American Society for Testing Materials, Special Technical Publication, Vol. 664, W. F. Adler, ed., Philadelphia, PA, pp. 320–342.

Hand, R. J., Field, J. E., and Townsend, D., 1991, "The Use of Liquid Jets to Simulate Angled Liquid Impact," *Journal of Applied Physics*, Vol. 70, pp. 7111–7118.

Heymann, F. J., 1969, "High Speed Impact between a Liquid Drop and a Solid Surface," *Journal of Applied Physics*, Vol. 40, pp. 5113–5122.

Lesser, M. B., 1981, "Analytic Solutions of Liquid-Drop Impact Problems," *Proceedings of the Royal Society of London*, Series A, Vol. 377, pp. 289–308.

Lesser, M. B., and Field, J. E., 1983, "The Impact of Compressible Liquids," *Annual Review of Fluid Mechanics*, Vol. 15, pp. 97–122.

Shi, H. H., and Field, J. E., 1992, "The Role of the Liquid Layer in High Speed Liquid/Solid Impact," *Proceedings of the Fourth Research and Publication Symposium of the Institute of Fluid Science*, Tohoku University, Japan, pp. 141–144.

Troyanovski, B. M., 1973, *Turbines for Nuclear Power Stations*, Energia, Moskva.

Wilson, M. P. W., and Brunton, J. H., 1970, "Wave Formation between Impacting Liquids in Explosive Welding and Erosion," *Nature*, Vol. 226, pp. 538–541.

van der Zwaag, S., and Field, J. E., 1983, "Rain Erosion Damage in Brittle Materials," *Engineering Fracture Mechanics*, Vol. 17, pp. 367–379.

M. R. Wang
Associated Professor.

D. Y. Huang
Graduate Assistant.

Y. C. Liu
Graduate Assistant.

Institute of Aeronautics and Astronautics,
National Cheng Kung University,
Tainan, Taiwan, 70101

Droplet Dynamics Near the Wall in a Vertical Rectangular Duct

Measurements of the droplet behavior near the wall in a vertical rectangular duct were conducted by a phase Doppler particle analyzer (PDPA). The test Reynolds number and drop size range is from 18,500 to 89,300 and from 5 μm to 110 μm, respectively. Results show that the negative slip-velocity of the drops near the free-stream region normally results in the reversed slip-velocity phenomenon in the boundary layer region. No negative slip-velocity of all drops are discovered for Reynolds number less than 38,300. This indicates no reversed slip-velocity phenomenon for the test drop size range under low Reynolds number conditions. However, when the Reynolds number is over 38,300, the free-stream slip-velocity of the bigger drops becomes negative. It is found that the negative slip-velocity and, hence, the reversed slip-velocity phenomenon may take place for drop size larger than 52 μm to 90 μm depending on the flow Reynolds number.

Introduction

Study of the two-phase suspension flow is important in many industrial applications. The suspended particles involved in the practical applications could be liquid droplets, solid particles, or air bubbles. The different inertias of the particle phase and the gas phase in the two-phase suspension flow normally result in a significant velocity difference between them. Such phenomenon, in turn, influences the transport processes of mass, momentum, and energy as well as chemical reactions in two phase turbulent flow. This phenomenon is very important in the understanding of phase interactions and deposition of the dispersed phase on the wall.

The effects of particle loading on the turbulent motion in a vertical up flow were studied by Lee and Durst (1982). Four kinds of glass beads with size of 100, 200, 400, and 800 μm were used as the dispersed phase in air flow. Their results showed that the mean velocities of 100 μm and 200 μm particles are lower than the air flow in the free stream but are higher than air flow near the wall region. It turns out that, for the two smaller particles, there is a radial matching location at which the relative velocity between the phases changes its direction in the central region and the wall region. The wall region where the relative velocity between the particle and the air flow changes its direction is called "reversed slip-velocity region" (Lee and Durst, 1982). They also found that the thickness of this reversed zone is about 20 percent of the pipe radius for the 100 μm particles and is only 10 percent of the pipe radius for the 200 μm particles. However, no reversed slip-velocity region was observed for the 400 μm and 800 μm particles. This implies that the existence of this reversed slip-velocity region depends on the particle size in the range 100 μm–800 μm. However, study of the reversed slip-velocity region in other size range was not carried out in their tests.

Contributed by the Fluids Engineering Division for publication in the JOURNAL OF FLUIDS ENGINEERING. Manuscript received by the Fluids Engineering Division October 22, 1992; revised manuscript received May 7, 1993. Associate Technical Editor: A. Prosperetti.

Lee and Einav (1972) investigated the migratory motions in a rectangular duct by laser-Doppler velocimeter (LDV) measurement. The water flow used in their experiment was filtered through a micronite in order to limit the size of the natural contaminants below 2 μm. Glass spheres with size of 30, 50, and 100 μm were utilized in the tests. The flow Reynolds number was from 400 to 600 and the particle Reynolds number from 0.01 to 0.13. Their measurements showed that the particle velocities always lag behind the fluid in the laminar boundary layer region. This indicates that there is no particle reversed slip velocity region in their test cases. However, the Reynolds number used in this test is much lower than the previous one (Lee and Durst, 1982) and the carrier phase is water instead of air. It seems that the interaction between the carrier phase and the dispersed phase may be dependent on the flow Reynolds number and the inertia of both phases.

Tsuji and Morikawa (1982) investigated the effects of particle size on the turbulent modulation in a horizontal pipe flow with a higher Reynolds number, i.e., 11,500–28,800. The air flow is loaded with plastic particles with size 200 μm and 3400 μm. Results show that there is a reversed slip-velocity zone near the wall for the 200 μm particles. Moreover, the flow turbulence is enhanced by the larger particles (i.e., 3400 μm) and is reduced by the smaller particles (i.e., 200 μm). It seems that the reversed slip-velocity region may take place in a higher Reynolds number range (Lee and Durst, 1982; Tsuji and Morikawa, 1982). An investigation of the particle behavior in a vertical air pipe flow was further carried out by Tsuji et al. (1984). Particle sizes of 200, 500, 1000, and 3000 μm in diameter were used in their tests. Results showed that the reversed slip-velocity phenomenon took place only for 200 μm particles, similar to the result described by Lee and Durst (1982). The data also showed that large particles resulted in the enhancement of the flow turbulence throughout the pipe section, but the small particles reduced it.

As a comparison, Rogers and Eaton (1989) further studied

Table 1 Comparison of the results under various experimental conditions

Author	Test tunnel flow direction	Flow Reynolds number	Phases flow/drop	Size	Results
Lee and Eiven 1972	Horizontal duct	400–600	Water/solid	30, 50, 100 μm glass bead	No reversal
Lee and Durst 1982	Vertical pipe Up flow	7,600	Air/solid	100, 200, 400, 800 μm glass bead	Reversal for 100–200 μm *T.M.
Tsuji et al. 1984	Horizontal pipe	11,500–28,800	Air/solid	200, 3400 μm/plastic	Reversal for 200 μm T.M.
Tsuji et al. 1984	Vertical pipe Up flow	15,000–38,000	Air/solid	200, 500, 1000, 3000 μm plastic	Reversal for 200 μm T.M.
Roger and Eaton 1989	Vertical duct Up flow	107,600	Air/solid	50, 90 μm/glass bead	No reversal T.M./normal direction No T.M./streamwise direction
Rashidi et al. 1992	Horizontal duct	2,500–7,500	Water/solid	120–1100 μm/polystyrene 88 μm/glass bead	No reversal T.M./120–1100 μm polystyrene No T.M./88 μm glass bead
This paper 1992	Vertical duct Down flow	38,300–89,300	Air/Liquid	20, 50, 80 μm Liquid drop	Reversal for 80 μm

* Turbulent Modulation

the response of solid particles under zero and adversed pressure gradient in a vertical turbulent boundary layer flow with a Reynolds number as high as 107,600. Glass beads with size of 50 and 90 μm at concentration of 2 and 20 percent were used to study the aerodynamic characteristics of the dispersed phase. The results demonstrated that the particles were able to respond to the fluctuations of the flow in the streamwise direction. However, the particle response was strongly attenuated in the direction normal to the wall. Their analysis also showed that the power spectrum of the particle velocity fluctuations in the normal direction shifts to higher frequencies relative to the streamwise fluctuations, indicating that the particles cannot closely follow the fluid fluctuations in the normal direction to the wall. These data also indicated that the gas velocity is always greater than that of the particles across the turbulent boundary layer and the reversed slip-velocity zone does not exist in this case.

A test at low Reynolds number in a water flow was also performed by Rashidi et al. (1990). They examined the effects of particle size, particle density, particle loading, and flow Reynolds number on the particle-wall interaction in a turbulent flow. The solid particles, i.e., spherical polystyrene with size range from 120 to 1100 μm and spherical glass bead with only one size of 88 μm, were loaded in the water flow. The flow Reynolds number based on flow depth is from 2,500 to 7,500. The data showed that turbulence intensities and Reynolds stresses increase when loaded with the larger polystyrene particles (i.e., 1100 μm) and decrease when loaded with the smaller polystyrene particles (i.e., 120 μm). These effects are enhanced as the particle loading is increased. However, they also found that the glass bead (i.e., 88 μm) is too heavy to cause any significant modulation on the turbulence. Moreover, it was found that the mean particle velocity always lags behind the fluid across the entire turbulent boundary layer in their experiments. This indicates that there is no reversed slip-velocity region similar to that described by Lee and Durst (1982).

The above results are summarized in Table 1. The reversed slip-velocity phenomenon depends on the flow Reynolds number, the properties of the fluid and dispersed particles, as well as the size of the particles but is insensitive to the orientation of the test tunnel. However, the reversed slip-velocity phenomenon of the air flow loading with liquid drops has not been explored. This paper intends to study the interaction between a polydispersed drop spray and air flow in a moderate Reynolds number range (i.e., 18,500–89,300).

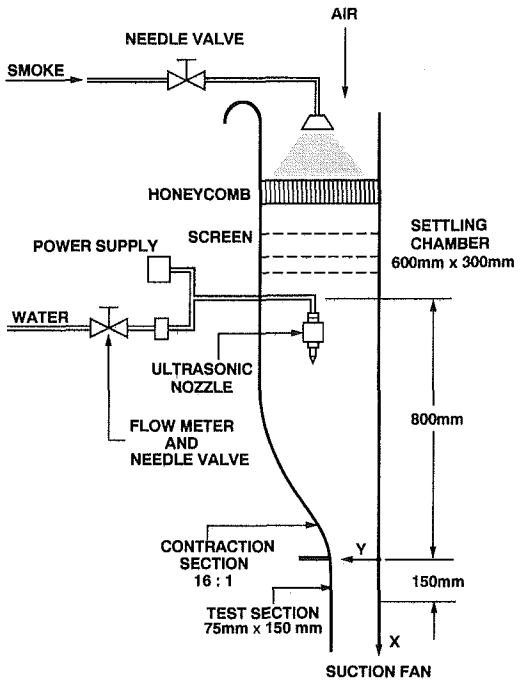

Fig. 1 Schematic of the experimental facility

Configuration of Wind Tunnel

A vertical suction type wind tunnel as shown in Fig. 1 was employed in this study. This wind tunnel is made up of the

Nomenclature

d_p = droplet diameter
Re = Reynolds number
U = streamwise velocity
U_f = gas streamwise velocity at the free stream
V = slip-velocity ($= U_p - U_g$)
X = streamwise coordinate
Y = transverse coordinate
δ = boundary layer thickness
$(Y/\delta)_R$ = reversal point
ν = kinematic viscosity of air
μ = dynamic viscosity of air

Subscripts

g = gas phase
p = droplet phase

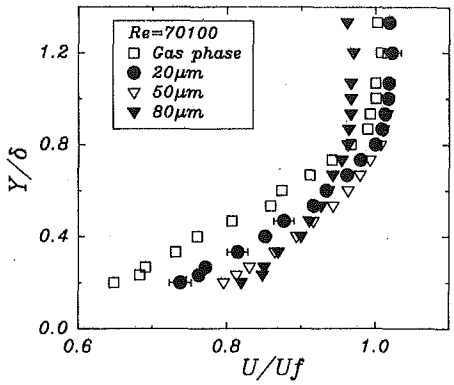

Fig. 2 Velocity distribution of the drops at Re = 70,100

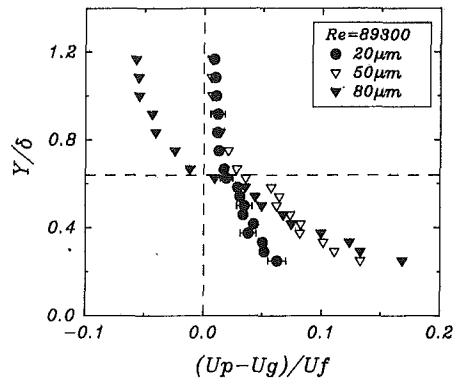

Fig. 4 Slip-velocity between the dispersed phase and the gas phase. (Re = 89,300, X = 145 mm, δ = 6.0 mm)

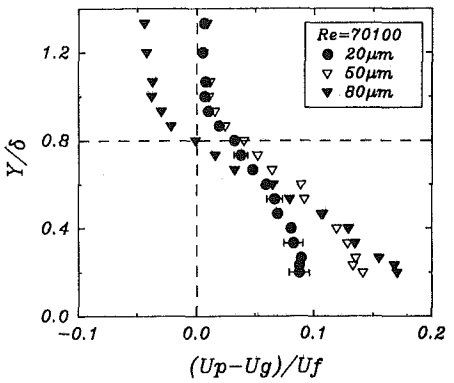

Fig. 3 Slip-velocity between the dispersed phase and the gas phase. (Re = 70,100, X = 145 mm, δ = 7.5 mm)

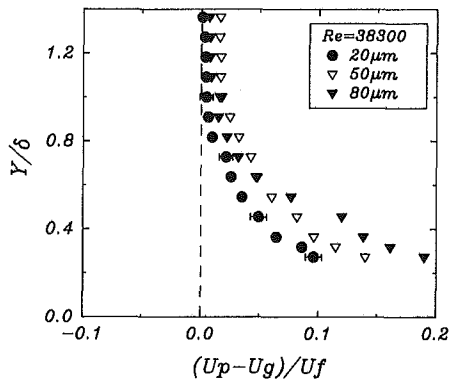

Fig. 5 Slip-velocity between the dispersed phase and the gas phase. (Re = 38,300, X = 145 mm, δ = 5.5 mm)

settling chamber, contraction section, test section, noise reduction chamber and suction fan. The contraction ratio of the tunnel is 16:1 with a cross-section area of 75 mm × 150 mm at the test section. The coordinate as shown in Fig. 1 was selected such that the transverse coordinate Y is positive away from the wall and the streamwise coordinate X is positive toward the downstream with the origin at the entrance of the test section.

Seeding Drop Generator

In order to distinguish the velocity of the continuous phase from the dispersed phase, kerosine drops were seeded to trace the gas flow. Seeding drops with size less than 2 μm were supplied by a seeding drop generator. The polydispersed drops were provided by a Sono-Tek ultrasonic nozzle located at 800 mm upstream of the test section. The arrangement of the ultrasonic atomizing nozzle system in the settling chamber is shown in Fig. 1. Since the cross-sectional area of the settling chamber is large enough and the flow velocity in the settling chamber is less than 1 m/s, the disturbance generated from the drops supply system is relatively small. The atomizing nozzle used in this study was operated at a water flow rate of (25.0 ± 0.75) cc/min with a sauter mean diameter of 53 μm.

Measurement System and Measuring Uncertainty

A two-component phase Doppler particle analyzer (Aerometric model PDP-3200) was used to measure the velocity distribution, particle size and number density of the polydispersed droplets in the two-phase boundary layer. The optical system consists of a transmitter and receiver modules. These packages are affixed to a single base. The transmitter and receiver may also be positioned around the test section to facilitate the required optical access for the measurement. Off-axis forward scatter light detection is used. The detailed description of the working principle had been given by Bachalo and Houser (1984). The local mean quantities are averaged by collecting 30,000 samples for every measurement point. The gas phase velocity is calculated by taking the data of particles smaller than 2 μm and the dispersed phase velocity is calculated from the rest of the particles. The phase Doppler particle analyzer was mounted on a three-axis transverse system which permits positioning to within 0.1 mm.

Uncertainties (Chang et al., 1992) in the mean and fluctuating velocities of the continuous phase using the PDPA are within 2 percent in comparison with the measurements of a pitot tube in the measuring range from 2 to 10 m/s. Repeatability in the mean and fluctuating velocities of both phases are also within 2 percent uncertainty under the test conditions. Mass conservation checks for liquid flow rates at each measuring axial station, by comparing with the metered liquid flow rate in the upstream water supply line, revealed that the uncertainty in the mean liquid flow flux was at most 10 percent. Calibration with monodispersed droplet showed that the error in diameter measurement by PDPA was below 5 percent.

Results and Discussion

In order to investigate the effects of the Reynolds number on the droplet motion within the two-phase boundary layer, experiments were first performed under flow conditions such that the free stream velocities were equal to 5.8 m/s, 11.2 m/s and 14.2 m/s, corresponding to Reynolds numbers based on the hydraulic diameter (i.e., 100 mm) 38,300, 70,100 and 89,300, respectively. The boundary layer thickness, δ, for the test conditions is 5.5 mm, 7.5 mm, and 6.0 mm, respectively.

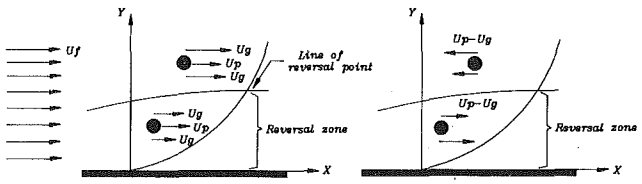

Fig. 6 Schematics of the velocity distribution of the 80 μm drop in the boundary layer. (*a*) Particle motion near the wall, (*b*) slip-velocity of the particle

The information of the drops at 20 μm, 50 μm, and 80 μm is discussed first.

Figure 2 shows the typical velocity distribution of the gas phase and the dispersed phase at Re = 70,100. It seems that the velocity distribution can be divided into two regions, one is near the wall, i.e., $Y/\delta \leq 0.8$, the other is near the free stream, i.e., $Y/\delta \geq 0.8$. In the region of $Y/\delta \geq 0.8$, the velocities of the smaller drops (i.e., 20 and 50 μm) and gas phase are almost the same within the measuring uncertainty, indicating that the equilibrium condition between the smaller drops and gas phase has been achieved. Since the momentum of the drops issuing from the nozzle is transferred from the gas phase, the velocity of the bigger drops (i.e., 80 μm) is less than others in this region because of their higher inertia. However, the velocity distributions are quite different in the near wall region (i.e., $Y/\delta \leq 0.8$). The velocity of the 80 μm drop is the highest in the near wall region while the velocity of the gas phase is the lowest (see Fig. 2). It seems that the viscous effect in the near wall region is significant and the influence of this effect on the drop velocities depends on their size. The velocity of the bigger drops in the near wall region is higher because of their higher inertia when entrained from the free stream.

This foregoing phenomenon can be further explained by the slip-velocity distribution illustrated in Figs. 3 and 4. The slip-velocity of the 80 μm drop turns from a negative value in the free stream region (i.e., $Y/\delta \geq 0.8$) to a positive value in the near wall region (i.e., $Y/\delta \leq 0.8$). It is found that the slip-velocity is zero at $Y/\delta = 0.8$ for 80 μm particles. Similar phenomenon has been reported by Lee and Durst (1982) and is called "reversed slip-velocity region" or "reversal zone." By comparing Figs. 3 and 4 with Fig. 5, it is also found that there exists a reversal zone for the larger drops (i.e., 80 μm) at higher Reynolds numbers (i.e., Re = 70,100 and Re = 89,300) but not for smaller Reynolds number (i.e., Re = 38,300 in Fig. 5). This phenomenon is called "reversed slip-velocity phenomenon" and takes place only for bigger drops, i.e., 80 μm drops in this case. The location where the slip-velocity between the drops and the fluid is zero is called the "reversal point" and is designated as "$(Y/\delta)_R$." It is interesting to find that the reversal phenomenon was not observed throughout the entire turbulent boundary layer for 20 μm and 50 μm drops in the test Reynolds number range (see Figs. 3–5).

The results also shows that there exists a negative slip-velocity between the larger drops (i.e., 80 μm) and the gas phase and it increases as Reynolds numbers increase from Re = 70,100 to Re = 89,300 (see Figs. 3 and 4). This result may imply a local nonequilibrium phenomenon of the larger drops and the gas phase in the region of $Y/\delta > (Y/\delta)_R$.

It is also interesting to see that the reversal point (i.e., $(Y/\delta)_R$) of the larger drop conspicuously moves farther away from the wall as Reynolds number decreases from Re = 89,300 to 70,100 (see Figs. 3 and 4), indicating that the reversal zone increases as Reynolds number decreases. This phenomenon can be explained by the aerodynamic lift force of the drop in the boundary layer region (Saffman, 1965). Figure 6 shows a schematic of the velocity distribution of the 80 μm drop in the boundary layer region. As can be seen from Fig. 6(*a*), the particle velocity leads the air flow velocity in the reversal zone and lags behind the air flow velocities in the region near the free stream. In an effort to study aerodynamic lift force, the slip-velocity is further illustrated in Fig. 6(*b*). In the reversal zone (i.e., $U_p - U_g > 0$), the drop is subject to a pressure difference because of the velocity difference at both sides of the drop. The slip-velocity at the bottom side of the drop is higher than that at the top side, implying that there is a lift force acting on the drop in the direction toward the wall. This lift force is called the Saffman shear-induced lift force (Saffman, 1965). On the other hand, the Saffman lift force acting on the drop is toward the free stream when the drop is outside the reversal zone. The above argument implies that the drop in the shear region with $U_p - U_g > 0$ are propelled toward the wall. This will, in turn, enhance the deposition of the drop on the wall.

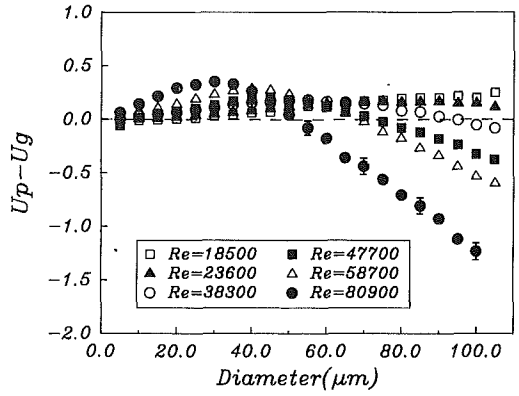

Fig. 7 Dependence of the slip-velocity distribution of the spray drops on the Reynolds numbers in the free stream

According to Saffman (1965), the shear-induced lift force on a small sphere in a creeping shear flow can be expressed as:

$$F_L = K\mu(U_p - U_g)\left(\frac{dU_g}{dy}\right)^{1/2}\frac{a^2}{\nu^{1/2}} \tag{1}$$

where F_L is the Saffman shear-induced lift force, $U_p - U_g$ is the slip velocity between the sphere and the fluid, a is the radius of the sphere, μ and ν are the dynamic and kinematic viscosity of the fluid, respectively, and K is a constant equal to 81.2. From this formula, it is known that a sphere moving through a very viscous fluid with velocity V (i.e., $U_p - U_g$) relative to the shear flow, experiences a lift force which deflects the trajectory of the particle normal to the direction of the relative velocity. The lift force on a small sphere may result from either the spinning motion of the sphere (i.e., Magnus effect) or the motion of a sphere through a shear flow. However, Saffman also found that the lift force due to particle rotation is less than that due to the shear by an order of magnitude when the Reynolds number is small. Hence the lift force on the drop is mainly attributed to the shear flow near the wall.

In an effort to investigate the effects of the Reynolds number on the drop behavior in the air flow, the above phenomenon are further studied under Reynolds numbers from 18,500 to 80,900. The measurements are performed at the location of $X = 145$ mm, $Y = 15$ mm which is in the free-stream region. Results are summarized in Fig. 7. It is found that the slip-velocity of the drops in the free stream depends on their size and flow Reynolds number. The slip-velocity for all the drops size range (i.e., 5 μm–110 μm) is positive and relatively small for Reynolds number less than 38,300. This indicates that no reversed slip-velocity phenomenon can be found for the test particle range under low Reynolds number conditions which is consistent with that reported by Lee and Einav (1972) and Rashidi et al. (1990). However, the slip-velocity turns from a positive values for the smaller drops to a negative values for

the larger drops for Reynolds number more than 38,300. Moreover, the diameter of the drops with a zero slip-velocity depends on the Reynolds number and is called "critical diameter." It is interesting to see that this critical diameter decreases from 90 μm to 52 μm as the Reynolds number increases from 38,300 to 80,900 (see Fig. 7).

As described earlier, the negative slip-velocity condition in the free-stream normally results in the reversal zone near the wall region (see Figs. 3 and 4). Hence, it can be concluded that the reversed slip-velocity phenomenon takes place for drop size larger than 90 μm at Reynolds number 38,300 and for drop size larger than 52 μm at Reynolds number 80,900. Figure 7 also shows that the negative slip-velocity of a specific drop size increases as the Reynolds number increases. In the smaller drop size range where the slip-velocity is always positive, there is a maximum slip-velocity at drop size of 30 μm.

Conclusion

The dynamics of the spray drops in the range of 5 μm to 110 μm near the wall at the Reynolds number from 18,500 to 89,300 are studied. Results show that the reversed slip-velocity phenomenon of the larger drops (i.e., 80 μm) near the wall takes place at the higher Reynolds number (i.e., Re = 70,100 and Re = 89,300). However, this phenomenon is not observed for the case of lower Reynolds number (i.e., Re = 38,300). Moreover, the reserved slip-velocity phenomenon is not observed for 20 μm and 50 μm drops for the test Reynolds number from 38,300 to 89,300. Results also show that the thickness of the reversal zone of the 80 μm drop increases as Reynolds number decreases. It is found that the drops near the wall are subject to a Saffman shear-induced lift force which will, in turn, result in the deposition of the drops on the wall. It is also found that the negative slip-velocity between the 80 μm drop and the gas phase in the region of $Y/\delta > (Y/\delta)_R$ increases as Reynolds number increases, implying that the equilibrium between the 80 μm drop and the gas phase has not been achieved. Furthermore, the negative slip-velocity near the free stream normally results in the reversed slip-velocity phenomenon near the wall. However, no negative slip-velocity near the free stream can be found for the smaller drops.

Measurement of the negative slip-velocity near the free stream is performed for Reynolds numbers from 18,500 to 80,900. No negative slip-velocity for all drops is discovered for Reynolds number less than 38,300. This indicates that no reversed slip-velocity phenomenon can be found for the test drops range under low Reynolds number conditions. On the other hand, slip-velocity near the free stream becomes negative for bigger drops when the Reynolds number is higher than 38,300. It is concluded that the negative slip-velocity may take place for drop size larger than 52 μm to 90 μm depending on the flow Reynolds number.

References

Bachalo, W. D., and Houser, M. J., 1984, "Phase/Doppler Spray Analyzer for Simultaneous Measurement of Drop Size and Velocity Distributions," *Optical Engineering*, Vol. 23, No. 5, p. 583.

Chang, K. C., Wang, M. R., Wu, W. J., and Liu, Y. C., 1992, "Theoretical and Experimental Study on Two-Phase Structure of Planar Mixing Layer," *AIAA Journal*, Vol. 31, No. 1, p. 68.

Lee, S. L., and Einav, S., 1972, "Migration in a Laminar Boundary Layer Measured by the Use of a Two-Dimensional Laser-Doppler Anemometer," *Progress in Heat and Mass Transfer*, Vol. 59, p. 385.

Lee, S. L., and Durst, F., 1982, "On the Motion of Particles in Turbulent Duct Flows," *International Journal of Multiphase Flow*, Vol. 8, No. 2, p. 125.

Rashidi, M., Hetsroni, G., and Banerjee, S., 1990, "Particle-Turbulence Interaction in a Boundary Layer," *International Journal of Multiphase Flow*, Vol. 6, No. 6, p. 935.

Rogers, C. B., and Eaton, J. K., 1989, "Particle Response and Turbulent Modification in a Flat Plate Turbulent Boundary Layer," ASME, FED-Vol. 80, *Turbulence Modification in Dispersed Multiphase Flows*, p. 15.

Rouhiainen, P. O., and Stachiewicz, J. W., 1970, "On the Deposition of Small Particles from Turbulent Streams," ASME *Journal of Heat Transfer*, Vol. 92, p. 169.

Saffman, P. G., 1965, "The Lift on a Small Sphere in a Slow Shear Flow," *Journal of Fluid Mechanics*, Vol. 22, p. 385.

Tsuji, Y., and Morikawa, Y., 1982, "LDV Measurements of an Air-Solid Two-Phase Flow in a Horizontal Pipe," *Journal of Fluid Mechanics*, Vol. 120, p. 385.

Tsuji, Y., Morikawa, Y., and Shiomi, H., 1984, "LDV Measurements of an Air-Solid Two-Phase Flow in a Vertical Pipe," *Journal of Fluid Mechanics*, Vol. 130, p. 417.

Analytical Solutions for Flow of a Dusty Fluid Between Two Porous Flat Plates

Ali J. Chamkha
Assistant Professor,
Mechanical Engineering Department,
Kuwait University,
Safat, 13060 Kuwait
Mem. ASME

Equations governing flow of a dusty fluid between two porous flat plates with suction and injection are developed and closed-form solutions for the velocity profiles, displacement thicknesses, and skin friction coefficients for both phases are obtained. Graphical results of the exact solutions are presented and discussed.

Introduction

This paper deals with the two-dimensional, steady, laminar, fully developed flow of a dusty fluid between two parallel porous flat plates. The plates are infinitely long and separated by a fixed distance of $h1$ (h multiplied by 1, a constant) with the lower plate being coincident with the plane $y=0$. The flow takes place due to the action of a constant pressure gradient applied in the x-direction. Uniform fluid-phase suction and injection are imposed at the lower and upper plates, respectively. The fluid and particulate phases are both assumed incompressible.

In the present work both phases (the fluid phase and the particle cloud) are treated as continua. The basic assumption in the theoretical analysis of such a suspension is that the average properties of the particles are described in terms of continuous variables. Extensive work based on the continuum modeling of particulate (particle-fluid) suspensions has been reported (see, for instance, Marble, 1970; Di Giovanni and Lee, 1974; Ishii, 1975; and Drew, 1979, 1983).

The mathematical model employed in the present work represents a generalization of the original dusty-gas model (a model restricted for particulate suspensions having small volume fraction. See, for instance, Marble, 1970) by allowing for finite particulate volume fraction. In this case the particle-phase viscous effects are important.

In the absence of particle-phase viscous effects (small particulate volume fraction), it was reported by Chamkha (1992) that a difficulty exists as to the appropriate particle-phase boundary conditions that need to be used for this problem. The purpose of this paper is to obtain a closed-form solution for the problem described above for uniform and finite particle-phase volume fraction by applying slip boundary conditions familiar from rarefied gas dynamics on the particle phase. This allows one to explore the qualitative behavior brought about by changes in boundary conditions and various parameters of the system.

Governing Equations

Consider steady laminar flow of a suspension of solid spherical particles uniformly distributed in a continuous carrier fluid between two infinite parallel porous flat plates due to a constant applied pressure gradient. The governing equations for this investigation are based on the balance laws of mass and linear momentum for both phases. These are given by

$$\nabla\cdot((1-\phi)\mathbf{V})=0, \tag{1a}$$

$$\nabla\cdot(\phi\mathbf{V}_p)=0 \tag{1b}$$

$$\rho(1-\phi)\mathbf{V}\cdot\nabla\mathbf{V}=-\nabla((1-\phi)p)+\nabla\cdot(\mu(1-\phi)(\nabla\mathbf{V}+\nabla\mathbf{V}^T))+\rho_p\phi(\mathbf{V}_p-\mathbf{V})/\tau, \tag{2a}$$

$$\rho_p\phi\mathbf{V}_p\cdot\nabla\mathbf{V}_p=\nabla\cdot(\mu_p\phi(\nabla\mathbf{V}_p+\nabla\mathbf{V}_p^T))-\rho_p\phi(\mathbf{V}_p-\mathbf{V})/\tau \tag{2b}$$

where ∇ is the gradient operator, ϕ is the particle volume fraction, $\mathbf{V}$ is the fluid-phase velocity vector, $\mathbf{V}_p$ is the particle-phase velocity vector, ρ is the fluid-phase density, ρ_p is the particle-phase density, p is the fluid pressure, μ is the fluid-phase dynamic viscosity, τ is the momentum relaxation time (time needed for the relative velocity between the two phase to decrease e^{-1} of its original value), and μ_p is the particle-phase dynamic viscosity, and a superposed T denotes the transpose of a second order tensor. It can be seen from Eq. (2b) that the partial pressure contributed by the particle phase and gravity are neglected. This situation arises when inertia and drag dominate over gravity forces. This obtains when the velocity in the x-direction and the suction velocity are large compared to the particles settling velocity. The last term in Equation (2a) accounts for the interaction between the two phases and is based on Stoke's linear drag theory. In the present work, ϕ, ρ, ρ_p, μ, μ_p, and τ will all be treated as constants.

It is convenient to nondimensionalize the governing equations given earlier by using the following equations:

$$\dot{y}=1\eta,\quad \mathbf{V}=\mathbf{e}_xV_cF(\eta)-\mathbf{e}_yV_w,\quad \mathbf{V}_p=\mathbf{e}_xV_cF_p(\eta)-\mathbf{e}_yV_w,\quad dP/dx=-\mu V_cG/1^2 \tag{3}$$

where $\mathbf{e}_x$ and $\mathbf{e}_y$ are unit vectors in the x and y directions, respectively, V_c is a characteristic velocity, and V_w is the suction (or injection) velocity and is a constant and positive. It can be noticed from Eqs. (2) that for steady-state and constant particulate volume fraction conditions the cross stream velocities for both phases have to be equal. The resulting nondimensional equations can be shown to be

Contributed by the Fluids Engineering Division for publication in the JOURNAL OF FLUIDS ENGINEERING. Manuscript received by the Fluids Engineering Division June 29, 1992; revised manuscript received May 24, 1993. Associate Technical Editor: M. W. Reeks.

$$F'' + \mathrm{Re}_w F' - \kappa\alpha(F - F_p) + G = 0, \quad (4a)$$

$$r_\nu F_p'' + \mathrm{Re}_w F_p' + \alpha(F - F_p) = 0 \quad (4b)$$

where a prime denotes ordinary differentiation with respect to η and

$$\mathrm{Re}_w = V_w 1/\nu, \quad \kappa = \rho_p\phi/(\rho(1-\phi)), \quad \alpha = 1^2/(\tau\nu),$$

$$r_\nu = \nu_p/\nu\,(\nu = \mu/\rho, \quad \nu_p = \mu_p/\rho_p) \quad (5)$$

are the wall Reynolds number, the particle loading, the inverse Stokes number, and the viscosity ratio, respectively.

Four boundary conditions (two for the fluid phase and two for the particulate phase) are needed to solve Eqs. (4). No slip fluid boundary conditions will be used at the walls. That is

$$F(0) = 0, \quad F(h) = 0 \quad (6)$$

While the exact form of boundary conditions to be satisfied by a particulate phase at a surface is unknown at present and since a particle cloud may resemble a rarefied continuum, slip boundary conditions similar to those used in rarefied gas dynamics are used at the walls. These are

$$F_p'(0) = \omega F_p(0), \quad F_p'(h) = -\omega F_p(h) \quad (7)$$

where ω is a constant and positive, and the negative sign is used to make $F_p(h)$ positive since $F_p'(h)$ is negative. In general, ω would be a function of the coefficient of viscosity. No attempt, however, is made in the present work to relate ω to the internal properties of the suspension.

Of special interest are the fluid-phase volumetric flow rate, the particle-phase volumetric flow rate, the fluid-phase skin friction coefficient at the lower plate, and the particle-phase skin friction coefficient. These can be defined, respectively, as

$$Q = \int_0^h F(\eta)d\eta, \quad Q_p = \int_0^h F_p(\eta)d\eta,$$

$$C = F'(0), \quad C_p = r_\nu\kappa F_p'(0) \quad (8)$$

Results and Discussion

The governing equations developed above will be solved subject to the boundary conditions given earlier in closed form. This will be done next.

Solving for F in Eq. (4*b*), taking the appropriate derivatives, and then substituting into Eq. (4*a*) yield a fourth-order, linear, nonhomogeneous, ordinary differential equation in F_p. It can be written as

$$F^{iv} + \mathrm{Re}_w(1+r_\nu)/r_\nu F_p''' + (\mathrm{Re}_w^2 - \alpha(1+\kappa r_\nu))/r_\nu F_p'' - \mathrm{Re}_w\alpha(1+\kappa)/r_\nu F_p' = \alpha/r_\nu G \quad (9)$$

Without going into the details, it can be shown that

$$F_p = C_1\exp(m_1\eta) + C_2\exp(m_2\eta) + C_3\exp(m_3\eta) + A_1\eta + B_1 \quad (10)$$

where m_1, m_2, and m_3 are the roots of the equation

$$m^3 + P^*m^2 + qm + r = 0$$

$$P^* = \mathrm{Re}_w(1+r_\nu)/r_\nu, \quad q = (\mathrm{Re}_w^2 - \alpha(1+\kappa r_\nu))/r_\nu$$

$$r = -\mathrm{Re}_w\alpha(1+\kappa)/r_\nu, \quad A_1 = \alpha G/(r_\nu r) \quad (11)$$

It should be pointed out that the particle-phase axial velocity F_p is indirectly dependent on V_w through Re_w. The coefficients B_1, C_1, C_2, and C_3 are constants determined by the application of the boundary conditions. These can be shown to be

$$B_1 = \mathrm{Re}_w A_1/\alpha - C_1E - C_2H - C_3I,$$

$$C_1 = (-A_1(2+\omega h) - C_2K - C_3L)/J$$

$$C_2 = (R - C_3P_1)/\mathrm{O}, \quad C_3 = (Q_1\mathrm{O} - MR)/(NO - MP_1) \quad (12)$$

where

$$E = 1 - m_1/\alpha(r_\nu m_1 + \mathrm{Re}_w), \quad H = 1 - m_2/\alpha(r_\nu m_2 + \mathrm{Re}_w)$$

$$I = 1 - m_3/\alpha(r_\nu m_3 + \mathrm{Re}_w),$$

$$J = (m_1 - \omega) + (m_1 + \omega)\exp(m_1 h) \quad (13)$$

$$K = (m_2 - \omega) + (m_2 + \omega)\exp(m_2 h),$$

$$L = (m_3 - \omega) + (m_3 + \omega)\exp(m_3 h)$$

$$M = JH(1 - \exp(m_2 h)) - KE(1 - \exp(m_1 h))$$

$$N = IJ(1 - \exp(m_3 h)) - LE(1 - \exp(m_1 h)) \quad (14)$$

$$\mathrm{O} = K(\omega E + m_1 - \omega) - J(\omega H + m_2 - \omega),$$

$$P_1 = L(\omega E + m_1 - \omega) - J(\omega I + m_3 - \omega)$$

$$Q_1 = JA_1 h + EA_1(2 + \omega h)(1 - \exp(m_1 h))$$

$$R = -(2 + \omega h)A_1(\omega E + m_1 - \omega) - JA_1 - (\mathrm{Re}_w\omega/\alpha - 1) \quad (15)$$

With F_p known, Eq. (4*a*) can now be solved for F. The solution for F can be shown to be

$$F = C_1E(\exp(m_1\eta) - 1) + C_2H(\exp(m_2\eta) - 1) + C_3I(\exp(m_3\eta) - 1) + A_1\eta \quad (16)$$

The appropriate solutions for Q, Q_p, C, and C_p can be written, respectively, as

$$Q = (B_1 - \mathrm{Re}_w A_1/\alpha)h + A_1h^2/2 + C_1E(\exp(m_1h) - 1)/m_1 + \mathrm{C_2H}(\exp(m_2h) - 1)/m_2 + C_3I(\exp(m_3h) - 1/m_3 \quad (17)$$

$$Q_p = B_1h + A_1h^2/2 + C_1(\exp(m_1h) - 1)/m_1 + C_2(\exp(m_2h) - 1)/m_2 + C_3(\exp(m_3h) - 1)/m_3 \quad (18)$$

$$C = A_1C_1Em_1 + C_2Hm_2 + C_3Im_3 \quad (19)$$

$$C_p = \kappa r_\nu(A_1 + C_1m_1 + C_2m_2 + C_3m_3) \quad (20)$$

It is difficult to gain insight into the behavior of the physical properties of the problem under consideration from the form of the solutions reported above. For this reason, graphical results are obtained by numerically evaluating the exact solutions and will be presented below.

It should be mentioned that when r_ν was made very small during the numerical evaluation of the solutions, it was found that the corresponding solutions approached the inviscid case ($r_\nu = 0$) reported earlier by Chamkha (1992) under the appropriate conditions. This is a further evidence that the no slip condition on the particle phase used by Chamkha (1992) in the inviscid case is reasonable.

Figures 1 through 4 are obtained by numerically evaluating Eqs. (17) through (20). These figures are chosen from a variety of results to elucidate the features of the problem under consideration.

Figures 1 through 4 present the behavior of the fluid-phase volumetric flow rate Q, the particulate phase volumetric flow rate Q_p, the fluid-phase skin friction coefficient C, and the particulate-phase skin friction coefficient C_p for various values of the particle loading κ and the inverse Stokes number α, respectively. In these figures the dotted lines correspond to the equilibrium limit (where both phases are moving together with the same velocity) attained at large values of α ($\alpha \to \infty$). Increases in the values of α increase the momentum transfer between the two phases causing the fluid-phase volumetric flow rate to decrease and the particle-phase volumetric flow rate to increase until equilibrium between the two phases for large values of α is reached. This is evident from Figs. 1 and 2. It can be seen from Figs. 1 through 4 that as the particle loading (or the particle density) increases, Q, Q_p, and C decrease (since the fluid-phase velocity decreases and the particle phase is being dragged along by the fluid phase) while C_p increases (see definition of C_p) for all values of α shown. As apparent from Figs. 3 and 4, there is a minimum in C and a corresponding maximum in C_p at some particular value of α. This type of behavior is well known and often observed in relaxation type flows. It should be mentioned that when the present results were compared with the results associated with the inviscid

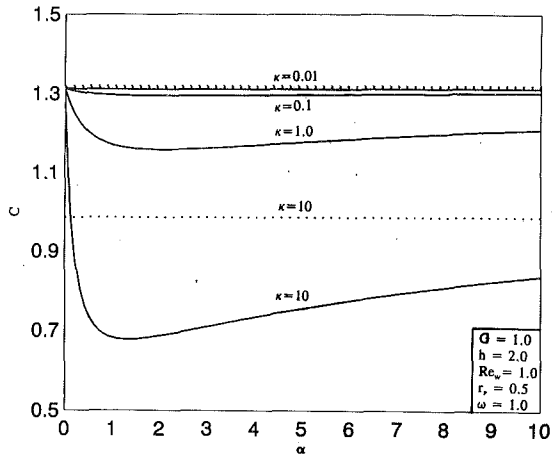

Fig. 1 Fluid-phase volumetric flow rate versus α

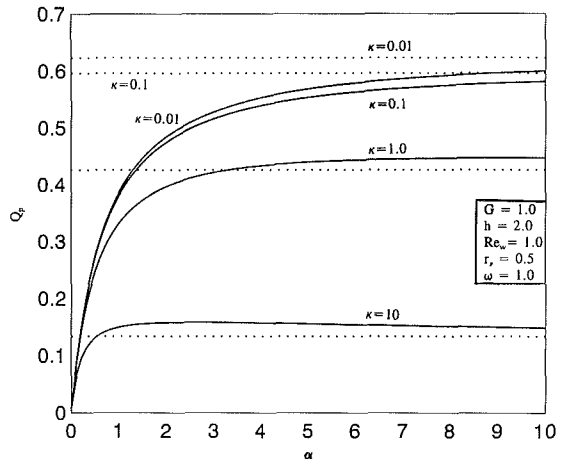

Fig. 2 Particle-phase volumetric flow rate versus α

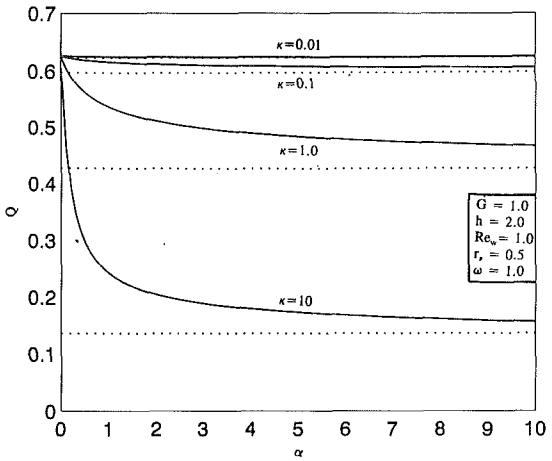

Fig. 3 Fluid-phase skin friction coefficient versus α

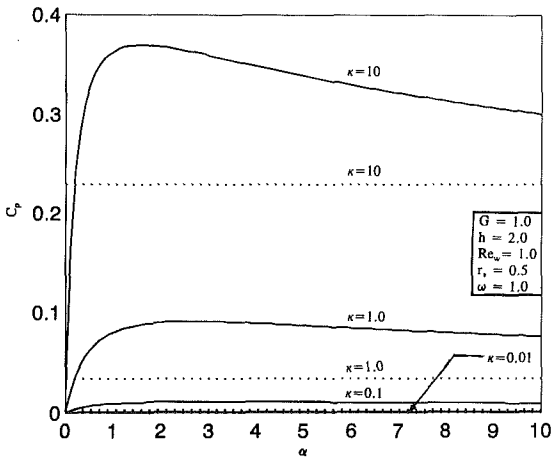

Fig. 4 Particle-phase skin friction coefficient versus α

particle phase case, significant decreases in the values of C and slight increases (for small values of α) followed by slight decreases (for large values of α) in the values of Q and Q_p were observed.

Conclusion

The problem of steady laminar fully developed flow of a particle-fluid suspension between two infinite parallel porous flat plates due to the action of a constant pressure gradient is solved in closed form. The particle-phase volume fraction is assumed finite and uniform. This assumption made it possible to investigate appropriate forms of particle-phase boundary conditions. Slip boundary conditions similar to those used in rarefied gas dynamics were utilized and appear to be reasonable. This provided a rational way in arriving at the appropriate boundary conditions for the case of small volume fraction where particle-phase viscous stresses are negligible. The influence of the particle loading on the volumetric flow rates and skin friction coefficients for both phases is presented graphically and discussed. It is hoped that the present model will be used for the investigation of different stress models and boundary conditions.

References

Marble, F. E., 1970, "Dynamics of Dusty Gases," *Annual Review of Fluid Mechanics*, Vol. 2, pp. 397–446.

Di Giovanni, P. R., and Lee, S. L., 1974, 'Impulse Motion in a Particle-Fluid Suspension Including Particulate Volume, Density and Migration Effects," ASME *Journal of Applied Mechanics*, Vol. 41, pp. 35–41.

Ishii, M., 1975, *Thermo-Fluid Dynamic Theory of Two-Phase Flow*, Eyrolles, Paris.

Drew, D. A., 1979, "Application of General Constitutive Principles to the Derivation of Multidimensional Two-Phase Flow Equations," *International Journal of Multiphase Flows*, Vol. 5, pp. 143–164.

Drew, D. A., 1983, "Mathematical Modeling of Two-Phase Flow," *Annual Review of Fluid Mechanics*, Vol. 15, pp. 261–291.

A. J. Chamkha, 1992, "Poiseuille Two-Phase Flow With Suction and Injection," *Development of Theoretical Applied Mechanics*, Vol. 16, pp. II4.16-II4.23.

Droplet Sizing Using the Shifrin Inversion

R. Albert

P. V. Farrell

Department of Mechanical Engineering,
University of Wisconsin-Madison,
Madison, WI 53706

A method for measuring droplet size distributions was investigated with an emphasis on limitations related to measurements in real spray environments. The method stores a photographic image of a plane of droplets within a spray and is capable of evaluating particle size distributions within the spray, one small region at a time. The method complements droplet velocity measurements made using Particle Image Velocimetry. In a typical experiment, a plane of the spray was illuminated by a laser light sheet and photographed. After processing, a small laser beam scanned the film and a diffraction pattern was generated for each region illuminated by the small laser. The diffraction pattern was inverted using a Shifrin inversion to solve for the particle size distribution within the illuminated region. In this paper we will discuss some of the limitations of this method and indicate one approach which seems to allow for improved inversions using data signal processing.

Introduction

A significant number of two-phase flow problems are of short duration, or exhibit important transient characteristics upon starting or stopping, or are in a turbulent flow field. Any of these conditions renders many of the details of the flow unsteady. Measurement of the spatially resolved transient behavior of the flow field may provide better understanding of two-phase flow behavior.

Current experimental techniques for measuring particle size and velocity have been carefully developed and appear to be mature techniques. These include Fraunhofer diffraction measurements (Swithenbank et al., 1976 and Yule et al., 1982), interferometric intensity type measurements (Farmer, 1972 and Bachalo, 1980), and phase Doppler type measurements (Bachalo and Houser, 1984). Comparisons of these techniques are given by Jackson and Samuelson (1987) and Dodge et al. (1987) and recent summaries are given by Hirleman et al. (1990).

These techniques make measurements at a single point or measurements averaged over some small area of the flow. They can make a series of measurements at a given location over time. For transient flows, particularly ones with significant turbulence and other stochastic characteristics, a collection of single point time records spanning some spatial region of interest is difficult to interpret. The various spatial locations would be sampled at different discrete times, for what may amount to different flow conditions. For many transient multi phase flow applications, measurements which span a spatial area or volume at a series of discrete times may be of greater utility in developing an understanding of the flow as well as for development and refinement of flow models.

Measurement Technique Background

The basis of the method for measuring particle size and velocity is similar to the developing technique of particle image velocimetry (PIV). A brief review of the concepts necessary for this measurement technique will be presented.

Particle image velocimetry has been described in a complete review by Adrian (1991). The general technique of PIV involves a multiple exposure photograph of a flow containing particles or droplets. A photographic image of the particles is obtained for a plane of particles which has dimensions of the height of an illuminating laser sheet, the width of the image plane, and the thickness of the laser sheet. Typical dimensions are 3 cm high by 5 cm wide by 200 μm thick. The light source is usually controlled to allow two exposures of the particle field to be recorded on the film. The time between the exposures is controlled and is presumed known. Particle velocity can be obtained by measuring the magnitude and direction of the displacement of a particle between exposures.

After development, the film is illuminated with an unexpanded laser beam. Sequential illumination of portions of the film provides information regarding particle displacement in the region illuminated. Each particle image generates a diffraction pattern in the far field (far from the film). The combination of the many diffraction patterns from many particle images illuminated by the laser beam produces an interference pattern, known as Young's fringes. The low frequency modulation of the fringe pattern is known as the diffraction halo.

Particle size information is available from the shape of the diffraction halo which modulates the Young's fringe pattern. Since the Fourier transform or far-field diffraction operator is linear, the effects of many particles may be interpreted through superposition. The diffraction halo is the same diffraction pattern for near forward scattering from particles which is observed for diffraction based particle sizing techniques (Swithenbank et al., 1976).

Inversion of the scattered intensity data, minus the higher frequency Young's fringe data, can provide a particle size distribution of the ensemble of particle images which appear within the interrogating laser beam. It may be noted that in

Contributed by the Fluids Engineering Division for publication in the JOURNAL OF FLUIDS ENGINEERING. Manuscript received by the Fluids Engineering Division November 29, 1992; revised manuscript received July 16, 1993. Associate Technical Editor: M. W. Reeks.

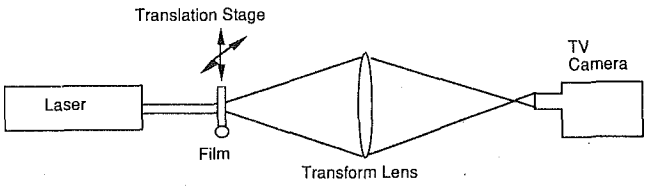

Fig. 1(*a*) Interrogation system for PIV and particle sizing method

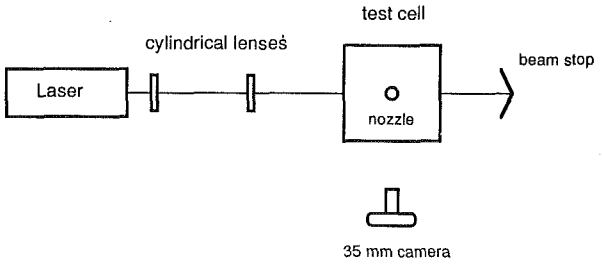

Fig. 1(*b*) Experimental arrangement for spray photography, plan view

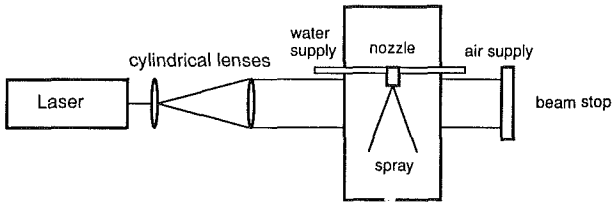

Fig. 1(*c*) Experimental arrangement for spray photography, elevation

dilute regions of a spray, the small sample volume interrogated may cover a few droplets, not enough to be reliably predicted with a continuous size distribution. Thus in inverting the diffraction halo intensity pattern to recover a particle size distribution, it is unlikely that an a priori selected distribution function will be successful.

For particle size measurements a TV camera is used to capture the diffraction pattern and Young's fringe pattern at the back focal plane of the lens, as shown in Fig. 1(*a*), along with a typical photographic setup in Figs. 1(*b*) and 1(*c*). The use of a TV camera as a detector has the advantage of simultaneous use for PIV applications and selectivity of geometry of data collection. With the camera, information on the intensity profile can be collected at different sector sizes and at different angles within each sector. A disadvantage of using a TV camera is the limited dynamic range of the attached frame grabber, which in our case is 8 bits for each pixel. In our analysis some high intensity information in the small diffraction angle region was sacrificed (overexposed or saturated) to pick up information at higher scattering angles.

The intensity pattern captured by the TV camera can be sampled in a variety of ways, using line scans of the image in selected directions, integrating rings at specified radii to imitate ring detectors (Kouzalis et al., 1988), or integrating over selected sectors of rings. In the experiments discussed here, little difference was seen in the results for line scans and sectors integrated over as much as 45 deg. Since line scans are much faster, these are used for the results.

The diffraction halo due to particle scattering is the low frequency portion of the Young's fringe pattern, which is given by the Airy formula

$$I_\theta = \frac{1}{k^2\theta^2 z^2}\int_{x_1}^{x_2} J_1^2(y)x^2 n(x)\,dx \tag{1}$$

where θ is an angle measured from the center of the diffraction pattern, I_θ is the normalized scattered intensity at an angle θ, $k=2\pi/\lambda$, λ is the wavelength of light, z is the distance from the diffracting object to the viewing plane, x is the particle size parameter $x=\pi d/\lambda$, x_1 and x_2 are limits on the expected particle size parameter, $n(x)$ is the particle size distribution, $\theta \cong \sin\theta$, $y=x\theta$, and J_1 is a Bessel function of the first kind of order unity. For some distributions $n(x)$ may be assumed to vanish at x_1 and x_2, giving

$$I_\theta = \frac{1}{k^2\theta^2 z^2}\int_{0}^{\infty} J_1^2(y)x^2 n(x)\,dx \tag{2}$$

Equation (2) may be considered a first-kind Fredholm integral equation. An inversion producing $n(x)$, known as a Shifrin inversion, is possible (Fymat and Mease, 1978) resulting in

$$n(x) = \frac{2\pi k^2 z^2}{x^2}\int_0^\infty J_1(y)\,Y_1(y)y\,\frac{d(\theta^3 I_\theta)}{d\theta}\,d\theta \tag{3}$$

where Y_1 is a Bessel function of the second kind of order 1.

This type of data inversion allows flexibility in the type of particle size distribution acquired, since no distribution is assumed. A major disadvantage of this integral inversion scheme is that the measured data I_θ, must be differentiated. Alternative inversion methods using the Shifrin inversion in other forms (Fymat and Mease, 1978 and Coston and George, 1991) and the use of other inversion schemes (Hirleman, 1991) have been suggested. Some of these inversions are aimed primarily at ring detector geometry, but others which may prove useful in this application have not yet been implemeted. It should be noted that the result of the calculation from Eq. (3) is a relative particle size distribution, and actual particle flux or mass flux of particles is not a result of Eq. (3). Estimates of total particle flux for diffraction based methods are usually made by measurement of the attenuation of the interrogating laser beam relative to a correlation for extinction as a function of flux.

The technique outlined has been tested on modeled and experimental single apertures, a variety of modeled polydisperse distributions, a fixed calibration reticule, and a monodisperse droplet stream (Farrell, 1991). The results of this previous work indicated that the inversion scheme worked well for both monodisperse and polydisperse size distributions using modeled intensity data. Using experimental data from single apertures, the method was able to accurately measure monodisperse distributions. Using a reticule with a Rosin-Rammler distribution of plated spots, the method was able to accurately measure the distribution. In the previous work, the method

Nomenclature

d = particle diameter
I_θ = intensity at an angle θ from the optical axis
k = wave number, $2\pi/\lambda$
$n(x)$ = particle distribution function
N_θ = number of data samples at discrete θ locations
x = particle size parameter, $\pi d/\lambda$
x_1 = limit of integration for size parameter in Eq. (1)
x_2 = limit of integration for size parameter in Eq. (1)
y = particle parameter, $x\theta$
z = distance from particle image to image plane for interrogation
λ = wavelength of light
θ = angle from optical axis
$\Delta\theta$ = angular spacing between sample points

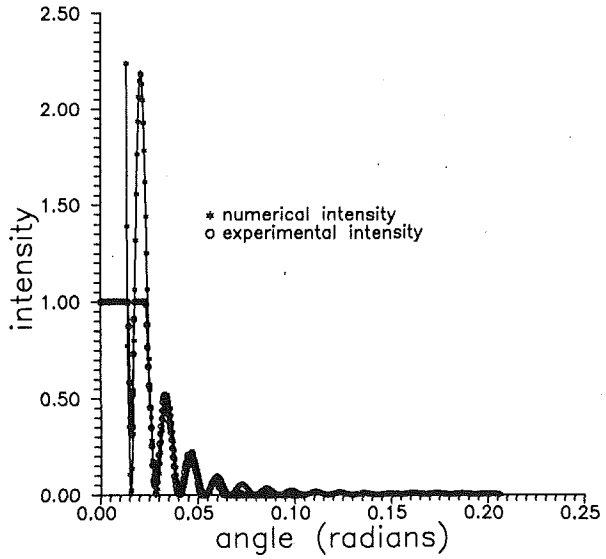

Fig. 2 Intensity profiles for numerical and experimental data for 50 μm aperture

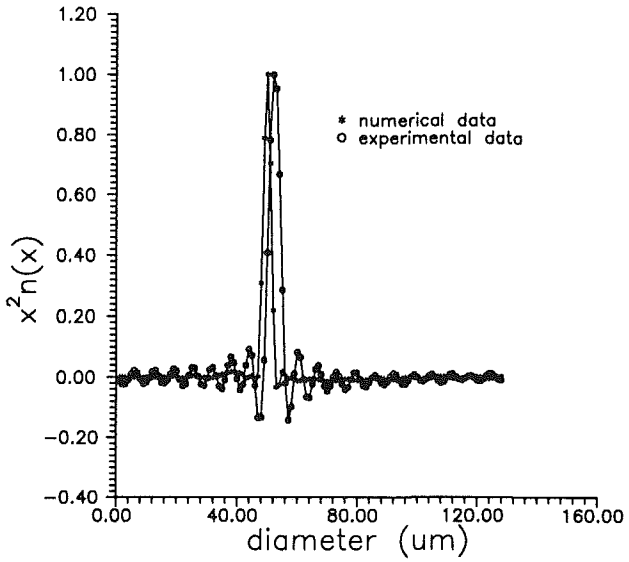

Fig. 3 Comparison of area weighted size distributions for numerical and experimental data for a μm aperture

had not been extensively tested in spray fields subject to laser speckle and other noise sources.

When the experimental method described was applied to a spray, several problems were observed which were not clearly evident in the single aperture and polydisperse reticule evaluations. For a typical application, a large spray field is photographed, either with single or double exposure, and interrogated on a scale of about 0.5 mm. For many regions of a spray, this geometric scale will include a small number of droplets. In these regions, system performance for monodisperse or multi mode size distributions is important.

Particle Sizing Method Improvements

The particle sizing method may be characterized using calculated intensity distributions for monodisperse or polydisperse particle distributions. Experimental monodisperse and polydisperse distributions can also be evaluated, although quantitative comparison for polydisperse distributions is difficult since the actual distribution is rarely known.

A calculated intensity profile for a 50 μm particle is shown

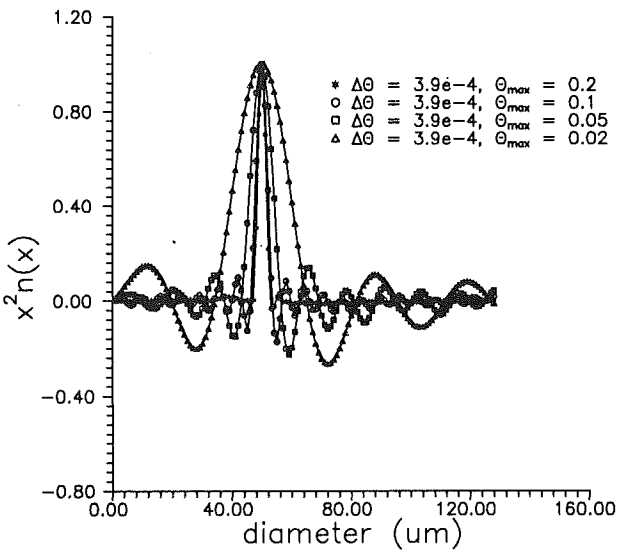

Fig. 4 Numerical data with rotation of θ_{max}, $\Delta\theta$ constant

in Fig. 2. This figure shows a slice through the cross section of the Airy pattern described in Eq. (2). The numerical intensity pattern has been truncated in the figure to expand the intensity scale at the lower intensity values, but the complete intensity profile is used in the inversion calculations. Using the Shifrin inversion, the area weighted number distribution, $x^2n(x)$, calculated using the Shifrin inversion is shown in Fig. 3. A 50 μm aperture intensity profile was measured experimentally, and the area weighted size distribution was calculated. These profiles are also shown in Fig. 2 and Fig. 3. Note that the experimental intensity profile in Fig. 2 has saturated the detector (TV camera) for the first two peaks. As indicated in Fig. 3, the actual aperture diameter was slightly larger than 50 μm. It was measured to be about 53 μm.

In comparison to the numerical intensity distribution in Figs. 2 and 3, the experimental distribution shows greater noise and a limited range of θ over which the intensity signal is above the noise floor. As a result, the integration in the Shifrin inversion is carried out over a smaller range of significant θ values, and the resulting distribution in Fig. 3 shows broader peaks and some "ringing" near the 50 μm peak. For this particular experiment, the noise in the intensity profile is primarily background optical noise (e.g., laser speckle) so camera and digitizer noise are not the major contributors. If the ripple in the distribution in Fig. 3 is considered to be random noise, an rms noise value can be calculated for each of the profiles in Fig. 3. The numerical profile has an rms noise figure of 0.761 percent of the peak signal, while the experimental profile has an rms noise figure of 3.465 percent of the peak signal. Clearly the noise in these distributions is not random, and the rms noise does not accurately characterize the ability to identify distribution peaks, but this type of calculation gives a numerical comparison of the ripple of the distribution function.

Reducing the range of θ over which the numerical intensity profile is sampled or has significant content produces characteristics similar to the experimental aperture results, indicating that the limitation to relatively small θ values has a significant impact on the calculated size distribution and the distribution pattern. The effect of reduced total angle over which data can be collected is shown in Fig. 4. In this figure, inversions were generated from numerically generated intensity profiles for a 50 μm particle have been truncated to smaller total sampling angles. In Fig. 4, the number of sample values in the intensity profile was changed while the $\Delta\theta$ was held constant. In a second numerical experiment, not shown, the number of sample values was held constant and $\Delta\theta$ was allowed

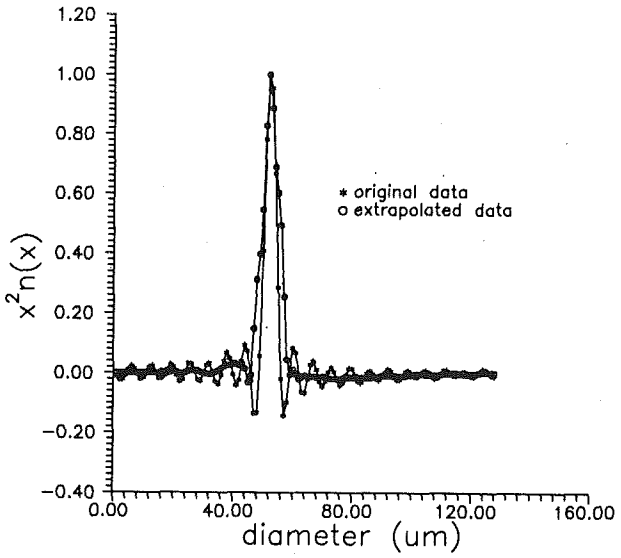

Fig. 5 Comparison of original experimental data with extrapolated data for 50 μm aperture

to vary, giving results similar to those shown in Fig. 4. In this figure, $\Delta\theta$ is the angular distance between adjacent sampled points in the data set. In either case, the overall angle for sampling, θ_{max}, has a significant effect on the size distribution pattern. The rms noise in the size distribution, calculated as for Fig. 3, ranges from .76 percent to 11.44 percent in Fig. 4. The results shown in Fig. 4 illustrate the fact that for low oscillation inversions with narrow peaks, the total collection angle, θ_{max} is more important than either the number of samples, N_θ , or the angular distance between samples, $\Delta\theta$.

When using intensity profiles for monodisperse distributions, the required range of θ is significantly larger than for the polydisperse case. This increase in required effective sampling angle for monodisperse distributions has been previously noted by Fymat and Mease (1978). In the current measurement method, a large portion of the particle image photograph lies in a region where a small number of particles will be sampled by the unexpanded laser beam at any one time. Thus, performance on monodisperse distributions or small numbers of particle sizes is important in the overall performance of the system.

Several approaches to "extrapolate" the measured data to larger θ values for monodisperse distributions have been tried, and one shows some promise. Theoretical particle size distributions produce intensity distributions which are essentially integrals of Bessel functions (Eq. (1)). A part of the kernel of the integral used in the Shifrin inversion is the term

$$\frac{d(\theta^3 I_\theta)}{d\theta} \tag{4}$$

which for numerically generated monodisperse size distributions is essentially a cosine wave. In order to extrapolate the range of θ over which this term is available (non-zero and not dominated by noise), the existing portion of the kernel is treated in a manner similar to those used for calculations of superresolution in optics (c.f. Harris, 1964). The kernel cited in Eq. (4), as a function of θ, is Fourier transformed using an FFT routine. In the Fourier plane, the available frequency values may be used to generate more values by interpolating between calculated frequency values. In our implementation, using a trapezoidal rule, this technique effectively doubles the number of frequency samples. Upon inverse Fourier transformation, the reduction of Δf by a a factor of 2 leads to an increase in the total θ range of the function by a factor of 2. This method assumes that all significant frequency content of the kernel is already present in the original data. The result represents extrapolated data which is consistent with the original values in terms of frequency content. In an effort to filter the high frequency noise typically present on experimental signals, we also window the frequency spectrum before inverse transformation using a Blackman-Harris type window. After this extrapolation procedure, the newly lengthened kernel is used in the Shifrin inversion to determine the particle size distribution.

This technique has almost no effect on numerically derived intensity distributions, since typically any range of θ values may be selected when the intensity distribution is generated. For monodisperse experimental data, the extrapolation of the data has a small effect, giving somewhat larger peak values for the area weighted size distribution, and less ripple in the size distribution. An example of the results of this type of data extrapolation is shown in Fig. 5. This figure shows the results of two inversions from an experimentally derived intensity distribution for a nominally 50 μm aperture. One of the inversions, labeled with the stars, is the inversion from the original data set, without extrapolation or filtering. The second profile, labeled with the circles, is from the transformed, interpolated, filtered, and inverse transformed data. The two profiles are clearly similar, but the extrapolated one exhibits a slightly wider profile at the 50 μm particle size, and significantly reduced ripple elsewhere. Using the rms noise as an estimate of the ripple in the size distribution, the "original data" in Fig. 5 has an rms noise of 3.46 percent and the "extrapolated data" has an rms noise of 1.82 percent.

Spray System

Experimental results from a water spray are shown to indicate how the method performs on an actual spray. With the system performance demonstrated in the previous sections of this paper, some confidence has been gained on the performance of the system. Since the size distribution in the regions interrogated by the laser is not known, only qualitative evaluations of the system performance is possible under these conditions. The measurement made with the current method differs significantly from the kind of measurement made with single point measurement devices, such as phase Doppler particle sizing. These single point devices measure a local spatial particle size for particles passing through a defined volume in the spray over time. The current method provides a particle size distribution over a spatial volume, typically larger than the PDPA volume for a specific time. Since the particle images are recorded on film for a relatively large field of view, there are a great number of such small volumes over which particle size distributions can be generated in a specific image. In general, direct comparison of single point multiple time with single time multi-point measurements are not appropriate.

A spray chamber was designed and built of acrylic with three windows to serve as entry and exit points for the laser sheet and as a window for photography. A Spraying Systems nozzle, which was an external mix, round spray, full cone atomizer (1/4J, 64SS air cap, 1650SS fluid cap, with No. 12810 liquid shut off needle) was used. The chamber allowed both horizontal and vertical nozzle translation relative to the laser sheet location. The air was supplied under pressure from the house supply directly to the nozzle and the liquid was siphon fed from a 500 ml beaker.

A doubled Nd:Yag laser supplied illumination of the spray by providing high intensity light in a pulse duration of about 6 ns operating at a wavelength of 532 nm. Two cylindrical lenses shaped the laser beam. The light was expanded by the first lens to a height of 40 mm at the test chamber. The second cylindrical lens decreased the 7 mm width of the beam to about 1 mm at the location of the spray. A sketch of the system is shown in Figs. 1(*b*) and 1(*c*).

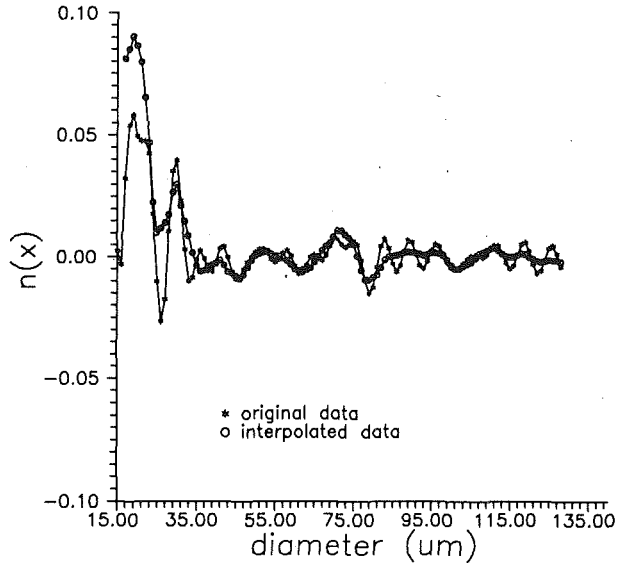

Fig. 6 Sample size distribution from spray

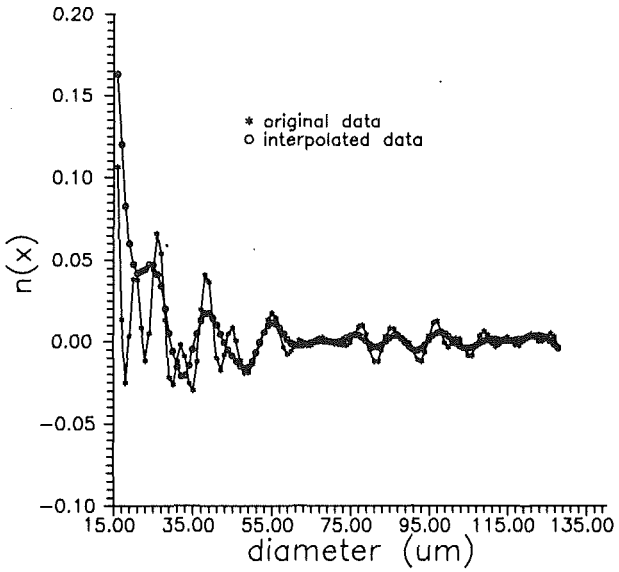

Fig. 7 Sample size distribution from spray

A 35 mm camera with a 105 mm focal length lens with a focusing tube was used to take the photographs of the spray. A magnification of 1:1 was chosen for simplicity. The imaged droplets at 90 deg scatter appeared as a front and a back arc, or in some cases as a disk. For the analysis scheme, filled-in images were needed. To solve this problem 2',7' Dichlorofluorescein was used to dope the water spray to provide fluorescence from the 532 nm source. The sprayed solution contained 1 g of the chemical for every 200 ml of water and the remaining solids were filtered with Whatman #1 filter paper. A hydrometer determined the specific gravity of the solution to be the same as that of water. The Dichlorofluorescein is listed as a low hazard material with usual industrial handling. A wet vacuum, equipped with a foam filter sleeve, was connected to the bottom of the spray chamber and the exhaust was vented directly into the outgoing building exhaust. Note that for other scattering angles and other droplet or particle materials, the fluorescent dopant may not be necessary. In fact, some previously taken backlit spatially filtered images for a monodisperse stream did not require any dopant (Farrell, 1991).

The parameters which could be varied during the experiment were the supply air pressure (which correspondingly altered the liquid flow rate) and the horizontal and vertical nozzle positions. For this paper, one setting of these values was used, since the emphasis was on the inversion scheme.

In the region of interrogation, the droplet images on the film typically range from 15 to 70 μm, and are relatively well dispersed. Extrapolated data results are plotted in Figs. 6 and 7 for samples taken at two different locations of the water spray from the air-assisted atomizer. These locations were chosen arbitrarily to indicate the general types of particle distributions available, and are not intended to comprehensively describe the spray itself. In each figure, a plot of the size distribution from unextrapolated data is shown in comparison with the distribution using extrapolated and filtered data. Note that for these figures the particle size distribution is plotted, not the area weighted distribution. The regions sampled have a few to several particles within the region, and the size distributions should reflect that kind of multi mode character. The extrapolated data appear to have somewhat reduced oscillation in the $n(x)$ profiles with respect to the unextrapolated versions. Each sampled region has only a few particles in it, so each peak in the size distribution may be interpreted as one or more particles at that size. Non-spherical particles within a sample area of the image will produce an ensemble diffraction signal corresponding to their shapes. Ellipsoidal particles which were oriented with major axis parallel to one another were evaluated producing major and minor axis dimensions (Farrell, 1991). For randomly oriented particle images within the 700 μm interrogation beam, the resulting size distribution will represent an average horizontal and vertical dimension of the particles resulting from the summation of their diffraction patterns.

The size distributions shown in Figs. 6 and 7 are not as well defined as those for the single apertures, in Fig. 4 for example. Figure 6 shows a large peak at about 20 μm and smaller peaks at about 30 μm and 70 μm, all of which are likely to represent single particles of these respective sizes. The remainder of the distribution in Fig. 6 shows remnants of the ripple seen on other examples, but looking at the "interpolated" results, the remaining peaks do not appear to rise above the background ripple. Using the rms noise calculation used in Fig. 4 comparisons, the extrapolated size distribution for Fig. 6 exhibits an rms noise value of 3.95 percent of the peak value, while the original data has an rms noise figure of 5.66 percent of the peak value. In Fig. 7, large values of the distribution function are evident at about 15 μm and again at about 25 μm, 39 μm, and 55 μm. Each of these peaks likely represents a single droplet of that size. The remainder of the distribution, at larger droplet sizes, appears to be primarily background ripple. The rms noise figure of 16.5 percent of the peak value. In both of these cases, the use of the extrapolation scheme appears to reduce the magnitude of the background ripple due to limited angular data range, making the distribution peaks more readily identifiable.

The inversions shown in Figs. 6 and 7 take about 2 s per location in the field of view, for a location about 0.7 mm in diameter. The total time to interrogate an entire image depends on the image size and density with which sampling is desired. Note that the images themselves were recorded in a single pulse of the laser, in about 6 ns.

Conclusions

This paper discusses a technique for droplet sizing in a polydisperse atomizer spray. The major focus of the paper is to indicate how the current inversion scheme's level of performance is affected by limited data collection range caused by experimental noise. A method is proposed for extrapolation of the data to larger sampling angles through interpolation in the frequency domain. Some examples of the performance of the system are presented for single apertures and for portions

of a spray. On single aperture data, the "noise" in the size distribution interpreted as random rms noise, decreases by a factor of almost 2, compared to a similar "noise" measurement on unextrapolated data. On experimental data from a water spray, size distributions are qualitatively improved and size peaks made more identifiable. The reduction in noise, using the calculated rms noise as a figure of merit, is smaller for the spray data than for the apertures, with typical reductions of about 1/3.

Acknowledgments

This work was supported in part by a grant from the national Science Foundation CTS-9106568, and by the designation of the Engine Research Center as a DOD Center of Excellence for Propulsion.

References

Adrian, R. J., 1991, "Particle Imaging Techniques for Experimental Fluid Mechanics," *Annual Review of Fluid Mechanics*, 1991, p. 261.

Bachalo, W. D., 1980, "Method for Measuring the Size and Velocity of Spheres by Dual-Beam Light-Scatter Interferometry," *Applied Optics*, Vol. 19, p. 363.

Bachalo, W. D., and Houser, M. J., 1984, "Phase/Doppler Spray Analyzer for Simultaneous Measurements of Drop Size and Velocity," *Optical Engineering*, Vol. 23, p. 583.

Coston, S. D., and George, N., 1991, "Particle Sizing by Inversion of the Optical Transform Pattern," *Applied Optics*, Vol. 30, p. 4785.

Dodge, L. G., Rhodes, D. J., and Reitz, R. D., 1987, "Drop-Size Measurements Techniques for Sprays: Comparison of Melvern Laser-Diffraction and Aerometrics Phase/Doppler," *Applied Optics*, Vol. 26, p. 2144.

Farmer, W. M., 1972, "Measurement of Particle Size, Number Density, and Velocity Using a Laser Interferometer," *Applied Optics*, Vol. 11, p. 2603.

Farrell, P. V., 1991, "Particle Sizing Using a Two-Dimensional Image," SAE Paper 910725.

Fymat, A. L., and Mease, K. D., 1978, "Reconstructing the Size Distribution of Spherical Particles from Angular Forward Scattering Data," *Remote Sensing of the Atmosphere, Inversion Methods and Applications*, A. L. Fymat and V. E. Zueu, eds., Elsevier.

Harris, J. L., 1964, "Diffraction and Resolving Power," *Journal of Optical Society of America*, Vol. 54, p. 931.

Hirleman, E. D., 1991, "General Solution to the Inverse Near-Forward Scattering Particle-Sizing Problem in Multiple-Scattering Environments," *Applied Optics*, Vol. 30, p. 4832.

Hirleman, E. D., Bachelo, W. D., and Felton, P. G., 1990, *Liquid Particle Size Measurement Techniques: 2nd Volume*, ASTM STP 1083.

Jackson, T. A., and Samuelson, G. S., 1987, "Droplet Sizing Interferometry; A Comparison of the Visibility and Phase/Doppler Techniques," *Applied Optics*, Vol. 26, p. 2137.

Kouzelis, D., Candel, S. M., Esposito, E., and Zikikout, S., 1988, "Particle Sizing by Laser Light Diffraction: Improvements in Optics and Algorithms," *Optical Particle Sizing*, G. Gousbet and G. Grehan, eds., Plenum.

Swithenbank, J., Beer, J. M., Taylor, D. S., Abbot, D., and McCreath, G. C., 1976, "A Laser Diagnostic Technique for the Measurement of Droplet and Particle Size Distribution," *Experimental Diagnostics in Gas Phase Combustion*, AIAA Vol. 53, *Progress in Astronautics and Aeronautics*, B. T. Zin, ed..

Yule, A. J., Seng, C., Felton, P. G., Ungut, A., and Chigier, N. A., 1982, "A Study of Vaporizing Fuel Sprays by Laser Techniques," *Combustion and Flame*, Vol. 44, p. 71.

Simulation of the Turbulent Flow Inside the Combustion Chamber of a Reciprocating Engine With a Finite Element Method

Y. Mao

M. Buffat

D. Jeandel

Laboratoire de Mécanique des Fluides
et Acoustique,
ECL, UCB, CNRS URA263, BP 163, 69131
Ecully Cedex, France

This paper presents numerical simulations of turbulent flows during the intake and the compression strokes of a model engine. The Favre average Navier-Stokes equations are solved with a k-ϵ turbulence model. The numerical procedure uses a time dependent semi-implicit scheme and a finite element method with a moving mesh (Buffat, 1991, Mao, 1990). Results of 2-D axisymmetrical calculations with and without inlet swirl are presented and compared to experimental data (Lance et al., 1991). The influence of different turbulence models and the numerical precision of the simulations are also discussed.

1 Introduction

The flows inside the cylinder of an internal combustion engine is nonstationary, compressible, and turbulent. The behavior of such flow is one of the most important features controlling the combustion processes and thus the performance of the engine. Therefore in design of modern engines, the prediction of the in-cylinder flow is gaining attention. During the last decade several multidimensional numerical codes have been developed (Amsden, 1973; Gosman, 1977). These investigations have given some important information on the in-cylinder flow structure during the intake and the compression stokes, with or without inlet swirl. These computer programs are generally based on finite difference or finite volume methods, and a k-ϵ two equations model is used in the calculations for modeling the turbulence.

In-cylinder flow motions are strongly dependent on the geometries of the chamber and inlet system. The shapes of the chamber and the structure of the inlet system are usually complicated, furthermore the movements of the piston and the valves impose additional difficulties on the calculations. Therefore the numerical simulations, based on finite difference or finite volume methods, usually did not include an inlet system and valves in their calculating domains because of the use of structured meshes. Consequently, certain hypothesis or experimental data must be used in the entrance of the cylinder as inlet boundary conditions. These made possible the calculations of in-cylinder flows, but the results are not completely independent of the experimental measurements.

In the present work, a finite element method with an unstructured mesh is used. This method is well adapted to Computational Fluid Dynamics (CFD) simulations in complex domains, and thus boundary conditions are easy to apply. The computational domain includes a main chamber, a piston with a bowl, a central valve and an inlet system. As far as we know, this is one of the first applications of the finite element method for the simulation of in-cylinder turbulent flows.

Two extensions of the k-ϵ model for compressible flows have been used: Watkins' model (Gosman, 1984) and Morel's model (Morel, 1992). We have compared their behavior during the compression stroke, and similar predictions have been obtained with both models. This is in agreement with the results reported by B. A. Befrui and A. D. Gosman (Ahmadi-Befrui, 1989) using three different versions of the k-ϵ model (Watkins, Morel, and El Tahry's models). At present, none of these models could be claimed as been superior. The only difference between them is the modification made in the production term of the ϵ transport equation in order to take into account of the effect of compression on turbulence. Although these models have given very different behaviors in special cases of compression and expansion of homogeneous turbulence, it appears that these modifications do not change the essential nature of the k-ϵ turbulence model in the general case.

2 Mathematical Formulations

The governing equations of the in-cylinder flow are the classical Navier-Stokes equations. A k-ϵ turbulence model is used to represent small scales of turbulence motions. Additional terms, due to the statistical average, are modeled using an eddy viscosity concept. We then have to solve density-weighted ensemble-averaged Navier-Stokes equations together with transport equations for the turbulence kinetic energy k and its dissipation rate ϵ.

The non-dimensional equations for the mean quantities are:

$$\frac{\partial \rho}{\partial t}+\frac{\partial \rho u_j}{\partial x_j}=0 \tag{1}$$

Contributed by the Fluids Engineering Division for publication in the JOURNAL OF FLUIDS ENGINEERING. Manuscript received by the Fluids Engineering Division April 15, 1991; revised manuscript received May 4, 1993. Associate Technical Editor: C. J. Freitas.

$$\frac{\partial \rho u_i}{\partial t}+\frac{\partial \rho u_i u_j}{\partial x_j}=-\frac{\partial \pi}{\partial x_i}+\frac{\partial}{\partial x_j}\left[2\left(\frac{1}{\mathrm{Re}}+\frac{1}{\mathrm{Re}_t}\right)S_{ij}\right] \quad (2)$$

$$\frac{\partial \rho T}{\partial t}+\frac{\partial \rho T u_j}{\partial x_j}=\frac{\partial}{\partial x_j}\left[\left(\frac{1}{\mathrm{Re\,Pr}}+\frac{1}{\mathrm{Re}_t\mathrm{Pr}_t}\right)\frac{\partial T}{\partial x_j}\right]+\frac{\gamma-1}{\gamma}\frac{dP}{dt} \quad (3)$$

where $\rho(\mathbf{x}, t)$ is the density, $P(t)$ is the mean thermodynamic pressure, $T(\mathbf{x}, t)$ is the temperature, $u_i(\mathbf{x}, t)$ and x_i are the i-direction velocity and coordinate, respectively. The non-dimensional variable π $(\mathbf{x}, t)$ is a normal stress divided by a reference kinetic energy. The total pressure $p(\mathbf{x}, t)$ is then given by:

$$p(\mathbf{x},t)=P(t)+\gamma Ma_0^2\left(\pi(\mathbf{x},t)-\frac{2}{3}\left[\left(\frac{1}{\mathrm{Re}}+\frac{1}{\mathrm{Re}_t}\right)\mathcal{D}+\rho k\right]\right) \quad (4)$$

where Ma_0 is a reference Mach number. Since the flow is subsonic ($Ma_0<1$), the contribution of the dynamic pressure π is neglected in the energy equation. $\mathcal{S}_{ij}$ and $\mathcal{D}$ are, respectively, the strain rate tensor and the mean velocity divergence, given by:

$$\mathcal{S}_{ij}=\frac{1}{2}\left(\frac{\partial u_i}{\partial x_j}+\frac{\partial u_j}{\partial x_i}\right) \text{ and } \mathcal{D}=\mathcal{S}_{kk}=\frac{\partial u_k}{\partial x_k}.$$

The turbulent Reynolds number Re_t is defined in term of two nondimensional scales of turbulence k and ϵ:

$$\frac{1}{\mathrm{Re}_t}=\mu_t=C_\mu\rho\frac{k^2}{\epsilon}$$

where μ_t is a nondimensional turbulent viscosity, and C_μ is an empirical constant ($C_\mu=0.09$).

Transport equations for the turbulent kinetic energy k and its dissipation rate ϵ are written as:

$$\frac{\partial \rho k}{\partial t}+\frac{\partial \rho k u_j}{\partial x_j}=\frac{\partial}{\partial x_j}\left(\frac{\mu_t}{\sigma_k}\frac{\partial k}{\partial x_j}\right)+2\mu_t\mathcal{S}_{ij}\mathcal{S}_{ij}-\frac{2}{3}(\mu_t\mathcal{D}+\rho k\mathcal{D})-\rho\epsilon \quad (5)$$

$$\frac{\partial \rho \epsilon}{\partial t}+\frac{\partial \rho \epsilon u_j}{\partial x_j}=\frac{\partial}{\partial x_j}\left(\frac{\mu_t}{\sigma_\epsilon}\frac{\partial \epsilon}{\partial x_j}\right)+2C_1\frac{\epsilon}{k}\mu_t\mathcal{S}_{ij}\mathcal{S}_{ij}-\frac{2}{3}C_1\frac{\epsilon}{k}(\mu_t\mathcal{D}^2+\rho k\mathcal{D})-C_2\rho\frac{\epsilon^2}{k} \quad (6)$$

This model was initially proposed by Launder and Spalding in 1974 (Lunder, 1972) for solving incompressible flows. σ_k and σ_ϵ are diffusion constants, with the following values:

$$\sigma_k=1 \text{ and } \sigma_\epsilon=1.3.$$

The molecular viscosity μ is a function of the mean temperature T, given by

$$\mu=\mu_0(1+T)^\alpha \text{ with } \alpha=0.8 \quad (7)$$

The values of the model constants are:

$$C_1=1.44,\ C_2=1.92,\ C_\mu=0.09.$$

3 Turbulence Models

In internal combustion (IC) engine research, the k-ϵ turbulence model is widely used, because of its simplicity and the generality of its governing equations (Jenning, 1988). Over the past ten years, several different versions of the k-ϵ model have been developed for compressible turbulent flows. For example, Gosman and Watkins (Gosman, 1984) have proposed the following modified ϵ equation:

$$\frac{\partial \rho \epsilon}{\partial t}+\frac{\partial \rho \epsilon u_j}{\partial x_j}=\frac{\partial}{\partial x_j}\left(\frac{\mu_t}{\sigma_\epsilon}\frac{\partial \epsilon}{\partial x_j}\right)+2C_1\frac{\epsilon}{k}\mu_t\mathcal{S}_{ij}\mathcal{S}_{ij}-\frac{2}{3}C_1\frac{\epsilon}{k}(\mu_t\mathcal{D}^2+\rho k\mathcal{D})-C_2\rho\frac{\epsilon^2}{k}+\rho\epsilon\mathcal{D} \quad (8)$$

The additional term $\rho\epsilon\mathcal{D}$ comes from the modeling of the production term in the ϵ transport equation for compressible flows. However Reynolds (Reynolds, 1980) has pointed out that, for a rapid spherical compression of a homogeneous turbulence, the predicted behavior of the length scale using the previous model is not plausible. Morel and Mansour (Morel, 1992) have proposed a modified version to account for the general case of compression, including the three basic compressions: axial, cylindrical radial, and spherical. They assumed that, during the compression or expansion strokes, the variation of the integral length scale L is directly related to the variation of the volume. In other words, the mass of an elementary turbulence volume remains constant, so that:

$$\rho L^n=\text{constant}, \quad (9)$$

where the exponent n is equal to 1, 2, and 3 for the three basic compressions respectively, and the turbulence integral length scale L is defined by:

$$L=\frac{k^{2/3}}{\epsilon} \quad (10)$$

The modified ϵ equation is:

$$\frac{\partial \rho \epsilon}{\partial t}+\frac{\partial \rho \epsilon u_j}{\partial x_j}=\frac{\partial}{\partial x_j}\left(\frac{\mu_t}{\sigma_\epsilon}\frac{\partial \epsilon}{\partial x_j}\right)+2C_1\frac{\epsilon}{k}\mu_t\mathcal{S}_{ij}\mathcal{S}_{ij}-\frac{2}{3}C_1'\frac{\epsilon}{k}\mu_t\mathcal{D}^2-\frac{2}{3}C_1''\rho\epsilon\mathcal{D}-C_2\rho\frac{\epsilon^2}{k}+\rho\epsilon\mathcal{D} \quad (11)$$

The new coefficients C_1' and C_1'' are given by:

$$C_1'=C_1+a^*(C_1+1.5),\ C_1''=3+\frac{3}{2n} \quad (12)$$

with

$$a^*=\frac{3(S_{11}^2+S_{22}^2+S_{33}^2}{(|S_{11}|+|S_{22}|+|S_{33}|)^2}-1 \text{ and } n=3-\sqrt{2a^*} \quad (13)$$

The coefficients C_1' and C_1'' vary over a moderate range ($C_1'=1.32\sim1.44$, $C_1''=3.5\sim4.5$) while in Watkins' model C_1 is equal to 1.44.

For the three basic compressions, with these coefficients, the exact expression of the product of the deformation tensor $\mathcal{S}_{ij}$. $\mathcal{S}_{ij}=1+a^*/3\ \mathcal{D}$ is obtained, and it insures that the term ρL^n is constant. For a general compression, this product is an interpolation between the three basic compressions.

As it has been expected, this model gives a decreasing turbulence length scale during the compression and an increasing turbulence length scale during the expansion for homogeneous turbulence.

4 Numerical Method

To integrate in time the system of partial differential Eqs. (1)-(3) and (5)-(6), we use a semi-implicit scheme (Buffat, 1991), which takes into account the deformation of the domain with a Lagrangian-Eulerian formulation and allows the linearization of the equations. Furthermore, the energy equation, the transport equation for k and ϵ, and the momentum equation can now be solved sequentially instead of simulataneously.

Let us define $\mathbf{W}=[u_1, u_2, u_3, T, k, \epsilon]$, the vector of state variables. Equations (1)-(3) and (5)-(6) can be expressed symbolically as:

$$\rho\frac{D\mathbf{W}}{Dt}=\mathrm{div}\,[\mathcal{K}(\nabla\mathbf{W})]+\mathcal{C}(\nabla\pi)+\mathcal{S}(\mathbf{W}) \quad (14)$$

$$\mathrm{div}\,\mathbf{u}=-\frac{1}{\rho}\frac{D\rho}{Dt} \quad (15)$$

where $\mathcal{K}(\nabla\mathbf{W})$ is the tensor of viscous fluxes, $\mathcal{C}(\nabla\pi)$ is the normal stress constraint in the momentum equation, and $\mathcal{S}(\mathbf{W})$ includes the remaining source terms.

The semi-implicit scheme then, is as follows:

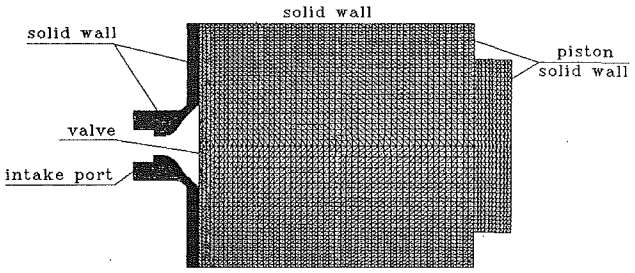

Fig. 1 Geometry of the axisymmetrical combustion chamber. Finite element mesh (2380 nodes).

$$\rho^{n+1}\left[\frac{\mathbf{W}^{n+51}-\mathbf{W}^{n}}{\Delta t}+(\mathbf{u}^{n}-\mathbf{s}).\Delta\mathbf{W}^{n+1}\right]=\operatorname{div}\left[\alpha_{w};\nabla \mathrm{cf3W}^{n+1}\right]$$
$$+\operatorname{div}\left[\tilde{\mathcal{K}}(\nabla\mathbf{W}^{n})\right]+\mathcal{JC}(\nabla\pi^{n+1})+\mathcal{S}(\mathbf{W}^{n},\mathbf{W}^{n+1}) \quad (16)$$

$$\operatorname{div}\mathbf{u}^{n+1}=-\frac{1}{\rho^{n+1}}\left[\frac{\rho^{n+1}-\rho^{n}}{\Delta t}+(\mathbf{u}^{n}-\mathbf{s})\nabla\rho^{n+1}\right] \quad (17)$$

where we have decomposed the viscous fluxes into a linear part $\alpha_W\nabla\mathbf{W}$ and a residue $\tilde{\mathcal{K}}(\nabla\mathbf{W})$. To improve the numerical stability of the scheme, some terms in $\mathcal{S}(\mathbf{W})$ are treated implicitly in the transport equations of k and ϵ (Mao, 1990). The velocity $\mathbf{s}$ corresponds to the deformation of each point in the moving domain. For the space discretization, we use a finite element method with a $P_1/\mathrm{iso}\,P_2$ element which gives a continuous and piecewise linear interpolation for the pressure π, associated with a continuous and piecewise linear interpolation for the velocity components u_i, the temperature T, k, and ϵ on a grid twice as fine as the pressure grid (each element is divided into four triangles). To take into account the deformation of the domain, the velocity $\mathbf{s}$ is imposed on each node of the grid.

A preconditioned Uzawa algorithm (Buffat, 1991) is used to decouple the velocity $\mathbf{u}$ and the pressure π. The resulting linear equations for the nodal values of the velocity components u_i, the temperature T, k, and ϵ are solved using a preconditioned conjugate gradient square (CGS) algorithm.

5 Calculating Conditions

The geometry of the axisymmetrical combustion chamber is drawn on Fig. 1. The calculating domain includes a main chamber, a piston with a bowl, a central valve and an intake system. The geometry and the boundary conditions correspond to the combustion chamber of a motored diesel engine installed in the laboratory, working at 250 rpm and having a compression ratio equal to 16. The finite element mesh has 2380 nodes and is refined near the valve.

5.1 Boundary Conditions. For all solid walls, classical "wall functions" are used to impose the values of the dependent variables in the near wall regions (Brun, 1988). To take into account the compression, a molecular viscosity which is a function of the temperature (7), is used in the expression of the wall laws. With a constant molecular viscosity, wrong boundary conditions values are predicted at the end of the compression stroke. At the entrance, the normal derivative of the axial and radial velocity is set to zero. Atmospheric pressure and ambient temperature are also imposed in the inlet section. The velocity fluctuation at the entrance is equal to 10 percent of the mean axial velocity u_1.

For calculations with an inlet swirl, the tangential velocity u_3 is imposed at the entrance as a function of the axial velocity u_1:

$$u_3 = 0.5 * u_1$$

With these boundary conditions and with the simulation of the movement of the valve, a hypothesis about the velocity profiles at the entrance of the chamber is not needed. The movement of the flow is entirely created by the moving piston and the valve.

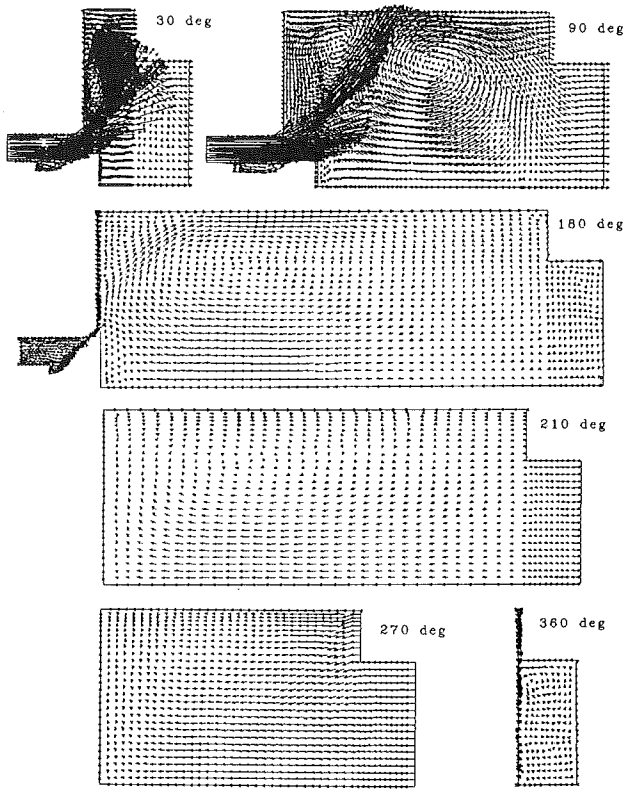

Fig. 2 Velocity vector fields without inlet swirl. Crank angles of 30, 90, 180, 210, 270, 360 deg from top to bottom.

5.2 Initial Conditions. Air in the chamber is initially at rest, pressure is equal to atmospheric pressure, and temperature is set to 293° K. The turbulence kinetic energy is equal to 1.1 percent of the kinetic energy of the mean piston speed V_p^2; that is to say, the fluctuating velocity is equal to 10 percent of the mean piston velocity. The length scale is estimated as 10 percent of the radius of the chamber. The initial dissipation rate ϵ is then determined by:

$$\epsilon = C_\mu^{3/4}\frac{k^{3/2}}{L}$$

By trying different initial values, we have found that the initial conditions have no major influence on the results.

6 Numerical Results

The calculation is performed with an engine speed of 250 rev/min. The numerical results are compared to experimental data measured in an identical combustion chamber of a motored engine installed in the laboratory (Lance et al., 1991). The measurements use a Laser Doppler Anemometry (Belmabrouk, 1991), to obtain the components of the mean and fluctuating velocity at different sections in the chamber.

6.1 Results Without Inlet Swirl. The velocity fields at different crank angles (CA) during the intake and the compression strokes are plotted on Fig. 2. During the intake stroke, a conical jet is formed and enters the chamber with a velocity which is about 10 times stronger than the velocity of the piston. The jet drives the air at rest in the chamber, and forms shear layers with very sharp gradients, which produce a high level of turbulent kinetic energy. As soon as the jet reaches the lateral wall of the cylinder, it splits into two parts: one moving

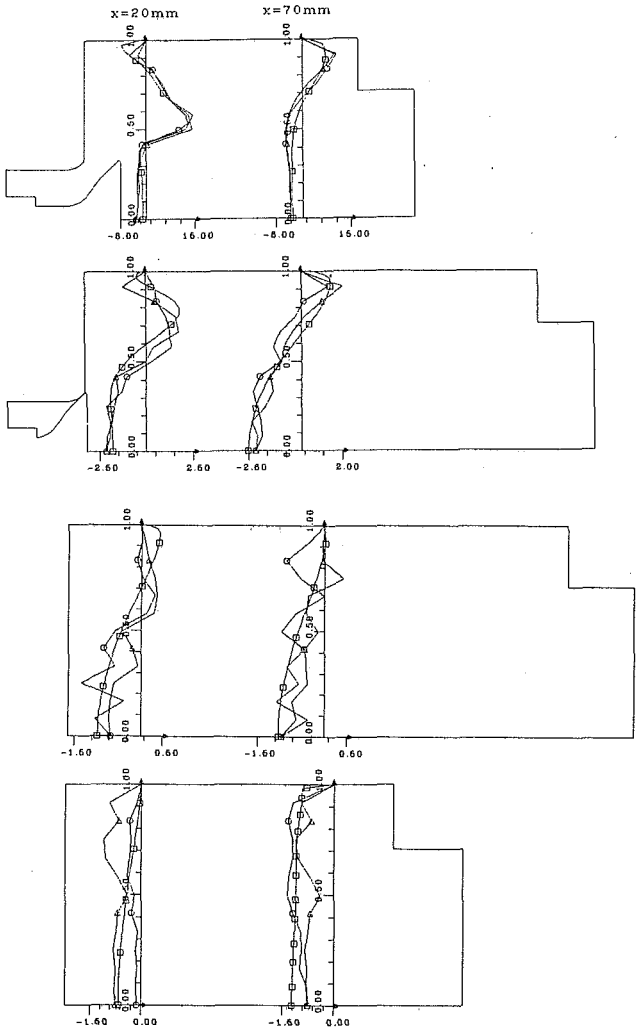

Fig. 3 Mean axial velocity profiles u_1 without inlet swirl. Sections $x = 20$ mm and 70 mm at crank angles of 90, 180, 210, 270 deg from top to bottom (⊖: predictions; ⊹, ⊖: experimental data (Lance et al., 1991)).

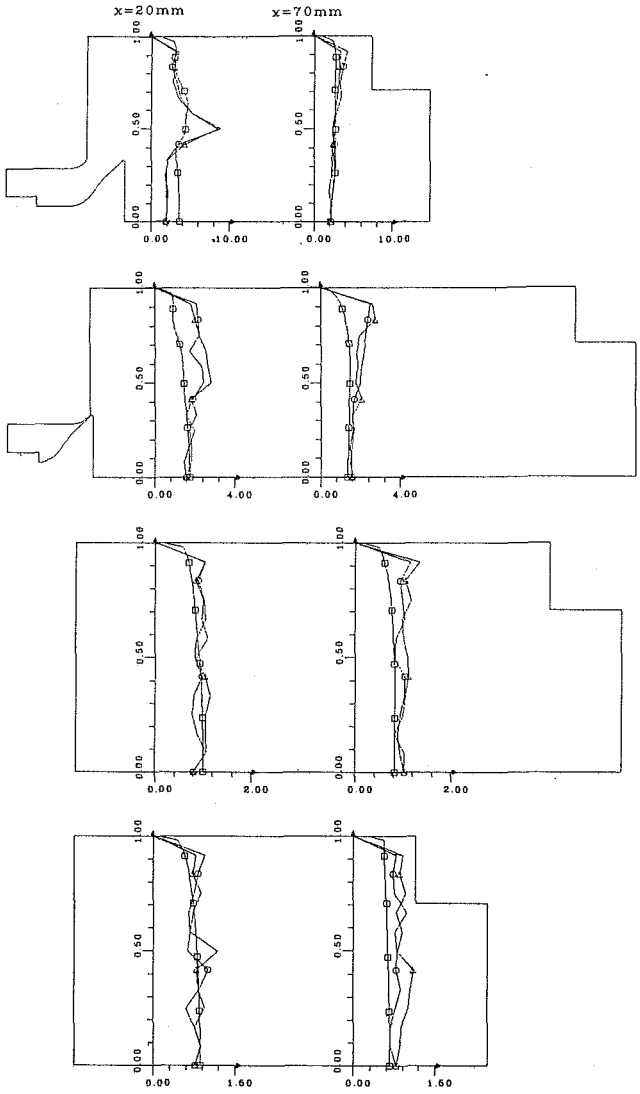

Fig. 4 Velocity fluctuation profiles u' without inlet swirl. Sections $x = 20$ mm and 70 mm at crank angles of 90, 180, 210, 270 deg from top to bottom (⊖: predictions ⊹, ⊖: experimental data (Lance et al., 1991)).

to the piston and another moving to the cylinder head. When the corner eddy takes all the space between the cylinder head and the lateral wall at about 60 deg CA, most of the inlet fluid moves in the direction of the piston and forms a large eddy in the chamber. These two eddies persist to the end of the intake stroke.

During the compression stroke (from 180 to 360 deg CA), the valve is closed. The eddies are dissipated by the effects of turbulence and compression. At about 270 deg, the eddies disappear entirely and the flow becomes almost one-dimensional, except in the near wall regions. At the end of the compression stroke, the "squish" phenomenon generates two eddies in the bowl of the piston, and increases the turbulence level in the bowl.

In Fig. 3, the profiles of the predicted mean axial velocity at different crank angles are compared to the experimental data measured in the sections $x = 20$ mm and $x = 70$ mm. The results of the calculation are in agreement with the measurements.

In Fig. 4, the predicted fluctuation u' is compared to the experiment in the same sections. The predicted RMS fluctuation is determined from the turbulence kinetic energy using an isotropic hypothesis:

$$u' = \sqrt{\frac{2}{3}k}$$

During the intake stroke, at the section $x = 20$ mm, the predicted profile does not present the peak in the shear layer region, and during the compression stroke, turbulence level is underestimated at section $x = 70$ mm, due to the turbulence modeling.

In conclusion, the numerical results compare well to the experimental data in a situation without swirl.

6.2 Influence of the Turbulence Models. Two turbulence models, the L.S.W model and the Morel's model, have been used during the compression stroke. The profiles of the mean axial velocity u_1 obtained with the two models are compared in Fig. 5. We did notice that the value of kinetic energy with the L.S.W model is a little stronger than that with the Morel's model, leading to a stronger eddy viscosity, and therefore a weaker mean velocity. However the gap between the two models is small (below 6 percent).

The predicted fluctuation u' using the two turbulence models are compared in Fig. 6. The results with the L.S.W model are a little stronger than those with the Morel's model and match better the experimental data, but the differences are also small.

Though these models have predicted very different behaviors in a homogeneous turbulence compression, they give almost the same results for the simulation of the compression stroke

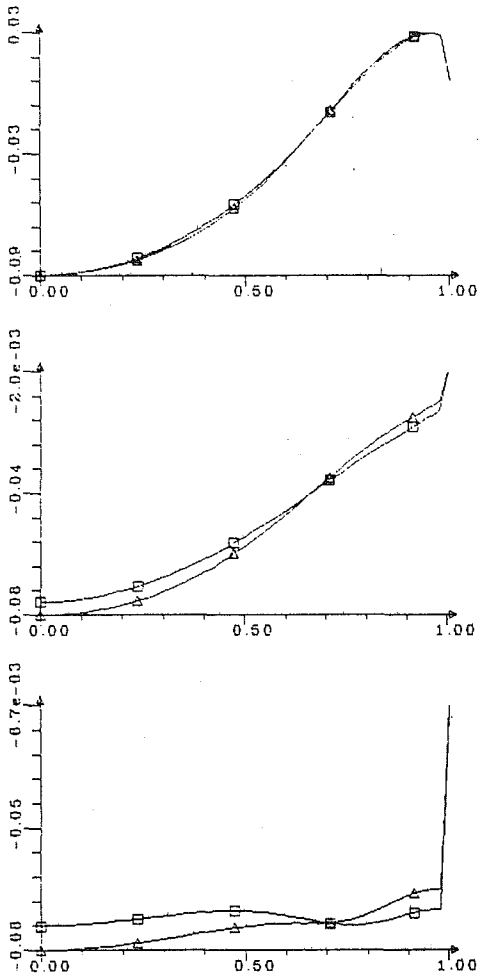

Fig. 5 Mean velocity u_1 with the two turbulence models during the compression stroke. Sections $x = 20$ mm and 70 mm at crank angles of 270 deg (top) and 360 deg (bottom) (⊖: Morel's model; -+-: Watkins' model; -⊕-: experimental data (Lance et al., 1991)).

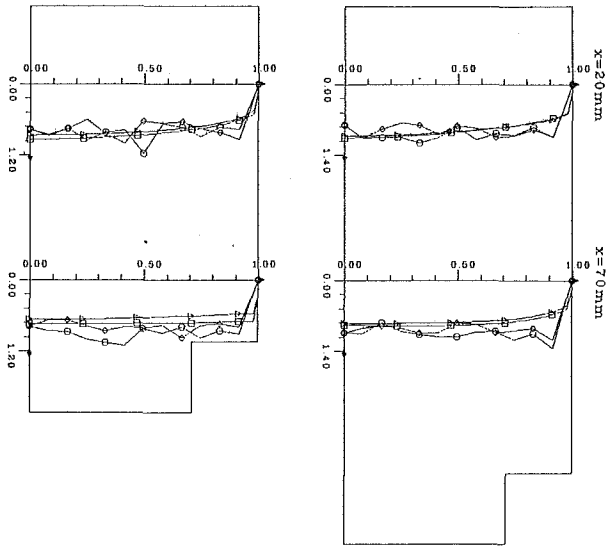

Fig. 6 Velocity fluctuation u' with the two turbulence models during the compression. Sections $x = 20$ mm and 70 mm at crank angles of 270 and 360 deg (⊖: Morel's model; -+-: Watkins' model; -⊕-: experimental data (Lance et al., 1991)).

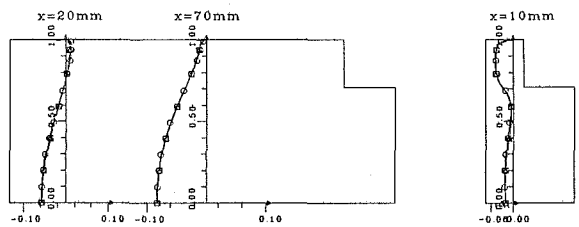

Fig. 7 Mean axial velocity u_1 during the compression with different meshes. Sections $x = 20$ mm and 70 mm at crank angles of 270 and 360 deg (⊖: coarse mesh and time step Δt; -+-: coarse mesh and time step $\Delta t/2$; -⊕-: refined mesh and time step Δt).

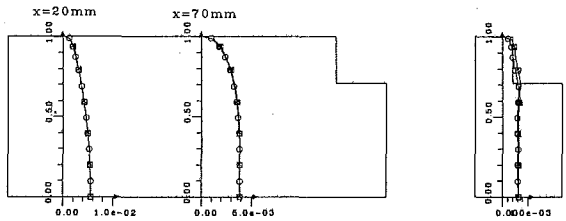

Fig. 8 Turbulent kinetic energy k during the compression with different meshes. Sections $x = 20$ mm and 70 mm at crank angles of 270 and 360 deg (⊖: coarse mesh and time step Δt; -+-: coarse mesh and time step $\Delta t/2$; -⊕-: refined mesh and time step Δt).

in a combustion chamber. In other words, the modifications made in the production term of the ϵ equation do not change the essential behavior of the k-ϵ model for flow with shear movements or in the presence of solid walls. Actually, the modifications appear only in the diagonal terms of the production. When shear movements are present, the non-diagonal terms are non negligible and could even become dominant, therefore the two models give almost the same results. It is therefore difficult to make a clear choice between these two models, and obviously more experimental data are needed to validate the turbulence model, especially near and at the end of the compression. For the following simulations, we have used the Morel's turbulence model.

6.3 Numerical Precision. To check the numerical precision, three simulations of a compression stroke have been compared: one with the original mesh and a time step Δt, one with a refined mesh and the same time step Δt, and one with the original mesh and a smaller time step $\Delta t/2$. The refined mesh is obtained by dividing each triangle of the original mesh into four.

As indicated by the profiles of the mean axial velocity u_1, plotted in Fig. 7, the differences between these three calculations are negligible. The profiles of the turbulence kinetic energy k are shown in Fig. 8, and the gaps between the three curves are also very small.

The numerical error in these simulations of a compression stroke is almost imperceptible, and therefore the differences between these calculations and the experimental results can be attributed mainly to the turbulence models used.

6.4 Results With an Inlet Swirl. A tangential velocity is now imposed at the entrance of the chamber with a ratio 0.5 to the axial velocity. The velocity fields at different crank angles during intake and compression strokes are plotted in Fig. 9. We can see a similar evolution of the flow structures as in the case without swirl. At the end of the intake stroke, the structure of the flow is characterized by a large eddy generated by the interaction of the inlet jet and the cylinder walls, and a small eddy in the corner between the wall and the cylinder head, as in the case without swirl (see Fig. 7 at the 180 deg CA).

Figure 10 shows a comparison of predicted mean axial velocity profiles with experimental data at different crank angles in sections $x = 20$ mm and $x = 70$ mm. During the intake stroke, the numerical results compare well with experimental data. During the compression stroke, at 240° CA, the experimental

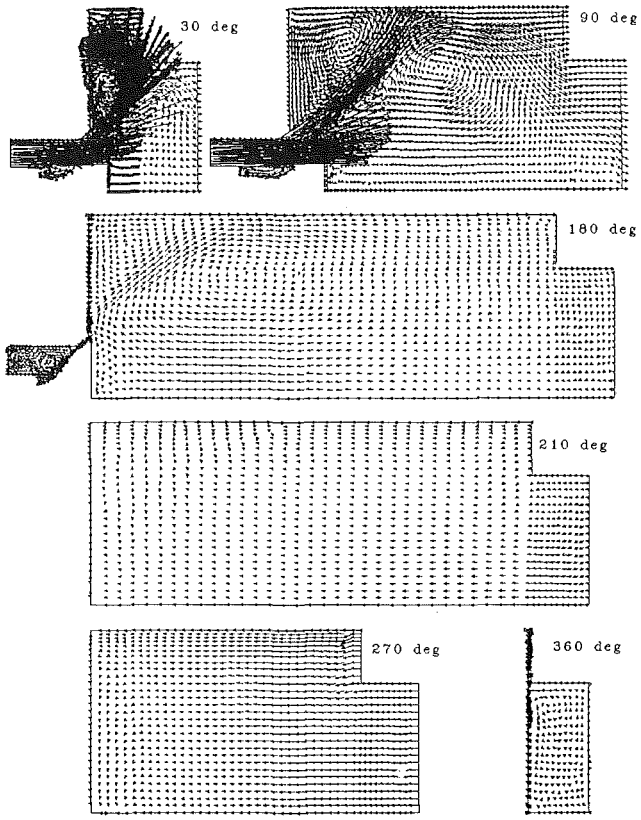

Fig. 9 Velocity vector fields with inlet swirl ($S = 0.5$). Crank angles of 30, 90, 180, 210, 270, 360 deg.

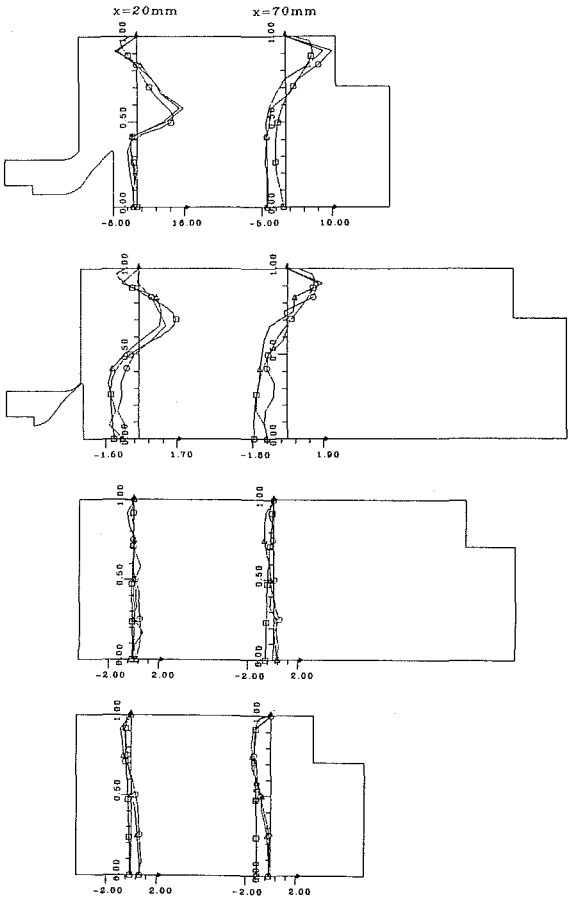

Fig. 10 Mean axial velocity profiles μ_1 with inlet swirl ($S = 0.5$). Sections $x = 20$ mm and 70 mm at crank angles of 90, 180, 210, 270 deg (⊟: predictions; ⊹, ⊖: experimental data (Lance et al., 1991)).

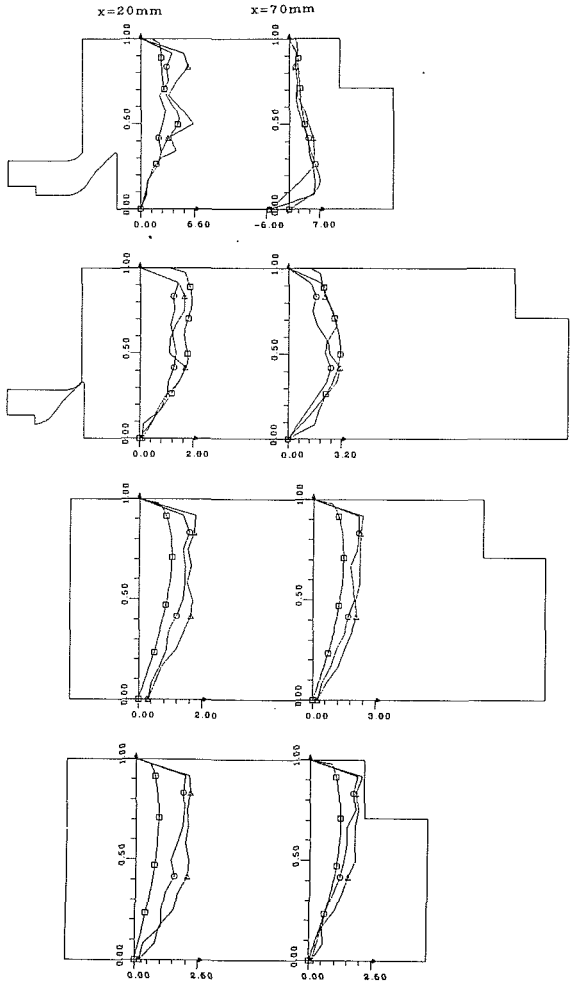

Fig. 11 Mean tangential velocity profiles u_3 with inlet swirl ($S = 0.5$). Sections $x = 20$ mm and 70 mm at crank angles of 90, 180, 210, 270 deg (⊟: predictions; ⊹, ⊖: experimental data (Lance et al., 1991)).

data show a positive axial velocity near the axis, suggesting an eddy rotating in the opposite direction of the large eddy at the end of the intake stroke. In the calculation however, we did not observe this eddy at 240 deg CA, but only a smaller one at 270 and 300 deg CA. Near TDC, all these eddies disappear, and the flow structure is dominated by the squish phenomenon.

Figure 11 shows the predicted mean swirl velocity and the experimental data at different crank angles. During the intake stroke the calculations approximate the experimental results, but during the compression stroke, the predicted velocity decreases more rapidly than in the experiment. These discrepancies may be attributable to the use of an isotropic turbulent viscosity.

Figure 12 shows the predicted fluctuating velocity u' with experimental results. Our predictions are supported by the experiments.

In the last figure (Fig. 13), the contour lines of the turbulent kinetic energy are drawn at different crank angles, showing the evolution of the turbulent kinetic energy with time. We can see that the maximums of turbulent kinetic energy are in the borders of the inlet jet where large shear stresses occur, namely near the walls of the valve and near the impinging point of the jet and cylinder wall.

7 Conclusion

A numerical code based on a finite element method with a Lagrangian-Eulerian formulation is used to simulate the turbulent flow inside a combustion chamber of a diesel engine.

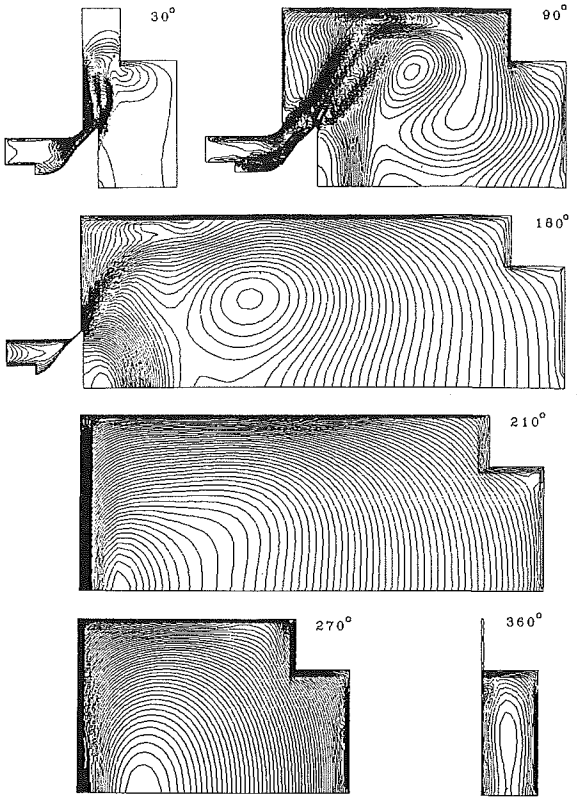

Fig. 12 Velocity fluctuation profiles u' with inlet swirl ($S = 0.5$). Sections $x = 20$ mm and 70 mm at crank angles of 90, 180, 210, 270 deg (⊕: predictions; ⊸, ⊸: experimental data (Lance et al., 1991)).

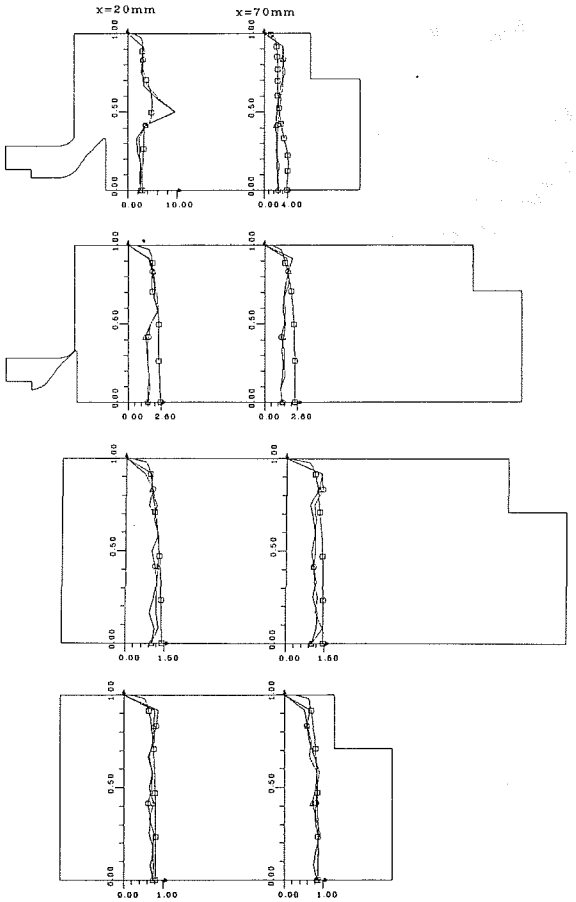

Fig. 13 Contour lines of the turbulent kinetic energy k with inlet swirl ($S = 0.5$). Crank angles of 30, 90, 180, 210, 270, 360 deg.

The predictions of the mean quantities by the numerical code are in agreement with the experimental measurements with the exception of the mean tangential velocity, which is underpredicted during the compression stroke. The turbulent quantities are also well predicted except some peaks in the profiles of the u' at section $x = 20$ mm.

Therefore the presented numerical method can now be used as a tool to study the internal aerodynamics inside the combustion chamber. Meanwhile, some improvements of the turbulence models are necessary in order to obtain a better predictions of the turbulent quantities, particularly the turbulent kinetic energy, which is under-predicted by the turbulence models during the compression stroke.

References

Ahmadi-Befrui, B., and Gosman, A. D., 1989, "Assessment of Variants of the k-ϵ Turbulence Model for Engine Flow Applications," *International Journal for Numerical Methods in Fluids*, Vol. 9, pp. 1073–1086.

Amsden, A. A., and Hirt, C. W., 1973, "YAQUI: An Arbitrary Lagrangian Eulerian Computer Program for Fluid Flows at All Speeds," *Los Alamos Scientific Laboratory Report*, LA-5100.

Belmabrouk, H., Lance, M., Grosjean, N., and Michard, M., 1991, "Turbulence Length Scale Measurements by Two Points Laser Doppler Anemometry in a Steady Flow," *International Congress and Exposition*, Detroit, MI, SAE paper 710474.

Brun, G., 1988, "Développement et Application d'une Méthode d'Élément finis Pour le Calcul des Écoulements Turbulents Fortement Chauffés," *Thèse de Doctorat*, Ecole Centrale de Lyon.

Buffat, M., 1991, "Simulation of Two and Three Dimensional Internal Subsonic Flows Using a Finite Element Method," *International Journal for Numerical Methods in Fluids*, Vol. 12, pp. 683–704.

Jennings, M. J., and Morel, T., 1988, "Observations on the Application of the k-ϵ Model to Internal Combustion Engine Flows," *Combustion Science*, Vol. 58, pp. 177–193.

Gosman, A. D., Khalil, E. E., and Whitelaw, J. H., 1977, "The Calculation of Two Dimensional Turbulent Recirculating Flows," *Proceedings of a Symposium on Turbulent Shear Flows*, Pennsylvania State University, Apr.

Gosman, A. D., Tsui, Y. Y., and Watkins, A. P., 1984, "Calculations of Three Dimensional Air Motion in Model Engine," SAE paper 840229.

Lance, M., Belmabrouk, H., Gervais, Y., Grosjean, N., and Michard, M., 1991, "Aérodynamique Interne d'un Moteur Axisymétrique Entraine," *La Combustion dans les Moteurs d'Automobiles GSM*, Edition Technips.

Launder, B. E., and Spalding, D. B., 1972, *Mathematical Models of Turbulence*, Academic Press.

Mao, Y., 1990, "Simulation Numérique par Éléments Finis de l'aérodynamique Interne des Chambres de Combustion des Moteurs á Piston," *Thèse de Doctorat*, Ecole Centrale de Lyon.

Morel, T., and Mansour, N., 1982, "Modeling of Turbulence in Internal Combustion Engine," SAE paper 820040.

Reynolds, W. C., 1980, "Modeling of Fluid Motions in Engine. An Introduction Overview," *Combustion Modeling in Reciprocating Engine*, Plenum Press.

Journal of Fluids Engineering

Technical Briefs

Characteristics of Swirling Flow in a Circular Pipe

Hui Li[1] and Yuji Tomita[1]

This paper examines experimentally the decay of swirl, the average dynamic, static and total pressures and the wall pressure in a pipeline 13 m in length and with an inside diameter of 80 mm for two Reynolds numbers and five different inlet swirls. The empirical correlations for the above quantities are derived, and by using these empirical correlations, the decay process and pressure distributions along the pipe for the swirling flow can be successfully computed by giving discharge velocity and a wall static pressure at any axial position.

1 Introduction

Swirling flow through a pipe is one of well-recognized techniques to organize and intensify certain working processes in industries such as enhancement of heat and mass transfer, and is particularly applied in aviation and rocket technology. Recently, swirling flow has been applied in pneumatic conveying technology to reduce pressure drop and power requirement, or to prevent particle deposition and blockage of pipeline (Li et al., 1992). Since the swirling flow dominates the performance of these technology, it becomes an important matter how to predict the characteristics of swirling flow. In particular, pressure distribution gives important information about the decay and energy loss of swirling flow. Until now, there are a few experimental and theoretical investigations reported in literature about the swirling flow in through pipes, and no clear generalized methods to compute the decay of swirl and the pressure distributions along the pipe.

Kreith and Sonju (1965) obtained a solution for the equation to predict the decay of swirl through pipe. Ito et al. (1980) analyzed the decay process of swirling flow and proposed a method to estimate the tangential velocity distribution. Kuroda et al. (1981) obtained an approximate equation of axial velocity distribution based on experimental results. Algifri et al. (1987) proposed a procedure to compute the swirl intensity, the tangential, and axial velocity distributions for given inlet flow conditions. Senoo et al. (1972) studied experimentally the swirling flow through pipes with different wall roughness and proposed a procedure to compute local wall pressure and average static pressure. Murakami et al. (1975) proposed a local relationship between average total pressure and wall pressure. However, these procedures are rather complicated and have limitations.

The present work includes development of more generalized correlations for the decay of swirl, the average dynamic, static and total pressures, and the wall pressure based on the measurements, and a proposition of the computation procedure of decay process and pressure distributions along the pipe for the swirling flow. To test the validity and extent of present approach, our measurements and correlations are compared with the available experimental data.

2 Experimental Apparatus and Procedure

The experimental apparatus consisted of a horizontal smooth acrylic tube of $D = 80 \pm 0.35$ mm inside diameter and about $L = 13$ m length, $L^* = L/D$ being 162.5. It was confirmed that the pipe is hydraulically smooth. Air from a blower was used as the working fluid. Swirling flows were generated at the pipe inlet by vaned swirlers of five different vane angles. The airflow rate was measured by a calibrated nozzle (Uncertainty in ± 0.44 percent). A three-holed spherical-head probe of 2 ± 0.05 mm diameter was used to measure the radial velocity and pressure profiles at fifteen different pipe sections. At each section, measurements were carried out at 20 radial locations with the resolution of ± 0.05 mm when the Reynolds number defined as $R_e = u_m D/\nu$ (u_m is discharge velocity) was 60,000 and 125,000 for five different intensities of inlet swirl. To check the accuracy of the velocity and pressure measurements, the flow rate determined by numerical integration of the axial velocity profile was compared with the flow rate measured by the nozzle meter in each measurement. The difference between these two measurements was within 5 percent referred to the flow rate.

3 Swirl Number and Velocity Profiles

Swirl number S has been successfully used to express the swirl intensity and used as an important similarity parameter of swirling pipe flow by several investigators (Senoo et al., 1975 and Algiferi et al., 1987). It is defined by

$$S = \int_0^R uwr^2 dr / R \int_0^R u^2 r dr \tag{1}$$

where u and w are axial and tangential velocity, respectively, R is pipe radius. Swirl number S is the ratio of the angular momentum flux to the product of the pipe radius and the axial momentum flux. We also use S to express the swirl intensity. In the following, the results are shown when S at x_1 section ranged from 0.58 to 1.12.

Figure 1 shows the result of dimensionless axial and tangential velocity profiles, which are referred to the average discharge velocity and pipe radius, for different axial locations

[1]PhD and Professor, respectively, Department of Mechanical Engineering, Kyushu Institute of Technology, Tobata, Kitakyushu 804, Japan.

Contributed by the Fluids Engineering Division of THE AMERICAN SOCIETY OF MECHANICAL ENGINEERS. Manuscript received by the Fluids Engineering Division March 19, 1992; revised manuscript received October 6, 1993. Associate Technical Editor: E. E. Michaelides.

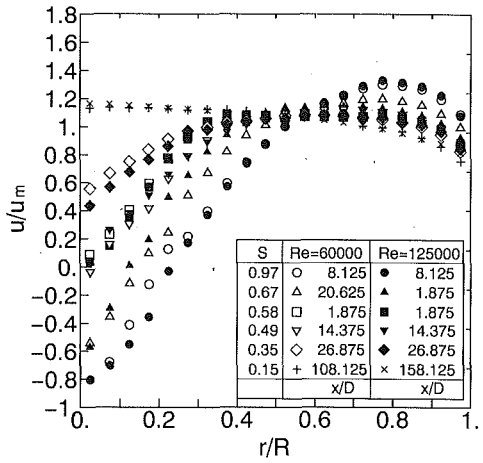

Fig. 1(*a*) Dimensionless axial velocity profiles (Uncertainty in $u = \pm 1.7$ percent in average)

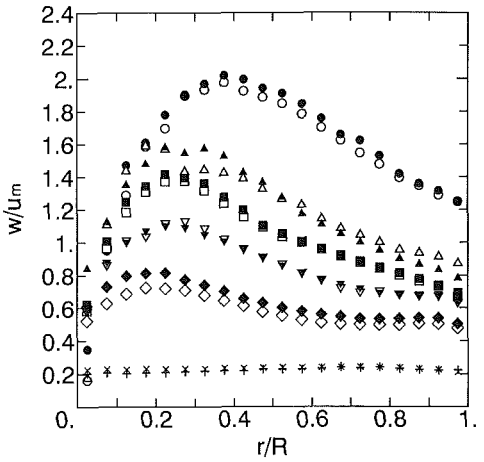

Fig. 1(*b*) Dimensionless tangential velocity profiles (Uncertainty in $w = \pm 2.2$ percent in average)

with S as a parameter for different Reynolds numbers. It is clear that the dimensionless velocity profiles are almost independent of Reynolds number, but also independent of the measurement location (e.g., for $S = 0.67$ in Fig. 1), and then the profiles are a function of local swirl number alone in our measurements.

4 Axial Decay of Swirl Number

An equation for the axial decay of swirl was obtained by Senoo et al. (1972) but underestimates the decay for the long pipe. So far, there is not a useful formula of axial decay of swirl number for a hydraulically smooth pipe of long length. We define inlet swirl number S_0 which is obtained by extrapolating experimental relationship between S and x to the origin of x. In Fig. 2, S/S_0 is plotted against $x^* = x/D$, the solid line being our experimental correlation of

$$\mathrm{Log}\,(S/S_0) = -0.01605x^{*0.8} \tag{2}$$

Data from Senoo et al. (1972) for $L^* = 60$ and Algifri et al. (1987) for $L^* = 100$ are also included in the figure. The maximum deviation of measurements from our correlation (2) is about 20 percent.

5 Pressure Distributions

It is well-known in a swirling pipe flow that the radial distribution of pressure is different in the downstream direction

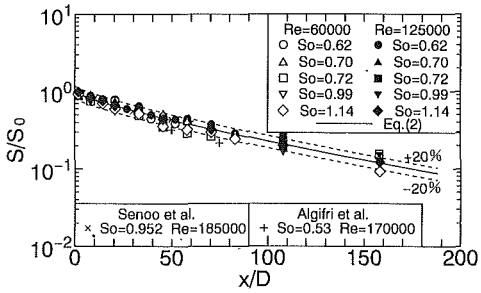

Fig. 2 Variation of swirl number along the axial direction (Uncertainty in $S = \pm 9.47$ percent in average)

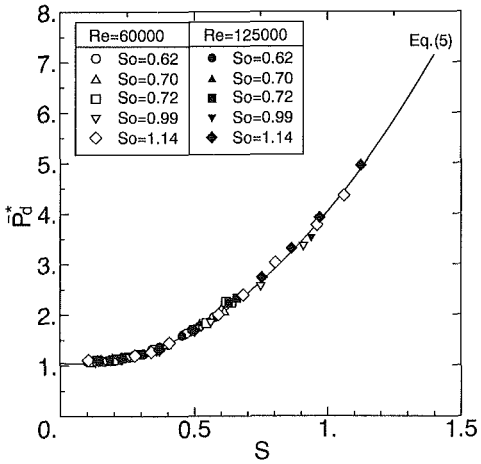

Fig. 3 Relationship between dimensionless mean kinetic energy and swirl number (Uncertainty in $\overline{P}_d^* = \pm 0.95$ percent in average)

with the decay of swirl. Such pressure profiles give important information not only about the decay of swirl but also about the energy loss of swirling flow. We examine the average dynamic, static, total pressures and the wall pressure as a function of local swirl number, where we will assume that those consist of independent contribution from the nonswirling flow and that from the swirling flow.

5.1 Average Dynamic Pressure. First, we define a dimensionless dynamic pressure as

$$P_d^* = u^{*2} + w^{*2} \tag{3}$$

and assume that the discharge average dynamic pressure $\overline{P}_d^*$ consists of

$$\overline{P}_d^* = I_a + I_s = 2\int_0^1 u_a^{*3} r^*\, dr + 2\int_0^1 \{(u^{*2} + w^{*2})u^* - u_a^{*3}\} r^*\, dr^* \tag{4}$$

where P_d^* is defined as $P_d/(\rho u_m^2/2)$, u^* and w^* are defined as u/u_m and w/u_m respectively, I_a is for the nonswirling flow, I_s is for the swirling flow and u_a is the axial local velocity of nonswirling flow of equal discharge velocity. In Fig. 3 $\overline{P}_d^*$ is plotted against local swirl number S. The measurements show that the dimensionless average dynamic pressure depends on the local swirl number alone and is a monotonous function of it. Within the experimental accuracy $\overline{P}_d^*$ is found to be independent of R_e, x^* and inlet swirl number S_0. We obtain the following empirical formula for $\overline{P}_d^*$ as a function of S

$$\overline{P}_d^* = 1.0522 - 0.4229S + 3.4121S^2 \tag{5}$$

where I_a is 1.0522. The solid line in Fig. 3 shows this relation.

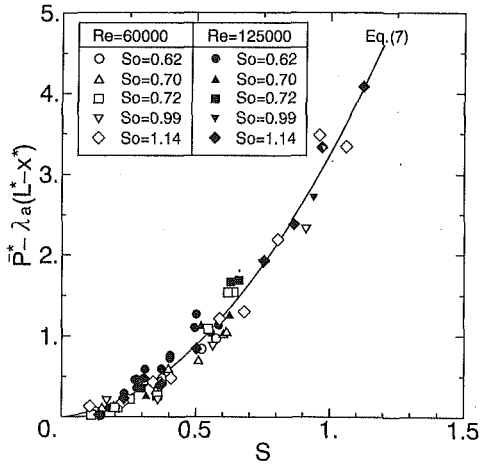

Fig. 4 Relationship between dimensionless mean static pressure drop and swirl number (Uncertainty in $\bar{P}^*$ = ±2.4 percent in average)

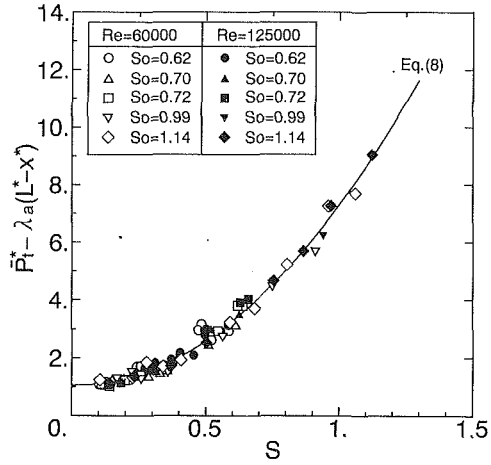

Fig. 5 Relationship between dimensionless mean total pressure drop and swirl number (Uncertainty in $\bar{P}_t^*$ = ±2.9 percent in average)

The average deviation of measurements from this correlation is 1.3 percent.

5.2 Average Static Pressure. The dimensionless average static pressure $\bar{P}^*$ is calculated by the same way as $\bar{P}_d^*$, where P is the gauge pressure. We assume that the static pressure at L^*-x^* from the pipe exit consists of the pressure drop due to nonswirling flow of equal discharge velocity and that due to the swirling flow. When the pipeline is a straight pipe of constant cross section, $\bar{P}^*$ is put

$$\bar{P}^* = P_a^* + \bar{P}_s^* = \lambda_a(L^*-x^*) + \bar{P}_s^* \tag{6}$$

where λ_a the pipe friction coefficient for the nonswirling flow and $\bar{P}_s^*$ the additional contribution due to the swirling flow. We show $\bar{P}_s^*$ against the local swirl number in Fig. 4, which indicates $\bar{P}_s^*$ is also a monotonous function of S. We get the following empirical formula for $\bar{P}^*$

$$\bar{P}^* = \lambda_a(L^*-x^*) + 0.2905S + 2.9572S^2 \tag{7}$$

The average deviation of measurements from this correlation is 3.1 percent.

5.3 Average Total Pressure. Since wall pressure drop along the pipe does not always correspond to the total energy loss in the swirling flow, the total pressure distribution along the pipe becomes important, and we examine the energy loss by using the average total pressure $\bar{P}_t^*$. From Eqs. (4) and (6), we have

$$\bar{P}_t^* = \bar{P}^* + \bar{P}_d^* = (I_a + P_a^*) + (I_s + \bar{P}_s^*)$$

and from Eqs. (5) and (7)

$$\bar{P}_t^* = \lambda_a(L^*-x^*) + 1.0522 - 0.1324S + 6.3693S^2 \tag{8}$$

The above correlation and the measurements are compared in Fig. 5 by $I_s + I_a$.

5.4 Wall Static Pressure. As above-mentioned, the wall static pressure P_w^* itself is no more than a representative quantity neither of overall static pressure drop nor of total pressure loss. However, it must have useful information to clarify the decay process of the swirling flow. We also assume that P_w^* consists of two parts, the one being the nonswirling flow and the other the swirling flow, and we put it as,

$$P_w^* = P_a^* + W_s = \lambda_a(L^*-x^*) + W_s \tag{9}$$

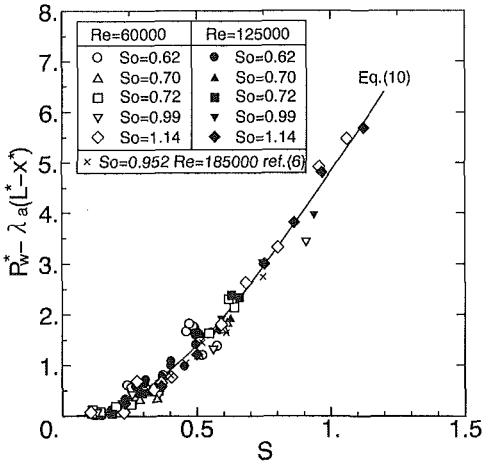

Fig. 6 Relationship between dimensionless wall static pressure drop and swirl number (Uncertainty in $\bar{P}_w^*$ = ±3.2 percent in average)

Thus W_s is considered to be additional wall pressure due to the swirling flow. In Fig. 6, W_s is plotted as a function of local swirl number S. It is found that W_s depends on the local swirl number alone and that it is also a monotonous function of S. We get the following empirical equation for W_s as

$$W_s = P_w^* - \lambda_a(L^*-x^*) = 0.7543S + 4.1633S^2 \tag{10}$$

The average deviation of measurements from the above correlation is 3.3 percent. In Fig. 6 the measurements by Senoo et al. (1972) for $L^*=60$ are plotted. The agreement is satisfactory.

6 Prediction of Decay Process by Wall Static Pressure

The above results indicate that the characteristics of swirling flow are a function of swirl number S, R_e, and L^* in a hydraulically smooth pipe. By the correlations obtained in this study, the decay of swirl number, the distributions of the average dynamic, static and total pressure along the pipe can be easily computed as follows:

(1) For given discharge velocity u_m, pipe length L and pipe diameter D, if the wall static pressure P_w at x^* is measured, the swirl number at x^* is obtained by Eq. (10) or by using Fig. 6.

(2) Substituting these S and x^* for Eq. (2) or using Fig. 2,

the inlet swirl number S_0 is obtained. Therefore, the swirl number at any section x^* is inferred by Eq. (2) or by using Fig. 2.

(3) The average dynamic, static, total pressure and wall static pressure at any axial section x^* can be determined by Eqs. (5), (7), and (8).

7 Conclusion

From the experimental study of swirling flow in a pipe it is found that the characteristics of swirling flow is a function of local swirl number, Reynolds number and pipe length-to-diameter ratio. These experimental results have been used to establish empirical relationships which express the swirl number as a function of distance-to-diameter ratio and those which express the wall static, average dynamic, static and total pressures as a function of local swirl number, Reynolds number and pipe length-to-diameter ratio. These experimental results and empirical relationships are in good agreement with measurements of other researchers. By using these empirical relationships, the characteristics of swirling flow in a pipe can be successfully computed by giving the discharge velocity and a wall static pressure at any axial position alone.

Acknowledgment

This work was performed as part of the research which was supported by a scientific research fund granted by Japanese Ministry of Education (No. 03650152).

References

Algiferi, A. H., Bhardwaj, R. K., and Rao, Y. V. N., 1987, "Prediction of the Decay Process in Turbulent Swirl Flow," *Proceedings of Institution of Mechanical Engineers*, Vol. 201, pp. 279–283.

Ito, S., Ogawa, K., and Kuroda, C., 1980, "Turbulent Swirling Flow in a Circular Pipe," *Journal of Chemical Engineering*, Japan, Vol. 13, pp. 6–10.

Kuroda, C., Ogawa, K., and Inoue, I., 1981, "An Approximate Equation of Axial Velocity Distribution in Turbulent Swirling Pipe Flow," *Journal of Chemical Engineering*, Japan, Vol. 14, pp. 158–160.

Kreith, F., and Sonju, O. K., 1965, "The Decay of a Turbulent Swirl in a Pipe," *Journal of Fluid Mechanics*, Vol. 22, pp. 257–271.

Li, H., Tomita, Y., and Funatsu, K., 1992, "Research of Swirling Flow Pneumatic Conveying System in a Horizontal Pipeline (1st Pressure Drop and Flow Patterns)," (In Japanese), *Trans. JSME*, Vol. 58, pp. 1599–1604.

Murakami, M., Kito, O., Katayama, Y., and Iida, Y., 1975, "Experimental Investigations of Swirling Flow in Circular Pipes," (In Japanese), *Trans. JSME*, Vol. 41, pp. 1793–1801.

Senoo, Y., and Nagata, T., 1972, "Swirl Flow in Long Pipes With Different Roughness," *Bull. JSME*, Vol. 15, pp. 1514–1521.

Mean Separation and Reattachment in Turbulent Pipe Flow Due to an Orifice Plate

N. K. Agarwal[1]

The mean flow in a pipe with turbulent separated flow due to an orifice plate is experimentally studied. Measurements of time-mean length of separation and reattachment regions, made using a surface fence gauge are presented for a range of orifice sizes. In a limited range of Reynolds number (based on orifice radial height) 3×10^4 to 7.3×10^4 studied, reattachment point location decreased from 12 to 9 step heights. The lengths of separation and reattachment regions are a function of orifice size and the Reynolds number based on the radial height of the orifice plate.

[1]Senior Scientist, Analytical Services & Materials, Inc., 107 Research Drive, Hampton, VA 23666. Mem. ASME.

Contributed by the Fluids Engineering Division of THE AMERICAN SOCIETY OF MECHANICAL ENGINEERS. Manuscript received by the Fluids Engineering Division July 27, 1992; revised manuscript received May 17, 1993. Associate Technical Editor: Ho, Chih-Ming.

Nomenclature

d = pipe diameter
d_c = choke throat diameter
d_o = orifice plate hole diameter
D_c = d_c/d
h = orifice plate radial height = $(d-d_o)/2$
h_1 = fence height
h_+ = h_1U_τ/ν
R, S_1, S_2 = mean reattachment, primary and secondary separation locations, respectively
$\mathrm{R_{eh}}$ = Reynolds number based on orifice radial height
U_τ = wall friction velocity
x = streamwise distance
X = x/d
β = d_o/d
ΔP = pressure differential across the fence
γ_p = forward flow fraction
τ_w = wall shear stress
ν = kinematic viscosity

Introduction

Most of the studies of the reattaching shear layer are confined to two-dimensional flows, such as steps and sudden expansions; good reviews of the available data have been presented by Bradshaw and Wong (1972), Eaton and Johnston (1981) and Morrison et al. (1988). Previous experimental determinations of the reattachment length for an orifice plate in a circular pipe have generally been made indirectly, by identifying reattachment with the position of maximum heat transfer rate in a heated pipe or with that of maximum turbulent axial velocity fluctuation. The reattachment length is the most important streamwise parameter on which to scale streamwise skin friction, downstream-upstream intermittency, static pressure recovery, and root-mean-square surface pressure fluctuations.

In this paper, results for the mean locations of flow separation and reattachment, in a fully developed turbulent pipe flow separated due to an orifice flow, are presented.

Pipe Flow Facility

The pipe flow facility is made up from smooth cold-drawn interchangeable sections of steel tubing with internal diameter of 72.54 mm. The downstream end of the pipe was connected to a vibration isolator, a sonic choke, and a remotely controlled quick acting valve to two large vacuum tanks. When the remotely controlled valve is opened, air enters from the atmosphere through the piping system to the vacuum tanks. Mass flow rate and the flow velocity in the pipe system are determined by the combination of the throat area of the sonic choke and the size of the orifice plate. Ten interchangeable sonic choke inserts with D_c in the range 0.39 to 0.86 and four orifice plates conforming to ASME and British Standards (refer to ASME MFC-3M, 1985 and British Standard 1042 Part I) with β in the range 0.62 to 0.83, were used. For all orifice plate/choke combinations used in these experiments, a fully developed turbulent velocity profile was established upstream of the orifice plate. More details of the pipe flow facility are contained in Agarwal (1994).

the inlet swirl number S_0 is obtained. Therefore, the swirl number at any section x^* is inferred by Eq. (2) or by using Fig. 2.

(3) The average dynamic, static, total pressure and wall static pressure at any axial section x^* can be determined by Eqs. (5), (7), and (8).

7 Conclusion

From the experimental study of swirling flow in a pipe it is found that the characteristics of swirling flow is a function of local swirl number, Reynolds number and pipe length-to-diameter ratio. These experimental results have been used to establish empirical relationships which express the swirl number as a function of distance-to-diameter ratio and those which express the wall static, average dynamic, static and total pressures as a function of local swirl number, Reynolds number and pipe length-to-diameter ratio. These experimental results and empirical relationships are in good agreement with measurements of other researchers. By using these empirical relationships, the characteristics of swirling flow in a pipe can be successfully computed by giving the discharge velocity and a wall static pressure at any axial position alone.

Acknowledgment

This work was performed as part of the research which was supported by a scientific research fund granted by Japanese Ministry of Education (No. 03650152).

References

Algiferi, A. H., Bhardwaj, R. K., and Rao, Y. V. N., 1987, "Prediction of the Decay Process in Turbulent Swirl Flow," *Proceedings of Institution of Mechanical Engineers*, Vol. 201, pp. 279–283.

Ito, S., Ogawa, K., and Kuroda, C., 1980, "Turbulent Swirling Flow in a Circular Pipe," *Journal of Chemical Engineering*, Japan, Vol. 13, pp. 6–10.

Kuroda, C., Ogawa, K., and Inoue, I., 1981, "An Approximate Equation of Axial Velocity Distribution in Turbulent Swirling Pipe Flow," *Journal of Chemical Engineering*, Japan, Vol. 14, pp. 158–160.

Kreith, F., and Sonju, O. K., 1965, "The Decay of a Turbulent Swirl in a Pipe," *Journal of Fluid Mechanics*, Vol. 22, pp. 257–271.

Li, H., Tomita, Y., and Funatsu, K., 1992, "Research of Swirling Flow Pneumatic Conveying System in a Horizontal Pipeline (1st Pressure Drop and Flow Patterns)," (In Japanese), *Trans. JSME*, Vol. 58, pp. 1599–1604.

Murakami, M., Kito, O., Katayama, Y., and Iida, Y., 1975, "Experimental Investigations of Swirling Flow in Circular Pipes," (In Japanese), *Trans. JSME*, Vol. 41, pp. 1793–1801.

Senoo, Y., and Nagata, T., 1972, "Swirl Flow in Long Pipes With Different Roughness," *Bull. JSME*, Vol. 15, pp. 1514–1521.

Mean Separation and Reattachment in Turbulent Pipe Flow Due to an Orifice Plate

N. K. Agarwal[1]

The mean flow in a pipe with turbulent separated flow due to an orifice plate is experimentally studied. Measurements of time-mean length of separation and reattachment regions, made using a surface fence gauge are presented for a range of orifice sizes. In a limited range of Reynolds number (based on orifice radial height) 3×10^4 to 7.3×10^4 studied, reattachment point location decreased from 12 to 9 step heights. The lengths of separation and reattachment regions are a function of orifice size and the Reynolds number based on the radial height of the orifice plate.

Nomenclature

d = pipe diameter
d_c = choke throat diameter
d_o = orifice plate hole diameter
D_c = d_c/d
h = orifice plate radial height = $(d-d_o)/2$
h_1 = fence height
h_+ = h_1U_τ/ν
R, S_1, S_2 = mean reattachment, primary and secondary separation locations, respectively
R_{eh} = Reynolds number based on orifice radial height
U_τ = wall friction velocity
x = streamwise distance
X = x/d
β = d_o/d
ΔP = pressure differential across the fence
γ_p = forward flow fraction
τ_w = wall shear stress
ν = kinematic viscosity

Introduction

Most of the studies of the reattaching shear layer are confined to two-dimensional flows, such as steps and sudden expansions; good reviews of the available data have been presented by Bradshaw and Wong (1972), Eaton and Johnston (1981) and Morrison et al. (1988). Previous experimental determinations of the reattachment length for an orifice plate in a circular pipe have generally been made indirectly, by identifying reattachment with the position of maximum heat transfer rate in a heated pipe or with that of maximum turbulent axial velocity fluctuation. The reattachment length is the most important streamwise parameter on which to scale streamwise skin friction, downstream-upstream intermittency, static pressure recovery, and root-mean-square surface pressure fluctuations.

In this paper, results for the mean locations of flow separation and reattachment, in a fully developed turbulent pipe flow separated due to an orifice flow, are presented.

Pipe Flow Facility

The pipe flow facility is made up from smooth cold-drawn interchangeable sections of steel tubing with internal diameter of 72.54 mm. The downstream end of the pipe was connected to a vibration isolator, a sonic choke, and a remotely controlled quick acting valve to two large vacuum tanks. When the remotely controlled valve is opened, air enters from the atmosphere through the piping system to the vacuum tanks. Mass flow rate and the flow velocity in the pipe system are determined by the combination of the throat area of the sonic choke and the size of the orifice plate. Ten interchangeable sonic choke inserts with D_c in the range 0.39 to 0.86 and four orifice plates conforming to ASME and British Standards (refer to ASME MFC-3M, 1985 and British Standard 1042 Part I) with β in the range 0.62 to 0.83, were used. For all orifice plate/choke combinations used in these experiments, a fully developed turbulent velocity profile was established upstream of the orifice plate. More details of the pipe flow facility are contained in Agarwal (1994).

[1]Senior Scientist, Analytical Services & Materials, Inc., 107 Research Drive, Hampton, VA 23666. Mem. ASME.

Contributed by the Fluids Engineering Division of THE AMERICAN SOCIETY OF MECHANICAL ENGINEERS. Manuscript received by the Fluids Engineering Division July 27, 1992; revised manuscript received May 17, 1993. Associate Technical Editor: Ho, Chih-Ming.

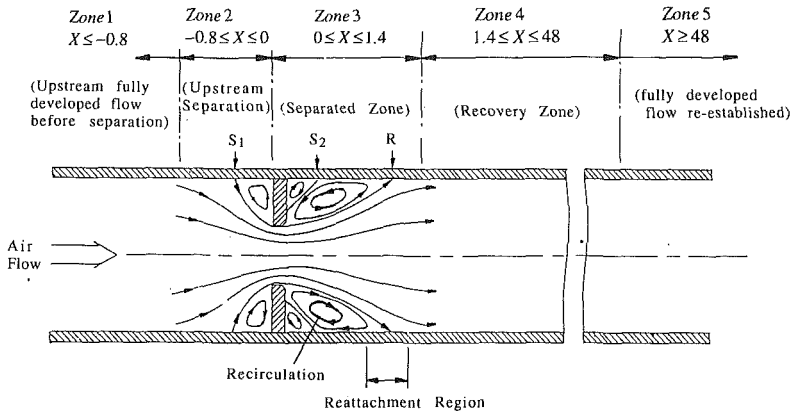

Fig. 1 Orifice flow

Instrumentation

Mean positions of separation and reattachment points, where the wall shear stress τ_w is zero, (this location is also where γ_P, the fraction of time that the flow moves downstream is 1/2) were determined by means of a surface fence gauge of the type described first by Konstantinov and Dragnysh (1955) and later by Vagt and Fernholz (1973). Basically, the "fence" consists of a rectangular projection of very small height positioned normal to the wall and to the flow direction. The differential pressure (ΔP), being the difference between the front and rear of the projection is related to the wall shear stress τ_w, which changes sign depending on the direction of local flow.

The results of Konstantinov and Dragnysh indicate that for very small projection heights ($h_+ \leq 3$) ΔP and τ_w are linearly related for a fixed value of h_1, i.e.,

$$\Delta P = K\tau_w, \tag{1}$$

but with K being dependent on the fence height. Later work (see Winter, 1977) suggests that more generally

$$(\Delta P/\tau_w) = f(h_+). \tag{2}$$

In the present investigation a 3 mm wide and 0.1 mm thick section of a razor blade was used as the fence. The top surface of the gauge body and the fence were carefully machined to match the pipe profile. A series of tests with different fence heights in the range 0.05 mm $\leq h_1 \leq 0.5$ mm showed that the location of the point at which $\tau_w = 0$ (i.e., $\Delta P = 0$), as indicated by the gauge, was insensitive to the fence height. Therefore, a value of 0.1 mm, corresponding to $10 \leq h_+ \leq 30$ over the range of the experimental flow speeds was used. Geometrical symmetry of the gauge was checked by repeating measurements with the gauge rotated through 180 deg.

A three-wire probe and the electronic circuit similar to the one described by Eaton et al. (1979) were used. The probe consisted of three parallel wires, a central heated velocity-sensing wire, and two temperature-sensing wires.

Experimental Uncertainty

The uncertainties in the mean velocity and the surface fence gauge measurements are mainly due to the uncertainties in the pressure measurements. The method of Kline and McClintock (1953) was used to estimate the uncertainty for the measurements, and are given below:

Mean axial velocity ±2.5 percent
Fence gauge pressure differential ±3 percent
x_R/h, x_{S1}/h, and x_{S2}/h ±0.045

Results

The mean flow in the piping system in the presence of an orifice plate can be usefully divided into the five characteristic zones and has the general character as shown in Fig. 1.

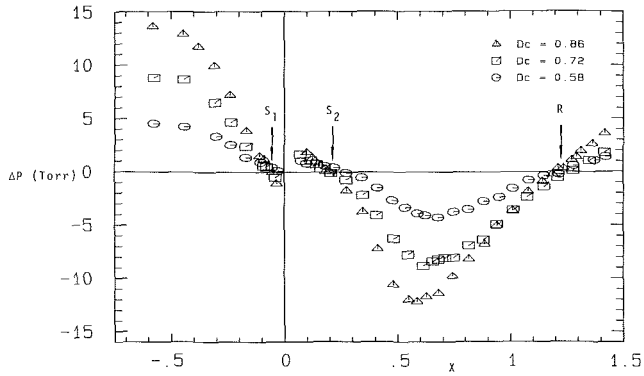

Fig. 2 Surface fence gage measurements, $\beta = 0.76$

Locations of mean separation and reattachment points were obtained by a fence gauge. Reattachment length in a few cases was also measured using a three-wire probe and the results obtained by these two gauges show good agreement. Typical variation of the pressure differential, ΔP, indicated by a fence gauge, through the separated-flow region and slightly beyond for an orifice plate with $\beta = 0.76$ with three different flow rates (corresponding to the chokes $D_c = 0.58$, 0.72, 0.86) is shown in Fig. 2. The zero-crossings of the curves of ΔP against X gives the positions of points of zero mean wall shear stress: thus the mean position of the primary separation can be identified as $X_{S1} \cong -0.08$, that of reattachment X_R in the range 1.3–1.4, and that of secondary separation as $X_{S2} \cong 0.20$.

Figures 3(*a–b*) show the X_R, X_{S1} and X_{S2} results, from Fig. 2 and similar plots for other orifice plates. All three points move toward the orifice plate as β increases (i.e., as the radial height of the obstruction decreases). The effect of increasing flow rate (i.e., increasing D_c) is also to move the location of these points towards the orifice plate; the effect is very small on X_{S1} but somewhat greater on X_{S2} and largest on X_R, and increases as β is reduced. Lines of constant X_R/h are also shown on Fig. 3(*a*). These indicate that the reattachment length expressed in terms of h is less strongly dependent on β than is X_R.

Figure 3(*b*) shows that when the same measured distances of separation and reattachment points from the orifice plate are expressed in terms of the radial height h of the obstruction caused by the orifice plate, they show a considerably weaker dependence on β. The position of primary separation x_{S1}/h, appears to be independent of β, while x_{S2} and x_R/h increase gradually with increasing β.

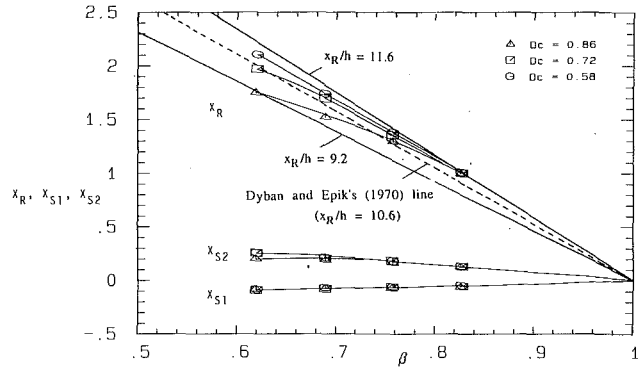

Fig. 3(*a*) Variation of reattachment and separation lengths with orifice size

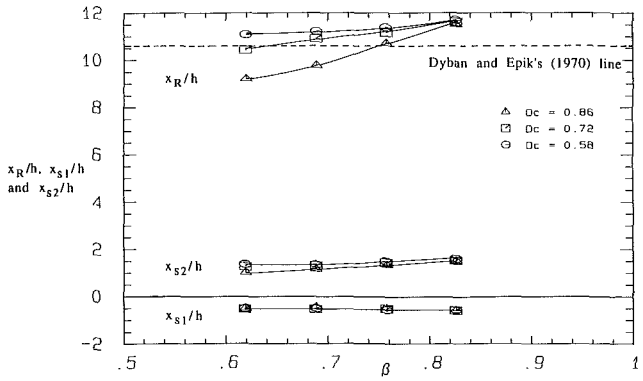

Fig. 3(*b*) Variation of reattachment and separation lengths with orifice size

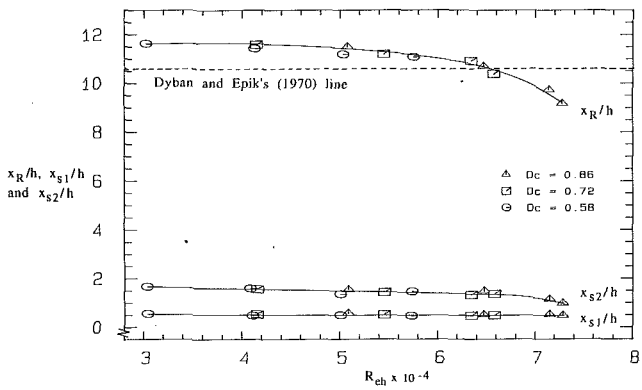

Fig. 4 Variation of reattachment and separation lengths with Reynolds number

On the assumption that compressibility effects are insignificant, and for a given orifice geometry (sharpness of edges, etc.), dimensional analysis would indicate that

$$X_{S1},\ X_{S2},\ X_R = \text{function}\ (\beta,\ R_e) \tag{3}$$

or

$$x_{S1}/h,\ x_{S2}/h,\ x_R/h = \text{function}\ (\beta,\ R_e) \tag{4}$$

where R_e is a Reynolds number. A fairly good collapse of the data can be obtained if h is used as the length scale and the values plotted as a function of the Reynolds number R_{eh}, as shown in Fig. 4. Thus Fig. 4 suggests that over the admittedly rather small, Reynolds number range of the present experiments, Eq. (4) reduces to

$$x_{S1}/h,\ x_{S2}/h,\ x_R/h = \text{function}\ (R_{eh}) \tag{5}$$

Dyban and Epik (1970) attempted to correlate reattachment length data, which cover orifice sizes $0.25 \le \beta \le 0.88$ and a Reynolds number range of $10^3 \le R_{eh} \le 4.0 \times 10^4$. The data show no systematic variation with Reynolds number and considerable scatter, values of x_R/h as low as 5 and as high as 18 being observed. Dyban and Epik give a mean line for the variation of X_R with β, which is shown in Figs. 3(*a-b*); it is equivalent to $x_R/h = 10.6$. This is close to $x_R/h \cong 10$, results of Back and Roschke (1972) in the flow through a sudden expansion (diameter ratio 0.39) in a circular pipe. Their results are for the flow with a thin boundary layer upstream of separation at R_{eh} of the order of 3×10^3. These results can be compared with the x_R/h values in the present case in the range 9.2 to 11.6, for just slightly higher Reynolds numbers.

The reattachment length for orifices in circular pipes expressed as x_R/h seems to be rather higher than the corresponding value for separation of a turbulent boundary layer from a backward-facing step in two-dimensional flow. From the data surveyed by Eaton and Johnston (1981) the latter ranges from 5 to 8.2.

Very little experimental information is available on either X_{S1} or X_{S2}. Adams et al. (1984) used a pulsed wire probe in their two dimensional flow downstream of a backward-facing step, with a Reynolds number, R_{eh}, of 36000 and measured the separation of the reversed flow at $x/x_R = 0.1$. Morrison et al. (1988) in an axisymmetric sudden expansion, measured the length of secondary recirculation zone as 0.8 step height (i.e., $x_{S2}/x_R \cong 0.13$). Data compiled by Morrison et al. for the flow through a sudden expansion show that the length of secondary recirculation region appears to be extending up to 1.5 step height. The length of secondary recirculation zone measured here varies between 1 to 1.9 step height (i.e., $x_{S2}/x_R \cong 0.1 - 0.13$) for a Reynolds number (R_{eh}) range of 30,000 to 73,000.

Conclusions

The mean positions of reattachment and separation points, expressed in terms of pipe diameters as X_R, X_{S1}, and X_{S2} or in terms of the radial height of the orifice as x_R/h, x_{S1}/h and x_{S2}/h are functions of orifice size β and the Reynolds number, R_e. Over the small Reynolds number range studied, x_R/h, x_{S1}/h, and x_{S2}/h appear to be functions of Reynolds number, R_{eh} based on the radial height of the orifice h. The reattachment length decreases from about $12h$ to about $9h$ as R_{eh} increases from 3×10^4 to 7×10^4.

The results obtained for separation and reattachment locations are broadly consistent with previously published work and appear to represent a more direct and systematic set of measurements than previously obtained for orifice plates in circular pipes.

Acknowledgment

This work was done at the University of Adelaide, South Australia. The author wishes to acknowledge many useful comments of Dr. M. K. Bull during the experimental program.

References

Adams, E. W., Johnston, J. P., and Eaton, J. K., 1984, "Experiments on the Structure of Turbulent Reattaching Flows," Report MD-43, Thermosciences Division, Department of Mechanical Engineering, Stanford University.

Agarwal, N. K., 1994, "Sound Field in Fully Developed Turbulent Pipe Flow due to Internal Flow Separation. Part 1. Wall Pressure Fluctuations," *Journal of Sound and Vibration*, Vol. 169, No. 1, pp. 89–109.

ASME MFC-3M, 1985, *Measurement of Fluid Flow in Pipes using Orifice, Nozzles, and Venturi*, New York, ASME.

Back, L. H., and Roschke, E. J., 1972, "Shear-Layer Flow Regimes and Wave Instabilities and Reattachment Lengths Downstream of an Abrupt Circular Channel Expansion," ASME *Journal of Applied Mechanics*, Vol. 94, pp. 677–681.

Bradshaw, P., and Wong, F. Y. F., 1972, "The Reattachment and Relaxation of a Turbulent Shear Layer," *Journal of Fluid Mechanics*, Vol. 52, pp. 113–135.

British Standard 1042 Part I, 1964, "Orifice Plates, Nozzles and Venturi Tubes".

Dyban, Y. P., and Epik, E. Y., 1970, "Effect of Turbulence on Calculating Heat Transfer Downstream of an Orifice in a Tube," *Heat Transfer-Soviet Research*, Vol. 2, No. 1, pp. 11–16.

Eaton, J. K., Jeans, A. H., Ashjaee, J., and Johnston, J. P., 1979, "A Wall-Flow Direction Probe for Use in Separating and Reattaching Flows," ASME JOURNAL OF FLUIDS ENGINEERING, Vol. 101, pp. 364–366.

Eaton, J. K., and Johnston, J. P., 1981, "A Review of Research on Subsonic Turbulent Flow Reattachment," *AIAA Journal*, Vol. 19, pp. 1093–1100.

Kline, S. J., and McClintock, F. A., 1953, "Describing Uncertainties in Single Sample Experiments," *Mechanical Engineering*, Vol. 75, pp. 3–8.

Konstantinov, N. I., and Dragnysh, G. L., 1955, "The Measurement of Friction Stress on a Surface," *Energomashinestroenic*, Vol. 176, pp. 191–200.

Morrison, G. L., Tatterson, G. B., and Long, M. W., 1988, "Three-Dimensional Laser Velocimeter Investigation of Turbulent, Incompressible Flow in an Axisymmetric Sudden Expansion," *Journal of Propulsion*, Vol. 4, No. 6, pp. 533–540.

Vagt, J. D., and Fernholz, H., 1973, "Use of Surface Fences to Measure Wall Shear Stress in Three-Dimensional Boundary Layers," *Aeronautical Quarterly*, May.

Winter, K. G., 1977, "An Outline of the Techniques Available for the Measurements of Skin Friction in Turbulent Boundary Layers," *Progress in Aerospace Sciences*, Vol. 18, pp. 1–57.

Mean Pressure Distribution and Drag Coefficient of Wire-Wrapped Cylinders

E. E. Yang,[1] H. R. Rahai,[1] and A. Nakayama[2]

Nomenclature

D = cylinder diameter, cm
d = wire diameter, cm
p = pitch spacing, cm
C_p = pressure coefficient, $\Delta P/(1/2)\rho U_\infty^2$
C_{p_b} = base pressure coefficient
C_{p_m} = minimum pressure coefficient
C_D = drag coefficient
U_∞ = free stream velocity, m/s
Re_D = Reynolds number, $\rho U_\infty D/\nu$
ρ = density, Kg/m^3
ν = kinematic viscosity, m^2/s
θ = circumferential angle, deg

1 Introduction

Flow past cylinders has been the subject of many investigations because of their importance in practical applications. The unique feature of flow past a cylinder is its separation from the surface at high Reynolds number, which results in a pressure drag quite distinct from viscous drag and is accounted for most of the total drag of the cylinder.

Destroying the symmetry of flow around a cylinder by applying roughness elements or axial or helical fins results in reduced structural oscillations and stress and the early transition of laminar boundary layer to turbulent results in smaller drag coefficient. There have been numerous studies on drag and shedding frequency of circular cylinders with either smooth, rough, or longitudinally ribbed surfaces in air at different Reynolds numbers. Examples are the studies of Achenbach (1968, 1971), Achenbach and Heinecke (1981), Guven et al. (1980), Walsh and Weinstein (1979), Walsh (1980) and Ko et. al. (1987). However, there have been very limited studies on wire-wrapped cylinders and that only at low Reynolds number. The experimental studies by Nassif et al. (1989) on flow over wire-wrapped cylinders below the sub-critical Reynolds number regime show that when the wire diameter is much less than the estimated size of the boundary layer thickness, there is no change in the drag coefficient as compared with the corresponding results for the smooth cylinder. However, when the wire diameter is much larger than the estimated boundary layer thickness, drag coefficient becomes higher than the corresponding value for the smooth cylinder.

Hsueh et al. (1991) performed measurements of turbulent wake of wire-wrapped cylinders with wire to cylinder diameter of 0.04 and pitch to cylinder diameter of 0.25, 0.5, and 1.0. The experiments are performed at Reynolds number based on the smooth cylinder diameter of 9000. Their results show that near the cylinder, the presence of wire causes increase in the maximum mean defect velocity as compared with the corresponding value for the smooth cylinder. However, the differences decrease and become negligible with increase in the downstream direction. Their results also show that the contribution of the longitudinal turbulent velocity to the momentum thicknesses are significant and should not be ignored. They did not investigate the effects of wire-wrapping on flow characteristics near the cylinder.

The objective of the present experiments is to study the effects of wire-wrapping on the drag coefficient of circular cylinders.

2 Arrangement and Techniques

The present study is divided into two parts. In the first part three smooth stainless steel cylinders of 2.54 cm diameter, D, each wrapped at different pitch, p, with stainless steel wire of 0.254 mm diameter, d, along with a smooth stainless steel cylinder of the same diameter are used. The various pitch (the spacing between adjacent loops) to cylinder diameter, p/D, for the wire wrapped cylinders were 0.25, 0.5, 1.0, and 2.0. In part two, the smooth cylinders are wrapped with wires of 0.254, 0.504, and 0.813 mm diameters where the ratio of wire diameter to the cylinder diameter d/D, are 0.01, 0.02 and 0.032, respectively. However, p/D are held constant at 1.0. The wires are wrapped tightly around the cylinders without any gap between the wires and the cylinders and the end are glued to cylinders ends. The entire length of the cylinders within the wind tunnel are wire-wrapped.

The blockage and aspect ratio are respectively 16.6 percent and 15. Drag coefficients are corrected for the blockage effect using the formula given by Allen and Vincenti (1944).

The experiments were carried our in the open-circuit blower tunnel of the Mechanical Engineering Department at California State University, Long Beach which has a cross-sectional area of 35×15 cm and is 91 cm long. In the range of 3 to 30 m/s, the mean velocity varies by less than 0.5 percent over the central portion of the test section and at all speeds the free stream turbulence intensity is less than 0.5 percent.

The smooth cylinder has one pressure tap of 1 mm diameter, placed at its mid point, while the wire-wrapped cylinders have three pressure taps of the same diameter, placed within the loop in the mid-section of the cylinder. The spacing between these pressure taps is approximately 3 mm for cylinders with $p/D = 0.5$ and 1.0 and approximately 1.5 mm for cylinder with $p/D = 0.25$.

Plastic tubing with outside diameter of 1 mm and inside diameter of 0.5 mm are inserted into the hole from inside of

[1]Graduate Assistant and Associate Professor, respectively, Department of Mechanical Engineering, California State University, Long Beach, CA 90840. Professor Rahai is a Mem. ASME.

[2] The Faculty of Engineering, Kobe University, Kobe, Japan.

Contributed by the Fluids Engineering Division of THE AMERICAN SOCIETY OF MECHANICAL ENGINEERS. Manuscript received by the Fluids Engineering Division August 18, 1992; revised manuscript received August 27, 1993. Associate Technical Editor: Ho, Chih-Ming.

Bradshaw, P., and Wong, F. Y. F., 1972, "The Reattachment and Relaxation of a Turbulent Shear Layer," *Journal of Fluid Mechanics*, Vol. 52, pp. 113–135.

British Standard 1042 Part I, 1964, "Orifice Plates, Nozzles and Venturi Tubes".

Dyban, Y. P., and Epik, E. Y., 1970, "Effect of Turbulence on Calculating Heat Transfer Downstream of an Orifice in a Tube," *Heat Transfer-Soviet Research*, Vol. 2, No. 1, pp. 11–16.

Eaton, J. K., Jeans, A. H., Ashjaee, J., and Johnston, J. P., 1979, "A Wall-Flow Direction Probe for Use in Separating and Reattaching Flows," ASME JOURNAL OF FLUIDS ENGINEERING, Vol. 101, pp. 364–366.

Eaton, J. K., and Johnston, J. P., 1981, "A Review of Research on Subsonic Turbulent Flow Reattachment," *AIAA Journal*, Vol. 19, pp. 1093–1100.

Kline, S. J., and McClintock, F. A., 1953, "Describing Uncertainties in Single Sample Experiments," *Mechanical Engineering*, Vol. 75, pp. 3–8.

Konstantinov, N. I., and Dragnysh, G. L., 1955, "The Measurement of Friction Stress on a Surface," *Energomashinestroenic*, Vol. 176, pp. 191–200.

Morrison, G. L., Tatterson, G. B., and Long, M. W., 1988, "Three-Dimensional Laser Velocimeter Investigation of Turbulent, Incompressible Flow in an Axisymmetric Sudden Expansion," *Journal of Propulsion*, Vol. 4, No. 6, pp. 533–540.

Vagt, J. D., and Fernholz, H., 1973, "Use of Surface Fences to Measure Wall Shear Stress in Three-Dimensional Boundary Layers," *Aeronautical Quarterly*, May.

Winter, K. G., 1977, "An Outline of the Techniques Available for the Measurements of Skin Friction in Turbulent Boundary Layers," *Progress in Aerospace Sciences*, Vol. 18, pp. 1–57.

Mean Pressure Distribution and Drag Coefficient of Wire-Wrapped Cylinders

E. E. Yang,[1] H. R. Rahai,[1] and A. Nakayama[2]

Nomenclature

D = cylinder diameter, cm
d = wire diameter, cm
p = pitch spacing, cm
C_p = pressure coefficient, $\Delta P/(1/2)\rho U_\infty^2$
C_{p_b} = base pressure coefficient
C_{p_m} = minimum pressure coefficient
C_D = drag coefficient
U_∞ = free stream velocity, m/s
Re_D = Reynolds number, $\rho U_\infty D/\nu$
ρ = density, Kg/m^3
ν = kinematic viscosity, m^2/s
θ = circumferential angle, deg

1 Introduction

Flow past cylinders has been the subject of many investigations because of their importance in practical applications. The unique feature of flow past a cylinder is its separation from the surface at high Reynolds number, which results in a pressure drag quite distinct from viscous drag and is accounted for most of the total drag of the cylinder.

Destroying the symmetry of flow around a cylinder by applying roughness elements or axial or helical fins results in reduced structural oscillations and stress and the early transition of laminar boundary layer to turbulent results in smaller drag coefficient. There have been numerous studies on drag and shedding frequency of circular cylinders with either smooth, rough, or longitudinally ribbed surfaces in air at different Reynolds numbers. Examples are the studies of Achenbach (1968, 1971), Achenbach and Heinecke (1981), Guven et al. (1980), Walsh and Weinstein (1979), Walsh (1980) and Ko et. al. (1987). However, there have been very limited studies on wire-wrapped cylinders and that only at low Reynolds number. The experimental studies by Nassif et al. (1989) on flow over wire-wrapped cylinders below the sub-critical Reynolds number regime show that when the wire diameter is much less than the estimated size of the boundary layer thickness, there is no change in the drag coefficient as compared with the corresponding results for the smooth cylinder. However, when the wire diameter is much larger than the estimated boundary layer thickness, drag coefficient becomes higher than the corresponding value for the smooth cylinder.

Hsueh et al. (1991) performed measurements of turbulent wake of wire-wrapped cylinders with wire to cylinder diameter of 0.04 and pitch to cylinder diameter of 0.25, 0.5, and 1.0. The experiments are performed at Reynolds number based on the smooth cylinder diameter of 9000. Their results show that near the cylinder, the presence of wire causes increase in the maximum mean defect velocity as compared with the corresponding value for the smooth cylinder. However, the differences decrease and become negligible with increase in the downstream direction. Their results also show that the contribution of the longitudinal turbulent velocity to the momentum thicknesses are significant and should not be ignored. They did not investigate the effects of wire-wrapping on flow characteristics near the cylinder.

The objective of the present experiments is to study the effects of wire-wrapping on the drag coefficient of circular cylinders.

2 Arrangement and Techniques

The present study is divided into two parts. In the first part three smooth stainless steel cylinders of 2.54 cm diameter, D, each wrapped at different pitch, p, with stainless steel wire of 0.254 mm diameter, d, along with a smooth stainless steel cylinder of the same diameter are used. The various pitch (the spacing between adjacent loops) to cylinder diameter, p/D, for the wire wrapped cylinders were 0.25, 0.5, 1.0, and 2.0. In part two, the smooth cylinders are wrapped with wires of 0.254, 0.504, and 0.813 mm diameters where the ratio of wire diameter to the cylinder diameter d/D, are 0.01, 0.02 and 0.032, respectively. However, p/D are held constant at 1.0. The wires are wrapped tightly around the cylinders without any gap between the wires and the cylinders and the end are glued to cylinders ends. The entire length of the cylinders within the wind tunnel are wire-wrapped.

The blockage and aspect ratio are respectively 16.6 percent and 15. Drag coefficients are corrected for the blockage effect using the formula given by Allen and Vincenti (1944).

The experiments were carried our in the open-circuit blower tunnel of the Mechanical Engineering Department at California State University, Long Beach which has a cross-sectional area of 35×15 cm and is 91 cm long. In the range of 3 to 30 m/s, the mean velocity varies by less than 0.5 percent over the central portion of the test section and at all speeds the free stream turbulence intensity is less than 0.5 percent.

The smooth cylinder has one pressure tap of 1 mm diameter, placed at its mid point, while the wire-wrapped cylinders have three pressure taps of the same diameter, placed within the loop in the mid-section of the cylinder. The spacing between these pressure taps is approximately 3 mm for cylinders with $p/D = 0.5$ and 1.0 and approximately 1.5 mm for cylinder with $p/D = 0.25$.

Plastic tubing with outside diameter of 1 mm and inside diameter of 0.5 mm are inserted into the hole from inside of

[1]Graduate Assistant and Associate Professor, respectively, Department of Mechanical Engineering, California State University, Long Beach, CA 90840. Professor Rahai is a Mem. ASME.

[2] The Faculty of Engineering, Kobe University, Kobe, Japan.

Contributed by the Fluids Engineering Division of THE AMERICAN SOCIETY OF MECHANICAL ENGINEERS. Manuscript received by the Fluids Engineering Division August 18, 1992; revised manuscript received August 27, 1993. Associate Technical Editor: Ho, Chih-Ming.

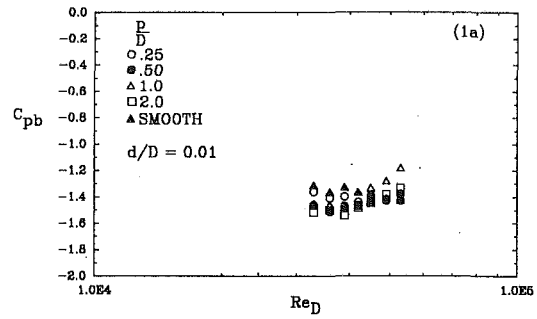

Fig. 1(*a*)

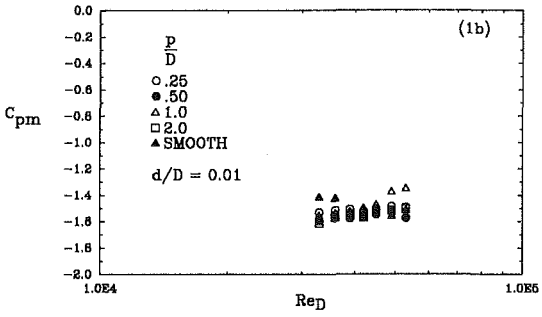

Fig. 1(*b*)

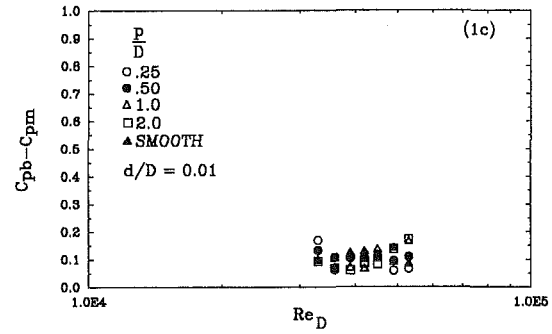

Fig. 1(*c*)

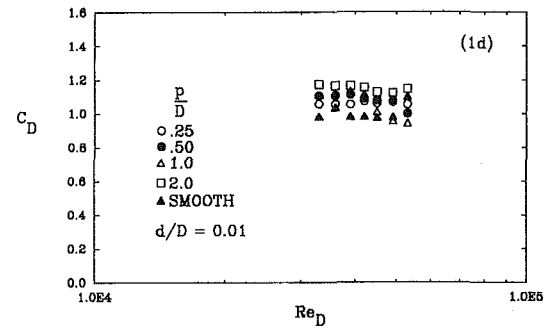

Fig. 1(*d*)

Fig. 1 Variation of the (*a*) base pressure coefficient, (*b*) minimum pressure coefficient, (*c*) pressure recovery, and (*d*) drag coefficient. Uncertainties in $C_p = \pm 0.05$ and in $C_D = \pm 0.02$.

the cylinders. The error in pressure measurements due to possible misalignment is less than 1 percent.

The experiments are carried out at seven different speeds from a minimum of 20 m/s to the maximum of 33 m/s which corresponds to the range of Reynolds numbers based on the smooth cylinder diameter of approximately 3.3×10^4 to 5.3×10^4. The estimated laminar boundary layer thicknesses for these Reynolds numbers, at 80 degrees from the front stagnation point are between 0.5 to 0.4 mm.

A Setra System pressure transducer model 339-1 is used for obtaining the pressure differential. At each position, 5000 samples of data are digitized and analyzed by using a 12 bit Metra Byte DAS-20 analog to digital converter connected to a 80386-based micro computer.

Mean pressure distribution is obtained by rotating the cylinders along their axes at 15 degrees interval and the drag force is obtained by integrating the pressure distribution along the whole cylinder in the plane perpendicular to the cylinder axis.

3 Results and Discussions

3.1 Part One, Variation of *P/D*. The pressure distributions are obtained from the center pressure tap. Initial measurements from all three holes showed existence of three dimensional boundary layer, especially near the wire. However, there were no change in the location of inflection point (boundary layer separation). Thus measurements are carried out using the center pressure tap only.

Figures 1(*a–d*) show variations of the base pressure coefficients, minimum pressure coefficients, pressure recovery, and drag coefficients for all cylinders. The base pressure coefficient for all wire wrapped cylinders are less than the corresponding values for the smooth cylinder up to $Re_D = 4.5 \times 10^4$. However, for higher Reynolds numbers, the base pressure coefficients of cylinders with $p/D = 0.25$ and 0.5 are nearly the same as the corresponding value for the smooth cylinder and for the cylinder with $p/D = 1.0$, it increases and becomes higher than the corresponding value for the smooth cylinder.

For cylinders with $p/D = 0.25$ and 0.5, the minimum pressure coefficient and pressure recovery are nearly the same as the corresponding value for the smooth cylinder. However, for $p/D = 1.0$, starting at $Re_D = 4.5 \times 10^4$, the minimum pressure coefficient and pressure recovery increase with increasing Reynolds number.

Results of Guven et. al. (1980) show that the pressure recovery is associated with the characteristics of the boundary layer. Our results indicate that when $p/D = 1.0$ and $d/D = 0.01$, the boundary layer becomes turbulent at Reynolds number of 4.0×10^4 which results in smaller momentum deficit and higher pressure recovery.

Cylinders with $p/D = 0.25$ and 0.5 have higher drag coefficients than the corresponding values for the smooth cylinder. However, when $p/D = 1.0$, the drag coefficient is initially higher than the corresponding value for the smooth cylinder and then it decreases to values less than the corresponding value for the smooth cylinder. The decrease in the drag coefficient corresponds to the increase in the pressure recovery which is consistent with transition of the boundary layer from laminar to turbulent state.

3.2 Part Two, Variation of *d/D*. Figures 2(*a–d*) show variations of the base pressure coefficient, minimum pressure coefficient, pressure recovery, and the drag coefficient when wire diameter is kept constant. Due to the space limitations, all the figures showing the variation of the mean pressure coefficients of these cylinders at different Reynolds numbers are excluded.

Results show that the base pressure coefficients for all wire-wrapped cylinders are initially lower than the corresponding value for the smooth cylinder up to the Reynolds number of 4.2×10^4. At this Reynolds number, the base pressure coefficient starts to increase and becomes higher than the corresponding value for the smooth cylinder at higher Reynolds numbers. The increase in the base pressure coefficient is higher for cylinder that has larger wire diameter.

The minimum pressure coefficients of wire-wrapped cylinders are initially less than the corresponding value for the

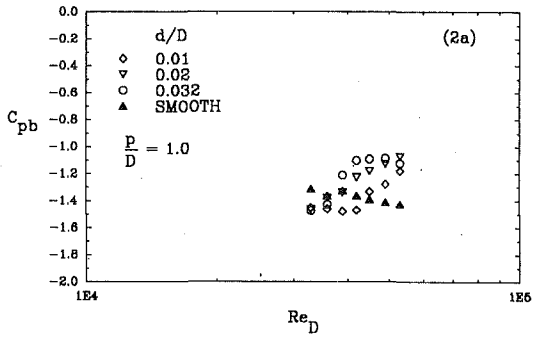

Fig. 2(*a*)

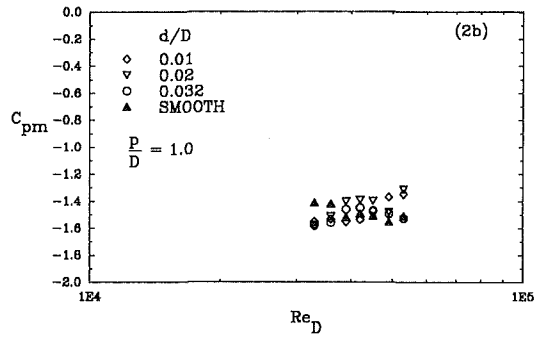

Fig. 2(*b*)

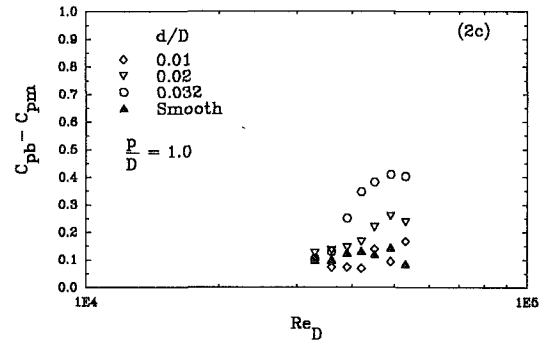

Fig. 2(*c*)

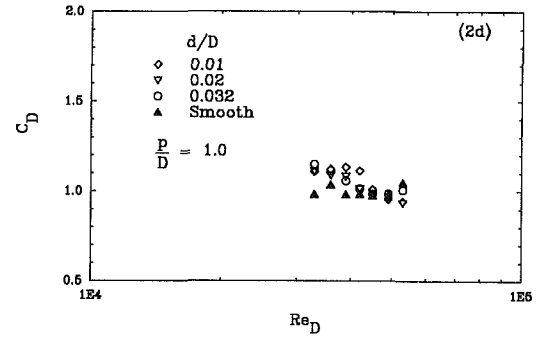

Fig. 2(*d*)

Fig. 2 Variations of the (*a*) base pressure coefficient, (*b*) minimum pressure coefficient, (*c*) pressure recovery, and (*d*) drag coefficient. Uncertainties are the same as Fig. 1.

smooth cylinder up to the Reynolds number of 3.9×10^4. However, as the Reynolds number increases, the minimum pressure coefficient increases for wire-wrapped cylinders with $d/D = 0.01$ and 0.02 and decreases when $d/D = 0.032$.

The pressure recovery of wire-wrapped cylinders show an increase for Reynolds number higher than 3.9×10^4 with the highest pressure recovery for the cylinder with $d/D = 0.032$. The increase in the pressure recovery corresponds to the decrease in the drag coefficient. The drag coefficients of wire-wrapped cylinders are initially higher than the corresponding value for the smooth cylinder. However, as the Reynolds number increases, the drag coefficients begin to decrease and the Reynolds number where the drag coefficient starts to decrease is decreased with increasing wire diameter. At the highest Reynolds number, the drag coefficients of all wire-wrapped cylinders are slightly less than the corresponding value for the smooth cylinder.

References

Achenbach, E., 1968, "Distribution of Local Pressure and Skin Friction Around a Circular Cylinder in Cross-flow up to $Re = 5 \times 10^6$," *Journal of Fluid Mechanics*, Vol. 34, p. 625.

Achenbach, E., 1971, "Influence of Surface Roughness on the Cross-flow Around a Circular Cylinder," *Journal of Fluid Mechanics*, Vol. 46, p. 321.

Achenbach, E., and Heinecke, E., 1981, "On Vortex Shedding from Smooth and Rough Cylinders in the Range of Reynolds Numbers 6×10^3 to 5×10^6, *Journal of Fluid Mechanics*, Vol. 109, p. 239.

Allen, H. J., and Vincenti, W. G., "Wall Interference in a Two-Dimensional Flow Wind Tunnel With Consideration of the Effect of Compressibility," *Journal of Fluid Mechanics*, Vol. 37, p. 577.

Farell, C., and Blessman, J., 1983, "On Critical Flow Around Smooth Circular Cylinder," *Journal of Fluid Mechanics*, Vol. 136, p. 375.

Farell, C., Carrasquel, S., Guven, O., and Patel, V. C., 1977, "Effect of Tunnel Walls on the Flow Past Circular Cylinders and Cooling Tower Models," ASME JOURNAL OF FLUIDS ENGINEERING, Vol. 99, p. 470.

Goldstein, S., ed., 1965, "Modern Developments in Fluid Dynamics, Dover Publications Inc.

Guven, O., Farell, C., and Patel, V. C., 1980, "Surface-Roughness Effects on the Flow Past Circular Cylinders," *Journal of Fluid Mechanics*, Vol. 98, p. 673.

Hsueh, L., Rahai, H. R., and LaRue, J. C., 1991, "Turbulent Wakes of Wire-wrapped Cylinders," *ASME Forum on Turbulent Flows*, FED-Vol. 112, pp. 95–100.

Ko, N. W. M., Leung, Y. C., and Chen, J. J. J., 1987, "Flow Past V-groove Circular Cylinders," *AIAA Journal*, Vol. 25, p. 806.

Nassif, M. Y., Tom, S., Rahi, H. R., and Nakayama, A., 1989 "Flow Over Wire-Wrapped Cylinders at Low Reynolds Number," *Bulletin of the American Physical Society*, Vol. 34, No. 10, Nov. Also Mechanical Engineering Report No. MEFT-89-3.

Walsh, M. J., and Weinstein, L. M., 1979, "Drag and Heat-transfer Characteristics of Small Longitudinally Ribbed Surface," *AIAA Journal*, Vol. 17, p. 770.

Walsh, M. J., 1980, "Drag Characteristics of V-groove and Transverse Curvature Riblets," *AIAA Progress in Astronautics and Aeronautics*, Vol. 72, p. 168.

Zukauskas, A., and Ziugzda, J., 1985, *Heat Transfer of a Circular Cylinder in Cross Flow*, Hemisphere Publishing Co.

A Note on Irrotational Curvilinear Flow Past a Weir

Amruthur S. Ramamurthy,[1] Ngoc-Diep Vo,[2] and R. Balachandar[3]

Curvilinear flows are commonly encountered in hydraulic engineering practice. Detailed velocity surveys of the curvilinear

[1]Prof. of Engineering, Concordia University, 1455 de Maisonneuve West, Montreal, Quebec, Canada, H3G 1M8.

[2]Research Assistant, Concordia University, Montreal, Quebec, Canada H3G 1M8.

[3]Research Scientist, Atomic Energy of Canada, Manitoba, Canada.

Contributed by the Fluids Engineering Division of THE AMERICAN SOCIETY OF MECHANICAL ENGINEERS. Manuscript received by the Fluids Engineering Division, September 15, 1992; revised manuscript received May 24, 1993. Associate Technical Editor: Ho, Chih-Ming.

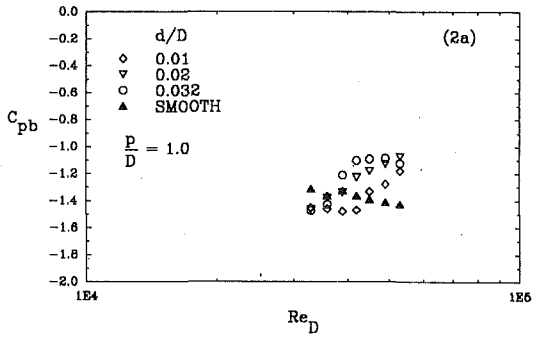

Fig. 2(*a*)

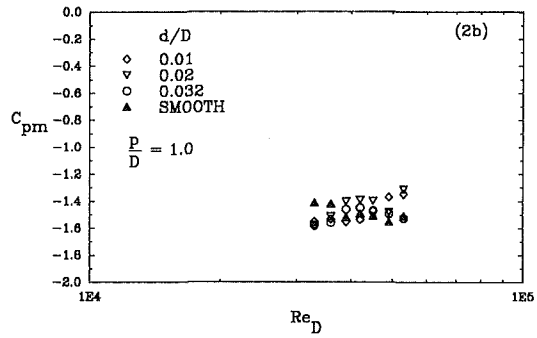

Fig. 2(*b*)

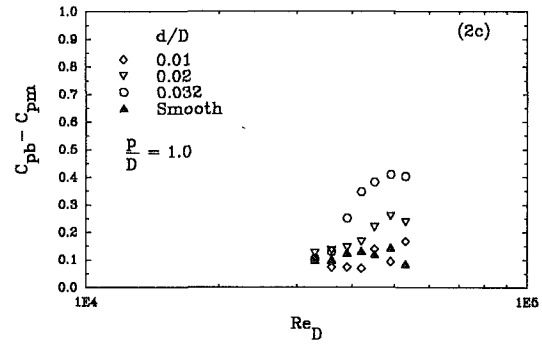

Fig. 2(*c*)

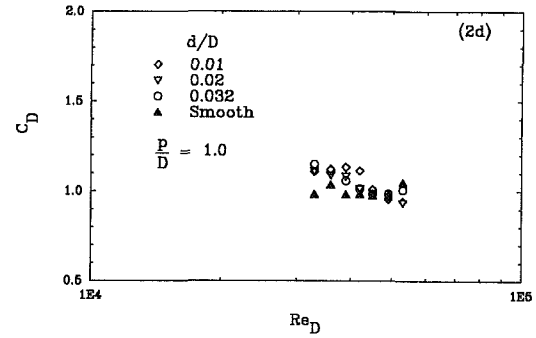

Fig. 2(*d*)

Fig. 2 Variations of the (*a*) base pressure coefficient, (*b*) minimum pressure coefficient, (*c*) pressure recovery, and (*d*) drag coefficient. Uncertainties are the same as Fig. 1.

smooth cylinder up to the Reynolds number of 3.9×10^4. However, as the Reynolds number increases, the minimum pressure coefficient increases for wire-wrapped cylinders with $d/D = 0.01$ and 0.02 and decreases when $d/D = 0.032$.

The pressure recovery of wire-wrapped cylinders show an increase for Reynolds number higher than 3.9×10^4 with the highest pressure recovery for the cylinder with $d/D = 0.032$. The increase in the pressure recovery corresponds to the decrease in the drag coefficient. The drag coefficients of wire-wrapped cylinders are initially higher than the corresponding value for the smooth cylinder. However, as the Reynolds number increases, the drag coefficients begin to decrease and the Reynolds number where the drag coefficient starts to decrease is decreased with increasing wire diameter. At the highest Reynolds number, the drag coefficients of all wire-wrapped cylinders are slightly less than the corresponding value for the smooth cylinder.

References

Achenbach, E., 1968, "Distribution of Local Pressure and Skin Friction Around a Circular Cylinder in Cross-flow up to $Re = 5 \times 10^6$," *Journal of Fluid Mechanics*, Vol. 34, p. 625.

Achenbach, E., 1971, "Influence of Surface Roughness on the Cross-flow Around a Circular Cylinder," *Journal of Fluid Mechanics*, Vol. 46, p. 321.

Achenbach, E., and Heinecke, E., 1981, "On Vortex Shedding from Smooth and Rough Cylinders in the Range of Reynolds Numbers 6×10^3 to 5×10^6, *Journal of Fluid Mechanics*, Vol. 109, p. 239.

Allen, H. J., and Vincenti, W. G., "Wall Interference in a Two-Dimensional Flow Wind Tunnel With Consideration of the Effect of Compressibility," *Journal of Fluid Mechanics*, Vol. 37, p. 577.

Farell, C., and Blessman, J., 1983, "On Critical Flow Around Smooth Circular Cylinder," *Journal of Fluid Mechanics*, Vol. 136, p. 375.

Farell, C., Carrasquel, S., Guven, O., and Patel, V. C., 1977, "Effect of Tunnel Walls on the Flow Past Circular Cylinders and Cooling Tower Models," ASME JOURNAL OF FLUIDS ENGINEERING, Vol. 99, p. 470.

Goldstein, S., ed., 1965, "Modern Developments in Fluid Dynamics, Dover Publications Inc.

Guven, O., Farell, C., and Patel, V. C., 1980, "Surface-Roughness Effects on the Flow Past Circular Cylinders," *Journal of Fluid Mechanics*, Vol. 98, p. 673.

Hsueh, L., Rahai, H. R., and LaRue, J. C., 1991, "Turbulent Wakes of Wire-wrapped Cylinders," *ASME Forum on Turbulent Flows*, FED-Vol. 112, pp. 95–100.

Ko, N. W. M., Leung, Y. C., and Chen, J. J. J., 1987, "Flow Past V-groove Circular Cylinders," *AIAA Journal*, Vol. 25, p. 806.

Nassif, M. Y., Tom, S., Rahi, H. R., and Nakayama, A., 1989 "Flow Over Wire-Wrapped Cylinders at Low Reynolds Number," *Bulletin of the American Physical Society*, Vol. 34, No. 10, Nov. Also Mechanical Engineering Report No. MEFT-89-3.

Walsh, M. J., and Weinstein, L. M., 1979, "Drag and Heat-transfer Characteristics of Small Longitudinally Ribbed Surface," *AIAA Journal*, Vol. 17, p. 770.

Walsh, M. J., 1980, "Drag Characteristics of V-groove and Transverse Curvature Riblets," *AIAA Progress in Astronautics and Aeronautics*, Vol. 72, p. 168.

Zukauskas, A., and Ziugzda, J., 1985, *Heat Transfer of a Circular Cylinder in Cross Flow*, Hemisphere Publishing Co.

A Note on Irrotational Curvilinear Flow Past a Weir

Amruthur S. Ramamurthy,[1] Ngoc-Diep Vo,[2] and R. Balachandar[3]

Curvilinear flows are commonly encountered in hydraulic engineering practice. Detailed velocity surveys of the curvilinear

[1]Prof. of Engineering, Concordia University, 1455 de Maisonneuve West, Montreal, Quebec, Canada, H3G 1M8.

[2]Research Assistant, Concordia University, Montreal, Quebec, Canada H3G 1M8.

[3]Research Scientist, Atomic Energy of Canada, Manitoba, Canada.

Contributed by the Fluids Engineering Division of THE AMERICAN SOCIETY OF MECHANICAL ENGINEERS. Manuscript received by the Fluids Engineering Division, September 15, 1992; revised manuscript received May 24, 1993. Associate Technical Editor: Ho, Chih-Ming.

flow field over a circular-crested two dimensional weir were obtained using laser doppler velocimetry (LDV). Using these test data, the basic assumptions related to the streamline geometry and irrotational of flow over weirs made in all existing theoretical weir models are verified. The test data yielded the pattern, slope and curvature of the streamlines. Water surface profiles were also obtained to determine the depth of flow over the crest and the radius of curvature of the surface streamline at the crest section. As part of the study, the velocity profile of the flow over the weir crest was integrated to obtain the weir discharge coefficient. The weir coefficient obtained on the basis of this empirical procedure is compared with the weir coefficient based on direct discharge measurement.

Nomenclature

A^* = area, velocity profile
C_d = coefficient of discharge
g = acceleration due to gravity
h = piezometric head, flow depth above crest level
H_1 = upstream total head measured above the crest level, at section (1)
H_δ = total head at edge of the boundary layer, at section (2)
H_s = total head at the free surface, at section (2)
p = weir height
P = pressure
q = discharge per unit width
r = radial distance, radius of curvature
R = radius of crest circular weir
u = horizontal velocity component
U = reference velocity ($U=\sqrt{2gH_1}$)
v = vertical velocity component ($v=u\tan\phi$)
V = tangential velocity, resultant velocity
x = x-direction; horizontal distance
y = y-direction, vertical distance, depth from bed
$\mathbf{y}$ = $\mathbf{y}=f(x)$, streamline
Y = total flow depth
z = elevation measured above channel bed
β = downstream slope angle
δ = boundary layer thickness
γ = specific weight of water
α = upstream slope angle
ϕ = inclination angle to horizontal, of streamline

Subscripts

1 = approach section 1, index
2 = downstream section 2, index
cr = at weir crest
Dir = direct discharge measurement
s = free surface
y = at depth y
Vel = velocity
δ = at edge of the boundary layer ($y=\delta$)

Introduction

Weirs are used for measurement of discharge and regulation of flow. Existing theoretical weir models assume the curvilinear weir flow to be irrotational. The simplest form of a circular-crested weir consists of a crest of radius R set tangentially to an upstream face and perpendicular to the direction of flow (Fig. 1). Denoting H_1 as the total head of the approach flow measured above the weir crest, the discharge coefficient C_d (Bos, 1978) and the flow per unit length of the weir crest q can be related by Eq. (1):

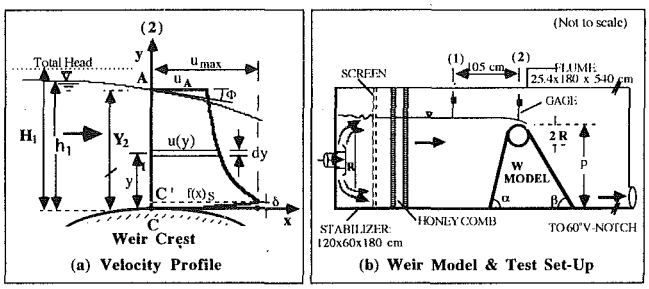

Fig. 1 Curvilinear flow past a weir

$$q = C_d \frac{2}{3}\sqrt{\frac{2}{3}\,g\,H_1^{1.5}} \tag{1}$$

Here, g = the acceleration due to gravity. Escande and Sananes (1959), Jaeger (1956), and Sananes (1957) studied circular-crested weirs to relate the minimum pressure on the weir surface $(P/\gamma)_{min}$ with the total head H_1, the crest flow depth Y_2, the crest radius R and a parameter m (Eq. (2)) which relates the radius of curvature r of the streamline with R. Thus, at point A in Fig. 1(a),

$$r = R + mY_2 \tag{2}$$

Bos (1978) has compiled and analyzed existing data to present a unified relationship between C_d and H_1/R for circular-crested weirs for which the downstream slope $\beta = 45$ deg (Fig. 1b). For flow over circular-crested weirs ($H_1/R \le 1.0$), Matthew (1963) outlined a simple theory which clearly explains the influence of surface tension, viscosity and radius of curvature r of the streamline on C_d. Using different forms of pitot tubes, Rajaratnam and Muralidhar (1971) presented detailed static pressure and velocity distributions for the curvilinear flow over a sharp-crested weir. A rational procedure to pass the maximum flood flow with a specified minimum crest pressure for standard spillways was proposed by Cassidy (1970). In the present study, velocity and pressure data were taken to verify the traditional theoretical assumptions related to the various characteristics of irrotational curvilinear flow over the weir crest. Further, an empirical approach is used to determine C_d by integrating the measured nondimensional velocity profiles in the region above the weir crest.

Basic Relations

The following assumptions are made in the development of the flow model: (1) The flow upstream of the weir is steady, two-dimensional and sub-critical; (2) Compared to the total head H_1 measured above the weir crest, the height p of the weir is large ($p/H_1 > 3$); (3) Frictional losses along the boundaries of the approach channel and along the weir surface are negligible; (4) The crest boundary layer thickness δ (Fig. 1(a)) is extremely small ($\delta/H_1 \ll 1$); (5) At the crest, in the region above the boundary layer ($y \ge \delta$), the curvilinear flow is irrotational and hence the total head is constant.

Determination of Streamline Curvature Parameter. For flow over the weir, defining the coordinate axes through the crest C (Fig. 1(a)), the functional representation of the streamlines for the flow over the crest can be written as,

$$y = f(x) \tag{3}$$

For any single streamline passing through a location y above the crest, knowing the form of $f(x)$, its radius of curvature r and inclination ϕ can be found. Thus,

$$\tan\phi = f'(x) \tag{4}$$

$$r = \frac{[1+(f'(x))^2]^{3/2}}{f''(x)} \tag{5}$$

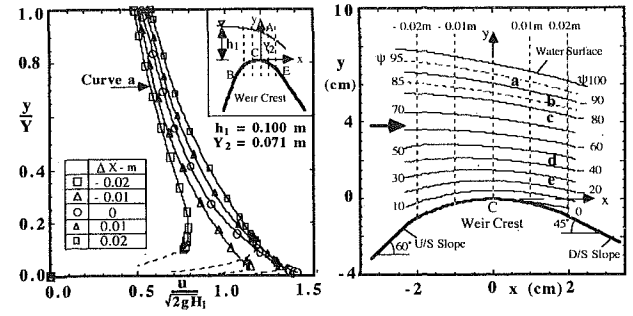

Fig. 2 (*a*) Velocity profiles of flow over weir crest; (*b*) water surface and streamlines over weir crest

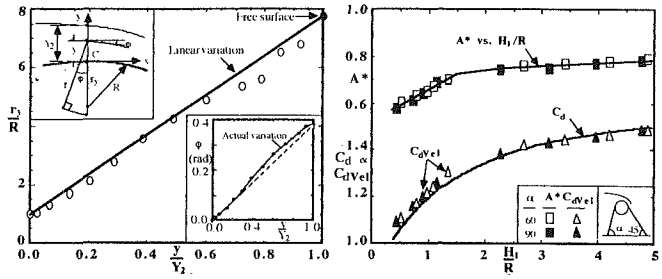

Fig. 3 (*a*) Variation of streamline radius r along flow depth Y_2. Insert: variation of streamline inclination ϕ along flow depth Y_2. (*b*) Variation of A^* and C_d with H_1/R.

$$r_y = \frac{r}{\cos\phi} \tag{6}$$

where, $f'(x)$ and $f''(x)$ denote the first and second derivatives of $f(x)$, respectively. At the free surface, it is easy to determine r directly from the depth profile. To obtain r at the interior points, one needs to known $f(x)$. For two-dimensional flow, $\psi_2 - \psi_1 = \int u dy$ denotes the discharge passing between the streamlines with stream function values ψ_2 and ψ_1. Hence, determining the velocity distribution (Fig. 2(*a*)) accurately at a few vertical sections in the vicinity of the crest, one can determine $f(x)$ (Fig. 2(*b*)). Subsequently, r and r_y (insert, Fig. 3(*a*), can be determined easily.

The assumptions related to the irrotationality of flow and the linear variation of r_y from the weir crest to the free-surface is central to the existing theoretical analysis of curvilinear flow over weirs (Jaeger 1956; Sananes 1957; Escande and Sananes 1959; Matthew 1963; Sarginson 1972). In the present study, detailed velocity distribution data was obtained experimentally for flow over the weir crest to determine the streamline pattern and verify the basic assumptions related to weir flow.

Determination of the Weir Discharge Coefficient C_d. Traditionally, C_d is evaluated from direct measurement of the total discharge and of the upstream total head (Eq. (1)). The velocity profile data over the weir crest C provides an alternate way of determining C_d using Eq. (7) (Fig. 1). Thus,

$$\int_0^{Y_2} u\, dy = q = C_d \frac{2}{3}\sqrt{\frac{2}{3}}\, g H_1^{1.5} \tag{7}$$

where, u is the horizontal velocity component measured at a depth y above the crest (Fig. 1). Using the parameters $U = \sqrt{2gH_1}$ and Y_2 to normalize u and y, Eq. (7) can be reduced to the following form:

$$\frac{q}{Y_2 U} = \int_0^1 \frac{u}{U}\, d\left(\frac{y}{Y_2}\right) \tag{8}$$

The above integral represents the area A^* of the dimensionless velocity profile. Hence,

$$\frac{q}{Y_2 U} = A^* \tag{9}$$

$$C_{d\text{Vel}} = \frac{3\sqrt{3}}{2}\left(\frac{Y_2}{H_1}\right) A^* \tag{10}$$

To verify the above empirical model, test data related to two different weirs were obtained.

Experimental Setup and Procedure

Machined plexiglas weir models were set in a stainless steel flume (Fig. 1). The test section was 25.4 cm wide, 180 cm high and 250 cm long. The side walls were equipped with transparent plexiglas windows to aid flow visualization. Sufficient stilling arrangements were provided to obtain a smooth flow without large scale turbulence. On the weir face, pressure taps were spaced at every 5 cm along the center line. On the weir crest, pressure taps were spaced at 5 degree intervals. The pressure head was measured on a manometer to the nearest 0.5 mm. All flow depths were measured to the nearest 0.3 mm.

A Laser Doppler Velocimeter (LDV) was used to survey the horizontal velocity distribution in the curvilinear flow field above the weir crest. The uncertainty in the velocity measurement was typically 0.5 percent and in the maximum velocity, it was much less than 1 percent. The maximum error in the discharge rate measured by a standard 60° V-notch was 3 percent. Horizontal velocity distributions along vertical sections were obtained on the crest C (Fig. 1) at span-wise locations 12.5 cm, 8.0 cm, 1.5 cm, and 0.5 cm from the sidewall for a fixed depth Y_2, to confirm the two-dimensionality of the flow.

Discussion of Results

Profiles of the horizontal velocity component u were recorded at the crest section C (Fig. 1*a*), covering the range $0.5 \le H_1/R \le 5.0$ for weir models with an upstream slope of $\alpha = 90$ and 60 deg and a downstream slope $\beta = 45°$.

Geometrical Characteristics of Streamlines. The insert of Fig. 2(*a*) shows the five vertical locations where the velocity profiles (Fig. 2*a*) were obtained at $H_1 = 0.100$m. In Fig. 2(*a*), the total area of the velocity distribution curve a denotes the dimensionless discharge q/Y_2U (Eq. (8)) passing through $x = -0.02$m. The actual discharges computed for the five selected sections agreed among themselves to within 2 percent.

Based on Fig. 2(*a*), the streamline pattern $y = f(x)$ was generated and plotted (Fig. 2(*b*)) to get r, r_y, and ϕ (insert, Fig. 3*a*) at the weir crest using Eqs. (4), (5), and (6). In Fig. 2(*b*), the free surface corresponds to $\psi = 100$. Fig. 3(*a*) indicates that the streamline radius parameter r_y does not vary linearly with depth in a section close to the free-surface ($0.6Y_2 \le y \le Y_2$).

Streamline Inclination ϕ. Insert of Fig. 3(*a*) shows that the streamline inclination ϕ deviates slightly from the linear variation along the depth at the crest section C. A maximum deviation of the order of 10 percent in the ϕ value occurs near the mid-depth of the flow over the crest. Since ϕ has generally a low value (0.2-0.3 rad), the corresponding variation of cos ϕ in Eq. (6) for the range of maximum deviation is of the order of 1 percent. Hence, Matthew's assumption (1963) of linear variation of ϕ between the value at the bed and that at the free surface will not lead to erroneous results.

Weir Discharge Coefficient $C_{d\text{Vel}}$. Equation (10) was used to determine the weir discharge coefficient $C_{d\text{Vel}}$ (Fig. 3(*b*)) using the areas of the velocity profiles for the two model weirs. Figure 3(*b*) also shows the variation of A^* and Y_2/H_1 with H_1/R.

Irrotationality of the Flow. The flow over the weir crest is treated as irrotational in the theoretical models. To indirectly

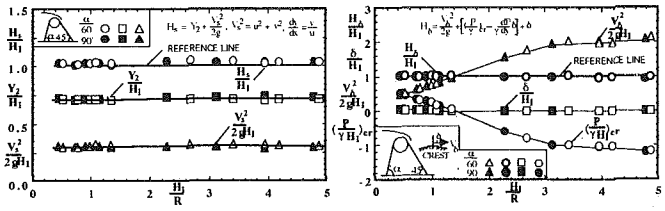

Fig. 4 Characteristics of weirs with *D/S* slope $\beta = 45$ deg ($0.5 \le H_1/R \le 5.0$). (*a*) Variation of Y_2/H_1, $V_s^2/2gH_1$, and H_s/H_1 with H_1/R; (*b*) variation of δ/H_1, $V\delta^2/2gH_1$, $(P/\gamma H_1)_{cr}$ and $H\delta/H_1$ with H_1/R.

verify the validity of this assumption, the velocity profile data was analyzed. For accelerating flow over the crest, the boundary layer is thin ($\delta \ll Y_2$). As such, while computing the total head H_δ at the edge of the boundary layer C' (Fig. 1), one can assume that the pressure at the edge of the boundary layer $(P/\gamma)_\delta \approx$ the crest pressure $(P/\gamma)_{cr}$. The total head at the edge of the boundary layer H_δ can be expressed as follows:

$$H_\delta = \frac{V_\delta^2}{2g} + \left[\left(\frac{P}{\gamma}\right)_{cr} - \frac{dP}{\gamma dy}\delta\right] + \delta \approx \frac{V_\delta^2}{2g} + \left(\frac{P}{\gamma}\right)_{cr} \qquad (11)$$

At the location A (Fig. 1*a*) of the free surface, the resultant velocity head at A is $V_s^2/2g = (u^2 + v^2)/2g = u^2\,(1 + \tan^2\phi)/2g$. Here, v denotes the vertical component of the velocity. Hence, with the crest C as the datum, the total head H_s at the free surface can be expressed as follows:

$$H_s = \frac{V_s^2}{2g} + Y_2 \qquad (12)$$

When the flow is irrotational in the region (excluding the boundary layer) between (1) and (2) of Fig. 1(*b*), the total head is conserved. Thus, $H_s/H_1 = H_\delta/H_1$. Figures 4(*a*) and 4(*b*) show that these ratios are in fact close to unity and hence indirectly confirm the irrotationality of the flow (assumption 5). For complete validation of irrotationality of the two dimensional flow in the region AC' (Fig. 1(*a*)), one can independently obtain accurate static pressure and velocity distributions at many locations above the crest, compute the local total head and compare them with the total heads at the free-surface and at C'. Alternatively, one can use the experimentally determined velocity component data and show that the net vorticity is zero at different locations along AC' (Fig. 1(*a*)), (Vo, 1992).

Conclusions

In existing theoretical models, the slope and curvature of the streamlines for flow over the weir are assumed to vary linearly from the weir crest to the free-surface. The present results indicate that the linearity assumption is quite valid over a wide range of depths, except in a narrow segment below the free-surface. The region of crest flow above the boundary layer is verified to be irrotational. This provides a verification of the basic assumptions related to the development of existing theoretical weir models. The value of C_{dVel} determined on the basis of the empirical procedure agrees very well with the previous results related to C_d obtained from direct discharge measurement. The alternate method suggested to determine the discharge coefficient of circular-crested weirs can be adopted for the case of other weir types. Lastly, the ability to measure the velocity field precisely in curvilinear flows enables one to indirectly estimate the precise pressure distributions in regions where the flow field is irrotational.

References

Bos, M. G., 1978, "Discharge Measurement Structures," Publ. 20, Institute of Land Recalamation and Irrigation, Wageningen, The Netherlands.

Cassidy, J. J., 1970, "Designing Spillway Crests for High Head Operation," *J. Hyd. Div.*, ASCE, Vol. 96, No. 3, pp. 745–753.

Escande, L., and Sananes, F., 1959, "Étude des seuils déversants à fente aspiratrice" (Weirs with Suction Slots). *La Houille Blanche*, Vol. 14, No. Spl B, pp. 892–902.

Jaeger, C., 1956, "Engineering Fluid Mechanics." Blackie & Son Limited, London, Glasgow, pp. 133–138.

Matthew, G. D., 1963, "On the Influence of Curvature, Surface Tension and Viscosity on Flow Over Round-Crested Weirs," *Proceedings of the Inst. of CE*, ASCE, Vol. 25, pp. 511–524.

Rajaratnam, N., and Muralidhar, D., 1971, "Pressure and Velocity Distribution for Sharp Crested Weirs," Journal of Hydraulic Research, Vol. 9, No. 2, pp. 241–247.

Sananes, M. F., 1957, "Ètude des seuils déversants à fente aspiratrice," IAHR, 7th Gen. Meet. Tran., Lisbon, Vol. II, pp. D24.1-D24.23.

Sarginson, E. J., 1972, "The Influence of Surface Tension on Weir Flow," *Journal of Hydraulic Research*, Vol. 10, pp. 431–446.

Vo, N. D., 1992, "Characteristics of Curvilinear Flow Past Circular-Crested Weirs," Thesis, presented at Concordia University, Montreal, Apr. 1992, in partial fulfillment of the requirements for the degree of Doctor of Philosophy.